

# 1991 International Aerospace and Ground Conference on Lightning and Static Electricity

(NASA-CR-3106-901-2) THE 1991 INTERNATIONAL  
AEROSPACE AND GROUND CONFERENCE ON LIGHTNING  
AND STATIC ELECTRICITY, VOLUME 2 (NASA)  
437 2

CSCL 043

NP1-37893

--THRU--

NP1-32737

Unclass

H1/47 0039644

*Proceedings of a conference held at  
Cocoa Beach, Florida  
April 16-19, 1991*

**NASA**

*NASA Conference Publication 3106, Vol. II*

# **1991 International Aerospace and Ground Conference on Lightning and Static Electricity**

*John F. Kennedy Space Center  
Kennedy Space Center, Florida*

Proceedings of a conference sponsored  
by the National Aeronautics and Space  
Administration, the National Interagency  
Coordination Group (NICG), and Florida  
Institute of Technology and held at  
Cocoa Beach, Florida  
April 16-19, 1991



National Aeronautics and  
Space Administration  
Office of Management  
Scientific and Technical  
Information Program

**1991**





## **NICG**

### **COMMITTEE CHAIRPERSONS**

<b>Chairman</b>	W. Jafferis NASA, KSC, Florida (407) 867-3185 or 3529 (407) 867-4079 (FAX)
<b>NICG Secretary</b>	M. Glynn FAA Technical Center (609) 484-4134
<b>Financial Coordinator</b>	Dr. A. Revay Florida Institute of Technology (407) 768-8020
<b>Conference Coordinator</b>	Eric Smith NASA, KSC, Florida (407) 867-3185
<b>European Coordinator</b>	J. L. Boulay ONERA, France

### **NICG STEERING COMMITTEE**

F. Pitts	NASA Langley Research Center
V. Mazur	U. S. Department of Commerce
D. Albright	U. S. Army Aviation Systems Command
L. Runke	Naval Research Laboratory
W. Walker	Naval Air Development Center
L. Walko	Wright Research and Development Center
M. Whittaker	Naval Air Test Center
B. Burrows	Culham Laboratory, England



## LAUNCHING INTO SPACE

The National Interagency Coordination Group (NICG) extends you a cordial invitation to attend the 1991 International Aerospace and Ground Conference on Lightning and Static Electricity.

Kennedy Space Center and Cape Canaveral Air Force Station are frequently called America's Spaceport. This title is earned through the integration of many skills in a wide variety of technical fields and successful implementation throughout labor and management levels that enables America to reach into space. Among the many challenges confronting the country's primary launch site are lightning protection, detection, and forecasting. This conference focuses on studies that attempt to solve these problems by presenting papers on active research on many appropriate topics.

The technical program for this year's conference consists of 119 papers and posters presented by investigators from fifteen countries making this a truly international effort. The conference is divided into twenty-six sessions based on research in lightning, static electricity, modeling, and mapping. These sessions span the spectrum from basic science to engineering, concentrating on lightning prediction and detection and on safety for ground facilities, aircraft, and aerospace vehicles. There is something for everyone, whether student or veteran to the field. I invite you to come to the conference and participate with us, sharing what you have learned and your concerns.

William Jafferis  
Conference Chairman

# TABLE OF CONTENTS

## Volume I of II

### SESSION I

Lightning Threat to Aircraft: Do We Know All We Need To Know? . . . . .	1-1
<i>V. Mazur</i>	

### SESSION 2A

Description and Interpretation of Aircraft Lightning Attachment Electric and Magnetic Fields Measurements and Video Observation . . . . .	2-1
<i>J. Moreau and S. Larigaldie</i>	
Intracloud Development of Lightning Strikes to Aircraft . . . . .	3-1
<i>V. Mazur</i>	
Current Waveform Observed During Lightning Strikes on Aircraft . . . . .	4-1
<i>J. Boulay</i>	

### SESSION 2B

Lightning Current Rate of Rise in the New Lightning Flash Model for the Space Shuttle Program . . . . .	5-1
<i>N. Bankston</i>	
Modeling of Electrically Thick Materials. Theoretical and Experimental Aspects . . . . .	6-1
<i>V. Gobin, F. Issac, and F. Jaillot</i>	
Sparking Characteristics of Carbon Fiber Composite Fastened Joints With Various Waveforms . . . . .	7-1
<i>D. Heidlebaugh and J. Carter</i>	
Investigations Into the Damage for Various Types of Unprotected Carbon Fibre Composites With a Variety of Lightning Type Arc Attachments . . .	8-1
<i>G. Reid</i>	



## TABLE OF CONTENTS (cont)

### SESSION 3A

Characteristics of Winter Lightning Currents Struck an Isolated Tower . <i>Y. Goto, K. Narita, and H. Komuro</i>	9-1
Thunderstorm Detection and Warning System Atmospheric Potential Monitor ..... <i>R. Markson and R. Wojtasinski</i>	10-1
Electrical Emissions of Airplanes Flying in Electrified Clouds and Their Effect on Airplane Measurements of Cloud Electric Fields ..... <i>J. Jones</i>	11-1
E and dE/dT Waveshapes for Narrow Bipolar Pulses in Intracloud Lightning ..... <i>P. Medelius</i>	12-1

### SESSION 3B

The Performance of Cable Braids and Terminations to Lightning Induced Transients ..... <i>D. Crofts</i>	13-1
Lightning Protection of the Fokker 100 CFRP Rudder ..... <i>A. Ruiter</i>	14-1
Protection of Electrical and Electronic Equipment Against Lightning Indirect Effects on the Airbus A340 Wing ..... <i>O. Spiller</i>	15-1
First and Subsequent Return Stroke Properties of Cloud-to-Ground Lightning ..... <i>S. Namasivayam and S. Lundquist</i>	16-1

## TABLE OF CONTENTS (cont)

### SESSION 4A

Characteristics of Return Stroke Electric Fields Produced by Lightning Flashes at Distances of 1 to 15 Kilometers .....	17-1
<i>Ch. Hopf</i>	
Electromagnetic Radiation Field of Multiple Return Stroke Lightning .....	18-1
<i>S. Gupta</i>	
Airborne Observations of Electric Fields Around Growing and Decaying Cumulus Clouds .....	19-1
<i>K. Giori and J. Nanevich</i>	

### SESSION 4B

Lightning Location System Supervising Swedish Power Transmission Network .....	20-1
<i>S. Melin</i>	
Range Estimation Techniques in Single-Station Thunderstorm Warning Sensors Based Upon Gated, Wideband, Magnetic Direction Finder Technology .....	21-1
<i>A. Pifer, W. Hiscox, K. Cummins, and W. Neumann</i>	
Thunderstorm Monitoring and Lightning Warning, Operational Applications of the SAFIR System .....	22-1
<i>P. Richard</i>	
VHF Discharge in Storm Cells Producing Microbursts .....	22A-1
<i>P. Laroche, C. Malherbe, A. Bondiou, M. Weber, C. Engholm, and V. Coel</i>	

### SESSION 5A

The QT Interval in Lightning Injury With Implications for the "Cessation of Metabolism" Hypothesis .....	23-1
<i>C. Andrews, M. Darveniza, and D. Colquhoun</i>	



## TABLE OF CONTENTS (cont)

Further Identification and Treatment Modalities in Telephone Mediated Lightning Strike .....	24-1
<i>C. Andrews and M. Darveniza</i>	
Step Voltage Analysis for the Catenoid Lightning Protection System ....	25-1
<i>J. Chai, D. Barker, R. Briet, and H. Eley</i>	
Hardening Communication Ports for Survival in Electrical Overstress Environments .....	26-1
<i>O. Clark</i>	

### SESSION 5B

P-Static Interference to Aircraft RF Receivers .....	27-1
<i>W. Devereux</i>	
Evaluation of the Observability of Electrostatically Charged Rotocraft ...	28-1
<i>P. McKenna, R. Dalke, R. Perala, and D. Steffen</i>	
Charge Control Experiments on a CH-53E Helicopter in a Dusty Environment .....	29-1
<i>C. Moore, J. Jones, and S. Hunyady</i>	
Results of Recent Precipitation Static Flight Test Program on the Navy P-3B Antisubmarine Aircraft .....	30-1
<i>M. Whitaker</i>	

### SESSION 6A

Launch Pad Lightning Protection Effectiveness .....	31-1
<i>J. Stahmann</i>	
Activation of the Navy's Indirect Effects Lightning Simulation Laboratory .....	32-1
<i>M. Whitaker</i>	
Characteristics of Vertical Electrical Fields and Associated Voltages Induced on an Overhead Power Line From Close Artificially Initiated Lightning .....	33-1
<i>M. Rubinstein</i>	

## TABLE OF CONTENTS (cont)

Lightning Protection for Shuttle Propulsion Elements .....	34-1
<i>C. Goodloe and R. Giudici</i>	

### SESSION 6B

Photographic Spark Detection Sensitivity With Various Film Types and Utilizing Multiple Spark Sources .....	35-1
<i>D. Dodrill and D. Heidlebaugh</i>	
Lightning Transient Monitoring on the Titan IV .....	36-1
<i>D. Downs</i>	
Influence of Configuration Effects on "Multiple Burst" Simulation Testing .....	37-1
<i>J. Emanuely and M. Cantaloube</i>	
Evaluation of the Damage Caused by Lightning Current Flowing Through Bearings .....	38-1
<i>E. Garbagnati, O. Celi, and A. Pigni</i>	

### SESSION 7A

A Transportable 50 KA Dual Mode Lightning Simulator .....	39-1
<i>K. Salisbury, S. Lloyd, and Y. Chen</i>	
Mathematical Models for Determining the Protected Spaces of the Vertical Lightning Rod .....	40-1
<i>I. Mladenovic and A. Vorgucic</i>	
Designs for Surge Immunity in Critical Electronic Facilities .....	41-1
<i>E. Roberts</i>	
The Sandia Transportable Triggered Lightning Instrumentation Facility .....	42-1
<i>G. Schnetzer and R. Fisher</i>	



## TABLE OF CONTENTS (cont)

### SESSION 7B

FD-TD Calculation With Composite Materials. Application to C160 Aircraft Measurements .....	43-1
<i>J. Alliot, J. Grando, F. Issac, and X. Ferrieres</i>	
Time Dependant Behavior of a Carbon Composite Case to Simulated Lightning .....	44-1
<i>M. Taylor</i>	
The Electromagnetic Environment in CFC Structures .....	45-1
<i>C. Hardwick and S. Haigh</i>	
A New Approach to Equipment Testing .....	46-1
<i>C. Hardwick, V. Dunkley, B. Burrows, and I. Darney</i>	

### SESSION 8A

Damage to Metallic Samples Produced by Measured Lightning Currents .	47-1
<i>R. Fisher and G. Schnetzer</i>	
An Assessment of Tailoring of Lightning Protection Design Requirements for a Composite Wing Structure on a Metallic Aircraft .....	48-1
<i>T. Hardwood</i>	
Lightning Protection Design and Testing of an All Composite Wet Wing for the Egrett .....	49-1
<i>B. Burrows, S. Haigh, C. Chessum, and V. Dunkley</i>	

### SESSION 8B

Lightning Protection of Full Authority Digital Electronic Systems .....	50-1
<i>D. Crofts</i>	
Simulation and Measurement of Melting Effects on Metal Sheets Caused by Direct Lightning Strikes .....	51-1
<i>A. Kern</i>	

## TABLE OF CONTENTS (cont)

Application of Designed Experiments Statistical Approach to Lightning Testing of Carbon Fiber Composites .....	52-1
<i>J. Ward and A. Booker</i>	

### SESSION 9A

A Survey of Laser Lightning Rod Techniques .....	53-1
<i>A. Barnes</i>	
Predicting Cloud-to-Ground Lightning With Neural Networks .....	54-1
<i>A. Barnes, D. Frankel, and J. Draper</i>	
The Electric Field Change Caused By a Ground Flash With Multiple Channels .....	55-1
<i>Z. Kawasaki</i>	

### SESSION 9B

FD-TD Numerical Simulation of an Entire Lightning Strike on the C160 Aircraft .....	56-1
<i>J. Alliot, J. Grando, J. Muller, and X. Ferrieres</i>	
Observations of Bidirectional Leader Development in Triggered Lightning Flash .....	57-1
<i>P. Laroche, V. Idone, A. Eybert-Beard, and L. Barret</i>	
Application of Surface Electrical Discharges to the Study of Lightning Strikes on Aircraft .....	58-1
<i>J. Boulay and S. Larigaldie</i>	
The Scale-Model Charge-Transfer Technique for Measuring Enhancement Factors .....	59-1
<i>J. Kositsky and J. Nanevich</i>	

## TABLE OF CONTENTS (cont)

### SESSION 10A

The Electric Field Changes and UHF Radiations Caused By the Triggered Lightning in Japan .....	60-1
<i>Z. Kawasaki, T. Kanao, K. Matsuura, M. Nakano, K. Horii, and K. Nakamura</i>	
The Detection of the Electric Field Vertical Distribution Underneath Thundercloud: Principle and Applications .....	61-1
<i>S. Soula and S. Chauzy</i>	
Discussions on a Long Gap Discharge to a Transmission Tower by a Rocket Triggered Lightning Experiment .....	62-1
<i>K. Nakamura, A. Wade, and K. Horii</i>	
Correlation Between Some Current Parameters and Optical Radiation Generated by 280 mm Long Laboratory Sparks .....	63-1
<i>D. Windmar, V. Cooray, and V. Scuka</i>	

### SESSION 10B

Modeling Structural Joint Lightning Currents for Direct Effects Evaluation .....	64-1
<i>J. Carter and J. Sutton</i>	
The Effects of the Exhaust Plume on the Lightning Triggering Conditions for Launch Vehicles .....	65-1
<i>F. Eriksen, T. Rudolph, and R. Perala</i>	
Power and Energy Dissipation in Subsequent Return Strokes as Predicted by a New Return Stroke Model .....	66-1
<i>V. Cooray</i>	
Horizontal Fields Generated by Return Strokes .....	67-1
<i>V. Cooray</i>	

## TABLE OF CONTENTS (cont)

### Volume II of II

#### SESSION 11A

Lightning Induced Currents in Aircraft Wiring Using Low Level Injection Techniques .....	68-1
<i>E. Stevens and D. Jordan</i>	
Observations of Lightning Processes Using VHF Radio Interferometry .....	68A-1
<i>X. Shao, C. Rhodes, P. Krehbiel, and R. Thomas</i>	
The Physics of the Oscillating Lightning .....	69-1
<i>P. Storebo</i>	
A System for Mapping Sources of VHF and Electric Field Pulses From In-Cloud Lightning at KSC .....	70-1
<i>E. Thomson and P. Medelius</i>	
A New Approach to the Determination of the Striking Distance From the Lightning Channel Photos .....	71-1
<i>A. Vorgucic and I. Mladenovic</i>	

#### SESSION 11B

Electromagnetic Topology: Characterization of Internal Electromagnetic Coupling .....	72-1
<i>J. Parmantier, J. Aparicio, and F. Faure</i>	
A Real Scale Simulator for High Frequency Lemp .....	73-1
<i>D. Gauthier and D. Serafin</i>	
A Theoretical Analysis of the Electromagnetic Environment of the AS330 Super Puma Helicopter External and Internal Coupling .....	74-1
<i>M. Gauthier, D. Serafin, F. Flourens, and T. Morel</i>	



## TABLE OF CONTENTS (cont)

### SESSION 12A

Three-Dimensional Time Domain Model of Lightning, Including Corona Effects . . . . .	75-1
<i>A. Podgorski</i>	
Surface Wind Convergence as a Short-Term Predictor of Cloud-to-Ground Lightning at Kennedy Space Center: A Four Year Summary and Evaluation . . . . .	76-1
<i>A. Watson, R. Holle, R. Lopez, and J. Nicholson</i>	
Assessment and Forecasting of Lightning Potential and its Effect on Launch Operations at Cape Canaveral Air Force Station and John F. Kennedy Space Center . . . . .	77-1
<i>N. Wyse, T. Graziano, M. Secrist, J. Weems, and C. Pinder</i>	

### SESSION 12B

Basic Studies on Sparks in Composite Carbone Fuel Tanks . . . . .	78-1
<i>P. Gondot, J. Avenet, S. Larigaldie, G. Hartmann, R. Haug, O. Farish, and M. Aked</i>	
Protection of Graphite Composite Fuel Tanks From Lightning Strike Damage and Fuel Vapor Ignition . . . . .	79-1
<i>R. Schmidt</i>	
Measurements of Some Parameters of Thermal Sparks With Respect to Their Ability To Ignite Aviation Fuel/Air Mixtures . . . . .	80-1
<i>S. Haigh, C. Hardwick, and R. Baldwin</i>	

### SESSION 13A

The Effect of the Earth's Oblate Spheroid Shape on the Accuracy of a Time-of-Arrival Lightning Ground Strike Locating System . . . . .	81-1
<i>R. Bent and P. Casper</i>	
Experience Gained in Operation of the VLF ATD Lightning Location System . . . . .	82-1
<i>A. Lee</i>	

## TABLE OF CONTENTS (cont)

Extension of and Improvements to the ERDC Low Frequency Magnetic Direction Finding System .....	83-1
<i>M. Lees</i>	
An Interactive Method for Obtaining the Optimum Lightning Location on a Spherical Surface .....	84-1
<i>G. Chao and M. Qiming</i>	

### SESSION 13B

Comparison of Lightning Location Data and Polarisation Radar Observations of Clouds .....	85-1
<i>A. Illingworth and M. Lees</i>	
The Spatial Variations of Lightning During Small Florida Thunderstorms	86-1
<i>E. Krider and T. Oram</i>	
Weak Positive Cloud-to-Ground Flashes in Northeastern Colorado .....	87-1
<i>R. Lopez, M. Maier, R. Holle, and J. Garcia-Miguel</i>	
Predicting the Onset and Cessation of Natural Lightning Hazards: Capabilities of Existing Sensor Systems as Illustrated by Two Case Studies .....	88-1
<i>M. Maier and L. Maier</i>	

### SESSION 14A

Lightning Mapping System .....	89-1
<i>C. Lennon and L. Maier</i>	
Lightning Testing at the Subsystem Level .....	90-1
<i>F. Luteran</i>	
Cloud-To-Ground Lightning Surveillance Capabilities at the U.S. Air Force Eastern Space and Missile Center .....	91-1
<i>M. Maier and R. White</i>	

## TABLE OF CONTENTS (cont)

A Continually Recording Method for Lightning Stroke Waveform . . . . .	92-1
<i>X. Lingen, G. Chao, and L. Xinkang</i>	

### SESSION 14B

Implementation of the FAA Research and Development Electromagnetic Database . . . . .	93-1
<i>D. Grush, D. Cook, R. McDowall, and M. Glynn</i>	
The New Section 23 of DO160C/ED14C Lightning Testing of Externally Mounted Electrical Equipment . . . . .	94-1
<i>B. Burrows</i>	
Design of Lightning Protection for a Full-Authority Digital Engine Control . . . . .	95-1
<i>M. Dargi, E. Rupke, and K. Wiles</i>	
Certification of Lightning Protection for a Full-Authority Digital Engine Control . . . . .	96-1
<i>M. Dargi, E. Rupke, and K. Wiles</i>	

### POSTER PAPERS (MEASUREMENTS)

On Error Sources During Airborne Measurements of the Ambient Electric Field . . . . .	97-1
<i>B. Evteev</i>	
Lightning to Upper Atmosphere: A Vertical Light Pulse From the Top of a Thunderstorm As Seen by a Payload Bay TV Camera of the Space Shuttle . . . . .	98-1
<i>O. Vaughan, W. Boeck, R. Blakeslee, B. Vonnegut, M. Brooks, and J. McKune</i>	
A Study of Point Discharge Current Observations in the Thunderstorm Environment at a Tropical Station During the Years 1987 and 1988 . . . .	99-1
<i>G. Manohar, S. Kandalgaonkar, and S. Sholapurkar</i>	

## TABLE OF CONTENTS (cont)

Portable Combined Optical and Electric Field Change Intracloud Lightning Detector .....	100-1
<i>R. Markson</i>	
Errors in Electric Field Measurements Using Instrumented Aircraft ....	101-1
<i>B. Evteev</i>	
Characteristic Features of Small, Average, and Large Ion Concentrations in Different Mobility Ranges, During Thunderstorms at Poona, India ...	102-1
<i>G. Srivastava</i>	
The Feedback Vibrating Capacitor Fieldmeter .....	103-1
<i>J. Vosteen and W. Vosteen</i>	
Optimal Parameters of Leader Development in Lightning .....	104-1
<i>N. Petrov and G. Petrova</i>	

## POSTER PAPERS (METEOROLOGY)

On Charging of Snow Particles in Blizzard .....	105-1
<i>H. Shio</i>	
On the Interactions of Positive Streamers With Hydrometeors .....	106-1
<i>T. Verma</i>	

## POSTER PAPERS (P-STATIC)

Development of a Portable P-Static Simulation Test Set .....	107-1
<i>W. Devereux</i>	

## POSTER PAPERS (AEROSPACE VEHICLES, TEST CRITERIA AND TECHNIQUES)

A Simulated Lightning Effects Test Facility for Testing Live and Inert Missiles and Components .....	108-1
<i>J. Craven, J. Knauer, T. Moore, and T. Shumpert</i>	

## TABLE OF CONTENTS (cont)

### POSTER PAPERS (MODELING)

Electron Distribution Functions in Electric Field Environments* .....	109-1
<i>T. Rudolph</i>	
Charge Transfer During Individual Collisions in Ice Growing by Riming .....	109A-1
<i>E. Avila and G. Caranti</i>	
How to Create Ball Lightning .....	110-1
<i>R. Golka</i>	
Experimental Modeling of Lightning Interaction Phenomena With Free Potential Conducting Objects .....	111-1
<i>C. Chernov, A. Lupeiko, and N. Petrov</i>	

### POSTER PAPERS (GROUND PROTECTION)

Diffuse Dispersive Delay and the Time Convolution/Attenuation of Transients .....	112-1
<i>B. Bittner</i>	
Advances in Lightning Protection That Satisfies Contemporary Standards	113-1
<i>R. Carpenter</i>	
Circuit Protection Devices for Transient Suppression .....	114-1
<i>R. Childers</i>	
Evaluating Lightning Hazards to Building Environments Using Explicit Numerical Solutions of Maxwell's Equations* .....	115-1
<i>R. Collier and P. McKenna</i>	
Voltages Induced on a Power Distribution Line By Overhead Cloud Lightning .....	116-1
<i>Z. Yacoub, M. Rubinstein, M. Uman, E. Thomson, and P. Medelius</i>	
Lightning Protection, Risk and Management Responsibility (Guidelines for a Proposed Lightning Protection Policy of a Golf Association or Tournament Sponsor) .....	117-1
<i>C. Hillyer</i>	

## TABLE OF CONTENTS (cont)

Influence of Channel Base Current and Varying Return Stroke Speed on the Calculated Fields of Three Important Return Stroke Models . . . . .	118-1
<i>R. Thottappillil, G. Diendorfer, and M. Uman</i>	
High Current Pulse Testing for Ground Rod Integrity . . . . .	119-1
<i>L. Walko</i>	

# ATTENDEES LIST

NAME	AFFILIATION	ADDRESS	CITY	STATE	ZIP	COUNTRY	TELEPHONE
Abbond	GE/MD34039	1000 Western Ave.	Lynn	MA	01910	USA	617-594-4365
Adamo	SRI International	333 Ravenswood Ave	Menlo Park	CA	94025	USA	(415) 859-2370
Albright	U.S.A Aviation Sys Com	4300 Goodfellow Bl	St. Louis	Missouri	63120-1798	USA	(314) 263-1634
Alliot	ONERA	8 Rue Vertugadins	Meudon		92190	France	33-1-4534-7501
Andrews	Univ. of Queensland	148 Jesmond Rd.	Indooroopilly	Qld	4068	Australia	61-7-878-2451
Armstrong	Los Alamos National	SST-7, MS D466	Los Alamos	NM	87545	USA	(505) 667-9517
Barkston	Rockwell International	10241 Lakewood Blvd.	Downey	CA	90241	USA	213-922-2456
Barker	The Aerospace Corp	P.O. Box 21205	KSC	FL	32815	USA	(407) 853-6666
Barnes	USAF	FL/GR/LYA	Hanscom AFB	MA	01731-5000	USA	617-377-2939
Baseley	USAF ASD/ENACE	Wright-Patterson AFB	Dayton	OH	45431-6503	USA	513-255-5078
Becker	NASA/KSC	TE-FAC	KSC	FL	32899	USA	407-861-2771
Beens	LRA	Haberweg 8	Braunschweig		D-3300	Germany	0531-23350
Bentti	NASA/KSC	TV-VPD-1	KSC	FL	32899	USA	407-867-4735
Berger	CNRS	ESE Plateau Du Moulon	GIF		91120	France	33-1-69-41-80-40
Bergman	Carl Bergman & Assoc.	12741 159th Lane, SE	Rainier	WA	98576	USA	206-446-7750
Binford	Mission Instruments Co	5937 E. Pima St.	Tucson	AZ	85712-4353	USA	602-795-0949
Bitner	Harris Corp.	2580 Clinton Dr. NE	Palm Bay	FL	32905	USA	407-727-6440
Boeck	Niagara University	DePaul Hall	Niagra Univ.	NY	14109	USA	(205) 544-1538
Bootsma	Boeing Canada/ Havil.	Garratt Blvd	Toronto	Ontario	M3K1Y5	Canada	416 375 4385
Boulay	ONERA	8 Rue des Vertugadins	Meudon		92190	France	33-1-45347501
Brahm	ABB Germany	7 Scheresberg	Birkenau		D-6943	Germany	011-49-6201-31466
Brewer	Instrument Specialties	P.O. Box A	Delwater Gap	PA	18327	USA	717-424-8510x113
Briet	The Aerospace Corp.	P.O. Box 92957, MS M4-934	Oxon	CA	90009	USA	213-336-1912
Burrows	LTT-Culham Laboratory	Abingdon	Denver	CO	80201	England	44-235-464243
Burtzlaiff	Martin Marietta Corp.	PO Box 179	Mannheim		D-6800	USA	303-977-1064
Busse	Bundesakademie fur	Seckenheimer Landstr 8-10	Cambridge	MA	02142	Germany	0621-418091
Canniff	US DOT/VTSC	Kendall Square	Toulouse		31056	USA	617-494-2581
Cantaloube	Centre Essais Aero. de	23 Ave Henri Guillaumet	5000 Cordoba	CO	80303	France	61-58-7320
Caranti	Nat. Univ. of Cordoba	Laprida 854	Boulder		32905	Argentina	5451-40669
Carpenter	Lightning Eliminators	6687 Atapahoe Rd	Palm Bay	FL	32905	USA	303-447-2828
Casper	Atmospheric Research	23 Commerce Park Dr.	Toulouse		31450	USA	(407) 725-8001
Catani	Centre National	18 Avenue Edward Belin	Milano		20134	France	(33) 61 273677
Celi	CESI	Via Rubattino 54	Los Angeles,	CA	90009	Italy	02-2125423
Chai	The Aerospace Corp.	P.O.Box 92957, MS M4-934	San Diego	CA	92123	USA	213-336-8341
Chan	Maxwell Laboratories I	8888 Balboa Ave.	Belmont		94002	USA	(619) 576-7852
Childers	Electromer Corp.	290 Harbor Blvd.	Tempe	CA	85281	USA	(415) 637-1830
Clark	General Semiconductor,	2001 W. Tenth Place	Ft.Lauderdale	FL	33301	USA	(305) 463-3451
Cline	Dayton Granger, Inc.	2605 Castilla Isle	San Rafael	CA	94903	USA	415-499-3900 x3918
Cohen	Panamax	150 Mitchell Blvd.	Lakewood	CO	80228	USA	(303) 980-0070
Collier	Electro Magnetic Appl	12567 W. Cedar Drive,					



# ATTENDEES LIST

NAME	AFFILIATION	ADDRESS	CITY	STATE	ZIP	COUNTRY	TELEPHONE
Conover	NASA/KSC	DL-ESS-23	KSC	FL	32899	USA	(407) 867-3404
Cooray	Inst of High Voltage R	Husbyborg	Uppsala		75592	Sweden	46 18 533636
Craven	U.S. Army	Redstone Technical Test	Redstone	AL	35898	USA	(205) 842-2952
Crofts	Raychem	Eddison Road	Swindon			U.K.	0793-482307
Currlin	Electronique 2000	8 Rue Rene-Camphin	Fontaine		38600	France	(33) 76264327
Davis	Bendix Engine Controls	717 N. Bendix Dr.	South Bend	IN	46620	USA	(219) 231-4464
Dellera	CESI	Via Rubattino, 54	Milano		20134	Italy	02-2125348
Demers	Pratt & Whitney Canada	235 Sherbrooke W. #1204	Montreal	Quebec	H2X 1X8	Canada	(514) 281-8405
Dhooze	Panamax	1878 Lodgepole Dr.	Milton	FL	62583	USA	904-626-0690
Druen	USBI	PO Box 1900	Huntsville	AL	35807	USA	205-721-2262
Dye	Peterson APB	4WW/DOOS	Colorado	CO	80914	USA	(719) 554-4269
Eberhardt	NASA/KSC	DL-DSO-23	KSC	FL	32899	USA	407-867-3185
Eckhoff	Boeing Aerospace Ops.	Mall Stop: FA-55	KSC	FL	32899	USA	(407) 867-2281
Kilts	Nat'l Severe Storm L.	1313 Halley Cr.	Norman	OK	73071	USA	405-366-0414
Eisenberger	Navy Sea System Comm	Code 665D	Washington	DC		USA	703-602-2080
Eley	The Aerospace Corp	P.O. Box 21205	KSC	FL	32815	USA	407-853-5581
Elkins	U.S. Army	STENT-Te-E-EM	Redstone	AL	35898	USA	(205) 876-3415
Emanuelly	Centre D'Essais Aero.	23 Av H. Guillaumet	Toulouse		31056	France	61587322
Engle	Gruuman Melbourne Sys	2000 NASA Blvd.	Melbourne	FL	32902	USA	(407) 751-5042
Eriksen	Electro Magnetic Appl.	P.O. Box 260263	Denver	CO	80226	USA	303 980 0070
Eybert-Bera	CEA	BP 85X 38041	Grenoble			France	33-76-88-30-87
Fanio	Aerospatiale	316 Route de Bayonne	Toulouse		31060	France	33 61 93 79 28
Felt	Office of Fed	6010 Executive Blvd.	Rockville	MD	20852	USA	301-443-8704
Fisher	Sandia National Labs	P.O. Box 5800	Albuquerque	NM	87185	USA	(505) 846-2419
Floret	Helita	16 Rue Bertin-Poirree	Paris		75001	France	33-1-45084747
Free	USAF	2542 Nobility Ave.	Melbourne	FL	32934	USA	407-242-7878
Frennberg	Saab-Scania AB A/C Div	S-581 88 Linkoping	Linkoping			Sweden	46-13-181211
Frick	F.A.A.	3229 E. Spring Street	Long Beach	CA	90806	USA	213-988-5250
Garry	FAA	FAATC, ACN-270	Atlantic City	NJ	08405	USA	(609) 484-6734
Gauthier	DGA/DREY/CEG		Gramat			France	65 105435
Gerlach	NASA/GSFC	E108	Mallopo	VA	23337	USA	804-824-1188
Giori	SRI International	333 Ravenswood Ave 408-30	Menlo Park	CA	94025	USA	415-859-3138
Glynn	FAA Technical Center	ACD 230	Atlantic City	NJ	08495	USA	609-484-4138
Gobin	ONERA	8 Rue Vertugadins	Meudon		92190	France	33-1-4534-7501x4445
Golka	Golka Associates	Box 676	Brockton	MA	02403	USA	(508) 586-7320
Gondot	Aerospatiale	12 Rue Pasteur	Suresnes		92152	France	
Goodloe	MSFC	EL56	MSFC	AL	35812	USA	205-544-2343
Goto	Mississippi State Univ	114 Alrport Rd.	Starkville	MS	39759	USA	(601) 325-8859
Goto	Tohoku Gakuin Univ.	1-13-1 Tagajo	Miyagi		985	Japan	22-368-1115
Grachan	Bendix/King, m/s 37	400 N. Rogers Rd.	Olathe	KS	66062	USA	(913) 782-0400

# ATTENDEES LIST

NAME	AFFILIATION	ADDRESS	CITY	STATE	ZIP	COUNTRY	TELEPHONE
Graby	GERAC	BP 505 31674	Labège Cedé			France	33-61-39-93-75
Crush	EG&G Idaho, Inc.	P.O. Box 1625, MS 2408	Idaho Falls	Idaho	83415-2408	USA	(208) 526-9406
Gumley	Int'l Protection Cons. Technopark		Hobart	Tasmania	7010	Australia	61-02-730066
Haigh	LTT - Culham Lab.	Abingdon	Oxon		OX143DB	England	235-464243
Haines	Naval Air Test CenterX Code SY84		Patuxent	MD	20670	USA	(301) 863-3872
Hardwick	LTT - Culham Lab.	Abingdon	Oxon		OX143DB	England	235-464243
Hargreaves	Rarger Lightning Prot	1066 Campus Drive	Mundelein	IL	60060	USA	(708) 362-4848
Harwood	Arc Inc.	2711 Jefferson Davis Hwy	Arlington	VA	22202	USA	704-418-6415
Hastbrouck	LINL	P.O. Box 808, L-154	Livermore	CA	94550	USA	(415) 422-1256
Heidlebaugh	The Boeing Co.	PO Box 3707, m/s 4A-11	Seattle	WA	98124	USA	206-655-6111
Heistand	Florida Power & Light	P.O. Box 1565	Homestead	FL	33090-1565	USA	305-246-6598
Herhold	Elite Electronic Eng	4309 N. Banana River	Cocoa Beach	FL	32931	USA	(407) 783-2360
Herring	Comptr Sciences	P.O. Box 4127 CSR 4600	Patrick AFB	FL	32925-0127	USA	(407) 853-5205
Hess	Honeywell, Inc	P.O. Box 21111	Phoenix	AZ	85036	USA	(602) 436-1285
Hillyer	CANRF	4700 Ortega Blvd	Jacksonville	FL	32110	USA	(407) 867-6330
Hohl	Lockheed Space Ops	1100 Lockheed Way	Titusville	FL	32951	USA	(505) 667-3406
Holden	Los Alamos National	Group SST-7, MS D466	Los Alamos	NM	87545	USA	303-497-6637
Holle	NOAA-NSSL	325 Broadway	Boulder	CO	80302	USA	(505) 662-2973
Holmes, Jr.	Los Alamos National	713 Kris Court	Los Alamos	NM	87545	USA	405-366-0433
Hondl	Nat'l Severe Storms	1313 Halley Cr.	Norman	OK	73069	USA	0049-89-6004-372
Hopf	University of Federal	W. Heisenberg - Weg 39	Neubiberg	CO	80818	USA	(719) 599-1961
Jackson	Kaman Sciences	1500 Garden of Gods Rd.	Colorado Spgs.	FL	32899	USA	(407) 867-3529
Jafferis	NASA/KSC	DL-SSS-23	KSC	Ontario	M5S 1A4	Canada	416-978-3116
Janischewsk	University of Toronto	Dept. of Electrical Eng.	Toronto	NV		USA	702-295-4589
Jenkins	Los Alamos National	P.O. Box 0 MS J900	Mercury	WA	98136	USA	206-938-4166
Jolly	Jon B. Jolly, Inc.	5416 California Ave., SW	Seattle	NM	87801	USA	505-835-5751
Jones	New Mexico Tech	Langmuir Laboratory	Socorro	Lancs	PR4-1AX	England	UK 772-854799
Jones	British Aerospace	Warton Aerodrome (W7G)	Preston	FL	32903	USA	407-727-1813
Kapryan	Retired NASA/KSC	316 10th Terr	Indianapolis	FL	32826	USA	(407) 658-6830
Karpinchik	CREOL UCF	12424 Research Parkway	Orlando	Osaka	565	Japan	81-6-877-5111
Kawasaki	Osaka University	Yamadaoka 2-1	Suita	FL	32899	USA	49-89-60043721
Kern	Univ. of the Federal	W. - Heisenberg - Weg 39	Neubiberg	WA	98124	USA	(708) 495-9770
Khandani	Boeing Aerospace	Mail Stop: FA-55	KSC	IL	60515	USA	(602) 621-6831
King	Boeing Commercial	PO Box 3707, M/S 9R-39	Seattle	AZ	85721	USA	(213) 593-9514
Klonda	Elite Electronic	1516 Centre Circle	Downers Grove	CA	92190	France	33-1-4534-7501
Krider	University of Arizona		Tucson		33701	France	33-56-55-2649
Kuhlman	McDonnell Douglas	3855 Lakewood Blvd.	Long Beach		GUI4 6TD	U.K.	(252) 24461 x 5730
Laroche	ONERA	8 Rue Vertugadins	Meudon				
Lebourg	Dassault	BP24	Merignac				
Lee	Meteorological Office	Bldg. Y70, Royal	Farnborough				

# ATTENDEES LIST

NAME	AFFILIATION	ADDRESS	CITY	STATE	ZIP	COUNTRY	TELEPHONE
Lee	Dr. M.I.	Electricity Res & Dev	Chester			U.K.	44-51-347-2309
Lehmann	Monty R.	K-Tech Corp.	P.O. Box 70	MD	20653	USA	301-863-8607
Lennon	Carl L.	NASA/KSC	TE-CID-3	FL	32899	USA	(407) 867-4020
Lohminger	Axel W.	U.S. Army	Picatinny Arsenal, Bldg	NJ	07806-5000	USA	201-724-3209
Lopez	Raul E.	NOMA-NSSL	325 Broadway	CO	80303	USA	303-497-6699
Luteran	Frank	R & B Enterprises	20 Clipper Road	PA	19428	USA	215-825-1960
Lyle	John	USAF	ASD/YSEF	Ohio	43433	USA	(513) 255-9526
Madusa	John T.	USAF	ESMC/WE	FL	32425	USA	(407) 494-5915
Magyar	Ernest A.	G4H Tech. Corp.	10169 New Hampshire Ave.	MD	20903	USA	(301) 431-3246
Maier	Launa M.	NASA	TE-CID-3	FL	32899	USA	(407) 867-4409
Maier	Michael W.	Computer Sciences/Rath	CSR 3220, P.O. Box 4127	FL	32925-0127	USA	407-494-4252/2012
Markson	Ralph	Airborne Research/Assoc	46 Kendal Common Rd.	MA	02193	USA	(617) 899-1834
Mayer	William J.	Los Alamos Nat. Lab	P.O. Box 1662, Mail	NM	87545	USA	(505) 667-4246
Maytrott	Craig	FL Solar Energy Center	300 S.R. 401	FL	32920	USA	407-783-0300 x 153
Mazur	Dr. Vladislav	Nat'l Severe Storms L.	1313 Halley Circle	OK	73069	USA	(405) 366-0406
McCartney	Gen. F.	NASA/KSC	Center Director	FL	32899	USA	(609) 383-8300
McDowall	Rosemarie	Computer Resource Mgt	200 Scarborough Dr.,	NJ	35630	USA	601-423-0672
McRae	Steve	AeroJet	1 NASA dr	MS	32611	USA	(904) 392-4241
Medelius	Pedro	University of Florida	311 Benton Hall	FL	16000	Yugoslavia	YU016-41-69655-642
Mladenovic	Ilija	Prof. Electronic/Faculty	Skopska 8		92552	France	33-1-47114194
Moreau	Jean-Patrick	Dassault Aviation/DGT/	78 Quai Marcel Dassault,	MA	01730	USA	(617) 271-3130
Mulvehill	Alice	The MITRE Corporation	Burlington Road		466	Japan	52-732-2111
Nakamura	Koichi	Nagoya Institute Tech	Gokiso Showa		471	Japan	565-32-3463
Nakano	Minoru	Toyota College of Tech.	Eisel-Cho		75244	Sweden	46 18 531293
Namasivayam	S.	Inst of High Voltage R	Husbyborg	CA	94025	USA	415-859-2609
Nanevich	J. E.	SRI	333 Ravenswood		32931	USA	407-799-2489
Neiman	Norman	Nyma, Inc.	1980 N. Atlantic Swt	FL	32899	USA	407-867-4564
Nguyen	Cuong C.	NASA, KSC	DF-FED-21	MD	20640-5000	USA	(301) 743-4130/4466
Nial, Jr.	John A.	U.S. Navy (DOD)	Naval Ord. Sta Code 6720	FL	32899	USA	407-867-2780
Nicholson	James R.	NASA/KSC	PT-AST	Beds.	101 3JJ	England	(+44) 582-450-042
O'Neill	Mike	Meas. Technology, Ltd.	Power Court	WA	98124-2207	USA	(206) 662-0121
Olson	Glenn O.	Boeing Mil. Airplanes	P.O. Box 3707, M/S 4C-69	AZ	85721	USA	(602) 621-6831
Oram	Timothy D.	Univ of Ariz (PAS 522)	Inst of Atmospheric Phy.	MS	39762	USA	(601) 325-3623
Owens	John K.	Mississippi State Univ	P.O. Drawer EE	Utah	84044-0157	USA	(801) 251-4137
Owens	Paula	Ministry of Defense	Liverpool		92552	France	(33) 1-37-11-41-94
Page	George D.	NAV PMO SSP DET	P. O. Box 157	IL	62225	USA	618-256-4858
Parmentier	Jean-P	Dassault Aviation/DGT/	78 Quai Marcel Dassault,	CO	80228	USA	303-980-0070
Patterson	Stephen D.	HQ Air Weather Service	Scott AFB	FL	32114	USA	(904) 239-6708
Parala	Dr. Rodney A.	Electro Magnetic Appl	12567 W. Cedar Dr., #250				
Phelps	Chris. T.	Embry-Riddle Aero.	Dept. of Math & Phys Sci				

# ATTENDEES LIST

NAME	AFFILIATION	ADDRESS	CITY	STATE	ZIP	COUNTRY	TELEPHONE
Pifer	Albert E.	Lightning Locat 4	Tucson	AZ	85706	USA	602-741-2838
Pitts	Felix L.	NASA-Langley	Hampton	VA	23665	USA	804-864-6186
Plumer	Andy	Lightning	Pittsfield	MA	01201	USA	413-499-2135
Podgoraki	Elizabeth	Transport Canada	Ottawa	Ontario	K1A 0N8	Canada	613-957-6947
Podgoraki	Dr. A.S.	NRC - Canada	Ottawa		K1A 0R6	Canada	613-993-4198
Pratt	Greg	LMSC	Iuka	MS	38852	USA	601-423-0596
Reid	G.W.	LIT - Culham	Oxon		OX143DB	England	235-464243
Reyay	Dr. Andrew	FIT	Melbourne	FL	32901	USA	407-723-0189
Richards	Philippe	Parc des Algorithmes	St Aubin		91194	France	1-69-41-27-01
Roberts	Ed	FAA, Airway Facil. Div	East Point	GA	30344	USA	(404) 763-7417
Robinson	Randy	Beech Aircraft Corp.	Wichita	KS	67201-0085	USA	(316) 676-7933
Ross	Fred L.	Lockheed Aer Systems	Marietta	GA	30063	USA	404-494-1406
Roth	Jan-Uwe	Dornier Luftfahrt GmbH	Friedrichshaf		7990	Germany	7545-84897
Rubinstein	M.	University of Florida	Gainesville	FL	32611	USA	(904) 392-4930
Ruhnke	Lothar H.	NRL	Washington	DC	20375	USA	202-767-2951
Ruiter	A.M.	Fokker Space & Systems	Amsterdam		1100AE	Holland	011-31-20-6056255
Rupke	Ed	Lightning Technologies	Pittsfield	MA	01201	USA	(413) 499-2135
Rustan	Pete	SDIO/TNI	Woodbridge	VA	22192	USA	(703) 693-1671
Salaun	Michal	Dassault	St. Cloud		92552	France	
Salisbury	Kenton	Maxwell	San Diego	CA	92123	USA	619-576-7866
Sanders	Gary	Sandia National Labs	Albuquerque	NM	87185	USA	505-846-0085
Sannicandro	Rocco	Boeing Aerospace Ops	KSC	FL	32899	USA	867-2281
Scheps	Richard D.	Rockwell International	Anaheim	CA	92803-3170	USA	(714) 762-3738
Schnetzer	George H.	Sandia National Labs	Albuquerque	NM	87185	USA	505-844-6185
Schroeder	Jack	Lightning Diversion Sy	Huntington	CA	92647	USA	714-841-1080
Serafin	Dominique	Centre d'Etude Granat	Gramat		46500	France	(33) 65105446
Shaheen	George	Honeywell	Glendale	AR	85030	USA	602-436-7237
Shao	Xuan-min	New Mexico Tech	Socorro	NM	87801	USA	(505) 835-5137
Shio	Dr. Hisashi	Hokkaido Univ.	Iwamizawa	Hokkaido		Japan	0126-22-1470-336
Shrier	Karen	Electroner	Belmont	CA	94002	USA	(415) 637-1830
Saith	Eric	NASA/KSC	KSC	FL	32899	USA	407-867-3185
Soula	Serge	L. Aerologie	Toulouse		31062	France	61-55-60-02
Spalding	Richard E.	Sandia National Labs	Albuquerque	NM	87185	USA	(505) 844-5934
Spiller	Olaf	Deutsche Airbus	Hunefeld St. 1-5		2800 Bremen	Germany	421-538-4423
St. Jean	Paul	Thiokol	Ogden	VT	84403	USA	(801) 863-3500
Stahmann	James R.	Beijing Aerospace Ops	KSC	FL	32899	USA	407-867-7507
Stevens	E.G.	ERA Technology Ltd.	Leatherhead	Surry	KT22 7SA	England	372-374151
Stoble	James G.	AF Office of Sci Res	Bolling AFB	DC	20332	USA	(202) 767-4960
Storebo	Per B.	Norwegian Def ResEstab	Kjeller		N-2007	Norway	47-6-807855
Taylor	Nathan	NASA/KSC	KSC	FL	23899	USA	407-861-2779

# ATTENDEES LIST

NAME	AFFILIATION	ADDRESS	CITY	STATE	ZIP	COUNTRY	TELEPHONE
Thomas Garland L.	NASA, KSC	RT-ENG-1	KSC	FL	32901	USA	(407) 867-4493
Thompson Paul J.	Lawrence Livermore Nat P.O. Box 45		Mercury	NV	89023	USA	(702) 295-2411
Thomson Ewen	University of Florida Dept. Electrical Eng.		Gainesville	FL	32611	USA	904-392-4041
Thottappillil Rajeev	University of Florida Dept. Electrical Eng.		Gainesville	FL	32611	USA	(904) 392-4930
Travis Joshua	NASA/KSC	DL-DSD-1	KSC	FL	32899	USA	
Uesugi Masato	NASDA	Sengen 2-1-1	Tsukuba	Ibaraki	300	Japan	81-298-52-2293
Uman M.	University of Florida Dept. Electrical Eng.		Gainesville	FL	32611	USA	
Veazey Don R.	US Army Atmos Sci	ATTN: SLCAS-DP	WSMR	NM	88002-5501	USA	(505) 678-5232
Vislocky Tim	NASA/KSC	3571 S. Atlantic Ave.	Cocoa Beach	FL	23931	USA	
Vorgucic Aleksandar	Prof. Electronic Fac.	T. Roksaudica 3	NIS		18000	Yugoslavia	38-18-46466
Vosteen James	Monroe Electronics Inc	100 Housel Ave.	Lyndonville	NY	14098	USA	(716) 765-2254
Wakerfield Charles T.	U.S. Navy	Naval Ordnance Station	Indian Head	MD	20640-5000	USA	(301) 743-4130/4466
Walker William	Naval Air Devel. Ctr.	Code 7021	Warminster	PA	18974	USA	215-441-2906
Walko Lawrence C.	USAF Aero Propulsion L	WL/PooX-3, WPAFB	Dayton	OH	45429-6563	USA	513-255-9634
Ward John M.	The Boeing Co.	PO Box 3707, M/S 4A-11	Seattle	WA	98124	USA	206-655-6111
Watson Andrew I.	NORAA/NSSL	325 Broadway R/E/NS1	Boulder	CO	80303	USA	303-497-6630
Weber R.	Aerospatiale	22 Rue Pasteur	Suresnes		92150	France	
Wheeler Mark M.	Comptr Sciences/Rayth	P.O. Box 4127	Patrick AFB	FL	32925	USA	(407) 853-5151
Whitaker Mike	U.S. Navy	NATC (SY84)	Pax River	MD	20670	USA	301-863-3868
Whitworth Daniel	NASA, KSC	SI-FSD-4	KSC	FL	32899	USA	407-867-7157
Wiedmann Dr. Juergen	Dornier	P.O. Box 7303	Friedrichshaf		7541-4961	Germany	
Willlett John C.	AFGL	105 Drummer Road	Acton	MA	01720	USA	(508) 263-1857
Wilson Michael J.	Lawrence Livermore N L P.O. Box 808, L-153		Livermore	CA	94550	USA	415-294-4011
Windmar Dan	Inst of High Voltage R	Husbyborg	Uppsala		75592	Sweden	
Wyse Neil R.	USAF	ESMC/WE	PAFB	FL	32925	USA	(407) 853-8492
Yokoyama Kiyooki	Mississippi State Univ	114 Airport Road	Starkville	MS	39759	USA	(601) 325-8859
Zimbalatti Anthony	Consultant	294 Crowell St.	Hempstead	NY	11550	USA	(516) 483-4742
Zischank Dr. Wolfgang	Fed. Armed Forces	Werner-Heisenberg - Weg	Neubiberg		0-8014	Germany	089-60043721

# ATTENDEES 228

# COUNTRIES 14

**Session 11A, Thursday 1:30**  
**Lightning Phenomenology**  
**Modeling 3**  
**Uman, Chairman**

## LIGHTNING INDUCED CURRENTS IN AIRCRAFT WIRING USING LOW LEVEL INJECTION TECHNIQUES

E G Stevens  
ERA Technology Ltd, UK

D T Jordan  
Royal Aerospace Establishment, UK

### ABSTRACT

Various techniques have been investigated to predict the transient current induced into aircraft wiring bundles as a result of an aircraft lightning strike. A series of practical aircraft measurements have been carried out together with a theoretical analysis using computer modelling. These tests have been applied to various aircraft and also to specially constructed cylinders installed within coaxial return conductor systems.

Low level swept frequency cw (carrier wave), low level transient and high level transient injection tests have been applied to the aircraft and cylinders. Measurements have been carried out to determine the transfer function between the aircraft drive current and the resulting skin currents and currents induced on the internal wiring. The full threat lightning induced transient currents have been extrapolated from the low level data using Fourier transform techniques.

The aircraft and cylinders used in these investigations were constructed from both metallic and CFC (carbon fibre composite) materials. The results demonstrate the pulse "stretching" phenomenon which occurs for CFC materials due to the diffusion of the lightning current through carbon fibre materials. TLM (transmission line matrix) modelling techniques have been used to compare the theoretical currents and the measured values.

### INTRODUCTION

This paper provides a summary of various ongoing lightning simulation techniques which have been investigated during trials by ERA and RAE to evaluate the indirect effects of lightning strikes to aircraft using low level cw and transient injection techniques.

The investigations have primarily been concerned with measurements of currents induced into the aircraft wiring harnesses as a consequence of low level injection into an aircraft fuselage. To investigate these effects various test rigs were erected around ground based aircraft and specially constructed test cylinders including:

- \* aluminium cylinder
- \* carbon fibre cylinder
- \* modern non-metallic helicopter
- \* modern carbon fibre aircraft
- \* modern metallic aircraft

Each of the test subjects were fitted with specially designed return conductor systems which were derived from the results of computer modelling such as "INDCAL", and using the experience and engineering judgement of the engineers involved.

### CYLINDER MEASUREMENTS

Two cylindrical tubes were constructed and installed within coaxial return conductor systems to investigate the effects of lightning coupling to a wire within the cylinder. One of the cylinders was constructed from aluminium and the other from CFC materials.

The primary objectives of the tests were to compare the results obtained using transient injection techniques with the cw injection techniques, using various termination load resistance values.

#### Cylinder Configuration

The cylinders were approximately 1.5 m long, 0.5 m in diameter and were constructed using material of approximately 2 mm in thickness. The ends of the cylinders were fitted with 60 degree tapered conical extensions made from eight copper bars (1/2" x 1/16") and were attached using a circular copper fixing band. Electrical contact to the CFC cylinder was achieved by electroless plating the ends of the cylinder using a solution of a copper salt.

In addition each cylinder was fitted with a coaxial return conductor system approximately 2.4 m long and 1.15 m diameter, made from eight copper conductors (1/2" x 1/16"). The return conductor system was tapered at each end to maintain a constant characteristic impedance of approximately 50  $\Omega$ . The cylinders were each fitted with internal test wires which could be terminated with various loads via "N" type connectors. The design of the cylinders and return conductor system is shown in Figs.1 and 2.

### Cylinder Tests

The transient injection tests were carried out at low level using a digital waveform generator which produced a double exponential signal with a peak amplitude of approximately 14 A, a risetime of 13  $\mu$ s (time to peak) and a half amplitude duration of 102  $\mu$ s.

Transient injection was also carried out at medium level using an RAE transient generator which produced a double exponential signal with a peak amplitude of approximately 1100 A, a risetime of 16  $\mu$ s (time to peak) and a half amplitude duration of 58  $\mu$ s.

The swept frequency cw injection tests were carried out over the frequency range 10 Hz to 100 MHz using a network analyser together with a selection of amplifiers. The magnitude and phase angle of the current induced on the test wire was normalised to the cylinder drive current to obtain the transfer function. The induced current measurements were made using current probes.

### Cylinder Results

The cw transfer function measurements have been normalised to the transient drive waveforms using Fourier transform techniques to compare the results obtained using the two methods.

Comparing the results from the transient injection tests carried out in the time domain with the cw injection tests carried out in the frequency domain shows that similar results are obtained.

Figs.3 and 4 show typical graphs which compare the wire current results obtained by the two test techniques for the 1100 A transient using the aluminium cylinder and the CFC cylinder terminated with 50  $\Omega$ . The X-axis time scale is logarithmic to allow the full transient waveform to be observed.

For the aluminium cylinder the initial wire transient shape approximates towards the differential of the driving transient followed by an overshoot and a "long tail". For the CFC cylinder the wire current is a similar shape to the drive current waveform.

The cw results have also been extrapolated to the "Component A and H" lightning waveforms as specified in the "Yellow" book Ref.[1] and in the "Orange" book Ref.[2], to compare the currents. The highest currents are induced with the CFC cylinder with short circuit loads on the both the wire and the cylinder.

For the "Component A" threat (Fig. 5) the peak wire current for the CFC cylinder is 49 kA at 61  $\mu$ s and for the aluminium cylinder the wire peak current is 2.3 kA at 7.8  $\mu$ s.

For the "Component H" threat (Fig 6) the peak wire current for the CFC cylinder is 450 A at 10  $\mu$ s and for the aluminium cylinder the wire peak current is 140 A at 0.3  $\mu$ s. The transient on the wire in the CFC cylinder is considerably "stretched" in time compared the "Component A and H" threat waveforms which peak at 6.4  $\mu$ s and 0.25  $\mu$ s respectively.

### Cylinder TLM Modelling

The cylinder and return conductor system have also been modelled using 3D (three dimensional) TLM modelling to predict the current induced on the cylinder wire, Ref [3]. The 3D model uses a regular mesh size of 0.05 m which represents a mesh cut-off frequency of 600 MHz (assuming 10 cells per wavelength).

As a consequence of the inherent symmetry in the return conductor system a parallel processing approach was used to enable the Sun3 to be used with transputers. The eight return conductors have been reduced to four to enable the four transputers to be implemented in the processing.

The induced wire current has been modelled at the same positions where the practical measurements were carried out. The impulse response has been filtered down to 100 MHz and convolved with a double exponential threat waveform with a peak amplitude of 1 A, a risetime of 1  $\mu$ s (time to peak) and a half amplitude duration of 20  $\mu$ s.



The predicted transient current is shown in Figs.7 and 8 respectively for aluminium and CFC cylinders terminated with a  $50\ \Omega$  load. The currents in the wire, the current in the cylinder and the current in the return conductor system are shown. The maximum time duration shown on the graph is only  $16\ \mu\text{s}$ , however the wire current for the CFC cylinder (shown as No 2 on the graph in Fig.8), has not yet reached its peak value, indicating a considerable time elongation of the transient.

The computer processing time required to calculate the currents is considerable and the work is currently being updated to include longer time durations for the predicted data.

## HELICOPTER MEASUREMENTS

As part of the AFARP 17 (Anglo-French aeronautical research programme) a series of lightning simulation tests have been applied to an Aerospatiale Ecureuil helicopter, Refs [4] and [5]. The tests were carried out at CEAT (Centre d'Essais Aeronautique de Toulouse) in France during 1989/90 by teams from RAE (Royal Aerospace Establishment) Farnborough UK, ONERA (Office National d'Etudes et de Recherches Aerospatiales) Meudon France, and CEAT.

The helicopter was installed within a coaxial return conductor system consisting of nine flexible conductors to form a coaxial line from the nose to the tail of the aircraft to simulate a nose to tail strike. A number of instrumentation wires were installed within the aircraft for the measurement of induced currents.

The return conductor system was terminated at the tail using various loads including the characteristic impedance of the transmission line (approximately  $50\ \Omega$ ) and also using an open circuit and also short circuit loads.

### Helicopter Tests

Various tests were applied by each of the trials teams and included:

- \* low level swept frequency carrier wave injection (by RAE)
- \* low and medium level transient injection (by CEAT)
- \* high voltage transient injection (by ONERA)

The low level transient injection tests were carried out using a reduced level waveform similar to lightning "Component H" (H/10), with a peak amplitude of approximately 1 kA, a risetime of 100 ns and a duration of  $4\ \mu\text{s}$ .

Transient injection was also carried out at medium level using a waveform similar to in shape to a lightning "Component D" (D/20) waveform with a peak amplitude of approximately 6 kA, a risetime of  $3\ \mu\text{s}$  and a duration of  $30\ \mu\text{s}$ . At higher levels the peak amplitude was increased to 50 kA (D/2) with a risetime of  $3\ \mu\text{s}$  and a reduced duration of  $15\ \mu\text{s}$ .

The swept frequency cw injection tests were carried out over the frequency range 1 kHz to 100 MHz using a network analyser together with a selection of amplifiers. The magnitude and phase angle of the current induced on the measurement wiring bundle was normalised to the aircraft drive current to obtain the transfer function. The induced current measurements were made using current injection and current measuring probes.

### Helicopter Results

A comparison has been made between results of the wire currents predicted from the cw measurements extrapolated to the aircraft threat test transient and the wire currents measured during the transient injection tests.

There is a very good agreement between the transient shapes obtained using the two test techniques although amplitude of the cw predictions is higher than the transient measurements. Typical graphs for different wires are shown in Figs.9 and 10 for the "Component D" waveform and in Figs.11 and 12 for the "Component H" waveform.

## CFC AIRCRAFT MEASUREMENTS

A series of lightning simulation tests have been applied to a modern jet aircraft constructed from CFC materials to investigate coupling phenomena.

High level transient injection and low level swept frequency cw injection transfer function tests were applied to investigate the degree of coupling between the airframe and the aircraft wiring bundles. The aircraft was installed on aircraft jacks within a return conductor system configured for a nose to wing tip lightning strike.

## **CFC Aircraft Tests**

The cw transfer function measurements were made between the drive current into the aircraft and the induced current on the aircraft wiring bundles and extrapolated to the test transient used during the aircraft. Measurements were made with the aircraft electrically inert and also electrically powered from a ground power unit to investigate any differences.

The transient injection was carried out at using a Culham LTT transient generator which produced a double exponential signal with a variable peak amplitude of up to approximately 40 kA, with a risetime of approximately 2.5  $\mu$ s (time to peak) and a half amplitude duration of 14  $\mu$ s.

## **CFC Aircraft Results**

A comparison has been made between results of the wire currents predicted from the cw measurements extrapolated to the aircraft threat test transient and the wire currents measured during the transient injection tests. There was no significant difference in the swept frequency cw transfer function measured with the aircraft powered and un-powered.

There is a good agreement between the cw and transient test techniques and the results obtained for two typical wiring bundles are shown in Figs.13 and 14.

The cw results for a typical wiring bundle have been normalised to the "Component A" and "Component H" waveforms in Figs.15 and 16. For the "Component A" waveform the peak current occurs at approximately 100  $\mu$ s with a level of over 400 A. Also for the "Component H" waveform it can be seen that considerable elongation has occurred.

## **METALLIC AIRCRAFT MEASUREMENTS**

A series of swept frequency cw skin current measurements have been applied to a modern metallic aircraft at the RAE (Royal Aerospace Establishment) Farnborough UK. The aircraft was installed within a return conductor system to simulate a lightning strike entering at the aircraft nose and exiting at the tail. The return conductor system consisted of twelve copper tubular conductors to form a coaxial line, Refs[6], [7] and [8].

### **Metallic Aircraft Tests**

Swept frequency cw skin current measurements of transfer function were made at various locations over the aircraft fuselage. The reference skin current was initially measured at the 1 m circumference position on the nose injection point on the aircraft. The transfer function was measured at various positions along the fuselage and out onto the wings of the aircraft as shown pictorially in Fig.17 (return conductor system omitted for clarity).

The return conductor system was terminated in turn by its characteristic impedance, by a short circuit and also by an open circuit. The measurements covered the frequency range 100 Hz to 100 MHz and were carried out using direct injection techniques into the aircraft nose and measurement of the transfer function using a skin current probe and a network analyser.

### **Metallic Aircraft Results**

The results are shown as the magnitude and phase angle of the skin current with respect to the nose injected skin current. In general the skin current was reasonably uniform for frequencies below approximately 3 MHz (resonance of return conductor system) and varied approximately as expected with the size of the surface circumference of the aircraft fuselage. At higher frequencies the skin current varied by up to +/- 30 dB at some of the resonant frequencies. Typical results are shown in the following section on modelling.

### **Metallic Aircraft TLM Modelling**

The aircraft and return conductor system have been modelled using 2D (two dimensional) and 3D (three dimensional) TLM (transmission line matrix) modelling to predict the cw response of the airframe Refs [9] and [10]. The 3D model uses a mesh size of 0.21 m (143 MHz mesh cut-off frequency) and represents the twelve return conductors as eight flat plates. The number of return conductors was reduced to allow a sufficient number of TLM nodes between the return conductors to obtain the correct magnetic field distribution.

The airframe skin current has been modelled at the same positions where the practical measurements of skin current were carried out. Both the magnitude and phase angle of the skin current have been modelled and compare well with the measured values at all locations. Figs.18 and 19 compare the magnitude and phase angle of the measured skin current transfer function with the modelled values.

It is hoped that these modelling techniques will be extended for future work to assist with the prediction of lightning transient currents on aircraft equipment and wiring bundles.

### CONCLUSIONS

Various swept frequency cw and transient injection techniques have been examined and compared to investigate the indirect effects of an aircraft lightning strike and the coupling to aircraft equipment and wiring bundles. There is a good correlation between the results obtained using these two techniques.

TLM modelling techniques have been used to predict the skin current distribution on aircraft and the currents induced onto wires inside cylinders. A good correlation has been achieved between the modelled values and practical measurements.

### ACKNOWLEDGEMENT

Acknowledgement is given to Messers S I Holland of ERA Technology Ltd and S J Holden of A&AEE Boscombe Down for carrying out the practical measurements to assist with the preparation of this paper.

### REFERENCES

- 1 Yellow Book, "Test waveforms and techniques for assessing the effects of lightning induced transients". SAE committee report AE4L-81-2, 15th December 1981
- 2 Orange Book, "Protection of aircraft electrical/electronic systems against the indirect effects of lightning", Recommended draft advisory circular. SAE AE4L-87-3 Committee Report, 4th February 1987.
- 3 Mallik A., "Convert TLM code to OCCAM and produce a 3D model of a CFC fuselage", KCC report 201/WS3, MOD contract AWL12C/2694, Kimberley Communication Consultants Ltd, Nottingham UK, July 1990.
- 4 Emanuely J.L, Daviose C., "Lightning simulations on a helicopter test-bed: pulse injection test results (Part 1: raw measurements)", Anglo-French research programme (AFARP) No 17, E88/681500 part 1, reference 001230, Centre D'essais Aeronautique de Toulouse (CEAT), France, 4 February 1991.
- 5 Emanuely J.L, Daviose C., "Lightning simulations on an helicopter test-bed. Part 2: Synthesis", Anglo-French research programme (AFARP) No 17, E88/681500 part 2, reference 002276 8 March 1991, Centre D'essais Aeronautique de Toulouse (CEAT), France.
- 6 Stevens E.G., "Assessment and application of whole aircraft lightning test techniques", ERA report 89-0312, ERA Technology Ltd, Leatherhead, Surrey, April 1990.
- 7 Stevens E.G., Jordan D.T., Holden S.J., "Whole aircraft lightning indirect effects evaluation using low level injection techniques", International conference on lightning and static electricity, University of Bath, 26 to 28 September 1989.
- 8 Stevens E.G., "Lightning test techniques using low level injection for indirect effects evaluation", draft ERA Report 90-0155, ERA Technology Ltd, Leatherhead UK.
- 9 Armour T., Mallik A., "Lightning interaction with aircraft". KCC Report No 146/5, Contract A85C/2420, Kimberley Communications Consultants Ltd, Nottingham, May 1987
- 10 Johns D.P., "TLM predictions of the response of a Jaguar aircraft in a lightning rig", KCC report 182/WS2, MOD contract AWL 12C/2612, Kimberley Communications Consultants Ltd, Nottingham, UK, 21 January 1991.

(C) British Crown Copyright 1991/MOD

Published with the permission of the Controller of Her Britannic Majesty's Stationery Office

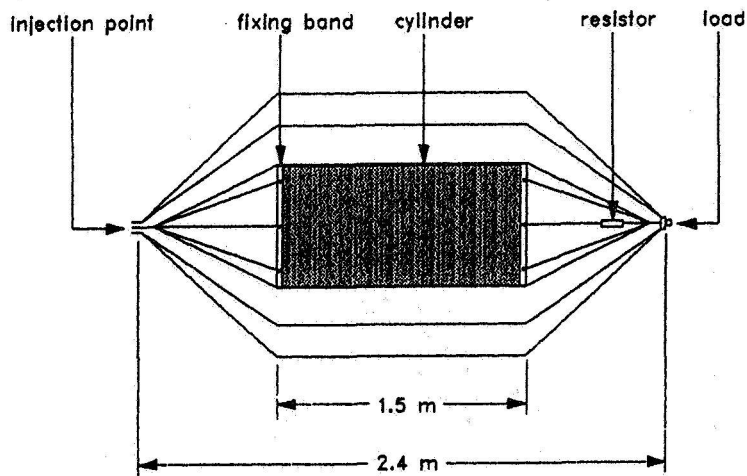


Fig.1 Cylinder and Return Conductor System  
(Side view)

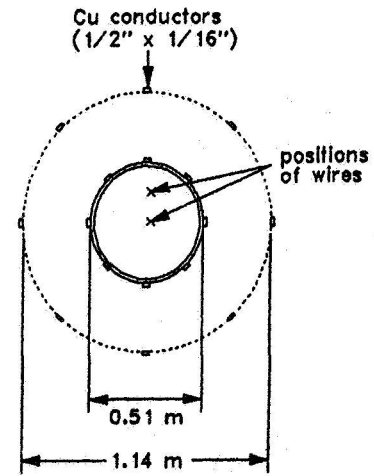


Fig.2 Cylinder and Return Conductor System  
(End view)

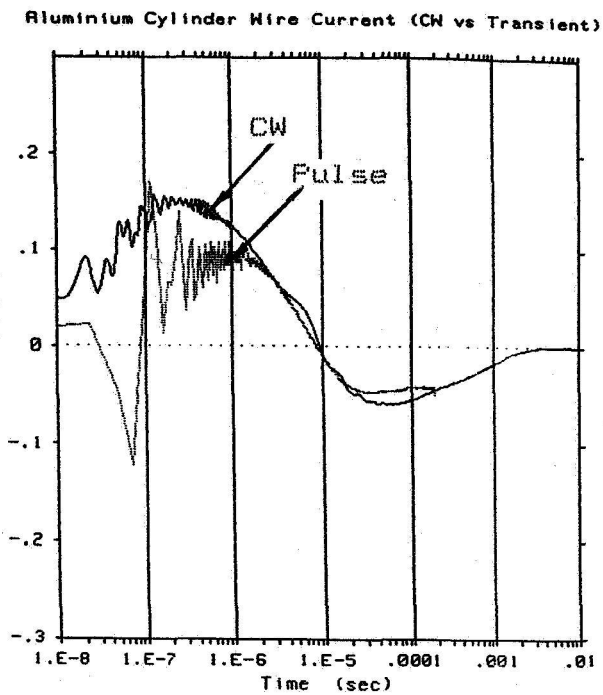


Fig.3 Aluminium Cylinder Wire Current  
(CW versus Pulse)

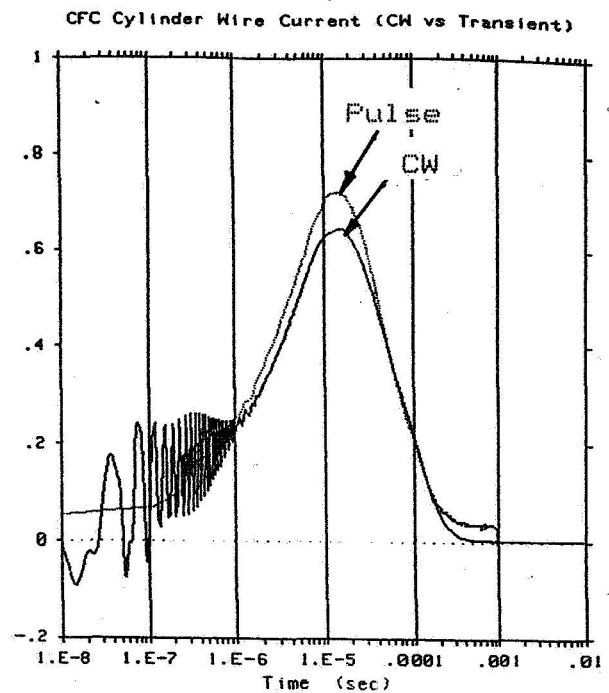


Fig.4 CFC Cylinder Wire Current  
(CW versus Pulse)

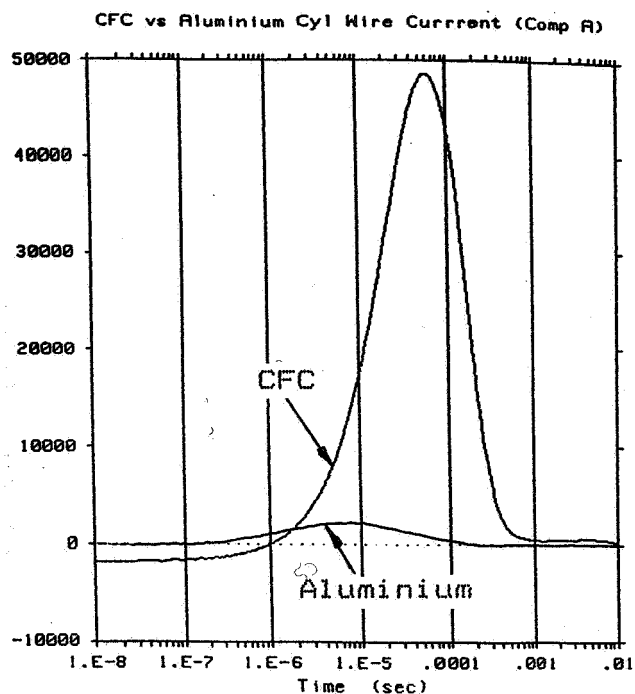


Fig.5 Aluminium versus CFC Cylinder Short Circuit Wire Current (Component A)

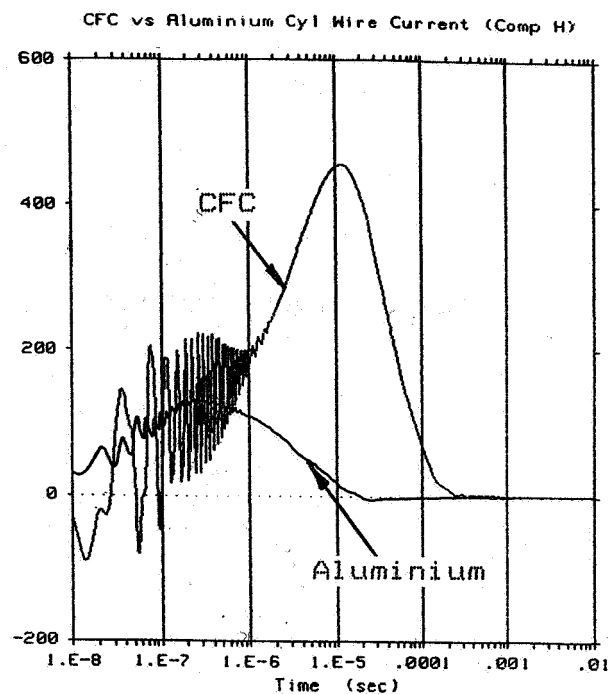


Fig.6 Aluminium versus CFC Cylinder Short Circuit Wire Current (Component H)

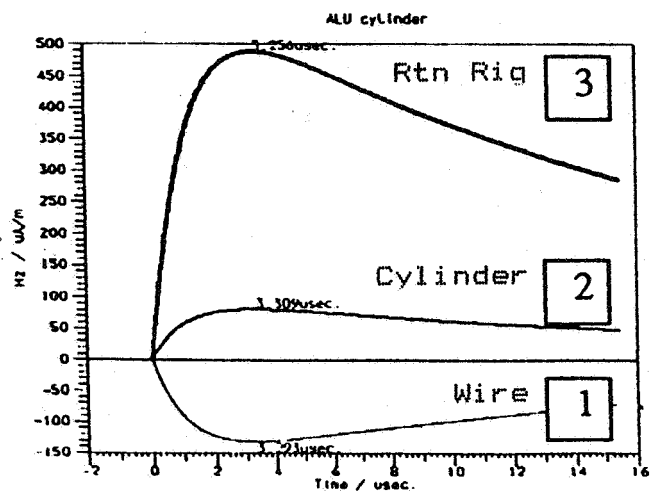


Fig.7 TLM Modelled Cylinder Currents (Aluminium Cylinder)

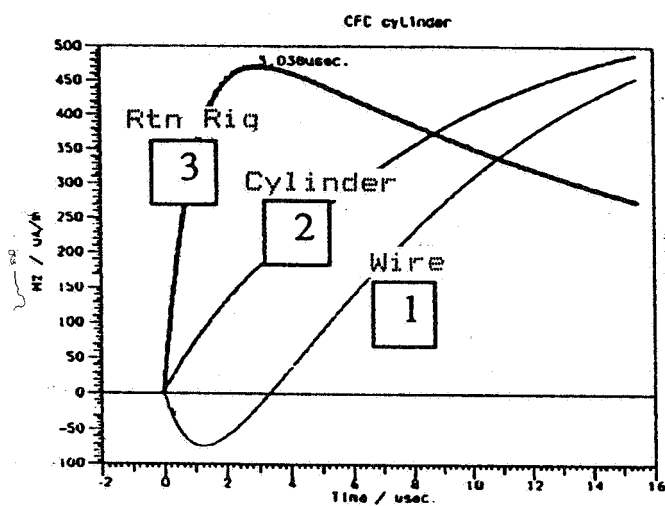


Fig.8 TLM Modelled Cylinder Currents (CFC Cylinder)

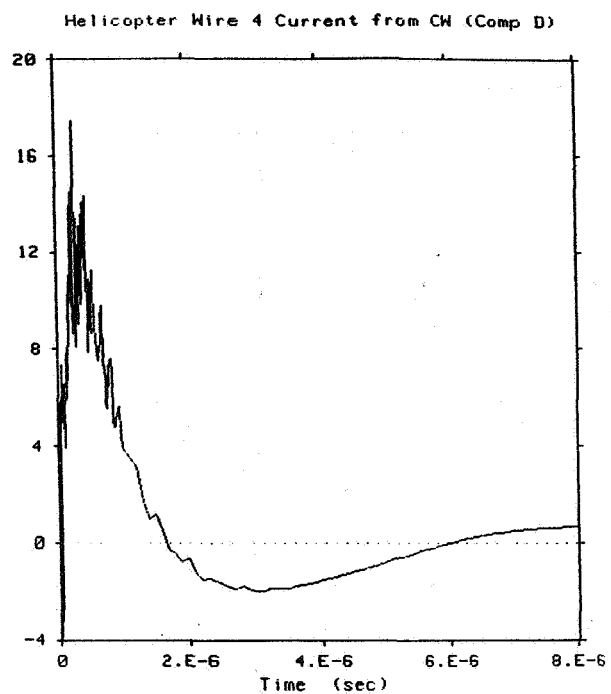


Fig.9 Helicopter CW Predicted Wire Transient  
(Wire 4, Component D)

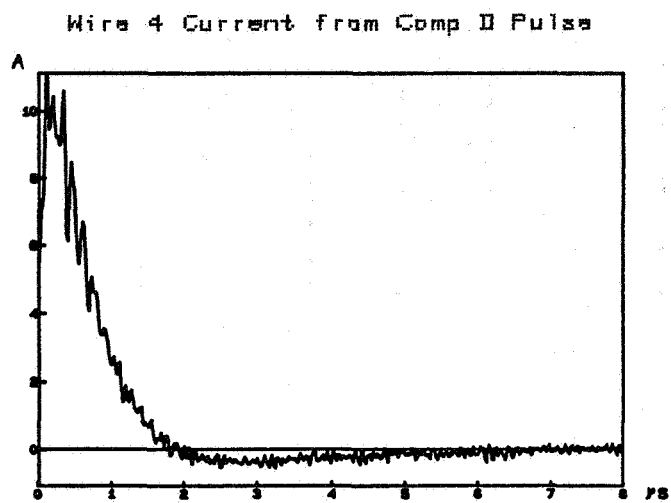


Fig.10 Helicopter Transient Wire Measurement  
(Wire 4, Component D)

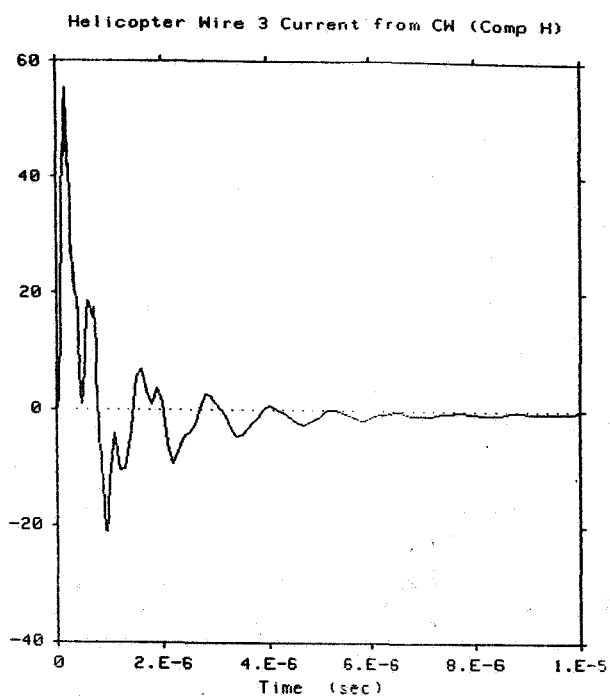


Fig.11 Helicopter CW Predicted Wire Transient  
(Wire 3, Component H)

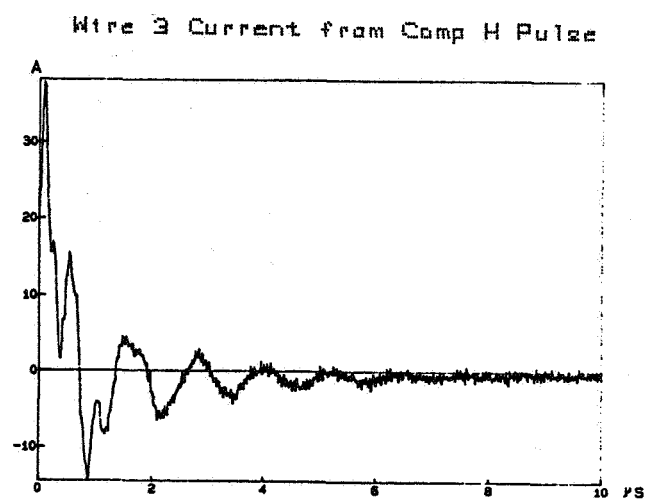


Fig.12 Helicopter CW Predicted Wire Transient  
(Wire 3, Component H)

CFC Aircraft Wire Current (CW vs Pulse)

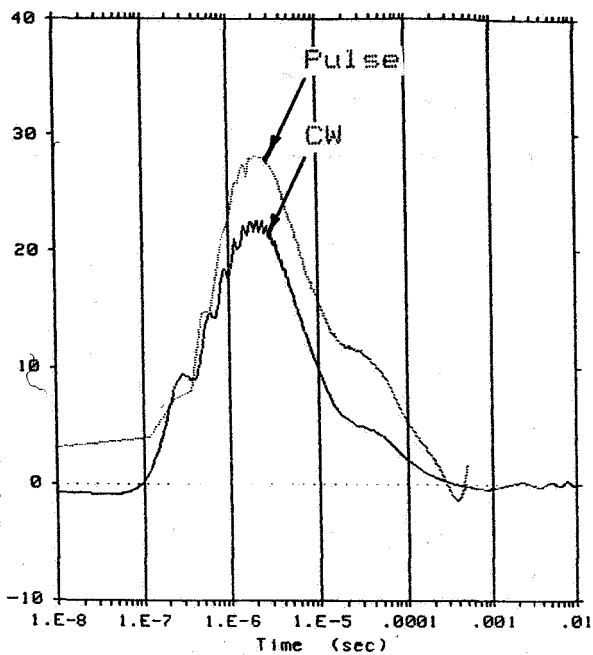


Fig.13 CFC Aircraft Typical Wiring Transient (CW versus Pulse)

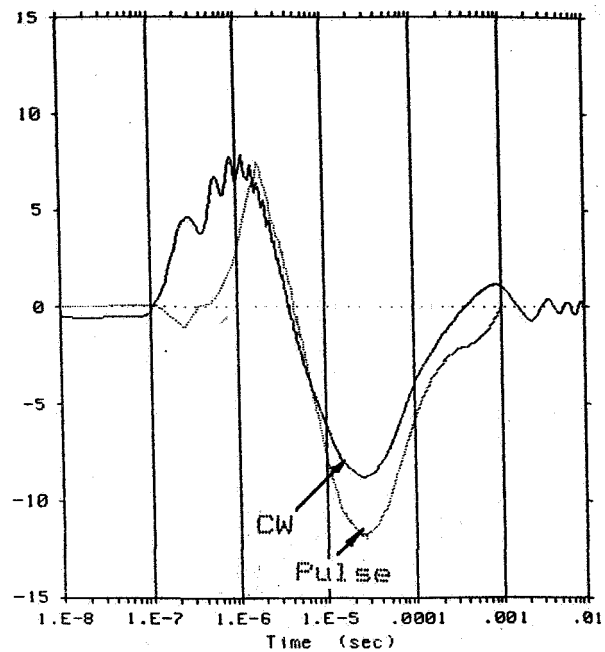


Fig.14 CFC Aircraft Typical Wiring Transient (CW versus Pulse)

CFC Aircraft Wire Current (Comp A)

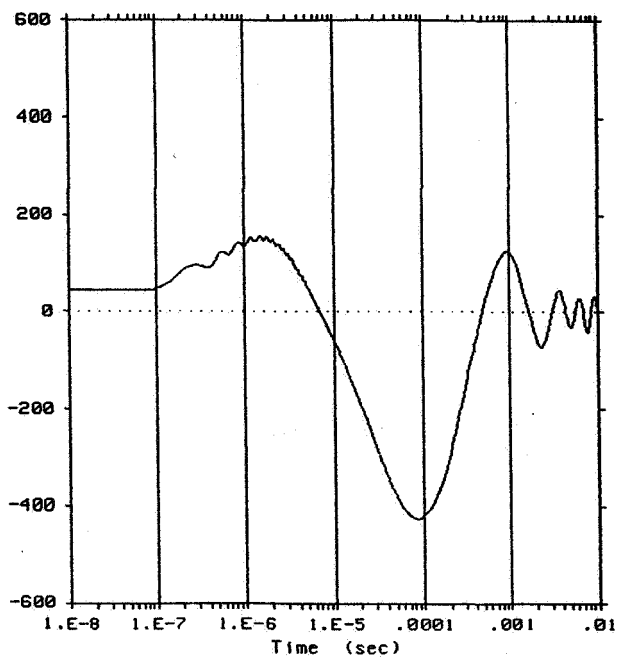


Fig.15 CFC Aircraft Typical CW Predicted Wiring Transient (Component A)

CFC Aircraft Wire Current (Comp H)

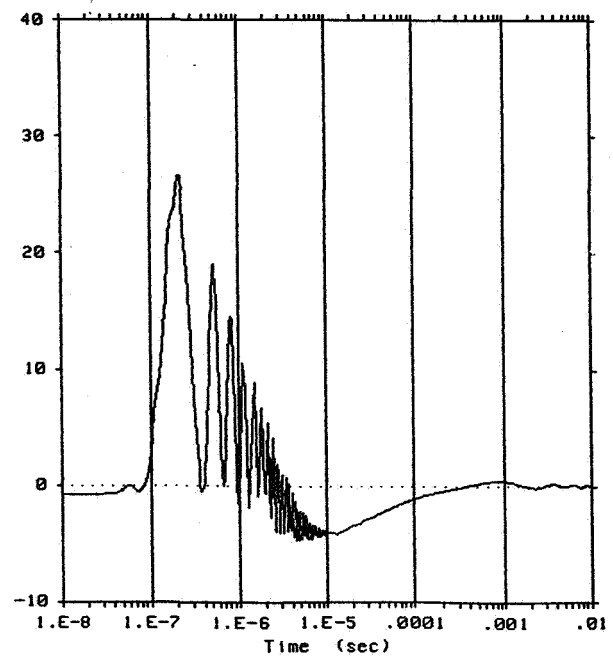


Fig.16 CFC Aircraft Typical CW Predicted Wiring Transient (Component H)

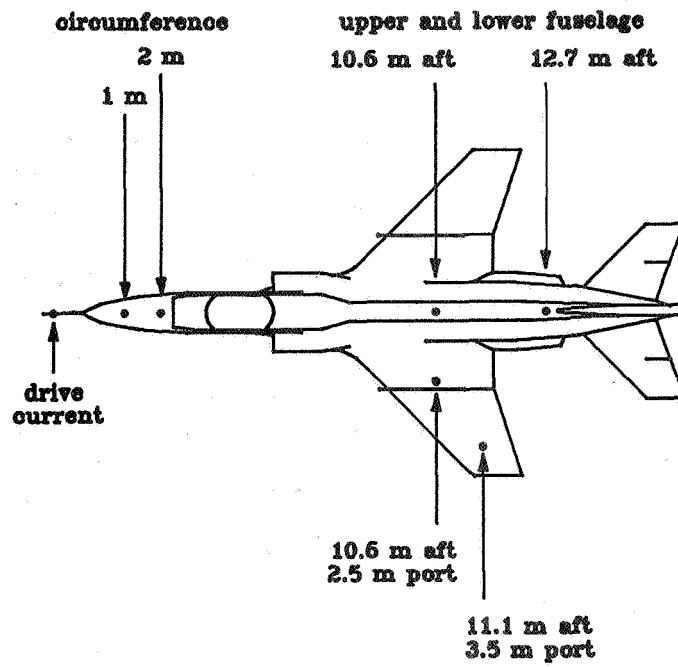


Fig.17 Metallic Aircraft Skin Current Measurement Locations

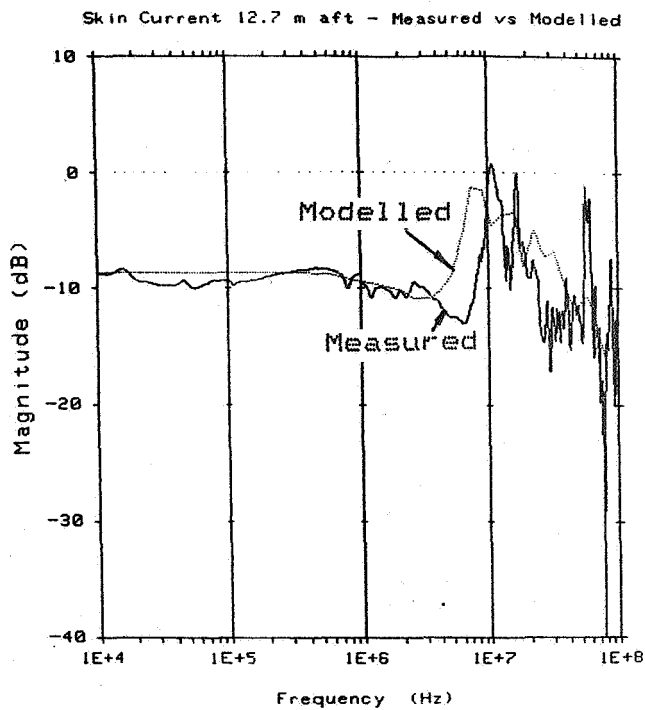


Fig.18 Metallic Aircraft Skin Current Magnitude Transfer Function (Modelled versus Measured)

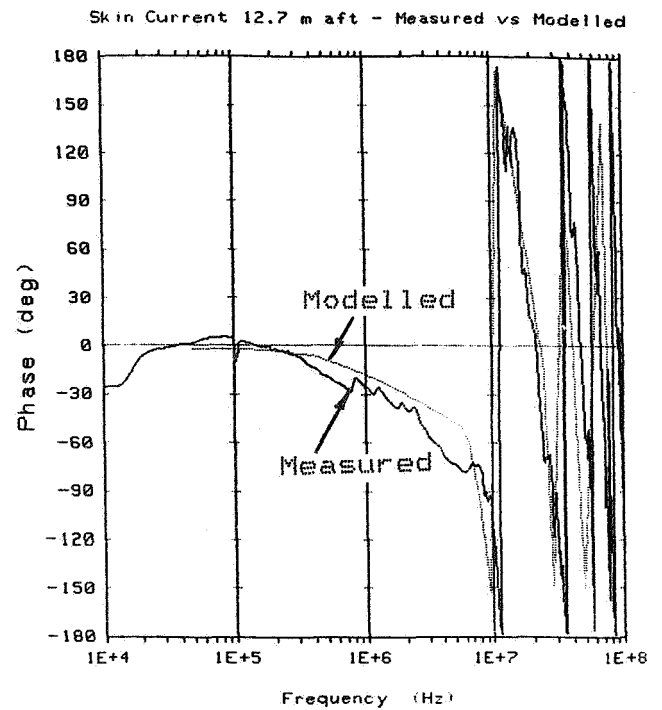


Fig.19 Metallic Aircraft Skin Current Phase Transfer Function (Modelled versus Measured)



OBSERVATIONS OF LIGHTNING PROCESSES USING VHF RADIO  
INTERFEROMETRY

C. T. Rhodes\*, X. M. Shao, P. R. Krehbiel and R. Thomas  
New Mexico Institute of Mining and Technology  
Socorro, NM 87801

## ABSTRACT

A single-station, multiple-baseline radio interferometer has been used to locate the direction of VHF radiation from lightning discharges with microsecond time resolution. Radiation source directions and electric field waveforms have been analyzed for various types of breakdown events. These include initial breakdown and 'K'-type events of in-cloud activity, and the leaders of initial and subsequent strokes to ground and activity during and following return strokes. Radiation during the initial breakdown of a flash and in the early stages of initial leaders to ground is found to be similar. In both instances the activity consists of localized bursts of radiation that are intense and slow-moving. Motion within a given burst is unresolved by the interferometer. Radiation from in-cloud K-type events is essentially the same as that from dart leaders; in both cases it is produced at the leading edge of a fast-moving streamer that propagates along a well-defined, often extensive path. K-type events are sometimes terminated by fast field changes that are similar to the return stroke initiated by dart leaders; such K-events are the in-cloud analog of the dart leader-return stroke process.

Radiation from the above processes is produced exclusively by negative-type breakdown, in agreement with the findings of other investigators. Radiation during return strokes initiated by dart leaders sometimes progresses away from the top end of the leader channel as an apparent positive streamer. These streamers appear to establish channel extensions or branches that are later traversed in the opposite direction by negative-polarity streamers of K- and dart-leader events. Finally, a new phenomenon has been identified whose electric field waveform resembles that of a highly branched, initial-type leader, but which transports negative charge horizontally and slowly away from the eventual channel to ground. The breakdown is observed to be terminated by a fast dart leader to ground from the source region of the activity.

## INTRODUCTION

Radio interferometry is continuing to provide a powerful technique for studying lightning discharge processes. The use of interferometric techniques for studying lightning has been discussed in detail by other investigators (e.g. Hayenga [1979], Richard and Auffray [1985], Rhodes [1989]). In this paper we present results from a two-dimensional interferometer system of different types of breakdown processes that occurred during two multiple-stroke discharges to ground, one of which was preceded by extensive intracloud activity. The discharges occurred over Socorro, New Mexico, during the 1988 summer thunderstorm season.

## THE INTERFEROMETER SYSTEM

Interferometric techniques determine the direction of arrival of radiation signals by measuring the phase differences of the radiation incident upon an antenna array. The array used in this study consisted of five antennas configured to form short- and long-baselines along each of two orthogonal directions in a horizontal plane. The long baselines were  $4\lambda$  in length and provided accurate but ambiguous estimates of the source direction. The short baselines were  $\lambda/2$  in length and provided coarse but unambiguous determinations of the source direction that were used to resolve the ambiguity of the long-baseline measurements.

The interferometer operated at a center frequency of 274 MHz with a 6 MHz bandwidth and a time resolution of 1 microsecond. Phase data from each of the short and long baselines was continuously recorded on a high density digital recorder along with separate measurements of the logarithmic RF power and fast electric field change. The electrostatic (slow) field change was sampled with 20  $\mu$ s time resolution and recorded along as part of serial housekeeping information. The decay time constant of the fast and slow electric field change measurements was 0.1 ms and 10 s, respectively. Data from lightning flashes of

\* Now at Los Alamos National Laboratories, Los Alamos, NM 87545.

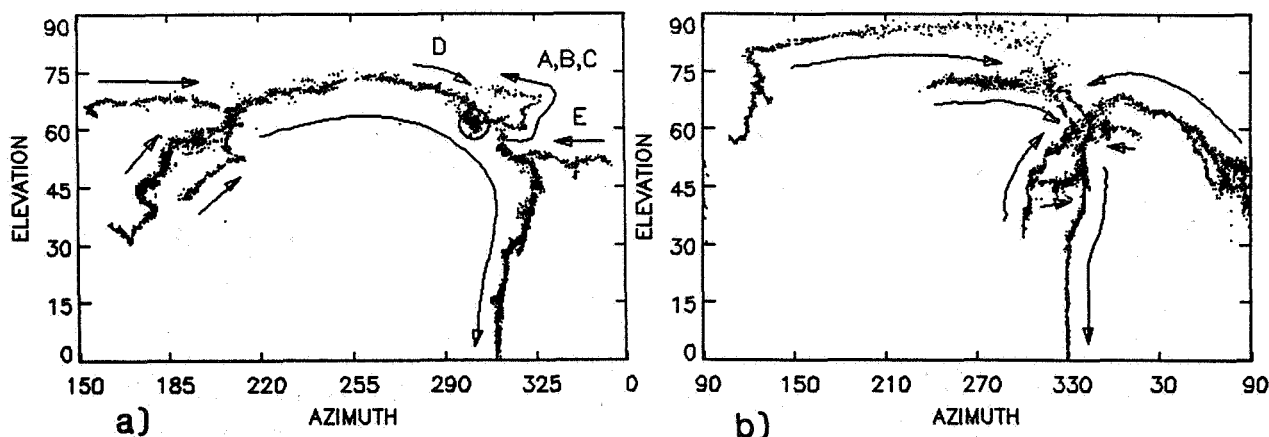


Figure 1: a.) Overview of Flash 153844. Composite of a K-event during the preliminary intracloud activity, dart leaders for strokes 3, 4, and 5, and several in-cloud streamers between stroke 4 and 5. b.) Overview of Flash 155325. Composite of leaders for strokes 3, 4, 7, 8, 9, and several streamers after continuing current stroke 8.

interest were played into an analysis computer where they were analyzed in detail using interactive graphics software.

## DATA AND RESULTS

Figure 1 shows composites of selected results for the two flashes, which occurred at 15:38:44 and 15:53:25 on Day 236 (August 23), 1988. Flash 153844 lasted about 1.2 seconds and consisted of 360 ms of intracloud activity followed by 5 strokes to ground. Flash 155325 lasted about 1 second and began with the initial leader to ground; it produced 9 strokes down the same channel. Both discharges went to ground 5-10 km north of the interferometer site and had in-cloud channels which developed toward and on the opposite side of the interferometer. The strokes of both flashes were of normal polarity, i.e. they lowered negative charge to ground.

The composites provide an overview of most of the channels and branches of each flash. The figures show the source directions in azimuth-elevation format and graphically depict the channel to ground. Cloud base was between 20° and 30° elevation along the vertical channel to ground, so that the channels above this point were inside the storm. The discharges are seen to have been substantially branched inside the cloud. Flash 153844 (Figure 1a) began at the location denoted by the circled region and established channels A - E during the intracloud phase of the flash. The initial leader to ground began near the flash start point and established the channel followed by subsequent leaders and strokes. The third stroke initiated a continuing current that originated along the D and E segments. Later strokes originated farther along the main left-hand channel on the other side of the interferometer.

Flash 155325 exhibited substantial and complicated branching into the top of the vertical channel to ground. The branches were followed by different strokes of the flash and by k-events late in the flash. The left branch extended overhead and past the interferometer site; other branches connected into the channel to ground from different directions.

### INITIAL BREAKDOWN

Flash 153844 began with a long interval of in-cloud breakdown that lasted about 360 ms and culminated in the development of an initial leader to ground. Figure 2(a) shows radiation source locations for the initial 70 ms of the in-cloud activity, termed interval A. Radiation during the first 60 ms of A (labelled A1) consisted of series of bursts whose sources drifted slowly in the direction of increasing azimuth, as indicated by the arrow. During each burst the radiation sources were localized and their extent or motion was not resolved by the interferometer, but the centers of successive bursts continually moved in the direction

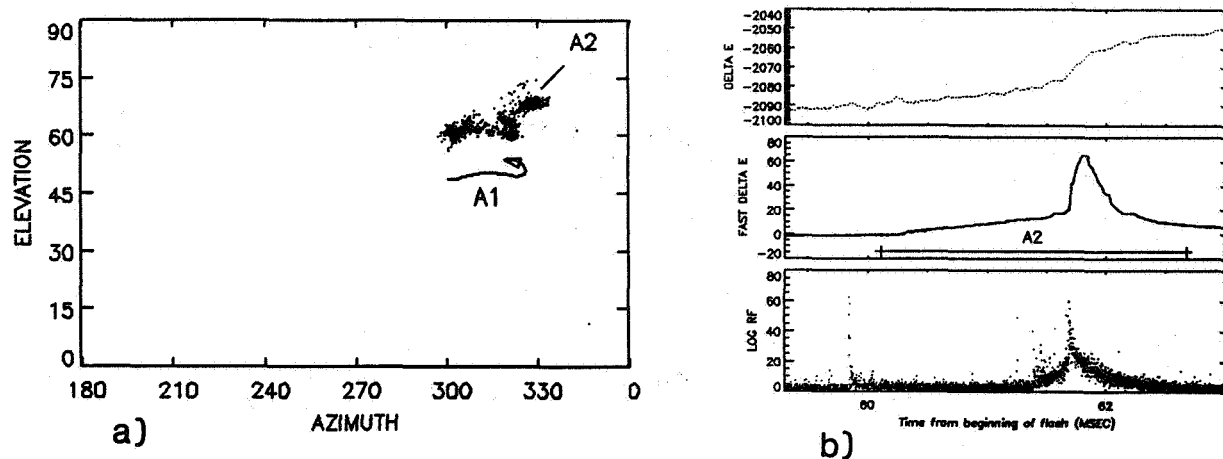


Figure 2: a.) Activity during the initial 70 ms of breakdown for Flash 153844. b.) Radiation and electric field waveforms for event A2 that completed the initial A activity.

of progression. The activity culminated with a strong burst of radiation just beyond the end of the A1 activity, labelled A2.

Figure 2(b) shows time waveforms for the A2 event. The event began with a brief burst of radiation from a localized region on the edge of A2 closest to A1. The electric field subsequently increased at a steady rate until, 1.5 ms later, radiation developed just beyond the region of the initiating burst and increased in intensity until a large, rapid electric field change occurred. During this time the radiation sources continued to be displaced away from the location of the initial burst and continued the overall progression of breakdown away from the flash start point.

The electric field change was positive during the entire A event, indicating that negative charge was transported away from the observation site, or, equivalently, that positive charge was transported toward the site. Later results for the flash show that the A activity progressed away from the observation site; the activity therefore transported negative charge in its direction of progression. (The negative-going change at the end of fast electric field record in Figure 2b was due instrumental decay, of 0.1 ms time constant.)

Assuming that the preliminary activity was 5-6 km above ground level (AGL), as found by Krehbiel et al. [1979] in a similar storm from the same area, and noting that the sources were at about  $60^\circ$  elevation, we infer that the initial activity was about 3 km plan distance from the interferometer. From this and from the angular extent of the source motion, the projected extent of the A progression was about 1 km. The projected average speed of progression was therefore about  $1.5 \times 10^4$  m/s.

#### K-TYPE EVENTS

Figures 3 and 4 show results for two K-type events which occurred 212 and 231 ms into Flash 153844. Both events retraced the path of the A activity of Figure 2 and extended the A path. The first K-event is labelled C and is shown in Figure 3. It began with 500  $\mu$ s of localized radiation in the flash start region (C1) and continued after a brief lull with a well-defined streamer (C2, the first streamer of the flash) that rapidly retraced the path of the A activity and extended the far end of the channel upward in elevation and backward in azimuth. The electric field increased continuously during the C2 streamer progression, again indicating the transport of negative charge away from the interferometer. As the streamer reached the end of its extent the radiation dropped abruptly in amplitude and the fast electric field signal saturated. Lower-amplitude radiation persisted for about 100  $\mu$ s at the far end of the streamer path, then a final burst of radiation (C3) progressed backward along the vertical segment midway along the streamer channel. The entire event lasted about 1 ms, typical of K-events.

Results for K-event D are shown in Figure 4. This event substantially extended the breakdown to the left of the flash start region. Two precursor events, D0 and D1, occurred at a distance beyond the flash start region and were directed toward the flash start region. D0 was a short streamer that propagated into the starting point of D1; D1 was a slightly longer and more intense streamer that propagated into

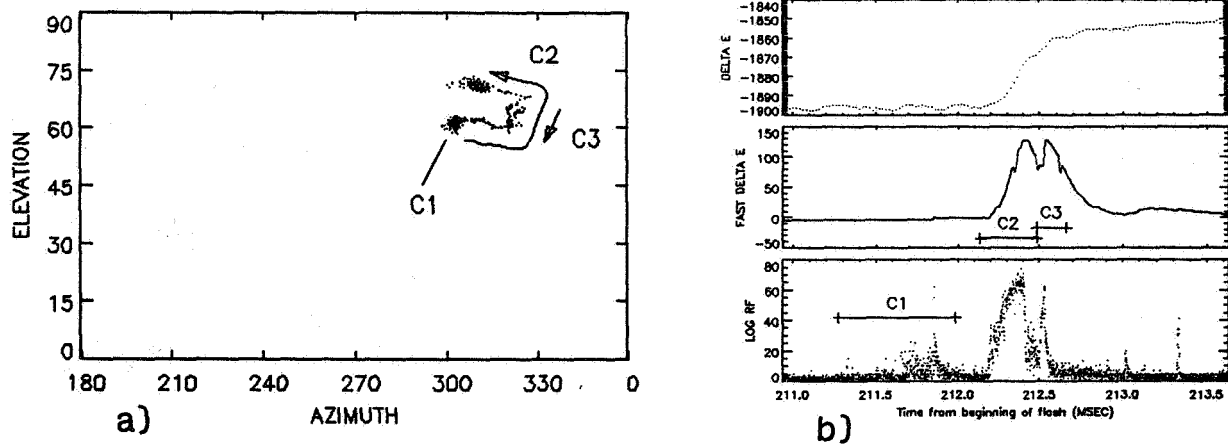


Figure 3: K-event C, 212 ms into the preliminary activity of Flash 153844.

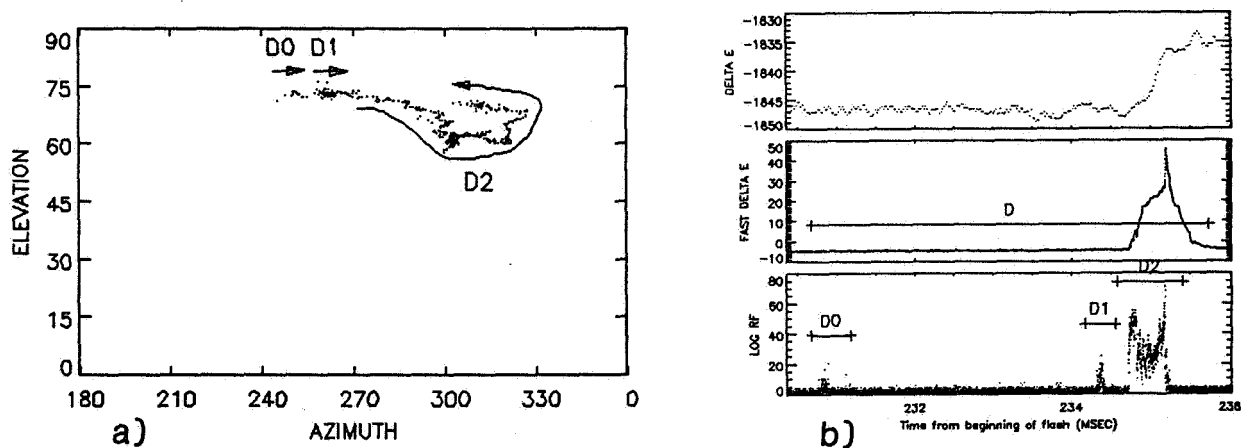


Figure 4: K-event D, 231 ms into the preliminary activity of Flash 153844.

the starting point of the final D2 streamer. D2 progressed rapidly into the flash start region and (without pause) along the full extent of the C channel. When D2 reached the end of its extent, a fast field change occurred and the radiation abruptly dropped in amplitude. The fast field change indicates that the current rapidly increased along the D channel.

Event D enables the polarity of the streamers to be clearly established. As will be seen later, the channel extension to the left of the flash start point (D0, D1, and the initial part of D2) was traversed in the same direction by negative-polarity dart leaders later in the flash. The electric field change of the dart leaders had the same polarity as the D streamers, indicating that the C and D streamers (as well as the A activity) were also of negative polarity. Knowing the polarity of the C and D streamers, the fact that each produced a positive field change implies that they progressed away from the interferometer site. The fact that the elevation angle of the streamers increased at their far end therefore indicates that they developed vertically upward in the cloud, or had an upward component. (The alternate possibility, that the elevation increase was caused by horizontal motion toward the interferometer, would have produced a field change of the opposite polarity.)

Assuming that the total length of the C streamer was 2-3 km, its velocity is inferred to have been  $1 - 1.5 \times 10^7$  m/s, several orders of magnitude greater than that of the A activity. The velocity of the D streamer was comparable to that of C.

Event D is significant for another reason. A careful analysis of the observations prior to D has shown that no radiation occurred along the channel extension established by D0, D1, and the initial part of D2.

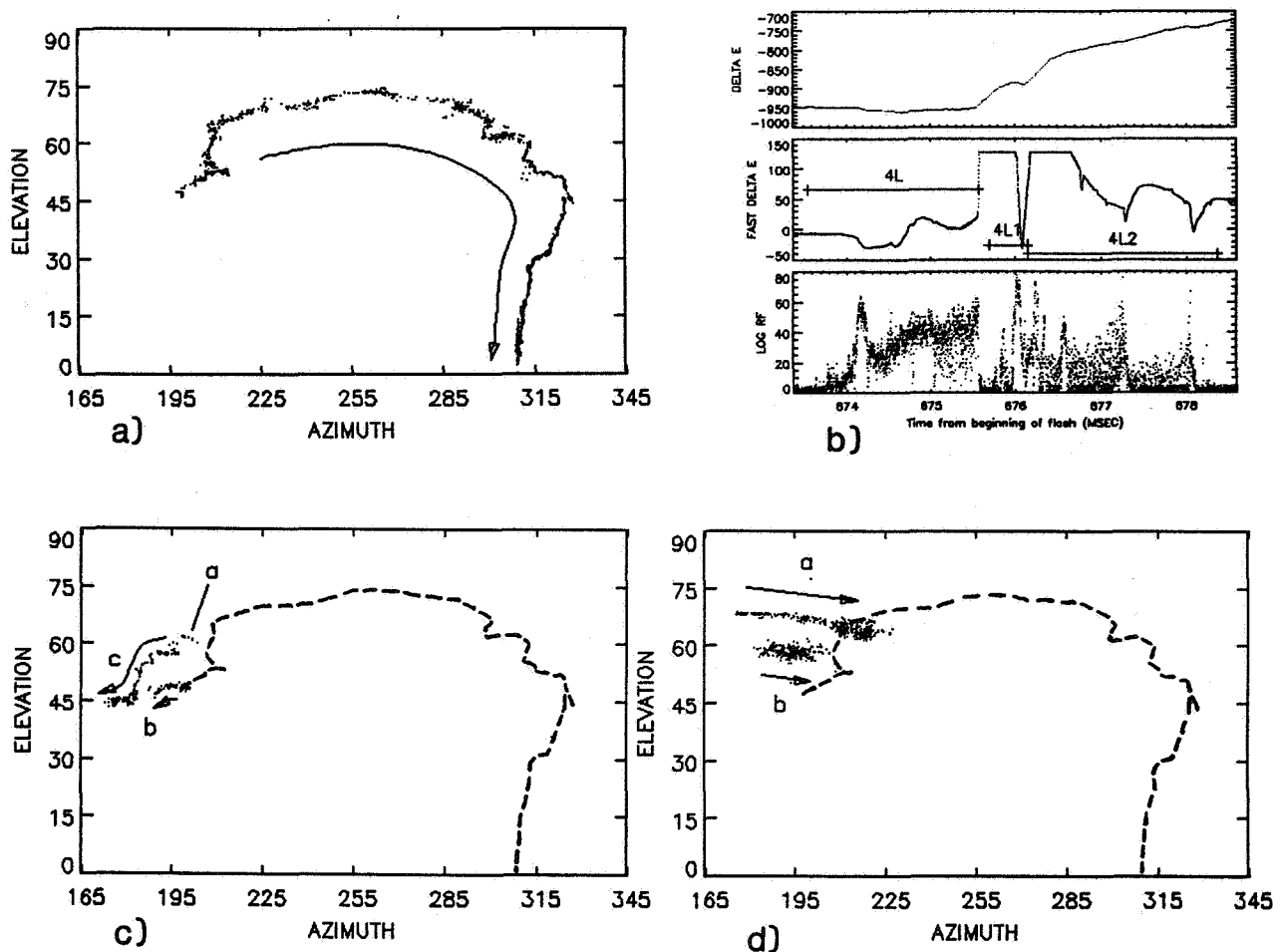


Figure 5: Results for the 4th stroke of Flash 153844. a.) Radiation sources for the dart leader; b.) time waveforms; c.) radiation sources at the end of the return stroke; d.) radiation sources following the return stroke.

The channel appeared to be extended by breakdown which began at a distance from previously-detected activity, and the extension streamer was fast even though no prior radiation was detected along the first half of its path. It is significant that several breakdown events preceded the final streamer; each appeared to enhance the local electric stress for the subsequent event.

#### DART LEADERS AND RETURN STROKES

Figure 5a shows radiation sources of a typical dart leader, in this case for the leader of the fourth stroke to ground of Flash 153844. Time waveforms for the leader are shown in Figure 5b. Dart leaders radiate strongly at their advancing tip and usually progress continuously along a well-defined channel to ground. In this instance the leader required 1.7 ms to reach ground and propagated over a substantial horizontal distance within the cloud before turning vertically downward to ground. The leader began south of the interferometer and propagated overhead and to the north, reaching a maximum elevation of about  $75^\circ$  while passing overhead. The radiation ceased at the beginning of the return stroke, whose electric field change saturated the fast field change channel.

During the return stroke the radiation remained quiet for about  $200 \mu\text{s}$ , after which time three radiation bursts occurred of increasing intensity (interval 4L1). The radiation sources for the bursts are shown in Figure 5c and progressed rapidly away from the far end of the leader channel. The field change of the final burst was strongly negative, indicating that positive charge was transported along the channels away from the interferometer. The events are therefore inferred to have been positive-type streamers and appeared to

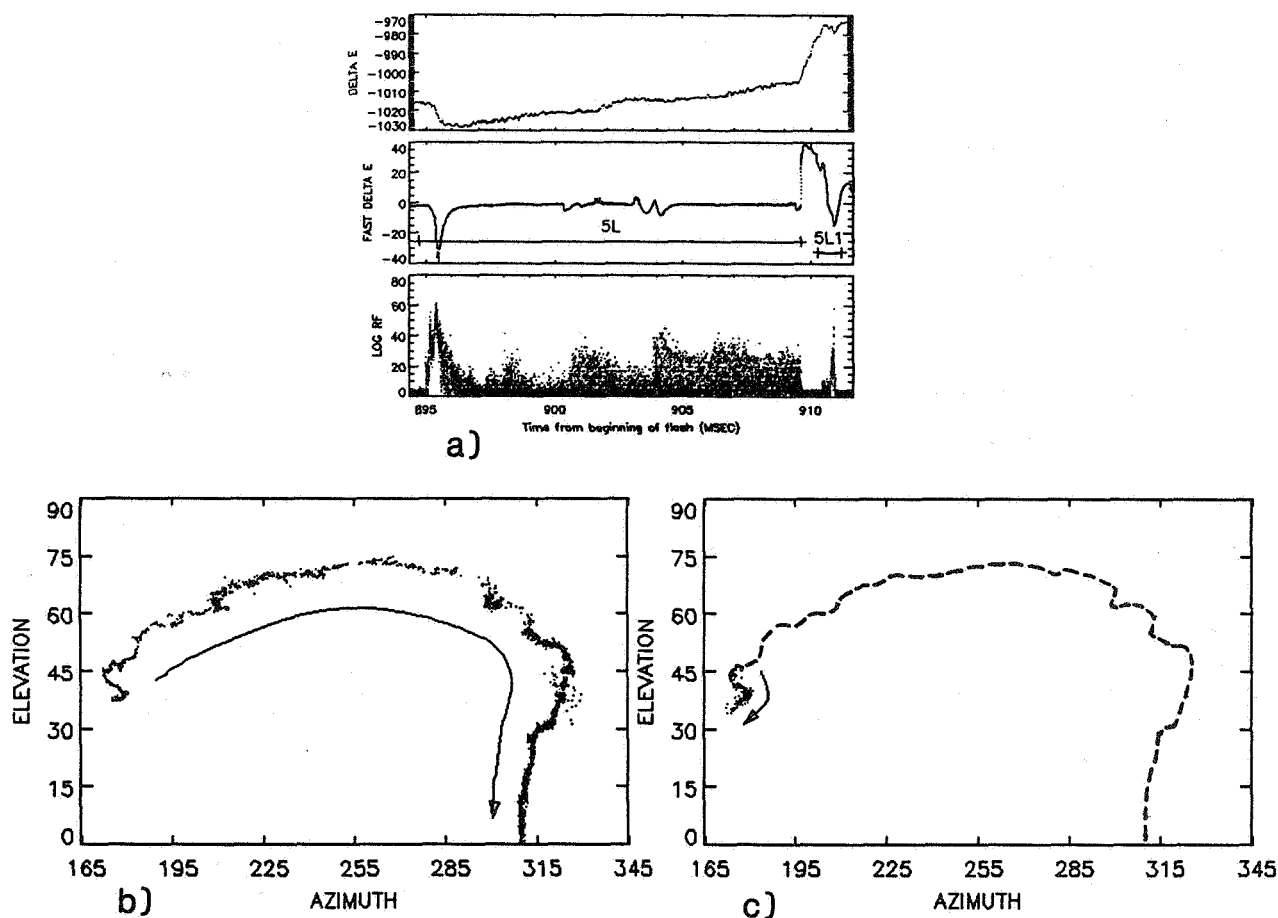


Figure 6: Results for the 5th stroke of Flash 153844. a.) Time waveforms, b.) radiation sources for the leader, c.) radiation sources at the end of the return stroke.

occur when the return stroke arrived back in the source region of the leader. Careful analysis of the activity prior to the fourth stroke indicates that no radiation occurred along the *a-c* branch or the *b* extension; therefore the streamer events appeared to create the branch and the channel extension. As we later show, the *a-c* branch was traversed by the next stroke of the flash.

Figure 5d shows radiation source locations for the remainder of the stroke (interval 4L2). For about 2 ms following the 4L1 bursts, negative-type streamers repeatedly propagated along two other branches into the channel of the dart leader and return stroke. These branches had been active during the interstroke interval between the third and fourth strokes. The electric field records of Figure 5b show that these events renewed the current flow in the channel and indicate that charge transported into the channel by the streamer events went all the way to ground. That no radiation was detected along the main channel during the return stroke or during the 4L2 events is typical and indicates that radiation is not produced by current flow along already conducting channels, but predominantly by breakdown processes.

The total length of the 4th-stroke leader is estimated to have been about 20 km, and the average speed of the leader as about  $1\text{--}1.5 \times 10^7$  m/s. This is similar to the speeds of the K-streamers. The return stroke is estimated to have taken 200  $\mu$ s to travel back along the channel (equal to the duration of the quiet period), and therefore travelled at a speed of about  $1 \times 10^8$  m/s.

Figure 6 shows results for the fifth and final stroke of Flash 153844. The leader for the stroke was initiated 220 ms after the fourth stroke and took a relatively long time to progress to ground (14 ms). The leader travelled rapidly (about  $10^7$  m/s) until reaching its approximate mid-point, close to the highest elevation angle, and then progressed more slowly (less than  $10^6$  m/s) to ground. The initial segment was along the *a-c* branch established at the end of the fourth stroke; this channel was retraced and extended

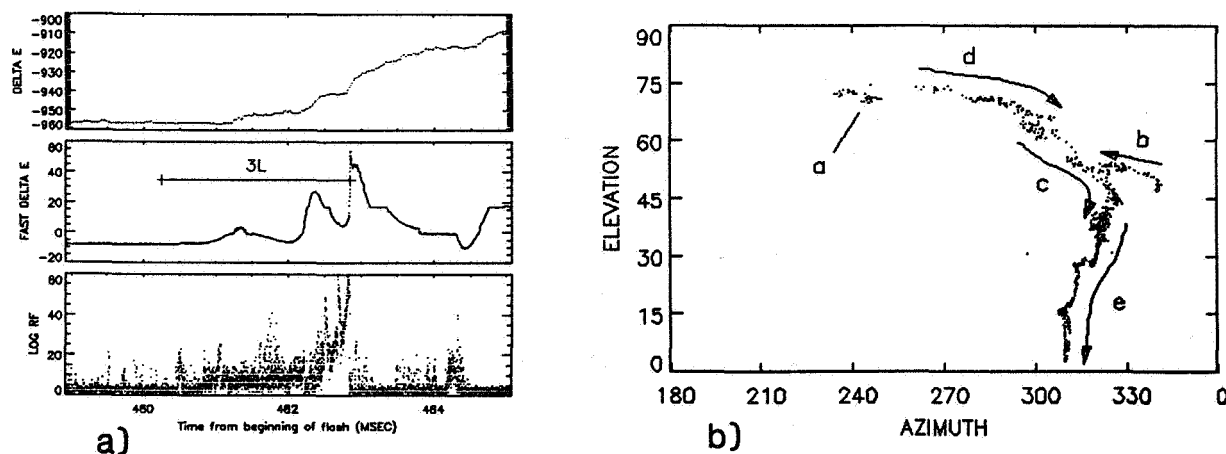


Figure 7: Results for the 3rd stroke of Flash 153844, which initiated a continuing current. a.) Time waveforms, b.) radiation sources for the leader.

numerous times during the intervening interstroke interval. The return stroke was less intense than the fourth stroke and did not saturate the electric field records. It was accompanied by a quiet period of about 1 ms duration in the radiation waveform, and then by a single burst of radiation back in the leader source region. As during the fourth stroke, the radiation sources of the burst progressed away from the source region of the leader and produced a field change indicative of a positive streamer. Assuming that the streamer was initiated by the arrival of the return stroke back in the source region, the speed of the return stroke was about  $2 \times 10^7$  m/s, a factor of five slower than the speed of the previous, more energetic stroke.

Figure 7 shows results for the leader of the third stroke of Flash 153844, which initiated a continuing current discharge to ground. The leader lasted about 2 ms and was comprised of an unusually complex sequence of breakdown events. The time sequence of the events is as indicated in the figure. Upon contacting ground, the radiation decreased in amplitude but, unlike the later strokes, did not become quiet. Rather, it radiated intermittently during the beginning of the return stroke, from successively higher points along the channel as the upward-moving return stroke encountered apparent branch points on the channel. Several M-type events occurred during the continuing current, the first of which can be seen just after 484 ms in Figure 7a. Radiation from this M-event began at a distance to the right of the right-hand branch and progressed into the branch, indicating that this was the charge source for the increased current flow to ground. Later M-events originated from the far end of the left-hand branch. The continuing current was therefore supplied with charge along both leader branches. Branching or leader complexity is not a necessary component of continuing current discharges, however, as a continuing current event during Flash 155325 was initiated by a simple dart leader.

Figure 8 shows results for one of the dart leaders of Flash 155325 and illustrates another type of post-leader radiation that was observed in several strokes of that flash. In particular, the radiation dropped abruptly in amplitude at the beginning of the return stroke but otherwise continued through the time of the return stroke, uninterrupted by quiet periods. After the leader reached ground, the radiation source switched immediately to region *a* to the left of the top of the leader. 150  $\mu$ s later, at about 100.9 ms, two larger-amplitude bursts occurred at the top of the leader channel (*b*) that signified the arrival of the return stroke at this location. (The time delay corresponds to a return stroke velocity of about  $0.5 - 1 \times 10^8$  m/s.) Because the *a* radiation preceded the arrival of the return stroke at the top of the channel and was smaller in amplitude than the final leader radiation, it appeared to be produced by breakdown that was concurrent with the leader and that was revealed only when the stronger radiation of the descending leader was extinguished. No direction of progression or charge transfer could be determined for the *a* activity, as the source locations were dominated by scatter and the fast electric field record had saturated. The *a* branch became the path of the leader for the next stroke of the flash; this is similar to results obtained for the stroke of Figure 5 with the difference in this case that the path was established as part of the leader activity, rather than by the return stroke.

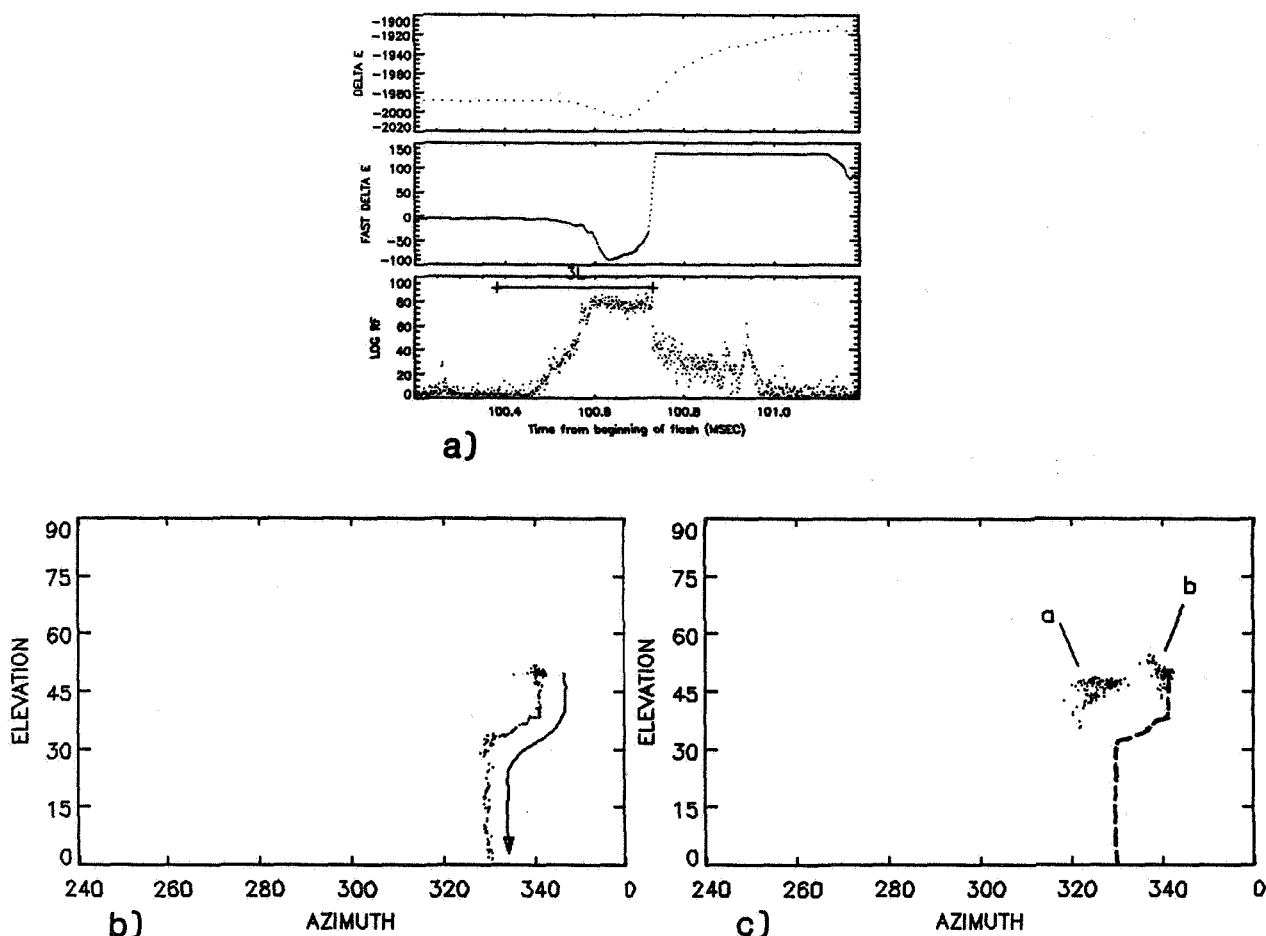


Figure 8: Results for the leader and return stroke of the 3rd stroke of Flash 155325. a.) Time waveforms, b.) radiation sources for the leader, c.) post-leader radiation sources.

#### INITIAL LEADER AND RETURN STROKE

Figure 9 shows time waveforms and radiation source locations for the initial leader to ground of Flash 153844. The total duration of the leader was 50 ms. The leader began abruptly with intense and localized bursts of radiation that began in the start region S and progressed slowly but steadily away from the start region along a relatively well-defined channel. As in the initial breakdown of Figure 2a, the extent or motion of the sources during a given burst was unresolved by the interferometer. About halfway through the leader, when the sources had moved down to about 30° elevation, the bursts increased in frequency and the radiation became continuous and more widespread. The radiation continued in this manner, increasing in intensity until reaching ground. The increased width of the channel below 30° elevation is indicative of branching; this is confirmed by results for the subsequent strokes of the flash, whose dart leaders delineated several slightly different branches along the lower channel to ground.

Superimposed on the main leader activity were a number of fast streamers that progressed into the leader start region, as shown in Figure 9b. The occurrence of these events can be seen in a time plot of the phase data, shown in Figure 9c. The streamers funneled negative charge into the developing leader along several channels that were established during the preceding intracloud activity.

The average speed of progression of the initial leader to ground is estimated to have been about  $1.5 \times 10^6$  m/s. It is not known when the leader became stepped, as the electrostatic component of the field change dominated over the radiation component due to the close proximity of the flash. Waveforms similar to those of Figure 9 are obtained for the initial leaders of other flashes (e.g. Rhodes and Krehbiel [1989]).

Figure 10 shows expanded time waveforms and source locations for a 2 ms time interval at the end



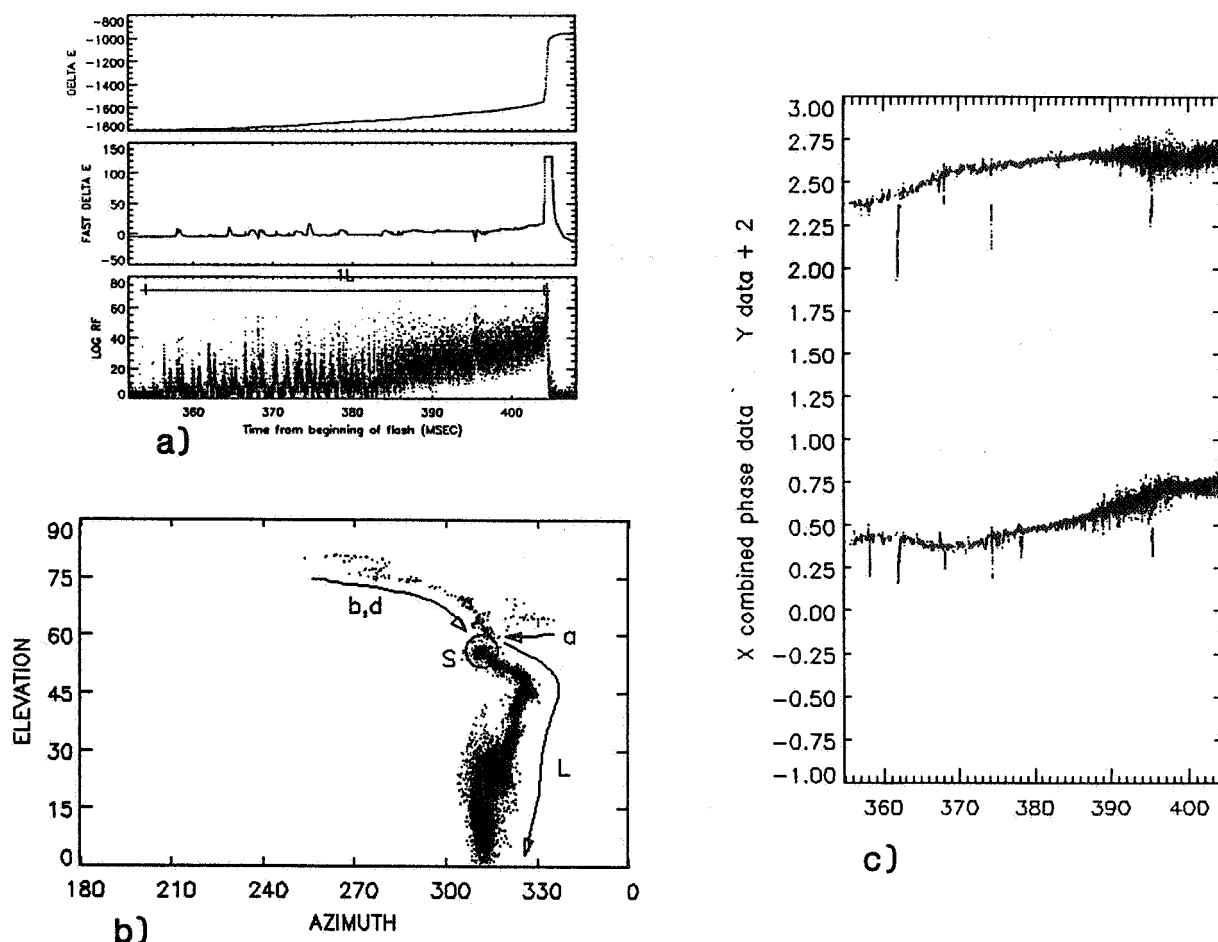


Figure 9: Results for the initial leader to ground of Flash 153844. a.) Time waveforms; b.) radiation source locations; c.) phase data vs. time.

of the initial leader through the time of the return stroke. The return stroke field change lasted about 0.6–0.7 ms and had several components. At its beginning, the fast field record shows the occurrence of a 20  $\mu$ s precursor change, indicative of an upward-moving streamer that completed the connection to ground. The ensuing return stroke quickly saturated the fast field change record, but, as seen on the less-sensitive slow field change record, produced only a small electrostatic field change. A larger stroke occurred 200  $\mu$ s later, simultaneous with a noticeable increase in the radiation intensity.

At the onset of the return stroke, the radiation amplitude did not change significantly from that of the leader but the source locations indicate that a sequence of two upward-moving events (*b* and *c*) occurred along the lower part of the channel. These are seen just after 404.1 ms in the elevation–time plot of Figure 10c, and initiated the small-amplitude initial return stroke. The larger-amplitude stroke just after 404.3 ms was accompanied by even stronger radiation that also moved rapidly up the lower part of the channel (*d*). The radiation moved up to about 30° elevation in about 100  $\mu$ s; after this it abruptly switched to higher elevation and progressed backward along the right-hand feeder channel of the leader (*e*, *f*). No radiation was detected along the unbranched upper half of the leader channel. The concentrated sources labelled *a* at the bottom of the channel in Figure 10b were produced at the end of the leader; no source motion was detected during the final connection event.

#### A NEW TYPE OF HYBRID LEADER EVENT

Figure 11 shows results obtained for the leader of the 6th stroke of Flash 155325. The static electric field change for this leader resembled that of a second initial-type leader along a new channel to ground, in

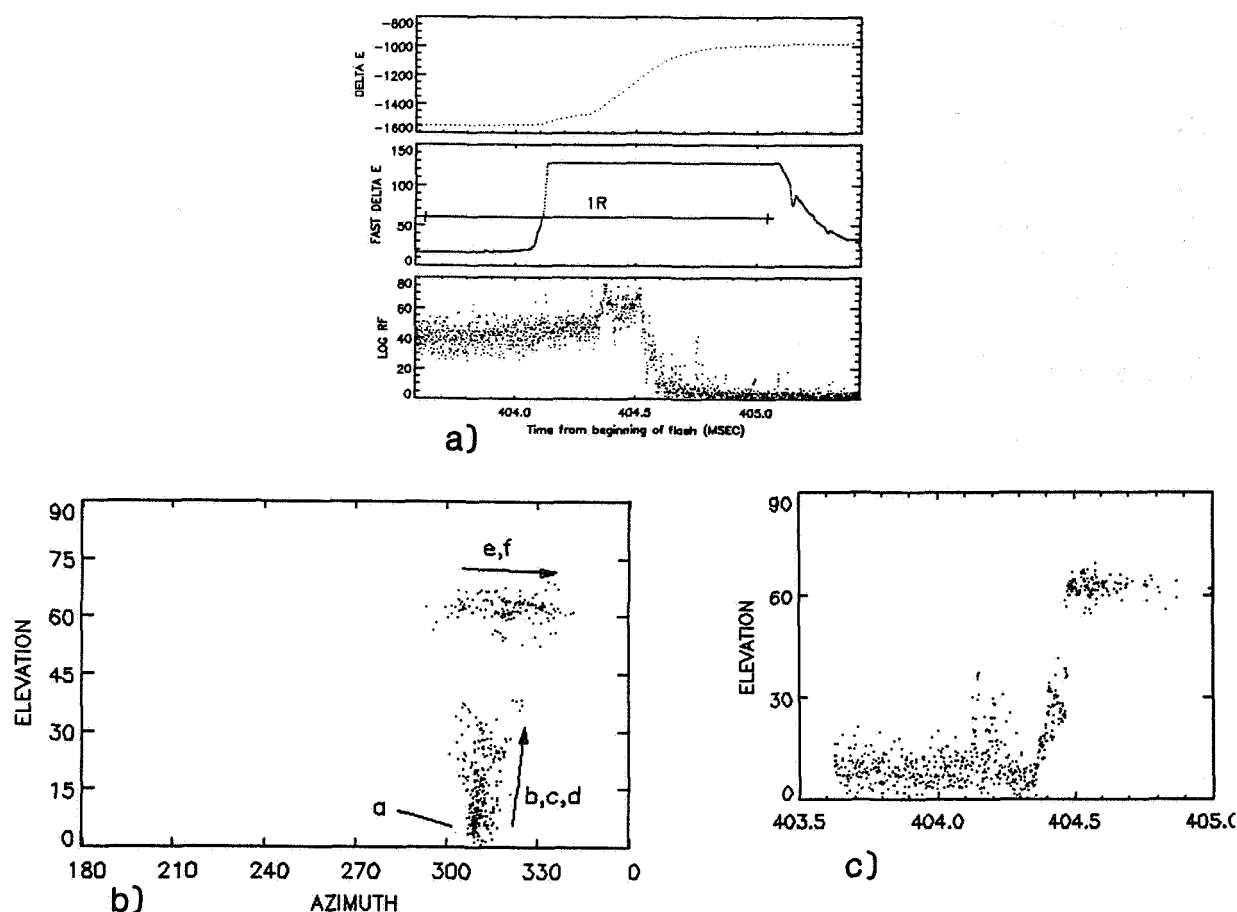


Figure 10: Radiation sources during the initial return stroke of Flash 153844: a.) Time waveforms, b.) radiation source locations, c.) elevation angle vs. time.

that it was long in duration and increasingly negative leading up to the return stroke (Figure 11a). But the radiation sources for the event show that it was a totally different and new type of phenomenon (Figure 11b). In particular, widespread, continuous radiation began at a low elevation angle in the direction of the previous channels to ground and progressed slowly and continuously toward and past the interferometer along an apparently horizontal path. The sign of the electric field change indicates that the breakdown transported negative charge in its direction of progression, i.e. that it was negative-type breakdown.

After about 60 ms, a dart leader originated back in the source region of the slow breakdown and progressed rapidly in the opposite direction to ground. The dart leader and stroke were also of negative polarity, therefore both the slow activity and the dart leader/stroke transported negative charge away from their common source region. We speculate that the slow moving radiation was produced by the highly-branched and slow-moving 'finger' type discharges that are sometimes observed to propagate horizontally through the base of older storm complexes. Further study is required for a better understanding of this hybrid phenomenon.

## SUMMARY AND DISCUSSION

VHF radiation from lightning typically occurs in bursts and can be classified as falling into one of two categories: a) that produced by fast-moving streamer events which propagate along well-defined channels during a given burst, at typical velocities of about  $10^7$  m/s, but sometimes down to  $\sim 10^6$  m/s, and b) localized, intense radiation whose motion within a burst is not resolved but whose centroid moves slowly from burst to burst. In both cases, the breakdown is predominantly negative, i.e. negative charge

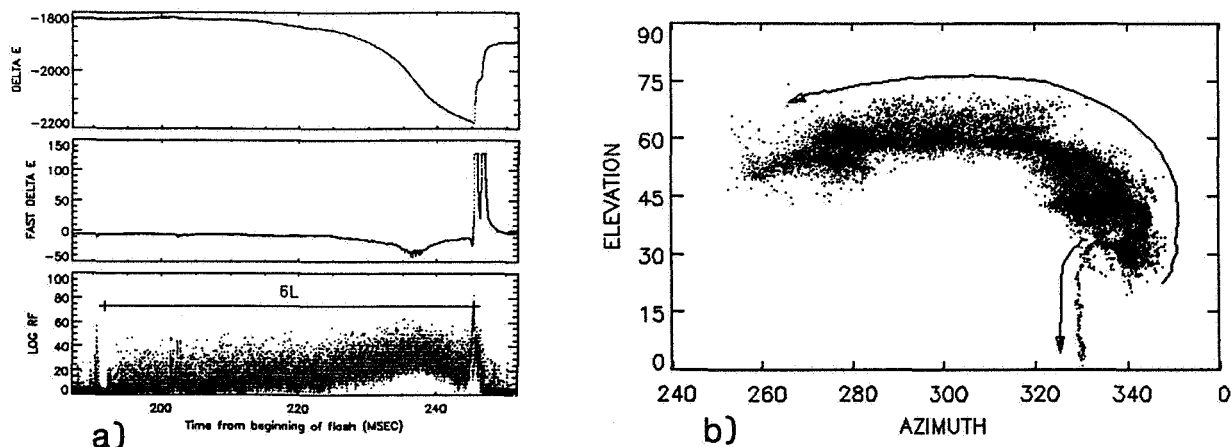


Figure 11: Results for the leader of the 6th stroke of Flash 155325: a.) Time waveforms, b.) radiation source locations.

is transported in the direction of progression; in agreement with the results of other studies (e.g. Proctor [1981, 1988], Richard et al. [1985]). Radiation is sometimes observed from positive breakdown events, however, as discussed later.

Fast-moving streamers are a feature both of in-cloud 'K' events and of dart leaders to ground, and appear to be the same process in both instances. Some K-events are terminated by fast field changes (Figure 4), which indicate a rapid increase in current along the streamer channel and are analogous to the return stroke initiated by a dart leader. Many K-streamers do not produce a fast field change, however, but simply die out after traveling some distance. Although not shown in this paper, aborted dart-type events are observed which also die out before reaching ground (Figure 8, Richard et al. [1986]; Rhodes [1989]). This essentially eliminates any distinction between the dart- and K-type events.

Localized, slow-moving radiation is observed during the initial breakdown of a flash and during initial leaders to ground (Figures 2 and 9, respectively). In these instances the speed of progression is on the order of  $10^5$  m/s. During initial leaders the radiation often becomes more widespread with time, indicating the occurrence of branching. A new type of hybrid breakdown event has been identified which resembles an initial-type leader in that the radiation sources are slow-moving and widespread, but which progresses horizontally within the storm and is observed to spawn a dart leader in the opposite direction to ground (Figure 11).

Several types of radiating events are observed during and after return strokes. For initial strokes, the radiation is observed to *increase* in amplitude during the return stroke and to progress rapidly up the lower part of the channel, either in one well-defined event or, in more complex situations, as a sequence of several upward-propagating events (Figure 10). Radiation later in the return stroke is observed from or beyond the source region of the leader.

For strokes initiated by dart leaders, the radiation is observed usually to *decrease* in amplitude when the leader ends and the return stroke begins. Often there is a quiet period of little or no radiation during the return stroke, as has been noted by other investigators (e.g. Hayenga, [1984]; Richard et al. [1986]). The quiet period is terminated by a burst or bursts of radiation back in the source region of the leader. Two types of post-quiet period bursts have been identified: those which travel away from the top end of the leader channel and those which travel into it. The former appear to be launched when the return stroke arrives at the upper end of the channel. From their direction of propagation and from the sign of their electric field change, these appear to be positive-type streamers. The streamers are fast and extend the channel or develop new branches that are sometimes followed by the leaders of subsequent strokes (Figure 5c). Bursts which travel into the top end of the leader channel do so as negative streamers that appear to renew the current flow along the entire channel to ground (Figure 5d).

Other strokes initiated by dart leaders do not have a quiet period during the return stroke. In these instances, also noted by Takagi [1969] and Hayenga [1984], the radiation continues with decreased amplitude

after the leader contacts ground (Figure 8). The radiation occurs from breakdown adjacent to the leader source region. Because the radiation is continuous and precedes the arrival of the return stroke back in the source region, it is likely that it is from breakdown that developed simultaneous with the leader and that is revealed only when the stronger radiation from the descending leader tip is extinguished. The polarity of the breakdown has not been established, but the breakdown appears to establish new channels or branches followed by subsequent activity. Delayed radiation is also observed which is associated with the arrival of the return stroke back in the source region of the leader.

Finally, radiation is sometimes observed which moves up the channel to ground during return strokes initiated by dart leaders (Rhodes [1989], Figure 7). In this instance, the radiation occurred at apparent branch points along the lower to middle part of the channel as the return stroke reached the branch points.

We turn now to a discussion of how new channels develop and extend during intracloud activity, prior to the occurrence of cloud-to-ground strokes. This happens either as a result of slow-moving negative breakdown, as in Figure 2, or in a retrograde manner by negative streamers which begin at a distance from previously detected activity (Figure 4). The retrograde streamers are observed to propagate at a fast speed ( $10^7$  m/s) even though no radiation has been detected along the extension path. This leads to the question whether the streamers have been preceded by other breakdown which was not detected – in particular by a positive streamer or streamers which propagated *away* from the earlier (negative) activity. The existence of such streamers has been proposed by Mazur [1989a] on the basis of gaps observed in the development of extensive intracloud discharges by Richard et al. [1985], and on the basis of observations of bi-directional breakdown in aircraft-triggered lightning. Mazur proposed that the disconnected, retrograde negative streamers were recoil events along the channels of VHF-invisible positive streamers that develop as part of a bi-directional breakdown process.

Other than the speed of the streamer, there is no indication that the D extensions of Figure 4 followed the path of invisible positive breakdown. Several points argue against the invisible streamer hypothesis. The first is that the extending D streamer required three breakdown attempts to get started. If it were a recoil event along a positive streamer channel it might be expected that one of the earlier attempts at the recoil would have been successful. Rather, the observed sequence of events behaved more like the local triggering of breakdown in enhanced fields generated at a distance from the prior activity. Second, positive streamers appear to be observed at other stages of a flash, as described earlier, that do radiate. This leads one to question the assumption that positive streamers in virgin air would be invisible at VHF. In the case of K-changes and dart leaders, it is the initiating (negative) streamer that radiates and the recoil (positive) event that does not radiate.

Event A2 of Figure 2 provides a possible example of a different kind of non-radiating positive streamer. For 1.5 ms between the initial and final radiation bursts of this event, the electric field increased steadily as if positive charge were being transported toward the interferometer site, but little or no radiation was produced. Then a final radiation burst occurred from negative breakdown which propagated away from the interferometer. This suggests sequential bi-directional breakdown away from the initial A2 burst location that is analogous to case 2) of aircraft-triggered lightning in the study by Mazur [1989b]. If this explains the observations, it is likely that the positive streamer progressed along the path established by the preceding A1 activity. The lack of radiation is then explained as being due to the existence of prior breakdown along the positive streamer path.

The streamer events of Figure 5c and Figure 6c are examples of (rapid) positive streamers that radiate and have not been preceded by detected breakdown. Positive streamers also occur at the beginning of rocket-triggered lightning (e.g. Laroche et al.; Nakamura et al.; this conference) that are not preceded by other breakdown, and it should be relatively easy to determine if these radiate detectably.

## REFERENCES

1. Hayenga, C. O., Positions and movement of VHF lightning sources determined with microsecond resolution by interferometry, *Ph.D. Thesis, Univ. of Colo., Boulder*, 1979.
2. Hayenga, C. O., Characteristics of lightning VHF radiation near the time of return strokes, *J. Geophys. Res.* 89, 1403-1410, 1984.

3. Krehbiel, P. R., M. Brook and R. A. McCrory, An analysis of the charge structure of lightning discharge to ground, *J. Geophys. Res.* 84, 2432-2456, 1979.
4. Laroche, P., V. Idone, A. Eybert-Berard and L. Barret, Observations of bidirectional leader development in triggered lightning flash, this conference.
5. Mazur, V., Triggered lightning strikes to aircraft and natural intracloud discharges, *J. Geophys. Res.* 94, 3311-3325, 1989a.
6. Mazur, V., A physical model of lightning initiation on aircraft in thunderstorms, *J. Geophys. Res.* 94, 3326-3340, 1989b.
7. Nakamura, K., A. Wade and K. Horii, Discussions of a long gap discharge to a transmission tower by a rocket triggered lightning experiment, this conference.
8. Proctor, D. E., VHF radio pictures of cloud flashes, *J. Geophys. Res.* 86, 4041-4071, 1981.
9. Proctor, D. E., R. Uytendogaardt and B. M. Meredith, VHF radio pictures of lightning flashes to ground, *J. Geophys. Res.* 93, 12,683-12,727, 1988.
10. Rhodes, C. T., Interferometric observations of VHF radiation from lightning, *Ph.D. Thesis, New Mexico Institute of Mining and Technology, Socorro*, 1989.
11. Rhodes, C. T. and P. R. Krehbiel, Interferometric observations of a single stroke cloud-to-ground flash, *Geophys. Res. Letters* 16, 1169-1172, 1989.
12. Richard, P. and G. Auffray, VHF-UHF interferometric measurements applications of lightning discharge mapping, *Radio Science*, 20 2, 171-192, 1985.
13. Richard, P., J. Appel, and F. Broutet, A three-dimensional interferometric imaging system for the spatial characterization of lightning discharges, *Proceedings, 10th International Aerospace and Ground Conference on Lightning and static Electricity*, Paris, France, 1985.
14. Richard, P., A. Delannoy, G. Labaune and P. Laroche, Results of spatial and temporal characterization of the VHF-UHF radiation of lightning, *J. Geophys. Res.* 91, 1248-1260, 1986.
15. Takagi, M., VHF radiation from ground discharges, *Proc. Res. Inst. Atmos. Nagoya*, 16, 163-168, 1969.

## THE PHYSICS OF THE OSCILLATING LIGHTNING

Per B. Storebø  
Norwegian Defence Research Establishment  
N-2007 Kjeller, Norway

## ABSTRACT

The lightning is proposed to start in a limited region of electric break-down field. A growing charge pool in a cumulonimbus cloud is likely to produce such a field in its outer layers. When the field is not aligned with the potential surfaces, the electric force pushes positive charge in one direction and negative in the opposite. Self-inductance develops and an embryo open electric circuit is born. Oscillations swiftly grow in strength when potential energy of the cloud is released. The channel extends in steps during those cycle-stages where charge is crammed into the channel terminals.

Electro-static consequences of a narrow conductor among the cloud charges are computed. The conductor is charged by influence to such a degree that the charge is bound to leak out to the ambient air and appear as a charge sheath some distance off the channel. Ample energy is released to sustain the oscillations. The period increases with channel length and agrees well with observed time between steps.

A ground strike leads to a shock-pulse travelling up the channel.

## INTRODUCTION

The start location of a lightning event is within a cumulonimbus cloud and therefore out of sight. The highly visible event, particularly during the night, is the final stage. That stage has been intensely studied by various photographic means. Electrostatic and electrodynamical instruments observe the lightning as an entity from some distance. The total description gathered lacks some detail and is felt to be puzzling in many respects.

A model for the phenomenon should obviously lead to lightning characteristics identical to those observed. The more important characteristics are the following:

- Before the lightning event the electric charges are on cloud droplets or in the air, i. e. on isolators. The lightning collects charge in a fraction of a second.
- The channel extends in steps of the order of 50 m over about 1  $\mu$ s. It apparently "rests" for some 50  $\mu$ s inbetween. The whole channel is visible when a new step takes place. It seems to become extinct inbetween.
- The return stroke shows up as a light pulse travelling upwards along the channel. Later strokes are light pulses as well,

going down and then up the channel.

- The electric current is more pronounced in the return stroke than in the stepped leader. Electric field changes associated with the lightning last longer than the visible lightning.

It is the purpose of this paper to point out that the characteristics above are those of a progressing aerial conductor undergoing free electric oscillations. Some electro-static consequences of such a conductor among the cloud charges must first be considered.

### ELECTROSTATIC CONSIDERATIONS

The cumulonimbus cloud is highly charged. Tens of coulombs of positive charge are present in the upper part and tens of coulombs of negative charge in the lower part, where a smaller amount of positive charge may also be found. If a vertical rod-shaped conductor is introduced in such a cloud, a radical redistribution of the rod charge takes place.

The fundamental requirement for a conductor is a common potential all over its surface. The common potential is achieved by a distribution of charge over the surface. Ambient potential deviations are locally balanced by the surface charge.

Charge and potential are connected. Let the mean ground potential be zero and the relative potential be called voltage. If the ground is considered to be a perfect conductor, a charge element  $\Delta Q$  causes a voltage increment  $\Delta U$  at a point in space

$$\Delta U = \Delta Q \cdot (1/e_1 - 1/e_2) / \epsilon \quad (1)$$

The equation is based on the model of a charge combined with a negative mirror charge below the ground, where  $e_1$  and  $e_2$  are the distances between the point and the two charge elements in question, while  $\epsilon$  is the permittivity of air. In order to find the voltage at a given point, the increments may be added for the whole charge distribution.

In a computer model the cloud electricity has been replaced by two charge pools shaped as cylinders. The charge in a pool has even density. A lower pool between 3 and 5.5 km height has radius 2.5 km and charge -20 C. An upper one between 8.5 and 11 km has radius 1.5 km and charge +10 C. The conductor is represented by surface-charges on a tube with radius 200 m; the height of the charge-terminals may be chosen at will. The tube has no net charge, but whenever it intersects the charge pools, the core charge is moved radially out to its surface. The cylinders and the tube have a common axis. The horizontal resolution is variable, but less than 250 m. The vertical one is 100 m.

The charge on the conductor surface cannot be found analytically, but it may be approximated by iteration. The iteration requirement is a common voltage for the tube axis. It is achieved by shifting charge along the tube. The total amount of positive charge must be equal to the total amount of

negative charge; this demand is sufficient to establish the value of the common axis voltage.

The voltage along the system axis is shown in figure 1 for different tube configurations. Wherever it is positioned, the tube-shaped charges have a pronounced effect on the voltage distribution. The common voltage established along the axis appears to be close to the mean value of the original distribution between the terminals.

When charge distribution and voltage distribution are known, the potential energy may be computed. If a charge on the ground is given zero energy, the potential energy  $W$  of the system is

$$W = \Sigma(0.5 \cdot \Delta Q \cdot U) \quad (2)$$

For the tubes with an upper terminal at 8.5 km, the system energy is plotted in figure 2 as a function of height of the lower terminal. When the tube charges are introduced, the energy is reduced from that represented by the cloud charges. This is also true for the tubes 3-5.5 and 8.5-11 km, where energies are 19.7 and 19.9 GJ respectively. The reduction increases with increased length of the tube, although the increment appears to be marginal for tube extensions outside the cloud charges.

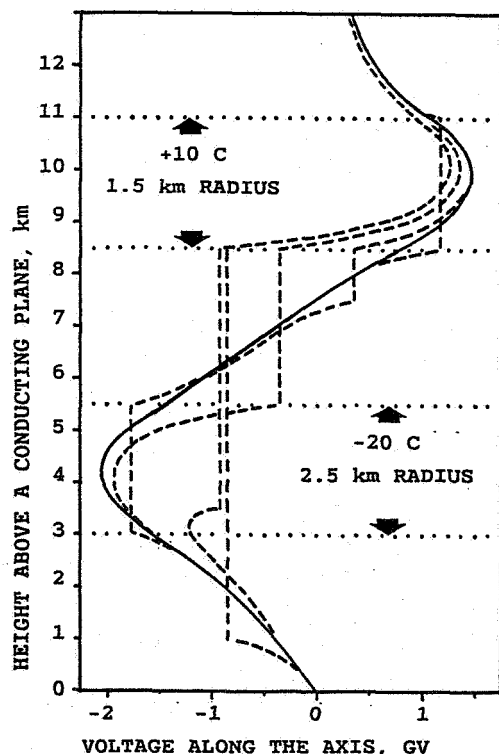


Fig. 1. Voltages in the Model  
The solid curve is the voltage for the cloud charges only, the dashed curves when additional tube-shaped charges are present. Radius 200 m. Various end points.

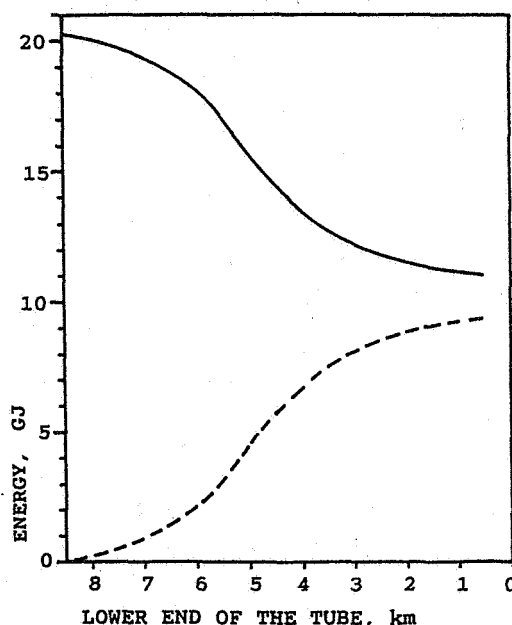


Fig. 2. Energy of the Configurations  
Upper tube end 8.5 km.  
Solid curve: Potential energy.  
Dashed curve: The energy released by introducing tube charges.



The energy deficit represents an energy conversion. If the tube is envisaged as a lightning channel, the released energy is dissipated or is available for further channel progression. The converted energy is plotted in figure 2 as well.

The vertical field at the ground is another quantity of interest. In the computer model it is only available as a mean for the lowest 100 m, and it is plotted in figure 3. One curve is drawn for the base of the axis, the other close to the outer cloud limit. The field is strongest in the central part, and it is very much influenced by tube charges close to the ground.

The charge distribution along the tube is plotted in figure 4. Within the cloud the extreme sections carry very large charges compared with the next ones. It is certainly qualitatively correct, but the vertical resolution is not good enough to bring about quantitative accuracy. A better resolution would undoubtedly give higher absolute values for the charge in the terminals.

The charges are nevertheless very high. At 9 km height the break-down field of air might be about 1 MV/m. For an infinitely long cylinder with a linear charge density of 20 mC/m, the field strength drops below this value at a distance of 360 m. The computer model is consequently artificial. If the charge distribution were ever brought into existence, ions would achieve ionization energy between collisions with neutral molecules. They would multiply, and an exchange of charge between cloud and tube would take place.

The tube charges in the lower terminal are lower, and the highest positive charge density corresponds to about 200 m radius for the breakdown region.

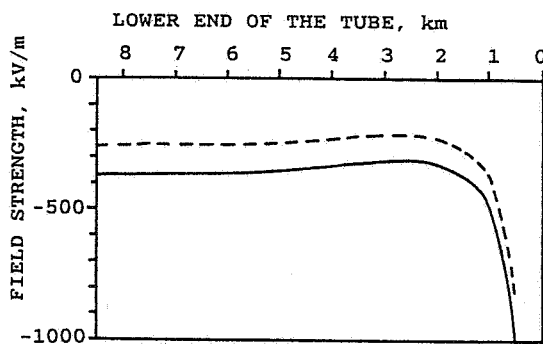


Fig. 3. Ground Voltage Gradient  
Solid curve: At the axis base.  
Dashed curve: 2.5 km off-base.  
Upper tube end at 8.5 km.

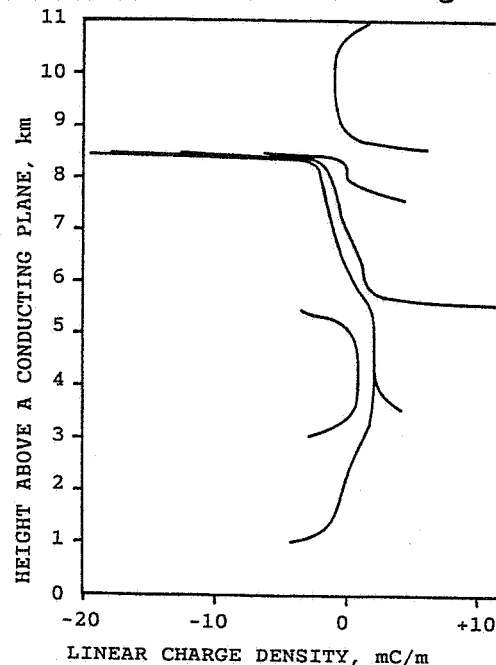


Fig. 4. Tube Charge Distribution  
Distributions corresponding to all the tubes in figure 1 are shown.

In the middle part of a long tube the computed charge-densities seldom give break-down radii greater than a few tens of meters. These charges are consequently able to remain on the surface.

The general conclusions in this section are meant to be used for the lightning phenomenon, but some caution must be applied. The computer-results depend very much on the charge configuration in the cloud, both on the quantities and on the positions in space. Some runs with a more impressive positive charge pool show a positive axis voltage when the terminal approaches the ground.

#### INITIATION OF A LIGHTNING

The charge generation in a cumulonimbus will not be discussed here. Charge pools of the order of tens of coulombs are formed. After a lightning event the charge lost may be replenished over some 20 s in a mature cloud. The charge build-up appears to be fast.

In an isolated and symmetric spherical pool with charge  $Q$  and radius  $r$ , the field  $E$  at the surface is

$$E = Q/4\pi r^2 \epsilon \quad (3)$$

The charge will in general build up as  $r^3$ , and the surface field should therefore increase and eventually surpass the break-down limit of some 1 MV/m. The configuration in a cloud is never ideal, and deviations from a radial field is the rule. The break-down field should therefore initially be surpassed over a limited region only, and the region is not likely to be aligned along equi-potential surfaces. A tilted electric field pushes positive charge into one end and negative charge into the other end of the region. Self-inductance leads to more separation than called for in the situation; a voltage drop develops in the opposite direction, and charge is pushed back. An embryo oscillating circuit has been brought into existence.

The air is heated to some sort of plasma. The outer plasma parts are exposed to cooling and recombinations, and the oscillating charges are likely to find a best path with low resistivity in the core part of the breakdown region: The electricity flow consequently contracts to a current in a narrow channel.

The channel is a conductor among the cloud charges. It is not the sturdy tube considered in the computer model, but the effect must be similar. The high charges formed by influence, most pronounced for the terminals, cause break-down fields exceeding by far the trigger-off field. Charge is immediately transferred to the very limit of the field, and the final result is a new configuration with charge neutralized in the cloud pool, but appearing anew, at a different place, as a charge sheath surrounding the channel. A common mean voltage for the channel is achieved by the sheath charges, not by charges in the channel proper.

The concept of a charge sheath led to the formulation of the computer model discussed in the electro-static section. The oscillations are not affected

by a shift of static charge from the channel to a surrounding sheath.

### THE STEPPED CHANNEL EXTENSIONS

The oscillation current is started by a potential difference between the terminals. It over-shoots because the current builds up self-inductance. And charge jammed in a terminal creates break-down field in the channel extension. The charge is then likely to proceed beyond the limit reached in the previous oscillation. The field is best aligned when the terminal charge is of the same type as that in the sheath, and those extensions should be most robust. The twisted shape of a channel may be caused by the more uncertain field of opposite charges, which occurs in every second step. Because the channel extends in a field of its own making, the direction of a new step may only be slightly affected by the original static field.

The channel lengthening is an involved electric phenomenon tied up with protuberances of an advancing tip. In this stage the current works against an increasing counter-potential, and the excess charge diminishes. The progress stops when the break-down field disappears.

A conductor extension requires a new "static" voltage pattern. It can only be established by way of the channel: In order to cope with the new configuration, a balance current shifts charge along the channel. The event is illustrated in figure 5. The charge brought into the terminal creates a general break-down field and immediately takes up a more permanent position as a charge sheath extension in the surrounding air.

The adjusted charge distribution has less potential energy than the old one, and the released energy is fed right into the channel by the balance current. The current is actually a pulse spanning over the extension time only. The sequence of pulses is synchronized with the oscillations. When the

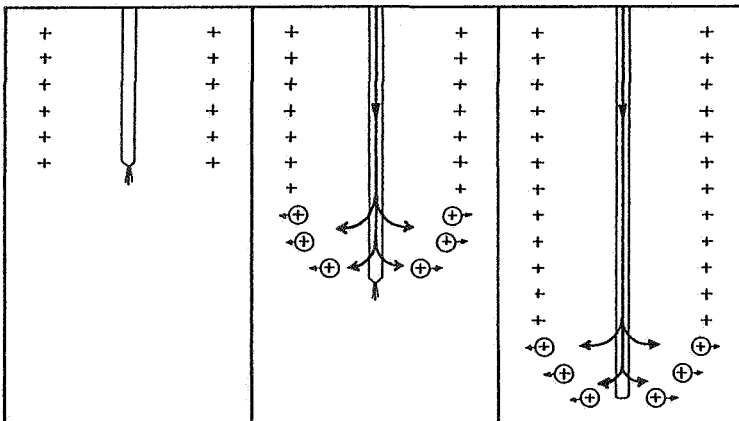


Fig. 5. The Charge Sheath Extension

The individual drawings show the initial, medium and final stages of a step. The balance current is indicated by the heavy curve with arrows. The charge elements are shown as +, those moving are inside circles. The drawing is not to scale.

balance and the oscillation charges are of the same type, oscillations are reinforced. When they are opposite, oscillations are damped. The former step type is likely to be most pronounced, and the oscillations are consequently sustained and amplified.

The balance current must be the main agent for heating the whole channel to luminosity. The charge distribution in figure 4 may be used for an estimate: The lowest terminal has a charge density of 3.5 mC/m. An extension of 50 m over 1  $\mu$ s demands a current of 175 kA. The secondary oscillating current is likely to be considerably weaker. Photographs agree with this concept. According to the idealized diagram of Schonland et al [1] and the photographs of Salanave [2], the whole channel is visible at the moment of extension and becomes extinct for a much longer time inbetween.

In the further course of events the channel apparently defies spread of the luminous molecules. In a cross-section the periphery is cooled between the current-pulses. The channel appears stable and narrow because new pulses again and again find their way along the best path in the core region and revitalizes the channel along its axis.

#### OSCILLATION CHARACTERISTICS

The lightning oscillations are defined by capacity and self-inductance. Standard radio formulas [3] may be used for an estimate. The electric quantities depend on the dimensions of the conductor. In the calculation a channel radius of 1 cm is assumed. Estimates in the literature range from millimeters to tens of centimeters. The results are given in table I.

Table I. Oscillation Characteristics for a Vertical Channel

Channel length, m	10	100	500	1000	4000	10000
Capacity, pF	80	604	2570	4830	16400	40000
Self-inductance, $\mu$ H	15	152	1150	2441	10900	29000
Period, $\mu$ s	0.2	2	11	22	84	215
Wave-length, m	65	570	3240	6470	25000	64000

The wave length is always long compared to the channel length. The whole channel will consequently oscillate without nodes. Two lightning steps should take place in a full oscillation. The oscillation period agrees well with reported stepped-leader intervals.

An estimate of the energy needed for heating and ionization is called for. Lightning temperatures above 25000 K have been measured, but are probably confined to a very narrow core. For the 1 cm channel let us assume 3000 K and a pressure of  $10^6$  Pa. The number of molecules per meter channel length is  $7.5 \cdot 10^{21}$ . If a mean ionization potential of 16 V is used, the calculated energy for singly ionized molecules is 1.2 kJ. Heating the molecules requires an other 1 kJ. These are the major energy requirements. Let us assume that a 1000 m channel is built up in 20 steps, i. e. heating and ionization must take place anew 20 times for a mean length of 500 m.

The energy need is 22 MJ. It is small compared with the 1.2 GJ, which according to figure 2 is the mean energy released.

The oscillation model seems to indicate a lightning path growing somewhat by chance. The released energy is however essential for driving the oscillation. The loss by way of heat radiation and ionization is considerable, and a path extending in the wrong direction cannot be held up for a long time. Some of the lightnings terminating in free air may simply have run out of working energy.

### THE GROUND STRIKE

The electro-static computations are meant to illustrate some aspects of the lightning event. With some justification the abscissa of figure 3 may be taken as time. The rate of change for a terminal close to the ground appears to be formidable. It is questionable if the less than perfect ground is able to keep on to a zero voltage in the striking point.

A voltage turmoil is likely to appear at the moment of strike. The model lightning of figure 1 should keep on to some of its negative voltage, but the short-circuited base would immediately be raised to zero. A positive pulse is thus fed into the channel and will start its way upward as a return stroke.

It should be noticed that neither the ground strike nor the return pulse has an immediate effect on the charge sheath outside the channel proper. A comparatively slow discharge must therefore follow. The oscillation model thus leads to a two-step electric signal, an instantaneous jump followed by a slower final discharge.

The present theory establishes the stepped leader as the main lightning stroke. It releases the bulk of the available electrostatic energy. It transfers the charge. It is, however, brought about in smaller steps, the mean is a "slow" transfer. The electro-magnetic radiation may for this reason be fairly weak, and instruments based upon sensing radiation may faultily record the first ground strike as a rather insignificant event.

### FURTHER MODEL POTENTIALITIES

Up to now only the lower end of a channel has been studied. The model does not imply any difference between the terminals. The other end is expected to extend out of the region where it was created.

An extension upwards could imply a lightning towards the ionosphere simultaneously with the lower flash. Such thoughts apparently have been put forward earlier, based upon observations. A discharge towards the more diffuse ionosphere is not so abrupt as that towards the ground, and the prerequisite for a following shock-pulse may not be present.

The upper terminal need not to proceed upwards at all. A horizontal or even downward growth meets the basic requirements. Some lightning

terminations into free air could be "the other end" channels.

Multiple strokes following the same channel are in general observed. The subsequent strokes appear as travelling light pulses. They could be pulses reflected from the upper channel. The model is open for other explanations as well, if a semi-free upper channel is allowed to roam about. On its way it might be able to tap energy from other charge configurations and thus have the power to mend a broken section of the channel. Continuous luminosity might be new and stronger oscillations with the ground as a lower condenser plate. Salanaves photographs indicate oscillations.

### CONCLUSION

If a long and narrow conductor is exposed to rapid changes of a strong electric field, electric oscillations tend to be generated. The lightning model proposed owes its characteristics to free electric oscillations. Channel extensions are triggered off when oscillating charge is crammed into the channel terminals.

Many characteristics can be tested against observations published on the lightning phenomenon, and they seem to agree well. Other characteristics are not explicitly mentioned in the literature and may be looked on as predictions. It is the hope of the author that these predictions will be tested.

### REFERENCES

- 1) Schonland, B. F. J., Malan, D. J. and Collens, H., 1935: Progressive lightning. II. Proc. Roy. Soc. A, 152, 595-625.
- 2) Salanave, L. E., 1980: Lightning and its spectrum, An Atlas of Photographs, The University of Arizona Press, Tucson, Arizona.
- 3) Hodgman, C. D., Weast, R. C., Selby, S. M., 1961: Handbook of Chemistry and Physics, pp. 3315-3325, Chem. Rubber Publ. Co., Cleveland, Ohio.

N91-32697

A SYSTEM FOR MAPPING SOURCES OF VHF AND ELECTRIC FIELD PULSES FROM IN-CLOUD  
LIGHTNING AT KSC

E.M.Thomson and P.J.Medelius  
Department of Electrical Engineering  
University of Florida  
Gainesville, FL 32611

ABSTRACT

The literature concerning VHF radiation and wideband electric fields from in-cloud lightning is reviewed. VHF location systems give impressive radio images of lightning in clouds with high spatial and temporal resolution. Using systems based on long- and short-baseline time-of-arrival and interferometry workers have detected VHF sources that move at speeds of  $10^5$ - $10^8$  m/s. The more slowly moving sources appear to be associated with channel formation but the physical basis for the higher speeds is not clear. In contrast, wideband electric fields are directly related to physical parameters such as current and tortuosity.

A long-baseline system is described to measure simultaneously VHF radiation and wideband electric fields at five stations at Kennedy Space Center. All signals are detected over remote, isolated ground planes with fiber optics for data transmission. The modification of this system to map rapidly-varying  $dE/dt$  pulses is discussed.

INTRODUCTION

The use of both direction finders and time-of-arrival techniques to locate VLF radiation from distant lightning is well-established (for example, [1,2]) These early systems could locate general regions of lightning activity with a spatial accuracy of about the scale of a storm. When these techniques were applied to VHF and UHF from close lightning within about the last decade sources could be mapped with much higher resolution in both time and space. Consequently, we now have VHF radio images of lightning, frequently in three dimensions, with spatial resolution of up to a few tens of meters and temporal resolution of the order of microseconds. Proctor [3] describes a system that locates VHF sources from lightning in three dimensions with an optimal resolution of about 100 m vertically and 25 m horizontally. Proctor used five receivers with a center frequency of 250 MHz and a bandwidth of 5 MHz located on 30 km and 40 km baselines. He presents detailed descriptions of the VHF development in five cloud flashes [4], 26 consecutive flashes in relation to radar pictures [5], and 47 ground flashes [6]. A similar long-baseline system using time-of-arrival is reported by Lennon [7] whose data was analyzed in Rustan et al. [8]. Following Oetzel and Pierce's suggestion [9] that line-of-sight direction finding was possible using much shorter baselines than Proctor's, hence obviating the problem of pulse identification at all stations when pulses arrive in different order at different stations, Cianos et al. [10] described a technique for two-dimensional location of VHF pulses at 30 MHz using stations separated by about 300 m with relative timing of about 10 ns. This technique was also implemented by Murty and MacClement [11] using sferics in the range 82-88 MHz. Taylor [12] reduced the distance between receivers to 14 m by increasing his bandwidth to 60 MHz (frequency range 20-80 MHz) and timing resolution to 0.4 ns and obtained three dimensional fixes by establishing two stations separated by several kilometers. Further results obtained by Taylor's system are reported in Taylor et al. [13]. A variation on the short baseline method was developed by Warwick et al. [14] who, instead of measuring time differences between stations, used an interferometer to measure phase differences and two-dimensional locations for VHF at 34 MHz. The advantage of interferometry over long-baseline time-of-arrival is that the source location can be found in near real time, as opposed to many months later as reported in

Proctor [3], and the tracking of faster VHF sources is possible owing to the short (about 1-5  $\mu$ s) time aperture needed for a single fix. Further results using this system are reported in Hayenga and Warwick [15] Hayenga [16] and Rhodes and Krehbiel [17]. An interferometer centered at 300 MHz has been described in Richard and Auffrey [18] and the results obtained have been discussed by Richard et al. [19], Mazur [20] and Bondiou et al. [21].

Wideband electric field measurements have been made with sufficient bandwidth to distinguish submicrosecond-scale variations by several workers within the last two decades. For a review of return stroke fields refer to Uman [22]. Wideband radiation electric field pulses from in-cloud processes have been observed in three distinct forms:- (i) bipolar pulses of about 40  $\mu$ s full width with 2-3 fast pulses riding on the initial half cycle [23]; (ii) unipolar pulses with halfwidths of typically 0.75  $\mu$ s that occur in regular sequences of 100-400  $\mu$ s duration [24]; and (iii) bipolar pulses of about 10  $\mu$ s halfwidth with smoother rise and smaller overshoot than those in (i) [25]. The Le Vine pulses were observed to accompany the largest amplitude rf noise at 3-295 MHz [25] and have 20 dB more spectral energy at 20 MHz than first return strokes [26].

Krehbiel et al. [27] describe a system for locating major charge transfers using a multiple station system with a bandwidth of close to DC to 1 kHz and give results for leaders, continuing currents and slow in-cloud processes in ground flashes. Despite the success of this method for ground flashes, Liu and Krehbiel [28] had difficulty interpreting the slow E fields after about 30 ms in intracloud flashes, presumably because of overlapping processes at different locations. Measurements of wider bandwidth electric fields have also been used to locate the strike point of return strokes by [7,29]. There are no reports in the literature concerning measurements of multiple wideband electric fields from in-cloud processes.

In this presentation we investigate the origins of VHF and wideband electric fields for in-cloud lightning processes, describe a system currently being implemented at KSC to measure and interpret these signals, indicate some important applications, and relate our recent results to the design of future high speed mapping systems.

#### ORIGINS OF VHF RADIATION

According to Proctor [3], the amplitudes of noise pulses at 250 MHz are not proportional to the charge lowered. Since some processes such as the dart leader tip did not radiate at all, Proctor concluded that "VHF noise occurs during the incipient stage of channel formation", a conclusion that was reinforced by his results for cloud flashes [4]. Proctor [3] differentiated between two types of discharge process in cloud flashes according to the VHF characteristics:- (i) new channel formation associated with VHF pulses; and, (ii) recoil streamers along existing channels that caused "Q noise". VHF pulses were emitted at rates from  $10^3$  to  $10^5$  pulses/second and were associated with sources that moved at speeds of  $6 \times 10^4$  m/s to  $10^5$  m/s. Q noise trains lasted from 10  $\mu$ s to over 2 ms and consisted of short pulses superimposed on a low frequency component that started and ended with gradual ramps lasting up to tens of microseconds. Q noise sources were deduced to be positive streamers, with one exception, and propagated at speeds of  $2.7 \times 10^6$  m/s to  $4.6 \times 10^7$  m/s. Proctor's figure showing how the Q noise was associated with the electric field waveshapes in one of the two K changes he showed is reproduced in Figure 1. The electric field antenna had a rise time of about 7  $\mu$ s and a decay time constant of 100  $\mu$ s. Note that in both this and the other case shown the VHF preceded the electric field rise and started ramping several tens of microseconds before the rapid portion of the K change. In his study of ground flashes, Proctor et al. [6] noted further that stepped leaders and intracloud streamers could not be distinguished, since both emit pulses and propagate at an average speed of  $1.6 \times 10^6$  m/s. He found that his single-station 3.5 kHz bandwidth electric fields were consistent with a model in which



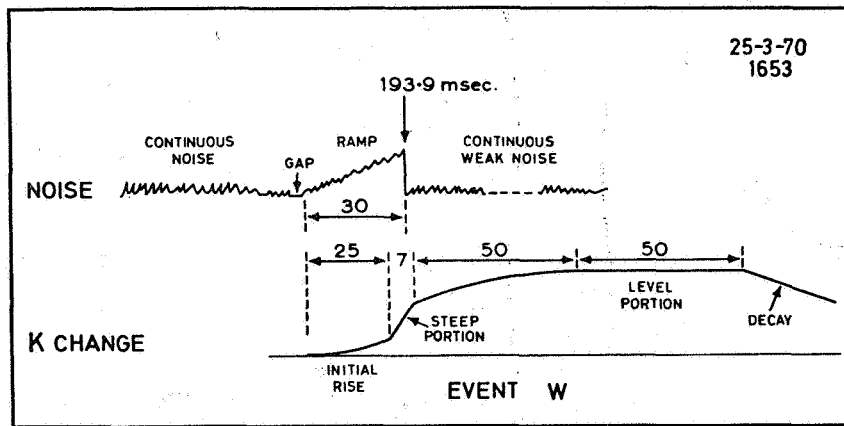


Figure 1. VHF noise and electric field change for a K change. Time intervals are in microseconds. Reproduced from Proctor [4].

charge is deposited at the position of the radio sources and depleted from the point of origin of each leader. Proctor et al. [6] found Q noise sources that propagated at  $10^8$  m/s during return strokes, and at a similar speed during interstroke periods. Individual components of these latter sources were directed vertically but there was an overall horizontal progression from one component to the next at an average velocity of  $2.2 \times 10^4$  m/s horizontally away from the starting points of the flashes. The median duration of these Q noise trains was 80  $\mu$ s and the median interval between them was 3.5 ms.

On the basis of interferometric measurements in a 3.4 MHz bandwidth centered at 34 MHz, Hayenga and Warwick [15] identified "acceleration of electrons in the high electric field at the tip of propagating breakdown streamers" as the source of VHF radiation in individual noise bursts, and a "propagation of the breakdown region" as the slower process responsible for the drifting motion from one burst to the next. During both the initial and intracloud portions of ground flashes, the bursts were typically 20  $\mu$ s long, occurred about every 100  $\mu$ s, extended about 1km in length, and propagated at about  $5 \times 10^7$  m/s. Fast burst origins drifted at a typical speed of  $2 \times 10^5$  m/s. Hayenga and Warwick show one cluster of fast bursts in the initial portion of a ground flash that appeared to move downward within bursts with a horizontal drifting from burst to burst. Hayenga [16] noted that fast bursts always accompanied K changes but also occurred when no K change was apparent. He considers his "fast bursts", Proctor's "Q noise" and the "solitary pulses" defined by Rustan et al. [8] to be the same phenomenon. Figure 2 is Hayenga's [16] locations, VHF power (rectified and integrated interferometer fringe output) and electric field for a typical fast burst. Note that the VHF precedes and overlaps the electric field pulse. Hayenga [16] identifies a further type of VHF source that is a precursor to dart leaders. These precursors moved into regions devoid of previous VHF in contrast to the bursts that travel through or on the edge of previously active regions. However, Hayenga cautions that the optical dart leader and the precursors are not correlated directly, although they are related, and therefore that the K change optical events (Brook and Kitagawa, 1977) are probably not correlated directly with the VHF fast bursts.

Using an interferometric system with a 600 kHz bandwidth centered at 300 MHz [18], Richard et al. [19] classified VHF sources into two types depending on the rate of pulse emission. (i) Low-rate pulsed radiation with rates of 1-20 pulses/microsecond ( $1 \times 10^6$  to  $2 \times 10^7$  pulses/s) consisted of pulses

usually narrower than 3  $\mu$ s width in pulse trains with durations of up to several hundred milliseconds. (ii) High-rate bursts of radiation appear as "dense pulsed radiation lasting from a few tens of microseconds to 1 ms". They

associated the high rate bursts with recoil streamers and K changes in the last few hundred milliseconds of an intracloud flash when the VHF sources in each burst propagated at about  $10^7$  m/s over distances of a few to 10 km with

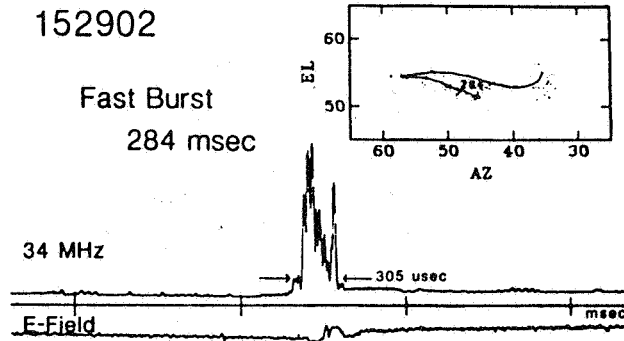


Figure 2. Loci of fast burst VHF movements. Postions within each burst were joined in their proper time sequence. Reproduced from Hayenga [16].

subsequent bursts following tens of milliseconds later along the same path. Mazur [20] noted that the radiation sources associated with K changes in the J-type stage of intracloud flashes originate in parts of the cloud where no radiation sources had been previously located and propagate towards the region of initiation. This observation contrasts with that of Hayenga [16] who observed fast pulses skirting or penetrated previously active regions. It is also different from the observation of Proctor [4] that most sources of Q noise were located near the flash origin and appeared to result from an overshoot of a wave that had returned along the main channel. Another major difference lies in Mazur's statement that "positive leaders are not detected by the interferometric system" in that Proctor [4] deduced that the sources of Q noise were positive streamers. Richard et al. [19] found decorrelations between electrical or optical discharge processes and sources of 300 MHz radiation, concluding that "the VHF-UHF electromagnetic phenomenolgy is distinct in some specific cases from the electric phenomenology". Specifically, they found higher velocities for VHF sources ( $10^7$  m/s) than have been previously observed for the luminous streamer in K changes, development of radio sources down the leader channel before the leader's electric field change, and return stroke radio sources that were generally spread out along the leader trajectory or within the cloud with a lack of spatial correlation to the precursor activity. Labaune et al. [30] determined that VHF-UHF radiation sources that propagate at:- (i)  $10^5$ - $10^6$  m/s correspond to the step and branching mechanisms of negative leaders; (ii)  $2 \times 10^7$  m/s, the most commonly observed phenomenon, cannot be interpreted in terms of known properties of dry air discharge; and (iii)  $10^8$  m/s arise from mechanisms triggered in the channel corona envelope as an indirect consequence, but not the propagation of, the return stroke. Labaune [31] and Weidman et al. [32] both measured the wideband electric fields in the VHF-UHF range (10-500 MHz). The typical pulse obtained by Labaune is

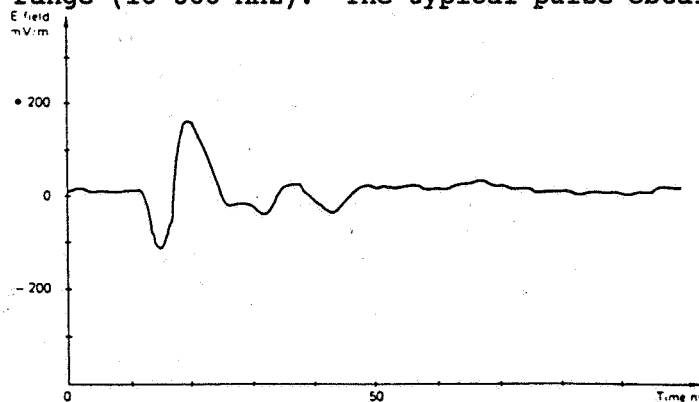


Figure 3. Broadband pulse typical of VHF-UHF radiation from lightning. Reproduced from Labaunne et al. [30].

given in Figure 3. This shows the short risetime of 5 ns that is consistent with the "streamer-leader" transition in negative streamers that Labaune et al.

[30] conclude to be the origin of VHF-UHF radiation. Similar measurements made by Weidman et al. [32], however, indicate risetimes of the order of 30 ns. Le Boulch and Hamelin [33] propose that Weidman's longer risetimes could be attributed to positive streamers.

#### IN-CLOUD ORIGIN OF WIDEBAND ELECTRIC FIELD PULSES

The bipolar pulses observed by Weidman and Krider [23] had fast (about 1  $\mu$ s width) pulses riding on the initial half cycle. They interpreted these as indicating the formation of the discharge channel in some stepped fashion since the fast pulses were similar to those produced by stepped leaders [34,35]. The bipolar component was then produced by a slower current surge which flows either while the channel is being established or just after. Krider et al. [36] found a clear tendency for the rf radiation to peak during the initial half cycle of these pulses with the temporal development of the rf being similar for all frequencies in the range 3-295 MHz. They note that this observation is consistent with Weidman and Krider's interpretation since predischARGE and leader processes do produce strong rf. Krider et al. [35] postulated that, for a stepped leader, a fast current pulse might propagate several hundred meters up the vertical leader channel before dissipating so that the radiation field  $E(t)$  in the first 1 or 2  $\mu$ s is related to the current  $I(t)$  by

$$E(t) = (-\mu_0 v / 2\pi D) i(t')$$

where  $v$  is the constant propagation speed,  $t' = t - D/c$ , and  $D$  is the horizontal distance to the base of the channel. This relationship is also valid for a vertical in-cloud current. Thomson [37] found a similar relationship for an in-cloud current pulse propagating along a channel of arbitrary orientation. Specifically, the radiation field was also proportional to the speed-current product with additional geometrical factors. Thomson [37] further found that four wideband radiation fields could be inverted to give the magnitude of the speed-current product, the current waveshape, and the direction of the velocity of propagation.

Krider et al. [24] interpret the trains of regular electric field pulses that they observed in terms of an intracloud discharge process similar to the dart-stepped leader. Noting a consistency between the speeds of dart-stepped leaders measured by Schonland et al. [38] and the speeds of streamers that produce K changes as suggested by Ogawa and Brook [39], they propose that "a significant fraction of any dartlike K changes develop in a stepped fashion and produce the observed uniform pulses". The 100-400  $\mu$ s durations of these pulse trains is consistent with Proctor's median duration of 80  $\mu$ s for Q noise that he attributes to K changes.

Le Vine [25] found that the strongest sources of rf radiation in the 3-300 MHz range were short duration (10-20  $\mu$ s) bipolar pulses that did not have fast unipolar pulses riding on the initial half cycle. He noted no apparent correlation between strength of the RF radiation and the size of the associated E pulse. Le Vine modeled these pulses as a fast ( $10^8$  m/s) K streamers that lower positive charge or raise negative charge. Subsequent results by Willett et al. [26] and Medelius et al. [40] indicate, however, that the Le Vine-type pulses are usually isolated and cannot be obviously attributed to any known lightning processes such as K changes.

The effect of channel tortuosity on wideband electric fields and radiation spectra was investigated by Le Vine and Meneghini [41,42]. Although they apply their model to a tortuous return stroke, their results are also applicable to a general current pulse propagating along an established channel. Le Vine and Meneghini [42] find that tortuosity renders the electric field waveshape less representative of the current pulse and more unipolar than theory predicts. Tortuous channels act as adjacent short channel lengths and behave mathematically as several point radiators located at the channel kinks. The

radiated waveform thus contains information on both the current waveshape and the channel tortuosity.

#### SYSTEM

The measurement system being constructed for this summer's experiment comprises five remote stations with two wideband channels (1 Hz to more than 8 MHz) per station. The remote stations are located at the eastern bank of the Indian river, the UC9 site on Playalinda Beach, Unified S-Band (USB), Hypergolic Maintenance Facility (HMF), and the central station is at the Shuttle Landing Facility (SLF). The distance between remote and central stations is about 10 km. Signals are sent back to a central recording station via either microwave links with a carrier of 10 GHz and 3 dB bandwidth of 1 Hz-8 MHz, or analog fiber optics links with a 3 dB bandwidth of 1 Hz to 14 MHz. Control of all functions at the remote stations is an enhancement of the technique using two-way coded audio tones that is described in Thomson et al. [43]. Control functions include gain, antenna, and calibration of the electric field sensors, and power, signal switching (50 MHz or 225 MHz), and miscellaneous system status features such as adequate battery voltage. Synchronization of remote stations is effected using the timing signals inherent in any TV broadcast. We will use WESH TV 2 that broadcasts from Orlando at 55.25 MHz.

Electric field changes at each station are detected by integrating the displacement current intercepted by a flat plate antenna. The 10-90% rise time of these integrators is 40 ns and they decay with a 1 ms decay time constant to a step electric field input. Triangle-wave and square-wave calibration signals can be applied through a known capacitance directly to the inputs of the integrators to simulate a electric field for linearity and absolute field calibrations as shown in Thomson et al. [43].

VHF radiation is received in a 5 MHz bandwidth at a center frequency of both 50 MHz and 225 MHz. Detection is with an envelope detector and each signal is compressed with a logarithmic amplifier. Envelope rather than product detectors are used to decrease signal distortion that may arise in product detectors as a result of IF frequency shifts.

The five electric field signals sent back from the remote stations are recorded at the central station in digital form in a 5-channel 8-bit Le Croy digitizing system interfaced with an 80386-based IBM clone PC. The signals are digitized at 20 MS/s for 100  $\mu$ s each time a trigger occurs. Consecutive trigger events are digitized sequentially with no dead time between triggers until the 128 kS Le Croy memory is full. Thus 64 trigger events can be recorded per lightning. The central channel has a 32  $\mu$ s pretrigger delay so that the signal radiated by a single event is recorded somewhere in each 100  $\mu$ s window. The electric fields are also recorded continuously on five FM channels of a Honeywell 101 magnetic tape recorder with 0-500 kHz 3dB bandwidth. The VHF signals, either 50 MHz or 225 MHz, are also recorded on the inner five channels of the seven tracks on a single headstack of our Honeywell magnetic tape recorder. Using DIRECT recording mode gives a bandwidth of 400 Hz to 2 MHz. The outer two channels of the headstack have modulated synchronization signals derived from WESH TV2 that are needed for deskewing the signals and providing accurate timing. Tape skew has proven to be an important problem in previous measurements of this type [44]. A common time code recorded in both the digitizer and tape recorder system is an amalgamation of IRIGB and TV synch signals that gives relative timing with 50 ns accuracy. Propagation delays along the microwave and fiberoptic links will be calibrated out by adding in to each channel either the horizontal synch signal (one pulse per 63  $\mu$ s) or a high frequency code derived from the WESH TV2 signal.

The locations of the VHF and electric field pulses recorded by the system will be found from the differences in times of arrival as described by Proctor [3]. The radiation electric fields will also be inverted to give the current-velocity product for each pulse origin as explained by Thomson [37].

## DISCUSSION

### APPLICATION TO FAST PULSES

The above literature review indicates that a major problem revealed by VHF mapping systems is the interpretation of the physical origin of VHF sources that are observed to propagate at speeds of  $10^7$  m/s and faster. Whereas VHF sources that propagate at  $10^5$ - $10^6$  m/s appear to be associated with ionization at the tips of extending streamers, the faster VHF sources are not attributable to known optical processes [28]. On the other hand, return stroke models relating electric field pulses to observed optical velocities and current waveshapes have been validated by experiment (for example, Willet et al., [45]). A straightforward extension of these models to in-cloud currents should yield results that are directly interpretable in terms of either the current propagation [37] or channel tortuosity [41,42]. By mapping both VHF and electric field pulse sources, as well as the current-velocity vector for each electric field pulse, we can investigate the physical relationship between these two signals. For example, if, as is proposed by Krider et al. [36], the VHF radiation preceding the electric field peak is associated with the formation of the channel while the electric field pulse arises from the current flow along that channel, we should detect an extending VHF source that is followed by a current-velocity vector originating at its tip and pointing back down the VHF extension. Similarly, if the small pulses riding on the leading edge of the bipolar pulses observed by Weidman and Krider [23] are also associated with the formation of the same channel that is the origin of the VHF pulses, then the locations and propagation directions of the sources of these pulses will be consistent with the movement of the VHF sources.

### SYSTEM MODIFICATION FOR DE/DT MAPPING

The dE/dt record has many interesting features. The narrow bipolar pulses first noted by Le Vine [25] have significant dE/dt fine structure throughout the whole bipolar E waveshape [26] that is frequently so large as to obscure the derivative of the microsecond-duration E pulse [40]. This dE/dt fine structure arises from short-duration pulses that ride on top of the microsecond-scale E pulse waveshape. The zero crossings of this dE/dt "noise" occur at the peaks of the short-duration pulses. Figure 4 shows dE/dt recorded at a digitization rate of 100 MS/s. This figure shows that dE/dt has significant variations on a 10 ns scale. In fact, we have recently recorded dE/dt with a 400 MS/s digitization rate that indicates fine structure on a several nanosecond time scale. These pulses are undoubtedly those that are detected by VHF location systems operating in this range. The effect of filtering these dE/dt signals through a bandpass VHF receiver is discussed further in Medelius et al. [40]. In order to establish the relationship between the dE/dt fine structure and the microsecond duration E waveshape simultaneous mapping is needed. The best way to map the dE/dt is probably with a short baseline system similar to that described by Taylor [12]. However, we require a much faster location rate than one per 40  $\mu$ s, as was obtained by Taylor. In fact, if all zero crossings are to be detected, a rate of one fix per few nanoseconds is desirable. Simultaneous mapping of E pulses and dE/dt would offer a powerful tool for investigating the nature of rapidly-propagating in-cloud currents, and these are precisely those whose VHF origins are least well understood.

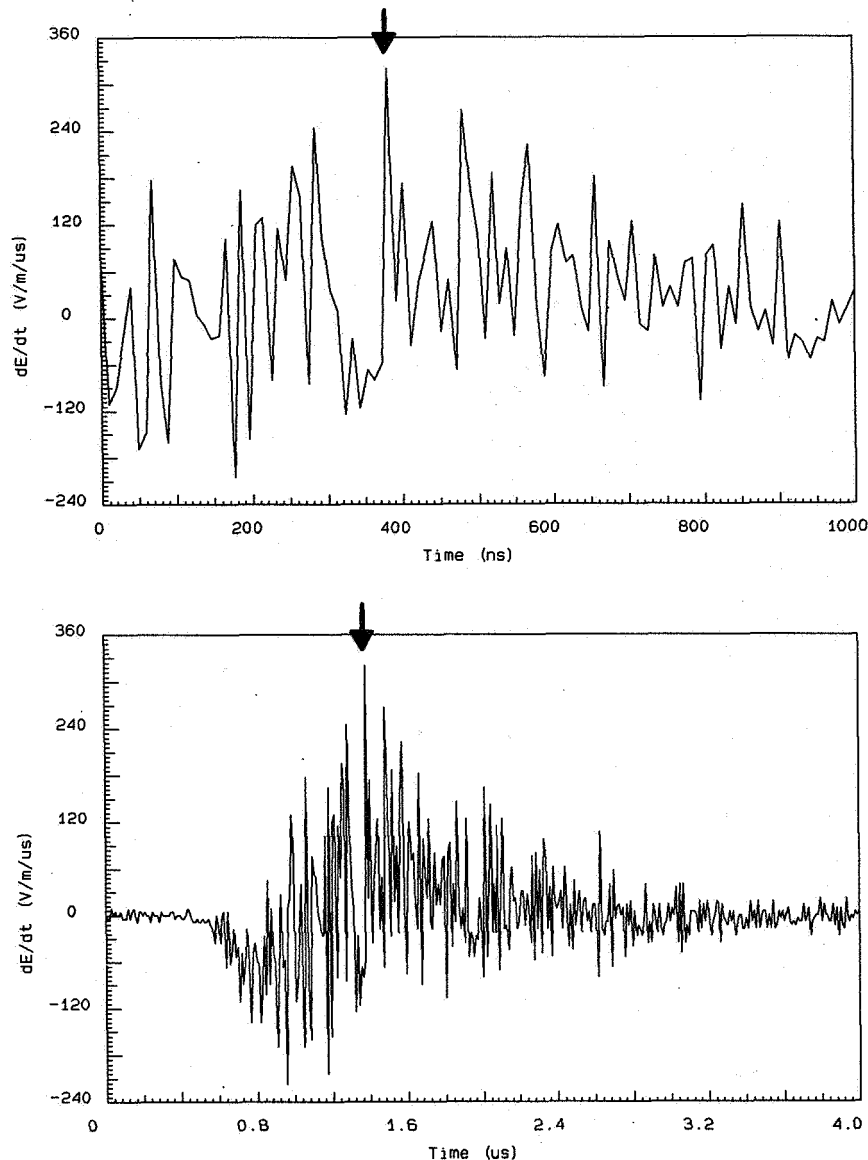


Figure 5.  $dE/dt$  waveshapes for a bipolar electric field pulse. The arrow indicates the same point on both traces.

#### REFERENCES

1. Horner, F., Radio noise from thunderstorms, in "Advances in Radio Research, Vol. 2, J.A. Saxton, (Ed.), pp 122-215, New York, Academic Press, 1964.
2. Lewis, E.A., R.B. Harvey and J.E. Rasmussen, Hyperbolic direction finding with sferics of transatlantic origin, J. Geophys. Res., **65**, 1879-1905, 1960.
3. Proctor, D.E., A hyperbolic system for obtaining VHF radio pictures of lightning, J. Geophys. Res., **76**, 1478-1489, 1971.
4. Proctor, D.E., VHF radio pictures of lightning, J. Geophys. Res., **86**, 4041-4071, 1981.
5. Proctor, D.E., Lightning and precipitation in a small multicellular thunderstorm, J. Geophys. Res., **88**, 5421-5440, 1983.
6. Proctor, D.E., R. Uytendogaardt, and B.M. Meredith, VHF radio pictures of lightning flashes to ground, J. Geophys. Res., **93**, 12,683-12,727, 1988.
7. Lennon, C.L., LDAR - a new lightning detection and ranging system, EOS Trans., AGU, **56**, 991, 1975.

8. Rustan, P.L., M.A. Uman, D.G. Childers, W.H. Beasley, and C.L. Lennon, Lightning source locations from VHF radiation data for a flash at Kennedy Space Center, *J. Geophys. Res.*, 85, 4893-4903, 1980.
9. Oetzel, G.N., and E.T. Pierce, VHF technique for locating lightning, *Radio Science*, 4, 199-201, 1969.
10. Cianos, N., G.N. Oetzel, and E.T. Pierce, A technique for accurately locating lightning at close ranges, *J. Appl. Meteorol.*, 11, 1120-1127, 1972.
11. Murty, R.C., and W.D. MacClement, VHF direction finder for lightning location, *J. Appl. Meteorol.*, 12, 1401-1405, 1973.
12. Taylor, W.L., A VHF technique for space-time mapping of lightning discharge processes, *J. Geophys. Res.*, 83, 3575-3583, 1978.
13. Taylor, W.L., E.A. Brandes, W.D. Rust, and D.R. MacGorman, Lightning activity and severe storm structure, *Geophys. Res. Letts.*, 11, No. 5, 1984.
14. Warwick, J.W., C.O. Hayenga, and J.W. Brosnahan, Interferometric position of lightning sources at 34 MHz, *J. Geophys. Res.*, 84, 2457-2468, 1979.
15. Hayenga, C.O., and J.W. Warwick, Two-dimensional interferometric positions of VHF lightning sources, *J. Geophys. Res.*, 86, 7451-7462, 1981.
16. Hayenga, C.O., Characteristics of lightning VHF radiation near the time of return strokes, *J. Geophys. Res.*, 89, 1403-1410, 1984.
17. Rhodes, C., and P.R. Krehbiel, Interferometric observations of a single stroke cloud-to-ground flash, *Geophys. Res. Letters*, 16, 1169-1172, 1989.
18. Richard, P., and G. Auffray, VHF-UHF interferometric measurements, applications to lightning discharge mapping, *Radio Science*, 20, 171-192, 1985.
19. Richard, P., A. Delannoy, G. Labaune, and P. Laroche, Results of spatial and temporal characterization of the VHF-UHF radiation of lightning, *J. Geophys. Res.*, 91, 1248-1260, 1986.
20. Mazur, V., Triggered lightning strikes to aircraft and natural intracloud discharges, *J. Geophys. Res.*, 94, 3311-3325, 1989.
21. Bondiou, A., I. Taudiere, P.R. et F. Helloco, Analyse spatio-temporelle du rayonnement VHF-UHF associe A L'Elair, *Revue Phys. Appl.*, 25, 147-157, 1990.
22. Uman, M.A., Lightning return stroke electric and magnetic fields, *J. Geophys. Res.*, 90, 6121-6130, 1985.
23. Weidman, C.D., and E.P. Krider, The radiation field wave forms produced by intracloud lightning discharge processes, *J. Geophys. Res.*, 84, 3159-3164, 1979.
24. Krider, E.P., G.J. Radda, and R.C. Noggel, Regular radiation field pulses produced by intracloud lightning discharges, *J. Geophys. Res.*, 80, 3801-3804, 1975.
25. Le Vine, D.M., Sources of the strongest RF radiation from lightning, *J. Geophys. Res.*, 85, 4091-4095, 1980.
26. Willett, J.C., J.C. Bailey, and E.P. Krider, A class of unusual lightning electric field waveforms with very strong HF radiation, *J. Geophys. Res.*, 94, 16,255-16,267, 1989.
27. Krehbiel, P.R., M. Brook, and R. McCrory, An analysis of the charge structure of lightning discharges to the ground, *J. Geophys. Res.*, 84, 2432-2456, 1979.
28. Liu, Xin-Sheng, and P.R. Krehbiel, The initial streamer of intracloud lightning flashes, *J. Geophys. Res.*, 90, 6211-6218, 1985.
29. Lyons, W.A., R.B. Bent, and W.H. Highlands, Operational uses of data from several lightning position and tracking systems (LPATS), *Proceedings, 10th International Conference on Lightning and Static Electricity*, pp347-356, Paris, 1985.
30. Labaune, G., P. Richard, and A. Bondiou, Electromagnetic properties of lightning channel formation and propagation, in "Lightning Electromagnetics", R.L. Gardner (ed.), pp 285-317, Hemisphere Publishing Corp., New York, 1990.
31. Labaune, G., The role of the transient arc in the generation of metric and decimetric radiation by a lightning flash, *Annales des Télécommunications*, 39, 5-6, 1984.
32. Weidman, C., J. Hamelin, and M. Le Boulch, Lightning VHF and UHF emissions and fast time resolved measurements of the associated electric field variations, *Proceedings, 10th International Conference on Lightning and Static Electricity*, pp175-184, Paris, 1985.
33. Le Boulch, M., and J. Hamelin, Rayonnement en ondes métriques et décimétriques des orages, *Ann. Telecommun.*, 40, 277-313, 1985.

34. Krider, E.P., and G.J. Radda, Radiation field wave forms produced by lightning stepped leaders, *J. Geophys. Res.*, 80, 2653-2657, 1975.
35. Krider, E.P., C.D. Weidman, and R.C. Noggle, The electric fields produced by lightning stepped leaders, *J. Geophys. Res.*, 83, 951-960, 1977.
36. Krider, E.P., C.D. Weidman, and D.M. Levine, The temporal structure of the HF and VHF radiation produced by intracloud lightning discharges, *J. Geophys. Res.*, 84, 5760-5762, 1979.
37. Thomson, E.M., Radiation field from an in-cloud lightning process with arbitrary orientation, *Proceedings, 8th International Conference on Atmospheric Electricity, Uppsala, 1988.*
38. Schonland, B.F.J., D.J. Malan, and H. Collens, Progressive lightning II, *Proc. Roy. Soc., London*, A152, 595-625, 1935.
39. Ogawa, T., and M. Brook, The mechanism of the intracloud lightning discharge, *J. Geophys. Res.*, 69, 5141-5150, 1964.
40. Medelius, P.J., J. Pierce, and E.M. Thomson, E and dE/dt waveshapes from close lightning at Kennedy Space Center, *Proceedings, International Conference on Lightning and Static Electricity, Cocoa Beach, 1991.*
41. Le Vine, D.M., and R. Meneghini, Electromagnetic fields radiated from a lightning return stroke: application of an exact solution to Maxwell's equations, *J. Geophys. Res.*, 83, 2377-2384, 1978a.
42. Le Vine, D.M., and R. Meneghini, Simulation of radiation from lightning return strokes: the effects of tortuosity, *Radio Science*, 13, 801-809, 1978b.
43. Thomson, E.M., P. Medelius, M.A. Uman, A remote sensor for three components of transient electric fields, *IEEE Trans. Ind. Electr.*, 35, 426-433, 1988.
44. Thomson, E.M., J.W. Stone, M.A. Uman, and W.H. Beasley, Location of lightning sources at VHF using cross correlation techniques, *Trans. Am. Geophys. Union*, 62, 880, 1981.
45. Willett, J.C., V.P. Idone, R.E. Orville, C. Leteinturier, A. Eybert-Berard, L. Barret, and E.P. Krider, An experimental test of the "transmission-line model" of electromagnetic radiation from triggered lightning return strokes, *J. Geophys. Res.*, 93, 3867-3878, 1988.



A NEW APPROACH TO THE DETERMINATION OF THE STRIKING  
DISTANCE FROM THE LIGHTNING CHANNEL PHOTOS

*A. Vorgučić and I. Mladenović*  
*University of Niš, 18000 Niš, Yugoslavia*

ABSTRACT

The paper is concerned with the emphasis of the possible influence the stepped leader movement on the value of the striking distance. The numerical values of the striking distances are most frequently verified from the lightning channel photos. There is some explanations for dispersion of the striking distance which appears specially on the tall structures. Unusually long striking distance, may be influenced by the positive space charge or prior upward flashes. One more indefiniteness which may have influence in estimation the striking distance is a complex charge motion in the leader channel. Through introduction of two types charge motion it is shown possible shortening of the striking distance seen on the lightning channel photos.

INTRODUCTION

In connection with the protecting space of a lightning rod the wide accepted electrogeometric model deals with the striking distance. They are more different numerical values of the striking distance from different authors. This different values, results from the different consideration of the critical value of electrical field, distribution of the electrical charge in the leader channel and so on. The numerical values of the striking distances is usually verify from the photos of the lightning channel, after the sharp bend in channel and simultaneous measurement or estimation of lightning current. Some measurements of the striking distance through photos of channel show a significant dispersion [1], with brought in doubt the relations between crest current and striking distance. Some explanations for dispersion of striking distance includes the space charge by tall structures [2]. It had be shown that periodical inordinate striking distances are, only apparent and that phenomenon could be occur on the tall structures and is influenced by the positive space charge from point discharge or prior upward flashes [3].

In [4,5] the authors of this paper are introduced the two types of movement of the stepped leader and pointed out that movement of the stepped leader may have influence on the estimation of the striking distance length from the photos of the lightning channel.

STRIKING DISTANCE

They are some definitions of striking distance. But all of them may be represented as: striking distance is the distance between the tip of the downmoving leader and the point on the earth or structure when, under electrical charge deposited in leader channel, electrical field reaches a critical value on the earth or structure. From point on earth or structure,

When electrical field reaches critical value, starts positiv connecting streamer (return stroke), which connects striking point and the tip of the downmoving negative leader. This is the lenght of the last step in the lightning development. It depends, generally of the electrical charge in the leader channel. The striking pont is not by anything determined in advance, but only by critical electrical field intensity due to downmoving leader. The charges in the leader channel are neutralized during the return stroke process. The crest of the lightning current depends on this charge. It follows that the striking distance could be introduced like function on crest lightning current. The determination of striking distance in function of lightning current was subject of many investigators. For the practical calculations, relation between striking distance  $r$  in m and crest value of the lightning current  $I$  in kA can be presented in the simplified form

$$r = kI^p.$$

Constants  $k$  and  $p$  have different values, what depends on the authors, and start from 3.3 to 10.6 for  $k$  and from 0.51 to 0.85 for  $p$ . The different values of the striking distance, for the same crest current, results from the different consideration of critical value of the electrical field, distribution of the charge in the leader channel and so on.

The point where the leader channel and the upward streamer meet, could be see in same photographs according the sharp bend in the lightning channel. From such a photos taken from two directions the striking distance could be determinated-estimated. By simultaneous taking od photographs and current measurement or magnitude current estimation from the lightning current effect, the accuracy of the proposed matematical expression for striking distance in function of lightning current may be examined. Some measurements of striking distance trough photographs of chaneel show a significant dispersion, what brought in doubt the relations between crest current and striking distance.

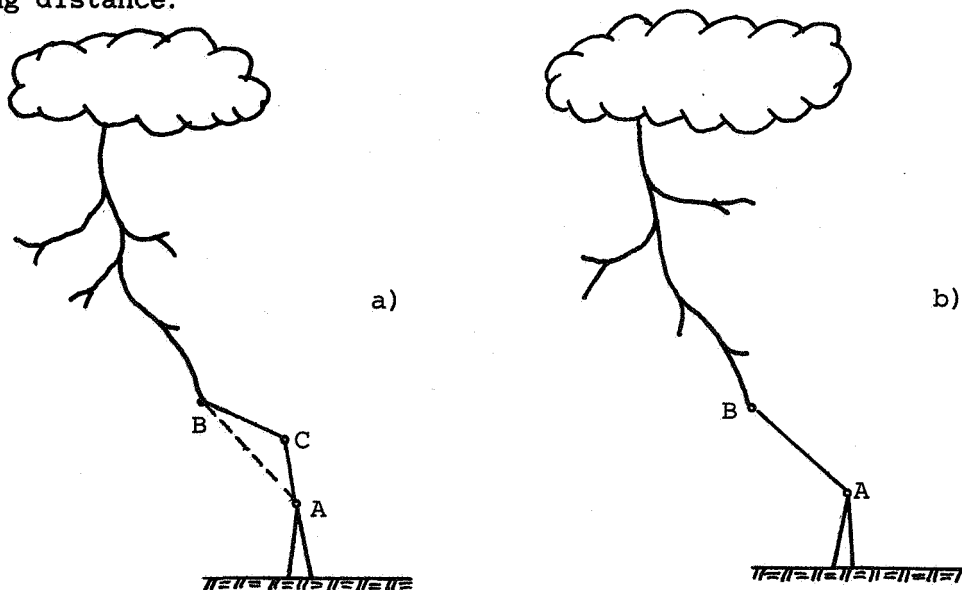


Fig.1 Paths of the lightning fllash: a) Case of inordinate seen striking distance; b) Normal case

Some explanations for dispersion of striking distance includes the space charge by tall structures. It had be shown that periodical inordinate striking distance are, only apparent and that phenomenon could be occur on the tall structures and is influenced by the positive space charge from point discharge or prior upward flaches. For the mechanism proposed by Mousa [3], photos of the lightning channel show two deviation points in the path of the lightning channel befor it terminates on the structure. In Fig. 1 are given two possible cases. Fig. 1a shows the situation when last step of downmoving leader conects structure over spark (AC) from prior upward flash and Fig. 1b when is this spark extinguished. In the first case striking distance is not AB but BC like in case b (BA). Posibility for the first case is greater for the short-time rate (flashes/minute). According Erikson, for the first case (Fig. 1a) the striking distance would be doted line (AB).

### INFLUENCE OF THE STEPPED LEADER

According to the photographs from the Bays cammera and measuring the electrical field on the earth, the cloud-ground discharge is initiated by streamer that develops downwards in a series of steps. Each of this steps observed as a sudden increase in luminosity of the channel of the ionized air at the tip of the streamer. This streamer is called stepped leader. The spark in its moving toward ground get over some distance, stops and after short time interval continue to move. The lenth of each step is about 50 m. After completing a step the tip of the streamers appears to pause for a time of the order 50  $\mu$ s, and the new step being much brighter then the rest of the streamer. When stepped leader in its moving, approaches the ground, starts the positive conecting streamer from the earth to the stepped leader. This conecting streamer, which is initiated by the critical electrical field, from the electrical sharge in the channel of the downmoving stepped leader, conects striking point with the leader channel. The stepped leader approaches the ground at the average velocity at about  $1,5 \times 10^5$  m/s. The second one ist velocity of the individual step motion value of about  $5 \times 10^7$  m/s.

They are more theory of the stepped leader, but it could be concluded that all of them includes that the average velocity for a negatively charged downmoving stepped leader is about  $1,5 \times 10^5$  m/s, like the velocity of the pilot streamer. The pilot streamer, which prepares the way for the step proces by ionizing the air, moves continually. The mean velocity of individual steps is about  $5 \times 10^7$  m/s, much higher then average velocity of the stepped leader. Time intervals between individual steps is about 50  $\mu$ s. Velocity of the conecting streamer is about  $5 \times 10^7$  m/s, like velocity of individual steps. Let us denote:  $V_1$  - velocity of the pilot streamer propagation also average velocity of the stepped leader,  $V_2$  - the velocity of the individual steps trough the already prepared channel by the pilot streamer and  $V_s$  - the velocity of the conecting streamer. The mean values of velocities are:  $V_1 = 1,5 \times 10^5$  m/s;  $V_2 = 5 \times 10^7$  m/s;  $V_s = 5 \times 10^7$  m/s.

Now we have to distinguish two tipes: tip of the pilot streamer moving

with the velocity  $V_1$  and tip of the individual step in the stepped leader moving with velocity  $V_2$ . It is possible that position of both tips may initiate the connecting streamer from the striking point because the both of them bears the charge. It is not the same which tip and from which position due the critical field on the striking point. If it is a tip of the individual step we have to take in consideration that it has the velocity like connecting streamer and it has already prepared way for its motion.

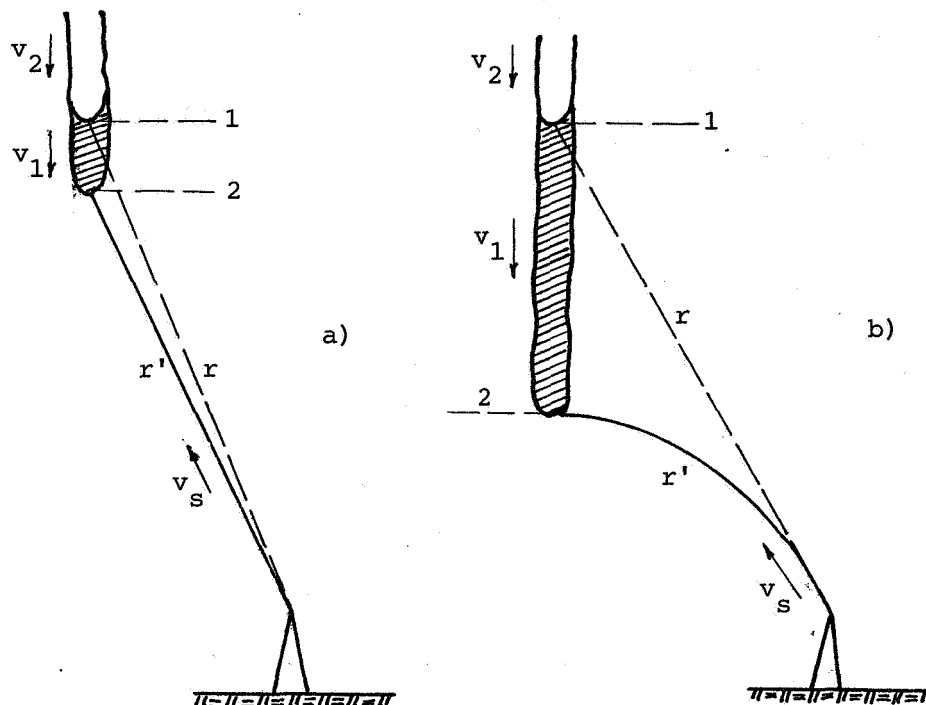


Fig. 2. Tip positions of stepped leader when starts connecting streamer:  
a) Case  $r \approx r'$ ; b) Case  $r' > r$

Fig. 2a shows position of individual step near to end of prepared way by pilot streamer, when is connected streamer initiated. Bending of channel could be much sooner and there is not big difference between  $r$  and  $r'$ .

Fig. 2b shows position of individual step tip initiating connecting streamer, when the tip is in beginning of its motion. The both, step and connecting streamer moves with equal velocities ( $V_2 = V_s$ ). The way of downmoving leader is determined. Meeting point "2" of two streamers, which is seen on the photographs like bend of channel is nearer to the striking point and the striking distance on the photographs is  $r'$  instead  $r$ . It is possible to see this channel with two deviation.

Dispersion of the striking distance are in both directions. Greater striking distances then expected, got from photos of the channel, are explained with the positive space charge and could be seen on photos with two deviation points. Our suggestion is that shorter striking distances could be explained with two tips with different velocities in the stepped leader (shown in Fig. 2).

In Fig. 3 are given two known examples of the lightning channel photos. If they are very strong strokes it could be taken that from point D the

downmoving leader initiates the connecting streamer which in beginning has direction toward point D (part AC). Step of the stepped leader moves along prepared channel (DB) by pilot streamer. The connecting streamer from A turn over C to B. But the some shape of the lightning channel could be in more way interpreted. Above metioned striking distance could be AD. According to Erikson definition striking distance is AB, according Mousa is BC and classical definition is AC.

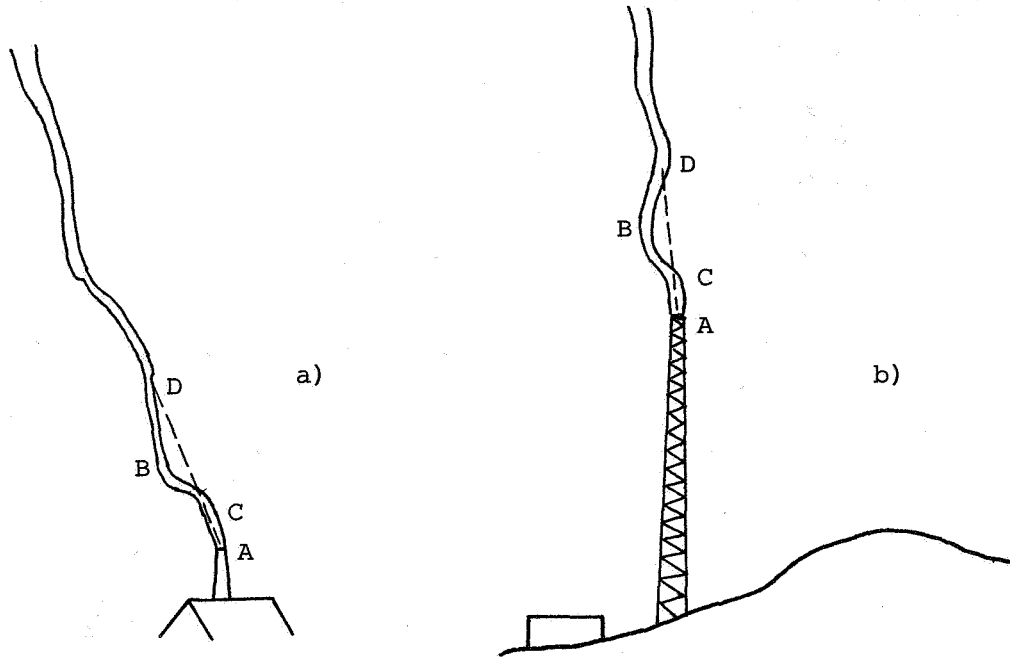


Fig. 3. The striking stroke in a) Chimney in Britain and b) tower in Monte Orsa.

### CONCLUSION

Some estimation or measurement the striking distance from the photos of the lightning channel shows a significant dispersion in both directions from established relations. Approaching to the more correct estimation in some cases is taking in account the remainder sparc of prior upward flashes as an extension of the structure. This could be seen on the lightning channel photos with two deviation points. Trough the introduction of two tipes with different velocities in the stepped leader is shown possible influence of its movement in estimation the striking distance. The movement the step of the stepped leader along the channel already prepared by the pilot streamer could be seen on the photos like shorter striking distance. To get more precisely striking distance from the lightning channel photos it must be taken in consideration all effects including also the shape of the channel and intensity of the lightning current.

#### REFERENCES

- [1] Eriksson A.J., Lightning and Tall Structures, Trans. Sount. African IEE, Vol. 69, No. 8, 1978, pp. 238-252.
- [2] Golde R.H., Lightning and Tall structures, Proc. IEE, Vol. 125, No. 4, 1978, pp. 347-351.
- [3] Mousa A.M., Efect of Height of structure on the striking Distance of a Downward Lightning Flash, Proc. Int. Communications and Energy Conference, Montreal, 1984, pp. 9-14.
- [4] Mladenović I., Vorgučić A., Stepped Leader and Striking Distance, 10th International Aerospace and Ground Conference on Lightning and Static Electricity, Paris, 1985, pp. 321-323.
- [5] Vorgučić A., Mladenović I., Some Consideration About Striking Distance, 19. International Blitzschutzkonferenz (ICLP) Graz, 1988, pp. 105-109.

**Session 11B, Thursday 1:30**  
**Aerospace Vehicles**  
**Modeling and Coupling Analysis 3**  
**Revay, Chairman**

**ELECTROMAGNETIC TOPOLOGY: CHARACTERIZATION OF INTERNAL  
ELECTROMAGNETIC COUPLING**

J.P. Parmantier\*, J.P. Aparicio\*\* and F. Faure\*\*

\*Dassault Aviation, B.P. 300, 92214 SAINT-CLOUD, FRANCE

\*\*Office National d'Etudes et de Recherches Aéronautiques  
B.P. 72, 92322 CHATILLON CEDEX, FRANCE

**ABSTRACT**

This paper presents the main principles of a method dealing with the resolution of electromagnetic internal problems: Electromagnetic Topology. A very interesting way is to generalize the multiconductor transmission line network theory to the basic equation of the Electromagnetic Topology: the B.L.T. equation.

This generalization is illustrated by the treatment of an aperture as a four port junction. Analytical and experimental derivations of the scattering parameters are presented. These concepts are used to study the electromagnetic coupling in a scale model of an aircraft, and can be seen as a convenient means to test internal electromagnetic interference.

**1. INTRODUCTION**

The study of the internal electromagnetic problem should, in the future, lead to the development of an electromagnetic design tool. An electromagnetic design can be carried out in four phases. The first one is to design a first prototype. The second phase is to calculate the interference in the system previously defined. In a third phase the system has to be optimized, to be in agreement with specific goals such as price, but also weight. The last phase is to establish maintenance specifications once the system is entirely defined.

Electromagnetic Topology is a powerful frequency method developed several years ago specially for aeronautics by C.E. Baum [1] in the USA, and that could answer these four phases. Nowadays, studies are being made to see how far this theory can be applied or modified or completed to be successful.

**2. OVERVIEW OF ELECTROMAGNETIC TOPOLOGY****FUNDAMENTAL APPROACH**

The main concept of Electromagnetic Topology, as defined by C.E. Baum, is to divide the space of interest into volumic zones in order to break down a total complex electromagnetic problem into a group of small problems independent of each other.



The topological diagram is a helpful abstract vision of the geometry of a system, taking into account the electromagnetic interactions between the different volumes. With this diagram, an inventory of all the penetration paths into the previous volumes can be made and then an interaction graph drawn: this description of the electromagnetic interaction between volumes is better suited than the diagram to computerization. Figure 1 represents a superimposition of a topological diagram with an associated interaction graph.

According to the theory, the calculation of the interference in the system is provided by deriving the topological network(s) associated to the interaction graph. Figure 2 is an example of such a network dealing with one external penetration path of the interaction graph presented in figure 1. A network is constituted by tubes related to each other through junctions. The signal propagating on the tubes is understood in terms of wave vectors  $W(z)$  and the coupling of external sources in terms of source wave vectors  $W_s$ . One can then derive relations involving all the waves on the network, considering supervectors (vectors of vectors) and supermatrices (matrices of matrices). The propagation equation relates the wave supervectors at each extremity of the tubes  $W(0)$  and  $W(L)$  by means of a propagation supermatrix  $\Gamma$ :

$$W(L) = \Gamma W(0) + W_s \quad (1)$$

The propagation equation relates the outgoing wave supervectors  $W(0)$  and the incoming wave supervectors  $W(L)$  by means of a scattering supermatrix  $S$ :

$$W(0) = S W(L) \quad (2)$$

Combining (1) and (2), a single equation can then be derived, taking into account all the electromagnetic interactions on the network: it is called the B.L.T. equation (Baum - Liu - Tesche):

$$(1 - S\Gamma) W(0) = S W_s \quad (3)$$

One can already measure how this equation can be useful to perform the optimization phase of an electromagnetic design. However, the main problem is to express the waves and  $S$  and  $\Gamma$  supermatrices in any coupling configuration.

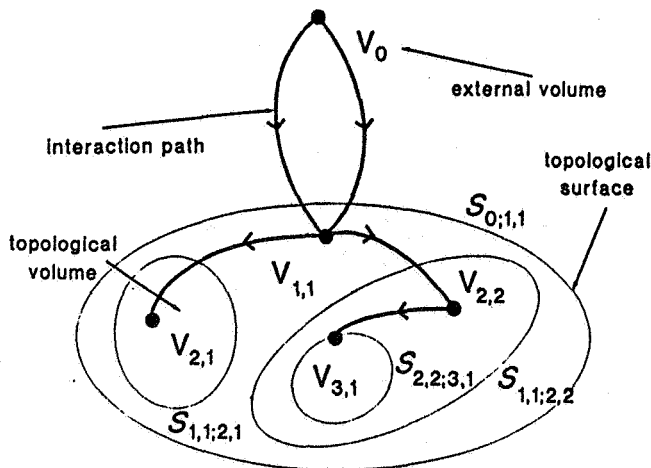
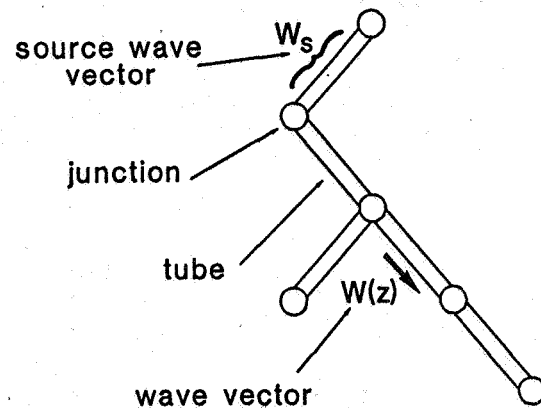


Figure 1: Topological diagram and associated topological graph.

Figure 2: Topological network.



### A QUALITATIVE APPROACH

In this approach, the concepts of topological diagram and graph remain valid. The difference is that all the evaluations of the interference are made by means of transfer functions. For this, judicious observables must be defined at each node of the graph, such as electromagnetic fields or currents and voltages and related by means of matricial expressions involving transfer operators  $T_{i,j;k,l}$  as defined in figure 3. As an example, the current and voltage at node 3.1  $\begin{Bmatrix} I \\ V \end{Bmatrix}_{3.1}$  is given with respect to external electromagnetic

field  $\begin{Bmatrix} E \\ H \end{Bmatrix}_0$  by the relation:

$$\begin{Bmatrix} I \\ V \end{Bmatrix}_{3.1} = T_{3.1;2.2} T_{2.2;1.1} \left( T_{1.1;0}^1 + T_{1.1;0}^2 \right) \begin{Bmatrix} E \\ H \end{Bmatrix}_0 \quad (4)$$

This tool is well suited to evaluate interference on a given structure and to propose maintenance specifications. The transfer operators can be measured or estimated (defining bounds with matricial norms for example) [1],[3]. The main problem is that this approach poorly lends itself to foresee the interference value when the geometry of the structure is modified.

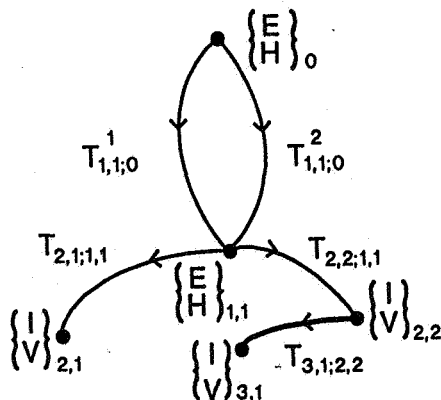


Figure 3: Transfer functions on a topological graph.

## A NEW APPROACH COMBINING QUANTITATIVE AND QUALITATIVE ASPECTS

The two previous fundamental approaches must progress each in its own way, but it must always be kept in mind, that they must meet and merge in a single approach in the future.

Today, an approach conciliating the two is developed, based on the fact that a very important way to propagate the interference is constituted by cables. As a matter of fact, the multiconductor transmission line network theory is well suited to the B.L.T. equation formalism because all the quantities defined in (3) can be easily expressed with respect to current  $I(z)$  and voltage  $V(z)$  observables all along the lines [2],[5]. Figure 4 shows the electrical modeling of a multiconductor line cell where  $Z$  and  $Y$  are the distributed shunt impedance and parallel conductance matrices respectively.  $V_s$  and  $I_s$  are the shunt voltage and parallel current generators dealing with the coupling of external sources on the wires.

A  $Z_c$  matrix can be defined on each transmission line by:

$$Z_c = (Z.Y)^{1/2} \quad (3)$$

which allows to express the waves  $W(z)$  as:

$$W(z) = V(z) + Z_c I(z) \quad (4)$$

$\Gamma$  and  $W_s$  quantities can also be easily derived from  $Z$  and  $Y$  matrices and  $V_s$  and  $I_s$  vectors.

To obtain a generalization of this network transmission line formalism for the treatment of a global electromagnetic internal problem, one may think of integrating other forms of electromagnetic couplings into this theory. Effectively, apertures, joints, seams, antennas are very common and important penetration points in aeronautical vehicles.

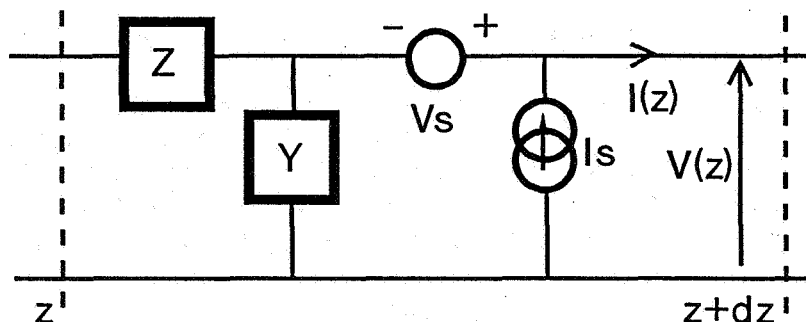


Figure 4: Electrical modeling of a multiconductor cell.

This can be done in two ways. The first one deals with distributing  $V_s$  and  $I_s$  generators all along the lines, using direct measurements or 3-dimensional codes. The second one consists in characterizing the coupling in terms of a network junction. This is what will be discussed now.

### 3. ELECTROMAGNETIC COUPLING THROUGH AN APERTURE DESCRIBED AS A JUNCTION

#### 3.1. COUPLING OF TWO WIRES LOCATED ON BOTH SIDES OF AN APERTURE

##### Geometrical configuration

The configuration is represented in figure 5. The aperture is circular, with a diameter  $d$ , but the study remains valid for any shape. Both wires of length  $l$  are parallel to a ground plane at heights  $h_1$  and  $h_2$  respectively. The main hypothesis here is that conducting wire paths always prevail on any external radiation field.

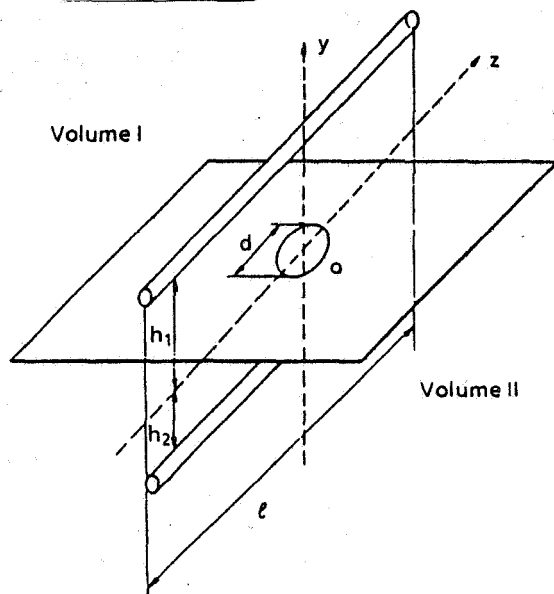


Figure 5: Coupling of two wires located on both sides of an aperture.

##### Electrical modeling and scattering parameters for small apertures

This model is valid insofar as the resonances of the aperture are not involved. The electrical scheme associated with this configuration is shown in figure 6 (the reaction of the inner wire is not taken into account). It can be shown that current  $I$  and voltage  $V$  in the upper volume, create in the lower wire shunt current  $I_{eq}$  and serial voltage  $V_{eq}$  generators [3], defined as:

$$V_{eq} = j\omega\alpha I \quad (5)$$

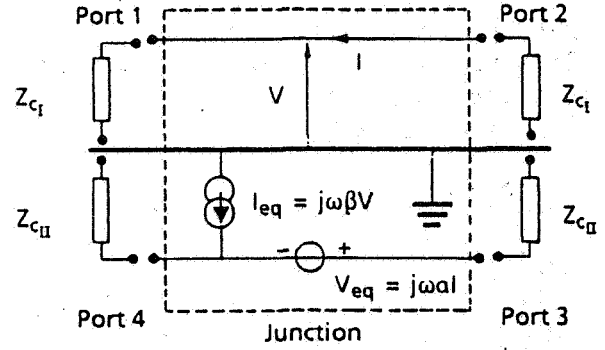
$$I_{eq} = j\omega\beta V \quad (6)$$

One can consider this configuration as a four port junction. The scattering parameters determination implies that each port is loaded on the characteristic impedance of the lines connected to  $Z_{cI}$  and  $Z_{cII}$  respectively (see figure 6).

A 4x4 matrix  $[S]$  is then derived and can be divided into four blocks as follows [4]:

$$[S] = \begin{bmatrix} S_{I,I} & S_{I,II} \\ S_{II,I} & S_{II,II} \end{bmatrix} \quad (7)$$

Figure 6: Electrical modeling of the junction dealing with the coupling of two wires through an aperture.



$S_{I,I}$  and  $S_{II,II}$  are 2x2 matrices dealing with the scattering parameters of a transmission line and are only slightly affected by the presence of the aperture. More important are the 2x2 blocks  $S_{I,II}$  and  $S_{II,I}$  dealing with the signal transfer from one side of the structure to the other. The expression of  $S_{II,I}$  components is given by:

$$S_{II,I} = \begin{bmatrix} \frac{j\omega}{2} \left( \beta Z_{cII} + \frac{\alpha}{Z_{cI}} \right) & \frac{j\omega}{2} \left( \beta Z_{cII} - \frac{\alpha}{Z_{cI}} \right) \\ \frac{j\omega}{2} \left( \beta Z_{cII} - \frac{\alpha}{Z_{cI}} \right) & \frac{j\omega}{2} \left( \beta Z_{cII} + \frac{\alpha}{Z_{cI}} \right) \end{bmatrix} \quad (8)$$

#### Scattering parameters for large apertures

It must be noted that the relation (8) still remains valid for low frequencies (before the resonances of the wires) and can inspire an efficient way to go back to  $\alpha$  and  $\beta$  values.

However, when the frequency increases, the best way to characterize the aperture coupling is the measurement. The scattering parameter determination is not made directly. The first step of the work generally consists in measuring the microwave parameters  $S_o$  of the 4-port junction with a network analyser [6]. These parameters have the same definition as the "topological" S parameters except the load impedance is fixed at  $Z_{co}$  generally equal to 50  $\Omega$ .

The second step is to go back to the Y parameters of the junction with such a matricial relation:

$$[Y] = \frac{1}{Z_{co}} ([1] + [S_o])^{-1} \cdot ([1] - [S_o]) \quad (9)$$

with  $[1]$ : the unit matrix.

One can then derive the  $[S]$  topological matrix, considering the local characteristic impedance matrix  $[Z_c]$  of the connected lines:

$$[S] = ([1] - [Z_c][Y]) \cdot ([1] + [Z_c][Y])^{-1} \quad (10)$$

Figures 7a,7b,7c illustrate as an example the variation of  $S_0$ ,  $Y$  and  $S$  parameters between port 1 and port 3.

It must be specified that when the length of the lines becomes greater than the aperture size, the B.L.T. equation formalism gives the opportunity to find the parameters in the actual reference plane of the junction.

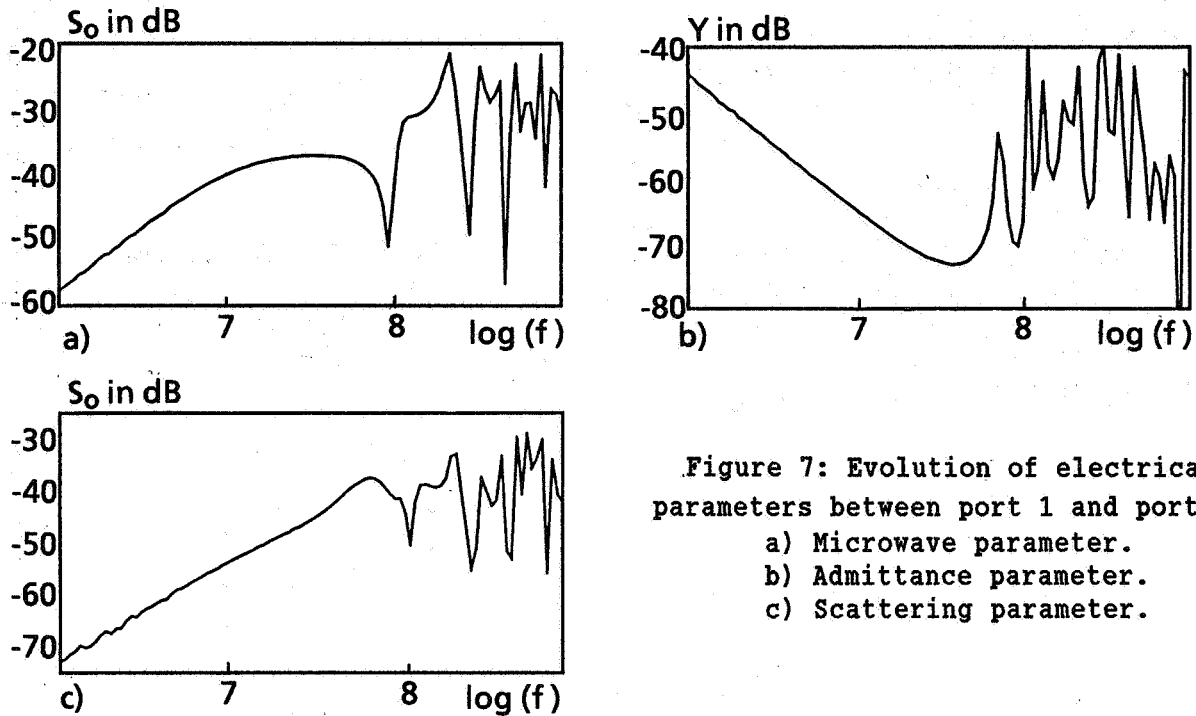


Figure 7: Evolution of electrical parameters between port 1 and port 3.

- a) Microwave parameter.
- b) Admittance parameter.
- c) Scattering parameter.

### 3.2. MODELING OF THE FIELD TO WIRE COUPLING

For this case, one must consider the geometrical configuration represented in figure 8. The upper wire in volume I has disappeared and has been replaced by an external electromagnetic plane wave. If the aperture is short circuited, this wave creates, short circuit electric  $E_{sc}$  and magnetic  $H_{sc}$  fields on it. The aperture must be supposed small enough to consider that the distribution of the fields is homogeneous.

Then the question can be asked what should the characteristic of the fictive wire in volume I be to create such an electromagnetic field distributions. For this, the E.M. fields created by a wire on a conductive plane can be calculated. According to the notations of figure 8, we have:

$$\vec{E}_{sc} = - \frac{V}{\pi} \frac{Z_0}{Z_c} \frac{d}{d^2 + y^2} \vec{e}_x \quad (11)$$

and

$$\vec{H}_{sc} = - \frac{I}{\pi} \frac{d}{d^2 + y^2} \vec{e}_y \quad (12)$$

where  $Z_c$  is the characteristic impedance of the wire,  $Z_0$  the impedance of the medium.

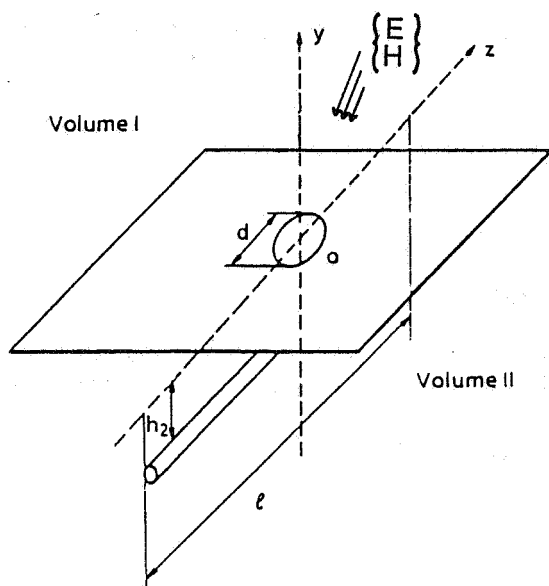


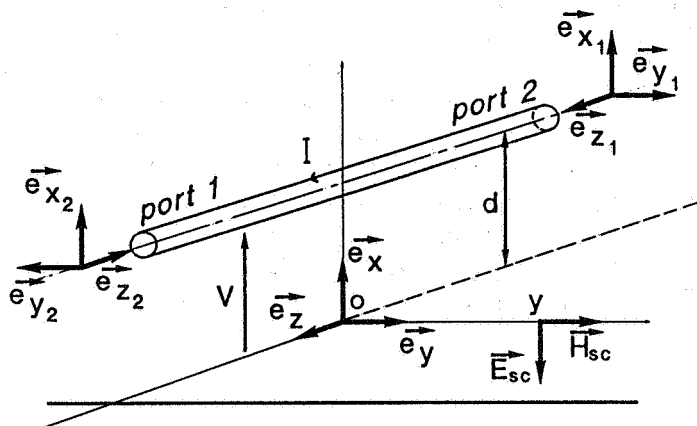
Figure 8: Coupling of a plane wave and a wire located under an aperture.

At each extremity (see figure 9), two orthogonal references can be created:  $(\vec{e}_{x1}, \vec{e}_{y1}, \vec{e}_{z1})$  at port 1,  $(\vec{e}_{x2}, \vec{e}_{y2}, \vec{e}_{z2})$  at port 2. The short circuit fields  $\vec{E}_{sc}$  and  $\vec{H}_{sc}$  can be expressed according to these new directions and become respectively  $\vec{E}_{sc1}, \vec{H}_{sc2}$ .

If I is introduced, an index dealing with volume I including indices 1 and 2, the topological wave for the fictive wire is defined by:

$$W_I^{\pm} = V_I \pm Z_{cI} I_I \quad (13)$$

Figure 9: Electromagnetic field created by a wire on a conductive plane.



where + or - indicates incoming and outgoing waves.

From (11) and (12), defining an equivalent length  $l_{eq}$  by:

$$l_{eq} = \frac{Z_c}{Z_o} \frac{d^2 + y_o^2}{d} \quad (14)$$

( $y = y_0$  at the center of the aperture), and a topological field wave  $W_{scI}^+$  by:

$$W_{scI}^+ = E_{scI} + Z_0 H_{scI} \quad (15)$$

a new scattering equation involving the observables at each port of the junction is derived:

$$\begin{pmatrix} W_{scI}^- \\ W_{II}^- \end{pmatrix} = [S'] \begin{pmatrix} W_{scI}^+ \\ W_{II}^+ \end{pmatrix} \quad (16)$$

If  $[S]$  is the scattering matrix dealing with the coupling of the fictive wire and the wire in volume II, defined in 4 blocks as in (8), it can be seen that  $[S']$  in relation (16) is equal to:

$$[S'] = \begin{bmatrix} S_{I,I} & -S_{I,II}/l_{eq} \\ -S_{II,I} * l_{eq} & S_{II,II} \end{bmatrix} \quad (17)$$

As the scattering parameter definition needs to have a ratio  $V/I$  equal to  $Z_c$ , it is seen that the ratio  $E(y)/H(y)$  remains equal to  $Z_0$ . So, by adjusting the value of the medium impedance, it is possible to simulate any direction of the incident plane wave.

In fact, a single wire can be shown as an approximate tool to simulate a plane wave but as a convenient system for testing a structure. One could also think of measuring the scattering parameters when the wire in volume I is replaced by a conductive plane, thereby defining a stripline.

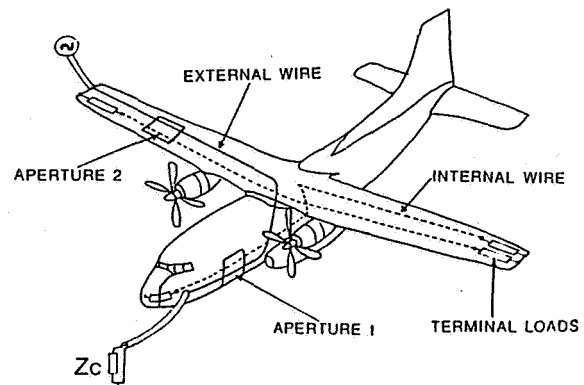
#### 4. APPLICATION OF THE TOPOLOGICAL CONCEPTS ON A SCALE MODEL

##### CHARACTERIZATION OF THE INJECTION

The previous results are applied on a scale model ( $1/10^{th}$ ) of the C160 Transall aircraft. Figure 10 shows the experimental set-up. Several wires (in dotted lines) run inside the structure and the external coupling paths are essentially constituted by two apertures 1 and 2.

An external wire excitation is chosen as in II.1, II.2 and II.3, but to maintain a constant characteristic impedance, the wire is replaced by a coaxial cable unshielded at the level of the apertures. This convenient means of excitation allows to easily choose the aperture to be irradiated. The frequency range can reach up to 100 MHz with less than a 3 dB variation and  $Z_c$  remains equal to  $50 \Omega$  except at the aperture level [7].

Figure 10: External and internal wire location on the scale model.





## HIGH FREQUENCY MODELING OF INTERNAL COUPLINGS

If interference precalculations are to be made, it is necessary to make circuit modelings of the couplings. This can be done using powerful personal computer codes such as "Touchstone". Such a code provides the opportunity to perform curve optimizations: specific goals are introduced and the adjustment of pertinent parameters is made automatically.

The electrical characterization of the scale model is made in a topological sense which means that each part is studied independently. As an example, figure 11 represents the different ports where measurements are performed on the wing. Considering this configuration as a four port system the  $S_{ij}$  parameters have been obtained and simultaneously, a modeling of the electrical circuit has been done. To take resonances in the aperture into account, several generator cells have been provided as reported in figure 12. Finally, a comparison between measured and modeled transfer functions can be performed using the B.L.T. equation. Figure 13 gives an example of the good agreement between both results at port 4. Consequently, we are now able to foresee the consequences of any modification on this geometry, by fitting the value of the pertinent circuit elements.

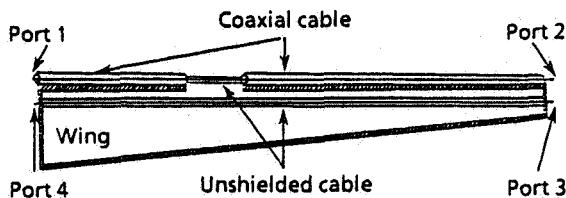


Figure 11: Different ports of measurement on a wing.

Figure 12: Electrical modeling of the coupling through the aperture taking resonances into account.

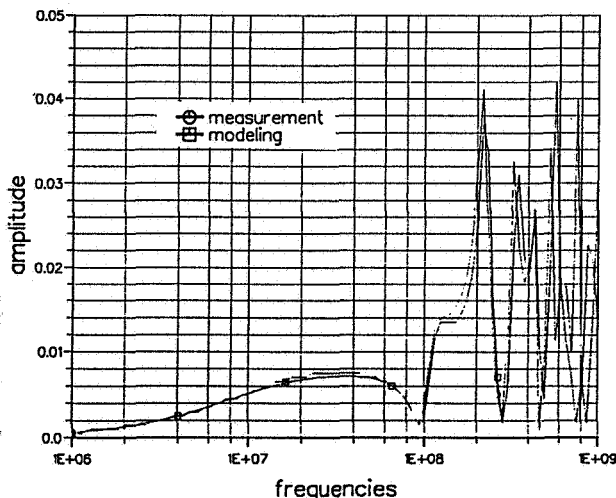
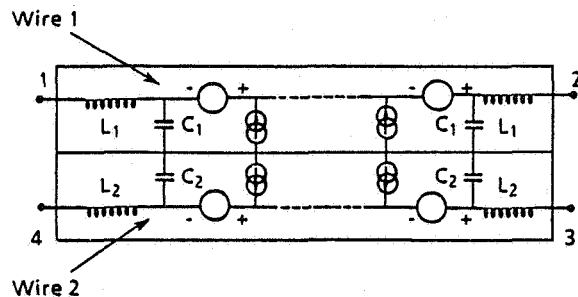


Figure 13: Comparison between measured and modeled transfer functions on port 4 of the wing.

## 5. CONCLUSION

The electromagnetic topology must lead to the definition of an electromagnetic design tool. Nowadays, several methods must be developed at the same time: the fundamental concepts, elaborated by C.E. Baum; a quantitative way dealing with the use of graph concepts. Another interesting method, combining the two previous ones, is to generalize the multiconductor transmission line network theory in the aim of integrating well known electromagnetic couplings in the formalism.

The treatment of an aperture as a four-port junction is an aspect of this development, and has proved itself to be a convenient means to test internal electromagnetics. In the future, other aspects such as antenna couplings and current diffusion will be treated.

In conclusion, the B.L.T. equation coupled with the multiconductor transmission line network formalism could become, in the future, the basis of an electromagnetic design tool.

## REFERENCES

- [1] C.E. Baum,  
Theory of electromagnetic interference control. Interaction Notes, Note 478, 28 December 1989.
- [2] C.E. Baum, T.K. Liu, F.M. Tesche,  
On the analysis of general multiconductor transmission line networks. Interaction Notes, No 350, November 1978.
- [3] F.C. Yang, C.E. Baum,  
Electromagnetic Topology: measurements and norms of scattering parameters of subshields. Electromagnetics 6, 47-59, 1986.
- [4] K.S.H. Lee,  
Principles, techniques and reference data (a complete concatenation of technology from EMP interaction notes). EMP Interaction Notes, 2.1, 1980.
- [5] J.P. Parmantier, G. Labaune, J.C. Alliot, P. Degauque,  
Electromagnetic coupling on complex systems: Topological approach. La Recherche Aéronautique, n°1990-5.
- [6] J.P. Parmantier, G. Labaune, J.C. Alliot, P. Degauque,  
Electromagnetic Topology: Junction characterization methods. La Recherche Aéronautique, n°1990-5.
- [7] J.P. Parmantier, J.P. Aparicio,  
Electromagnetic Topology: coupling of two wires through an aperture. Proceedings, Zurich, 1991.

**A REAL SCALE SIMULATOR FOR HIGH FREQUENCY  
LEMP**

D. GAUTHIER - D. SERAFIN

CENTRE D'ETUDES DE GRAMAT  
46500 GRAMAT

**ABSTRACT :** The paper describes the real scale simulator designed by the Centre d'Etudes de Gramat (CEG) to study the coupling of fast rise time Lightning Electromagnetic pulse with a fighter aircraft. The system capability of generating the right electromagnetic environment has been studied using a FDTD computer program. First data of inside stresses are then shown. A time domain and a frequency domain approach are exposed and compared.

**1. INTRODUCTION**

Nowadays aircrafts become more and more sensitive to the high frequency electromagnetic pulses generated during a lightning strike event. This is due to the extensive use of both composite material in the fuselage and digital electronic whose susceptibility towards High Frequencies (HF) is important. Recent in flight lightning measurement campaign [1], [2] have revealed significant single current pulses whose rise time can be much faster than the micro second range. Such pulses seem to originate from the re-ignition phase when the lightning channel is already ionized. Their spectrum can show a significant frequency content up to few tens of Megahertz.

It is not yet well established whether this new kind of threat has to be normalized or not and taken into account during qualification process. In order to study the coupling of such high frequencies Lightning Electromagnetic Pulse (LEMP) with inner aircraft cables a simulator has been designed by the Centre d'Etudes de Gramat (CEG).

The fast rise times associated with high current amplitude suggest to use a coaxial return path technique to be able to simulate faithfully the electromagnetic environment created by lightning.

**2. OVERVIEW OF THE SIMULATOR DESIGN**

The simulator is based upon the coaxial return path technique. This technique has previously been used with Transall and Mirage Scale Model Studies [3]. The aircraft under test is considered as the central conductor of a coaxial line whose outer conductor is made by a set of wires surrounding the aircraft (see fig 1). Under the aircraft the return current is driven through a copper ground plane. The distance between the central core and the return path is adjusted to avoid any air breakdown during the high voltage tests. Two other parameters which are of great importance for the set up of the return wires are the electric field at the fuselage surface and the characteristic impedance of the line. We tried to maintain the second around the fixed value of  $50\Omega$ , while the first one is compared with 3D computer calculations (see next section).

The aircraft stands on metallic adjustable posts. Those three posts are situated inside the line. It has been checked that the change in the characteristic impedance due to this configuration does not affect strongly the rise time of the injected current. The current is injected at the nose of the aircraft, the end of the line can be terminated by various charge impedance or short circuited.

The following experiments have been performed using a low level generator ( $I_c = 500$  A). Future works will be proceeded with a variable (5 - 15 kA) high level generator whose rise and decay times will as well be adjustable.

### 3. OUTER COUPLING

As a first step it seems of the greatest interest to measure the electromagnetic environment created by the simulator using Finite Difference Time Domain (FDTD) computer program. The code called GORFF-VE has previously been used to interpret the data from in flight lightning measurement campaign [4]. The good agreement between real data and numerical calculations has allowed to get a good confidence in the ability of the code to reproduce in flight lightning electromagnetic environment. Hence numerical calculations are now used to validate the simulation tool.

Accurate description of the GORFF-VE 3D code can be found in numerous publications [5], [6].

The current shapes injected at the nose of the aircraft experimentally and numerically are presented figure 2.

Electric and magnetic fields have been measured for various points on the half of the total fuselage by reason of symetry. Measurements have been performed using active sensors and fiber optic link. Mappings of the peak values of the electric and magnetic fields are reported figure 3 and 4.

For a better understanding temporal shapes of the recorded signals are compared with numerical ones. This is only possible using a transfer function technique because of the difference in the experimental and numerical injected currents (see fig 2).

To be consistent and to eliminate the mismatch problems at the aircraft nose, value of the major magnetic field component at the nose ( $H_{y1}$ ) is taken as a reference.

Only the time domain derivative is compared for the electric field because the numerical decay time is strongly dependent upon the aircraft capacitance.

Both equations are used :

$$H_{y,x}(\omega) \times \frac{H_y^{\perp \text{ para}}}{H_y^{\perp \text{ conf}}}(\omega) = MIR(\omega) \quad (1)$$

$$-\frac{dE_{\text{Gorff}}^n(\omega)}{dt} \times \frac{E_z^1 \rho_{\text{cous}}}{E_z^1 \text{Gorff}}(\omega) = d\text{Mir}^n(\omega) \quad (2)$$

Fourier transform analysis are performed in the  $10^4 - 10^8 \text{Hz}$  range. After inverse Fourier transform (1) and (2) are compared with the experimental signals (fig 5, 6). A study of all the experimental points allow to conclude that two zones appear on the aircraft :

- *Booster and back fuselage zone* where experimental recordings are much higher than what is expected from the calculations,
- Everywhere else experimental signals fit quite well the theoretical predictions.

Hence, comparison between the electromagnetic environment created by the simulator and calculated from the 3D FDTD GORFF-VE code indicates that the coaxial return path simulation is appropriate to reproduce the fast rise time lightning electromagnetic stress. Due to the good agreement on the outer electromagnetic peak values and time domain shapes, inner coupling results should be representative of the in-flight situation.

#### 4. INNER COUPLING

Ten different points have been instrumented inside the Mirage aircraft. Six cable currents have been measured and for four points inner fields have been recorded. The levels recorded are significant, six typical recordings are presented fig. 7. As well as time domain measurements, frequency domain measurements have been performed using a vectorial network analyser. From those experiments transfer functions up to 200 MHz, normalized to Hy1 value are deduced (fig. 8).

Using these functions and the Fourier transform of Hy1 at the nose of the aircraft, we have been able to deduce stresses inside the aircraft. These stresses are compared with the measured one for four different cases (two currents, two H fields).

As the frequency spectrum of Hy1 is well defined only up to 20 MHz a good agreement can be obtained as long as the inner signal does not contain too high frequencies (HYIPPB, ITPBC). If this is not the case discrepancies are observed (HXIS, ITSER) because the high frequency excitation is not the same in the two cases (fig 9). As the frequency spectrum of Hy1 is limited to 20 MHz (due to the 80 dB dynamic measurement range), only noise is then recorded after this limit and the frequencies higher than 20 MHz are then altered. Limiting the analysis up to 20 MHz then cancel out those frequencies.

#### 5. CONCLUSION

We have presented a real scale simulation tool able to reproduce quite faithfully the electromagnetic environment generated by fast rise time lightning pulses.

The first series of measurements inside the aircraft have been presented. They show the limitations of the frequency domain analysis. Still more work has to be done on a more realistic aircraft and at real threat to define Thevenin equivalent generators for the stress on the inner cable bundles and to compare those values with advisory circular recommended waveforms for aircraft certification.

A link between Thevenin generators and cables bundle currents would also be helpful for future qualification tests.

### ACKNOWLEDGEMENTS

This work was supported by DRET (Direction des Recherches, Etudes et Techniques) of French Ministry of Defence.

### REFERENCES

- [1] J.P. MOREAU - J.Y. JOUAN - F. ISSAC  
*Transall 88 lightning characterisation program*  
1989 ICOLSE - Bath.
- [2] V. MAZUR  
*Lightning initiation on aircraft in thunderstorms*  
Aerospace and ground conference on lightning and static electricity - Oklahoma city  
1988.
- [3] D. GAUTHIER - D. SERAFIN  
*Simulation des effets impulsionnels de la foudre par ligne coaxiale adaptée*  
Colloque CEM - Evian 1989
- [4] F. FLOURENS - D. GAUTHIER - D. SERAFIN  
Exploitation de mesures acquises lors de la campagne 1988 de caractérisation de la foudre sur un aéronef en vol.  
N.T. 90-73 - CEG - 1990
- [5] F. FLOURENS - D. GAUTHIER - D. SERAFIN  
*Lightning strike simulation using coaxial line technique and 3.D linear injection current analysis*  
1989 ICOLSE Bath.
- [6] F. FLOURENS - D. SERAFIN  
*Remarques sur la simulation de l'espace libre au sein du programme GORFF et sur la modélisation des extrémités de fils électriquement adaptés.*  
NE 88.04 - CEG - 1988.

ORIGINAL PAGE  
BLACK AND WHITE PHOTOGRAPH

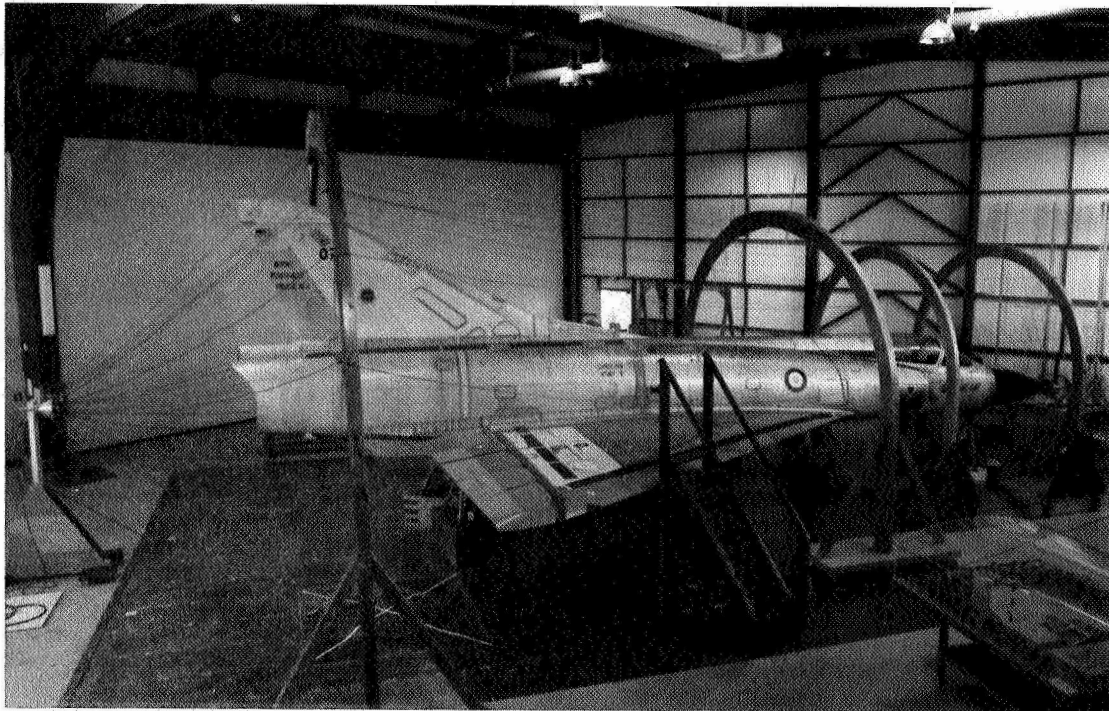


FIGURE 1 : Picture of an overall view of PARSIFAL simulator

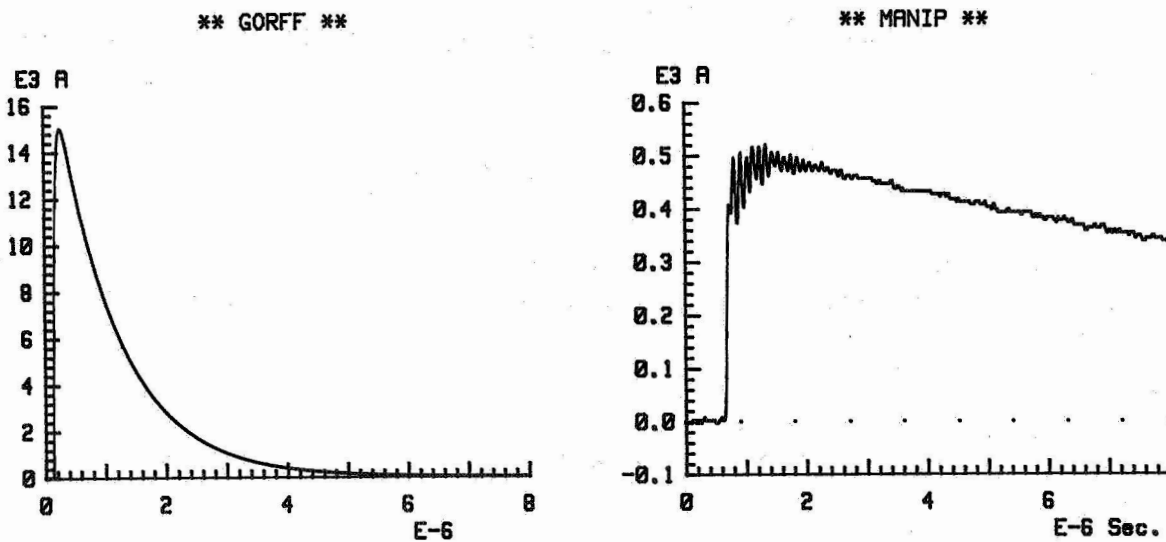
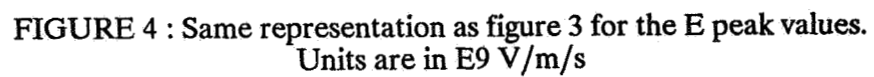
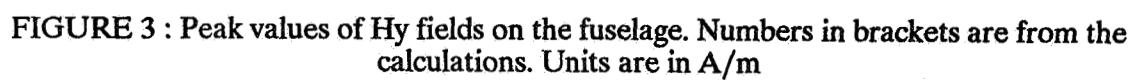


FIGURE 2 : Time domain behavior of the experimental  
and the numerical currents injected on the Mirage





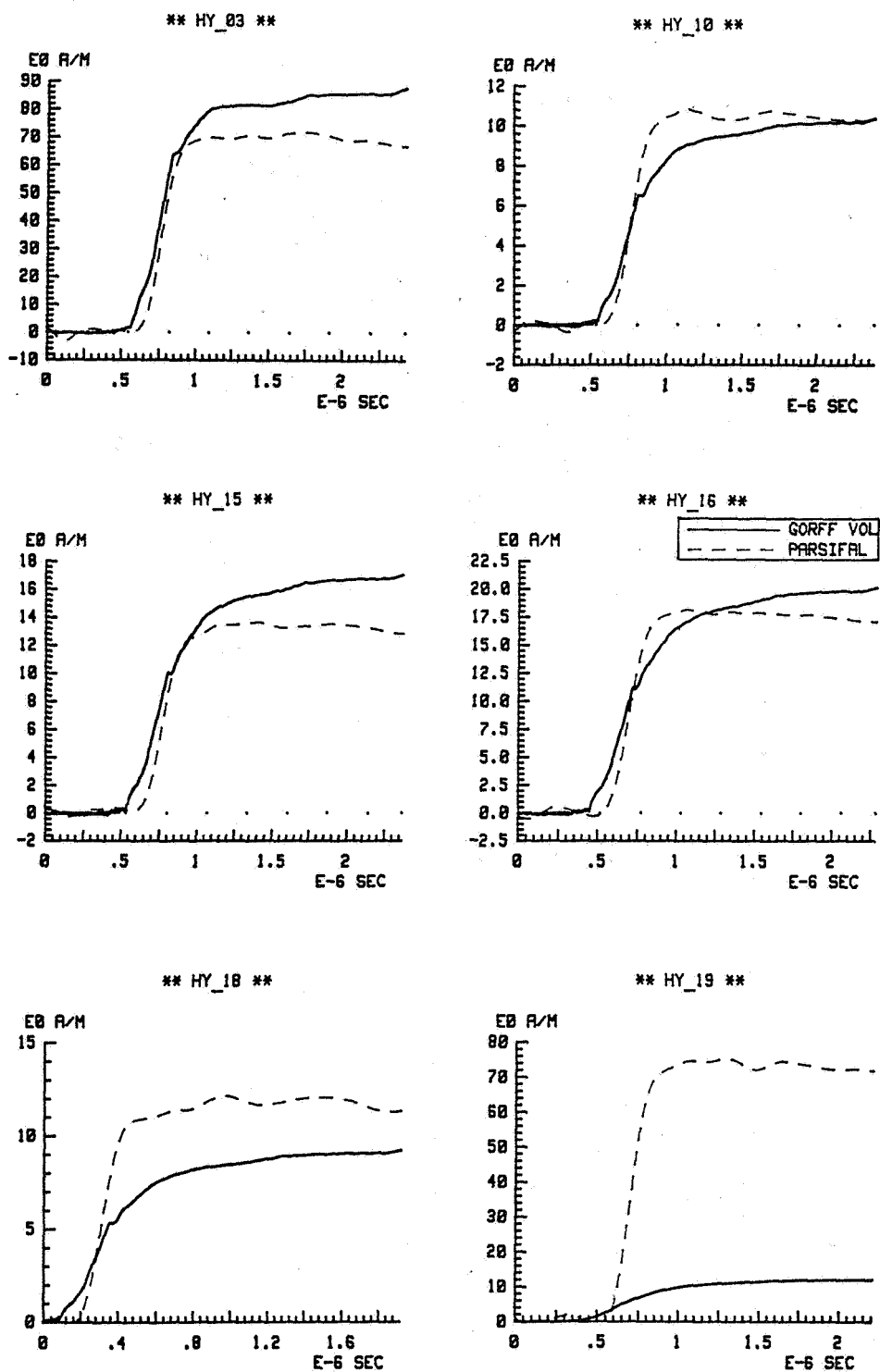


FIGURE 5 : Time domain comparison for 6 Hy points of the fuselage

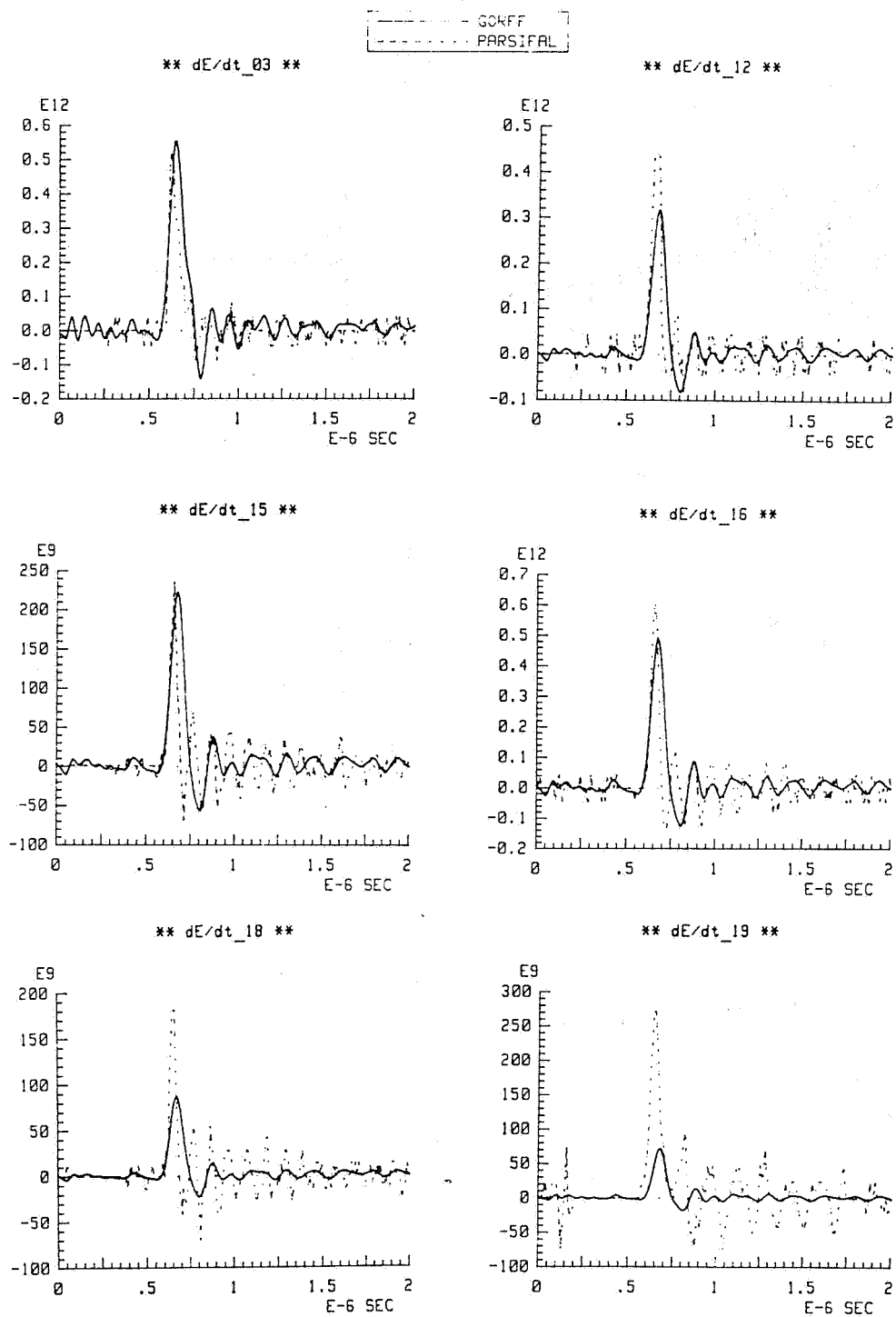


FIGURE 6 : Same comparison as figure 5 for the  $\dot{E}$  time domain values

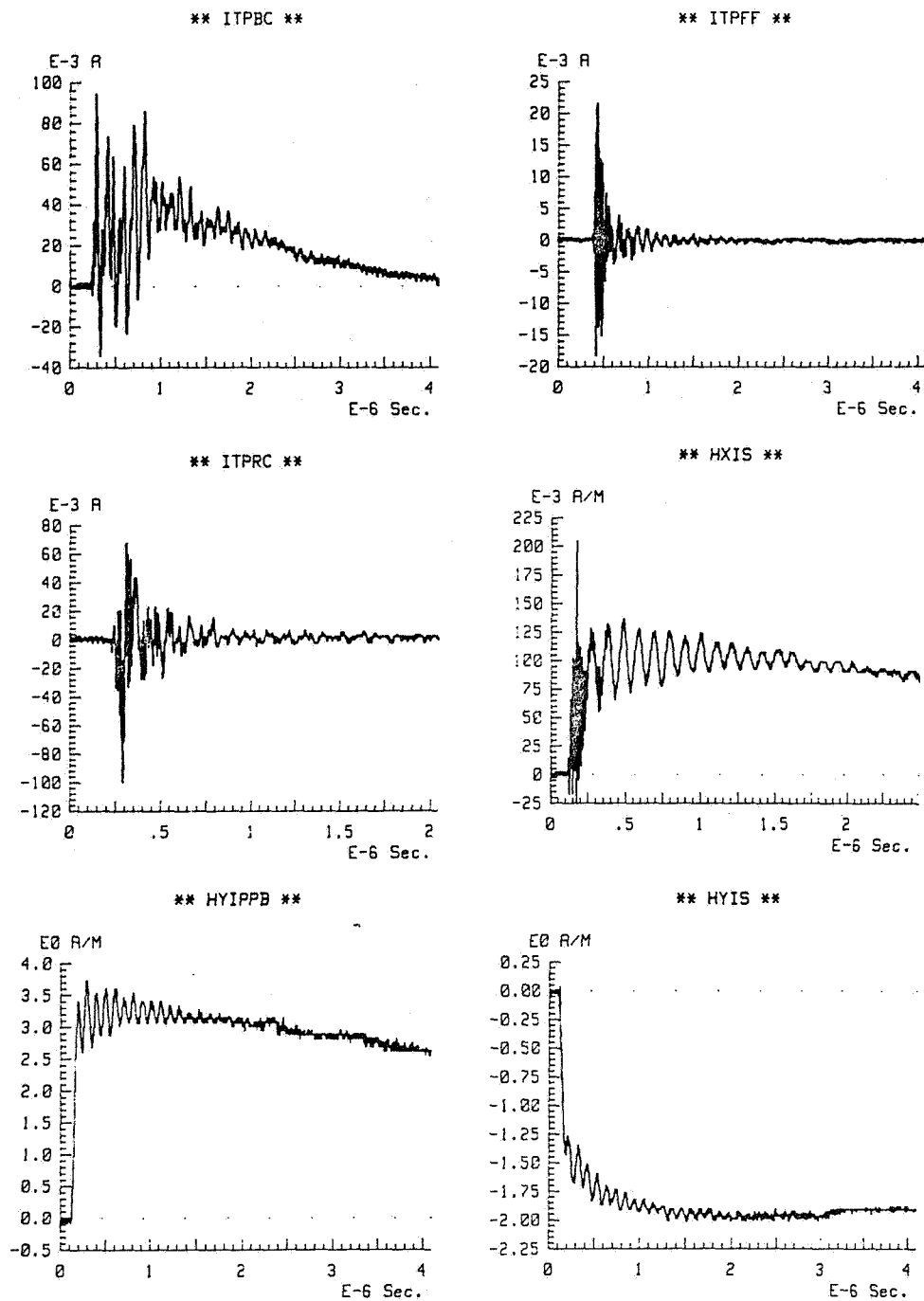


FIGURE 7 : Samples of currents and fields measured inside the aircraft

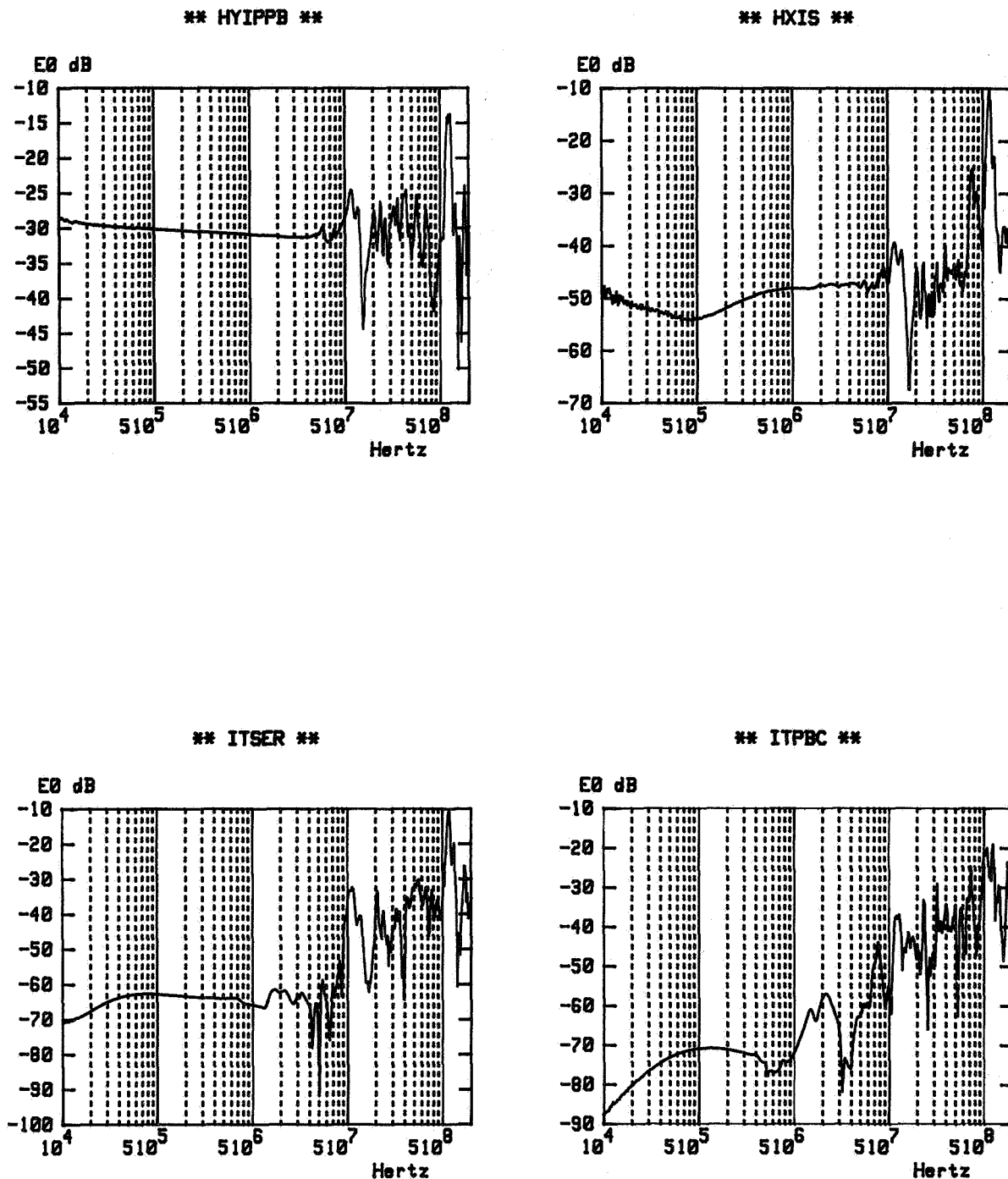


FIGURE 8 : Examples of transfer function measured with a network analyser :

HYIPPB : Hy field in the cockpit, near the UHF command box  
 HXIS : Hx field in the equipment compartment  
 ITSER : current on the cable bundle of the emitter  
 ITPBC : current on the cable bundle of the UHF emission box

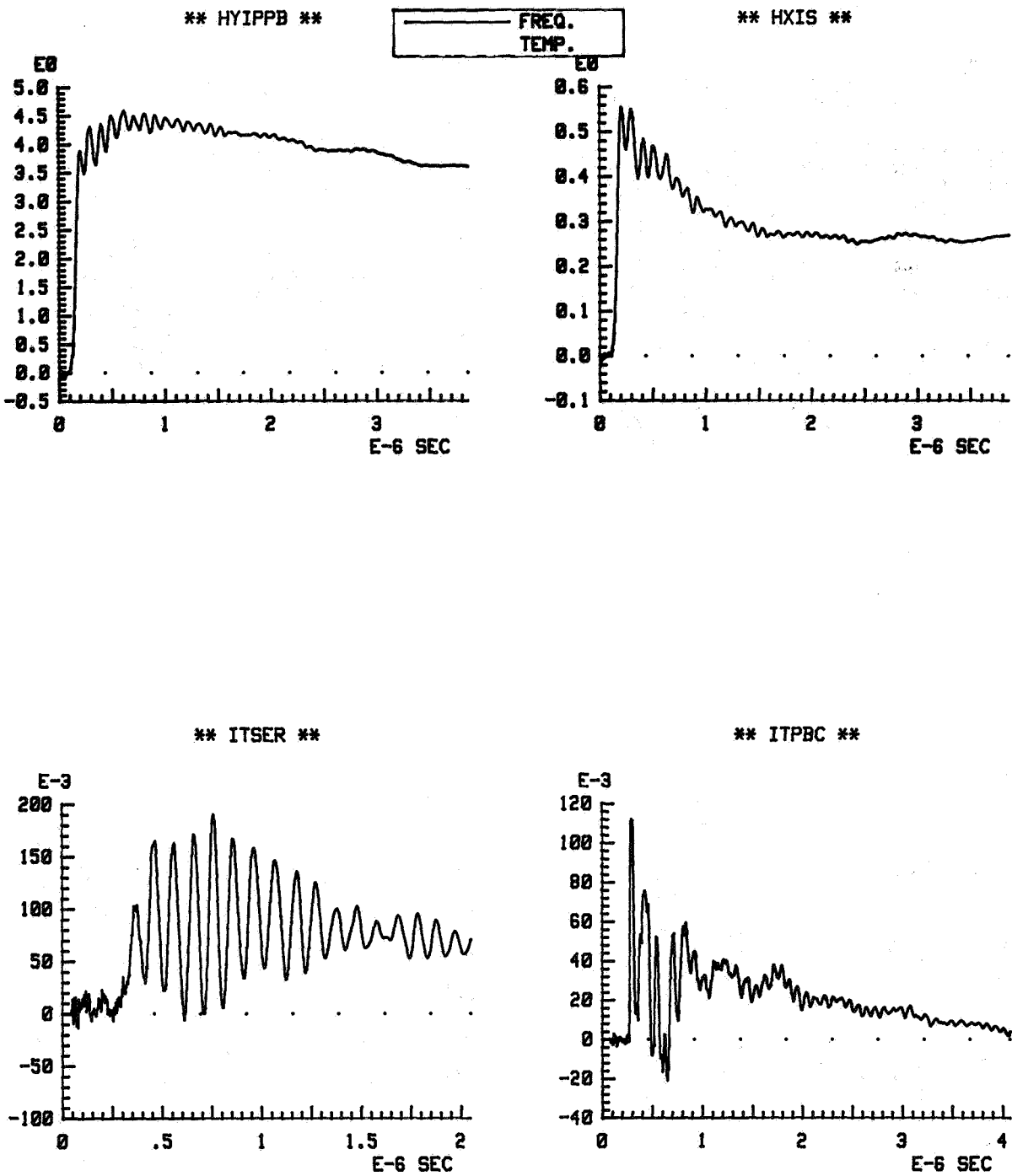


FIGURE 9 : Experimental and frequency domain calculated inner currents and fields.  
The points presented are the same as for figure 8

**A THEORETICAL ANALYSIS OF THE ELECTROMAGNETIC ENVIRONMENT  
OF THE AS330 SUPER PUMA HELICOPTER  
EXTERNAL AND INTERNAL COUPLING**

**F. FLOURENS - T. MOREL**  
GERAC - B.P. 19 - 46500 GRAMAT - FRANCE

**D. GAUTHIER - D. SERAFIN**  
CENTRE D'ETUDES DE GRAMAT - 46500 GRAMAT - FRANCE

**ABSTRACT :** Numerical technics as FDTD computer programs, that have first been developed to analyse the external electromagnetic environment of an aircraft during a wave illumination, a lightning event or any kind of current injection, are now very powerful investigative tools. The program called GORFF-VE, has been extended to compute the inner electromagnetic fields that are generated by the penetration of the outer fields through large apertures made in the metallic body. Then, the internal fields can drive the electrical response of a cable network. The coupling between the inside and the outside of the helicopter is implemented using Huygens's principle.

Moreover, the spectacular increase of computer resources, as calculations speed and memory capacity, allows the modelization structures as complex as these of helicopters with accuracy.

In this paper, this numerical model has been exploited, first, to analyse the electromagnetic environment of an in-flight helicopter for several injection configurations, second to design a coaxial return path to simulate the lightning aircraft interaction with a strong current injection. The E-fields and current mappings are the result of these calculations. Among the results, the resonance modes of the global structure have been emphasized.

## **1. INTRODUCTION**

From recent in-flight lightning measurements, it has been noted that fast rise time pulses were associated with the discharge. The study of the coupling phenomena of these pulses with either electronic on-board devices or on-board cables, necessitates to threaten a real scale aircraft with a fast rise time generator. The use of a coaxial return path technique allows to simulate the electromagnetic environment created by the direct injection of a fast rise time current pulse. This technique of simulation has previously been used for a TRANSALL aircraft and a M2000 fighter (1), (2). In the latter cases, the electromagnetic environment was evaluated using a theoretical model like a FDTD computer code, and using experimentations on scale models. The results obtained by the two methods have agreed quite rightly.

The FDTD computer code was used to evaluate the performances of the coaxial return path technique for the simulation of fast rise time lightning pulses on an helicopter. The theoretical improved model allows the calculation of both the outer and inner electromagnetic environment of the structure. Then, the results of several injection configurations are compared one with the other. The two main configurations are, first the injection of the pulse at the front of the in-flight helicopter when an exit channel is connected at its rear, and, second, the same injection but using a coaxial return path technique.

## 2. OVERVIEW OF THE THEORETICAL METHOD

### 2.1. Basics of the model

The theoretical model solves MAXWELL's equations in the time domain using finite difference approximations for the partial derivatives in time and space. This method which is suitable for transient analysis has already been reported several times (3), (4). The three dimensional finite difference representation of the helicopter is implemented in the centre of a 3D finite difference space grid ; this representation is constituted by a set of unit metallic surfaces. The inner and the outer fields can be computed together, during the same computer run for two reasons : first, because we computed the total electromagnetic fields in the grid and second because we didn't need different cell sizes for the inner and outer representation of the helicopter. The space domain is discretized as a set of elementary parallelepipedic cells. Six field components are evaluated in each cell of the grid. Figure number 1 shows where the electric (E) and magnetic (H) components are computed inside the cell. Then, the structure under study is modeled as a set of unit surfaces that are the sides of elementary cells. The electric field components that are tangential to its surfaces are forced to zero. Now, if there is an aperture in the structure at this location, the tangential fields are computed in the same way as in free space. However, this very simple method for the apertures is accurate only if their dimensions are superior to the size of the cell. The ratio between aperture dimensions and cell size must be superior to five in order to get good results.

A thin wire formalism that uses a transmission line approximation has been added to the code to model the lightning channel, cables and wires of a coaxial return path. All these wires can have non parallel direction with the cell axes and can be connected to metallic surfaces or one to the others. Generators and impedances can electrically load the wires.

The computer program called GORFF-VE has previously been used to interpret the data obtained from in-flight measurements (5) ; the good agreement observed between these data and the calculations, has validated the code for computing the in-flight lightning electromagnetic environment.

### 2.2. FDTD model of the helicopter

The FDTD representation of the structure is presented on figure number 2. The apertures are presented on figure number 3. The size of an elementary cell is 10 cm x 15 cm x 20 cm. These dimensions give a time step equal to 250 picosecond and allow frequency spectrum up to 300 MHz for the calculated signals.

The largest aperture of the structure is the windows of the canopy. This set of windows is an important way of penetration for the electromagnetic fields during the current injection. Two cables were set inside the helicopter, to compute an open circuit voltage and a short circuit current. These two signals are both evaluated during a single run. The wires are situated 60 cm above the floor, and oriented from the rear to the front of the cabin. They are 5,4 meters long each. The position of the wires is shown figure number 4.

The coaxial return path is composed of six wires surrounding the helicopter. The structure is the inner conductor of the coaxial transmission line which characteristic impedance is about 50 ohms. The coaxial return path is simulated in a very simple way with the thin wires formalism ; this is displayed figure number 5. The generator is matched to the line impedance and the line can be terminated by various charge impedance or short circuited. For the following simulations, the charge impedance is the characteristic impedance of the injection line.

### 2.3. Results of the models

The electromagnetic results given by the computations are :

- the E-fields and H-fields in the time domain for several inner and outer observation points (see figure number 6). These results are FOURIER transformed to point out resonance frequency,
- the mapping of the maximum values of the H-fields on the outer surface of the structure,
- the mapping of the maximum values of the inner E-fields and H-fields on the symmetry-plane of the helicopter cabin,
- the current and the voltage generated on the wires ends.

These results are obtained for several injection configurations. Two configurations are reported :

- in-flight injection at the nose of the helicopter,
- injection at the nose of the helicopter with a coaxial return path.

### 2.4. Injected current

The shape of the injected current is an arch of a square sinusoide. The rise time (0 - 100 %) of these signals is about a 50 nano second. The shape of the time functions and its FOURIER transformation are given figure 7.

## 3. OUTER RESPONSE OF THE HELICOPTER

### 3.1. In-flight calculations

The outer response of the helicopter was computed when the apertures had been closed and then opened. The same differences exist between these two calculations. The results obtained for several typical observation points are displayed in the next array, for a 1000 Amp injected current.

The apertures modify the electromagnetic fields only in their vicinity. Generally speaking, the values of the fields are reinforced when the apertures are opened. Figure number 8 shows the H-field distribution on the structure with and without apertures.

Several resonances are observed on the outer response, both with or without apertures. The two main values of resonance are 7 MHz and 10 MHz, as shown on the E and H-fields for the observation point n°3 (figure 9). The first frequency of 7 MHz is issued from the longitudinal resonance of the helicopter. The wavelength of this resonance ( $= 43$  m) is greater than twice the length of the helicopter ( $= 32,5$  m) because its cross section is large compared to its



length. A corrective factor of 1,3 must be applied to find the correct resonance value (6). The second resonance of 10 MHz is issued from the blades of the main rotor. The wavelength of this resonance (= 30 m) is exactly four time the length of the blade (7,5m).

Observation point	E <sub>MAX</sub> (kV/m)			H <sub>MAX</sub> (A/m)		
	without appert.	with appert.	Difference	without appert.	with appert.	Difference
1	26	75	+ 188 %	262	213	- 19 %
2	27	30	+ 11 %	255	270	+ 7 %
3	32	37,5	+ 17 %	112	146	+ 26 %
4	26	30	+ 15 %	93	100	+ 6 %
5	20	23	+ 15 %	68	70	+ 3 %

### 3.2. Coaxial return path calculations

The result obtained from the in-flight calculations are compared with the results calculated with the coaxial injection structure, on the following array.

Observation point	E <sub>MAX</sub> (kV/m)			H <sub>MAX</sub> (A/m)		
	In-flight	Return path	Discrepancy	In-flight	Return Path	Discrepancy
1	75	70	- 6 %	213	183	- 14 %
2	30	40	+ 33 %	270	203	- 25 %
3	37,5	43	+ 15 %	112	130	+ 7 %
4	30	67	+ 123 %	93	225	+ 142 %
5	23	30	+ 30 %	68	83	+ 22 %

The value of the simulated charge densities and current densities with the coaxial technique are quite similar, except for the observation point number 4. This point is located at the back of the structure. The difficulty to realize a good adaptation of the coaxial transmission line in this part of the structure, generates an overestimated value for the E-field. Moreover, the concentration of the current density lines along the fuselage generates an overestimation of the H-field values.

Generally speaking, as one can see on figure number 10, the coaxial transmission line injection technique reproduces correctly the in-flight external environment.

## 4. INNER RESPONSE OF THE HELICOPTER

The calculations of the inner environment for the in-flight injection and for the coaxial injection have displayed the same evolution for both the E-field and H-field. The analysis of the results is done, first when the cables are in-place and, second, when the cables are removed.

### 4.1. E.M. environment of the structure without cables

The internal results are the E and H space fields. The value of these two fields decreases of about 50 dB between the front of the canopy and the back of the metallic cabin. The same values of attenuation are observed for the two configurations of injections as one can see on figure number 11. Cavity resonances are observed inside the structure. Their frequencies can be evaluated by the basic relation used for a rectangular cavity :

$$f_{m, n, p} = \frac{c}{2} \sqrt{\frac{m^2}{a^2} + \frac{n^2}{b^2} + \frac{p^2}{d^2}}$$

where  $c$  is the speed of light and  $a, b, d$  the dimensions of the cavity. Applied to the helicopter cavity dimensions, this relation gives the following resonance frequencies :

TE <sub>101</sub>	->	65 MHz
TE <sub>102</sub>	->	78 MHz
TE <sub>103</sub> /TM <sub>110</sub>	->	96 MHz
TE <sub>111</sub> /TM <sub>111</sub>	->	100 MHz

Upper modes ( $f > 100$  MHz) can also be driven by the incident electromagnetic fields. The FOURIER transformation of the electric fields calculated in the middle of the cabin are given figure 12. The transformation shows the cavity resonance frequency, overlaid with the outer ones. The only discrepancy observed between the in-flight results and the coaxial return results lies in the relative importance of the cavity resonances. The highest modes ( $f > 100$  MHz) are dominant for a coaxial injection while they are not for an in-flight injection for two reasons. First, because of the shorter rise time of the current density when the coaxial return path is employed and second, because of the different way of field penetration through the apertures. This is not important for field levels, but it may become important if cables can couple energy in this frequency domain.

### 4.2. E.M. environment of the structure with the cables

The presence of the cables inside the helicopter doesn't modify the external electromagnetic environment but drastically increases the field levels inside the cabin. The ratio between middle and front fields become inferior to 25 dB compared to the 50 dB observed without any cables. The cables resonances affect the internal response as one can see on the Fourier transformation of the inner electric field (see figure 13). In this case, the presence of the cables has no effects on the value of the cavity frequency resonance. The influence of these cables is important because they run just behind the canopy apertures. The induced signals conducted along these wires pollute all the cabin.

The voltage and the current induced on the wires show resonances. Their wavelengths are multiples of the wires length. These signals are displayed figure 14, in the time and the

frequency domain. The response of the wires are the same in voltage and current, for the in-flight injection and for the coaxial one. The mappings of the inner electromagnetic fields are given figure 15 for this two configurations and one can see a good adequacy between the results.

## 5. CONCLUSION

The current injection on an helicopter using a coaxial return path for the currents allows to reproduce faithfully the electromagnetic environment generated by a fast rise time lightning pulse, when the attachment point is located on the nose of the helicopter. Additional study may be necessary to analyse other configurations of injection.

Nevertheless, if some discrepancies are observed at the rear of the structure for the outer environment, the inner electromagnetic fields are very close between the two way of simulation. The reason is that the major way of coupling between the exterior and the interior are the windows of the canopy located at the front of the helicopter. Consequently, electrical signals generated on wires are quite in accordance.

Numerical simulation is a powerful tool to analyse the fields involved during a lightning event, or during a lightning test with a simulator. This way of investigation shows that coaxial technique is able to reproduce the lightning environment of an helicopter, although the theoretical model of the coaxial return path was simplified. For real simulation test, this return path may be of a better geometry and may give better results than numerical simulations.

## AKNOWLEDGEMENTS

This work was supported by DRET (Direction des Recherches, Etudes et Techniques) of the French Ministry of Defense.

## REFERENCES

- [1] F. FLOURENS - D. GAUTHIER - D. SERAFIN  
*Lightning strike simulation using coaxial line technique and 3.D linear injection current analysis*  
1989 ICOLSE Bath.
- [2] D. GAUTHIER - D. SERAFIN  
*Simulation des effets impulsionsnels de la foudre par ligne coaxiale adaptée*  
Colloque CEM - Evian 1989
- [3] F. FLOURENS - T. MOREL - B. PECQUEUX - R. VEZINET  
*Evolution du programme GORFF-VE de résolution de problèmes électromagnétiques impulsionsnels - Adaptation au procédé de calcul vectoriel et au système d'exploitation NOS-VE sur ordinateur CDC.*  
Note technique T 89-60 - Centre d'Etudes de Gramat - Octobre 1989.
- [4] A. REINEIX - B. JECKO - P. BREUILH  
*Détermination par la méthode des différences finies des champs électromagnétiques dans une cavité illuminée via une ouverture de grandes dimensions*  
Colloque CEM - Limoges 1987
- [5] F. FLOURENS - D. SERAFIN  
*Exploitation de mesures acquises lors de la campagne 1988 de caractérisation de la foudre sur un aéronef en vol.*  
Note technique T90-73 - Centre d'Etudes de Gramat - Décembre 1990
- [6] Y. SHIAU - L. DUNCAN  
*EMP guidelines for navy ship platform hardening*  
IRT Corporation 1983

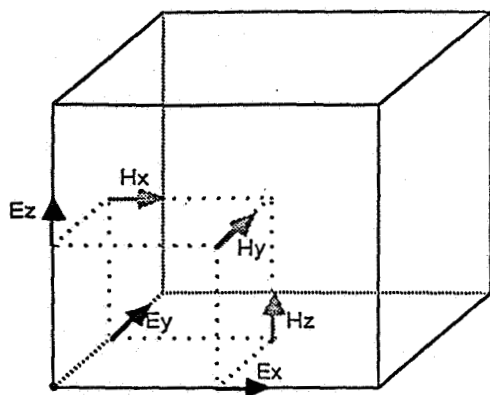


FIGURE 1 : Calculation points

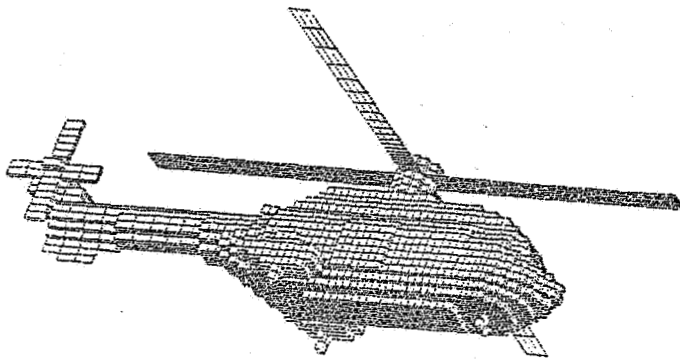


FIGURE 2 : Helicopter DFDT Model

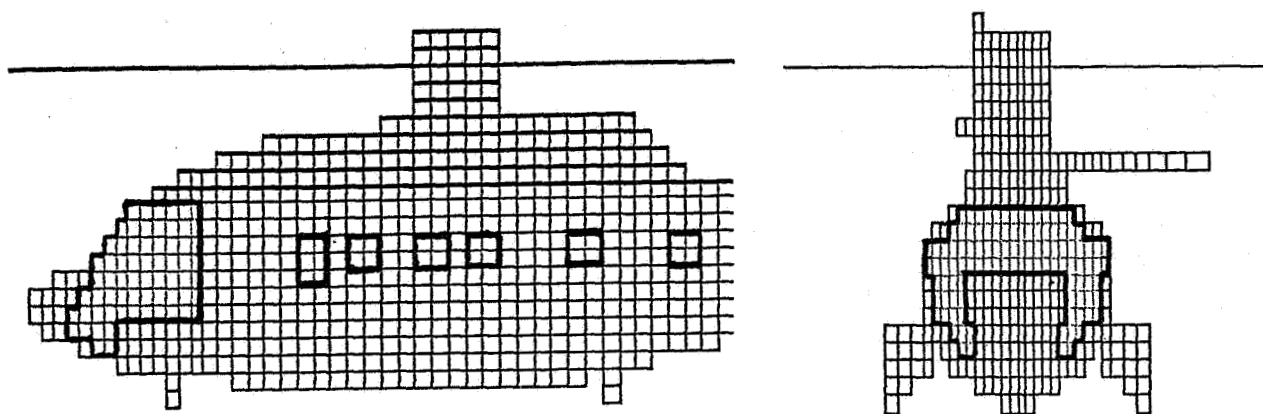


FIGURE 3 : Apertures geometry

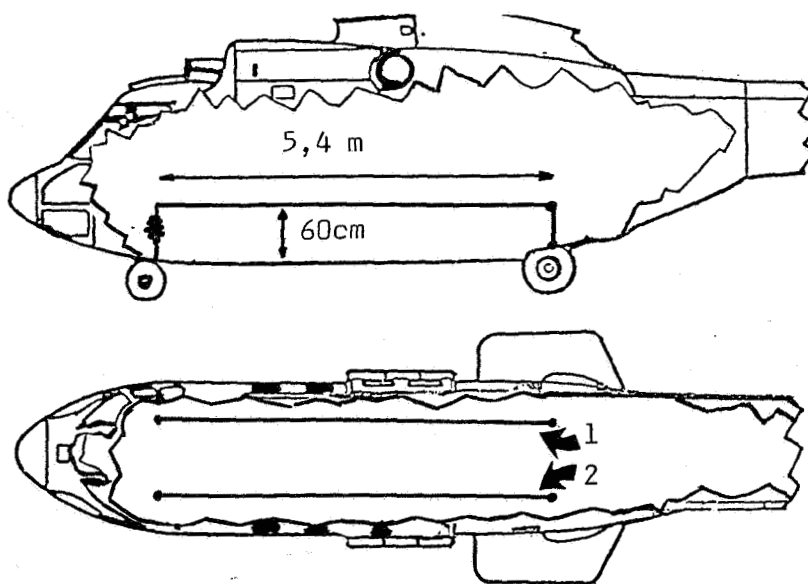


FIGURE 4 : Wires locations

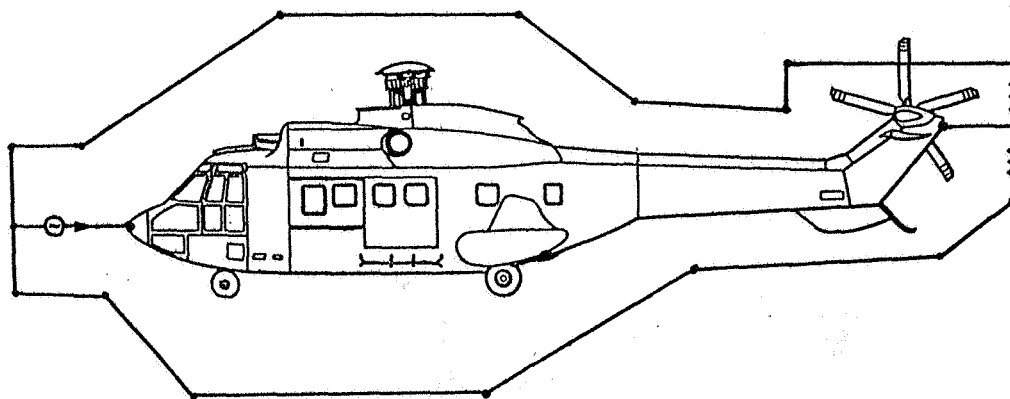


FIGURE 5 : Structure of the coaxial line

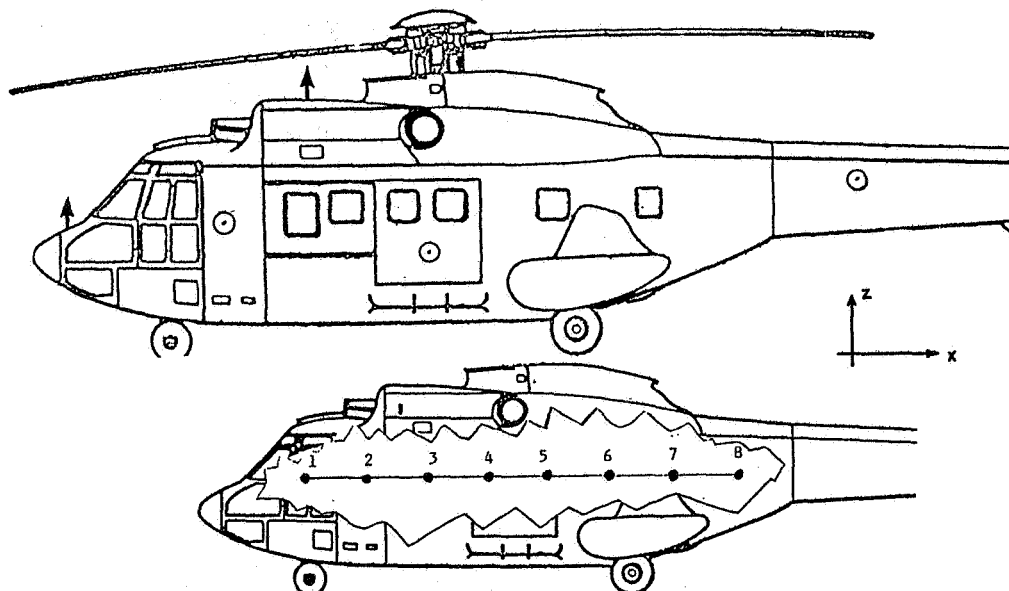


FIGURE 6 : Observation points

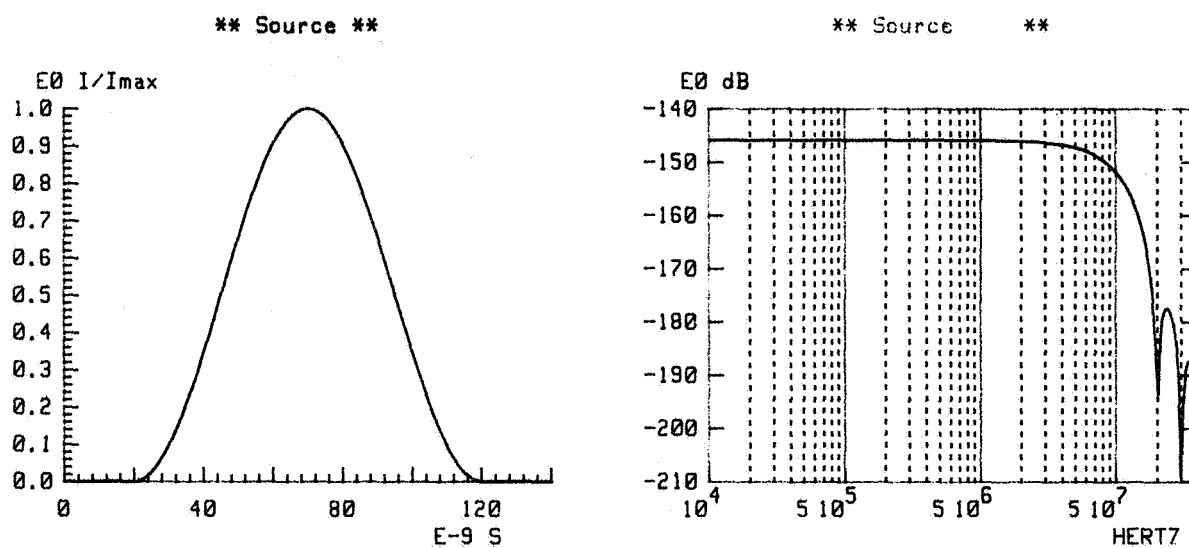
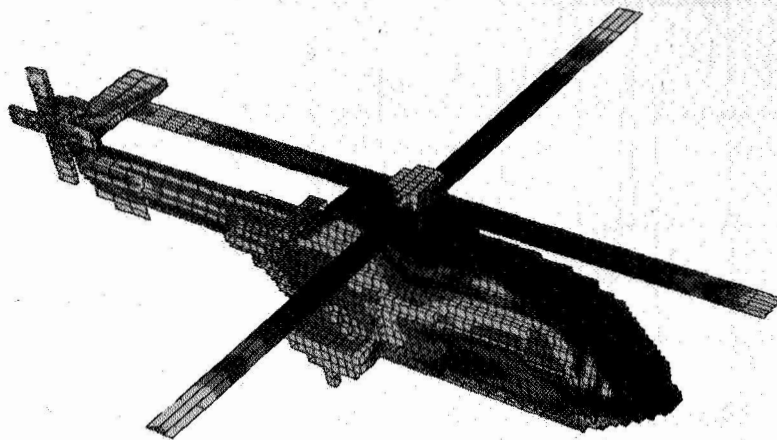
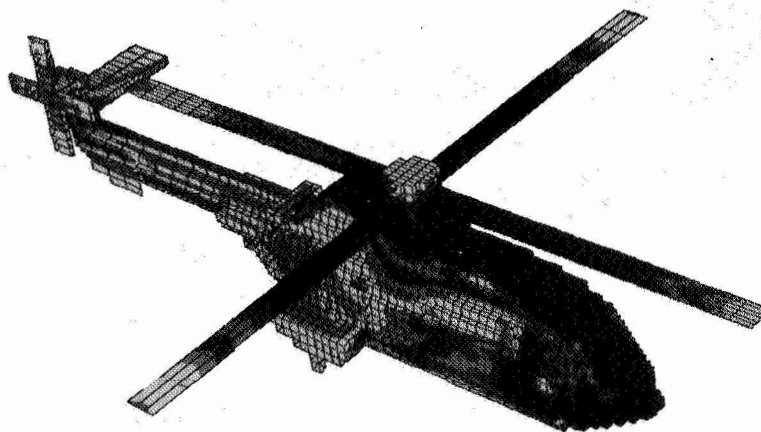


FIGURE 7 : Injected current



Without apertures



With apertures

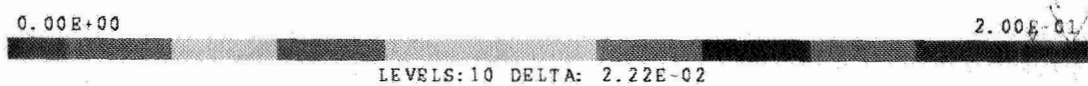


FIGURE 8 : H-field repartition -  $I_{\text{INJECTED}} = 1,6 \text{ Amp}$

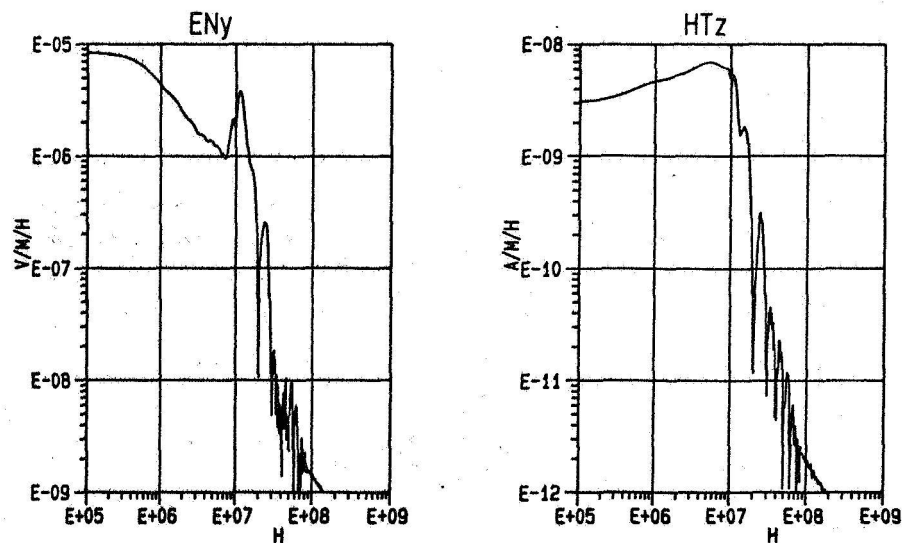


FIGURE 9 : E and H field - Observation point n° 3

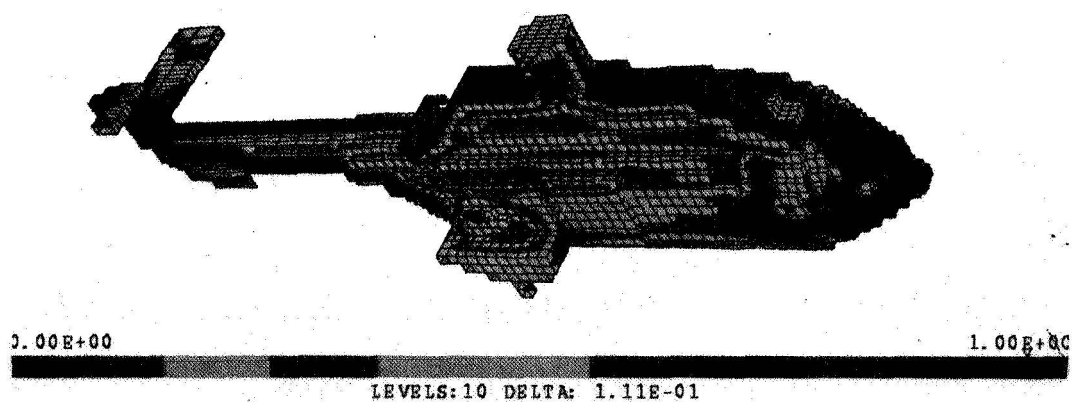
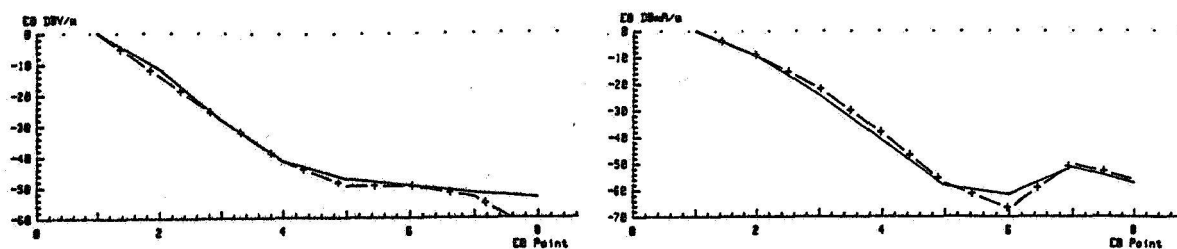


FIGURE 10 : H-field repartition -  $I_{\text{INJECTED}} = 6 \text{ Amp.}$



— : in-flight    -+--+ : coaxial return path

FIGURE 11 : Inside field attenuation

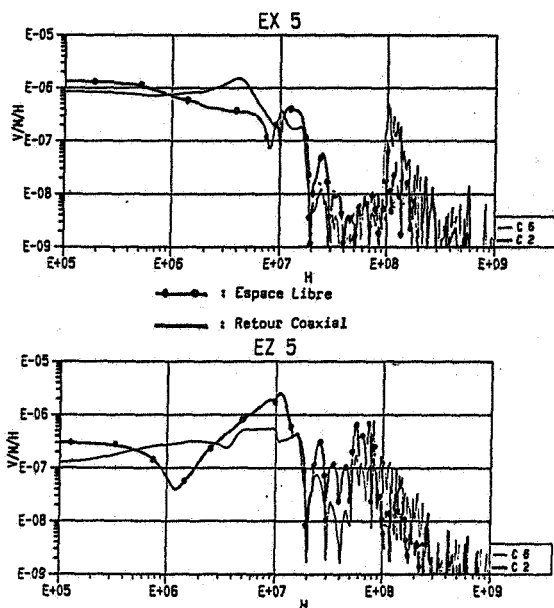


FIGURE 12 : FOURIER transform of inside field without wires

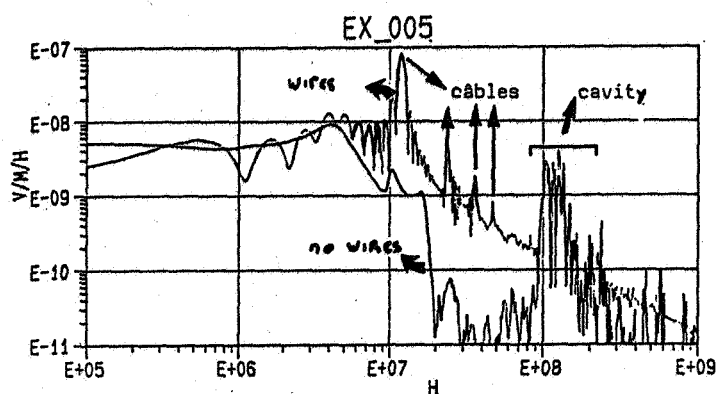


FIGURE 13 : FOURIER transform of inside field with wires

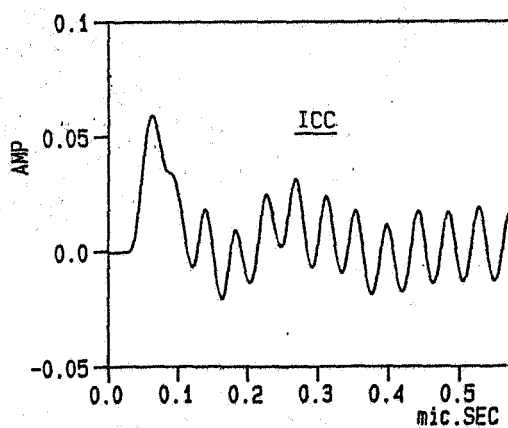
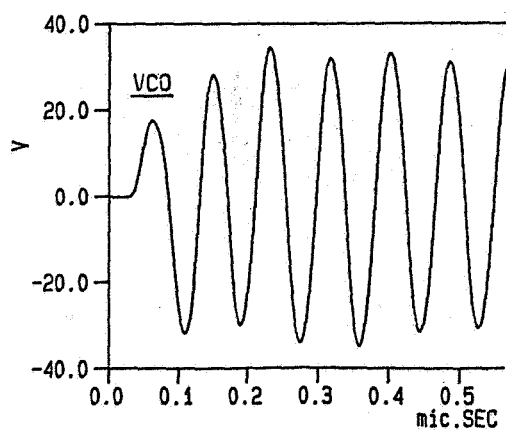
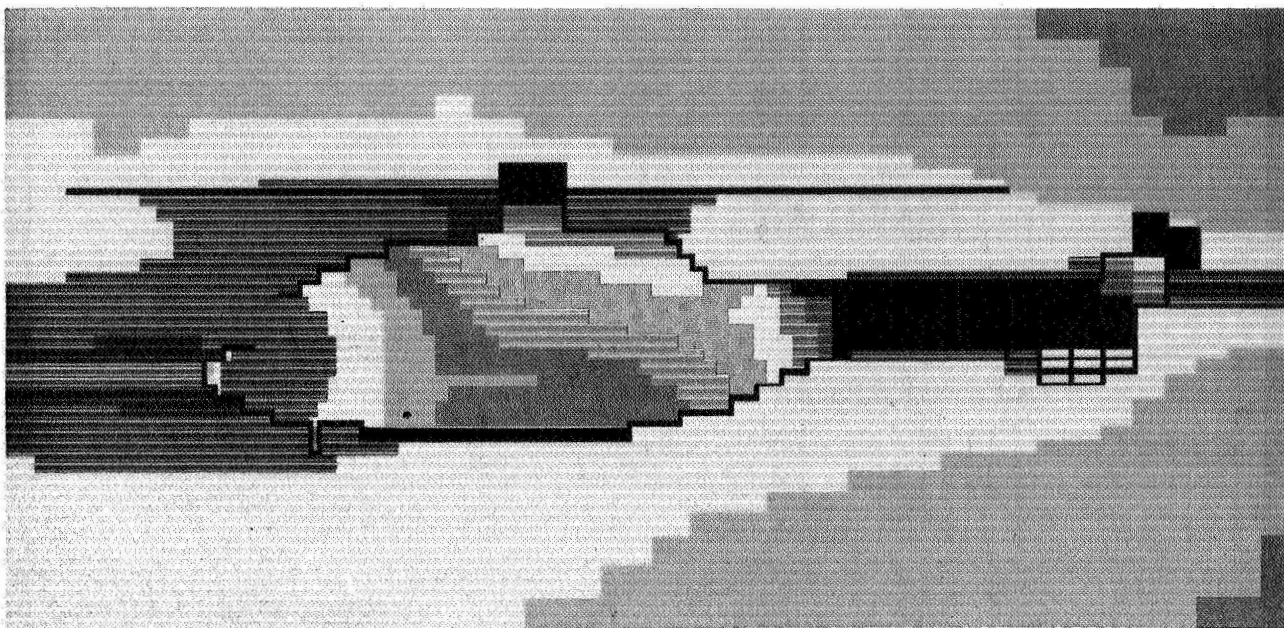
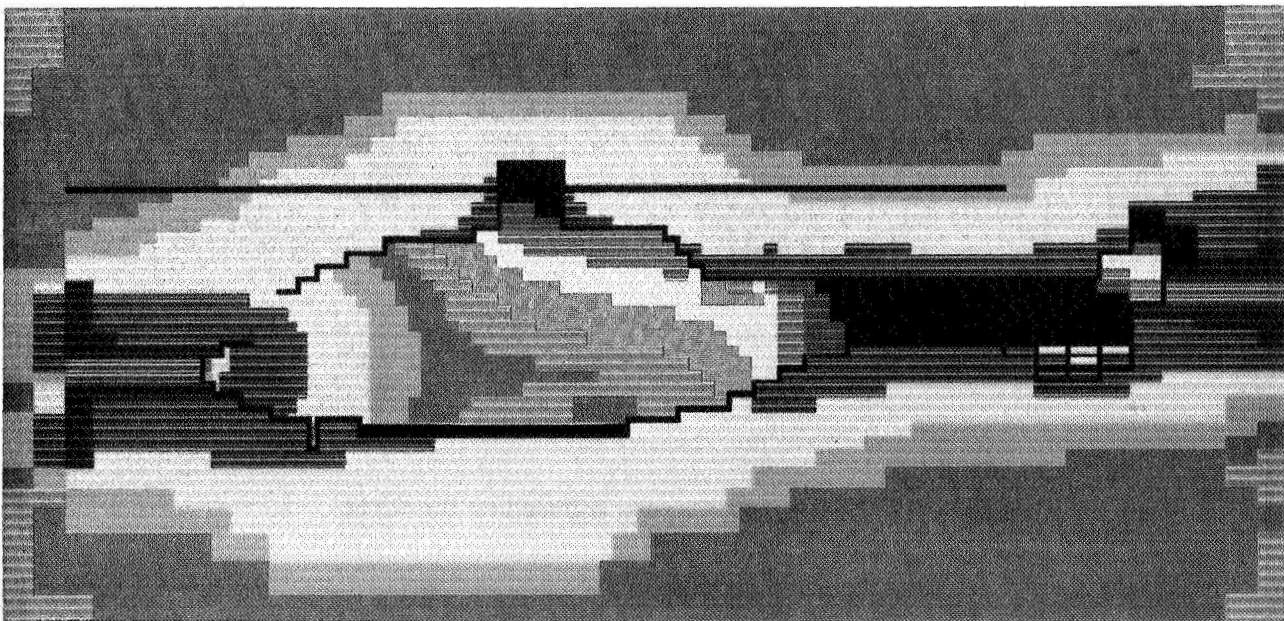


FIGURE 14 : Voltage and Current induced on the wires





**In flight injection**



**Injection with coaxial return path**

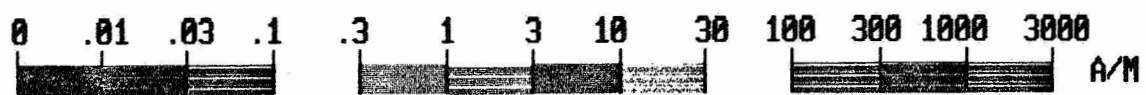


**FIGURE 15 : Mapping of inner electromagnetic fields**

**Session 12A, Thursday 3:45**  
**Lightning Phenomenology**  
**Meteorological Relationships 1**  
**Hasbrouck, Chairman**

# THREE-DIMENSIONAL TIME DOMAIN MODEL OF LIGHTNING INCLUDING CORONA EFFECTS\*

Andrew S. Podgorski

Electromagnetic Protection Group, Institute for Information Technology  
National Research Council of Canada, Ottawa, Canada K1A 0R6

## ABSTRACT

A new 3-D lightning model that incorporates the effect of corona is described for the first time. The new model is based on a Thin-Wire Time Domain Lightning (TWTDL) Code developed previously. The TWTDL Code was verified during the 1985 and 1986 lightning seasons by the measurements conducted at the 553-m CN Tower in Toronto, Ontario.

The inclusion of corona in the TWTDL code allowed study of the corona effects on the lightning current parameters and the associated electric field parameters.

## INTRODUCTION

To overcome problems resulting from the straight line channel approximation, the pre-defined channel current distribution, and the pre-defined channel current propagation speed, the author previously introduced the first fully 3-D time domain model of lightning based on the Thin-Wire Time Domain Code [1].

This new 3-D model not only accepted the 3-D geometry of the lightning channel but also calculated the lightning current distribution and speed of propagation of lightning current in the channel. In the model the provision was made for resistive and non-linear loading of the lightning channel, consequently permitting studies of the stepped leader and of the channel branching. The most important asset of the proposed model was the ability to model the effect of structures (towers, airplanes, etc.) on lightning current and vice versa. This led to the development of a unified lightning threat concept [2] that allowed definition of lightning parameters describing the lightning currents measured on the ground, towers, or airplanes [3,4,5].

Lightning that was modelled using proper resistance of the lightning channel demanded that the final breakdown point be located <20 m from the top of the tower. Considering this, it was always the

intention of the author to include the effects of corona in the proposed model of lightning, to account for measurements indicating that the location of the final breakdown point can be >100 m from the top of the tower. The corona model presented here was supported by a publication describing experiments on coronas generated in laboratories [6].

## THE THIN-WIRE TIME DOMAIN LIGHTNING MODEL

The Thin-Wire Time Domain Lightning model is based on a concept presented in Fig. 1 and it is obtained by combining the basic four models of positive, negative, upwards, and downwards lightning models of Berger [7] into one return stroke model. To form a new 3-D Thin Wire Time Domain Lightning Code (TWTDL), the Thin-Wire Time Domain (TWTD) Code and the Waterloo Analysis and Design (WATAND) Code are combined. The new TWTDL Code permits calculation of the currents of thin-wire structures using a moment method solution of the

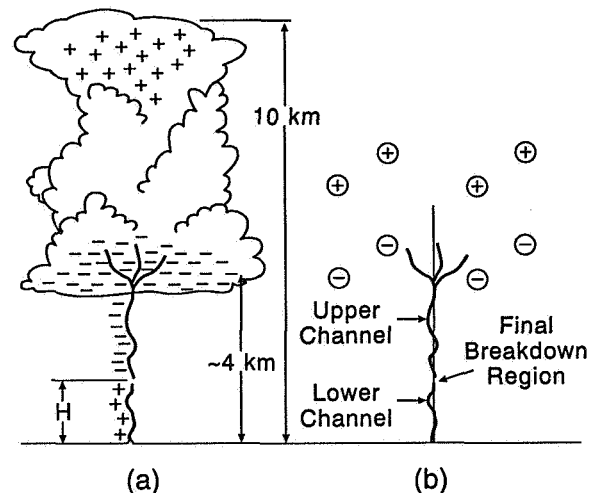


Figure 1. Return stroke phase of a lightning channel: (a) presented in Ref. 7; (b) used in the TWTDL model

\* NRC No. 31801

electric field Maxwell's integral equations. The Code computes a time domain solution by setting up a geometry-dependent matrix that relates the applied electric field to the induced currents and solves the matrix equation as an initial-value problem for the time-dependent induced current distribution. The induced currents are then used to find the time-dependent radiated and scattered fields. The thin-wire approximation used in the TWTDL Code is well suited for modelling of lightning since the diameter of the lightning channel is much smaller than its length.

The original TWTDL Code permitted modelling of only simple non-linear loads such as diodes. The addition of the Waterloo Analysis and Design (WATAND) computer code resulted in the ability of the TWTDL Code to accept resistances, capacitances, inductances, and non-linear and piecewise-linear voltage and current controlled resistances. The implementation of piecewise-linear resistances (switches) into the TWTDL Codes allowed the modelling of lightning branching and the implementation of voltage and current controlled resistances permitted modelling of non-linear effects during the attachment process. An example of the modelling of the effects of channel elongation process (stepped leader) on the lightning currents is shown in Fig. 2.

The TWTDL Code does not allow for DC charging of the lightning leader due to the requirement that the net charge on the modelled system always be zero. However, since the charge can be divided among different segments of the structure, the lightning channel charging can be accomplished by imposing a step charge at the cloud represented by multiplicity of short segments and by waiting long enough for stabilization of the initial charge and the field disturbance to occur (Fig. 3). Because of the 3-D character

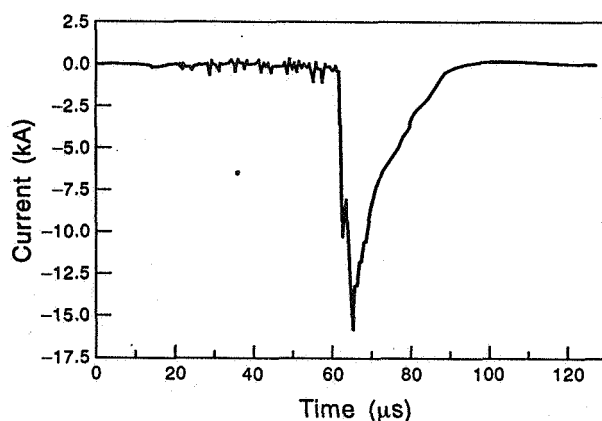


Figure 2. Time domain response of the lightning current that includes the effects of channel elongation process (stepped leader)

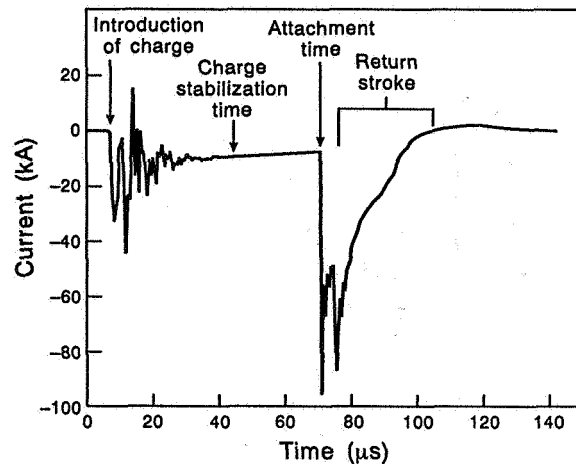


Figure 3. Charging mechanism in the TWTDL Code

of the TWTDL Code and its novel charging mechanism it was possible to model not only the cloud-to-ground lightning-tower interaction but also the intracloud and intercloud interaction of aircraft with lightning.

The validation of the TWTDL Code was accomplished through lightning current measurements conducted at the tallest free standing structure in the world, the 553-m CN Tower in Toronto, Canada. The CN Tower was chosen because of its free-standing character, dominating height, small overall diameter, and easy access to the location near the top of the tower where the free from the ground reflection lightning current measurements had to be made. The lightning current measurement system [8] installed at the CN Tower in 1985 had a response time of 50 ns. During the 1985-86 lightning seasons 94 lightning strokes were recorded. With the new measuring system, lightning current rise times in the order of 100 ns were recorded on tall towers for the first time. The measured rise time values compared very well with the values predicted by the TWTDL computer model. The same applies to the waveshape comparison, as can be seen on Fig. 4 where small details such as the effects of the attachment process, the ground reflection, the length of the lightning channel, and the height of the attachment region are correctly displayed. The comparison of measured and calculated waveforms revealed the presence of large numbers of measurements containing waveforms with very short 100 ns rise times.

The modelling of the 100 ns rise times required the placement of the final breakdown point at a distance of a few metres from the top at a tower, if the value of channel resistance was not to be decreased below acceptable levels. However, the presence of the final

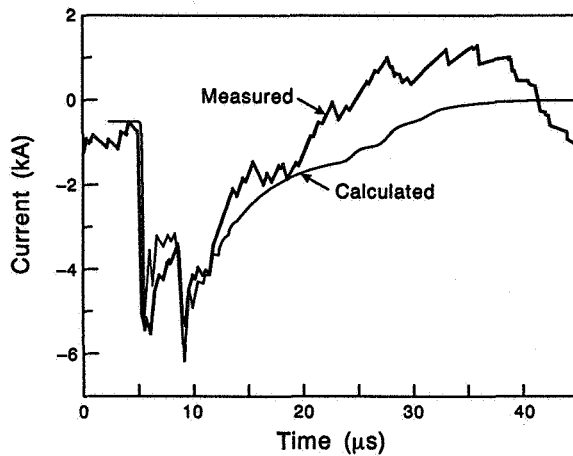


Figure 4. Calculated and measured lightning current waveform at the CN Tower

breakdown point so close to the top of the tower is not supported by video recordings. In the computer model, the distance of final breakdown point from the top of the tower could only be increased if there was a mechanism that could decrease the losses (resistance) and therefore the rise time of the current waveform. The only mechanism that could be responsible for such a decrease of risetime could have been the presence of corona. The description of cold and relatively dark corona around a lightning channel given in Ref. 6 allows the inclusion of the corona effects into the previous lightning model based on the use of the TWTDL Code.

### MODELLING OF CORONA EFFECTS

Reference 6 stipulates the presence of corona not only during the interstroke interval but in all phases of the lightning discharge. The corona charge is deposited around the thin lightning channel by a radial electric field pushing it away from the channel.

In relatively large electric fields existing near the channel, the radial electric field will carry the corona charge away at the speed of light. Reference 6 suggests that the radius of lightning corona expands up to 120 m and implies that a corona envelope of this size is relatively dark and not easily observable.

In order to model the effects of radial corona, radially resistively loaded wires were added to the previous lightning model. Figure 5 shows the structural geometry of the new lightning model. In this model the lightning, corona channels, and the CN Tower are described in terms of 3-D straight wire segments loaded with resistances. The segment length rule for the TWTDL Code is defined by:

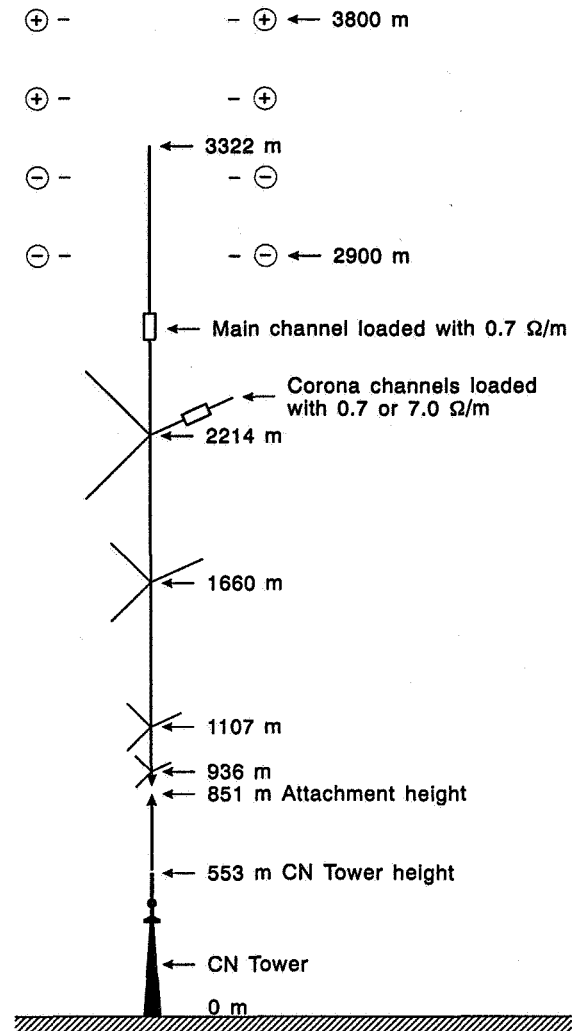


Figure 5. A 3-D view of a TWTDL input structure simulating corona effects

$$L \leq c \Delta t \quad (1)$$

where  $\Delta t$  is the duration of the time step and  $c$  is the velocity of light in vacuum.

Since it was the author's intention to analyze the lightning behavior using a time resolution comparable to the shortest rise time reported, a time step of a 140 ns was used. For 140 ns time step the model required 78 segments to model the main lightning channel and an additional 120 segments to model the effects of corona.

The thin-wire approximation used in the TWTDL Code required that the segment diameter be less than the segment length. While the exact limits have not

been determined, the following has been found to give good results:

$$D \leq 1.2L \quad (2)$$

where  $D$  is the segment diameter and  $L$  the segment length. The attachment region of the model Fig. 5 was modelled by a non-linear (voltage or current controlled) resistor, with an OFF resistance of  $10 \Omega$  and ON resistance of  $3 \Omega$ , series inductor and parallel capacitor.

The resistive loading of the lightning channel was determined from the experiments conducted at the CN Tower. A resistance value of  $30 \Omega$  for a 42-m segment ( $0.7 \Omega \text{ m}^{-1}$ ) was used, as this value was found to give the best results when the measured and calculated waveshapes of analyzed lightning were compared. The resistive loading of the corona channel was varied between  $0.7$  and  $7 \Omega \text{ m}^{-1}$ .

### STUDY OF LIGHTNING CURRENT

In the study of corona modelling it was assumed that the lightning channel is vertical and straight. This assumption was not required by the model but it greatly simplified the analysis. To account for an average lightning stroke response the height of the attachment region was placed at a height of 277 m over the top of the 553-m tall CN Tower. The height was chosen on the basis of the current rise time that for such a height has an average value of about 500 ns for models that either include or do not include corona. Figure 6 presents the values of the peak current amplitude of the lightning current as a

function of the position along the lightning channel. The changes are drastic and indicate introduction of losses into propagation along the lightning channel. The corona peak current reduction is smallest at the attachment point and equals 25% of the peak current without the corona. At a height of 2000 m above the attachment point the effect of corona results in a 40% reduction in a peak current amplitude.

The rise time of the lightning current waveform along the lightning channel is displayed by Fig. 7. It can be seen that, in the regions on both sides of the attachment point, a 30% reduction of the current rise time occurs. The region of the rise time reduction extends 200 m up and 200 m down from the attachment point. In regions further away from the attachment point the presence of corona increases the rise time of the lightning current waveform. However, this increase does not exceed 20% up to a height of 2 km above the attachment point.

The effect of corona on the rise time of the lightning current explains the presence of 100 ns rise times measured at the CN Tower [2]. Figure 7 shows that without the presence of corona the variation of the height of the attachment point with respect to the top of the tower cannot be larger than 20 m in order to provide for the rise times shorter than 340 ns. The presence of corona extends this variation of the height of the attachment point to 100 m. The presence of the attachment region at a height of 100 m above the top of the CN Tower is easily supported by the video recordings.

The increase of rise time as a result of the presence of corona explains the presence of high peak current

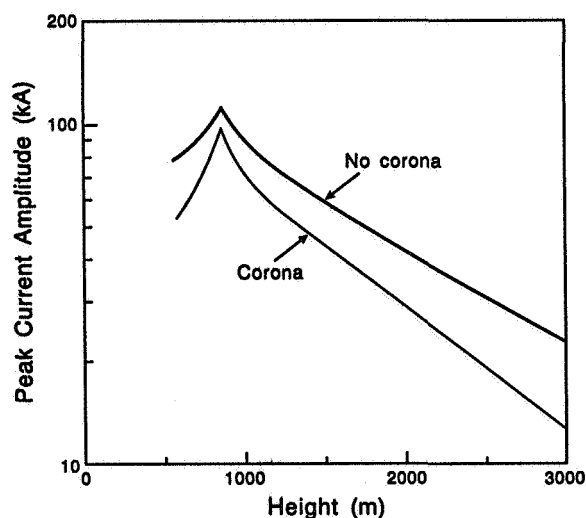


Figure 6. The peak current amplitude of the lightning current as a function of the position along the lightning channel

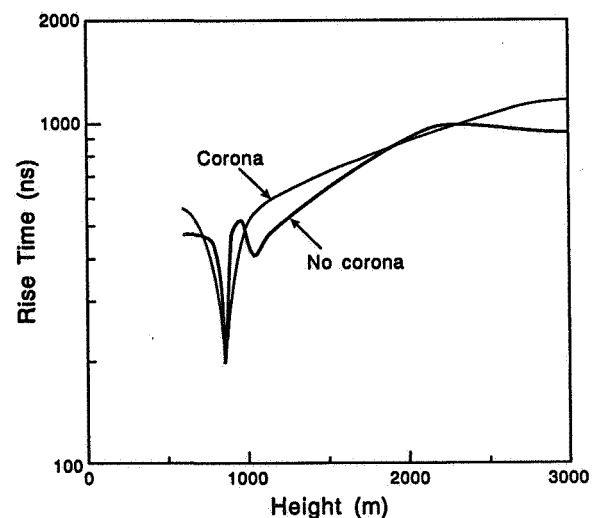


Figure 7. The rise time of the lightning current as a function of the position along the lightning channel

derivatives measured at towers and airplanes [4]. Figure 8 indicates that, in proximity to the attachment region, the presence of corona extends the region of high peak current derivatives. It is interesting to note that outside of the attachment region the corona reduces the peak current derivative by about 40%.

One of the parameters that created much controversy in the past is the velocity of current wavefront in the lightning channel. Figure 9 shows the velocity of the current wavefront normalized to the speed of light. It should be noted that this calculation was made for a straight lightning channel. Therefore, assuming channel tortuosity of 50%, one can easily divide the normalized velocity numbers of Fig. 9 by a factor of two and obtain average velocity in order of 40 to 45% of the velocity of light.

The important conclusion from Fig. 9 is, however, related to the variation of the velocity of propagation of low and high frequency components of the propagating current wavefront. Figure 9 displays the velocity of propagation of two points at the front of the current waveform. One of these points is located in the middle (50%) of the waveform and the other at its peak. The 50% point can be related to the high frequency components of the waveform, while the peak point can be related to the low frequency components of the waveform. Figure 9 reveals that the high frequency components (50% point) are propagating with the velocity close to the velocity of light, while the low frequency components travel with velocity considerably lower than the velocity of

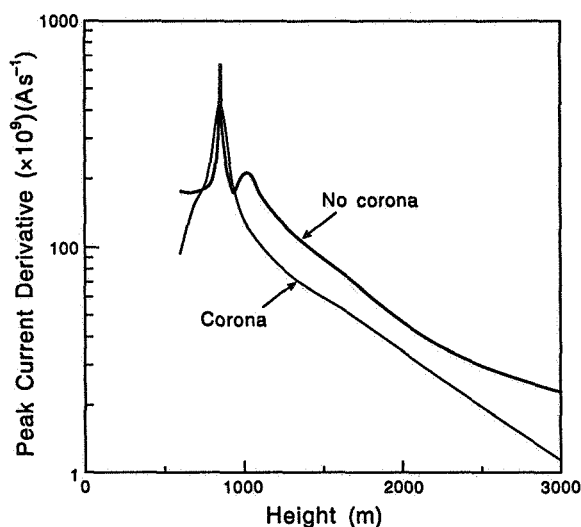


Figure 8. The peak current derivative as a function of the position along the lightning channel

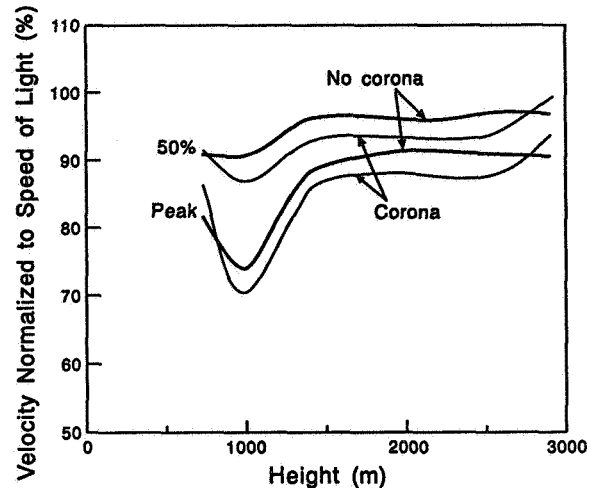


Figure 9. Velocity at propagation of the lightning wavefront as a function of the position along the lightning channel

light. The slowest velocity of propagation occurs in the attachment point region.

It is interesting to note the very small effect of corona on the velocity of propagation of both the low and high frequency components of the current waveform. The corona decreased the velocity of propagation of the two waveforms by only 5%. However, the presence of corona has a substantial effect on the electric field perpendicular to the surface of the lightning channel, as shown in Fig. 10. This field responsible for propagation of corona is reduced by the presence of corona channels. Figure 10 indicates that, in cases without corona, the region with the electric field higher than 1 MV/m extends up to a height of 600 m above the attachment point. With the presence of corona the field of 1 MV/m extends only to a height of 200 m above the attachment point. It appears that the corona is self-confining.

This finding is better displayed in Fig. 11 where a comparison of charge density of lightning channel with corona (charge  $Q_c$ ) and without corona (charge  $Q_{nc}$ ) is presented. Figure 11 shows that up to the height of 800 m above the attachment region the charge of the lightning channel is increased by 15% in the presence of corona.

## STUDY OF RADIATED FIELDS

In the TWTDL Code, the values of the radiated electric fields (E-fields) are calculated from previously determined lightning current values. However, a perfectly conducting ground is assumed for the purpose of calculation of the E-fields generated

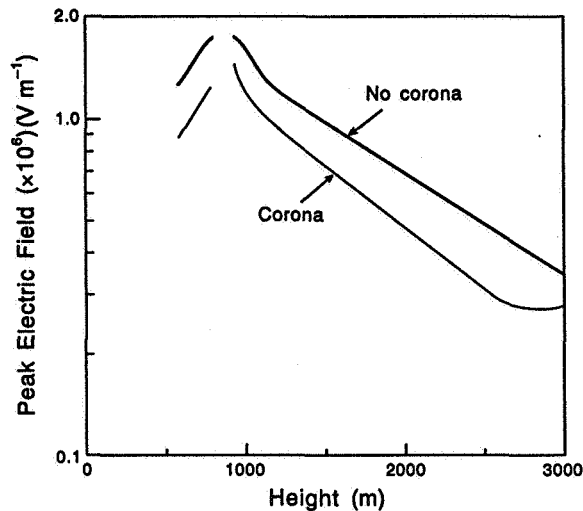


Figure 10. Peak of the electronic field perpendicular to the lightning channel as a function of the position along the channel

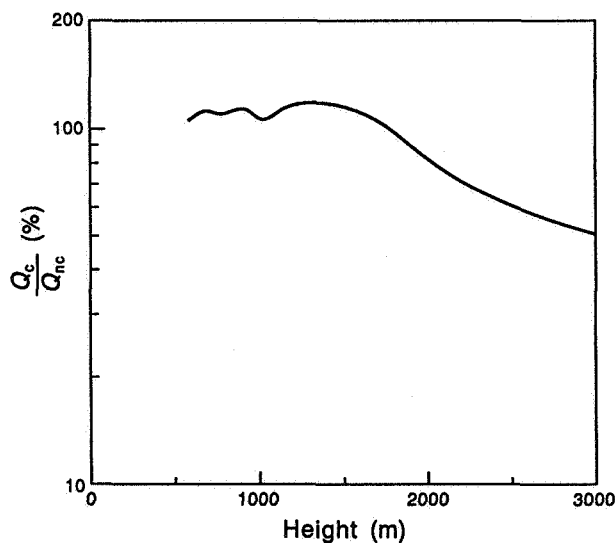


Figure 11. Comparison of charge density of lightning channel with corona ( $Q_c$ ) and without corona ( $Q_{nc}$ )

by the lightning channel. This simplification allows the total field to be calculated by summarizing the effects of previously calculated lightning currents and their underground images. The approximation used gives very good results for high frequency radiated components of the E-field, but it may create some problems for middle frequency components as these components can be trapped in a wave propagating parallel to the ground. The perfect grounding assumption permits accurate prediction of the

E-fields of the lightning channel located over the sea water, a distance of a few kilometres from the shore.

The TWTDL Code permits the verification of the relationship between lightning current and electric fields parameters. The peak E-field amplitude calculated as a function of distance from lightning channel using the TWTDL Code is shown in Fig. 12. From Fig. 12 it should be noted that the E-field peak amplitude decreases with the inclusion of corona. It can be seen that the low resistance corona, modelled with a corona channel resistance of  $0.7 \Omega \text{ m}^{-1}$ , is responsible for much greater field reduction than the corona modelled with a corona channel resistance of  $7 \Omega \text{ m}^{-1}$ . Corona appears to be responsible also for the narrowing of the near field region. It can be seen that the near field region is reduced from 5 km, for a case where there is no corona, to about 1 km, if the effect of corona is included. A very interesting phenomena can be observed at a distance less than 1 km from the lightning channel; for the high resistance corona the E-field values are higher than the E-field calculated when no corona is considered. With the use of Figs. 6 and 12 one can easily establish the relationship between the peak current amplitude and the peak amplitude of E-field. One can show that the coefficient defining the relationship between the peak current amplitude and the peak amplitude of the E-field varies up to  $\pm 20\%$  totally, for the near and the far field, for the case with or without corona, and for different heights of the attachment point. One should realize, therefore, that these large errors will result in substantial errors if peak current levels are determined from the E-field measurements. This approach, however, is used

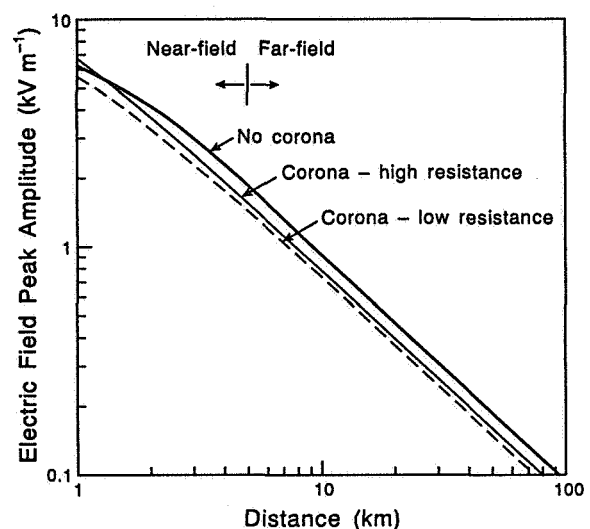


Figure 12. The peak E-field amplitude as a function of the distance from the lightning channel



when establishing a significant lightning current data base (10 million strokes) is required. Assuming  $\pm 20\%$  error, one can estimate that the peak current amplitude may be contained anywhere between 20 and 30 kA. Consequently, for high accuracy of peak current amplitude data, only direct measurements of the lightning currents should be considered.

On the contrary, the estimating of lightning current rise time through the measurements of the rise time of the E-fields results in exceptionally small error. However, the measurements of the rise time of E-field should be conducted at a distance not greater than 1 km from the lightning, channel as displayed in Fig. 13. Comparison between Fig. 7 and Fig. 13 indicates that the lightning current rise time at the attachment point and the rise time of the peak E-field are closely related. Slightly slower rise time of the peak E-field results from the corona shielding effect of the radiated field that is being measured on the ground.

## CONCLUSIONS

One of the important challenges faced by researchers working in the area of lightning is the measurement of lightning parameters. The direct lightning measurements provide researchers with a limited data set, such as peak current amplitude, rise time, and peak current derivatives. It is obvious that, if the data set is to be expanded into the low probability of lightning occurrence region, one will have to estimate the lightning current parameters from the electromagnetic field generated by lightning. The TWTDL code provides an excellent tool since using a 3-D analysis of electromagnetic field allows very accurate

derivation of the relationship between the lightning current and radiated electromagnetic field. The inclusion of the effect of corona further expands the capabilities of the Code and makes it the most comprehensive tool for modelling the lightning interaction with structures.

## REFERENCES

- [1] Podgorski, A.S., and Landt, J.A., "Three Dimensional Time Domain Modelling of Lightning", *IEEE Transactions on Power Delivery*, Vol. PWRD-2, No. 3, pp 931-938, July 1987.
- [2] Podgorski, A.S., "A Case for a Unified Lightning Threat", *Proceedings of the International Aerospace and Ground Conference on Lightning and Static Electricity*, Oklahoma City, OK, pp. 118-122, April 19-22, 1988.
- [3] Podgorski, A.S. and Podgorski, E.M., "Lightning Standards for Protection of Ground Electronic Systems", *Proceedings of the International Aerospace and Ground Conference on Lightning and Static Electricity*, Oklahoma City, OK, pp. 324-327, April 19-22, 1988.
- [4] Podgorski, A.S., "Lightning Standards for Aircraft Protection", *Proceedings of the 1990 IEEE International Symposium on Electromagnetic Compatibility*, Washington, DC, pp. 218-223, August 21-23, 1990.
- [5] Podgorski, A.S., "The Low Probability Lightning Threat.", *Proceedings of the EMC EXPO - 91 Conference*, Orlando, FL, June 25-27, 1991. In press.
- [6] Heckman, S.J., and Williams, E.R., "Corona Envelopes and Lightning Currents", *Journal of Geophysical Research*, Vol. 94, No. D11, pp. 13287-13294, September 30, 1989.
- [7] Berger, K., "Lightning", *Physics of Lightning*, R.H. Golde, Ed. Academic Press, Vol. 1, pp. 119-190, 1977.
- [8] Podgorski, A.S., "A New System for Measurement of Lightning Currents on Towers", *Proceedings of the IEEE Instruments and Measurement Technology Conference*, Boulder, CO, pp. 71-73, March 25-27, 1986.

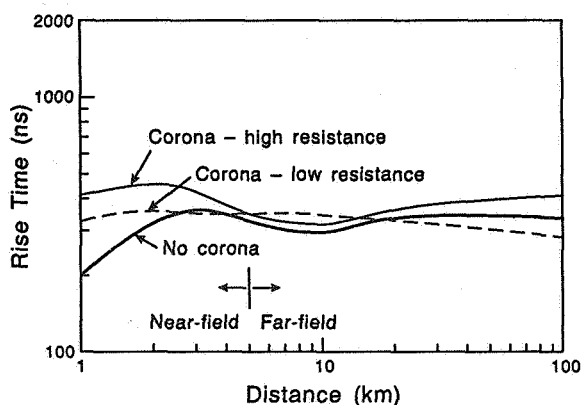


Figure 13. The rise time of the E-field as a function of the distance from the lightning channel

# **SURFACE WIND CONVERGENCE AS A SHORT-TERM PREDICTOR OF CLOUD-TO-GROUND LIGHTNING AT KENNEDY SPACE CENTER: A FOUR-YEAR SUMMARY AND EVALUATION**

Andrew I. Watson, Ronald L. Holle, Raúl E. López  
NOAA/ERL/National Severe Storms Laboratory  
Boulder, Colorado

and

James R. Nicholson  
National Aeronautics and Space Administration  
Kennedy Space Center, Florida

## **ABSTRACT**

Since 1986, USAF forecasters at Kennedy Space Center (KSC) have had available a surface wind convergence technique for use during periods of convective development. In Florida during the summer, most of the thunderstorm development is forced by boundary-layer processes. The basic premise is that the life cycle of convection is reflected in the surface wind field beneath these storms. Therefore the monitoring of the local surface divergence/convergence fields can, in most cases, be used to determine timing, location, longevity, and specifically, the lightning hazards which accompany these thunderstorms. This study evaluates four years of monitoring thunderstorm development using surface wind convergence, particularly the average over the area. Cloud-to-ground (CG) lightning is related in time and space with surface convergence for 346 days during the summers of 1987 through 1990 over the expanded wind network at KSC. The relationships are subdivided according to low-level wind flow and midlevel moisture patterns. Results show a one in three chance of CG lightning when a convergence event is identified. However, when there is no convergence, the chance of lightning is negligible. By itself, the convergence nowcasting technique is a very good simple technique. But when used with other observational platforms, the convective forecast is greatly enhanced. The 1990 deployment of a 5 direction finder (DF) network with a positive flash option is also examined and related to surface convergence and convective development.

## **1. INTRODUCTION**

The responsibility for thunderstorm prediction as well as all other weather support at the Kennedy Space Center (KSC) rests with USAF forecasters. The USAF forecasters are responsible for issuing weather advisories with 30-minute lead times for numerous locations at KSC and Cape Canaveral Air Force Station CCAFS. They are required to provide weather information for NASA, USAF, U.S. Navy, and commercial launches. This responsibility demands that the forecasters continue to provide a more timely and improved forecast product. In 1988, during the four convective summer months, the percent of man-hours lost due to lightning warnings within 5 miles of Complex 40 and 41 was 9.2% (Maj. A. Dye, private communication). A preliminary study of shuttle processing time lost during the four

summer months of 1988 indicated that for each hour during which negative ground flashes were observed within 5 miles of Complex 39 by the lightning mapping system, there were, on the average, 13 hours of warning duration (R. Benti, private communication).

Watson *et al.* [1 and 2] have shown the feasibility of using surface wind convergence as a short-term predictor of thunderstorms, especially cloud-to-ground (CG) lightning. These recent studies examined the ability of surface convergence in a relatively small network to anticipate the onset as well as the cessation of lightning in this network. Much of the convection in Florida during the summer is triggered by processes in the boundary layer. The life cycle of these thunderstorms is likely to be reflected in the surface wind field beneath the storms. This assumption, however, does not

always hold true for thunderstorm development in a more midlatitude environment [3] or during other seasons in Florida. The convergence technique presented here uses surface convergence, particularly the average over the area, to identify the potential for new, local thunderstorm growth, which can be used to specify the likely time and location of lightning production during the life cycle of the convection.

In 1987, NASA expanded the surface wind network onto the mainland west of KSC. The network area increased from near 800 km<sup>2</sup> to over 1600 km<sup>2</sup>. This study reports the results of this expansion using four years of wind and lightning information collected during June, July, August, and September of 1987-1990.

## 2. DATA AND ANALYSIS

The wind-tower locations and the 1600-km<sup>2</sup> analysis area are shown in Figure 1. Although individual towers have varying instrumentation, this study used winds sampled mainly at 16.5 m (54 ft), which is the highest available level for all the sites and is above all the vegetation. The wind data were recorded in increments of 5-min averages. The analysis area

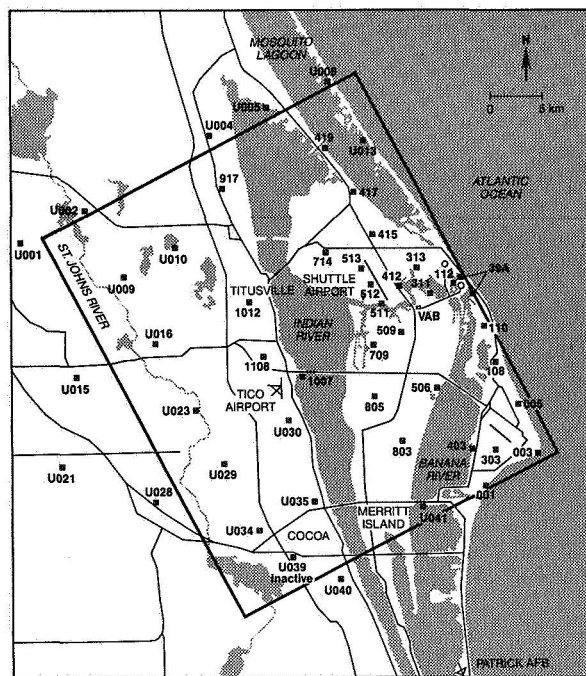


Figure 1. Kennedy Space Center and Cape Canaveral Air Force Station area. The rectangle marks the wind mesonetwork boundary. Solid squares indicate meteorological stations.

was divided into a 13-by-17 grid of equally spaced (2.8 km) points. The divergence quantities were then computed using an objective analysis scheme [1, 2, and 4].

CG lightning information was obtained from a medium gain network of three direction finders (DF) with a mean distance between DFs of 69 km. Only flashes recorded in the analysis area shown in Figure 1 were considered. Krider *et al.* [5 and 6] described the lightning location system, Mach *et al.* [7] described network performance, and López and Holle [8] described the lightning data processing. Unfortunately, only negative flash information (i.e., lightning lowering negative charges to the ground) was available for the three DF network. In 1990, data from the Melbourne, Florida DF were unusable, reducing the system to a two DF network. Considering the baseline problems which resulted over the northern half of the KSC wind network, the data could not be used.

Fortunately, a new five-DF low-gain lightning location network came on-line in 1990 with a mean distance between DFs of 45 km. Processing of the raw DF information was performed using a Passi and López [9] algorithm which calculates site errors and optimizes the flash position using information from all DFs detecting the flash. Since many more flashes seem to be detected with this network, this flash information was only used in examining positive flashes.

## 3. DIVERGENCE-LIGHTNING RELATIONSHIPS

If conditions in the middle troposphere are favorable, thunderstorms are likely to develop and be sustained in the sea-breeze zone and, through the process of downdrafts and outflows, produce new flanking convection which may migrate into other areas. Planetary boundary-layer convergence initiates these convective events.

### TOTAL-AREA DIVERGENCE

Total-area divergence is a term coined by Cunning *et al.* [10] for area-averaged divergence, that is, the sum of the divergence values at gridpoints divided by the total number of gridpoints. It is equivalent to the line integral of

the normal component of the wind around the domain boundary divided by the area. In a region the size of the KSC network, the value of total-area divergence quantifies the amount of horizontal mass into or out of the network boundaries, which approximates the average vertical motion in the region. Total-area divergence senses the prestorm environment as well as the formative, mature, and dissipation stages of convective development.

Figure 2 shows profiles of total-area divergence and 5-min CG flash totals in the network for 10 July 1988. Two relatively strong convergence-divergence couplets are shown with associated lightning. The convergence-divergence couplets in the total-area-divergence time series occur repeatedly as a sign of convective development. In the stages of convective development described by Byers and Braham [11], the cumulus or *formative* stage is characterized by updrafts throughout the cloud or cell. In the total-area divergence profile, the *formative* stage is from beginning convergence to maximum convergence, when there is predominantly inflow into the developing storm. The *mature* stage has both updrafts and downdrafts occurring throughout the thunderstorm. In the total-area divergence profile, this stage begins at maximum convergence and continues to maximum divergence. Throughout this period, convergence and divergence zones coexist in the network. Convergence begins to decrease while

downdrafts and precipitation cause increasing divergence. Finally, the *dissipation* stage is characterized by downdrafts. This stage begins at maximum divergence and ends when the total-area-divergence time series returns to near zero values as the downdrafts weaken and precipitation ceases.

CG lightning begins a short time before maximum convergence as convective clouds, in response to boundary-layer convergence, become deep and vigorous enough to support electrical discharges. Peak lightning occurs in the middle of the mature stage near the cross-over from convergence to divergence, which is described by Watson *et al.* [1]. CG lightning ends after peak total-area divergence as divergence settles back to quiescent values.

The magnitudes in the convergence-divergence couplet in the total-area divergence profile vary considerably from case to case. Because of the position of convective development in the network, one stage or another may be lost as cells move in or out of the network. Complicated patterns may form because of clashes of intersecting outflows. Signal may be lost because of the inhomogeneity of the station spacing (Fig. 1), and smaller-scale development may be lost until sensed by several sites because only the network average of divergence is being considered. Convergence-lightning episodes are usually not as dramatic as in Fig. 2. Figure 3 depicts an average day (21 June 1989) where convective development is weak.

### POSITIVE CG FLASHES AT KSC

In 1990 a low-gain CG flash detection network was installed at KSC which detects positive as well as negative CG flashes. The old lightning network did not contain the positive flash option. Therefore, there was little known about the concentration of positive flashes during convective development in the immediately vicinity of KSC and their association to surface convergence.

Positive CG flashes are considered to constitute a small fraction of the total number of flashes. Positive flashes are generally considered to have large currents and charge transfers. A literature review of positive flashes can be found in López *et al.* [12].

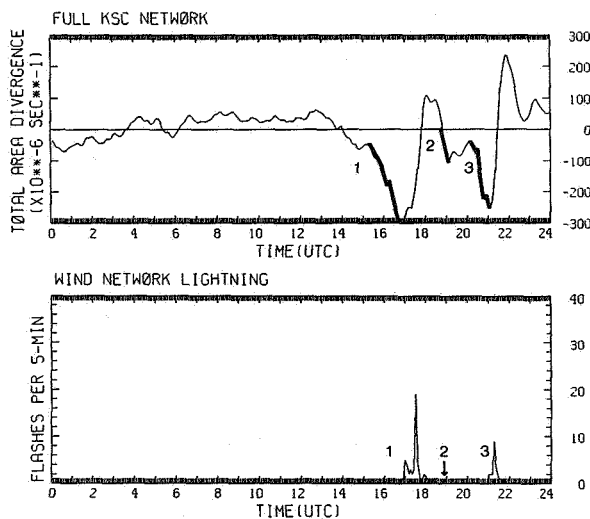


Figure 2. Time profiles (5-min resolution) of (top) total-area divergence, and (bottom) CG lightning for the KSC network on 10 July 1988. Bold lines identify convergence events.

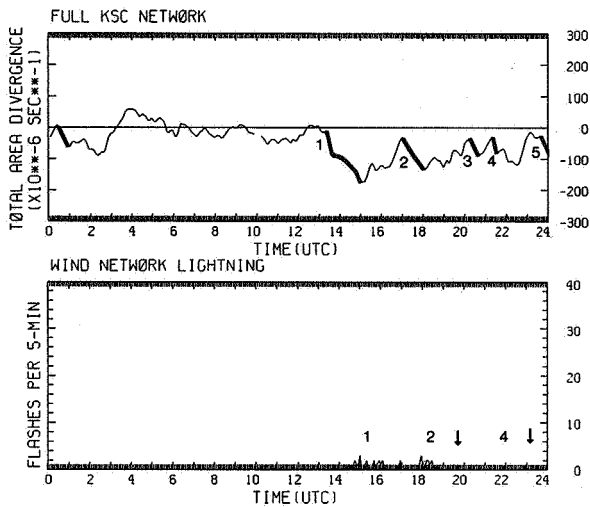


Figure 3. Same as Fig. 2, except for 21 June 1989.

Figure 4 shows time profiles of total-area divergence, total CG flashes, and positive flashes in the KSC wind network on 24 July 1990. A convergent/divergent couplet begins at 1600 UTC and ends near 2200 UTC. Network flashes begin at 1745 UTC immediately before the minimum in total-area divergence (convergence peak). The lightning peak occurs just before the peak in divergence during convective maturity as stated in the last section. Lightning ends at 2140 UTC as total-area divergence slips back towards zero. During the nearly 3 hours of CG flashes, positive flashes occur only for one hour and a half, peaking with 5 flashes in 5 minutes at maximum flash intensity with 8% of the flashes being positive. It appears that the majority of positive flashes occur during the mature stage of convective development in this example.

In a second example (Fig. 5), another strong convective event occurred on 17 August 1990. Development begins after 1600 UTC. CG flashes begin in the network at 1830 UTC, nearly 45 minutes before maximum convergence. Peak lightning occurs at the cross-over from convergence to divergence, that is, during the mature portion of the convective event. Positive flashes again straddle peak lightning activity. Main CG activity ends at 2010 UTC. Several flashes occur later as weak convergence occurs at 2130 UTC. Again, it is evident that most of the positive flashes exists in the mature stage of the convection. Figure 6 shows the surface situation at

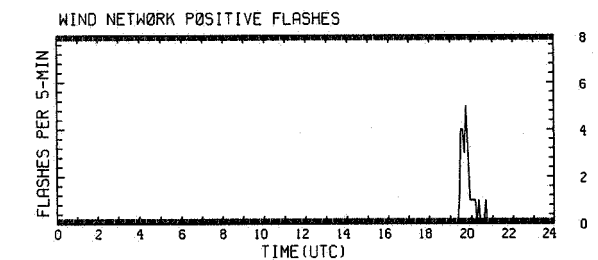
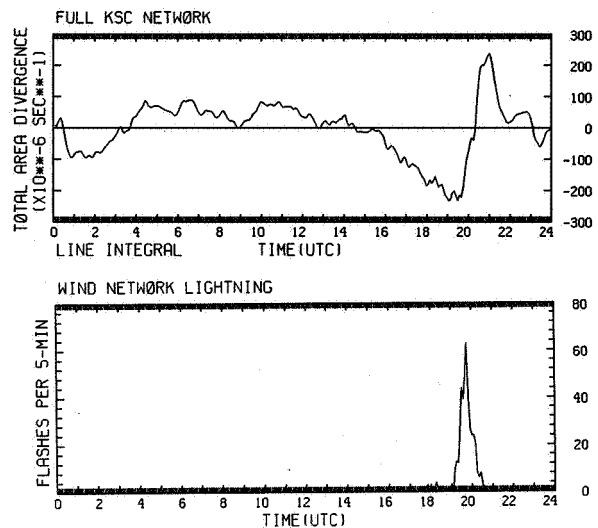


Figure 4. Time profiles (5-min resolution) of (top) total-area divergence, (middle) total CG flashes, and (bottom) positive CG flashes in the KSC wind network on 24 July 1990.

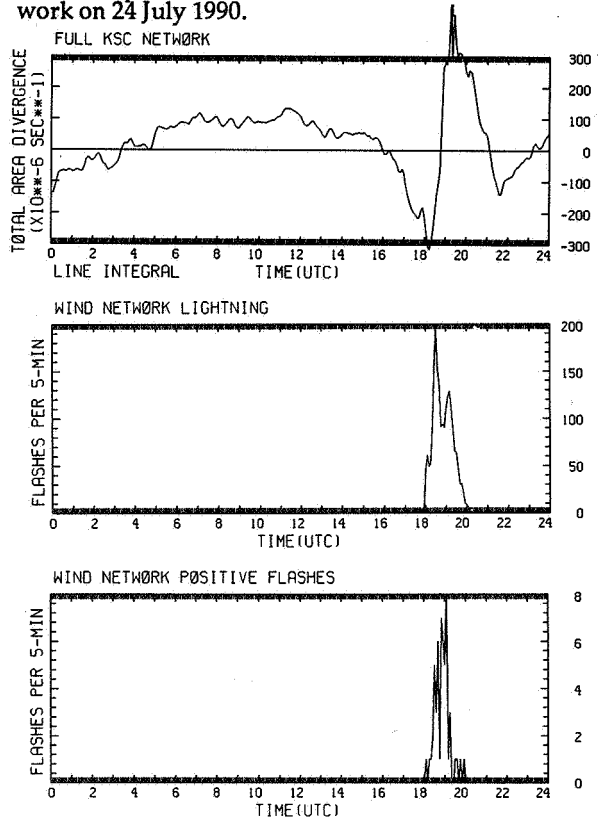


Figure 5. Same as Fig. 4, except for 17 August 1990.

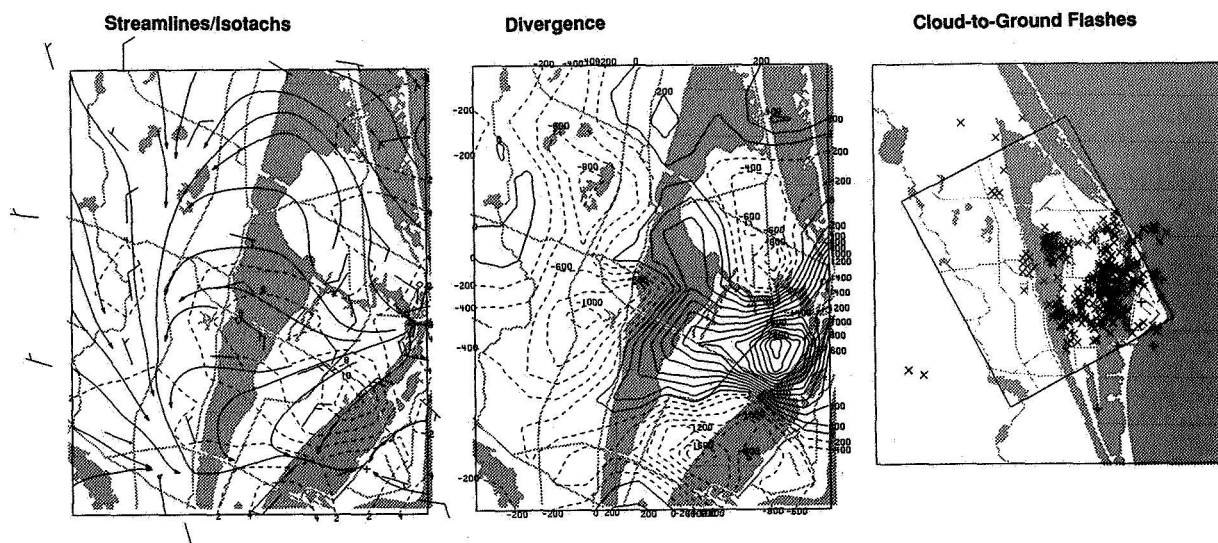


Figure 6. KSC mesonetwork analyses for 5-min period beginning at 1830 UTC (1330 EST) on 17 August 1990. Left: streamlines and isotachs ( $\text{m s}^{-1}$ ). Center: divergence ( $10^{-6} \text{ s}^{-1}$ ). Right: Larger area view of 10-min CG flashes centered at 1830 UTC.

maximum convective development.

What about these positive flashes? Are these positive flashes lowering intense positive charges to ground? The variation of signal strength versus distance from the center of the lightning DF array is shown in Fig. 7. Notice that the majority of these flashes are weak and are attenuated very quickly with range. These weak positive CGs have also been reported in analysis of Colorado flash structure [12].

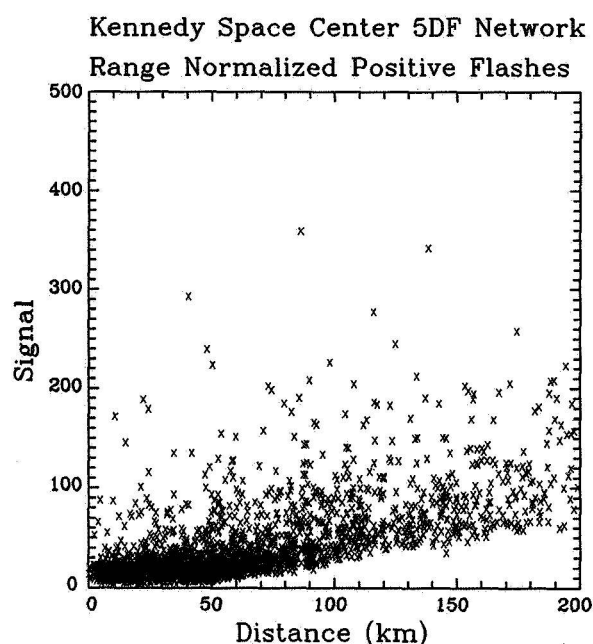


Figure 7. Variation of positive flash signal strength with distance during July and August 1990.

## A CONVERGENCE EVENT

The nearly monotonic drop in total-area divergence during the formative stage occurs before the onset of precipitation or CG lightning (see Fig. 2). Therefore, this increase in convergence can be used to anticipate convective development and production of precipitation or lightning during the mature and dissipation stages.

Watson *et al.* [1 and 2] developed convergence-event criteria for relatively small ( $280\text{-km}^2$  and  $800\text{-km}^2$ ) KSC networks. Their assumptions were that flow must be into the network, which can be converted into upward vertical motion. Therefore, the total-area divergence profile must be at zero or less. To filter noise from the total-area divergence profile, a three-point running mean (15-min average) is applied. For the expanded KSC network, an event is then defined as a sustained or monotonic drop in total-area divergence exceeding  $50 \times 10^{-6} \text{ s}^{-1}$  (called 50 units hereafter) for more than 10 minutes. Slight hesitations in this drop in divergence are ignored.

## A LIGHTNING EVENT

To statistically relate lightning to convergence events, a lightning-event criterion must also be developed. A lightning event is defined as the occurrence of one or more nega-



tive CG lightning flashes within the limits of the mesonet. An individual lightning event must be separated from previous or future lightning events by at least 30 min without flashes. Figure 2 shows three lightning events on 10 July 1988 associated with three convergence events. Figure 3 shows five convergence events, three of which have related lightning. Two lightning events (arrows) have no associated convergence.

#### 4. IMPORTANCE OF WIND DIRECTION

The patterns and locations of Florida convection are directly related to the synoptic wind field [13]. This and other studies emphasized the importance of the interaction between the synoptic wind field and the sea-breeze circulation in determining the timing and location of convective activity across the Florida peninsula. López and Holle [14] have also shown that the spatial CG lightning distribution in central Florida is determined in large part by this interaction.

The sea-breeze circulation assumes different characteristics depending on whether the prevailing wind has an onshore or offshore component. The larger-scale flow can accelerate or impede the daily progress of the sea breeze inland; the same is true for convection. Onshore flow along the Gulf coast normally produces vigorous convection inland. This convection may then drift eastward across KSC. Onshore flow along the Atlantic coast usually generates less vigorous convection, which results in less lightning. If convection occurs, it usually develops by midmorning and drifts westward across the state.

To estimate sea-breeze and thunderstorm motion, a mean vector wind [1,14],  $V_{0.3}$  from the surface to 3 km (10,000 ft) was computed each day using the Cape Canaveral sounding released daily between 0900 and 1300 UTC. Five wind-regime classes were selected, depending on  $V_{0.3}$ . One class was calm for  $V_{0.3} \leq 2$  m  $s^{-1}$ , and the other four classes were mutually exclusive 90° sectors centered on the average Florida east coastline in the vicinity of KSC; these classes were northeasterly (NE), 023°-113°; southeasterly (SE), 113°-203°; southwesterly (SW), 203°-293°; and northwesterly (NW), 293°-023°.

Table 1 gives the distribution of daily CG flashes in the KSC wind network for the study period, June-September 1987-1989, based on the mean vector wind  $V_{0.3}$ . SW flow contributes 66% of the total network flashes. NE and NW flow have the smallest percentage of flashes. The percent of regime days with lightning ranges from 30% (NE) to 73% (SW).

Table 1. Distribution of CG flashes in KSC wind network for June-September 1987-1989.

Flow Regime	Regime Days	% Days with Ltg.	Avg. No. of Flashes	Peak Daily Flashes	Total Flashes	% of Network Flashes
All	346	55	132	982	25223	100
NE	71	30	14	121	303	1
SE	101	63	64	823	4077	16
SW	103	73	221	982	16583	66
NW	19	42	58	189	464	2
Calm	52	44	165	657	3796	15

#### 5. EFFECT OF MIDDLELEVEL MOISTURE

In south Florida studies, Burpee [15] found greater amounts of midtropospheric moisture on rainy sea-breeze days than on dry sea-breeze days. Watson and Blanchard [16] found better surface convergence-convective rainfall relationships when midlevel moisture was more abundant. Figure 8 presents the distribution of midlevel relative humidity (RH) averaged in the 700-500-mb layer from the morning sounding over the KSC region for the total ensemble and for the five low-level wind directions. Box-and-whisker plots depict the distributions of relative humidity on days when lightning and no lightning were reported in the KSC network. For the total set, midlevel moisture was greater for the lightning cases than for the cases of no lightning in the network; the corresponding median values of relative humidity were 46% and 67%, respectively. The no-lightning days in the NE regime were the driest, and the lightning days in the SE wind regime were the wettest. Each wind regime held true; the greater the midlevel relative humidity, the more likely the chance for lightning. Precipitable water (not shown) for the entire atmospheric column also shows similar differences. However, low-level moisture (below 700 mb) was always present and therefore shows no correlation.

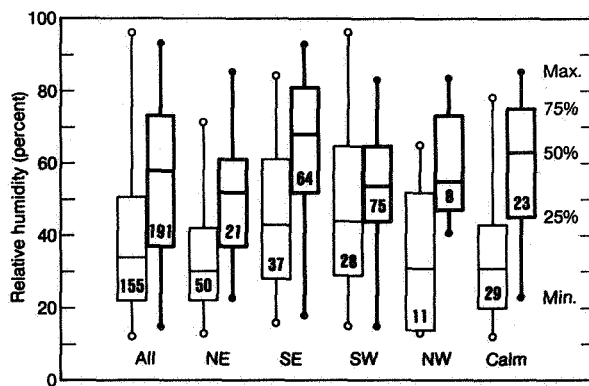


Figure 8. Distribution of midlevel RH (700-500 mb) according to low-level wind direction. Box-and-whisker plots represent the distributions of RH on days when lightning (bold boxes) and no lightning were reported in the KSC wind network. Rectangles represent the middle 50% of the sample; lines within the rectangles indicate the median; the extreme dots represent the maximum and minimum. Numbers in the boxes indicate the number of days in each sample.

## 6. VERIFICATION SUMMARY

Criteria for convergence and lightning events were given in Section 3. All convergence events were determined only by the total-area-divergence time series. No distinction was made as to how convergence cells were situated in the network.

### CONVERGENCE-LIGHTNING EVENT SUMMARY

Table 2 summarizes the convergence-lightning event results. There were 545 convergence events; 185 of these events had lightning. There were 140 lightning events with no related convergence; 63 of these misses had only one

flash. The associated summary measures testing predictability are also provided in Table 2 and in tables which follow. These summary measures include the probability of detection (POD), the false alarm ratio (FAR), the critical success index (CSI), and true skill statistic (TSS). The TSS is presented formally by Doswell and Flueck [17]. The TSS is provided because it uses all the information contained in a 2 x 2 contingency table, and provides a measure of the observed skill to perfect skill. It has a fixed range of -1 to +1, where TSS = +1 is perfect skill, and TSS = 0 shows zero correlation between the observed and predicted values.

### EFFECT OF LOW-LEVEL WIND DIRECTION AND MIDDLELEVEL MOISTURE

Table 2 also subdivides the convergence-lightning event summary according to low-level wind direction. SW flow is the major lightning producer; NE flow has the lowest lightning output. POD and TSS are highest under Calm and SW flow. False alarms are greatest under NE flow with only 17 lightning events occurring with 97 convergence events.

Table 3 separates the convergence-lightning event summary according to midlevel relative humidity. The morning midlevel RH values (700-500 mb) for the period were separated into quartiles, ranging from RH < 41%, 41-52%, 53-67%, and RH > 67%. For the driest conditions (RH < 41%), the FAR is very (.81). Only 24 lightning events occurred with 128 convergence events. As RH increases, so does TSS.

In the following Tables (4 and 5), the low-level wind regimes are subdivided accord-

Table 2. Total-area divergence versus CG lightning, based on 1987-1989 KSC wind network for a convergence-event threshold of  $50 \times 10^{-6} \text{ s}^{-1}$  separated according to low-level wind direction.

	Regime Days	Related		Avg. Total Flashes	Lt看. Misses	Avg. Total Flashes/Miss	POD	FAR	CSI	TSS
		Conv. Events	Lt看. Events							
All	346	545	185	121	140	17	.57	.66	.27	.43
NE	71	97	17	11	17	6	.50	.82	.15	.39
SE	101	194	56	58	56	12	.50	.71	.22	.35
SW	103	147	74	208	47	18	.61	.50	.38	.49
NW	19	23	6	61	8	14	.43	.74	.19	.33
Calm	52	84	32	100	12	54	.73	.62	.33	.59



Table 3. Total-area divergence versus CG lightning, based on 1987-1989 KSC wind network for a convergence-event threshold of  $50 \times 10^{-6} \text{ s}^{-1}$  separated according to midlevel relative humidity.

	Regime Days	Related		Avg. Total Flashes	Lt看. Misses	Avg. Total Flashes/Miss	POD	FAR	CSI	TSS
		Conv. Events	Lt看. Events							
All	346	545	185	121	140	17	.57	.66	.27	.43
RH < 41%	125	128	24	184	25	8	.49	.81	.16	.35
RH (41 - 52%)	68	111	40	94	34	19	.54	.64	.28	.38
RH (53 - 67%)	74	140	53	123	34	25	.61	.62	.30	.43
RH > 67%	79	166	68	114	47	15	.59	.59	.32	.50

ing to midlevel RH. As found in Table 2, SW flow is the major lightning producer. When SW flow is subdivided according to midlevel RH (Table 4), the POD increases as RH increases, FAR decreases as RH increases, and TSS increases as RH increases.

Calm flow (Table 5) may be the most important regime for the convergence technique, since convection develops in place (i.e., little movement) under this regime. Again, the FAR is high during dry conditions but decreases as RH increases. The TSS is quite good throughout the RH classes. Notice the one large lightning "bust" in RH (53-67%).

The remaining directions are not present due to space limitations. A summary is given instead. The NE wind regime is the weakest lightning producer. Under the two driest quartiles, there is little chance for a lightning event to occur with convergence. However, as midlevel RH increases, the chance for lightning improves. The summary measures (POD, etc.) also improve as RH increases. The RH values under SE flow provide some puzzle-

ment. The usual situation under low RH values appears consistent with other directions, i.e., low POD, high FAR, and low TSS. The lack of skill (low TSS) at higher RH values may be attributed to more disturbed conditions when there is less association between surface convergence and lightning as convection develops by other means than surface heating. The NW regime had too few samples to be meaningful.

When compared to the 2-year study of Watson *et al.* [2] encompassing the smaller 800-km<sup>2</sup> network, the forecast statistics have decreased in skill. The TSS has dropped approximately 0.2 in nearly all cases. The principal reason is that many small storms are imbedded in a large network. The encouraging aspects are that the statistics appear most favorable for calm flow, which is the most difficult wind regime, since extrapolation and persistence techniques do not work when development occurs in place. In the case of calm flow, the TSS has increased by 0.05 to 0.59. The probable cause for this is that much of the entire life cycle of convection occurs within the boundaries of the larger network. The use of the convergence-lightning

Table 4. Total-area divergence versus CG lightning, based on 1987-1989 KSC wind network for a convergence-event threshold of  $50 \times 10^{-6} \text{ s}^{-1}$  separated according to midlevel relative humidity for the SW wind regime.

SW Flow	Regime Days	Related		Avg. Total Flashes	Lt看. Misses	Avg. Total Flashes/Miss	POD	FAR	CSI	TSS
		Conv. Events	Lt看. Events							
	103	147	74	208	47	18	.61	.50	.38	.49
RH < 41%	29	37	14	247	12	15	.54	.62	.29	.39
RH (41 - 52%)	23	36	17	138	16	28	.52	.53	.33	.37
RH (53 - 67%)	30	43	22	250	13	11	.63	.49	.39	.48
RH > 67%	21	31	21	196	6	17	.78	.32	.57	.70

Table 5. Total-area divergence versus CG lightning, based on 1987-1989 KSC wind network for a convergence-event threshold of  $50 \times 10^{-6} \text{ s}^{-1}$  separated according to midlevel relative humidity for the Calm wind regime.

Calm Flow	Regime Days	Related		Avg. Total Flashes	Lt看. Misses	Avg. Total Flashes/Miss	POD	FAR	CSI	TSS
		Conv. Events	Ltg. Events							
	52	84	32	100	12	54	.73	.62	.33	.59
RH < 41%	26	30	5	179	3	2	.63	.83	.15	.48
RH (41 - 52%)	7	12	6	116	4	7	.60	.50	.38	.46
RH (53 - 67%)	8	18	10	38	1	595	.91	.44	.53	.75
RH > 67%	11	24	11	113	4	6	.73	.54	.39	.55

technique as a nowcasting tool is a very good simple single rule. In practice, the technique is not used alone, but should be combined with other platforms such as radar, satellite, lightning maps, visual observations, etc.

## 7. SUMMARY

During the three summers of data collection, 25,223 flashes were detected in the KSC wind network covering  $1600 \text{ km}^2$ . The convergence-lightning technique accounted for 89% of the network flashes in 185 convergence events. Synonymous with dry conditions was NE flow; there was little chance for lightning under these conditions. There also were high false alarm rates with NE flow as moderate onshore flow produced implied convergence at coastal wind sites which oscillated at times to create convergence events.

More midlevel moisture was available on days when lightning was reported in the KSC wind network than on days when no lightning was reported. Overall, as midlevel RH decreased, the less the chance for lightning. As RH increased, the greater the chance for lightning to occur with convergence.

The summer of 1990 provided the first opportunity to study the relationship of positive CG flashes to the life cycle of convection as viewed through the surface total-area divergence profile. Most positive CG flashes were found to be weak and occurred during the mature stage of convective development. After reviewing several months of convergence and lightning (both positive and negative CG flashes) for 1990, it can be concluded that due to the small percentage of positive flashes (3.7% in

wind network) and their time of occurrence (convective maturity), little has been lost in previous years' convergence-lightning summaries which did not contain positive flashes, because the positives always occurred during peak negative activity, and not at the end of the storm.

The technique is currently implemented at KSC for use by USAF forecasters and has met with great success. However, the technique cannot be used in a vacuum; it must be incorporated into a total mesoscale observing and forecasting system. The likelihood of thunderstorms must be determined from the synoptic situation. Monitoring the total-area divergence time series and horizontal fields is but one aid that will help the forecaster determine the timing, longevity, and possibly, the intensity of the lightning episode.

## 8. ACKNOWLEDGMENTS

The authors wish to thank the following individuals, and many of their colleagues at their respective facilities, for support during the collection, processing, and interpretation of the data used in this study: William Jafferis (NASA, KSC), Ron Wojtasinski (NASA, KSC), Michael Maier (CSR, KSC), and John Weems (USAF). The research was supported by NASA.

## 9. REFERENCES

1. Watson, A.I., R.E. López, R.L. Holle, and J.R. Daugherty, 1987: The relationship of lightning to surface convergence at Kennedy Space Center: A preliminary study. *Wea. Forecasting*, 2, 140-157.

2. Watson, A.I., R.L. Holle, R.E. López, R. Ortiz, and J.R. Nicholson, 1991: Surface wind convergence as a short-term predictor of cloud-to-ground lightning at Kennedy Space Center. *Wea. Forecasting*, 6, In press.
3. Watson, A.I., and R.L. Holle, 1982: The relationship between low-level convergence and convective precipitation in Illinois and south Florida. Tech. Rept. No. 7, NOAA/ERL, Boulder, and Illinois State Water Survey, Champaign, 67 pp.
4. Cressman, G.P., 1959: An operational objective analysis system. *Mon. Wea. Rev.*, 87, 367-374.
5. Krider, E.P., R.C. Noggle, A.E. Pifer and D.L. Vance, 1980: Lightning direction finding systems for forest fire detection. *Bull. Amer. Meteor. Soc.*, 61, 980-986.
6. Krider, E.P., R.C. Noggle and M.A. Uman, 1976: A gated, wideband magnetic direction finder for lightning return strokes. *J. Appl. Meteor.*, 15, 301-306.
7. Mach, D.M., D.R. MacGorman, and W.D. Rust, 1986: Site errors and detection efficiency in a magnetic direction-finder network for locating lightning strikes to ground. *J. Atmos. Oceanic Technol.*, 3, 67-74.
8. López, R.E., and R.L. Holle, 1986: Diurnal and spatial variability of lightning in northeastern Colorado and central Florida during the summer. *Mon. Wea. Rev.*, 114, 1288-1312.
9. Passi, R.M., and R.E. López, 1989: A parametric estimation of systematic errors in networks of magnetic direction finders. *J. Geophys. Res.*, 94, 13,319-13,328.
10. Cuning, J.B., R.L. Holle, P.T. Gannon and A.I. Watson, 1982: Convective evolution and merger in the FACE experimental area: Mesoscale convection and boundary layer interactions. *J. Appl. Meteor.*, 21, 953-977.
11. Byers, H.R., and R.R. Braham, Jr., 1949: *The Thunderstorm*. U.S. Government Printing Office, Washington, D.C., 187 pp.
12. López, R.E., M.W. Maier, J.A. García-Miguel, and R.L. Holle, 1990: Weak positive cloud-to-ground flashes in northeastern Colorado. Preprints, 1991 International Conference on Lightning and Static Electricity, 16-19 April, Cocoa Beach FL.
13. Byers, H.R., and H.R. Rodebush, 1948: Causes of thunderstorms of the Florida peninsula. *J. Meteor.*, 5, 275-280.
14. López, R.E., and R.L. Holle, 1987: The distribution of summertime lightning as a function of low-level wind flow in central Florida. NOAA Technical Memorandum ERL ESG-28, Environmental Research Laboratories, Boulder, CO, 43pp.
15. Burpee, R.W., 1979: Peninsula-scale convergence in the south Florida sea breeze. *Mon. Wea. Rev.*, 107, 852-860.
16. Watson, A.I., and D.O. Blanchard, 1984: The relationship between total area divergence and convective precipitation in south Florida. *Mon. Wea. Rev.*, 112, 673-685.
17. Doswell, C.A. III, and J.A. Flueck, 1989: Forecasting and verifying in a field research project: DOPLIGHT '87. *Wea. Forecasting*, 4, 97-109.

N91-32704

ASSESSMENT AND FORECASTING OF LIGHTNING POTENTIAL AND  
ITS EFFECT ON LAUNCH OPERATIONS AT CAPE CANAVERAL AIR FORCE STATION  
AND JOHN F. KENNEDY SPACE CENTER

J. Weems, N. Wyse, J. Madura, M. Secrist, and C. Pinder

United States Air Force, Detachment 11, 4th Weather Wing  
Cape Canaveral Air Force Station, Florida

ABSTRACT

Lightning plays a pivotal role in the operation decision process for space and ballistic launches at Cape Canaveral Air Force Station (CCAFS) and John F. Kennedy Space Center (KSC). Lightning forecasts are the responsibility of Detachment 11, 4th Weather Wing's Cape Canaveral Forecast Facility (CCFF). These forecasts are important to daily ground processing as well as launch countdown decisions. The methodology and equipment used to forecast lightning are discussed. Impact on a recent mission is summarized.

INTRODUCTION

Lightning and its effects can significantly impact safe and timely operations of space and ballistic launch systems from Cape Canaveral, Florida. Determining location, time, and strength of lightning and predicting lightning potential are key support elements provided to CCAFS and KSC by the U.S. Air Force Detachment 11, 4th Weather Wing's Cape Canaveral Forecast Facility. Decision makers and launch operations managers are continually updated on lightning occurrences and forecast probabilities. An extensive network of instrumentation and output displays are available to evaluate these phenomena. New techniques to determine the onset and cessation of lightning are constantly reviewed and applied to both day-to-day operations and launch countdown support. However, implementation of new capabilities is based on safety and operational requirements vice just technical feasibility. During launch countdowns the launch weather team must also evaluate the threat of triggered lightning from high electric field potential aloft. The team requires "clear and convincing evidence" to verify the environment is not dangerous prior to the "go for launch" call by the Range Safety Officer. Continuous instrument and procedure improvements have enhanced the quality of lightning forecasts for these extremely weather sensitive launch operations.

LIGHTNING FORECAST REQUIREMENTS

A major problem confronting forecasters at the CCFF is prediction of the precise time and location of convective activity and its associated weather phenomena, particularly lightning. These storms directly affect a myriad of activities including space and ballistic launch operations and routine

ground processing and gantry operations. Costs associated with lightning induced delays such as cessation of hazardous operations, pad evacuations, and limitation of most outdoor activity are substantial.

Lightning is a year-round concern at Cape Canaveral but the bulk of activity occurs during the months of May through September (see Fig. 1).

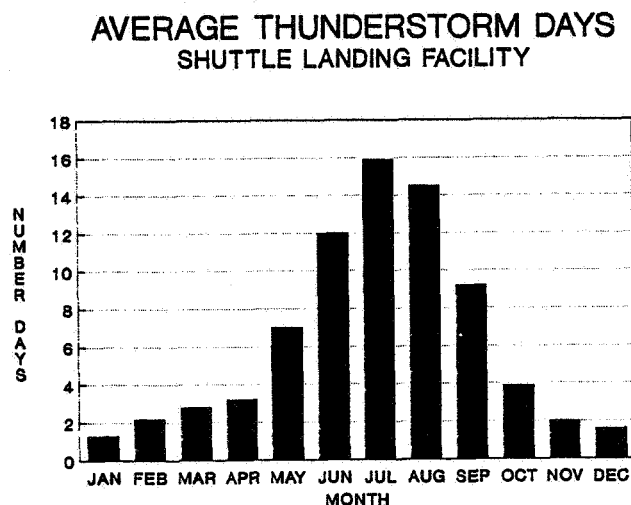


Fig. 1. Average Thunderstorm Days at the Shuttle Landing Facility, Kennedy Space Center, Florida [1].

Lightning assessments are used for planning and real-time operational decisions. Support specifics depend on the type of operation (e.g., daily ground/pad processing or launch) and time requirements. While daily ground operations support requires very precise forecasts of natural lightning for specific places (pads) and periods of time, the decision to launch also includes stringent concerns for triggered lightning.

Lightning forecasts beyond one day are used for planning purposes only. For instance, approximately 5 days in advance of Launch Readiness Reviews (LRR) and daily thereafter, customers are given the probabilities of violating Launch Commit Criteria (LCC) and an overall probability (see Table I). (Table II contains a complete listing of all lightning related LCC.) A critical lightning forecast is given prior to vehicle fueling--launch minus 9 hours for Shuttle and launch minus 5 hours for Expendable Launch Vehicles (ELV). The final launch decision requires the launch weather team to be clearly convinced no weather launch commit criteria are violated.

#### GROUND PROCESSING SUPPORT

Routine ground processing tasks normally require short-term forecasts. Most commonly, for day to day processing, the forecaster must predict lightning

TABLE I. Launch Constraint Probability Forecast Example

LTG WITHIN 10 NM OF LAUNCH SITE/PLANNED FLT PATH W/IN 30 MIN PRIOR TO LAUNCH UNLESS CONDITIONS CAUSING LTG HAVE MOVED >10 NM AWAY FROM LAUNCH SITE OF PLANNED FLT PATH:	<5%
THRU CU CLOUDS WITH TOPS HIGHER THAN THE +5°C LVL	10%
THRU OR W/IN 5 NM OF CU CLOUDS WITH TOPS HIGHER THAN THE -10°C LVL:	10%
THRU OR W/IN 10 NM OF CU CLOUDS WITH TOPS HIGHER THAN THE -20°C LVL:	10%
THRU OR W/IN 10 NM OF THE NEAREST EDGE OF ANY CB OR TSTM CLOUD INCLUDING ITS ANVIL:	<5%
ONE MINUTE AVERAGE FIELD MILL VALUES EXCEED 1KV/M WITHIN 5 NM DURING THE 15 MINUTES PRIOR TO LAUNCH:	<5%
FLIGHT PATH THRU VERTICALLY CONTINUOUS CLOUD LAYER DEPTH OF 4500 FEET OR MORE WITH ANY PART LOCATED BETWEEN 0° AND -20°C LEVELS:	20%
FLIGHT PATH THRU ANY CLOUDS THAT EXTEND AT OR ABOVE FREEZING LVL AND ARE ASSOCIATED WITH DISTURBED WEATHER:	10%
THRU TSTM DEBRIS CLOUDS OR WITHIN 5 NM OF TSTM DEBRIS CLOUDS NOT MONITORED BY FIELD MILLS OR PRODUCING RADAR RETURNS:	10%

within 5 nautical miles (nm) of a specific area with lead times of 30 minutes. However, sometimes resources are exposed over long periods of time. For instance, the rollout of the Shuttle from the Vertical Assembly Building (VAB) to the launch complex requires a forecast of a 90 percent probability of no lightning within 20 nm of vehicle rollout path for a period of about 8 hours.

An assessment of lightning advisories issued for the Titan Integrate, Transfer, and Launch (ITL) area, located near Launch Complex 40/41, illustrates the impact to one ELV customer. Figure 2 depicts the time lost due to these advisories in 1989 and 1990. In 1990, the CCFF issued a total of 98 advisories for lightning within 5 nm. Manpower impact is quite large considering the additional time lost exiting from and returning to the pad(s) and platforms. Furthermore, many tests underway were re-initiated from the beginning when prematurely terminated. For instance, Wyatt and Kintigh [2] estimates Titan launch flows are interrupted nearly 380 work force hours per year by lightning advisories. Martin Marietta Corp. (prime Titan Contractor) estimated, on the average, \$57,000 per day for manpower costs under normal operations. This translated to an approximate \$1 million per year in manpower losses for only one of four major launch systems at the CCAFS. This cost will escalate as Titan launch rates rise. Thus, improving lightning advisories is a top priority.

## GROUND PROCESSING LIGHTNING PRODUCT ENHANCEMENTS

Comparisons of 1989 and 1990 advisory data (shown in Fig. 2) suggest recent CCFF enhancements to lightning advisory procedures are reducing downtime. An added manpower position in 1990 allowed the CCFF to dedicate one trained individual to continually evaluate lightning and severe weather potential. Figure 2 also denotes a decrease of more than 10 percent in average lightning advisory duration from 1989 to 1990. A natural consequence of advisory duration reductions is manpower savings. During the non-convective season when not dedicated to day to day support, the individual produces simulations and studies on local effects, and then trains all CCFF forecasters. Initial results are quite favorable.

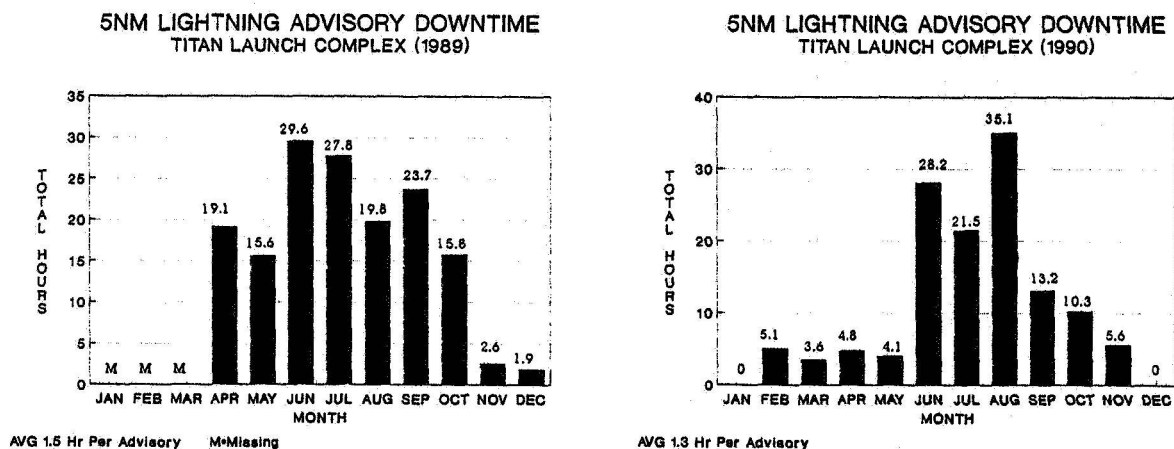


Fig. 2. Lightning Advisory Downtime at Complex 40/41 on Cape Canaveral Air Force Station, Florida in 1989 and 1990.

To reduce the impact of lightning advisories on similar KSC ground operations, a two-tiered (phase 1 & 2) advisory process was tested in summer 1990. The CCFF forecaster issued the initial advisory (phase 1) with a 30 minute lead time when the potential for lightning was expected to move within 5 nm of specified key KSC ground operations areas. This advisory was upgraded to phase 2 when lightning was considered imminent, that is, the threat had actually moved to (or formed) within 5 nm--so called zero minute lead time advisory. Since not all operations required 30 minute lead time, some were allowed to continue until phase 2 was in effect, thus reducing lost man hours. In addition, since phase 2 advisories were not forecasts, they virtually eliminated the false alarms and timing errors of phase 1 advisories. Limited data collected thus far indicates the phase 2 advisories were in effect only 42% of phase 1 advisory time. This two-tiered advisory will continue at KSC and is now being investigated for use on CCAFS in summer 1991.

## LIGHTNING ASSESSMENT INSTRUMENTATION

To reduce lost manpower costs and maintain the highest safety standards, the CCAFS and KSC developed a highly sophisticated network of instrumentation. Cape Canaveral Air Force Station/KSC and the surrounding area are host to a myriad of sensing equipment including a lightning detection network, a ground based field mill network, and wind/temperature sensors located on 46 towers at heights ranging from 2 to 165 meters. In addition, a WSR-74C (5 cm wavelength) radar was modified to produce volumetric data sets by McGill University [3]. These data are created at 24 elevation angles ranging from 0.6 degrees to 35.9 degrees over five minute intervals. Data digitization allows forecasters to construct and display constant altitude plan position indicator (CAPPI), vertical cross-sections, and echo tops; animate displays; and extract point information such as maximum tops and radial location. The digitized data is also transmitted to the Meteorological Interactive Data Display System (MIDDS) for processing and display over Closed Circuit Television (CCTV) and merged with other data such as lightning plots or satellite imagery. Location of the radar antenna at Patrick AFB, 21 miles south of Cape Canaveral, reduces ground clutter data loss and produces a full volume scan over CCAFS/KSC.

Equipment falls into four categories: (1) measurement of environmental parameters from which convection initiation can be forecast: Weather Information Network Display System (WINDS)--a network of wind and temperature sensors throughout the CCAFS and KSC complex, see Fig. 3; and the Meteorological Sounding System (MSS)--receives and processes upper air soundings; (2) detection/measurement of lightning associated parameters: Radar (WSR-74C and McGill processor described above); (3) measurement of potential: Ground Based Field Mill (GBFM), also known as the Launch Pad Lightning Warning System (LPLWS)--network of 31 ground based field mills for measuring surface electric potential, see Fig. 4; and (4) detection of actual lightning: Lightning Detection System (LDS), also referred to as Lightning Location/Protection (LLP)--a system of five detectors used to locate and measure cloud-to-ground lightning, and Arthur D Little Lightning Detector--determines occurrence in radial distances, including cloud-to-cloud discharges.

## LIGHTNING ASSESSMENT PROCESS

Detection of lightning and/or lightning potential is the focal point of CCFF instrumentation. First the potential for convection is determined from synoptic scale analyses. Next a mesoscale analysis begins with the local upper air sounding released daily at approximately 0615 local time. During the period May through September, a computerized Neumann/Pfeffer [4] climatological regression analysis provides a probability for afternoon/evening thunderstorm occurrence. Examination of satellite imagery and local/regional radar networks identifies mesoscale interactions, e.g., boundary intersections. Meanwhile, the local meteorological sensing networks are monitored to provide important local precursor data for convection initiation (winds, temperature, dewpoint). Techniques developed by the Environmental Research Lab (ERL) in Boulder, CO [4], using total average area divergence are used to identify areas of potential convective



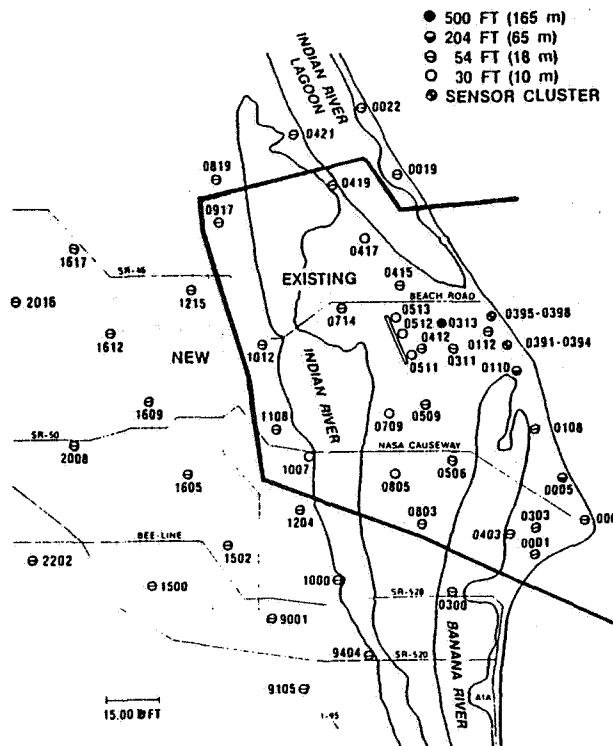


Fig. 3. Weather Information Network and Display System Tower Locations at CCAFS and KSC.

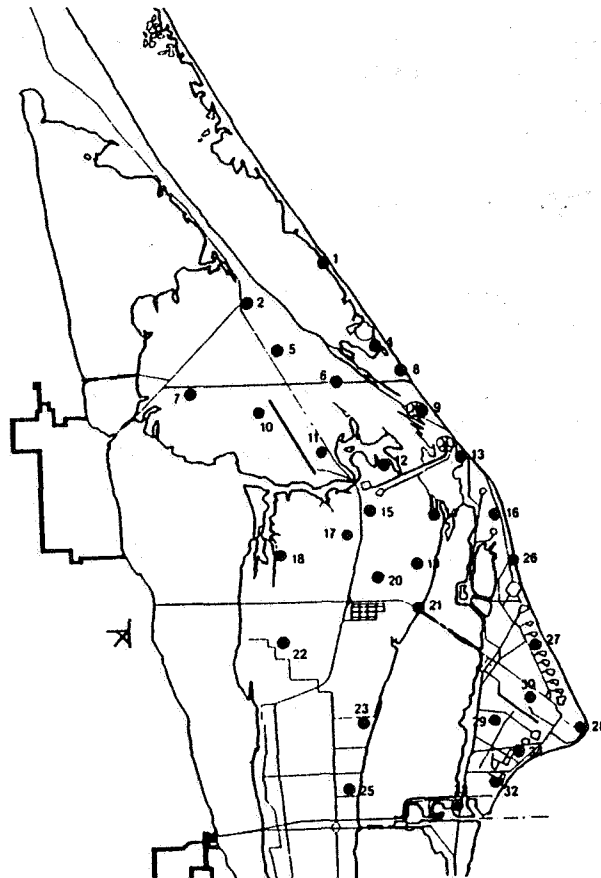


Fig. 4. Ground Based Field Mill (GBFM) Locations at CCAFS and KSC.

growth and hence lightning initiation. When these areas are defined, realtime evaluation intensifies. Radar and satellite are the primary tools to locate developing convection. The GBFM system detects, measures, and contours electric field charge centers and LDS identifies cloud-to-ground lightning occurrence. Integration of all tools is necessary to implement an effective lightning forecast and advisory program.

Forecasting the latter stages of convective decay is also operationally critical. Ground workers are anxious to resume work but typically the threat still exists. This "threat" is not as obvious as when towering clouds, strong winds, rain, and frequent lightning were prevalent. Charge lingers, becomes more concentrated and occasionally initiates powerful lightning discharges.

The debris stage is also critical for launch operations. Space launch vehicles transiting charge-laden clouds from decayed thunderstorms can initiate triggered lightning. On 26 March 1987, an Atlas-Centaur (AC 67) launch vehicle was launched from Pad 36B at CCAFS. At about 48 seconds into its flight, the vehicle was struck by triggered lightning and subsequently destroyed [6]. This incident emphasized the important role weather and weather support play in launching space vehicles. An increased aware-

ness of weather emerged and new lightning constraints were developed. The following constraints (Table II) were formulated by a joint effort of the operational, scientific and academic communities [7].

TABLE II. Range Safety Constraints for Natural and Triggered Lightning

THE LAUNCH WEATHER OFFICER MUST HAVE CLEAR AND CONVINCING EVIDENCE THE FOLLOWING CONSTRAINTS ARE NOT VIOLATED:

A. DO NOT LAUNCH IF ANY TYPE OF LIGHTNING IS DETECTED WITHIN 10 NM OF THE LAUNCH SITE OR PLANNED FLIGHT PATH WITHIN 30 MINUTES PRIOR TO LAUNCH UNLESS THE METEOROLOGICAL CONDITION THAT PRODUCED THE LIGHTNING HAS MOVED MORE THAN 10 NM AWAY FROM THE LAUNCH SITE OR PLANNED FLIGHT PATH.

B. DO NOT LAUNCH IF ANY OF THE PLANNED FLIGHT PATH WILL CARRY THE VEHICLE:

1. THROUGH CUMULUS CLOUDS WITH TOPS THAT EXTEND TO AN ALTITUDE AT OR ABOVE THE PLUS 5 DEGREE CELSIUS LEVEL; OR
2. THROUGH OR WITHIN 5 NM OF CUMULUS CLOUDS WITH TOPS THAT EXTEND TO AN ALTITUDE AT OR ABOVE THE MINUS 10 DEGREE CELSIUS LEVEL; OR
3. THROUGH OR WITHIN 10 NM OF CUMULUS CLOUDS WITH TOPS THAT EXTEND TO AN ALTITUDE AT OR ABOVE THE MINUS 20 DEGREE CELSIUS LEVEL; OR
4. THROUGH OR WITHIN 10 NM OF THE NEAREST EDGE OF ANY CUMULONIMBUS OR THUNDERSTORM CLOUD INCLUDING ITS ASSOCIATED ANVIL.

C. DO NOT LAUNCH IF, FOR RANGES EQUIPPED WITH A SURFACE ELECTRIC FIELD MILL NETWORK, AT ANY TIME DURING THE 15 MINUTES PRIOR TO LAUNCH TIME, THE ONE MINUTE AVERAGE OF ABSOLUTE ELECTRIC FIELD INTENSITY AT THE GROUND EXCEEDS 1 KILOVOLT PER METER WITHIN 5 NM OF THE LAUNCH SITE UNLESS:

1. THERE ARE NO CLOUDS WITHIN 10 NM OF THE LAUNCH SITE; AND,
2. SMOKE OR GROUND FOG IS CLEARLY CAUSING ABNORMAL READINGS.

NOTE: FOR CONFIRMED INSTRUMENTATION FAILURE, CONTINUE COUNTDOWN.

D. DO NOT LAUNCH IF THE PLANNED FLIGHT PATH IS THROUGH A VERTICALLY CONTINUOUS LAYER OF CLOUDS WITH AN OVERALL DEPTH OF 4,500 FEET OR GREATER WHERE ANY PART OF THE CLOUDS ARE LOCATED BETWEEN THE ZERO DEGREE AND THE MINUS 20 DEGREE CELSIUS TEMPERATURE LEVELS.

E. DO NOT LAUNCH IF THE PLANNED FLIGHT PATH IS THROUGH ANY CLOUD TYPES THAT EXTEND TO ALTITUDES AT OR ABOVE THE ZERO DEGREE CELSIUS LEVEL AND THAT ARE ASSOCIATED WITH DISTURBED WEATHER WITHIN 5 NM OF THE FLIGHT PATH.

F. DO NOT LAUNCH THROUGH THUNDERSTORM DEBRIS CLOUDS, OR WITHIN 5 NM OF THUNDERSTORM DEBRIS CLOUDS NOT MONITORED BY A FIELD MILL NETWORK OR PRODUCING RADAR RETURNS GREATER THAN OR EQUAL TO 10DB.

TABLE II (CONTINUED)

## G. GOOD SENSE RULE

IF HAZARDOUS CONDITIONS EXIST THAT APPROACH THE LAUNCH CONSTRAINT LIMITS OR IF HAZARDOUS CONDITIONS ARE BELIEVED TO EXIST FOR ANY OTHER REASONS, AN ASSESSMENT OF THE NATURE AND SEVERITY OF THE THREAT SHALL BE MADE AND REPORTED TO THE TEST DIRECTOR OR LAUNCH DIRECTOR.

## DEFINITIONS:

1. DEBRIS CLOUD - ANY CLOUD LAYER OTHER THAN A THIN FIBROUS LAYER THAT HAS BECOME DETACHED FROM THE PARENT CUMULONIMBUS WITHIN 3 HOURS BEFORE LAUNCH.
2. DISTURBED WEATHER - ANY METEOROLOGICAL PHENOMENON THAT IS PRODUCING MODERATE OR GREATER PRECIPITATION.
3. CUMULONIMBUS CLOUD - ANY CONVECTIVE CLOUD THAT EXCEEDS THE MINUS 20 DEGREE CELSIUS TEMPERATURE LEVEL.
4. CLOUD LAYER - ANY CLOUD BROKEN, OVERCAST LAYER, OR LAYERS CONNECTED BY CLOUD ELEMENTS; E.G., TURRETS FROM ONE CLOUD TO ANOTHER.
5. PLANNED FLIGHT PATH - THE TRAJECTORY OF THE FLIGHT VEHICLE FROM THE LAUNCH PAD THROUGH ITS FLIGHT PROFILE UNTIL IT REACHED THE ALTITUDE OF 100,000 FEET.
6. ANVIL - STRATIFORM OR FIBROUS CLOUD PRODUCED BY THE UPPER LEVEL OUTFLOW FROM THUNDERSTORMS OR CONVECTIVE CLOUDS. ANVIL DEBRIS DO NOT MEET THE DEFINITION IF IT IS OPTICALLY TRANSPARENT.

TABLE III. Equipment Applied to Launch Commit Criteria

CONSTRAINT	EQUIPMENT/SYSTEMS USED TO EVALUATE CONSTRAINT
A	LDS, GBFM, SURFACE OBS, A D LITTLE
B.1.	RADAR, SATELLITE, MSS, ACFT
B.2.	RADAR, SATELLITE, MSS, ACFT
B.3.	RADAR, SATELLITE, MSS, ACFT
B.4.	RADAR, SATELLITE, MSS, ACFT, SURFACE OBS
C	GBFM (including strip charts)
D	RADAR, SATELLITE, MSS, ACFT
E	RADAR, SATELLITE, MSS, ACFT
F	RADAR, SATELLITE, MSS, ACFT, SURFACE OBS
G	ALL

Table III illustrates the interaction required among instrumentation used to assess launch commit criteria. Common to most constraint assessments are three basic observation processes. First, a process to evaluate conditions necessary to produce/develop mechanisms forming lightning (thunderstorms), i.e., satellite, winds, temperature, etc. Second, a capability to

determine the presence of lightning (LDS, GBFM, A D Little). Finally, a capability to assess the in situ conditions (surface observer, weather aircraft, wind towers).

#### LAUNCH SYSTEM SUPPORT

The following synopsis illustrates how several tools can be used to evaluate LCC.

Six attempts to launch Eastern Test Range (ETR) Operation #1445 (Delta II) were made 20 May 89 through 10 June 90. Three of the five scrubs were directly related to weather LCC violations with two being especially noteworthy since the equipment and methodology used were unique.

On 23 May thunderstorms were widespread across the northern half of Florida with minor vorticity centers moving across central Florida. These vorticity maximums coupled with a seabreeze convergent boundary produced storms in the local area. The storms were clearly evident in early and mature stages within 10 nm of the launch pad on both satellite and radar but as anvils became detached and moved across the Cape area, volumetric radar data became invaluable. The ability to animate both echo tops and CAPPIs provided clear evidence of anvil origin. The increased resolution of radar data, both spatial and temporal, versus GOES satellite data, left no question of thunderstorm anvil proximity to the launch complex. Dissemination of the data over CCTV enabled the Launch Weather Officer to clearly describe and relay constraint status to decision makers. As the anvil moved over the Cape, field mills became active and exceeded the LCC of 1000 v/m within 5 nm of the launch site.

Two constraints were clearly violated.

- A. Do not launch if the planned flight path is through or within 10 nm of the nearest edge of any cumulonimbus or thunderstorm cloud including its associated anvil. Determined by radar.
- B. Do not launch if at any time during the 15 minutes prior to launch time, the one minute average of absolute electric field intensity exceeds 1 kilovolt per meter (1 kv/m) within 5 nm of the launch site. Determined by GBFM.

Launch attempt on 9 June was similar as thunderstorm anvils over the area were detected by satellite imagery and parent cells by radar. An extensive cirrus layer over central Florida masked convection below the canopy. Cells were observable on satellite only in areas where cirrus was not present or tops penetrated the layer. Radar was essential to detect the sources of convection and, in conjunction with satellite data, to determine if the overhead cirrus was thunderstorm associated anvil. Again two separate pieces of equipment were used together to determine constraint status. Analysis showed the parent storms remained outside of 10 nm radius; however, attached debris/anvil were within 10 nm. Thus, as before, the thunderstorm debris LCC was violated and the launch scrubbed.

On 10 June 1990 the satellite and radar data verified no LCC were violated and the Delta was successfully launched.

#### FUTURE ENHANCEMENTS

Several projects are underway to enhance support. Although not all inclusive, a short summary of new programs is shown below.

AirBorne Field Mill (ABFM) Program. The ABFM program was recommended by the AC 67 investigation committee. Purpose of the ABFM is to gather data to better understand/quantify the meteorological conditions favorable for electric charge aloft and then: (1) evaluate/revise current launch constraints and (2) possibly develop concept of operation to use an ABFM on day of launch. The ultimate goal is to safely increase launch availability and to reduce the chance for weather holds and delays.

A NASA Lear Jet with extensive instrumentation has been flying to 50,000 feet to obtain cloud electrification data in the vicinity of CCAFS. Forty missions were flown in July and August 1990 to calibrate the Lear Jet's five field mills and gather data to revise the LCC. A data analysis report is expected in Spring 1991. Two deployments are scheduled during 1991: February - March and June - July.

Lightning Mapping System. A new Lightning Detection and Ranging (LDAR) System is under development at KSC. The system will map the location of in-cloud and cloud-to-ground lightning based on the time of arrival (TOA) of VHF radiation [8].

Advanced Ground Based Field Mill (AGBFM) System. New more efficient and reliable field mills are being developed as a joint Air Force/NASA project. These mills will replace the current network and have independent processing capability vice the current need for processing on the ETR Cyber Computer.

Applied Meteorology Unit (AMU). The AMU will facilitate the development and transition of new techniques and equipment (such as LDAR) into the co-located CCFF. The AMU will be managed by KSC, manned by contractors, and contain close to a mirror image of CCFF equipment--the AMU will address both the CCFF and the Johnson Space Center's Spaceflight Meteorological Group Shuttle weather requirements.

Improved Weather Dissemination System (IWDS). IWDS is a micro VAX based system designed to simplify and accelerate the transmission of weather forecasts, observations, advisories, and warnings directly to individual user groups. System software is currently under development for CCAFS and KSC. Installation is expected by summer 1991. IWDS will eliminate time consuming dissemination processes and allow for increased forecaster concentration on convective activity.

#### SUMMARY

Lightning affects time critical launch and ground processing operations at

Cape Canaveral AFS and Kennedy Space Center, Florida. Detachment 11, 4th Weather Wing's Cape Canaveral Forecast Facility produces specific forecasts which allow appropriate personnel to evaluate risks of proceeding with or canceling time sensitive/high cost operational/launch events. Data from an extensive network of sensing equipment is used to evaluate specific launch commit criteria. Methods to reduce lightning impacts without increasing risks are constantly under study. These include both procedural reviews and instrumentation improvements.

#### ACKNOWLEDGEMENTS

The authors wish to convey a sincere appreciation to Mr Bill Boyd (Det 11, senior scientist) for his complete technical review of this document.

#### REFERENCES

1. Surface Observation Climatic Summaries for Shuttle Landing Facility, 1989. Prepared by OL-A, USAF Environmental Technical Applications Center, Asheville, North Carolina.
2. Wyatt, D and D. Kintigh, 1989: Internal US Air Force Study For Manpower Impact due to Weather for Launch Complex 40/41. Personal Conversation.
3. Austin, G.L., A. Kilambi, A. Bellon, N. Leoutsarakos, M. Ivanich, B. Boyd and C. Golub, 1988: Operational, Highspeed Interactive Analysis And Display System For Intensity Radar Data Processing. Preprints Fourth International Conference for Interactive Information and Processing Systems for Meteorology, Oceanography, and Hydrology, 79-84.
4. Neumann, C.J., 1971: The Thunderstorm Forecasting System at the Kennedy Space Center. J. Appl. Meteor., 10, 921-936.
5. Watson, A.I., R.L. Holle, R.E. Lopez, R. Otiz and J.R. Nicholson, 1990: Surface Wind Convergence as a Short Term Predictor of Cloud-To-Ground Lightning at Kennedy Space Center. Preprint of Article Submitted to Weather and Forecasting.
6. Christian, H.J., V. Manzur, B.D. Fisher, L.H. Ruhnke, K. Crouch, and R.P. Perala, 1989: The Atlas/Centaur Lightning Strike Incident. J. Geophysical Res., 94, 13,169-13,177.
7. Fisher, B.D., 1989: Effects of Lightning on Operations of Aerospace Vehicles. Presented at AGARD Flight Mechanics Panel Symposium on Flight in Adverse Environmental Conditions. AGARD Paper Number 26.
8. Lennon, C. and L. Maier, 1991: Lightning Mapping System. Unpublished Preprint to the 1991 International Conference On Lightning and Static Electricity, April 16-19, 1991.

**Session 12B, Thursday 3:45**  
**Aerospace Vehicles**  
**Protection of Fuel Systems**  
**Frick, Chairman**

**Basic Studies on Sparks in Composite Carbone Fuel Tanks**  
*by P. Gondot, J. Avenet, S. Larigaldie, G. Hartmann, R. Haug, O. Farish,*  
*and M. Aked*

**No paper available.**



**Protection of Graphite Composite Fuel Tanks From Lightning Strike  
Damage and Fuel Vapor Ignition**  
*by R. Schmidt*

**No paper available.**

# MEASUREMENTS OF SOME PARAMETERS OF THERMAL SPARKS WITH RESPECT TO THEIR ABILITY TO IGNITE AVIATION FUEL/AIR MIXTURES

S J Haigh, C J Hardwick, R E Baldwin Culham Lightning Test and Technology

## 1 ABSTRACT

This report describes a method used to generate thermal sparks for experimental purposes, and methods by which parameters of the sparks such as speed, size and temperature were measured.

Values are given of the range of such parameters within these spark showers.

Titanium sparks were used almost exclusively, since it is particles of this metal which are found to be ejected during simulation tests to CFC joints.

Tests were then carried out in which titanium sparks and spark showers were injected into JP4/(AVTAG F40) mixtures with air. Single large sparks and dense showers of small sparks were found to be capable of causing ignition.

Tests were then repeated using ethylene/air mixtures, which were found to be more easily ignited by thermal sparks than the JP4/air mixtures.

## 2 INTRODUCTION

During a lightning simulation test, joints which carry a high current density may produce showers of 'thermal sparks'. This is particularly true of carbon fibre bolted joints, and questions as to the fuel ignition capabilities of such sparks are clearly important where 'wet-wings' are concerned.

The particular question is whether the testing standards which are now used are valid for the threat of thermal sparks, since such standards evolved by anticipating that the threat was from voltage sparks. In other words, will cameras detect all of those sparks, both voltage and thermal, which are a threat to fuel vapours, and are the defined test mixtures using ethylene or propane more likely to be ignited by such sparks than the 'worst' fuel/air mixture?

There is evidence to stimulate such concern. For example the ignition temperatures quoted for propane (470°C) and ethylene (425°C) are much higher than those of kerosine (210°C) and the higher hydrocarbons such as hexane (230°C), and in this sense the diagnostic gases appear less sensitive than the mixtures they are intended to protect. Although this question extends more directly to "Hot-Spot" ignition, which may be addressed at a later date, it may also affect the mechanism by which thermal sparks ignite fuel vapours. It is thermal spark mechanisms only which are considered in this report.

This report continues the work programme on fuel ignition hazards funded by the Culham Lightning Club, and there has been additional support in this part of the work from the UK Ministry of Defence Procurement Executive.

## 3 THERMAL SPARK GENERATOR (TSG)

Creation of thermal spark showers is carried out by discharging a 80V/10,000µF capacitance into a titanium junction. The experimental arrangement by which these spark showers are produced is shown in Figure 1. The sparking occurs between a spinning titanium rod and a static titanium rod, with the relative motion of the two intended to prevent the junction from welding itself together during the discharge. Only a tiny fraction of the sparks which are produced enter the cell where the fuel vapour is contained, by passing through two narrow collimating slits.

## 4 MEASUREMENT OF SPARK PARAMETERS

### 4.1 Temperature

#### 4.1.1 Measurement

Temperature is an obvious parameter to try to measure, since we would expect a cool particle to present less of an ignition risk than a hot particle

The approach to perform the measurement was based on two colour spectroscopy, whereby the intensity of colours in different parts of the spectrum is compared; in this case bands in the blue/violet and deep red regions of the spectrum separated by a diffraction grating, and incident onto photomultiplier tubes. The system is shown in Figure 2.

Titanium thermal sparks generated light which was collected by the fibres and fed to the colour analyser; both single, large sparks and showers of very many small sparks were subject to measurement. The results showed that there was a consistent ratio of blue/red in the emitted light (Figure 3), rarely varying by more than 10%. This implies a virtually constant temperature for these particles.

Temperature reference points were provided by fusing wires of Nickel (melting pt. 1455°C) and Tungsten (mpt. 3422°C) with current pulses. The results are summarised below.

TABLE 1  
Red/Blue Ratios vs Temperature

	Temperature	Ratio	
Aluminium Sparks	not known	0.11-0.54	(Figure 5)
Titanium Sparks	not known	0.24-0.26	(Figure 3)
Fused Tungsten Filament	(3300-3422°C)	0.26. min	
Fused Nickel Filament	(1400-1455°C)	6.1. min	

It has been assumed here that the particles and the fused wires emit as black bodies, or that their emissivities are in the same ratio at the different colours.

#### 4.1.2 Discussion on Temperature

Temperature estimates derived in this way for titanium particles indicate values in the range 3300-3600°C; the range including calibration errors. The temperature variation measured for different particles or showers is nearer to 150 °C

Titanium has a boiling point of 3422°C, which puts this value as an upper limit on the temperature of the particles, and the measured values are to this. It is possible that the explosive disintegration of the titanium spark occurs because the particle reaches, or slightly exceeds its boiling point, and then begins to 'boil' violently.

Aluminium sparks behaves very differently; they have a colour temperature which exhibits sudden changes and oscillations so that measured values range from 2600->4500 C, well above the aluminium boiling point (Figure 3). This behaviour is probably due to the fact that the particle is boiling, but in a manner which causes jets of burning vapour to be ejected, so that the particle then jets and spins, following a typically erratic path.

For both titanium and aluminium it seems that the particle itself is at or close to boiling point and therefore the same for all sparks of the same metal. Incendivity then depends on the rate at which energy is dumped into the particles track; this was discussed in Reference 1.

## 4.2 Particle Size

### 4.2.1 Measurement

#### 4.2.1.1 Introduction

If the titanium spark particles are of virtually constant temperature then we have a relatively straightforward method of estimating their size, since the amount of light emitted by hot particles of a given material is a function of temperature, emissivity and size. Since temperature is eliminated as a variable the intensity of emitted light becomes a function of size only and proportional to the emitting surface area, if emissivity is constant.

The intensity of the emitted light can be measured in various ways, the best being to look at the signal voltage from a photomultiplier tube: study of the density of photographic images is also useful in providing rough comparisons, especially for comparing photographs of particles of known size with those seen during simulation testing.

#### 4.2.1.2 Calibration

To provide a known reference point particles of known size need to be produced; in this case titanium particles 0.12mm in diameter were produced by fusing a short length of very fine titanium wire with a current pulse. The wire melts and shrinks to form a single burning bead. These 0.12mm diameter sparks burned with such brilliance that they were clearly larger than those generally seen during simulation testing, but they provide a calibration against which other particles can be referenced.

#### 4.2.1.3 Photomultiplier Measurement

These relatively large calibration particles were compared with particles produced in more typical TSG showers by recording the light signal detected by a photomultiplier tube. A few spark showers produced particles whose signal range was typically 1/16-1/80 of the size of the calibration particles. However there were clearly particles even smaller, but as these tended to be emitted in showers with other much larger sparks it was difficult to ascribe a brightness to them.

Since the light emitted is assumed to be proportional to the area of the particle then we can deduce that the diameter of the unknown sparks produced by the TSG during these few showers lie largely in the range of 0.01 to 0.03mm, but with some even smaller particles.

#### 4.2.1.4 Physical Method

It is also possible to collect a small proportion of the sparks in a shower by allowing them to strike an aluminium plate, so that a small proportion weld themselves to it. Size can then be determined with a travelling microscope. Whether a particle sticks to the plate or not may depend on its size, so that it is not a rigorous means of obtaining a population cross-section. 80% of the particles were 0.008-0.02mm in diameter, and <0.1% were greater than 0.1mm dia.

#### 4.2.1.5 Photographic Method

It is useful to be able to look at a photograph of a spark shower and give an estimate of some of the particle sizes involved. Again it is possible to do this by relating the appearance of the 0.12mm diameter 'calibration' particles to those recorded on film by spark showers. It is not completely straightforward because particle speed is also involved, so that a slower particle of the same size as a faster one leaves a denser image track on film. However some of the effects of speed can be overcome using the "streak-camera" described in the next section. In general the larger the sparks the wider and denser is the image recorded on film. Their physical size is far too small to be resolved, so the image size of all particles is effectively determined by factors such as the lens, focussing, and the grain size of the film.

For example, some of the larger sparks seen during the testing of JP4 with spark showers (Section 6) appeared at f/5.6 to be approximately as bright as 0.12mm sparks photographed at f/16. This implies that the sparks seen during testing, which were found to pose an ignition hazard, have a diameter of approximately 0.04mm or greater. More typically the particles appear to be <0.02mm diameter.

#### 4.2.2 Comments on Measured Particle Size

The camera system used to photograph most of the TSG sparks employed a lens set at f/5.6, 400 ASA film and an object distance of 300mm. In terms of sensitivity this makes it roughly equivalent to 3000 ASA f/4.7 system with a field of view of 0.5m at the plane of the object, which is a typical set up during simulation tests. Certainly photographed sparks during these tests vary over roughly the same visibility range as do particles from the TSG, although where large particles occur in real tests they are usually accompanied by such a large bright shower that it is difficult to distinguish individual particles.

During simulation tests where severe sparking occurs, the ensuing pitting may appear to be light. This is a further indication of how little material needs to be ejected to create a large spark shower.

#### 4.3 Speed of the Particles

In this approach a simple 'streak' camera was constructed, by modifying an Olympus OMI camera and fitting a motor, so that film could be wound through the camera at constant speed whilst the shutter was held open. Otherwise the film, camera and lenses were as standard, and of the type used during simulation testing. In photographs taken using this the particle tracks, which are vertical in practice, appear to bend as the particles decelerate. Initially they are moving much faster than the film-to-image "streak velocity" and paths appear straight and nearly vertical; subsequent deceleration causes a bending effect which is visible in Figure 7 and from which the particle speed may be deduced.

In Figure 4 some typical particle paths are plotted, as a function of speed versus time and showing explosive disintegration as "\*" where it occurs.

Those particles represented by a steep slope are decelerating very rapidly, and such particles are faint and generally die rapidly. Particles which have a lower deceleration rate are larger and brighter.

## 5 INCENDIVITY OF THERMAL SPARKS WITH RESPECT TO FUEL/AIR MIXTURES

### 5.1 Introduction

In this part of the report we discuss some less abstract, aspects of the work, looking at whether particular titanium sparks or spark showers are liable to cause ignition to JP4.

For most of these fuel tests sparks showers were generated using the TSG described in Section 3.

### 5.2 Mixing of JP4/Air

Aviation fuels are complex mixtures. Their many constituent components exhibit various degrees of volatility and flamability and the collective product is then not nearly as well behaved or reproducible as a pure gas. For guidance the advice and works of HWG Wyeth (RAE Farnborough) have been greatly appreciated. As Crouch (Reference 2) and others have pointed out, fractional distillation can occur from a liquid fuel, so that for example the drawing off of fuel vapour from a liquid headspace slowly reduces the fraction of volatiles. For these tests therefore the fuel was metered and transferred only in liquid form, and for each test a given volume of liquid fuel was allowed to come into equilibrium with the fixed volume of air in the test cell. The remaining liquid was discarded after each test. To further reduce fractional distillation effects the initial 20 litres of fuel was split into many small volumes so that no volume of fuel was subjected to many repeated exposures to air and loss of its volatile components. An unopened container had an RVP of 20, whilst one which had suffered repeated exposure to the air (more than that to which such a volume would be subjected in practice) had a slightly reduced RVP of 19.

Figure 5 shows the apparatus built to create the equilibrium fuel/air mixture. An air circulator blows air over the surface of the fuel and recirculates it through the test cell, keeping the largely unevaporated liquid isolated from the test cell, and from the risk of ignition.

The system has the advantage that equilibrium is achieved quickly; a gas analysis system within the cell showed that the system reached 90% of its equilibrium richness within 60 seconds for a relatively weak equilibrium mixture. For the tests a standard equilibrating time of 10 minutes was used.

### 5.3 Testing With Voltage Sparks

Initially the fuel/air mixtures were tested by ignition with voltage sparks to establish how the most flammable mixtures were created and also to compare ignition energies with those of Crouch

The method of determining spark energy was essentially that in Reference 3, although corrections were necessary as the breakdown voltage of a fuel/air mixture was higher than that of air.

The determination of ignitability was a little crude. Sparks of a defined energy were applied to the mixtures, 10 over a period of approximately 30 seconds. If an ignition occurred then a (v) was designated, if not a (x) and these symbols are plotted against energy and mixture in Figure 6. The mixture is given as the percentage of the total volume taken up by liquid.

Given the statistical nature of this approach, results agree fairly well with those of Crouch.

### 5.4 Thermal Sparks Generator and Test Set up

This was described earlier and was shown in Figure 1. The collimator was designed not only to limit the sparks to those travelling vertically but also to act as a 'quench' to prevent flame fronts created outside the slit from propagating back into the test cell.

The test procedure was to add the appropriate amount of liquid fuel into the reservoir, seal the apparatus and allow the air circulator to operate for 10 minutes (see Figure 5). Thermal spark showers were then injected into the mixture which was at the same time filmed using the "streak camera". Two useful film speeds were available, these provided an effective speed of the field of view of 1.8 or 4.5m/second relative to the camera. At the faster speed only 2 or 3 events could be captured on 36 exposure film, so there were time and cost penalties here and most shots are carried out at 1.8m/second. Frequent remixing of the vapour, changing of films and tuning of the TSG meant that the programme did not permit a large number of shots to be made.

## 6 RESULTS

The results of the programme are assessed by looking at the streak camera results for each of the fuel mixture tests, and identifying differences between those showers which did, or did not, cause ignition. Mixtures covered the range .22% to 1.1%, and in all over 80 spark showers of notable size were discharged. The 13 ignitions which did occur have been split into three classes as follows, and examples of each are shown in Figure 7:

### 6.1 Ignition by a Single Large Particle

This event was observed with certainty four times:

- a) by a massive (~0.1mm dia) particle igniting a .35% mixture.
- b) twice by a smaller, but still relatively large particle (~0.04mm) to a .4% mixture.
- c) once by a large spark of undefined size (recorded on video) to a .4% mixture.

In all these cases ignition occurred when the particle was travelling relatively slowly (< 1 metre/sec), and on two occasions this was because the particle had struck a wall.

### 6.2 Ignition by a Dense Shower of Particles

There were several occasions where ignition occurred during a shower in which no particularly large sparks were present, but in which there was a shower of perhaps 15-25 particles, with high local spark density.

- This occurred:
- a) Twice to a .31% mixture.
  - b) Twice to a .40% mixture.

Dense showers were a fairly frequent occurrence during the tests to all the mixtures, but did not always cause ignition. It was difficult to see why one shower ignited, whereas another equal or even apparently larger shower, did not.

### 6.3 Spurious Ignitions of Unattributed Cause

The remaining ignitions were curious in that they occurred without any apparent cause, although always a short time after a spark shower had occurred.

One of the possible causes is that ignition occurred within the volume between the collimating slits, so that an ignition developed within this space, and propagate through the narrow exit slit, failing to quench. Alternatively a single large particle might have stopped at or just above the slit exit and caused ignition, since there is 1mm above the slit which is blind to the camera.

### 6.4 Large Sparks and Spark Showers which did not cause Ignition

No ignitions whatsoever occurred in the 15 showers generated into .55%, .62% and 1.1% mixtures. Other large particles and showers which appeared similar to those which caused ignition, did not cause ignition. A well defined pattern is therefore difficult to establish; but Table 2 summarises the results.

TABLE 2

FUEL %	
.22	XXXXXXXX
.31	XXXXXXXX
.31	XXXXXXXXSS
.35	XXXXXX?L
.40	X ? S
.40	S
.40	XXXXXXXX??LL
.43	X X X ? ?
.55	X X X X X X
.62	XXXXXXXXXX
1.1	XXXXXXXXXX

Summary of the ignitions which occurred to JP4/Air mixtures.  
 S= Spark Shower initiation  
 L= Large single spark initiation  
 ?= Undefined initiation type  
 X= Sparks/Shower not igniting

## 7 IGNITION OF ETHYLENE BY THERMAL SPARKS

The exercise of injecting spark showers of the type used for JP4 is repeated here for ethylene to attempt a correlation of their ignitabilities by thermal sparks. It has previously been noted that ethylene is far more sensitive than fuel in detecting voltage sparks (References 2 and 3).

Because it was anticipated from this that the ethylene had greater sensitivity, the size of the slot was reduced to 3 small holes less than 0.5mm in diameter, to improve the quenching performance of the slit, and to reduce the number of particles entering the cell as well as the width of the showers.

Eleven showers of relatively small sparks were produced, of which 2 caused ignition. One was caused by a single particle igniting the gas the second was caused by a group of particles.

### 7.1 Discussion

The spark showers and particles which ignited ethylene/air are smaller than those required to ignite JP4/air although it is difficult to be quantitative. The single particle which ignited the ethylene/air mixture is perhaps  $\frac{1}{2}$  -  $\frac{1}{3}$ rd the diameter of the smallest single spark which ignited a JP4/air mixture, simply on the basis of visual assessment of image density.

However spark showers which do not ignite the mixture are clearly visible on film suggesting that cameras are a more sensitive technique - so long as the source of sparks can be anticipated, viewed and sharp focus achieved.

## 8 CONCLUSIONS

Temperature of aluminium and titanium thermal sparks appears to be close to the boiling point of the metals, and for aluminium jetting of vapour appears to occur from the spark.

A thermal spark generator has been built to produce showers of thermal sparks from a current carrying contact; such particles are found to be emitted at speeds of at least a few tens of metres per second, decelerating rapidly to perhaps only a few metres per second before disintegrating. Smaller particles are generated faster and last for a shorter time.

Size of the particles produced is commonly the range 0.005mm diameter to 0.05mm diameter.

A JP4/air mixture is created by recirculating the air headspace rapidly over a metered fuel reservoir to achieve equilibrium. Approximate minimum ignition energies are slightly less than those quoted by Crouch.

Ignition of fuel mixture can occur from the titanium thermal spark showers; either by large, slow single sparks estimated to be  $\geq 0.04$ mm in diameter, or by a dense showers of smaller sparks.

Ethylene appears to be more easily ignited by thermal sparks than is JP4.

For detecting thermal sparks the defined photographic techniques are more sensitive than gas testing using ethylene (and much more sensitive than using fuel), but only so long as observed sparks can be guaranteed to be in focus.

## 9 REFERENCES

1. Haigh, Hardwick, Baldwin. Fuel Ignition Hazards from Thermal Sparks ICOLSE 1989. Bath, U.K.
2. Crouch Minimum Ignition levels of aircraft fuel constituents to lightning related ignition sources. ICOLSE 1986. Dayton.
3. Haigh, Baldwin, Banks. The detectability of voltage sparks by flammable gas and optical techniques. ICOLSE 1988. Oklahoma City.

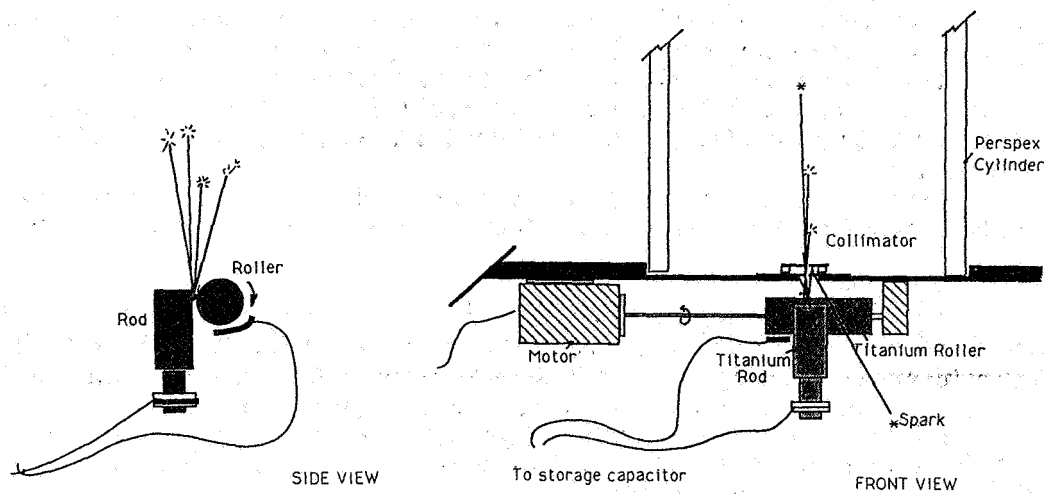


FIGURE 1  
Generation of Titanium Thermal Sparks

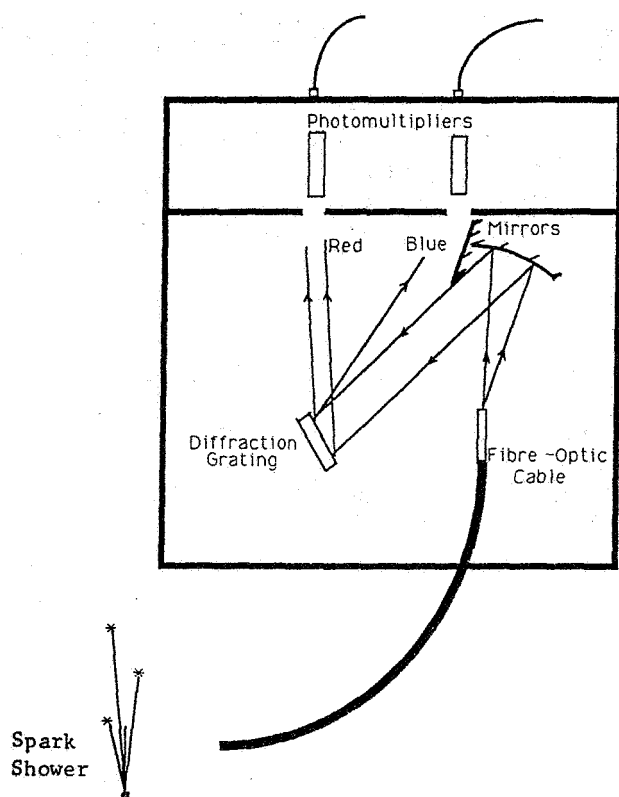


FIGURE 2  
Measurement of Spark Temperature



# TITANIUM SPARK SHOWER

# ALUMINIUM SPARK SHOWER

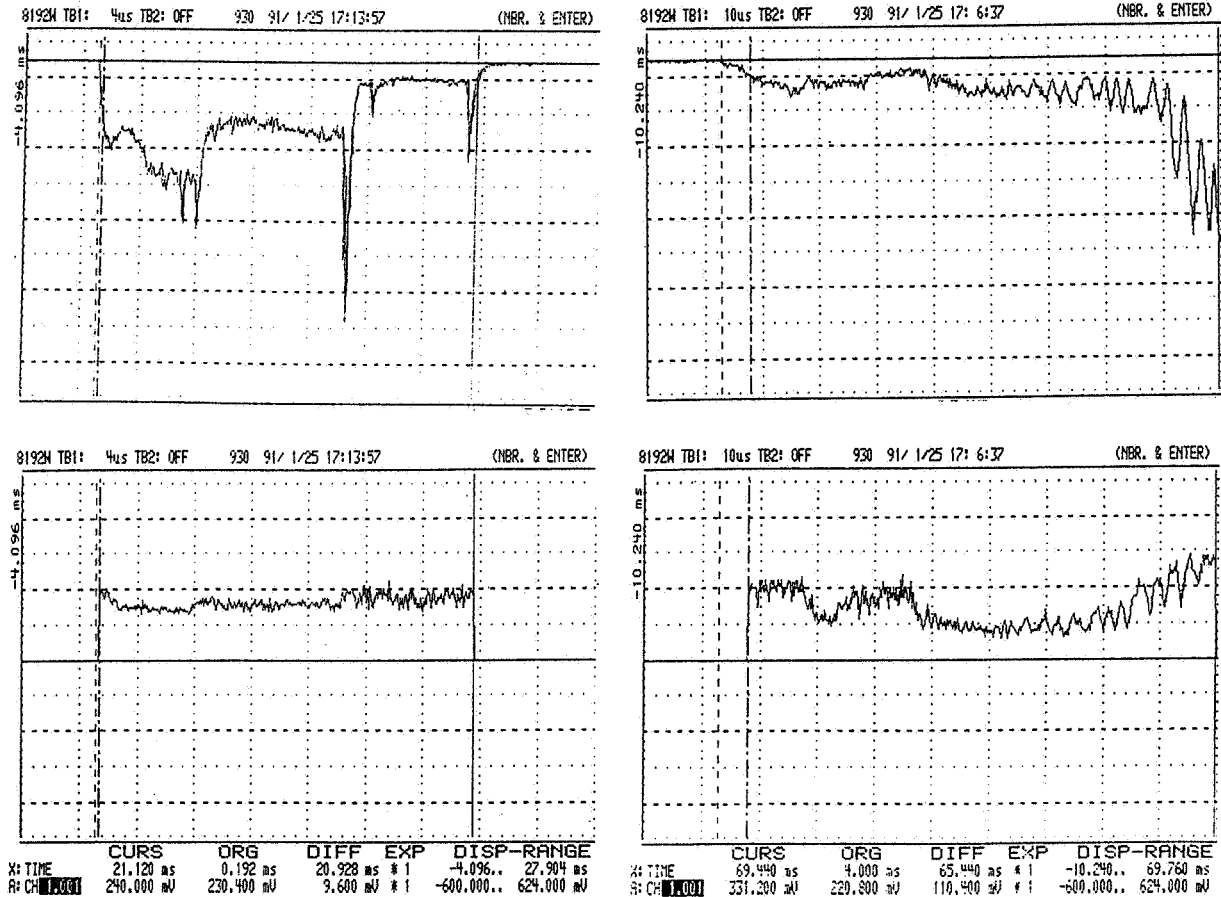


FIGURE 3

Recorded signals during the measurements of spark temperature

Upper Trace: Red Colour Signal (-ve going)

Lower Trace: Red/Blue Ratio (+ve going)

Left hand traces are for a Titanium spark shower, right hand for Aluminium.

**FIGURE 4**  
Decay of spark particle speed with time

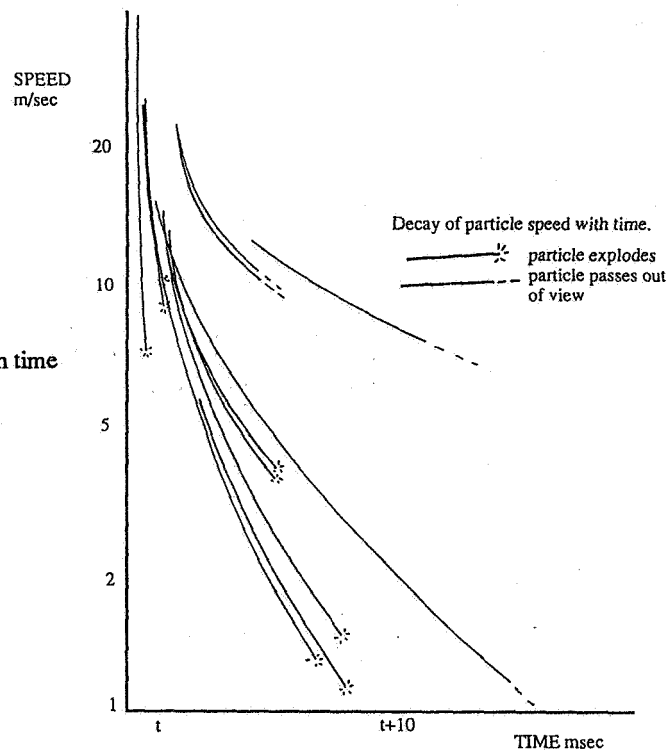


**FIGURE 5**  
Generation of Fuel/Air Mixture

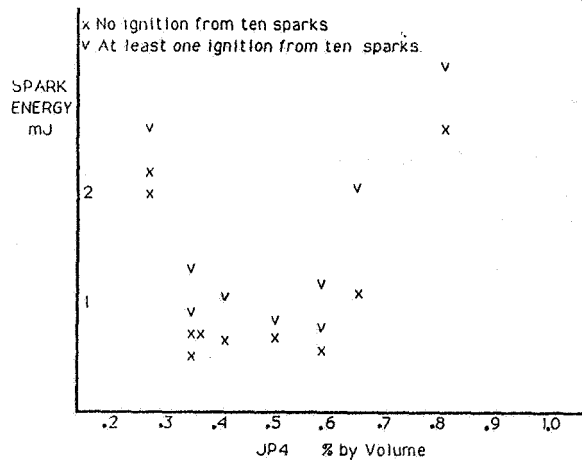
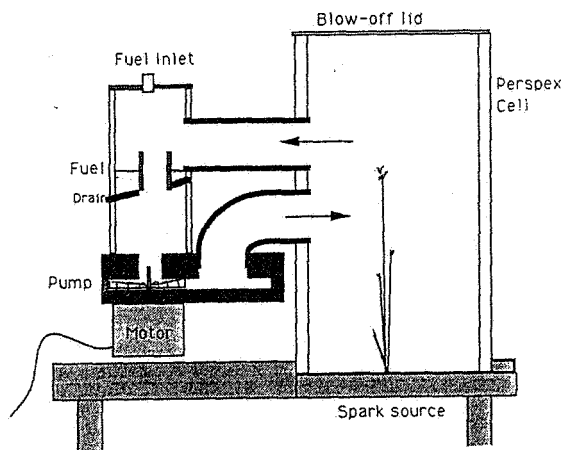


**FIGURE 6**  
Ignition of JP4/Air mixtures of various concentrations by low energy voltage sparks.

ORIGINAL PAGE  
BLACK AND WHITE PHOTOGRAPH

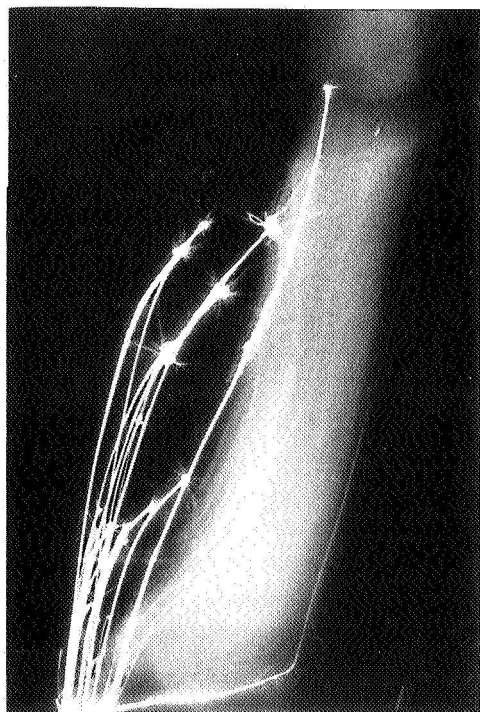


FIGURE 7

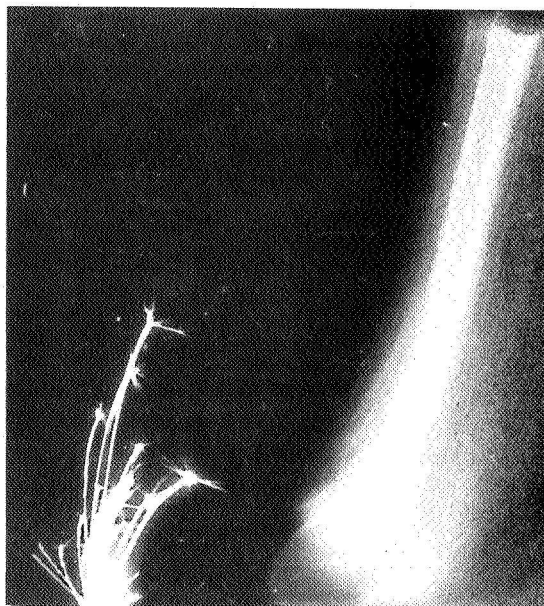
Three typical ignition sequences recorded by the Streak Camera. (JP4 Fuel)

The events are photographed through a wide slit, and the field of view appears as if it is moving rapidly from right to left. Ignited gas regions appear as a fairly uniform glow.

TOP LEFT: Ignition by a single large particle.  
LOWER LEFT: Ignition by a dense local shower.  
LOWER RIGHT: A "spurious" ignition.



0.1  
m  
Scale  
0



**Session 13A, Friday 8:00**  
**Lightning Mapping Systems 2**  
**Mazur, Chairman**

# THE EFFECT OF THE EARTH'S OBLATE SPHEROID SHAPE ON THE ACCURACY OF A TIME-OF-ARRIVAL LIGHTNING GROUND STRIKE LOCATING SYSTEM

Paul W. Casper, PE and Rodney B. Bent, Ph.D.

Atmospheric Research Systems, Inc.  
2350 Commerce Park Drive, NE, Suite 3  
Palm Bay, Florida 32905  
U.S.A.

## ABSTRACT

The algorithm used in previous technology time-of-arrival lightning mapping systems was based on the assumption that the earth is a perfect spheroid. These systems yield highly-accurate lightning locations, which is their major strength. However, extensive analysis of tower strike data has revealed occasionally significant (one to two kilometers) systematic offset errors which are not explained by the usual error sources. It has been determined that these systematic errors reduce dramatically (in some cases) when the oblate shape of the earth is accounted for. The oblate spheroid correction algorithm and a case example is presented in this paper.

## INTRODUCTION

Lightning ground strike tracking systems based on the time-of-arrival (TOA) technique, in combination with wideband waveform detection have been in operation for almost a decade. The accuracy of these systems has steadily improved as more has been learned about the fine characteristics of timing synchronization signals, propagation effects on lightning waveforms and software processing methods for accuracy enhancement. One of the more recent improvements has been accomplished by refinement of the mathematics to more accurately accommodate the oblate shape of the earth spheroid.

Earlier versions of TOA lightning tracking systems used mathematics based on a spherical approximation of the earth. This is usually not seriously in error, especially if the accurate earth's radius for the region of interest is used in the approximation. However, when accuracies otherwise are approaching a few hundred meters,

it becomes essential to base all mathematics on an extremely accurate earth model.

Tracking systems using terrestrial timing synchronization signals (e.g., LORAN) are doubly affected by the earth's oblate shape. The following section identifies the affected parameters and discusses the methods for improvement. Subsequent sections contain illustrations of the magnitude of each effect.

## MATHEMATICAL PROCEDURE

The oblate shape of the earth spheroid directly affects TOA system accuracy in two ways:

- a. Calculation of time clock offsets due to timing reference signal differential propagation delays
- b. Calculation of lightning stroke coordinates given a set of accurate receiver time differences

Different mathematical processes are involved in each of these steps. Derivation of the equations

is beyond the scope of this paper (consult references [1, 2, 3]), but the methodology for each is described in the following two subsections.

#### CALCULATION OF TIME CLOCK OFFSETS

Receiver sites and a terrestrial timing reference signal transmitter are at fixed locations. Therefore, the clock offsets due to timing signal differential propagation delays need only be calculated one time and stored in the system software. In order to determine these differential offsets, very accurate geodesic distances between the timing transmitter and each LPATS receiver must be first computed. A geodesic is defined as the curve of minimum length between two points on the surface of a spheroid [1].

Geodesic distances can be estimated fairly accurately by using a perfect sphere model of the earth with a radius equivalent to the earth radius at the mean latitude of the network. However, data to be presented in later sections shows that to achieve systematic location errors of less than several hundred meters, the actual shape of the earth must be properly accounted for.

The non-iterative solution by Sodano [1] provides a highly-accurate means of calculating geodesic distances. Sodano developed a system of equations that are easily programmed and solved in double precision using a personal computer equipped with a mathematic co-processor. The input to this set of equations is only the latitude and longitude (accurate to the fourth decimal place) of the two points of interest. Navigation receivers using the satellite-based Global Positioning System are most convenient for determining the coordinates of receivers to the required accuracy.

Once accurate geodesic distances are available, they must be converted to an equivalent propagation time. For this, we need an accurate ground wave propagation velocity figure, applicable for the high-energy frequencies radiated during the first ten microseconds of a lightning ground stroke. A figure for frequencies in the 50 to 300 KHz range is appropriate, such as the 100 KHz

figure provided by the U.S. Coast Guard for the LORAN navigational system. This 100 KHz velocity figure is determined as follows:

$$V' = V/n \quad (1)$$

where:  $V'$  = 100 KHz ground wave velocity

$n$  = index of refraction at the earth's surface for 100 KHz (1.000338)

$V$  = free space velocity (299,792,458 meters/second)

Accurate time clock offsets are then easily calculated:

$$T_{12} = V' (D_1 - D_2) \quad (2)$$

where:  $D_1$  = geodesic distance from receiver 1 to the timing transmitter

$D_2$  = geodesic distance from receiver 2 to the timing transmitter

Equation (2) produces the time offset between clocks in receivers 1 and 2. This figure for each clock pair in the system is stored by the central software and used to correct the time differences actually reported by the receivers.

#### CALCULATION OF STROKE COORDINATES FROM TIME DIFFERENCES

The second part of the problem is computation of the stroke coordinates given accurate input time differences. Razin [2] describes the mathematics for accomplishing this computation for both the spherical earth approximation and for the more exact oblate spheroid case. However, Razin does not present the equations for the oblate case. Fell [3] fills in this void. The full set of equations is quite complex and extensive, and the reader is referred to both Razin and Fell for the details. The computational procedure will be described here to provide general understanding of the process.

The first step in the process is to map the receiver coordinates from the spheroid (earth) onto an osculating sphere, internal to the spheroid, which is tangent to the spheroid at a point  $P_O$ . This tangent point is selected near the center of the receiver network. Figure 1 illustrates this arrangement in two dimensions for clarity. Once all the receiver coordinates ( $P_R$ ) are mapped onto the osculating sphere ( $P'_R$ ), the solution process proceeds as if the earth is a perfect sphere, using the  $P'_R$  set of receiver coordinates. When the stroke coordinates on the osculating sphere are computed ( $P'_S$ ), they are mapped back to the spheroid ( $P_S$ ) using a very simple equation pair.

Note that the osculating sphere receiver coordinates need only be computed one time. They can then be stored as fixed constants in the LPATS central computer software and used with the reported time differences to calculate each stroke's coordinates. The burden on the real time central computer software is substantially unchanged from the all-spherical case.

#### ERROR DUE TO TIME CLOCK OFFSETS

Offsets in the receiver time clocks, because of spherical approximation error in the offset correction constants, can be significant. Here we will examine an actual case to illustrate the point.

The five Florida LPATS network receiver locations are shown in Figure 2, plus the Jupiter, Florida, LORAN transmitter that is used for synchronization. This network has been in operation for several years, and a substantial archive of data has accumulated. In an effort to objectively assess the accuracy of this network, the data base was searched over a complete lightning season in the vicinity of three very tall, attractive objects ("Bithlo towers") to determine if an expected pattern of strikes existed. Each of these towers are over 1,000 feet in height. The location of the three Bithlo towers relative to the network is shown on Figure 2. The pattern of strikes in the vicinity of these towers is shown in Figure 3. Note that there is an unmistakable stroke cluster near each tower, which can only be

actual tower strikes. Although the cluster pattern is identical to the tower pattern, there is an apparent systematic offset to the southwest. After investigation of all the usual sources of systematic error (receiver coordinates, computational error, etc.), it was determined that the error was substantially due to time clock propagation offsets and the spherical approximation stroke coordinate solution mathematics. Here we will examine the error due to time clock offsets and address mathematical error in the next section.

Figure 4 is a blow-up of the area around towers #1 and #2. A 200m x 200m grid has been superimposed to aid in scaling distance. The centroid of the cluster near tower #1 is seen to be approximately 590 meters southwest of the tower. The same is true of the #2 tower and stroke cluster. The circles around the tower indicate the approximate attractive radius of each tower due to its height. It was determined from the data base that receiver triad 1-4-5 was used to locate virtually all the strokes in the Bithlo tower clusters, which is in fact the triad the system should have used since it is the optimum combination (least affected by timing errors for the Bithlo area). We will concentrate on this receiver triad to examine the spherical approximation time clock offset error.

The centroid of the actual tower #1 cluster is shown in Figure 5 (point A). Point B is a theoretical point, computed as follows:

- a. A stroke location at the exact coordinates of the tower was assumed.
- b. The exact propagation times to receivers 1, 4 and 5 were computed using the Sodano method.
- c. The relative stroke time differences seen by each receiver pair were then computed using the propagation times. These time differences should be exactly what the system actually saw, to the extent that it is possible to predict them.

- d. The 100 KHz timing signal propagation times from Jupiter to receivers 1, 4 and 5 were computed in two ways: 1) with spherical approximation mathematics, and 2) with Sodano's oblate spheroid mathematics. Secondary correction factors (due to earth conductivity effects) were added to all times.
- e. Time clock offset errors were computed by taking the differences between the spherical and oblate times by receiver.

Point B in Figure 5 is what results when actual time differences from step "c" are corrupted with the time clock offset errors predicted in step "e". This very closely approximates the operating condition of the system at the time, which was using time clock offset correction constants computed with spherical approximation mathematics. Point B is 405 meters southwest of the tower, short of the actual 590 meters, but certainly explaining the majority of it. Point B was computed with spherical approximation coordinate solution mathematics, exactly the same as the system was using.

We had to include the time clock offset errors determined in step "e" to simulate actual system conditions and calculate point B. We can just as easily remove the errors and observe the change in system accuracy that should result. Point C indicates the solution location with zero time clock offset error, using the step "c" time differences and spherical approximation coordinate solution mathematics. This point is 415 meters northeast of the tower, which is actually a slight degradation in accuracy. However, there remains a second source of error due to inaccurate solution mathematics, which was based on a spherical earth approximation. This error source is examined in the next section.

#### ERROR CAUSED BY SOLUTION MATHEMATICS

As noted at the beginning of Section 2, approximating the earth as a perfect sphere affects not only the accuracy of time clock offset calculations, but also the accuracy of stroke coordinate

computation given receiver time differences. The magnitude of this error contribution is illustrated here.

Refer again to Figure 5. With the time clock offset errors removed, the solution moves from B to C. Point C was calculated using the same solution mathematics as used by the system at the time, which was based on a spherical earth approximation. If we instead use the oblate spheroid mathematics as described previously, point C moves to D, which is only 205 meters from the tower. The net result of removing the time clock offset and improving the mathematical accuracy is a 50 percent reduction of error from 405 meters (point B) to 205 meters (point D).

The residual error of 205 meters is still under investigation but is believed to be due to approximations in the derivation of the oblate mathematics. Further findings will be presented at the conference.

#### DISCUSSION

We have seen that moderate systematic error in the TOA LPATS can arise in two ways from using a spherical earth approximation: 1) determination of time clock offsets, and 2) calculation of stroke coordinates from detected time differences. In the example presented in Section 3, removing time clock offset error resulted in an 820-meter shift in the computed coordinates. In this particular example, the radial position error happened to remain about the same, but this was only a fortuitous result. With a different triad of receivers or a stroke in a different location, it is possible that resulting error could be even larger than the original error as long as spherical solution mathematics is still used. Multiple errors can sometimes combine such that remaining error is larger when one error source is removed. It is important to reiterate that time clock offset error is quite easy to avoid in a system with a terrestrial timing reference signal by using accurate propagation time prediction software that accommodates the oblate earth shape (i.e., the method of Sodano). In systems



that are synchronized by satellite signals, the earth's oblate shape is handled differently, by including in the line-of-site calculations the elevation of the receiver site above sea level combined with the accurate earth radius for the applicable latitude.

The example illustrated that oblate solution mathematics can also provide a substantial systematic error reduction, in this case 50 percent. Even though the oblate mathematics is more complex than spherical mathematics, almost all of the additional complexity is involved in the initial one-time system set-up constant calculations, and there is practically no additional load on the real time LPATS Central Analyzer software.

The accuracy of all lightning ground strike tracking technologies in current use is affected by the earth's oblate shape. It has been shown in this paper that errors in a TOA system, due to approximating the earth as a perfect sphere, can be significant enough to warrant attention, especially when inherent system accuracy is good enough to be limited in large part by this error source.

#### REFERENCES

- [1] O'Conner, J. J., "Transformations Applicable to Missile and Satellite Technology", Technical Memorandum ETV-73-27, Air Force Eastern Test Range, Patrick Air Force Base, Florida, 26 April 1973 (specifically, Appendix F Part A entitled "Sodano's Noniterative Solution of the Inverse Geodetic Problem").
- [2] Razin, S., "Explicit (Noniterative) LORAN Solution", J. of Inst. of Navigation, Vol. 14, No. 3, Fall 1967, pp. 265-269.
- [3] Fell, H., "Comments on LORAN Conversion Algorithm", J. of Inst. of Navigation, Vol. 22, No. 2, Summer 1975, pp. 184-185.

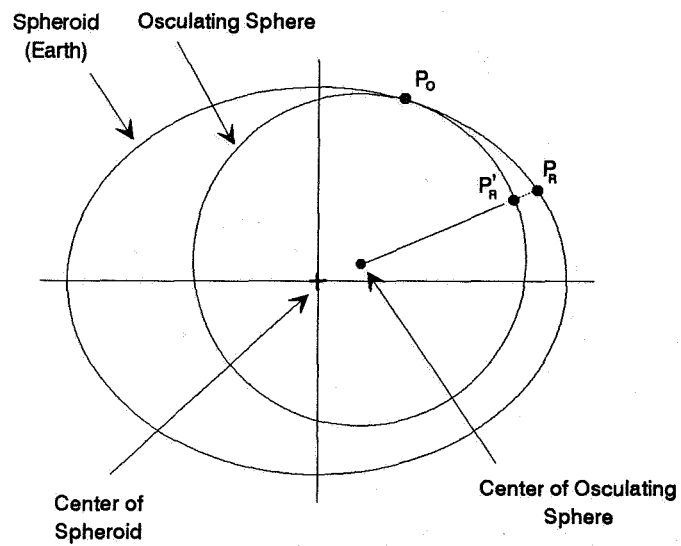


**Figure 1: Mapping a Point  $P_R$  on the Spheroid to a Point  $P'_R$  on an Osculating Sphere.**

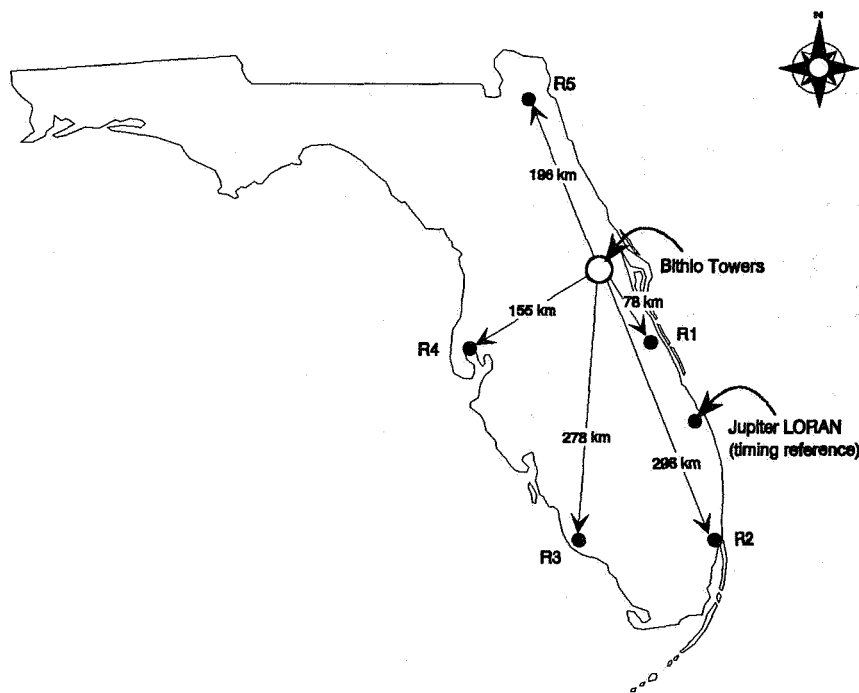


**Figure 2: Florida LPATS Network**

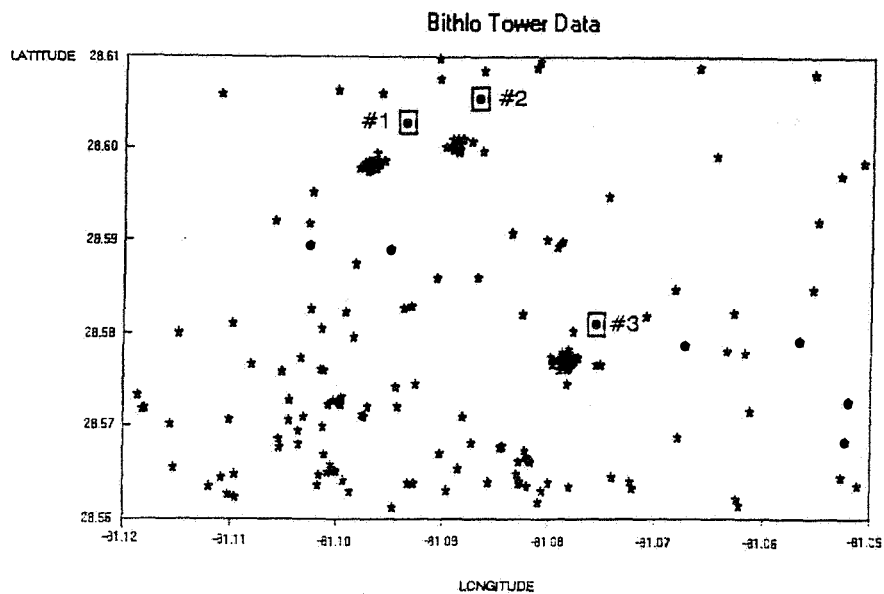
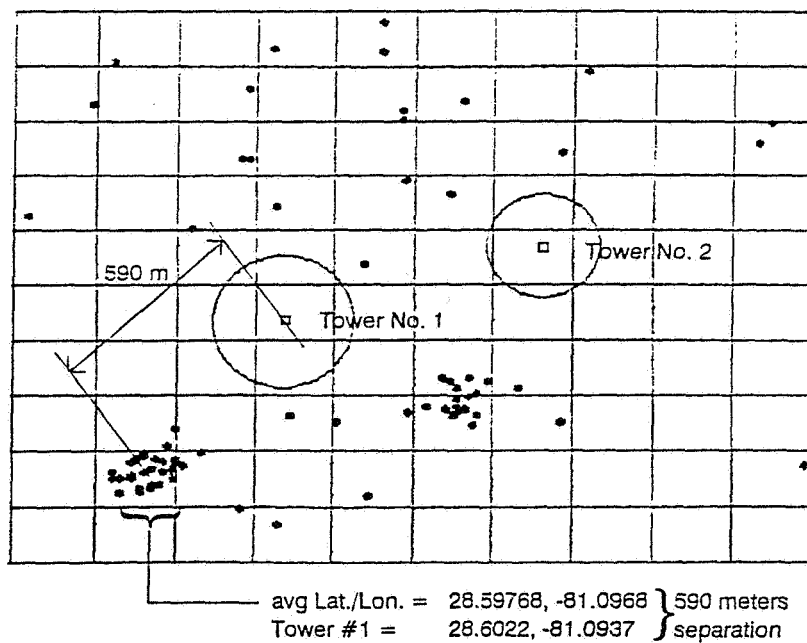


**Figure 3: Bithlo Tower Lightning Strikes**



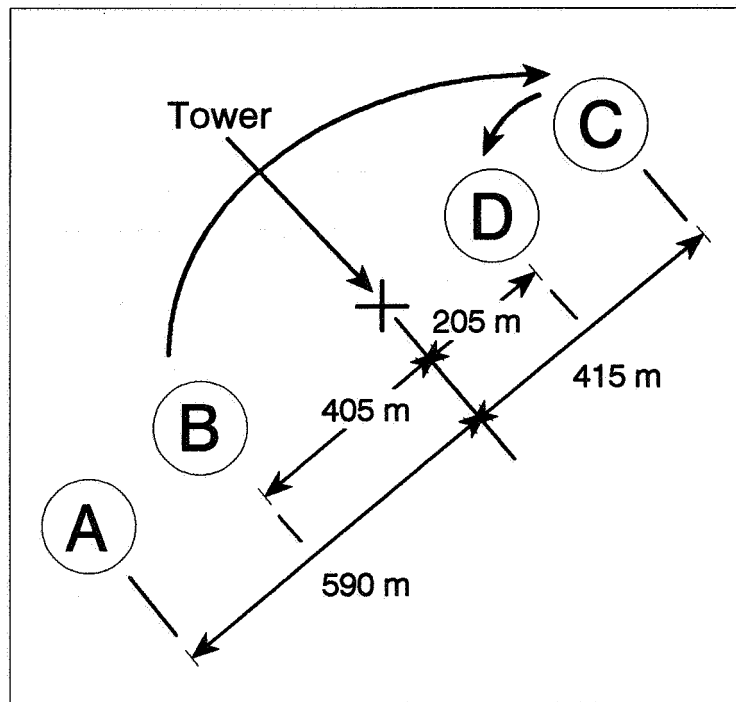
TV Towers No. 1 and No. 2

Center of graph:      Latitude: 28.6034 N  
                                  Longitude: -81.0903 W

Grid size:              2 km x 2 km

Cell size:              200m x 200m

**Figure 4: Strikes to Bithlo Towers #1 & #2**



- A** Centroid of the stroke cluster for tower #1.
- B** Theoretical solution, with predicted timeclock offsets.
- C** Theoretical solution, with timeclock offsets removed.
- D** Theoretical solution, timeclock offsets removed and math error removed.

**Figure 5. Triad 145 Solutions, as Affected by Timeclock Offset**

## EXPERIENCE GAINED IN OPERATION OF THE VLF ATD LIGHTNING LOCATION SYSTEM

Anthony C. L. Lee  
Meteorological Office, Bracknell,  
Berkshire, RG12 2SZ, United Kingdom

### ABSTRACT

The UK Meteorological Office's VLF Arrival Time Difference (ATD) system for long-range location of lightning flashes started automatic international issue of lightning-location products on 17 June 1988. Data from before and after this formal start-date have been carefully scrutinised to judge performance. Techniques for estimating location accuracy include internal consistency and comparisons against other systems. Other areas studied were range (up to several thousand km); detection efficiency, saturation effects in active situations, and communications difficulties (for this redundant system); and spurious fix rate.

Care has been taken to assess the potential of the system, in addition to identifying the operational difficulties of the present implementation.

### INTRODUCTION

The Meteorological Office's Arrival Time Difference (ATD) system for long-range lightning-flash location operates in the very low frequency (VLF) band, where lightning atmospherics ('sferics') at frequencies near 10 kHz propagate within the earth-ionosphere waveguide to great distances [1, 2]. The system has a nominal service area of 40W-40E 30-70N, which exceeds the combined areas of the USA and Canada, although strokes can be usefully located well outside this area at ranges of several thousand kilometres. The bulk of the nominal service area is shown in Fig. 1, and this is serviced by just seven ATD outstations whose eventual deployment is shown.

### OPERATION OF THE ATD SYSTEM

In the ATD system, a single lightning stroke produces sferic waveforms which are received through their vertical electric field, and are band-limited (eventually to 3 dB limits at 8.1, 11.7 kHz) at the unmanned outstations. From each outstation the digitised sferic waveform, together with the instant of time (or epoch) of the first digitisation sample for the waveform, is communicated to the control station. The detailed technique involves each outstation storing all the data that it observes above an analogue threshold, and forwarding selected data on request to the control station.

At the control station one waveform is chosen as a reference, and the other waveforms are each corre-

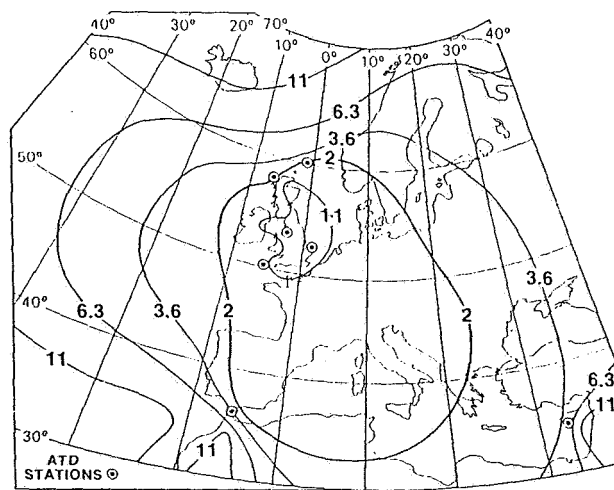


Figure 1: Seven outstations (five UK; Gibraltar, Cyprus) cover the 40W-40E 30-70N service area. Contours of RMS km fix error, for 5  $\mu$ s ATD errors, are superimposed. Smaller ATD errors are realistic, with proportionally reduced fix errors.

lated against this to extract the arrival time difference of the sferics against the reference. Although digitisation samples are spaced at intervals of several microseconds, the sferic waveform is limited to a frequency range well below the Nyquist constraint, so that the underlying continuous waveform is arbitrarily well represented, and each measured arrival time difference value ( $ATD_M$ ) can be estimated with adequate resolution — in this case well below a microsecond.

The most likely lightning stroke location (or 'fix') is estimated by its iterative adjustment to minimise the weighted differences between a set of theoretical arrival time difference values ( $ATD_{TH}$ ) based on the assumed stroke fix, the known outstation receivers' coordinates, a modelled spheric phase velocity, and a spheroidal earth; and the set of measured arrival time difference values ( $ATD_M$ ).

## ESTIMATION OF FIXES, AND FIX ERRORS

The fixing process can be described more formally as the minimisation of  $RESIDUAL^2(\theta, \lambda)$  with respect to the stroke coordinates  $\phi, \lambda$ , where:

$$RESIDUAL^2(\phi, \lambda) = \frac{1}{(m-2)} \times \sum_{r=1}^m \left\{ \frac{ATD_{TH}(r, \phi, \lambda) - ATD_M(r)}{\sigma(r)} \right\}^2 \quad (1)$$

and:

- $m$  = No. of non-reference outstations (No. of  $ATD$  values).
- $r$  = Index of non-reference outstations.
- $ATD_{TH}$  = Theoretical  $ATD$  value.
- $ATD_M$  = Measured  $ATD$  value.
- $\phi$  = estimated stroke latitude.
- $\lambda$  = estimated stroke longitude.
- $\sigma(r)$  =  $ATD$  standard deviation for non-reference outstation.

The normalising factor  $(m-2)$  accounts for the number of degrees of freedom (DOF) involved in fixing, so that with correct  $\sigma(r)$  values the expectation for the minimum value of  $RESIDUAL$  is unity. This can be used to form the basis of a technique for estimating the root mean square (RMS) values of  $\sigma(r)$  provided some relation is assumed between them (eg. they are equal), and provided that measurements are averaged over many strokes.

Once the  $ATD$  standard deviations  $\sigma(r)$  are known, they can be used to predict charts of absolute fix accuracy. Fig. 1 shows fix error (RMS km) of the eventual  $ATD$  outstation deployment over most of the service area under the assumption that  $\sigma(r) = 5 \mu s$ , and that all seven outstations are involved in every fix.

In practice there may be bias in the differences between theoretical and measured  $ATD$  values, due to errors in the algorithms converting local timescale

values to International Atomic Time ('timescale errors'), and modelling spheric velocities ('propagation errors'). Lee [3] extends the above argument by considering many strokes occurring within a short time-period (timing errors are constant) and within a fairly small geographical region (propagation errors are constant), so that any systematic bias offsets will be constant, and may be estimated as degrees of freedom along with the stroke locations.

If this is done, the remaining  $ATD$  standard deviation  $\sigma(r)$  will be reduced from values representative of absolute fix error to a measure of the the irreducible  $ATD$  scatter remaining after bias removal. In this case the charts of fix 'error' for bias-reduced  $\sigma(r)$  will correspond to charts of scatter in the fixing process. This information is important as it represents the limiting  $ATD$  system performance if bias errors can be adequately alleviated.

## ABSOLUTE AND RELATIVE FIX ERRORS FROM INTERNAL EVIDENCE

### TRIALS RESULTS

Initial indications come from 1978-9 trial results, with just four experimental outstations — three in the UK and one in Gibraltar [1].

In winter conditions lightning tends to occur in isolated clusters, mainly over the ocean:

- On one occasion, of 41 Mediterranean flashes no fewer than 17 occurred in groups of 1.7-10.7 km diameter — in spite of the 1000-2600 km range to most outstations.

This is likely to be an over-estimate of fixing scatter, as the observed scatter must include the physical separation of the observed strokes.

Absolute  $ATD$  system errors were estimated from  $\sigma(r)$  from the trial data:

- Over the entire trial,  $\sigma(r)$  values for absolute errors (no biases removed) were found to fall within the range 3.3-10.9  $\mu s$  — with the larger values associated with minor equipment failures.
- The more representative lower value is smaller than the 5  $\mu s$  used in Fig. 1.

With full operational outstation deployment, Fig. 1 suggests  $\sigma(r) = 5 \mu s$  gives 1.5-2 km fix errors in the Mediterranean. However, the more restricted trial outstation deployment degrades predicted absolute fix errors to 7-12 km. As expected, this is somewhat larger than the apparent fixing scatter, but not to such an extent that these results are inconsistent.

Table I. Pre-Operational Results for daytime strokes over southern UK [3].

Date:	Jul 29, 1987	Sep 05, 1987
GMT:	1500–1511	1430–1900
Strokes:	41	275
Absolute $\sigma(r)$ :	6.5 $\mu$ s	—
Abs. Fix Error:	3 km	—
Relative $\sigma(r)$ :	1.6 $\mu$ s	1.3 $\mu$ s
DOF:	47	365
Scatter :	700 m	630 m

A trial case [4] involved a tight group of intense sferics apparently associated with an organised storm near 45N 3E on the Massif Centrale in France. ATD variance over several strokes indicated an absolute fix error of around 5 km in this region. The RMS spatial scatter of this group was 1.1 km, but it appeared to travel consistently with local winds:

- If a uniform velocity fitted to this data is subtracted, the best estimate RMS Lagrangian spatial scatter (taking correct account of lost DOF) is reduced to 0.5–0.6 km.

However, as this group contained only 3–5 flashes, all that can be said with reasonable (90%) confidence is that the fix scatter was representative of a population scatter that fell within 2.5 km RMS.

No attempt was made to eliminate bias from small regions of trial data, because data rates were too low to produce results at high confidence level.

### PRE-OPERATIONAL SYSTEM RESULTS

During its pre-operational phase, the five UK outstations of the non-experimental ATD system were installed, and the system tested with frequent re-booting of sub-systems and other experimental activities. Routine sanitisation activities such as spectral calibration were not carried out, and minimum attention was paid to epoch calibration. In spite of this, the data were amenable [3] to determination of bias-removed  $\sigma(r)$  because such systematic offsets are eliminated; results are presented in Table I.

NAVSTAR Epoch calibration was carried out at all outstations shortly before the Jul 29 case, so local outstation timescales were well established:

- During 1500–1511 GMT 41 strokes were received in the southern UK. Their analysis (during which offsets were set to zero, implying no bias corrections) yielded  $\sigma(r) = 6.5 \mu$ s.

If all five outstations contributed to each fix in the southern UK region with  $\sigma(r) = 6.5 \mu$ s, then

fix errors would have been 3 km. A comparison was made [3] with 5 km radar rainfall data, and close agreement was found between sferic fixes and isolated squares of intense rainfall, although it is known that peak rainfall and lightning are not precisely co-incident.

Allowing fitted offsets to eliminate bias effects reduced  $\sigma(r)$  to its (relative or scatter) error of 1.6  $\mu$ s, giving a fix scatter of 700 m. Such small scatter levels are physically realistic [5]. Clearly, there was substantial bias in the absolute fix error — perhaps due to propagation effects.

A similar exercise was carried out on a much greater data set from Sep 05 (Table I). This data occurred 38 days later, after power re-starts and operator re-establishment of epoch using Loran-C data only. The offsets were different between the two dates, and gave clear evidence that relative to the Beaufort Park epoch, other outstations had been shifted by 10, 20 or 30  $\mu$ s ( $\pm 1 \mu$ s) because of the 10  $\mu$ s cycle ambiguity of Loran-C.

- Any system which relies only on Loran-C timing can suffer ambiguities of multiples of 10  $\mu$ s if no steps are taken to remove the problem. In the ATD system the problem can be identified and removed using the techniques presented here, or by using Omega reception facilities.

For this reason the absolute  $\sigma(r)$  values were larger, and are not considered here.

Bias elimination reduced  $\sigma(r)$  to a similar 1.3  $\mu$ s, and a scatter of 630 m for five-station fixing.

### EARLY OPERATIONAL DATA

The Gibraltar and Cyprus outstations were subsequently deployed to the operational configuration, although communications initially proved troublesome, limiting data availability.

With long-baseline deployment, interest lies in whether the effects of long-range propagation degrade  $\sigma(r)$ . The most stable VLF propagation occurs around local mid-day over the path, and data were found for 1000–1200 GMT on Dec 04, 1987 covering three distinct groups of strokes (first four columns of Table II) located west of Portugal (group A), 1200 km east of Atlantic City (group B), and 1000 km west of Sierra Leone (group C).

Analysis results allowing offsets to eliminate bias are presented. The three  $\sigma(r)$  values were  $\sim 30\%$  larger than the UK-stroke values at 1.91, 1.75, 1.80  $\mu$ s respectively. The associated (relative) fix scatter based on seven outstations (6 for C, as no sferics were received at Cyprus) are 1.3, 7.3, and 7.3 km — small values in spite of the great ranges involved.

Table II. Analysis of three mid-day groups of strokes for Dec 4, 1987. These are analysed to find Relative  $\sigma(r)$  separately; and also as a single composite group with fitted phase velocities [3].

Group:	A	B	C	A+B+C
Location:	W of Portugal	1200 km E Atlantic City	1000 km W Sierra Leone	—
Lat, Long:	38.3N, 11.6W	40.3N, 61.1W	8.2N, 21.1W	—
Strokes:	34	48	48	130
Rel. $\sigma(r)$ :	1.91 $\mu$ s	1.75 $\mu$ s	1.80 $\mu$ s	3.30 $\mu$ s
DOF:	88	140	170	394
Scatter:	1.3 km	7.3 km	7.3 km (6-station)	—

The three groups were composited, using a single set of offsets, to see how the wide geographical area would further degrade  $\sigma(r)$ . The sferic paths lay over regions of quite different surface conductivity, including sea, normal land, and the Sahara desert — so phase velocities would be different. To make a crude allowance for this, different phase velocities were used for groups A, B; and two phase velocities were used for group C, depending on whether the path lay over land/sea or desert. The phase velocities were fitted as part of the overall minimisation process — and a further four degrees of freedom were subtracted to give consistent statistics.

The fitted sferic phase velocities were reasonably consistent with theoretical values. Scatter results are shown in the last column of Table II. A rather larger  $\sigma(r)$  of 3.30  $\mu$ s is produced, highlighting the crudity of the model phase velocity used. Nevertheless, this degree of timing scatter is considerably smaller than experienced as absolute timing errors — demonstrating that bias reduction can be effective even with geographically coarse propagation information.

During the previous evening (Dec 03) 49 strokes were observed to the far south-west of the service area, during a twilight and night-time path: results are presented [3] in Table III. Biases were eliminated by fitting offsets, but when all strokes were composited the extended range and variation in twilight conditions produced a large scatter of 11.9  $\mu$ s. Breaking the data into more limited geographical and temporal ranges (but still retaining useful numbers of degrees of freedom) gave  $\sigma(r)$  values of 1.3–2.0  $\mu$ s, except for one result of 6.1  $\mu$ s where it is likely that rapid twilight changes were taking place.

#### CONCLUSIONS FROM INTERNAL EVIDENCE

From the above discussion conclusions are:

- If no allowance for bias is made then  $\sigma(r)$  estimates for absolute stroke locations are obtained. Values vary with details such as operator errors in setting timescales etc., but under correct operating conditions values of 3–7  $\mu$ s are found.

Table III. Analysis of long-range night-time Caribbean and tropical Atlantic clusters for Dec 03, 1987 [3]. Offsets were fitted to eliminate bias.

Group	GMT	Lat/Long	DOF	$\sigma(r)$ ( $\mu$ s)
All	1900–2230	—	157	11.9
D	1925–2044	10.8N, 44.7W	21	1.3
E	2129–2214	11.1N, 39.4W	5	2.0
F	1906–2045	11.0N, 76.5W	18	6.1
G	2051–2214	11.5N, 74.4W	32	1.8
H	1909–2227	14.4N, 79.0W	46	2.0

- If suitable offsets can be found or predicted, then  $\sigma(r)$  values associated with relative locations (or scatter) of around 1.4–2.0  $\mu$ s can be obtained, even under twilight conditions.
- Twilight conditions will be the most difficult to predict because conditions change rapidly.
- Absolute fix errors, or scatter in fixing, are calculated by scaling charts like Fig. 1.

#### CURRENT ATD SYSTEM PROBLEMS

##### CYCLE MIS-MATCHING IN ATD EXTRACTION

Sferics travelling in the earth-ionosphere waveguide have a phase velocity which varies with frequency and path, associated with a group-velocity less than the phase velocity. Thus sferic waveforms change with propagation, and have a slightly different shape when received at each outstation.

This distortion may modify waveforms differentially to the point where the correlation peak used for ATD-extraction is highest for a mis-matched cycle — and an ATD value an approximate multiple of 100  $\mu$ s (one carrier period) in error is obtained. This situation is usually associated with two similar-height peaks in the correlation, so that a warning



of possible mis-match is obtained. In the present system the  $\sigma(r)$  for that particular stroke and non-reference outstation is set to 100  $\mu\text{s}$ . This is usually large enough to down-weight this *ATD* to the point where it plays little part in subsequent fixing.

Early experience demonstrated that this 'fail-safe' approach produced unacceptable data-loss. The problem could be bypassed by correcting waveforms to some intermediate range using an initial fix and a spectral propagation model. This has not been done, but a partial solution has been implemented by fitting a group velocity to experimental data, and using this to correct the envelope position of sferic waveforms to match the phase velocity.

Nevertheless, where the outstation complement is reduced and cycle mis-matching occurs, the result can be data-loss; or if the error is not detected, a poor fix.

Current alleviation of cycle mis-match wastes data. The quantity  $\sigma(r)$  represents a conceptual Gaussian distribution of error. Recognition of a cycle-slip does not imply a Gaussian error distribution of width 100  $\mu\text{s}$ ; rather the Gaussian error distribution remains at the normal level, but there is a high probability of a catastrophic jump. Alternative *ATD* values are easily found from alternative correlation peaks, and the 'correct' value may be identified by examination of *RESIDUAL*. By this means the outstation data associated with the cycle-slippage is not lost, can take part in the fixing to provide redundant data (and hence maintain accuracy), and maintains redundancy for assessment of 'wrong cycles'.

The discrimination of this process depends on the ability to detect 100  $\mu\text{s}$  *ATD* errors, flagged by unlikely values of *RESIDUAL*; and its sensitivity depends on the value of  $\sigma(r)$ . In practice, under current arrangements  $\sigma(r)$  is not monitored by any on-line or off-line process, but is assigned by an operator. The value used is generally around 13  $\mu\text{s}$  (rather than 3–7  $\mu\text{s}$ ), largely because of the perceived probability of an operator setting local timescales to an incorrect Loran-C zero-crossing! Unfortunately this is something of a self-fulfilling prophecy, because with such a large  $\sigma(r)$  value any such incorrect operator settings are not highlighted by consistently significant values of *RESIDUAL*. Reduction of  $\sigma(r)$  by bias-reduction techniques would sharpen discrimination.

#### COMMUNICATIONS PROBLEMS

Communications between outstations and control station is currently through dedicated low-speed (110 bits  $\text{s}^{-1}$ ) telegraph lines. All are subject to surprisingly frequent outages, and if immediate reporting action is not taken (implying manpower-intensive

monitoring) outages may become prolonged. This reduces outstation availability. The lines suffer higher bit-error rates than that for which the error-correction protocols were designed, causing some communications congestion.

For the UK outstations greater availability may be obtained by the redundancy and lower error-rate inherent in a properly maintained digital packet switched network, such as the Meteorological Office Weather Information System; and such systems may carry their own transparent fault detection and reporting systems. The variable packet-switched delays need not be a problem in this system.

The worst communications problems exist on the two overseas stations. This is unfortunate as the cramped deployment of UK outstations makes the overseas stations crucial to long-range fixing. Cyprus suffers particular problems as it is a low-priority shared line, which on frequent occasions becomes unavailable. Loss of Cyprus data degrades long-range performance to such an extent that there may well be a false economy in shared use. An earlier shared link to Gibraltar has now been replaced by an exclusive line.

If outstation spatial deployment were more uniform, alternative (possibly additional) communications through techniques such as meteorscatter could extend the packet network; the extra redundancy would improve channel availability and automatic monitoring.

The burden of monitoring communications lines and reporting outages is currently borne by the control station operators, mandating their presence. Line-fault detection must become more automated, with automatic reporting of outage to the permanently manned Meteorological Office communications desk for remedial action.

#### ISOLATED OUTSTATIONS

Current outstation deployment has most outstations cramped within the UK, with two isolated overseas stations, making fix accuracy crucially dependent on overseas outstations. Fig. 2 shows location error for 5  $\mu\text{s}$  *ATD* errors using just five UK outstations in their current deployment (with the 'Aughton' outstation at the unfavourable Beaufort Park location). The 2 km fix error that existed over much of the Mediterranean is degraded to around 40–80 km, although degradation is less dramatic near the UK.

Long base-lines reduce fix error, but strokes observed by UK outstations may appear weak at the overseas outstations. Because of their low latitudes the Cyprus and Gibraltar outstations suffer reception of frequent sferics from intense tropical storms,

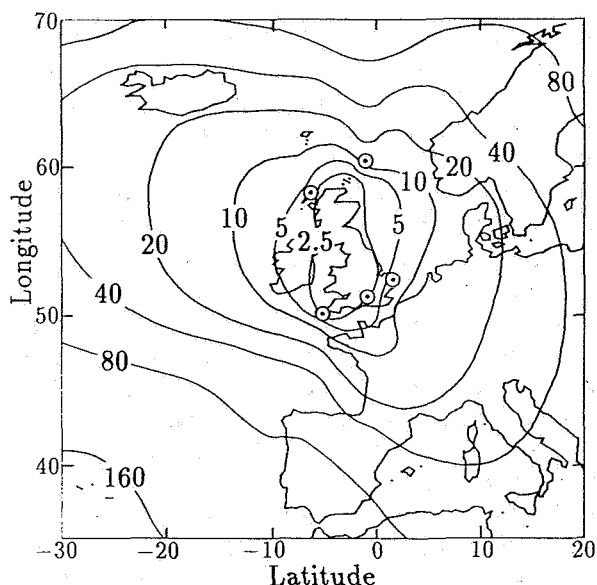


Figure 2: As Fig. 1, for five UK outstations in their current deployment. The 'Aughton' outstation is currently located at Beaufort Park.

which may prevent reception of the 'wanted' weak sferics. In particular, strokes to the north of the UK may not be received at either overseas outstation; and strokes in the western Atlantic will often not be received at Cyprus. This problem, added to communications outage, reduces overseas outstations availability — with a disproportionate effect on fix error.

If some UK outstations were re-deployed into Europe or Scandinavia, the Gibraltar and Cyprus outstations would become less critical. Re-deployment of the Cyprus outstation further north onto the European mainland could well improve communications and selected sferic reception, without significantly degrading seven-outstation performance in the southern limits of the service area.

#### RECEIVER RESOURCE SATURATION

The ATD technique is useable at high data rates and detection efficiencies, but the present system was engineered as an economic replacement for the much slower manual CRDF system.

The current ATD system is limited mainly by control-station processing capability to 400 strokes  $\text{h}^{-1}$ , averaged over several minutes, although this could be cheaply upgraded. A 'clean' 110 bits  $\text{s}^{-1}$  communications capacity would become saturated at around 3–6 times this data rate. Resources are limited, so the system is designed to make a semi-randomised selection from all available sferics (including weaker ones) using an outstation analogue

threshold, and an adjustable 'dead-time' imposed on the control station after sferic selection [2].

Outstation receivers have two independent gain-settings. One (adjusted by the control station) determines gain between antenna and digitiser circuits, and should be set so that sferics from strokes at 'appropriate' ranges do not saturate the electronics (special circuits 'tag' near-overload and overloaded signals). The other adjusts the threshold above which electric-field waveforms are judged sufficiently 'sferic-like' for their processed signals to be stored — awaiting requests for forwarding from the control station. The latter is adjusted locally to control the volume of data temporarily stored in outstation random access memory (RAM). The control station directly adjusts the 'selector' outstation threshold to adapt control station fixing rates to 400 strokes  $\text{h}^{-1}$ ; thus system detection efficiency is a function of activity [2].

However, an operational practice has crept in whereby control station operators attempt to acquire 'all' sferics from UK strokes (a user ideal) by setting the antenna-to-digitiser gains, and dead-time, to minimum. This causes problems when storms occur near an outstation; because local activity rapidly fills up outstation buffer RAM, raising the threshold, and making the outstation less sensitive — and therefore unavailable to sferics from more distant strokes. The problem is compounded if the control station attempts to fix strokes closely spaced in time (ie. with short dead-time) as the RAM buffer is emptied slowly.

In practice locally-generated data are 'distorted' by unusually short ranges, and so are of little use for ATD-extraction. Increasing the antenna-to-digitiser gain to levels appropriate to sferics from more 'normal' ranges will cause most abnormally short-range sferics to overload — and be tagged as such. Overloaded waveforms are currently not reported to the control station; an outstation software modification would ensure that they were discarded without occupying RAM space, while expending minimal outstation resources. This would break the cycle of RAM congestion from local activity, prevent threshold raising, and allow the outstation to continue reporting sferics from distant ranges provided they are not actually masked by simultaneous local activity.

#### AMBIGUOUS FIXES

Atkinson et al. [6] highlighted the possibility of ambiguous four-station fixes: a potential problem for both ATD and Time of Arrival (TOA) systems [7], although soluble by appropriate outstation deployment. A 'flat-earth' discussion is presented below.

If two intersecting lines can be drawn through

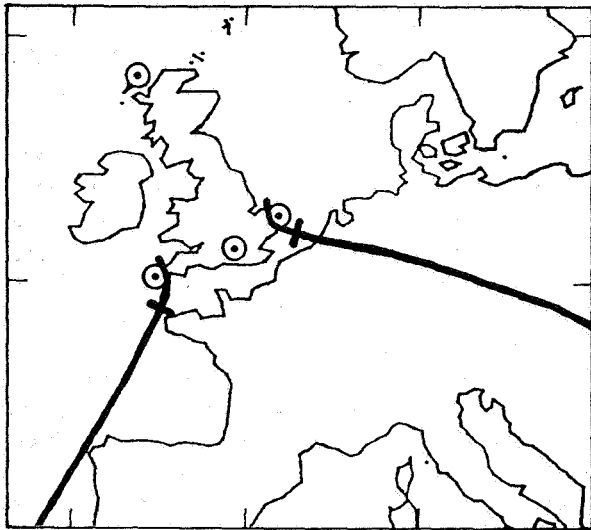


Figure 3: Two ambiguous paired loci for the four Outstations Camborne, Beaufort Park, Hemsby and Stornoway. The divergent paired loci are crossed at their common coincident-foci 'intersection'. Loci close to the outstations hook around Camborne and Hemsby; while their divergent pairs spread beyond Biscay, and towards south-east Europe.

four outstations, all lying on one side of a third line through the intersection, then the two lines may be considered as a limiting pair of hyperbolae with coincident foci at the intersection. In this case, a family of 'four-station' hyperbolae may be drawn with all members having one hyperbola passing through the four outstations; and the hyperbolic foci follow loci diverging from the intersection point.

For any point on a hyperbola, the difference between focal distances is constant. Thus it may be shown that a zero-*RESIDUAL* fix at the focus of one four-station hyperbola is ambiguous with a similar fix at the other focus. This holds for all family members, so any fix lying on a focal locus is ambiguous with a paired focus on the opposite focal locus, and cannot be distinguished by time-difference (*ATD* or *TOA*) alone.

Similar ambiguous fix loci exist over a curved earth. Fig. 3 illustrates two sets of divergent loci for fixes obtained using the four UK outstations shown (five as currently deployed, less Lerwick). Similar loci occur for the five UK outstations less Stornoway — the 'hooks' scarcely move, and the loci are rotated slightly clockwise. Strokes located on the lengthy half-loci are ambiguous (for the four-outstation sets cited) with fixes near the UK on the shorter half-loci, and vice versa.

In practice, apart from 'near coincident' ambiguities close to the intersection point, ambiguous fixes are widely spaced — and can be distinguished through relative outstation amplitudes or waveshapes.

Low  $\sigma(r)$  values would make it easier to distinguish non-zero *RESIDUAL* fixes in the vicinity of the loci. In the current system the potential problem areas are known, and fixes found in an ambiguous region are explored by starting the search minimiser (1) near both ambiguous fixes and inspecting the result. A fix is reported when only one solution is likely. The problem is best resolved by having further outstation observations — an option not readily available with short-range outstations.

Deploying three of the outstations in a triangle with the fourth near the centroid prevents the intersecting lines being drawable. Note from Fig. 1 that this is the UK outstation situation when the Beaufort Park outstation is finally deployed at Aughton, whichever of the two northern outstations is lost.

### SPURIOUS FIXES

Under unfavourable circumstances, particularly when the above effects conspire to reduce outstation observations, the system makes occasional grossly incorrect fixes — as opposed to fixes with errors comparable to the estimated error based on  $\sigma(r)$  values and fixing geometry. These appear to be associated with undetected cycle mis-matches, sometimes in conjunction with the current ambiguous fix mechanism (there is some evidence of identified spurious fixes in the UK area preferentially occurring near the ambiguous fix loci).

During the Jul-Sep 1989 operational trial, particular care was taken to identify 'spurious fixes' which did not correlate with other meteorological evidence:

- Positively identified spurious fixes (mainly near the UK) represented around 0.004% of the total number of fixes [8].

The proportion is small, but forecasters see this as the most significant problem for the current *ATD* system, because of the resulting loss of confidence. The current system's low detection efficiency was of much lower concern.

### ATD SYSTEM HEALTH MONITORING

Indices of overall system health, derived from (1), were designed into the *ATD* system; not all are currently in routine use.

- Setting  $\sigma(r)$  values in (1) to non-dimensional unity makes *RESIDUAL*<sup>2</sup> a measure of  $\sigma(r)^2$ ,

to be filtered, displayed as mean  $\sigma(r)$ , and used for fixing.

The algorithm must avoid 'downweighting' procedures, if necessary re-selecting correlation peaks. Reducing bias improves  $\sigma(r)$ , and quality control — including cycle-slippage detection.

- Setting  $\sigma(r)$  values in (1) to measured averages allows the significance of *RESIDUAL* to be evaluated realistically, and automatically, for each stroke.

The algorithm is based on an F-test. Outliers (at, say, 0.5% or 0.1% significance level) should be rejected, ensuring normal population fixes. Significance levels should be scrutinised, and any tendency to frequent high significance investigated.

Measured  $\sigma(r)$  values allow error ellipses to be evaluated. Strokes with fix errors outside agreed limits for their position are rejected, or tagged. Currently default  $\sigma(r)$  values of 13  $\mu$ s are used, making the estimate sensitive to fix location and available data, but not to scaling for *ATD* uncertainty.

- Estimation of bias, and scatter  $\sigma(r)$ , allow long-term estimates of corrections for bias-reduction, and resolution of epoch ambiguity; and estimates of irreducible scatter.

Plots of average  $\sigma(r)$ , three forms, provide an overall 'health score'. Degradation requires immediate warning, diagnosis, and remedy. In the system design many potential degradations were automatically maintained, but not all mechanisms are used:

Several epoch sources are provided, including Loran-C and Omega (different ambiguity periods) and inter-comparison techniques; as are automatic means for detecting and responding to hardware timescale jumps. Bias-estimation also detects timescale changes. Recently, NAVSTAR has been added to some outstations. However, operators have tended to use only one epoch source, and have become vulnerable to its weaknesses. Loran-C cycle-slippages of 10  $\mu$ s have been common — although these are easily detected ([3], Appendix A) and corrected.

The design included automatic closed-loop monitoring and correction of deficiencies in hardware filters. This has not been properly integrated.

Electronically variable notch filters are provided to protect distant (weak) sferics from man-made transmissions. Currently, they are little used.

## COMPARATIVE SYSTEM RESULTS

The following studies of comparative fixes and 'detection efficiencies' estimated during Jul-Sep 1989 are detailed by Atkinson and Kitchen [8]; only a summary is presented here.

### WMO SYNOP REPORTS

Observer thunderstorm reports (WMO SYNOP present weather codes 17, 29, 91-99) at three-hourly intervals were plotted over the service area, together with comparable *ATD* fixes. A thunderstorm 'detection index' was defined as the percentage of SYNOP thunderstorm observations for which there was an *ATD* fix within 100 km. For synoptic purposes it is unnecessary to detect each thunderstorm cell: 'areas' of activity are adequate. Different criteria may be important for short-term forecasting.

Over the entire service area, the two-weekly average detection index was close to the 80% mean, although wider variations occurred on shorter time-scales. Over the UK and near continent the index was >90%, falling to less than 50% at the edges of the service area in Eastern and Northern Europe and North Africa. Detection efficiency depends on threshold gain, and areas of distant activity may be masked due to system saturation by nearby storms.

### UK ERDC SYSTEM

Within the UK, the five UK-outstation *ATD* network offers <2.5 km fix errors (assuming 5  $\mu$ s *ATD* errors), improving to 1.1 km for a seven-outstation network. Predicted scatter should be a factor of 5/1.5 or 3.3 smaller.

Fix comparisons (based on strokes at corresponding times) were made with the Electricity Research and Development Centre (ERDC) 1 kHz direction-finding network [9]. Initial results on Humberside and Leicestershire storms (150 km from two operating ERDC outstations) showed *ATD* fixes biased 6 km south-west of ERDC fixes. Comparisons with data over the North Sea suggested systematic ERDC bearing errors of a few degrees on this day, so bias was removed to plot scatter comparisons.

The *ATD* system estimated absolute errors for each fix, based on (probably pessimistic) assumed 13  $\mu$ s *ATD* errors, were typically 3-10 km for these fixes which included some Gibraltar and Cyprus data. If 1.5  $\mu$ s *ATD* scatter is assumed, the fix scatter should be a factor 13/1.5 smaller, or 0.4-1.2 km.

Bias-removed results gave 8.5 km standard deviation for ERDC-*ATD* fix discrepancies <30 km. KEMA-*ATD* scatter (below) was similar in an area where predicted *ATD* system scatter was much

larger, suggesting that ERDC-ATD scatter is largely attributable to the ERDC system.

The ERDC system's high detection rate allows an estimate of ATD system stroke detection efficiency. During a two-hour period, 46 strokes were seen by both systems, from 53 ATD fixes and 168 ERDC fixes. This suggests an ATD detection efficiency of 27% for ERDC-detected strokes, with ATD selector at Camborne having 21 dB threshold gain. Flash detection efficiency may be a little higher if ERDC detected multiple strokes. Similarly, the ERDC detected only 87% of the ATD fixes, although this could be because it is less sensitive to cloud-flashes than the ATD system.

#### NORWEGIAN TRANSINOR SYSTEM

The TransiNor system uses 18 LLP magnetic direction-finding outstations [10,11], operating in Norway, Denmark, Sweden, and Finland. Fix times identified corresponding strokes, and fix comparisons were made mainly in southern Norway. TransiNor fixes can be made with up to eight outstations, although most used only 2-3.

In this northern region few ATD data from Gibraltar or Cyprus were available. Fig. 2 indicates that the five UK outstations alone, assuming  $\sigma(r) = 5 \mu\text{s}$  ATD error, give fix errors in southern Norway of 12-26 km. However, the current system does not estimate  $\sigma(r)$ , so the default value of 13  $\mu\text{s}$  was assumed — to estimate a (probably pessimistic) 30-60 km error for ATD system fixes.

The normal population discrepancies between ATD and TransiNor fixes varied widely: the largest were for oceanic TransiNor fixes to the south-west of Norway. However, these used just two TransiNor stations at Oslo and Satenas; the latter appearing to give bearing errors varying with azimuth, as found by Schutte et al [12], implying dominant TransiNor errors. More typically, fix discrepancies were around 65 km; although it is believed that the TransiNor system contributed a sizeable portion as there appeared to be little correlation between estimated ATD fix error and fix discrepancy. Other occasions gave rather lower discrepancies — down to 35 km.

LLP observations were used to deduce ATD system detection efficiency. In Southern Norway on 8 Aug, the apparent stroke detection efficiency (based on TransiNor detections) was 25% between 0900-1200 GMT (at a selector threshold gain of 21 dB), falling to 13% from 1200-1500 GMT (threshold gain 15 dB). These may be slight under-estimates of flash detection efficiency, as some TransiNor strokes were part of multiple-strokes, but are otherwise broadly typical.

#### DUTCH KEMA SYSTEM

Keuring van Elektrotechnische Materialen (KEMA) operate a 5-outstation LPATS network [7], and local fixes were studied at 52.5-54 N and 3-4.5 E. The  $\pm 1.5$  s LPATS timescale uncertainty caused difficulties, but comparisons were made with ATD system fixes.

ATD system accuracy depends on available outstations: seven (and assumed 5  $\mu\text{s}$  ATD error) imply fix errors of 1-1.5 km; degraded to 5-12 km with only five UK outstations, which was more typical.

Initial comparisons highlighted an 8 km bias between ATD and KEMA fixes, mainly through a 10  $\mu\text{s}$  Loran-C zero-crossing error in the Stornoway timescale. The ATD fixes appeared more spread geographically than KEMA fixes, suggesting KEMA fixes in this area are more precise, as might be expected for the five-outstation ATD network.

The bias was removed, and resulting fix discrepancies found to fit a distribution with a standard deviation 8.5 km for discrepancies less than 30 km.

This ATD system result suggests useful accuracy consistent with predicted absolute fix errors in this area, but is slightly disappointing as scatter appears larger than the 2-5 km that might have been expected from an assumed 2  $\mu\text{s}$  ATD scatter.

LPATS timing problems compromised estimates of ATD system stroke detection efficiency, but with a Camborne selector gain of 21 dB this was around 25%, in agreement with above estimates.

#### FLORIDA ARSI SYSTEM

Atmospheric Research Systems Inc (ARSI) manufacture the LPATS system, and operate a five-outstation network covering 24-32 N, 85-77 W. Both ATD and ARSI systems observed a storm 200-300 km off the east coast of Florida for a mid-day path on 14 Sep, 1979. Agreement in absolute fix positions was fair, with discrepancies <100 km — although an assumed 5  $\mu\text{s}$  ATD error would have suggested a 36 km error. ATD system detection efficiency was only a few percent at this range, and only 8 coincidences were observed.

Assuming 'correct' ARSI fixes, the measured ATD values (from Beaufort Park) were compared with theoretical ones. This highlighted 10  $\mu\text{s}$  timescale biases at two outstations (Loran-C!). More importantly, although the random difference between ATD values was 2-3  $\mu\text{s}$  at most outstations, the Lerwick value was around 6  $\mu\text{s}$ . This is larger than expected, is inconsistent with observed propagation effects ([3] Appendix A), and was not observed at 'nearby' Stornoway. This may imply a fault or local influence at Lerwick, perhaps explaining the over-

large scatter in KEMA comparisons. This is being investigated.

## LOOKING AHEAD

For the ATD system we have:

	UK Area	Wide Area
• Absolute $\sigma(r)$ :	3–7 $\mu\text{s}$	3–7 $\mu\text{s}$
Relative $\sigma(r)$ :	1.3–1.6 $\mu\text{s}$	1.3–2.0 $\mu\text{s}$

The above  $\sigma(r)$  errors have been estimated, and Figs. 1, 2 relate these to fix errors. Absolute errors can be reduced to make the system less vulnerable to outstation loss. Quality needs protection by tightening identified closed-loop procedures. Accidental timescale misalignments (by ambiguities of 10  $\mu\text{s}$ ) have been common, but are easily detected by available techniques, especially if bias is reduced. A possible problem with Lerwick is currently being investigated.

- Comparisons with KEMA and ARSI systems lend credence to  $\sigma(r)$  fix error estimates. ERDC and TransiNor comparison discrepancies are probably dominated by the comparison system.
- Fix errors become degraded if outstations are unavailable. This currently happens through communications problems, poor outstation deployment, and receiver resource saturation. All are tractable problems.
- A combination of poor outstation deployment, unavailable outstations, and bias-degraded  $\sigma(r)$  leads to a spurious fix rate of 0.004%. Although not large, this is considered the most important system problem for the forecaster. Improvements are achievable in all causative areas.
- Stroke detection efficiencies are low at around 25% near the UK, although adequate for synoptic purposes. Nevertheless, higher detection efficiency is desirable — and is achievable through improved processing (and possibly communications) resources.

The system can be upgraded. Trade-offs between real benefits and increased costs need to be considered.

## ACKNOWLEDGEMENTS

My thanks are due to N.C. Atkinson for discussions, and for sight of the draft paper by Atkinson and Kitchen, and to M.R. Blackburn. The comparisons summarised here are largely the work of N.C. Atkinson, M. Kitchen, and R. Johnson who have studied operational aspects of the ATD system.

## REFERENCES

1. Lee, A.C.L., 1986: An experimental study of the remote location of lightning flashes using a VLF arrival time difference technique, *Quart. J. Roy. Meteor. Soc.*, 112, 203–229.
2. Lee, A.C.L., 1986: An operational system for the remote location of lightning flashes using a VLF arrival time difference technique, *J. Atmos. and Ocean. Tech.*, 3, 630–642.
3. Lee, A.C.L., 1990: Bias elimination and scatter in lightning location by the VLF arrival time difference technique, *J. Atmos. Ocean. Tech.*, 7, 719–733.
4. Lee, A.C.L., 1989: Ground truth confirmation and theoretical limits of an experimental VLF arrival time difference lightning flash locating system, *Quart. J. Roy. Meteor. Soc.*, 115, 1147–1166.
5. Lee, A.C.L., 1989: The limiting accuracy of long wavelength lightning flash location, *J. Atmos. and Ocean. Tech.*, 6, 43–49.
6. Atkinson, N.C., M.R. Blackburn, and M. Kitchen, 1989: Wide area lightning location using the UK Met Office arrival time difference system, *1989 Int. Conf. on Lightning and Static Electricity*, 26–28 September, University of Bath, UK, Royal Aerospace Establishment, 2B.3.1–6.
7. Bent, R.B., and W.A. Lyons, 1984: Theoretical evaluations and initial operational experiences of LPATS (lightning position and tracking system) to monitor lightning ground strikes using a time-of-arrival (TOA) technique, *Seventh Int. Conf. on Atmospheric Electricity*, June 3–8, Albany, N.Y., Amer. Meteor. Soc., 317–324.
8. Atkinson, N.C., and M. Kitchen, 1991: The operational performance of the ATD thunderstorm location system, *in draft*.
9. Scott, L., 1988: A lightning location system for the UK electricity supply industry, *Int. Aerospace and Ground Conf. on Lightning and Static Electricity*, 19–22 April, Oklahoma City, Nat. Oceanic and Atmos. Admin., 391–395.
10. Krider, E.P., R.C. Noggle, and M.A. Uman, 1976: A gated wideband magnetic direction finder for lightning return strokes, *J. Appl. Meteor.*, 15, 301–306.
11. Herrman, B.D., M.A. Uman, R.D. Brantley, and E.P. Krider, 1976: Test of the principle of operation of a wideband magnetic direction finder for lightning return strokes, *J. Appl. Meteor.*, 15, 402–405.
12. Schutte, Th., E. Pisler, and S. Israelsson, 1987: A new method for the measurement of the site errors of a lightning direction finder, *J. Atmos. Ocean. Tech.*, 4, 305–311.

EXTENSION OF AND IMPROVEMENTS TO THE  
ERDC LOW FREQUENCY MAGNETIC DIRECTION FINDING SYSTEM

M I Lees  
Electricity Research & Development Centre  
Chester  
UK

ABSTRACT

In 1985 a three station direction finding lightning location system was established in the UK. In this paper a description is given of its evolution from an experimental system to a five station commercial system providing both on-line and historical location information. A method of error reduction which enables simultaneous optimisation of strike location and calculation of aerial twist error is described, together with results of the analysis of four station data from 1989. It is demonstrated that one station with a twist error can produce an apparent bearing dependent error in a station without errors. Application of the bearing corrections has significantly improved the accuracy of the system. Average location errors of better than 1km can be achieved at a distance of 200km from the stations.

INTRODUCTION

Damage by lightning to the distribution systems of the UK regional electricity companies, together with the associated costs of interruption of supply to customers is a significant cost to the businesses. It has been estimated that, in the mid 1980's, this cost was of the order of £4 million per annum [1].

By 1985 an experimental three station direction finding (df) lightning location system was established in the UK. The positions of the stations and the coverage of the system for strikes of 7 kA and greater is shown in figure 1. Earlier work [2,3] had showed that the errors in wide band df systems could be attributed to the downcoming horizontally polarized wave produced by reflections at the ionosphere. The experimental system therefore operated at a VLF frequency of 2 kHz, which is the cut-off frequency for horizontally polarized waves propagating in a plane waveguide with a separation between horizontal conductors of 75 km. This distance is the effective daytime height of the ionosphere for VLF waves. The df stations used 3 vertical loops differing in azimuth by 120 degrees. This avoided the need for polarity sensing to determine the bearing quadrant, and also avoided the need for accurate measurement of very small voltages, since the largest two signals will not vary by more than 1:0.5 in relative magnitude because the bearing to a strike must always be within 60 degrees of the planes of at least two of the three loops.

The system was operated intermittently during 1985 and 1986. Raw bearing and signal strength data from the stations was collected by a DEC PDP11/73 computer, with analysis and location being performed off-line on a Prime main-frame. Simple error analysis, consisting of the calculation of the "strike error radius" (defined as the root mean square of the perpendicular distance of the located strike position to the bearings from each of the stations), together with a few observer reports indicated that the system was only accurate to between 15 and 20 km at night. The operating frequency was therefore reduced to 1070 Hz with a bandwidth of 350 Hz. A similar analysis of the 1987 data indicated a mean accuracy of location of 6 km.

SYSTEM EXPANSION AND IMPROVEMENTS

Following the improvement in performance, a decision was made to increase the coverage and accuracy of the system by adding more stations. Also, the value of the system for producing early warning of impending lightning was appreciated, and a decision was made to develop the system to locate and broadcast lightning strike data to customers in real

time. During 1989, it became clear that the chosen sensitivity was inadequate, as a small number of strikes which had caused damage were sensed by only one or no stations. The threshold level at which the stations reported was therefore reduced. These improvements introduced a small number of problems to be overcome and these together with improved methods of location of strikes and error analysis are described below.

### CHOICE OF NEW SITES

The original sites were chosen so that the overall level was within 1 degree over 1 km radius with mean level constant over 10 km. The geography of the UK, together with a requirement to position stations with a separation of 300 km, and approximately 1 km from 11 kV power lines has prevented the installation of stations on such favourable sites. The principle need for more stations was to increase coverage of Scotland. At least one station was required in northern or central Scotland, with a second in northern England or southern Scotland. The hilly nature of the north of England and Scotland in general has led to most urban development being restricted to the low-lying coastal areas. The consequent need for electricity in these areas has resulted in a high density of transmission lines and hence reduced the number of sites which would otherwise be acceptable. However, four potentially acceptable localities were found.

Upon more detailed surveys of the areas, two sites were chosen as more acceptable than the others. These sites were both in Forestry Commission land, minimizing the risk from future development. The first, Harwood forest is some miles north west of Newcastle upon Tyne, whilst the second, Rhynie forest, is some miles north west of Aberdeen. The mean level of the Harwood site slopes by 0.03 degrees SE to NW, with the overall level within 1.2 degrees. The mean level of the Rhynie site slopes by 0.12 degrees E to W with the overall level within 1.2 degrees. The effects of these departures from the "ideal" sites are discussed in the section on errors below. At present all 5 stations are operating. The position of the new stations and the present coverage for strikes of 5 kA and above is also shown in figure 1.

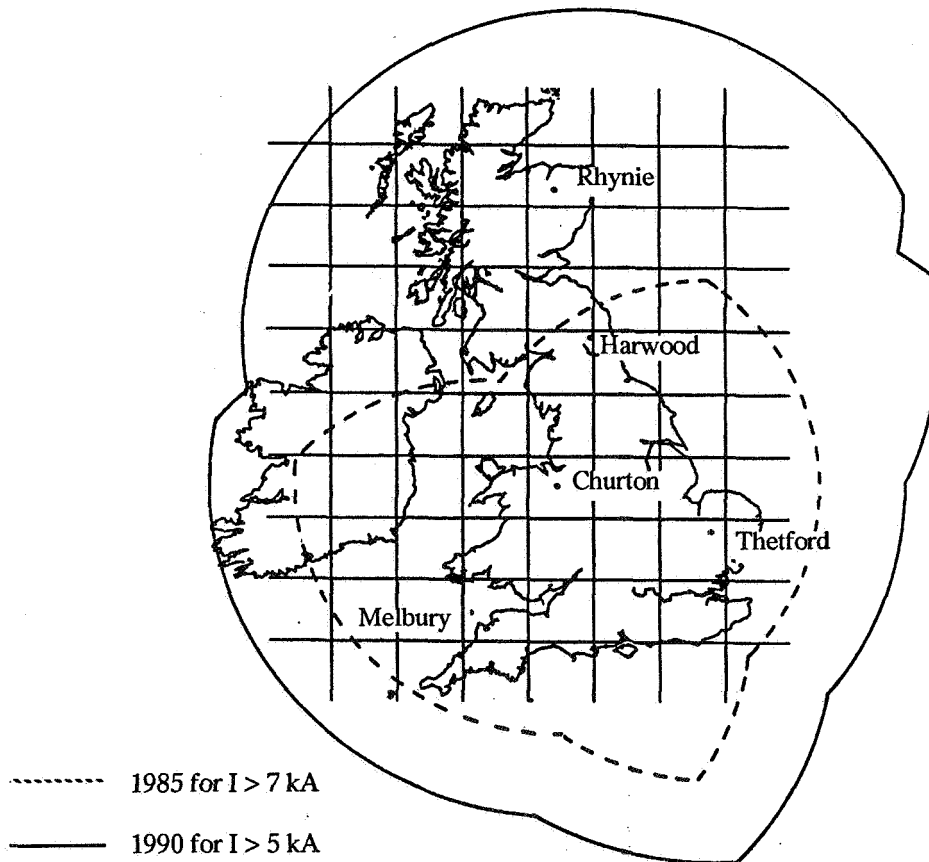


Figure 1. Position of DF Stations and coverage of system in 1985 and 1990



## DEVELOPMENT OF THE REAL-TIME ON-LINE SYSTEM

Collection of data and calculation of location. The df stations can sense a strike, calculate bearings and signal strength, and transmit the encoded data at a rate of 40 per second. However, it soon became clear that the PDP11 computer could not collect, time tag and store the data, and in addition calculate the strike location at rates significantly above one per second. This was acceptable for an off-line system, providing the input buffers were not filled. An on-line system, operating at this mean rate, could result in location information being sent to customers up to 15 minutes after the strike occurred. This is unacceptable for a "real-time" system.

The duties of the central computer were therefore distributed. The PDP11 continued to collect, time tag and store the data, whilst calculation of the location and transmission to remote displays was performed by a Sun 3/160 computer under Unix. This operating system was chosen as it allowed development of the various components of the system as separate programs to be run as separate processes.

There are three main process running live on the Sun. Communication between the various processes is by a low level Unix method known as "sockets". The first process collects the packet of data as made up by the DEC. It stores the raw data on disc and passes it on to the analysing process. This calculates the location, produces an estimate of accuracy of location and current of the strike, then tests the data against a series of rules in order to assess whether the strike has been incorrectly located. These test were of great importance in the early days when only two stations were operating, and became of importance again when the threshold of the system was reduced.

The analyser passes the location data, together with date, time, accuracy, number of re-strikes, current and flags indicating the results of the rules' test to the third main process. This encodes the data for transmission to remote displays and transmits it. Simultaneous connection of the analyser to more than one "post analysis" process is possible. It is therefore possible to filter data to a customer's needs, for example restricting the area of coverage, without making any change to the analysis program.

This system design makes the system more robust, since failure of one process does not affect the others. It also is of great assistance when bringing a station on-line, whilst it is being calibrated. Two complete systems can be run on the same machine, one without the new station, one with, and the results compared in a separate process without interfering with the live system.

In 1989 the Sun was upgraded to a 4/260 10 MIPS machine. In addition all the processes were streamlined to make them more time efficient. The result of this was to increase the processing speed by a factor of eight. The continuous rate is now well in excess of that which the data circuits to customers are able to support. A second DEC and a second Sun computer have been added to the system. These are inter-switchable with the original computers to provide hardware redundancy. As a consequence of this, although damage to stations has occurred, collection of data from at least two stations has not been interrupted for two years and within this period, excluding problems with data circuits, customers have only been off-line for a total of 44 hours.

On-Line Display terminals have been developed to provide a real-time graphical display of strikes. The display software runs on IBM PC and PS2 compatible machines within the Microsoft 'Windows' environment. Flashes are displayed within seconds of their occurrence in a window displaying an outline map of the British Isles and the north west coast of Continental Europe. The program is menu driven and includes facilities for pan and zoom of the display and sizing of the window. Various overlays are available displaying the 400 kV, 275 kV and 132 kV networks, power stations and sub-stations. User defined overlays are easy to produce and can be included in the display.

The strike position indicators are colour coded, representing the time of the strike. Data on any specific strike can be extracted by positioning cross hairs over the strike using the mouse. Clicking the mouse button opens a window which shows the details of the strike including the latitude, longitude and Ordnance Survey National Grid Eastings and Northings of the strike position; the uncertainty of the fix, the current of the strike, the date and time to the nearest hundredth of a second. In addition for restrikes a multiplicity counter is included. Hard copy of both the screen display and details of strikes within a given time period can be produced by a Microsoft 'Windows' supported printer.

Historical data can be replayed in a similar windowed display on the same machine without stopping the collection and display of live data.

**Effects of the reduction in Threshold** The analogue circuitry of the df stations have a dynamic range limited by external noise of 80 dB (power) from a reference of 22.5 nT magnetic flux density. The original working range was chosen to be 36 dB. This was chosen to limit the number of strikes detected at distances of above 1000 km, and also because of limitations in the resolution of the A/D converters. From work by Erskin [4], using the far field approximation for the ELF magnetic field due to lightning current given by Watt [5] and Uman [6] the minimum current against distance for a strike to be detected is shown in curve A figure 2. Using the flash current population from 1988 data [4] this gave a detection efficiency at 400 km of 99.5% (93% at 1000 km). The detection efficiency at 400 km using flash current population data measured by Berger et al. [7] was 99.5% for negative first strokes, 82% for negative following strokes and 95% for positive strokes. Using data of Popolansky [8] gave a detection efficiency of 94%.

However, there still remained incidents on the distribution network which were caused by strikes which were detected by one station only. The threshold was therefore reduced to 190 pT giving a dynamic range of 42 dB. This gives a minimum current for detection as shown in curve B figure 2. The detection efficiency is now 99.9% at 400 km and 99.5% at 1000 km (from [4]); greater than 99.9% for negative first strokes, 97% for negative following strokes, and greater than 95% for positive strokes all at 400km (from [7]); and approximately 98% for all strokes at 400km (from [8]). The coverage of the system for currents of 5kA and above is shown in figure 1.

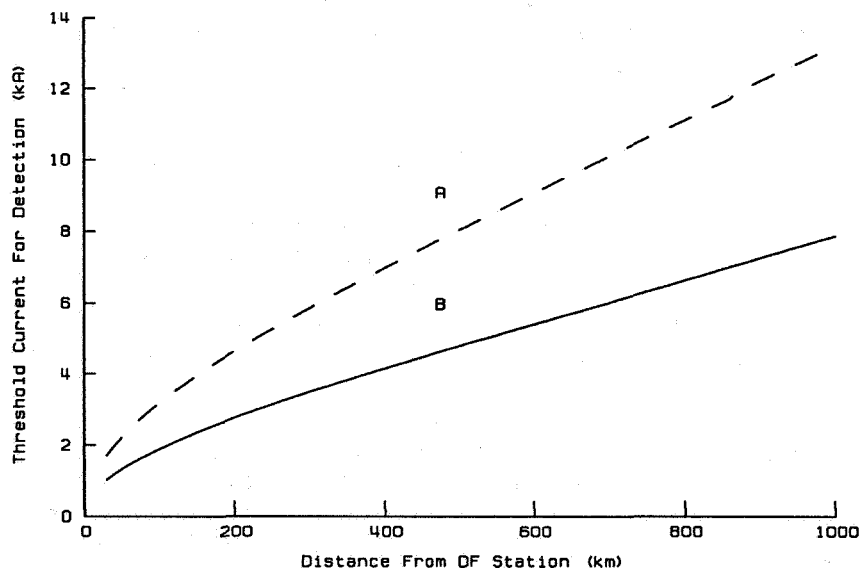


Figure 2. Effective range of DF stations as a function of strike current

Because the collection efficiency of the ERDC system is a function of distance from a station, the area over which strikes are detected is greater for strong strikes than for weak strikes. This effect is not allowed for in [4], and therefore the distribution may be weighted to larger currents. It is intended to analyse 1989 and 1990 data to determine the degree of weight resulting from this effect.

The greater sensitivity led to a much greater number of strikes in southern and central Europe being detected. Unfortunately the digitising errors from the weak signals caused large errors in the location of these strikes. The increase in number of stations meant it was possible for a strike to lie close to the baselines between three stations, a situation which was not possible with the three station system. There was also an indication that the approximation that the signal travels along a great circle was not sufficiently good for accurate location of strikes at distances in excess of 2000 km. The rules were therefore adjusted to prevent strikes occurring for example in northern Spain being incorrectly located in Brittany. The correct trapping of these strikes has been confirmed by correlation with data from the Meteorological Office.

## IMPROVED METHOD OF LOCATION

The original location method used plane geometry with corrections for the difference between true and grid north at the stations. The root mean square of the perpendicular distance of the location from the bearings was minimised. This is unsatisfactory when the variation in the distances from the strike to the stations is not small compared with the distances, and when the distance is greater than 300 km. From 1988 the locations were determined in spherical coordinates using the eigenvector method of Wangness [9]. This is essentially the same as the method described by Orville [10]. The point which is least far from all the bearings in a least squares sense, is found by calculating the smallest eigenvalue  $\lambda$  of the equation

$$(A' \cdot A - \lambda I) \cdot x = 0$$

where  $I$  is the unit matrix,  $x$  is a unit vector from the origin in the direction of the strike,  $A'$  is the transpose of  $A$ , and  $A$  is the matrix of the unit normals to the bearing planes. All vectors are expressed in a spherical coordinate system with the origin at the centre of the earth. In 1990, following the increase in speed of the system, the method was improved by determining the distance to the strike from each station and repeating the calculation with the elements of  $A$  divided by the corresponding distance to give the optimum location of the strike. This is a first order approximation to minimizing the sum of the squares of the difference between the measured and optimum location azimuths.

The increase in number of stations produces redundancy in data for producing the fix and error assessment. Were all measurements to be made with equal accuracy then an increase in stations would naturally lead to an increase in accuracy. However, increased distance from a strike reduces signal strength and increases digitising errors, and also a given bearing error results in a linear error which increases with distance. These effects combine to make measurements at stations close to a strike more reliable than those further away. The latter effect is normalised by dividing the elements of  $A$  by the corresponding distance to the strike as described above.

## ASSESSMENT AND REDUCTION OF SITE ERRORS

A brief review of the subject of site error estimation has been given by Passi & Lopez [9]. They divide the approaches to the problem into parametric and non-parametric methods. In the former method a two cycle sinusoid is fitted to the differences  $\epsilon_i$  for each strike between the measured and optimum location azimuths. This is performed for each df station independently. In the latter method no functional form of the error is assumed and the mean value of  $\epsilon_i$  is calculated for angular sectors independently for each d.f. station. Both of these approaches are amenable to feedback in the sense that the corrections found can be applied to the data set in order to produce better optimum locations, and the error assessment repeated. However, as pointed out in [9], errors determined by either of these methods are not the actual site errors of df stations, since they are determined from optimum positions which were biased by site errors. It is by no means certain that the solution will converge, indeed we have found that it is possible using this method to produce a small decrease in mean error radius, but at the cost of moving the locations to positions which are known to be in error. Passi and Lopez assumed that the errors in the bearings were induced by scattering objects near to a df station and that therefore the site errors could be represented by a harmonic series based on two cycle sinusoids. They showed that with this approximation it was possible to decouple the site error estimation from the localisation optimisation. They applied the method to a system with gross errors (up to 20 degrees) and showed convergence was possible using a function with two harmonics.

The dimensions of scattering objects must be a significant fraction of the wavelength of the radiation being scattered. The wavelength utilised by the ERDC system is 280 km. Hence the size of scattering objects is large and may be positioned at large distances from the d.f. station. There is no certainty that a back-scattered wave will have sufficient amplitude to interfere with the incoming wave at a station. It therefore cannot be assumed that the site error can be represented by harmonics of two cycle sinusoids unless very high harmonics are used.

## SIMULTANEOUS OPTIMISATION OF FLASH LOCATION AND SITE ERROR ESTIMATION

The principles of the method used were derived by Waddington [10]. The true errors  $\beta_j$  of the  $j$ th station cause apparent errors  $\epsilon_i$  to be measured at the  $i$ th station. Thus all stations can appear in error when in fact only one is, as is

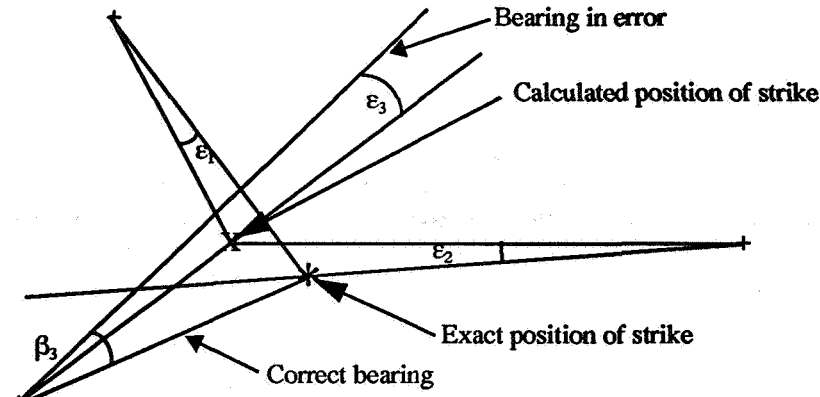


Figure 3. Definition of symbols and demonstration of the apparent error in all stations from a true error in one

shown in figure 3 for a three station system. It is this effect that can result in the calculation of incorrect corrections when not optimising the location simultaneously with calculation of site errors. It is clear from figure 3 that it is not possible to calculate the true errors from the apparent errors for one strike, although the reverse problem can be solved. However, it is possible to produce an estimate to the true errors if sufficient strikes are distributed over a large area. For an N station system the apparent errors  $\epsilon_i$  of station i are related to the true errors  $\beta_j$  of station j by the equation:

$$\begin{bmatrix} \epsilon_1 \\ \epsilon_2 \\ \dots \epsilon_N \end{bmatrix} = \begin{bmatrix} J_{11} & J_{12} & \dots J_{1N} \\ J_{21} & J_{22} & \dots J_{2N} \\ \dots J_{N1} & \dots J_{N2} & \dots J_{NN} \end{bmatrix} \cdot \begin{bmatrix} \beta_1 \\ \beta_2 \\ \dots \beta_N \end{bmatrix} \quad \text{where} \quad J_{ij} = w \cdot \frac{\partial \epsilon_i}{\partial \beta_j}$$

This is the first term in a Taylor expansion. It is assumed that the apparent errors are a continuous function of the true errors and that both are small. The elements of the jacobian are calculated by deliberately introducing small errors to each of the measured bearings in turn and re-calculating the optimum location of the strike. The elements of the jacobian are multiplied by a weighting factor  $w$  which is related to the mean, over all reporting stations, of the probable instrumental error in the measurement of the bearings. This quantity is dependent on the strength of the wave at the stations. If a station has not reported then the weighting factor for that station is zero. Hence the method can be applied to strikes with reports from a variable number of stations, as long as there are three or more. In addition, strikes of varying strengths and hence accuracies can be used, without weak inaccurate strikes having a disproportionate influence on the calculated corrections.

There will be an equation of this type for every strike, giving  $n$  estimates to the jacobian for  $n$  strikes, and producing an overdetermined system of  $M = nN$  linear equations for a  $N$  station system. The  $M$  equations cannot be satisfied exactly, but the residual angular error over all strikes can be minimised in a least squares sense. That is, minimise:

$$R = \sqrt{\sum_{k=1, M} r_k^2} \quad \text{where} \quad r_k = \epsilon_k - \sum_{j=1, N} J_{k,j} \cdot \beta_j$$

It can be shown [11] that the minimum value of  $R$  is given by the solutions  $\beta_j$  of the following equation:

$$\begin{bmatrix} J_{11} & J_{12} & \dots J_{1M} \\ J_{21} & J_{22} & \dots J_{2M} \\ \dots J_{1N} & \dots J_{2N} & \dots J_{MN} \end{bmatrix} \cdot \begin{bmatrix} \epsilon_1 \\ \epsilon_2 \\ \dots \epsilon_M \end{bmatrix} = \begin{bmatrix} J_{11} & J_{12} & \dots J_{1N} \\ J_{21} & J_{22} & \dots J_{2N} \\ \dots J_{1N} & \dots J_{2N} & \dots J_{MN} \end{bmatrix} \cdot \begin{bmatrix} \beta_1 \\ \beta_2 \\ \dots \beta_N \end{bmatrix}$$

It will be appreciated that no single optimised location has been used in determining the errors. Rather the effect of variation of a single station bearing on the error in the bearings from all other reporting stations, for each station, for each strike has been used in order to produce a global minimisation of errors over all strikes simultaneously. Once an estimate to the error has been found then the bearings can be corrected and the method repeated for a more refined estimate.

## EVALUATION OF THE METHOD

Since it is difficult to obtain a statistically significant sample of ground truths with which to compare the validity of calculated corrections it is necessary to have great confidence both in the method used to find the corrections and in the data sample used. Hence the method was tested on the 1989 data set in the following manner. Firstly optimised locations were calculated from the raw data set. The bearings from the stations to these locations were then calculated to produce a new data set which gave negligible location errors. Errors were then added to these bearings. These took the form of a constant and a part which was random within a range determined by the instrumental error for the strength at a station for a given strike. The introduced errors were therefore very similar to those which would be expected in the original raw data, but in this case they were known. The constant part of the error was taken to be a fraction of a degree for all but one station, which was set at 4.5 degrees. This large figure was included to assess the ability of the method to find small errors on one station in the presence of gross errors from another. The results of the analysis are shown in the table below. It can be seen that the method was able to extract the errors within 0.03 degrees.

Station	Thetford	Churton	Melbury	Harwood
Constant part of fake error	0.44	0.1	-0.3	4.5
Extracted error	0.417	0.069	-0.323	4.427
Standard deviation	0.039	0.059	0.034	0.041

## RESULTS OF ERROR ANALYSIS OF 1989 DATA

The angular differences, before corrections were applied, between the bearing from a station to the optimised location of a strike and the measured bearing at the station  $\epsilon_i$  were collected in 2.5 degree bins for each of the four stations which were operating in 1989. The variations with bearing of the mean of the apparent errors are shown in figure 4. The error bars show one standard deviation from the mean. The standard deviation over all angles is quoted in each graph.

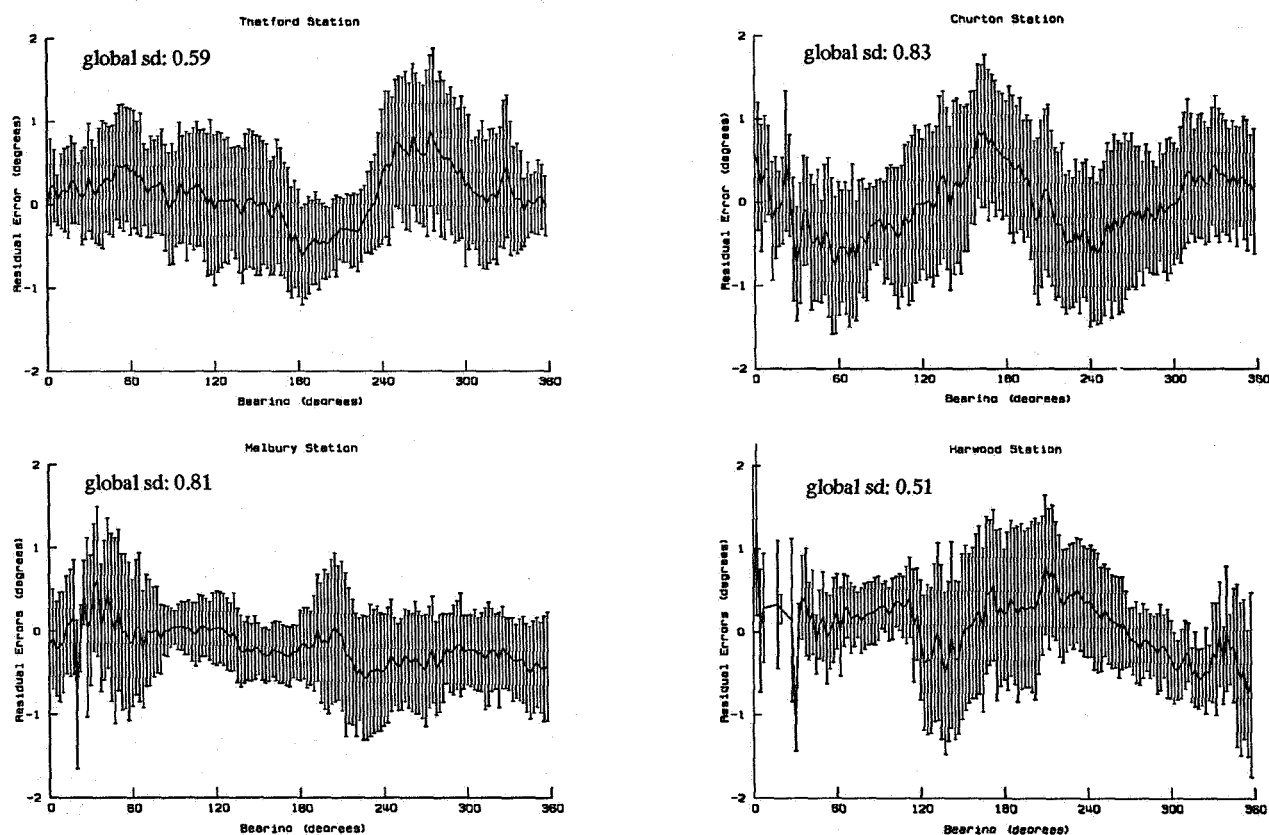


Figure 4. Variation of the apparent error in the bearing of a strike from each station as a function of the bearing.

It is apparent that a good fit to a two cycle sinusoid would be made by the data from Churton. Thetford, Melbury and Harwood also show features with a two cycle form. It will be noticed that the data for Harwood between 5 and 30 degrees is not as good as for the rest of the range, or for the other stations. This is most likely due to the geometry of the network of stations. The analysis requires a fix of a least three stations. One would expect a lower number of multi-station reports from this region, as it lies furthest from the Churton, Thetford and Melbury stations. However, there may be some meteorological reason for the lack of data in this region.

#### EVALUATION OF THE DEPENDENCE OF RESIDUALS ON BEARING

The bearing dependence of the mean residual in 2.5 degree bins after global correction for each station is shown in figure 5. The standard deviation over all angles is again quoted in each graph. The influence on location errors of correcting for the bearing dependent residual was investigated. This has not been subjected to the same critical test as described for the global error and therefore confidence in the results is not as great. Correcting for bearing dependent error and re-calculating the global error had only a small effect on the global correction of each station, as can be seen from the table below. Hence bearing dependent errors are a second order effect. The standard deviation over all angles was reduced by a similar amount upon correcting for the bearing dependent error, for all stations excepting Churton which was reduced to 0.54 degrees.

Station	Thetford	Churton	Melbury	Harwood
Global Correction before	0.95	0.60	-0.31	0.67
Bearing dependent correction				
Global Correction after	0.92	0.62	-0.33	0.67
Bearing dependent correction				

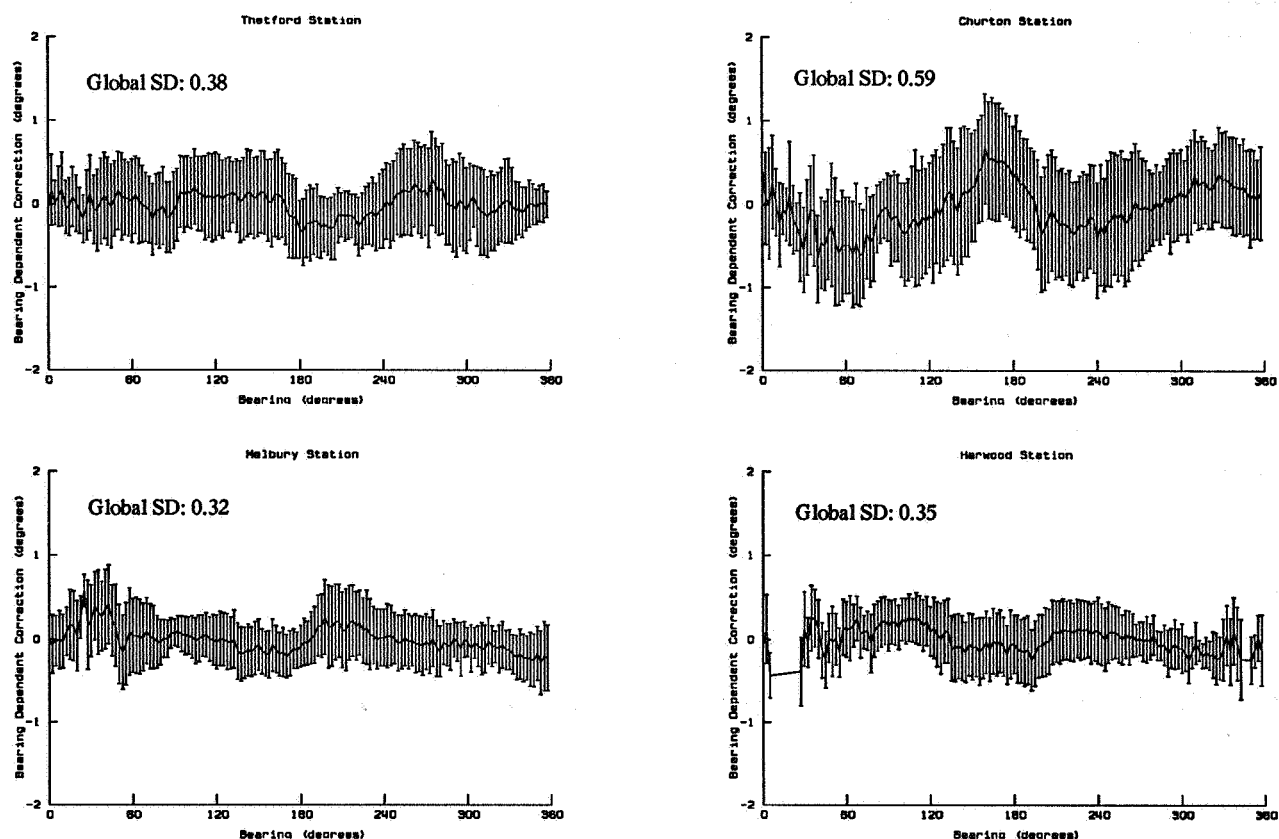


Figure 5. Variation with bearing of the apparent station error after global corrections applied

The effect on the accuracy of the location fixes resulting from the application of these corrections was marked. The mean rms linear error was calculated over all strikes in 100km square areas. In the centre of the network (at a distance of 200km from the stations) the mean rms linear errors decreased to less than 1km.

It is apparent that, following the global corrections, only the bearing dependent corrections for Churton station are double sinusoid in form. The most striking reduction in errors is shown by Harwood. The errors have changed from having a strong apparent bearing dependency, albeit with large scatter, to having small scatter and negligible bearing dependency. Melbury's errors show the same small scale dependence on bearing, with the large scale trend to greater negative errors between 120 degrees and 360 degrees removed by the global correction. An analysis of a three station system similar to that shown in figure 3 has been made. Churton and Harwood stations were assumed to be without errors. Bearings from each of the stations to 10000 strikes evenly spaced in latitude and longitude were calculated. The extracted twist error was then subtracted from the bearings from Thetford. The effective errors introduced on Harwood station by this twist error were calculated and are shown in figure 6. These should be compared with the graph for Harwood station in figure 4. The similarity in the functional dependence of the residual error on bearing is striking in view of the simplicity of the model. It is likely that the changes in the Melbury and Harwood errors are mainly due to the correction of the large twist error which was found in the Thetford station, and that Churton Station does display a real bearing dependent error. It is also evident that great care should be taken in applying bearing dependent corrections which have been extracted from the apparent errors of a station without first extracting the global twist errors in the manner described in this paper.

It is interesting that the shortcomings of the Harwood site have not had the expected effect on the errors of the station. It is probable that, were a good sample of data to have been collected between bearings of 5 and 30 degrees, Harwood would display lower errors than the other stations. Churton is sited on level ground in agricultural pasture that extends more than 10km in every direction. However it displays the greatest bearing dependent residual after correction for twist error on all the stations. This unlikely result is probably due to the long wavelength used by the system. Local potential scattering centres are of less importance than features with dimensions that are a significant fraction of a wavelength in size.

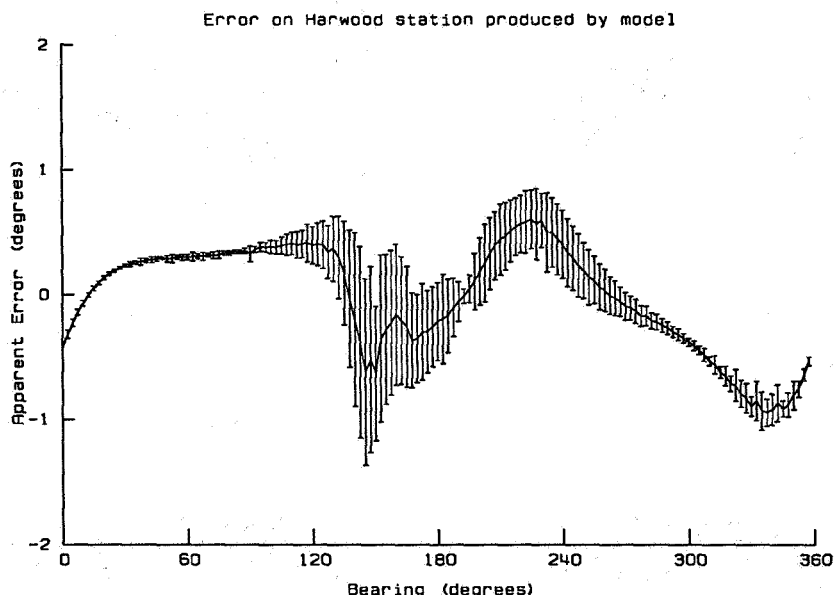


Figure 6. Apparent errors introduced on Harwood station by a twist error in Thetford station. Only Harwood, Thetford and Churton stations contributing to the analysis of 10000 simulated strikes.

#### IMPROVEMENTS IN PROGRESS

Although great improvements have been made in the accuracy of the system through analysis of historical data there

remains a random residual which is of the order of the mean digitising error taken over all strengths of signal. Although the resolution is 0.05 degrees for the strongest signals, it decreases as the signal strength is reduced, as a consequence of the method of analogue to digital conversion of the signal. Examination of the rms residual as a function of signal strength indicates that 12 bit resolution over the entire range would reduce the rms random residual by a further factor of two. A replacement A/D converter circuit which is designed to give better than 12 bit resolution over a full dynamic range of 60 dB (power) is presently being fitted to the stations.

The present system uses a central clock for timing and is therefore dependent upon the propagation time for data along a private circuit to remain constant, hence repeat request error correction is not possible. The system is therefore very sensitive to the quality of the data circuit. Modification of the stations to include local clocks to remove this dependency is also underway. This will ultimately make the aged DEC computers redundant, and will allow more flexibility in choice of communication medium and position of future stations.

## CONCLUSIONS

The development of the system from a three station system of limited coverage to a five station system with increased coverage, reliability and accuracy has been described. Particular attention has been paid to the analysis of station errors. A method of calculating the global twist errors of all stations simultaneously with optimising strike locations for all the strikes recorded by the stations, and hence extracting the true bearing dependent errors has been described.

The results of applying this method to four station data for 1989 have been presented. Application of the bearing corrections has significantly improved the accuracy of the system. Average location errors of better than 1km can be achieved at a distance of 200km from the stations. It is anticipated that further significant improvements in the accuracy of the system will result from the replacement of the existing A/D converters.

It is apparent that a degree of caution is needed when applying bearing dependent corrections which have been extracted from the apparent errors of a station without first extracting the global twist errors in the manner described in this paper.

## ACKNOWLEDGEMENTS

The author would like to thank the Electricity Research & Development Centre for permission to publish this work. I would also like to thank Mr. G Bulmer and Mr. B Wendl for undertaking many and varied electronic and computing tasks on the job, and generally contriving to keep the service operating efficiently and reliably. Finally, many thanks are due to Laura Scott, who designed and developed the system. Laura has recently retired from the Centre.

## REFERENCES

- [1] Scott L J, Int. Conference on Lightning and Static Electricity (1988)
- [2] Scott L J, International Conference on Lightning and Power systems IEE conference Publication no. 236, June (1984).
- [3] Challinor R A J. Atmos. & Terr. Physics, Vol 29, pp803-810, (1967)
- [4] Erskin A, Universities Power Engineering Conference pp565-568, (1989)
- [5] Watt J R, "Electromagnetic waves in stratified media", Pergamon Press, NY, (1962)
- [6] Uman M A "Lightning", McGraw-Hill, NY, (1969)
- [7] Berger K, Anderson R B & Kroninger H, Electra no. 41, pp23-27 (1975).
- [8] Popolansky F, Electra no. 22, pp139-147, (1972)
- [9] Passi R M & Lopez R E, J. Geophysical Research vol 94, pp13319-13328, (1989)
- [10] Waddington J F, ECRC internal report no ECRC/M2370 (1989)
- [11] Rice J R, "Matrix computations and mathematical software", McGraw-Hill, (1981)



An Iterative Method for Obtaining the Optimum  
Lightning Location on A Spherical Surface

Gao Chao

Ma Qiming

Center for Space Science and Applied Research  
Chinese Academy of Sciences

ABSTRACT

According to Orville, briefly introduced the basic principle of eigent technique for Obtaining the optimum source location using multiple direction finders on a spherical surface. This technique taking the distance of source-DFs as a constant should be improved. Pointed out that using a weight factor of signal strength is not a idealest method because of the inexact inverse signal strength-distance relation and the inaccurate signal amplitude. Presented an iterative calculation method using distance from source to DF as a weight factor. This method has higher accuracy and needs only a little more calculation time. Showed some computer simulations for a 4DFs system so as to show the improvement of location by using the iterative method.

1. INTRODUCTION

Lightning direction-finding networks [1] have been widely used for the purpose of determining cloud-ground lightning locations. For obtaining the optimum source location we have to resolve the problem of doing optimum calculation under presence of site errors and random errors.

Site errors as high as getting to even  $15^\circ$  are systematic errors [2.3]. These errors have been discussed [4. 5] and some methods have been presented to identify and remove them. The remained problem is simplified to do the optimization location only under the presence of random errors. It has also been solved satisfactorily [6.7]. Especially Orville[6] presented an analytical solution in spherical coordinates for the source on the earth's surface. The analytical solution was obtained by reducing the question to an eigenvalue problem. This method is also called symmetric minimization. It needs only very short time for getting the optimum position using all DF's data. Therefore the eigen technique is very suitable for real time operation.

For mathematical tractability Orville suggested all the distances between source and DFs are the same. This approximation will bring some errors into results. For improving the optimization accuracy, he introduced a method that used a signal strength, which varies inversely with the range from a DF to the flash, to weight the related elements. But it is not a best method because of the unregular properties of signal strength. We will present a simple iterative method based on Orville's eigen technique. We will also introduce some simulation examples for comparison.

## 2. SYMMETRIC MINIMIZATION

We assume there are no site errors in observations. In Fig. 1, a hypothetical ground flash occurs at point  $P(\sigma, \Omega)$  where  $\sigma$  and  $\Omega$  are latitude and longitude of the flash location respectively. A direction finder DF<sub>i</sub> at  $(\sigma_i, \Omega_i)$  detects the point lightning flash at an angle from the true azimuth, at a distance of  $\delta_i$  to the flash. The great-circle distance from the flash to the bearing line of DF<sub>i</sub> is  $h_i$ . We know

$$\sin \mu_i = \sin h_i / \sin \delta_i \quad (1)$$

For getting the optimum flash location we need to minimize

$$\sum_{i=1}^n \sin^2 \mu_i = \sum_{i=1}^n \sin^2 h_i / \sin^2 \delta_i \quad (2)$$

where  $n$  is the total number of DFs. For mathematical tractability Orville proposed to minimize  $\sum \sin^2 h_i$  instead of  $\sum \sin^2 \mu_i$  and presented an eigen technique, which is quite elegant and fast. But the approximation that let  $i=\text{constant}$  will bring some errors to the results. Although it is pointed out that the signal strength reported by DF can be used as a weight factor, its improvement is still limited because of the inexact inverse relation between and signal strength or the bigger measuring error of signal strength (up to 20%).

## 3. ITERATIVE METHOD

First based on Orville's eigen method [6], let  $\delta_i = \text{constant}$ , we can get the first location approximation  $(\sigma, \Omega)$ . Then using the relation

$$\cos \delta_i = \sin \sigma_i \sin \sigma + \cos \sigma_i \cos \sigma \cos(\Omega - \Omega_i) \quad (3)$$

we can get the approximate  $\delta i$ . Put the new  $\delta i$  into (2) to find the minimum value

$$\frac{\partial}{\partial \delta} \Sigma \sin^2 \mu_i = \frac{\partial}{\partial \delta} \frac{\sin^2 h_i}{\sin^2 \delta_i} \quad (4)$$

$$\frac{\partial}{\partial \Omega} \Sigma \sin^2 \mu_i = \frac{\partial}{\partial \Omega} \frac{\sin^2 h_i}{\sin^2 \delta_i} \quad (5)$$

Here  $\sin i$  is a known value. Let a weight factor

$$W_i = 1/\sin \delta_i \quad (6)$$

we can obtain following new eigents:

$$\hat{X}_1 = \begin{bmatrix} W_1 (x_1)_1 & W_2 (x_1)_2 & \dots & W_n (x_1)_n \\ W_1 (y_1)_1 & W_2 (y_1)_2 & \dots & W_n (y_1)_n \\ W_1 (z_1)_1 & W_2 (z_1)_2 & \dots & W_n (z_1)_n \end{bmatrix} \quad (7)$$

$$\hat{A}_1 = \begin{bmatrix} \Sigma W_i^2 (x_1)_i^2 & \Sigma W_i^2 (x_1)_i (y_1)_i & \Sigma W_i^2 (x_1)_i (z_1)_i \\ \Sigma W_i^2 (y_1)_i (x_1)_i & \Sigma W_i^2 (y_1)_i^2 & \Sigma W_i^2 (y_1)_i (z_1)_i \\ \Sigma W_i^2 (z_1)_i (x_1)_i & \Sigma W_i^2 (z_1)_i (y_1)_i & \Sigma W_i^2 (z_1)_i^2 \end{bmatrix} \quad (8)$$

$$\hat{X}_3 = \begin{bmatrix} W_1 (x_3)_1 & W_2 (x_3)_2 & \dots & W_n (x_3)_n \\ W_1 (y_3)_1 & W_2 (y_3)_2 & \dots & W_n (y_3)_n \\ W_1 (z_3)_1 & W_2 (z_3)_2 & \dots & W_n (z_3)_n \end{bmatrix} \quad (9)$$

$$\hat{A}_3 = \begin{bmatrix} \Sigma W_i^2 (x_3)_i^2 & \Sigma W_i^2 (x_3)_i (y_3)_i & \Sigma W_i^2 (x_3)_i (z_3)_i \\ \Sigma W_i^2 (y_3)_i (x_3)_i & \Sigma W_i^2 (y_3)_i^2 & \Sigma W_i^2 (y_3)_i (z_3)_i \\ \Sigma W_i^2 (z_3)_i (x_3)_i & \Sigma W_i^2 (z_3)_i (y_3)_i & \Sigma W_i^2 (z_3)_i^2 \end{bmatrix} \quad (10)$$

The difference between eigents above and those of Orville's is that each term above is weighted by factor  $W_i$ .

The following formulas should be same as Orville's:

$$\hat{R}_1 \hat{A}_1 = \hat{A}_3 \hat{R} \quad (11)$$

$$\hat{A}_3 = \begin{bmatrix} w & u & 0 \\ u & v & 0 \\ 0 & 0 & r \end{bmatrix} \quad (12)$$

$$\hat{V}_3 \hat{A}_1 = r \hat{V}_3 \quad (13)$$

Using the same calculation procedure we will obtain the iterated results, each is the new optimum probable location  $(\sigma, \Omega)$ . Of course we can do the iterative procedure several times so as to reach higher accuracy, but we have also found it is perfectly enough for general location to do iterative only once.

#### 4. RESULTS COMPARATION

For understanding the improvement of using iterative calculation, we have done some computer simulation. Assume there is a 4DFs network on the earth's spherical surface roughly in a square geometric figure with the center at latitude 39 N and longitude 115 E. The baseline of adjacent DF is about 90KM and the discussed area is about 200\*200KM. For any arbitrary point in this area, we know its exact direction related to every DF. Add 300 random errors to the ideal directions in an angle range of 1. Using two algorithms: unweighted symmetric minimization and iterative method respectively, we can get two sets of 300 new simulated lightning locations (to do iterative once) and further the distances between them and the ideal point. Take average of two sets distances we will obtain the statistics location error related to two methods. Repeat this simulation at different point (400 points) in whole area and compare their location errors, the improvement of iterative calculation will be clearly showed on Fig. 2-Fig. 4. Generally saying, iterative method will decrease the location error by 20% and extend the equal precision area much more.

For discussing the necessary iterative times we have tested iteration four times and compared the distance from center to the calculation points. Table I shows some examples of ten points and from the results we can conclude that once iteration is enough for acceptable accuracy.

#### 5. DISCUSSION

An iterative method for getting optimum lightning location has been presented. This method is an improvement on Orville's eigent method. It needs only the first distance opproximation of flash to DF as a weight factor to repeat the eigent technique once more. So it spends only a little more time during the real time calculation, but gets more accurate location result.

This technique has been used in a lightning location network around Beijing and we are satisfied with it.

#### REFERENCES

- [1]. Orville, R. E. , R. W.Henderson, and L.F.Bosart, An east coast lightning direction finder network, Bull.Am.Meteorol.Soc., 64, 1029-1037, 1983.
- [2]. Horner, F. , The accuracy of the location of sources of atmospherics by radio direction finding, Proc.IEEE.Radio Sect., 101, 383-390, 1954.
- [3]. Gething, P. J. D., Radio Direction Finding and the Resolution of Multi-component wave fields. 329pp., Peter Peregrinus. England, 1978.
- [4]. Hiscox, W.L., et al, A systematic method for identifying and correcting "site errors" in a network for magnetic direction finders, Presented on 1984, 26-28.
- [5]. Mach, D. M ., D.R.MacGorman, W.D.Rust, and R.T.Arnold. Site errors and detection efficiency in a magnetic direction-finder network for locating lightning strikes to ground. J.Atmos.Oceanic Technol., 3, 67-74. 1986.
- [6]. Orville, R. E., Jr., An analytical solution on obtain the optimum source location using multiple direction finders on a spherical surface, J.G.R., 1987. Vol, 92, No.D9, 10877-10886.
- [7]. Goodman, S.T., Optimization methods for locating lightning flashes using magnetic direction finding network, AIAA Aerospace Sciences meeting, Reno NV, Jan, 1989, 9-12.

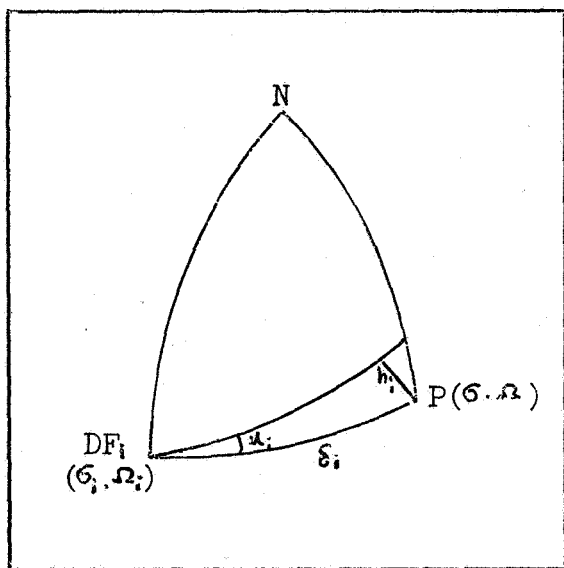


Fig. 1. Spherical sketch geometry for optimum flash location.

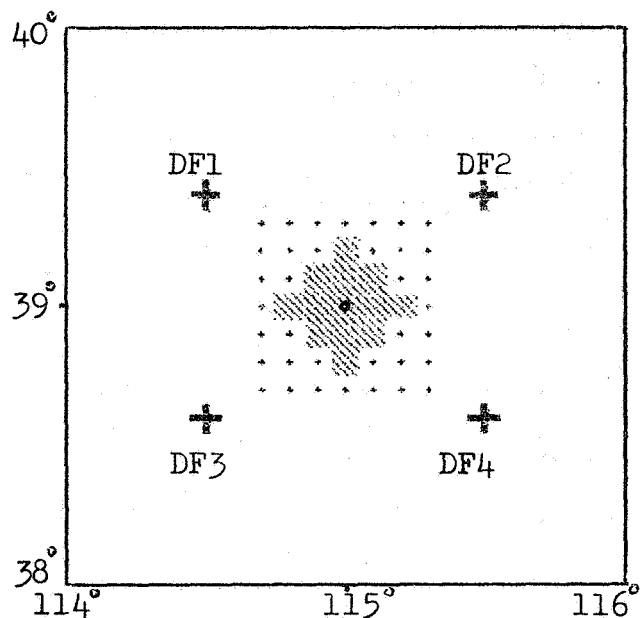


Fig. 2. Simulation results with 0.6KM location accuracy. Shadow represents the area using symmetric technique, dots are the expended area by iterative method.

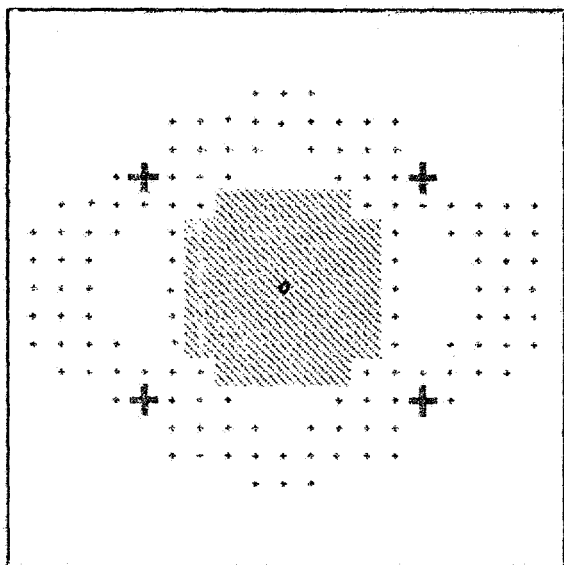


Fig. 3. Same as Fig. 2, but with 0.7KM location accuracy.

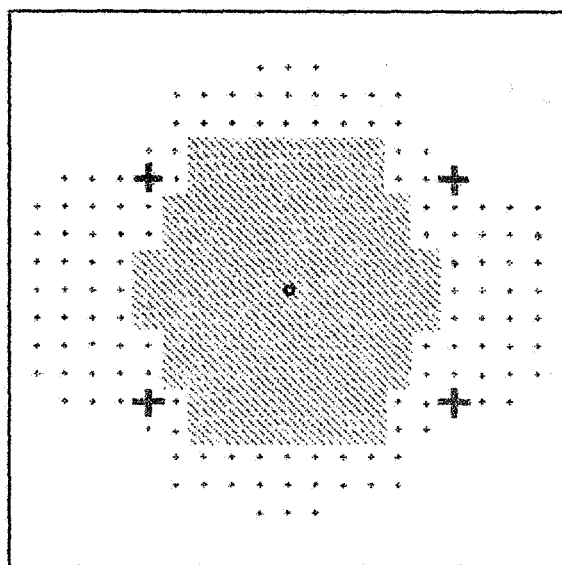


Fig. 4. Same as Fig. 2, but with 0.8KM location accuracy.

Table I. Comparison of the source-centre distance by using different calculation methods.

Source Number	Calculation Method					
	True	Symmetric	Iterative			
			1st	2ed	3rd	4th
1	127.49	128.27	127.50	127.49	127.49	127.49
2	99.78	100.11	99.78	99.79	99.78	99.78
3	124.77	124.67	124.77	124.77	124.77	124.77
4	78.61	78.65	78.61	78.61	78.61	78.61
5	0.60	0.59	0.59	0.60	0.60	0.60
6	77.48	76.99	77.48	77.48	77.48	77.48
7	128.55	129.05	128.55	128.56	128.55	128.55
8	99.79	100.11	99.79	99.79	99.79	99.79
9	125.02	125.14	125.02	125.02	125.03	125.03
10	33.66	33.63	33.66	33.66	33.66	33.66

**Session 13B, Friday 8:00**  
**Lightning Phenomenology**  
**Meteorological Relationships 2**  
**Pitts, Chairman**



COMPARISON OF LIGHTNING LOCATION DATA AND  
POLARISATION RADAR OBSERVATIONS OF CLOUDSA J Illingworth\* and M I Lees<sup>†</sup><sup>\*</sup>Dept. of Physics, UMIST, Manchester M60 1QD, UK<sup>†</sup>Electricity Research and Development Centre,  
Capenhurst, Chester CH1 6ES, UK

## ABSTRACT

Simultaneous observations of both the precipitation and the lightning associated with thunderstorms show that the lightning is within 3km of the maximum precipitation echo. The intensity and type of the precipitation is observed with 500m spatial accuracy using an S-band polarisation radar and the position of lightning is inferred from a low frequency magnetic direction finding location system. Empirical adjustments to the angles using the redundancy of the lightning data reduce this error. Radar echoes above 45dBZ may be caused by soft hail or hailstones, but similarly intense echoes may result from melting snow. Our data show that a new polarisation radar parameter, the linear depolarisation ratio, can distinguish between soft hail and melting snow, and that the intense radar echoes associated with melting snow pose no threat of lightning. A lightning risk only exists when the radar indicates that the clouds contain soft hail or hailstones.

## 1. INTRODUCTION

In this paper we examine the accuracy of a lightning location system by comparison with radar data, and examine how a new polarisation radar parameter can identify those clouds which contain soft hail or hailstones and pose a risk of lightning before natural lightning has occurred. In Section 2 we describe the Chilbolton polarisation radar. A brief description of the lightning location system is provided in Section 3. The lightning location system operates 24 hours a day, and aims to record every flash to ground over England, but the radar is a research instrument which can scan only slowly and is not operated continuously. In Section 4 we present the results from case studies on different days and discuss the results in Section 5.

## 2. CHILBOLTON RADAR

The Chilbolton radar (1) situated in Hampshire, operates at S-band (10cm) and, with a 25m dish, has a beamwidth of only a quarter of a degree. The conventional radar reflectivity,  $Z$ , is proportional to  $ND^6$ , where  $N$  is the concentration of particles of diameter  $D$ , summed over all sizes.  $Z$  is usually expressed in units of dB relative to the signal from a 1mm raindrop per cubic meter. The reflectivity of a raindrop is 7dB higher than the equivalent mass of ice, but from  $Z$  alone it is not possible to distinguish rain from ice. Neither can  $Z$  be used to differentiate between the various forms of frozen hydrometeors (snow, soft hail, hailstones etc).

The linear depolarisation ratio, LDR, is a new parameter which is a measure of the fall mode of the precipitation particles. It appears to be an excellent indicator of wet ice and can identify regions of cloud containing soft hail. LDR is defined as:

$$\text{LDR} = 10 \log(\text{ZVH}/\text{ZH}) \quad (1)$$

where ZVH is the (horizontal) cross-polar return from a vertically polarised transmitted pulse, and ZH is the conventional reflectivity (the co-polar, horizontal, return for horizontally polarised transmission).

A cross-polar return occurs only when oblate hydrometeors fall with their major or minor axis at an angle to the vertical. The highest values of LDR are found at the melting level and are associated with particles which are wet, oblate and tumbling (2). Simultaneous in-situ aircraft measurements of particle shapes and LDR measurements have confirmed (3) two distinct regimes for LDR:

- i) An LDR of about -15dB indicates melting snowflakes (low density aggregates of crystals with a mean axial ratio of about 0.5).
- ii) LDR values of about -24dB are associated with melting soft hail, which is much more spherical than melting snow.

Radar data taken when the aircraft was struck by lightning as it penetrated a cloud confirmed the above description (4). The lightning occurred when the LDR indicated soft hail and not in the regions where the radar suggested the presence of snow. An LDR of -20dB seems a reasonable criterion to separate the two types of precipitation particles.

### 3. THE ERDC LIGHTNING LOCATION SYSTEM

The lightning location system operated by the Electricity Research and Development Centre is described in more detail by Scott (5) and Lees (6). It is a magnetic direction finding system operating at 1kHz with a bandwidth of 350Hz. Five stations are available with a typical separation of 300km, but for most of the data in this paper three stations were used, each being about 200km from the radar. The error of the fix was estimated from the scatter of the three intersections of the three direction vectors. In 1988 the accuracy of the directions angles was limited by the precision of the coil alignments. In 1990 the redundancy of the data was used to make empirical adjustments to the direction angles so that the fixes were more consistent (6). These improved bearings are used for the locations reported in this paper.

### 4. CASE STUDIES

We shall consider data gathered on five different days. On 15 May 1988 a small isolated shower was observed for three hours; during this time it gave 24 flashes, the only ones detected over the UK on this day. On 10 May 90 a rather larger sheared cloud gave four flashes. This contrasts with 11 June 1990 where a much more intense echo gave no lightning, the radar indicating that the high Z was caused by melting snow. Four flashes were observed on 24 September, one from a very small isolated storm of low Z. Finally, on 15 October 150 discharges were observed in 40 minutes; the discharges were associated with a high Z region containing soft hail, whereas no lightning was observed from an intense echo 40km away which did not contain soft hail.

#### 4.1 15 May 1988

An isolated shower was observed for three hours during which time it steadily moved 100km in a westerly direction. There were three periods of electrical activity: 1251-1309 (ten flashes); 1334-1356 (six flashes); and 1551-1557 (eight flashes). All times are GMT. Figure 1 shows part of a radar PPI (scan in azimuth at low and constant elevation) taken at 1309. The scales indicate North-South and East-West distance from the radar and the superposed numbers are the minute of the flash, starting at 1253 and finishing at 1307. For simplicity three Z contours are shown; 10dBZ to outline the extent of the precipitation, 30dB, and 45dBZ. Using an empirical relationship of the form  $Z = 284R^{1.47}$ , these Z values are equivalent to a rain rate (R) of about 0.1, 2.5 and 25mm/hr respectively. Melting snow has a very high radar reflectivity ('the bright band'), in which case rain rates calculated from Z may be overestimated by up to a factor of six.

The errors quoted for the lightning fixes in Figure 1 are about 1km; the actual locations of these flashes seem to be about 3km N of the very localised 45dBZ echo (extent only 2km by 2km). If we consider that the echo was probably 8km further west at 1253, then the locations are within 3km of the 30dBZ echo. The PPI at 1251 confirms this. A similar proximity to the echo maximum is apparent for the 1334-1356 period.

Figure 2 is a radar scan at 1556 during the third period of lightning which lasted from 1551-1557. The 45dBZ echo is still 15km N of Chilbolton, but in the two hours since Figure 1 has moved 100km to be between 20 and 25km west of Chilbolton. During the period of the lightning it would have moved westwards by less than 3km. The computed errors for these eight flashes are typically 2km, and the Figure shows that the fixes are within 3km of the 45dBZ maximum echo. The two flashes which are rather further distant (1556) have a quoted error of 2.8km. These results indicate that the accuracy of these lightning fixes is approaching 3km.

Implicit in the above argument is the assumption that the lightning strike to ground must be coincident with the regions of highest reflectivity. It is known, for example, that lightning can occur from anvils, and there is some evidence that lightning rates are lower in regions of the very highest reflectivity which probably contain large hail. Figure 3 displays an RHI (vertical section) of Z and LDR through maximum echo in Figure 2. It is typical for the data on this day. There is no anvil, and the LDR at the melting layer (2km altitude) is about -24dB. This indicates that the clouds contained soft hail, but not large hail which would have taken a longer time to melt and given these values of LDR all the way to the ground. Note that the cross-polar power is less than the co-polar, and so when Z is low the cross-polar power falls below the radar sensitivity and is not plotted in the Figure. The value of LDR in the rain and the dry ice in Figure 3 is -32dB (the antenna limit). The low altitude echo from 10 to 20km range is ground clutter.

#### 4.2 10 May 1990

Four flashes were observed with coincident radar data. On this day the clouds were sheared with anvils and LDR indicated regions of both snow and soft hail. The best coincident data is shown in the RHI in Figure 4 taken at 1220.41 and an azimuth of 223°. The lightning at 1221.24 was located at an azimuth of 222.3° and a range of 34.1km (error 300m). Although the maximum

Tape 8134 Raster 89 Scan 1 On 15 May 88 At 13:09:52  
Elevation 0.98deg SC 4(C)

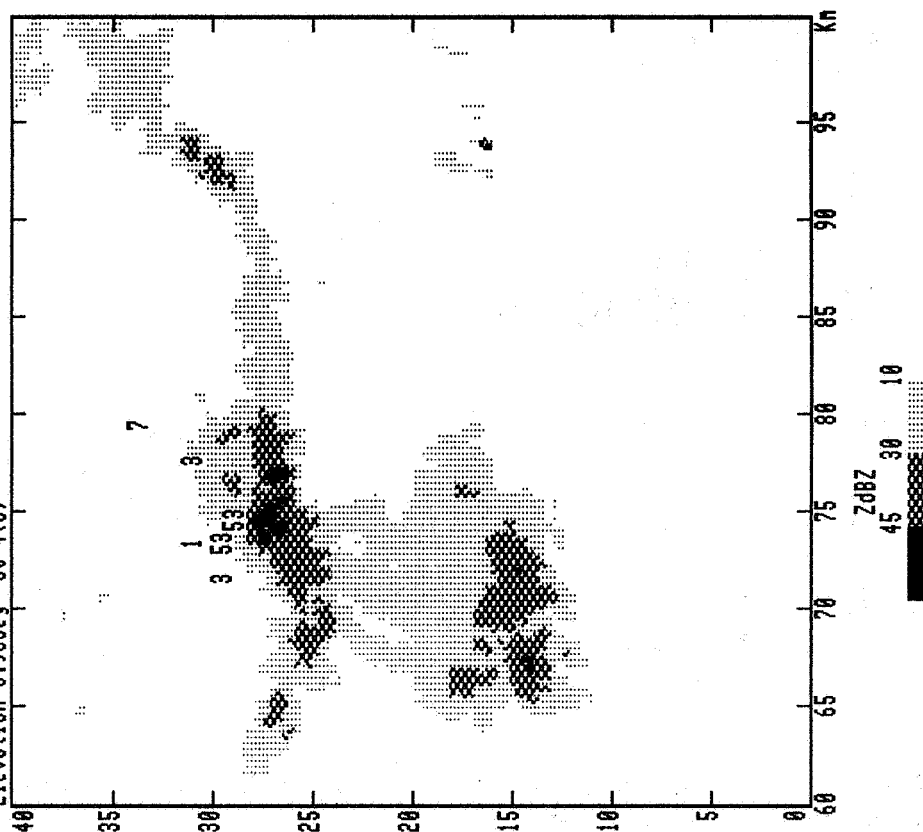


Figure 1. A PPI of the radar reflectivity on 15 May 1988 at 1309. The axes mark the distances in km from the radar (E-W and N-S). The position of the lightning flashes is indicated by the superimposed digits, with the number indicating the time in minutes.

Tape 8136 Raster 61 Scan 1 On 15 May 88 At 15:56:11  
Elevation 2.72deg SC 4(C)

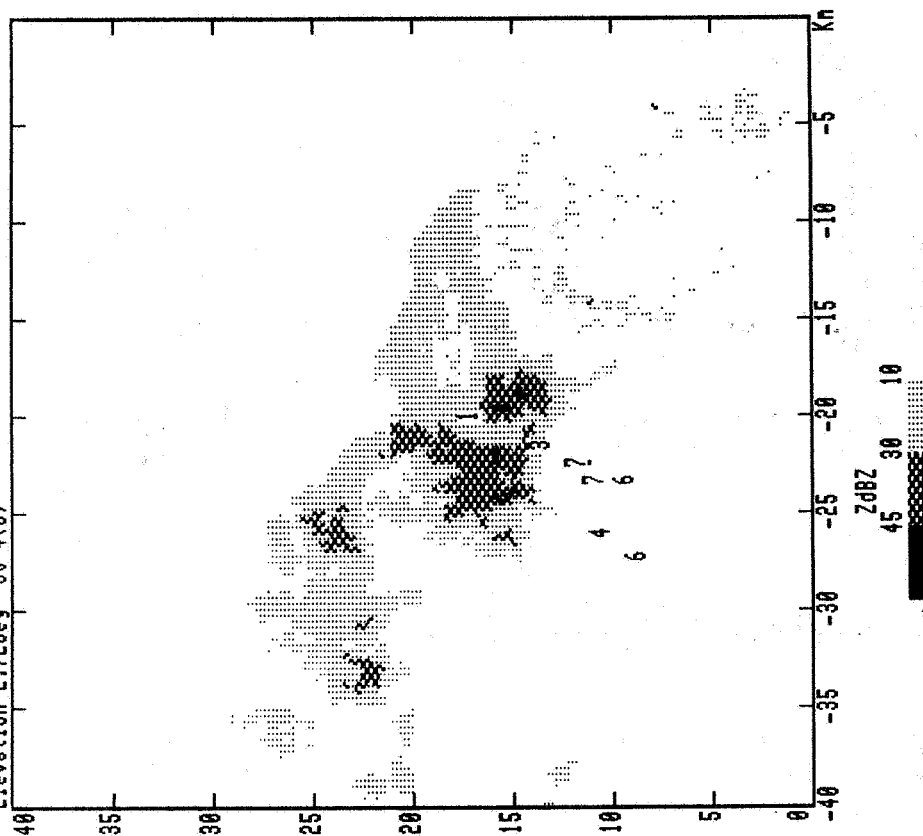


Figure 2. As for Figure 1 but at 1556, with the superimposed digits indicating the lightning position and time in minutes between 1551 and 1557. Computed errors 2km, but 2.8km for the 1556 fixes.

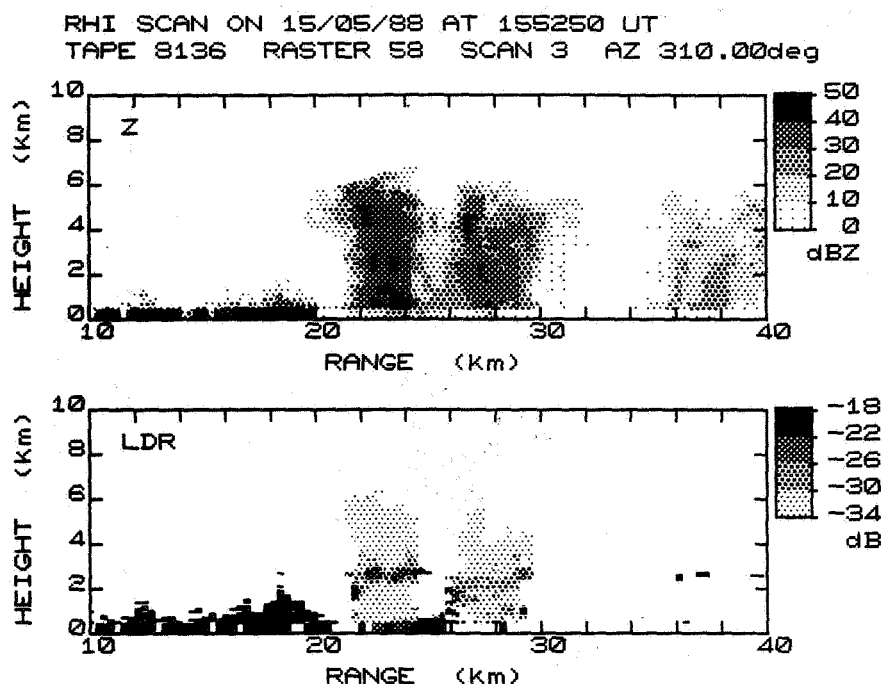


Figure 3. An RHI of the reflectivity, Z, and the linear depolarisation ratio, LDR, taken through the cloud in Figure 2. LDR of -24dB at the melting level indicates melting soft hail. The low level echo from 10 to 20km is ground clutter.

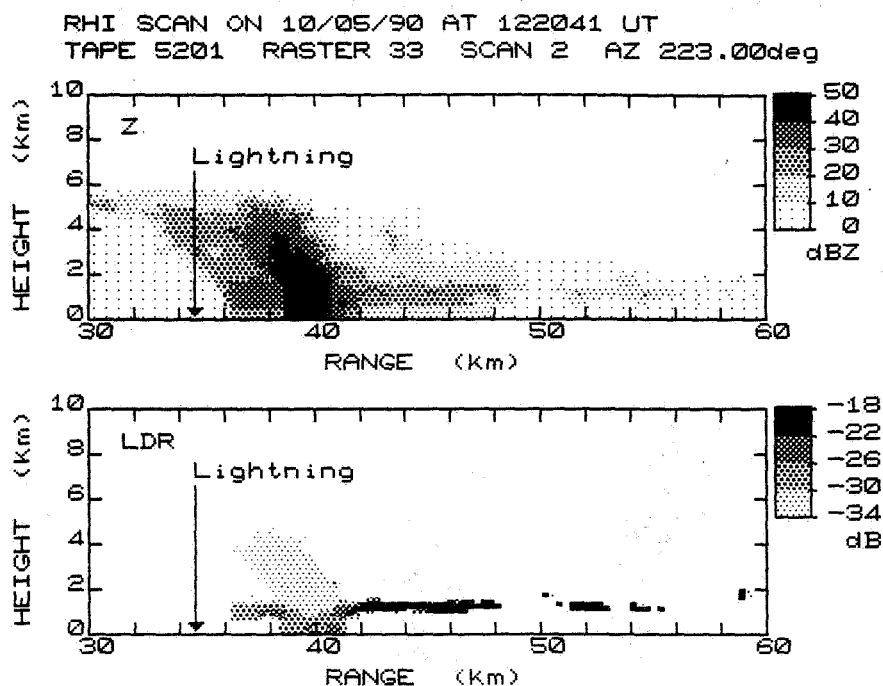


Figure 4. An RHI in Z and LDR obtained on 10 May 1990. The position of the lightning is shown by an arrow; there are indications that this was a positive discharge LDR indicates the presence of graupel at ranges 36 to 41km range.

echo is at 39km range, at 34km range there is an arvil type echo at 4km height with a Z above 30dBZ. The lightning fix waveforms indicate that this discharge had positive polarity.

The LDR data in Figure 4 provide additional information. Note the melting layer at 1km altitude signifies graupel from 36km to 41km range but snow at greater ranges. Other RHIs show that the bright band values due to melting snow exceeded 45dBZ. The sloping region of LDR -32dB (the antenna limit) at altitudes from 1 to 4km is due to dry graupel; because the Z value is so high the cross-polar return is still detectable even though it is 32dB down.

#### 4.3 11 June 1990

The PPI shown in Figure 5 shows a much larger region of high Z than on any of the cases discussed so far, yet on this day the closest lightning was 100km due south of the radar, about 140km distant from the echo in the Figure. The echo in Figure 5 appears to be that of a vigorous shower, Z exceeds 30dBZ over an area about 20km by 20km, with a central region 10km by 3km where Z is above 45dBZ; 40km away from the central region the echo is below the 10dBZ limit. However the LDR data in Figure 6 reveal that the LDR values are above -20dB and that the precipitation is thus in the form of low density half melted snowflakes. An RHI through this cloud confirms the existence of a distinct bright band. Actual rain rates at the ground are much lower than these values of Z would suggest.

It is often thought that stratiform rain is uniform, and that the bright bands can be recognised as concentric rings of enhanced reflectivity whose range depends on the elevation of the PPI. Such rings are occasionally visible in very light widespread rain, but this is unusual, rainfall fields are usually vary variable in space. It is our experience in the UK that most areas with Z above 45dBZ are in fact melting snow.

#### 4.4 24 September 1990

Four coincident radar and lightning fixes were achieved on this day. On the first two occasions the fixes occurred where the echo structure was ill defined with no definite localised maximum and for the third flash the radar and lightning data were separated by eight minutes. The location of the fourth flash is shown in Figure 7; it is an isolated echo contains only a few range gates where Z exceeds 30dBZ. During its lifetime this cell produced only one flash; it occurred one minute after the radar scan with a quoted error of 1.6km and was within 1km of the maximum echo. This cell was never very intense, but 10 minutes earlier the 30dBZ echo had an area of about 1km<sup>2</sup>. The LDR data showed that this small echo contained soft hail.

#### 4.5 15 October 1990

Over 150 coincident lightning locations and fixes were achieved on this day within the space of just 40 minutes. An example is given in Figure 8 which displays the nine fixes within one period of 700msec. LDR shows that the high Z is due to soft hail. It appears that this was a complex flash with strokes to ground at different positions. It is encouraging to note how seven of the fixes are centred on a Z region above 45dBZ and fall within the 30dBZ contour. This day was of particular interest because the lightning producing echo was embedded in a large area of high Z as shown in Figure 9 which displays the Z and LDR data and superimposed lightning data over a 50° PPI sector to a range of 150km. The lightning is associated with the high Z

Tape 5211 Raster 15 Scan 4 On 11 Jun 90 At 13:24:36  
Elevation 0.43deg SC 4(C)

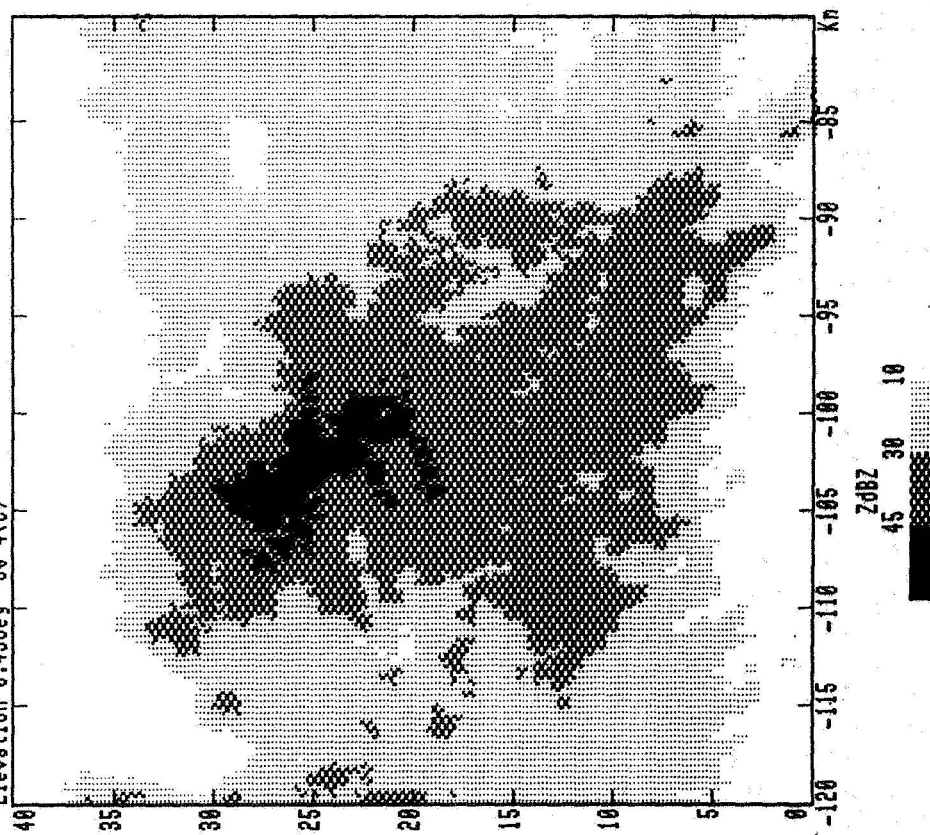


Figure 5. A PPI of the reflectivity on 11 June 1990. No lightning was observed.

Tape 5211 Raster 15 Scan 4 On 11 Jun 90 At 13:24:36  
Elevation 0.43deg SC 4(C)

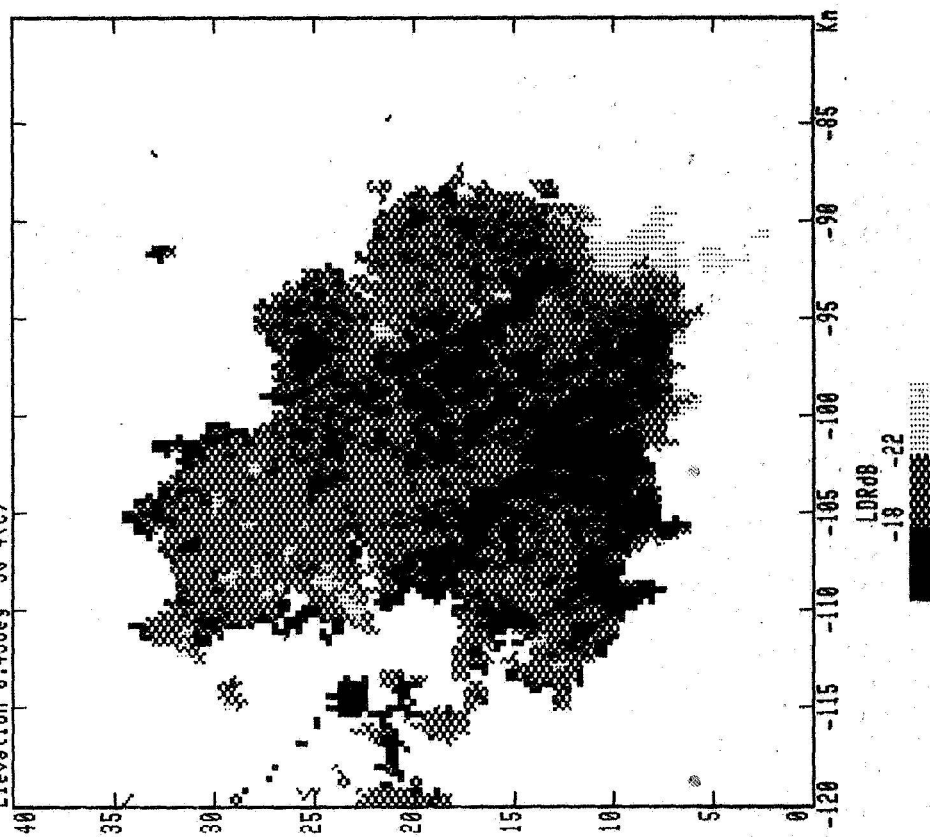


Figure 6. Values of LDR indicating melting snow for the PPI in Figure 4.

Tape 5223 Raster 14 Scan 1 On 24 Sep 90 At 14:44:21  
Elevation 0.92deg Sc 4(C)

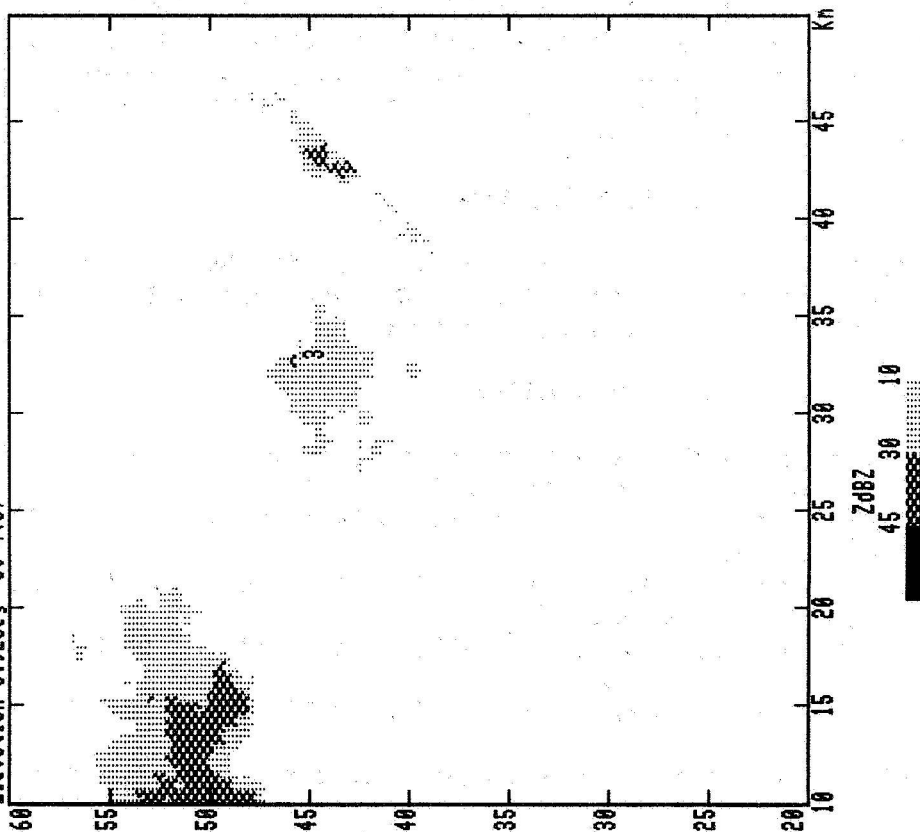


Figure 7. 24 September 1990. Radar echo which produced a single lightning flash at 1443.

Tape 5227 Raster 9 Scan 6 On 15 Oct 90 At 16:36:46  
Elevation 1.62deg Sc 4(C)

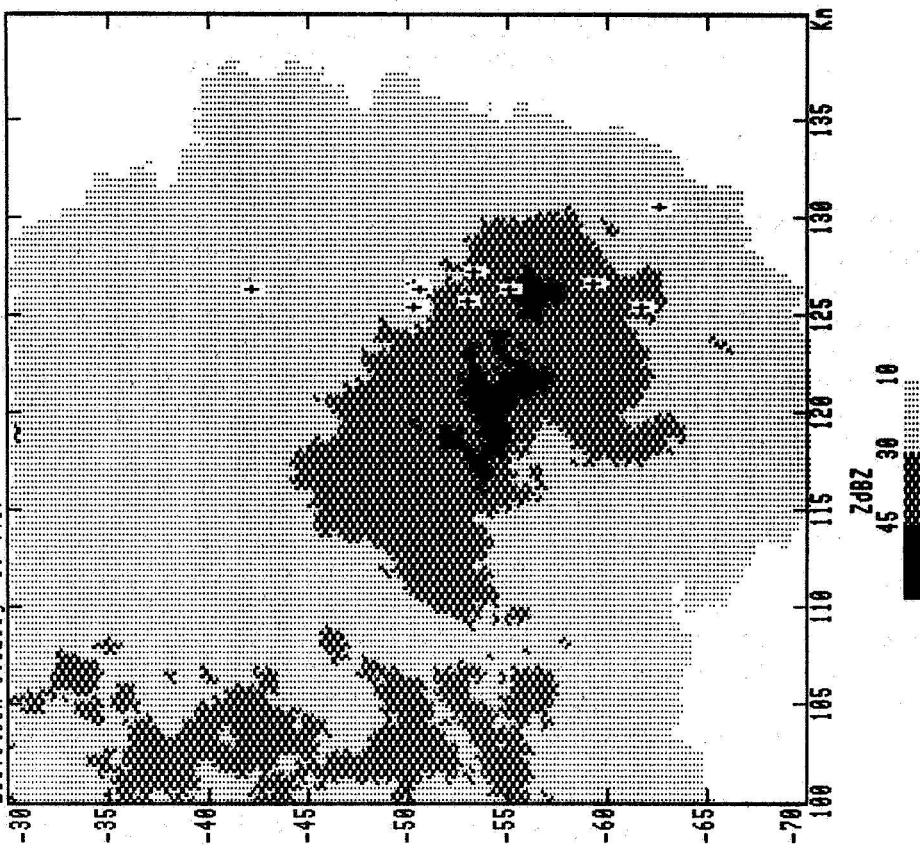


Figure 8. 15 October 1991. Radar reflectivity and nine lightning fixes (+) during a 700ms period; probably individual strokes of a single flash.



regions at ranges of 90 to 140km which contain soft hail, but there is no lightning in the high Z region at about 60km range where there is melting snow.

## 5. DISCUSSIONS AND CONCLUSIONS

The exact mechanism by which thunderstorms become electrified is still a matter of some debate (7). The findings presented here demonstrate that the lightning is associated with the presence of soft hail and lend support to the theory that charge separation occurs when ice crystals collide with and separate from small hail pellets. The absolute value of reflectivity is not crucial, occasional lightning being observed with maximum values below 45dBZ, whereas much more intense and extensive echoes which are not associated with hail pellets produce no lightning at all.

The presence of soft hail as revealed by the LDR radar signature appears to be a necessary condition for lightning, but small showers with soft hail are observed which fail to give lightning. However, we can assume that some charge separation is occurring in such clouds, and though the field is not sufficient for natural lightning, the presence of an aircraft may be sufficient to enhance the field to trigger a discharge. In the UK a much more common occurrence is to have more intense echoes but no soft hail present, and on these occasions there would not appear to be any risk of triggered lightning.

Comparisons of the lighting fixes with the coincident reflectivity patterns suggest that a very high accuracy is being achieved. For such comparison the ideal echoes should be of very limited spatial extent, moving slowly and with no shear. In such circumstances the data are unambiguous and it appears that, although the locating stations are 200km distant, the locations are correct to better than 3km. Agreement of 1km has been observed from data taken under these circumstances in 1990.

## 6. ACKNOWLEDGEMENTS

This work was made possible with a grant from USAF SPC-90-4005 and NERC GR3/5896. John Goddard at RAL implemented the LDR technique. We thank him and the staff at Chilbolton for their help in this project.

## 7. REFERENCES

1. Cherry S M and Goddard J W F (1982) URSI Symposium on Multiple Parameter Radar Measurement of Precipitation, Bournemouth UK, 49-54.
2. Illingworth A J and Caylor I J (1989) Preprints 24th Radar Meteorol Conf, Amer Meteor Soc, Boston, 323-327.
3. Frost I R, Goddard J W F and Illingworth A J (1991) Preprints 25th Radar Meteorol Conf, Amer Meteor Soc, Boston.
4. Frost I R, Illingworth A J and Caylor I J (1989) Int Conf on Lightning and Static Electricity, Bath, UK, 1A.1.1-8.
5. Scott L (1988) Int Conf on Lightning and Static Electricity, Oklahoma City, USA, 391-395.
6. Lees M (1991) Int Conf on Lightning and Static Electricity, Cocoa Beach, Florida, USA.
7. Illingworth A J (1985) J Geophys Res, 90, 6041-6046.

Tape 5227 Raster 9 Scan 6 On 15 Oct 90 At 16:36:46  
 Elevation 1.62deg Central Az 110.00deg  
 SG 4(C) LDR Trigger Level 3.00dB

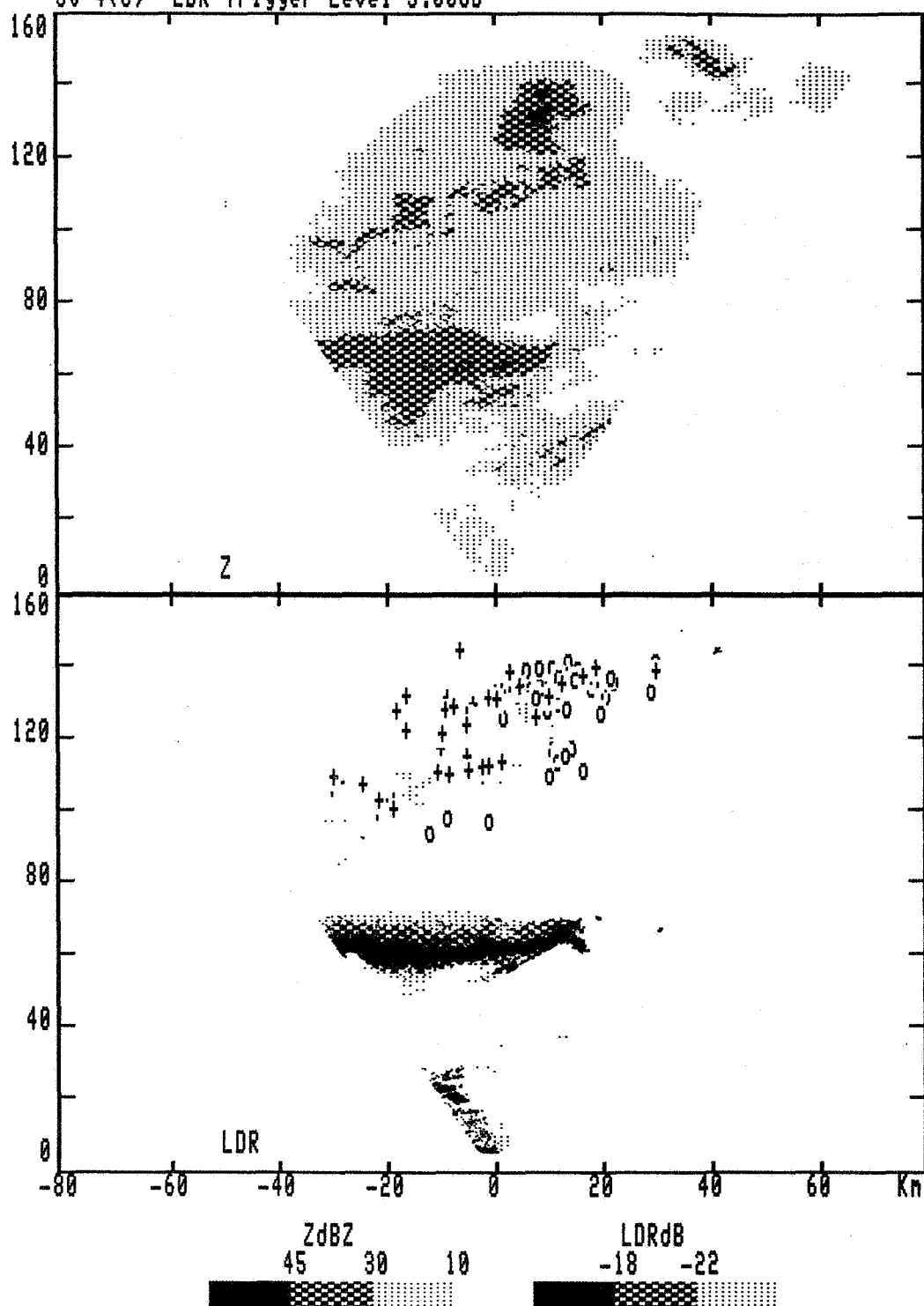


Figure 9. 15 October 1991. PPI of Z and LDR over a 50° sector. Lightning is restricted to areas where LDR indicates soft hail.

Lightning fixes: O, 1630-1639; +, 1640-1649.

# THE SPATIAL VARIATIONS OF LIGHTNING DURING SMALL FLORIDA THUNDERSTORMS

Timothy D. Oram and E. Philip Krider  
Institute of Atmospheric Physics  
University of Arizona  
Tucson, Arizona 85721

## ABSTRACT

Networks of field mills (FMs) and lightning direction finders (LDFs) have been used to locate lightning over the NASA Kennedy Space Center (KSC) on three storm days. Over 90 percent of all cloud-to-ground (CG) flashes that were detected by the LDFs in the study area were also detected by the FM network. 27 percent of the FM lightning events were correlated with CG flashes detected by the LDFs. About 17 percent of the FM CG events could be fitted to either a monopole or a dipole charge model. These projected FM charge locations are compared to LDF locations, i.e. the ground strike points. We find that 95% of the LDF points are within 12 km of the FM charge, 75% are within 8 km, and 50% are within 4 km. For a storm on July 22, 1988, there was a systematic 5.6 km shift between the FM charge centers and the LDF strike points that might have been caused by the meteorological structure of the storm.

## INTRODUCTION

The forecasting and detection of atmospheric electrical hazards at the USAF Eastern Space and Missile Center (ESMC) and the NASA Kennedy Space Center (KSC) are critical for safe launch and ground operations. Following the Apollo 12 incident in which the Saturn V rocket was struck twice by lightning, the USAF and NASA installed a network of field mills to measure cloud electric fields near the launch complexes. The field mill network can also be used to detect and locate lightning [1]. Also, a network of gated, wideband magnetic direction finders, manufactured by Lightning Location and Protection, Inc. (LLP), is used to locate CG lightning [2,3] in the ESMC-KSC area. These sensors respond to the magnetic fields produced by the return strokes in negative CG lightning, and they do not respond to cloud discharges. USAF and NASA launch criteria currently state that vehicles may not be launched if a 1 minute average of the absolute value of the cloud electric field exceeds 1000 Volts per meter within 5 nm (9.25 km) of the launch site within 15 minutes prior to launch. In addition, a launch cannot take place if lightning is detected within 10 nm (18.5 km) of the launch complex [4].

Several authors [5-8] have described methods of determining lightning charge locations using the field mill network. It is usually assumed that the spatial pattern of the abrupt field changes that are due to lightning can be described by either a monopole or dipole charge model. The monopole or point-charge model is thought to be the best description of CG lightning, while the dipole describes intra-cloud lightning [6]. In our analyses, we have tried both models on each lightning event, and we have systematically varied the parameters of these models until we have an optimum description of the measured field changes. We measure "the goodness of fit" using a standard chi-square function,

$$\chi^2 = \frac{1}{N_f} \sum \frac{(E_i - E_{mi})^2}{\sigma_i^2}$$

where  $N_f$  is the number of degrees of freedom (number of measurements minus the number of model parameters),  $E_i$  is the measured field change,  $E_{mi}$  is the modeled field change, and  $\sigma_i$  is the random error expected in the measurement at site  $i$ .

Several authors have tested the general accuracy of the FM locations by comparing them to visible lightning channels, television records or thunder measurements [5,9,10]. To the best of our knowledge, no one has yet

compared the FM locations of CG lightning to the LDF locations. Obviously, a study such as this might have important consequences for the evaluation of launch constraints and the methods that are used to detect and locate lightning and to measure lightning distances.

In the following, we will describe the sources of our data, the analysis procedures, and our attempts to estimate the errors in the locations. The effectiveness of the two detection systems will be discussed, and then we will give preliminary results on the spatial variations of the FM charge centers and the LDF ground strike points.

## DATA AND ANALYSIS PROCEDURES

**GROUND STRIKE LOCATIONS:** The LDF network computes the locations of the ground strike points from the intersection of magnetic direction vectors. The sensors are located at the Melbourne Regional Airport (DF #1), located about 70 km south of the rocket triggered lightning site (see Figure 1), the Orlando International Airport (DF #2), about 70 km west, and DF #3, about 2 km south of the rocket triggered lightning site. The measured angles are subject to both random and systematic or "site" errors. The systematic errors can be estimated and corrected using a procedure discussed by Hiscox et al. [11] and Lopez and Passi [12]. In order to estimate the true location, a site correction factor is applied to each LDF. The intersection of the corrected angles then gives the location of the ground strike point. When all three LDFs detect a flash, an "error triangle" may be formed from the intersections of three vectors.

In order to verify that we have derived the proper site correction factors, we have examined the locations of rocket-triggered flashes that were produced in the KSC Rocket Triggered Lightning Program. The dates, times, location, and position differences for these events are summarized in Table I. Note that for LDFs 1 and 2, the measured angles are all within the 1 degree random error that we expect in an LDF, that the East-West (X) components of the location errors are typically 0.5 km, and that the errors in the North-South (Y) components are less than 2.0 km. Rocket-triggered events almost always cause LDF 3 to over-range, so the location of these events are determined just by the intersections of LDFs 1 and 2. We expect that the rather large Y errors are caused by the large baseline distance from the RTL site to DF 2 (Orlando).

TABLE I: ROCKET TRIGGERED LIGHTNING EVENTS

DATE	TIME	A N G L E S			ERRORS (km)	
		DF 1	DF 2	DF 3	$\Delta X$	$\Delta Y$
IDEAL		352.2	64.4	355.2	0.	0.
7/25/88	21:18:52	351.6	65.7	NA	-0.4	-2.2
8/20/88	21:38:25	351.9	64.6	(344)	-0.2	-0.7
8/20/88	21:51:43	351.6	64.7	(0.4)	-0.5	-1.0
8/22/88	21:37:33	351.8	65.5	(233)	-0.2	-1.9
8/25/88	16:08:19	352.6	65.4	(356)	0.7	-1.3

**ELECTRIC FIELD:** The field mill sensors and sites have been described previously by Jacobson and Krider [5]. During 1988, the locations of the FM sites were as shown in Figure 1. (Note: The field mills are numbered from 1 to 34, but mills 3, 24 and 31 were not in service during 1988.) The electric field was digitized with 30 V/m resolution over a dynamic range that went from -15 kV/m to 15 kV/m. The field values were recorded at about 5 samples per second together with the hour, minute and second of the observation. For those events where only four samples were taken in a 1 second period, the value of the fourth measurement in the second was used for the fifth so as to "pad" the data.

The analysis procedure began by using an interactive program to identify the approximate time of each lightning discharge from simultaneous, abrupt changes in the electric field. An automatic slope projection algorithm was then used to determine the initial and final field values at each FM site and the change in the electric field was

calculated. A Marquardt algorithm was then used to find the model parameters that minimized the chi-square function. The values of the model parameters at the minimum are assumed to be the optimum location and magnitude of the lightning charge or the dipole moment. Previous authors have required that there be a minimum field change value at a given number of FM sites before the flash was analyzed. Here, there was no analysis threshold except the practical limit of about 90 V/m.

The algorithm began with an initial guess for the X and Y parameters that were assumed to be the same as the X and Y location of the field mill with the largest electric field change. A search was then conducted on a 3 by 3 by 3 grid with dimensions 10 km by 10 km horizontal and 4 km vertical centered at an altitude of 8 km to improve the starting parameters. The starting charge was assumed to be 10 C for a monopole solution, and the starting vertical dipole moment was -50 C-km for a dipole solution. The Marquardt algorithm was run 27 times using the grid starting parameters for each model type, and then the solution with the lowest root mean square error was chosen as the best solution. For those FM lightning events that coincided with an LDF location, the Marquardt algorithm was re-run using the LDF location in place of the reference field mill starting location. This new ensemble of 27 solutions was then compared to the previous best and then the final best was selected. A solution was rejected if the chi-square value was significant at less than the 80 percent level or if the uncertainties in the X, Y or Z parameters were greater than 1 km.

In order to estimate the effect of random measurement errors on the model parameters, known charges were placed on a grid above the network and then the ideal field change was computed at each field mill site. A random error was then added to these field changes and the analysis algorithm run as described above. This procedure was repeated 100 times at each grid point, and then an average parameter error and standard deviation was calculated. We found that there were no significant systematic errors until the X location of the ideal charge was less than 0 km or greater than 35 km (See Figure 1). Standard deviations of the X-Y position errors were less than 1.5 km over the entire study area and were less than 1 km over most of this area.

## CASE STUDIES

JULY 21, 1988: This storm produced the most lightning in the study area. A line of thunderstorms associated with a sea-breeze convergence moved from the mainland of Florida into the study area around 1845Z (1345L). Several areas of activity developed, but most of the lightning identified by the FM network occurred in two areas. The first was to the west of FM site 18 over the Indian River between 1900Z and 1920Z. The second began near FM site 15 to the southeast of the Shuttle Landing Strip between 1920Z and 1940Z. Altogether, the FM network detected 951 lightning events between 1700Z and 1955Z when the data ended. The LDF detected 312 CG flashes in the study area in the same time interval. Of these 312 CG flashes, 279 (89%) were coincident with FM events. Of the 38 which were not detected by the FM network, 18 were within 1 second of another LDF flash and hence were probably missed by the FM analysis algorithm. We were able to derive 34 satisfactory monopole fits to the FM events and 72 dipole fits. 30 of the monopole fits coincided with an LDF event. Figure 2 shows the X-Y location of all acceptable monopole and dipole fits for 7/21/88, and Figure 3 shows the locations of all LDF events. Figure 4 shows explicitly the horizontal separation between the locations provided by each system for the coincident lightning events.

JULY 22, 1988: There were two main areas of convection on this day; the first occurred southwest of FM site 10 between 1840Z and 1900Z. Here, the FM events produced 7 dipole solutions while the LDFs located two CG strikes. The second cell developed northwest of FM site 1 between 1900Z and 1930Z, and there were 22 LDF events in this interval. There were 111 FM discharges between 1835Z and 1940Z. All of the 24 LDF flashes in the study area were coincident with a FM event. Of the 24 CG flashes, 17 fit the monopole model. One CG flash was best fit by the dipole model, and the dipole moment of this flash was nearly horizontal. Figure 5 shows a map of the locations of all acceptable monopole and dipole fits for 7/22/88. Figure 6 shows a map of the LDF events, and Figure 7 shows the horizontal separation for coincident events.

AUGUST 9, 1988: Most activity on this day was west of FM site 7, and there were 61 FM flashes between 1830Z and 2015Z. There were 20 LDF flashes in this interval and 18 were coincident with a FM event. In the

cases where the FM network did not detect a LDF flash, both were within 0.5 seconds of another LDF flash. 8 of the LDF flashes provided satisfactory FM solutions. 15 FM events fit the monopole model and 9 fit the dipole model. Figure 8 shows a plot of the locations of FM events on 8/9/88. Figure 9 shows all LDF flash locations and Figure 10 shows the horizontal separation between the coincident flashes.

## DISCUSSION

The FM network was able to detect over 90 percent (321 of 356) of the CG flashes that were detected by the LDFs on all three days. When an LDF event was missed, 20 (of 35) occurred within 1 second of another LDF event. If we assume events that occur within 1 second of each other produce a single change in the electric field, 95 percent of the CG events were detected by the FM network. This assumption is reasonable since the sampling rate of 5 samples per second may not be sufficient to resolve 2 lightning flashes within a one second period. Altogether, 28 percent of FM lightning events were coincident with a CG event detected by the LDFs. This is a reasonable fraction of CG lightning at KSC [13].

On the above three storm days, we were able to fit 56 FM solutions that were coincident with an LDF location; i.e., about 17 percent of all the CG flashes. In addition, 17 percent of all FM events could be fitted satisfactorily within the limits imposed by our acceptance criteria. The percentage of satisfactory fits varied significantly on the different days: 11 percent on July 21, 31 percent on July 22, and 43 percent on August 9.

Figure 11 shows a histogram of the differences in the horizontal distance between the projected charge center and the LDF ground strike points for these 56 flashes. Note that these differences include errors in both detections systems and that 95% of the values are within 12 km, 75% are within 8 km, and 50% within 4 km. These results are somewhat larger than the horizontal variations found by Jacobson and Krider [5], where 95% were within 8 km and 75% were within 5 km. It is interesting to note that one of the differences in this study exceeded the 18 km (10 nm) launch criteria.

The average X,Y and standard deviation (in parenthesis) of the coincident FM and LDF locations are shown in Table II for each storm day. For the July 21 storm, we are showing only the 19 flashes in the Banana River cell with X parameters between 0 and 10 km and Y parameters between 10 and 22 km. The 17 events north of FM site 1 are used for the July 22 storm, and all 8 events are used for August 9.

TABLE II: AVERAGE LOCATIONS FOR STORM DAYS

DATE	AVG X FM(km)	AVG Y FM(km)	AVG X LDF(km)	AVG Y LDF(km)	$\Delta X$ (km)	$\Delta Y$ (km)
7/21	8.4 (2.2)	17.1 (2.4)	7.8 (1.6)	19.6 (3.3)	0.6	-2.5
7/22	15.5 (1.2)	36.8 (1.1)	9.9 (3.5)	38.9 (2.1)	5.6	-2.1
8/9	6.0 (0.6)	31.8 (1.9)	6.1 (2.0)	33.4 (3.5)	-0.1	-1.6

Note that the differences in the average X and Y coordinates are about what one would expect, given the errors in the measurements and the above standard deviations, except for a 5.6 km shift in the X position on 7/22/88 (see Fig. 7). We have checked for possible systematic errors in both the LDF and FM locations in this storm region and have concluded that this shift is, in fact, real and not an artifact. Note also that the standard deviations in the FM locations are about 50 percent less than the standard deviations in the LDF locations in the small storms on July 22 and August 9.

## CONCLUSIONS

We estimate that the detection efficiency of the FM network is between 90 and 95 percent on lightning in the study area, assuming that the LDF network detects all negative CG flashes. The FM network detects many more lightning events than the LDF network because the FMs also detect intra-cloud lightning. Only 17 percent of the FM events could be modeled (monopole or dipole) using a fairly strict set of rejection criteria. This percentage varied on the three storm days and was significantly higher on days with low flashing rates. Therefore, the utility of the FM network would appear to be limited by modeling requirements rather than by its ability to detect a lightning event.

In most cases, when the FM network missed a CG discharge, it was because there were two LDF flashes within 1 second of each other, an interval that exceeded the time resolution of the FM network.

The distribution of the horizontal distances between the FM charge centers and the associated LDF locations have been summarized in Figure 11. The largest cause of these distances is undoubtedly the quasi-random 'stepped' development of the initial leader channel from the 7 or 8 km altitude of the cloud charge [8] to the ground. These distances also include a random error in each detection network that is on the order of one kilometer. The large system shift that we have noted on 7/22/88 (see Table II) may well have been caused by a preferred direction of propagation that was introduced perhaps by the meteorological structure of the storm or a preferred region in the cloud for lightning initiation. In any case, the variability shown in Fig. 11 suggests that the 10 nm (18.5 km) 'stand-off distance' in the present launch rules is indeed safe.

Since the standard deviations of the FM locations under small storms tend to be less than the LDF positions, such locations might provide a better estimate of the source of lightning in the cloud. For example, the launch criteria could possibly say 'within N nm of the lightning charge center' rather than 'within 10 nm of lightning', since the FM charge centers provide the locations of developing charge rather than where channels actually strike the ground. More data will be needed to determine what distance is optimum for a threat radius for each detection system. In the future, we plan to continue studies such as this with other meteorological information, such as the surface wind divergence and weather radar data.

## ACKNOWLEDGMENTS

The authors wish to thank Detachment 11, 2WS, NOAA/NSSL (Ron Holle, Raul Lopez and Irv Watson) and Hal Herring of CSR for their help in gathering the field mill and LLP lightning data. They are also indebted to Bill Koshak, for his insight and helpful discussions, and to Margaret Sanderson Rae, for editing and preparation of the final manuscript.

## REFERENCES

1. Christian, H. J., V. Mazur, B. D. Fisher, L. H. Ruhnke, K. Crouch, and R. P. Perola. 'The Atlas/Centaur Lightning Strike Incident.' Journal of Geophysical Research, Vol. 94, 13169-13177, 1989.
2. Krider, E. P., R. C. Noggle and M. A. Uman. 'A Gated Wideband Magnetic Direction Finder for Lightning Return Strokes.' Journal of Applied Meteorology, Vol. 15, 301-306, 1976.
3. Krider, E. P., R. C. Noggle, A. E. Pifer and D. L. Vance. 'Lightning Direction-Finding Systems for Forest-Fire Detection.' Bulletin of the American Meteorological Society, Vol. 61, 980-986, 1980.
4. 'Shuttle Launch Commit Criteria and Background.' JSC-16007 (Preliminary). July, 1988.
5. Jacobson, E. A. and E. P. Krider. 'Electrostatic Field Changes Produced by Florida Lightning.' Journal of the Atmospheric Sciences, Vol. 33, 103-107, 1976.

6. Maier, L. M. and E. P. Krider. 'The Charges That are Deposited by Cloud-to-Ground Lightning in Florida.' Journal of Geophysical Research, Vol. 91, 13275-13289, 1986.
7. Koshak, W. and E. P. Krider. 'An Analysis of Field Changes During Active Florida Thunderstorms.' Journal of Geophysical Research, Vol. 94, 1165-1186, 1989.
8. Krider, E. P. 'Electric Field Changes and Cloud Electrical Structure.' Journal of Geophysical Research, Vol. 94, 13145-13149, 1989.
9. Uman, M. A., W. H. Beasley, J. A. Tiller, Y. T. Lin, E. P. Krider, C. D. Weidman, P. R. Krehbeil, M. Brook, A. A. Few, Jr., J. L. Bohannon, C. L. Lennon, H. A. Poehler, W. Jafferis, J. R. Gulick, and J. R. Nicholson. 'An Unusual Lightning Flash at Kennedy Space Center.' Science, Vol. 201, 9-16, 1978.
10. Nisbet, J. S., T. A. Barnard, G. S. Forbes, E. P. Krider, R. L. Lhermitte and C. L. Lennon. 'A Case Study of the Thunderstorm Research Project Storm of July 11, 1978: 1. Analysis of the Data Base.' Journal of Geophysical Research, Vol. 95, 5417-5433, 1990.
11. Hiscox, W. L., E. P. Krider, A. E. Pifer and M. A. Uman. "Systematic Method for Identifying and Correcting 'Site Errors' in a Network of Magnetic Direction Finders." A paper delivered at the International Aerospace and Ground Conference on Lightning and Static Electricity, Orlando, FL, 1984.
12. Passi, R. M. and R. E. Lopez. 'A Parametric Estimation of Systematic Errors in Networks of Magnetic Direction Finders.' Journal of Geophysical Research, Vol. 94, 13319-13328, 1989.
13. Livingston, J. M. and E. P. Krider. 'Electric Fields Produced by Florida Thunderstorms.' Journal of Geophysical Research, Vol. 83, 385-401, 1978.



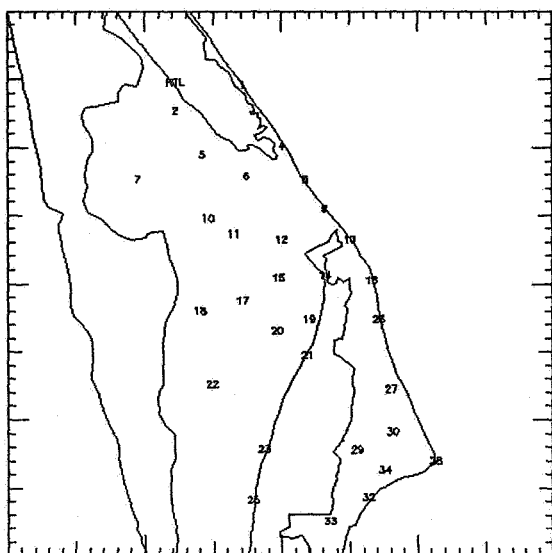


**Figure 1-** Locations of the Field Mills (1-34) and the Rocket Triggered Lightning Site in 1988. The lower left hand corner is the origin of our coordinate system. Each tick mark is 1 km.

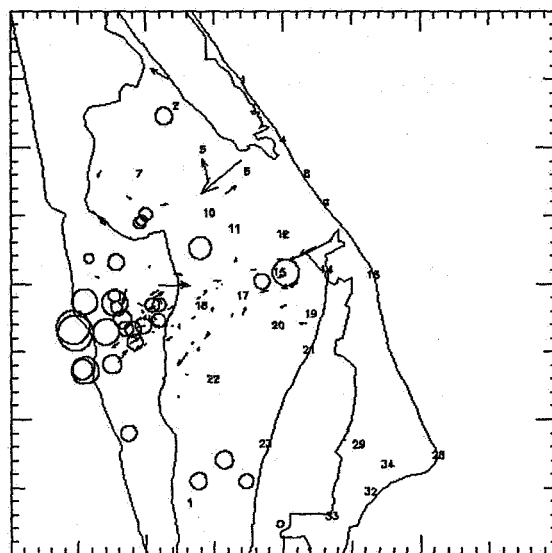


**Figure 2-** Monopole (circle) and dipole (arrow) fits for July 21, 1988. The location of FM sites with bad data are not plotted on this and similar figures.

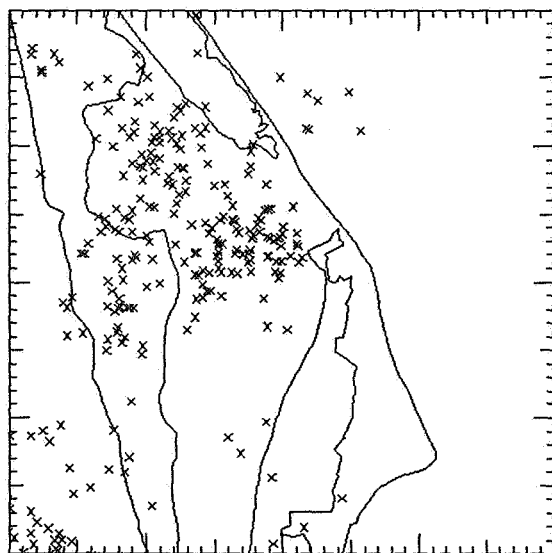


**Figure 3-** Locations of LDF lightning events for July 21, 1988.

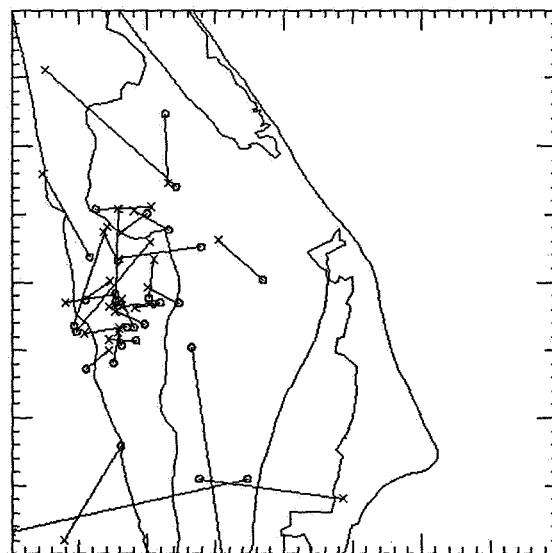


**Figure 4-** Horizontal separation between coincident FM (circle) and LDF (crosses) events for July 21, 1988.

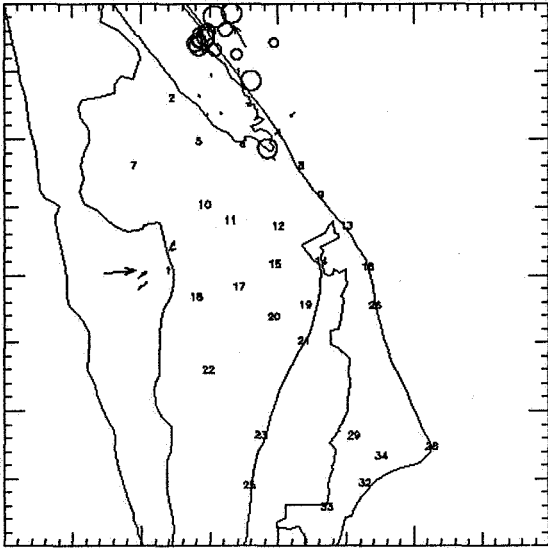


**Figure 5-** FM fits for July 22, 1988.

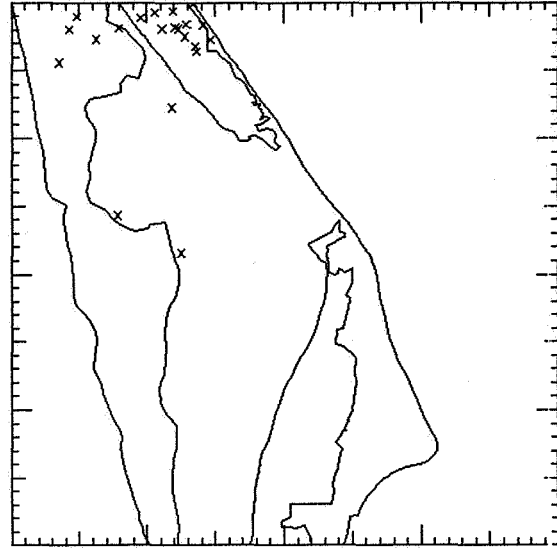


**Figure 6-** LDF flashes for July 22, 1988.

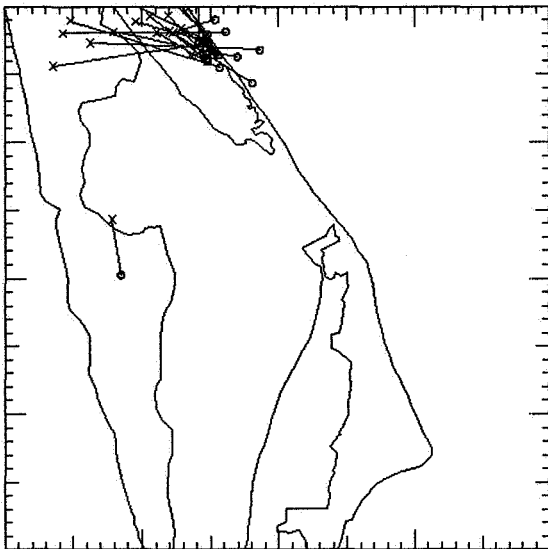


**Figure 7-** Horizontal separation between coincident FM and LDF events for July 22, 1988.

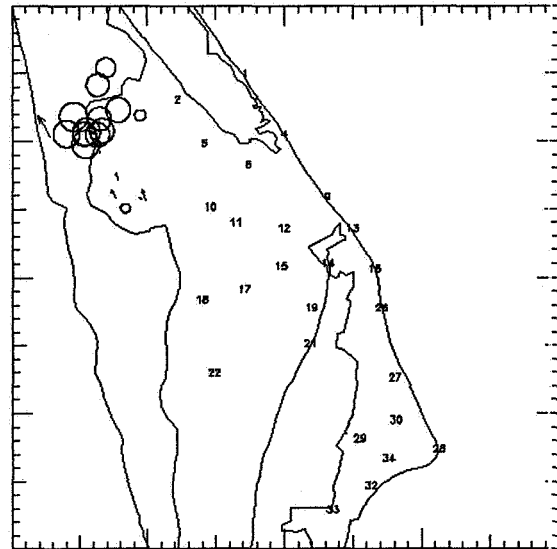


**Figure 8-** FM fits for August 9, 1988.

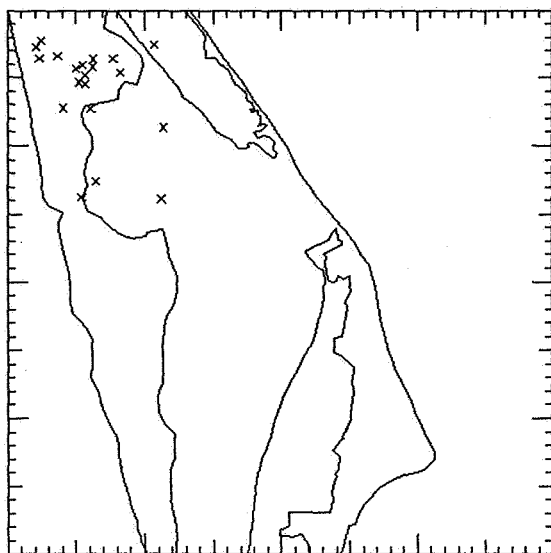


**Figure 9-** LDF lightning events for August 9, 1988.

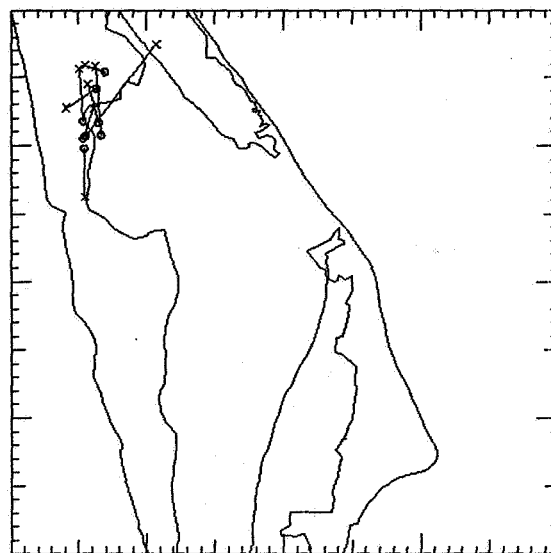


**Figure 10-** Horizontal separation between coincident FM and LDF flashes.

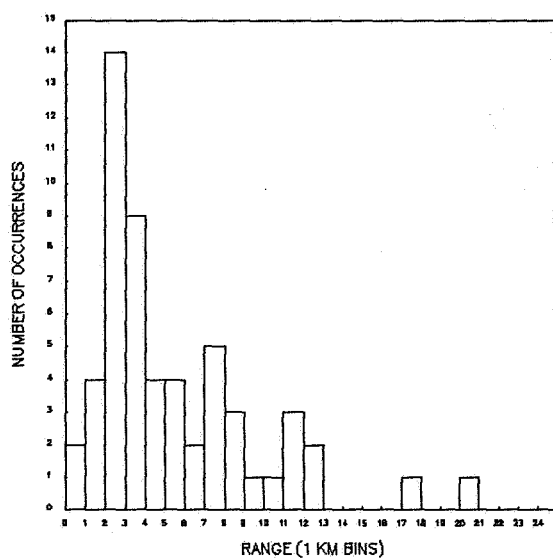


**Figure 11-** Histogram of horizontal differences between coincident FM and LDF flashes.

# WEAK POSITIVE CLOUD-TO-GROUND FLASHES IN NORTHEASTERN COLORADO

Raúl E. López<sup>1</sup>, Michael W. Maier<sup>2</sup>, Juan A. García-Miguel<sup>3</sup>, and Ronald L. Holle<sup>1</sup>

<sup>1</sup>National Severe Storms Laboratory  
National Oceanic and Atmospheric Administration  
Boulder, Colorado 80303

<sup>2</sup>Computer Sciences Raytheon  
(A joint venture of Computer Sciences Corporation  
and Raytheon Company)  
Cocoa Beach, Florida 32931

<sup>3</sup>Universidad Complutense  
Madrid, Spain

## ABSTRACT

The frequency distributions of the peak magnetic field associated with the first detected return stroke of positive and negative cloud-to-ground (CG) flashes was studied using lightning data from northeastern Colorado. These data were obtained during 1985 with a medium- to high-gain network of three direction finders (DFs). The median signal strength of positive flashes was almost two times that of the negatives for flashes within 300 km of the DFs, which have an inherent detection-threshold bias that tends to discriminate against weak signals. This bias increases with range, and affects the detection of positive and negative flashes in different ways, because of the differing character of their distributions. Positive flashes appear to have a large percentage of signals clustered around very weak values that are lost to the medium-to-high gain Colorado detection system very quickly with increasing range. The resulting median for positive signals thus could appear to be much larger than the median for negative signals, which are more clustered around intermediate values. When only flashes very close to the DFs are considered, however, the two distributions have almost identical medians. The large percentage of weak positive signals detected close to the DFs has not been explored previously. They have been suggested to come from intracloud discharges and thus are improperly classified as CG flashes. Evidence in hand, however, points to their being real positive, albeit weak CG flashes. Whether or not they are real positive ground flashes, it is important to be aware of their presence in data from magnetic DF networks.

## 1. INTRODUCTION

Positive cloud-to-ground (CG) lightning flashes generally constitute a small fraction of the total number of flashes striking a given region during a year. They are, however, of considerable interest because of the large currents and charge transfers that have been measured in association with some of them [1, 2]. Positive CG flashes are also interesting because of the situations in which they occur. Thus, positive flashes have been principally studied in connection with lightning discharges

to structures [1, 2] and with wintertime thunderstorms in Japan [3, 4] and the Scandinavian peninsula [5, 6]. However, they also have been found in spring thunderstorms in Oklahoma [7], and summer thunderstorms in Florida [8] and Montana [9].

With the establishment of magnetic direction-finder (DF) networks, positive flashes have been identified in large numbers in the northeastern U.S. [10-12], Oklahoma [7, 13-15], and Sweden [16, 17]. In the past, sample sizes from a particular region have been rather

limited, especially those pertaining to lightning discharges that did not occur to tall buildings and towers. The new networks provide the opportunity to obtain large samples of positive flashes to study their characteristics.

A network of three DFs of medium to high gain in northeastern Colorado was used in [18] to study the effect of local topography on the location and timing of negative CG flashes in the region. Using the same network, data on positive CG flashes were also collected during 1985. The data will be used in this paper to explore the distribution of the peak amplitudes of the magnetic field associated with positive CG return strokes in northeastern Colorado. The main emphasis is to compare signal strength distributions of positive and negative flashes.

## 2. FLASH DATA

The lightning detection network used in this study [18] consisted of three DFs of medium to high gain located in the vicinity of Denver in a relatively flat area adjoining the Front Range of the Rocky Mountains; the mean distance between DFs was 81 km. The network used the commercial lightning mapping system based on magnetic direction-finder technology [19, 20] manufactured by Lightning Location and Protection, Inc. (LLP) of Tucson, Arizona.

The peak amplitude of the magnetic field of each flash's first detected return stroke was recorded by the system as detected by each antenna. This amplitude for each DF was then multiplied by the distance between the DF and the flash, then an average was taken for all DFs that detected the flash. This average was then normalized to 100 km by dividing by 100. The normalized values are expressed in uncalibrated units of peak magnetic radiation. This parameter is related to the peak current in the first return stroke [21]. No attempts have been made in this study either to calibrate the signal strength values or to relate them to peak current, as the main thrust of this paper is to examine the relative magnitudes of the signals from negative and positive CG flashes.

## 3. PREVIOUS MEASUREMENTS OF POSITIVE FLASH INTENSITY

It appears that positive strokes can have very large peak currents and peak magnetic radiation fields, which are larger than the maximum ones for negative strokes [1, 2, 3, 11]. Flashes with very weak signals, however, can also constitute a large percentage of all positive flashes [3, 17]. The average values seem to be larger for positives than for negatives [11, 16, 17]. It should be realized, however, that direct measurements of peak stroke currents have been made only for positive flashes to tall structures. Most of those flashes are due to upward-propagating flashes triggered by the structures. To our knowledge, no direct measurements of peak stroke currents have been made for downward-propagating positive flashes to flat ground. The natural lightning observations by Brook *et al.* [3] refer to charge transfers and the continuing currents of positive flashes. The peak signal observations by networks of DFs provide indications of the relative peak currents in positive and negative strokes, and allow for the study of large samples. However, because experience with these data is limited, they should be critically examined before conclusions are drawn from the frequency distributions of signal strength. The present paper reports a study with that purpose.

## 4. SIGNAL STRENGTH DISTRIBUTIONS FROM COLORADO

### REGIONAL SIGNAL STRENGTH DISTRIBUTIONS

Figure 1 portrays the cumulative frequency distribution of the signal strength of all positive and negative flashes lying within 300 km of at least one DF for 1985 in the Colorado network. Again, the signal strength is the magnitude of the peak magnetic radiation field associated with the first return stroke of a flash, in uncalibrated units and normalized to 100 km. Because of the large skewness and wide spread of the data, the distribution is plotted on a logarithmic scale in the ordinate. For the abscissa, a probability scale has been used.

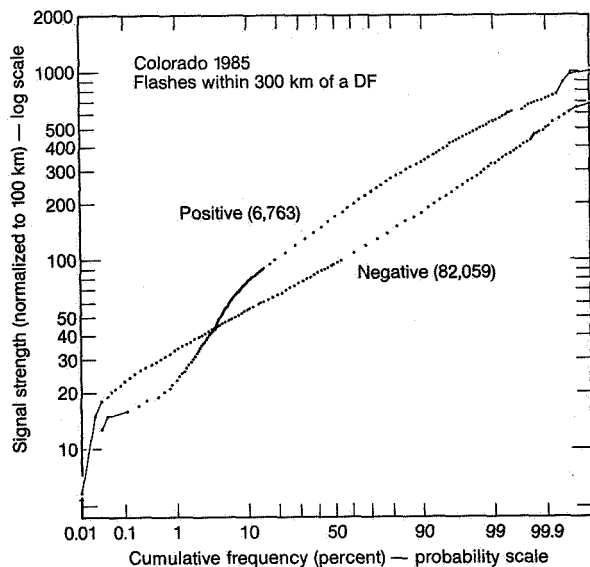


FIGURE 1. Cumulative frequency distribution in logarithmic-probability scales of peak signal strength of positive and negative return strokes within 300 km of a DF antenna for all of 1985. Signal strength in uncalibrated units of magnetic field strength normalized to 100 km.

According to Figure 1, the positive flashes have a larger median signal strength than the negatives (167 versus 94). Notice, however, that the negative frequency distribution curve is much more regular than the positive one and approximates much better a lognormal distribution (a straight line in this coordinate system). There is a larger percentage of flashes with very low peak signals in the positive than in the negative frequency distribution; notice how the positive curve lies to the right of the negative one on the left side of the graph. For example, the percentage of positive flashes with signal strengths less than 20 is 17 times that of the negatives. From 20 on, however, the percentage of weak flashes in the positive distribution decreases rapidly with increasing signal strength, so that eventually there is the same percentage of flashes with signal strengths less than 44, the crossover point, in both the negative and the positive distributions. The positive curve turns rapidly upward between signal strengths of 20 and 80, in relation to the negative curve. In that signal strength interval of the positive flash curve, there is a large percentage deficit of flashes compared with the distribution of the negatives. There are 24% fewer flashes with

signal strength less than 80 in the positive distribution than in the negative. For signals strengths greater than 140 the two distributions have approximately the same slope, but because of the earlier deficit of intermediate values, the overall median of the positives is 79% more than that of the negatives. Actually, there are only three positive flashes in the sample with signal strengths greater than the largest negative signal. Compared with the negative frequency distribution, then, the positive distribution has the following characteristics:

- More flashes with weak signals (<20),
- A smaller percentage of intermediates (20-80),
- About an equal percentage of large ones (>80).

The present median values are of the same order of magnitude as those reported for the U.S. East Coast network [11], but are 29% (positive) and 27% (negative) lower. This might be due to the different DF gains of the two networks. The Colorado system is set half way between medium and high gain; the eastern system is set at high gain. Also, the present results agree with the observations [17] in Sweden, where many positive strokes had rather large or rather weak signals, but not many had intermediate strengths.

However, the frequency distributions of Figure 1 for a large region around the DFs should be considered with caution. Although these curves probably preserve the overall characteristics of the distribution of signal strength, they also contain sampling and measuring biases. For the correct comparison of the signal strengths of positive and negative flashes, these different biases and their effects on the measured distributions of signal strength should be explored. Figures 2 and 3 illustrate some of these biases for the Colorado network. The lower series of points in each figure portrays the variation with distance of the minimum of all the normalized signals detected at the same range by all DFs. The upper series of points represents the maximum, and the middle one the average. To produce these figures, each flash in the study area was assigned to a particular range increment relative to each DF that detected it. Thus, the same flash could have been assigned to two or three different range increments corresponding to the different DFs. For convenience, the

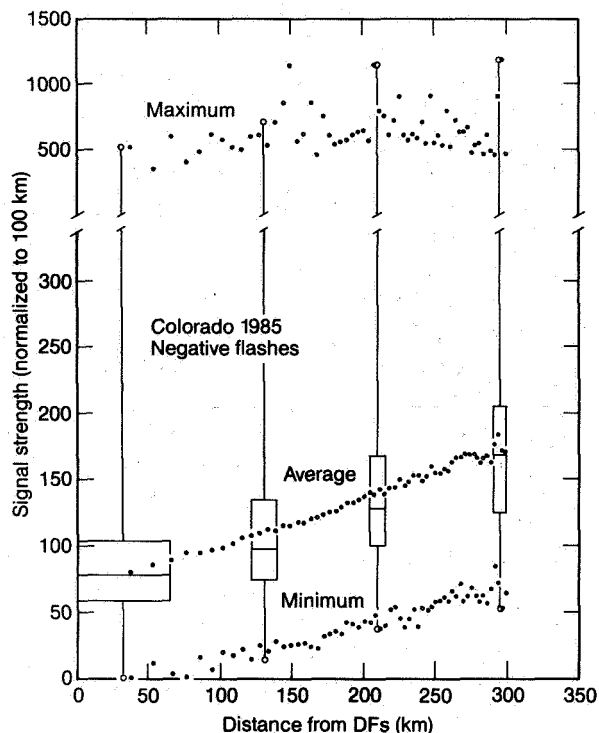


FIGURE 2. Variation with distance of minimum, average, and maximum of all normalized signals of negative flashes detected at the same range by all DFs. Note scale break in ordinate. Superimposed are box-and-whisker depictions of frequency distributions at related range intervals. Adjacent rectangles represent second and third quartiles; open circles represent maximum and minimum values. Range increments and boxes decrease in width with range because they represent annuli of equal areas.

flashes falling in the same range increment with respect to all three DFs were considered together in determining the parameters of Figures 2 and 3. The range increments were selected in such a way that the areas of the annuli they define are always the same; thus, radially, they are of decreasing magnitude. In this way, range samples have roughly the same number of flashes (this is not exactly true, of course, because the density of flashes is not uniform in the area of study). This precaution is desirable when comparing the extreme values (maxima and minima) of samples from populations that have slowly rising and decaying frequency distributions. The box-and-whisker diagrams are discussed below.

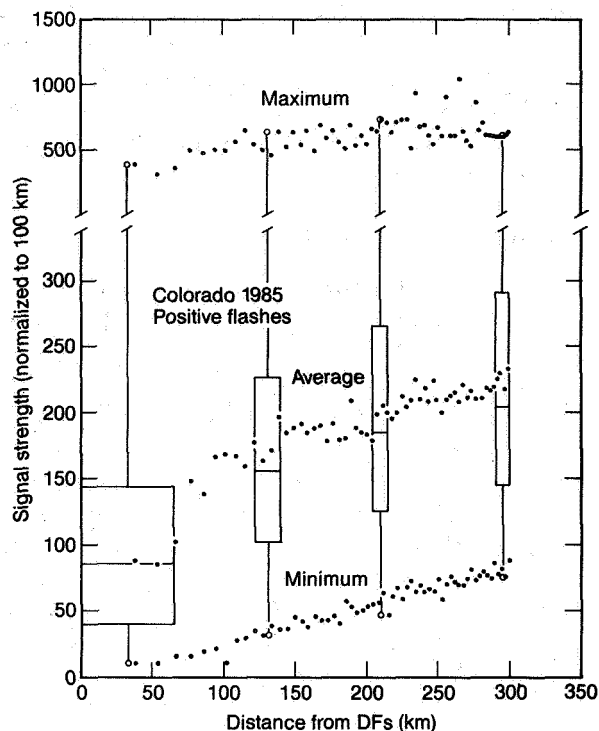


FIGURE 3. Minimum, average and maximum signal strengths, as in Figure 2, but for positive flashes.

### MINIMUM DETECTABLE SIGNAL BIAS

One of the most important sampling problems is the inevitable bias with range toward flashes with very strong signals. Because of the range dependency of the magnetic field of a flash, weak signals coming from distant ranges are not detected, as their magnetic fields reach the antenna with a strength that is below the threshold level of the DF. This level is set above the ambient noise level. As the distance increases, progressively stronger signals are lost in this way. This effect is illustrated by the lower curves in Figures 2 and 3, where the minimum detected signal strength increases linearly with radius for both positive and negative flashes. Notice the progressive erosion with range of detected weak signals indicated by the minimum curve. The minimum values for the positive flashes appear to be slightly larger than those for the negatives. This is so because the acceptance threshold, the minimum voltage that needs to be generated in the antennas before a signal is accepted for processing, was set by LLP at around 350 mV for positive flashes, and 120 mV

for negatives. A higher threshold for the positives was set by LLP to eliminate weak positive signals that were coming from very distant flashes (>1000 km) that were assumed to be ionospheric (inverted) reflections of negative ones.

### **DF SATURATION BIAS**

By contrast, the maximum values detected by the DFs (upper curves) do not seem to be affected as much with range as the minimum values (note a factor of ten difference between the upper and lower scales of the figures). These signals are way above the detection threshold, so that even when coming from 300 km they are still picked up by the DFs. Only three values in the positive curve are above the maximum value in the negative one. However, there is a slight drop in the values of the detected maximum signals from about 100 km inwards towards the DFs. This reduction could be due in part to another bias, the problem of DF saturation. Flashes striking close to the antennas can saturate the electronics of the DFs even if their normalized signals are not too high; the closer the flash position to a DF, the smaller the signal required to achieve saturation. Saturated detections were not considered in deriving the maximum signal curves. In Figures 2 and 3, the closest ring goes out to 39 km, and the maximum normalized signal observed within that ring for the negative flashes was 523. According to the linear decay of signal strength with range, that would give a value for the maximum absolute signal that a DF can detect before saturating of 1350 LLP units, which is a reasonable number for these systems. By 55 km (the extent of the second ring), that saturation threshold could tolerate a normalized signal of 739 before saturating the DF. The observed maximum for both positive and negative flashes in the second ring can be seen from Figures 2 and 3 to be considerably under that value. So, although the effect of saturation might account for some of the apparent reduction in maximum signal measured from 100 km inwards, the sampling variability and regional distribution of flashes are probably the major factors. A very sharp decrease in maximum signal values, however, could have been detected if the closest rings had been much smaller.

There is a striking difference between the curves depicting the average signal strengths (middle curves), in contrast to the basically similar character of the maximum and minimum curves of positive and negative flashes. The curve for negative values increases monotonically and smoothly with range, almost paralleling the curve for minimum values. The curve for the positives, however, although it starts out with an average that is similar to that of the negatives, jumps very quickly by 140 km to more than twice the value at close ranges (equivalent to that attained by the negatives at 300 km). From that point on, the increase is gradual and follows the increase in the minimum values. Thus, if the frequency distributions for negatives and positives are compared at close range (say, less than 70 km) they appear to have the same mean and extreme values. Throughout most of the region, however, the positives appear to have a very much larger mean, although the extremes are similar.

### **DIFFERENT RESPONSES OF POLARITY DISTRIBUTIONS TO BIASES**

Why is there such a difference between the two distributions at different ranges? Figure 3 displays box and whisker representations of the frequency distribution of the positive signal strength for different range intervals. Notice how the first two quartiles of the portrayed distribution closest to the DFs lie very low on the signal strength scale. The quartile levels rise rapidly in the second distribution, but in the next two the rise is gradual and parallels the rise in minimum value. Thus, it appears that the distribution of positive signal strengths observed closest to the DFs contains a large proportion of very weak signals. If the distribution of positive signals over the entire region was the same, such weak signals (most of the first quartile) would quickly become undetected with range, modifying greatly the character of the observed distribution. The negative flashes, however, have a more regular distribution that is not so skewed toward the weak signal strengths. Therefore, the effect of losing the weak signals with range would be reflected in a more gradual change in the distribution with



range. Recalling that the acceptance threshold for the positive flashes was about three times higher than for negatives, the true distribution of positive signals corresponding to the first box-and-whisker representation of the graph probably had an even higher percentage of weaker values. Also, because of the different acceptance thresholds, the erosion of weak values with range is much faster in the case of the positives. Even if the thresholds were the same, however, the effect of the detection bias would have been different for each polarity because of the even more marked disparity in the proportion of weak flashes between the two. Although, conceivably, there are geographical inhomogeneities in the signal strength distributions, these two different responses (both because of the different thresholds and the different basic distributions) to the detection bias of weak signals are obviously an important factor in explaining the difference between the curves depicting the average signal with range for positive and negative flashes.

#### SUMMARY OF SAMPLING BIASES

Thus, although the frequency distributions portrayed in Figure 1 for a large region around the DFs probably preserve the overall characteristics of the distribution of signal strength, they are biased toward flashes with strong signals and do not give enough weight to the weak flashes. Furthermore, since it appears that the positive and negative flashes have different signal strength distributions, especially for weak flashes, the range bias has quite different effects on the signal strength distributions of flashes of different polarities. In addition, there is a bias against large signals caused by the saturation of the DFs by flashes that strike close by. This effect is most important for flashes that fall within a few tens of kilometers from the DFs. Although those flashes are detected, their position and normalized signal strength cannot be accurately determined unless three DFs detect them (one saturated and two normal detections).

It should be emphasized, however, that the particular way in which the sampling and measuring biases affect the signal distributions with range depends on the gain of the network. The Colorado network used in

this paper has a medium-to-high gain. In networks with lower gain, the range detection bias would produce an even more dramatic modification of the signal strength distributions with range. Networks with high gain would see weaker flashes much farther away and the modifications to the signal distributions would be noticed only at larger distances, although the saturation effect will be worse at high gain. On the other hand, lower gain networks are usually designed to cover small areas, while higher gain networks are intended to monitor regions of a large extent.

It is virtually impossible to obtain a totally unbiased sample of flashes detected by a DF network to study their signal strength distribution. However, one could obtain a sample from an area that is close to the DFs and thus minimize the effect of the range attenuation, but not so close to the DFs that the saturation problem is severe. Figure 4 shows a plot of the frequency distribution of such a sample for positive and negative signals in log-probability coordinates for flashes that lie no farther than 60 km from at least one DF and not closer than 20 km from any DF. Flashes that saturated one DF but were detected correctly by two others were included in the two samples, as in this case both flash location and normalized signal strength can be estimated from the two non-saturated DFs. Saturating flashes detected by only two DFs were not considered. The two resulting distributions are probably close to the unbiased ones, although some deterioration has

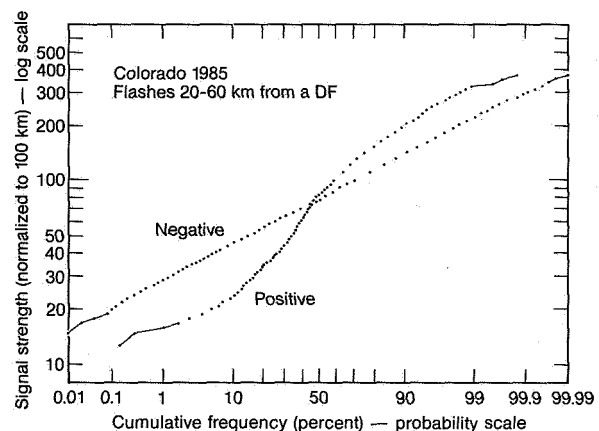


FIGURE 4. Same as Figure 1, but within 20 to 60 km of any DF.

undoubtedly already occurred in the chosen interval. These frequency distributions, however, should correspond better to the original, unbiased populations of positive- and negative-flash signal strengths in the area of study. Thus, a comparison of positive and negative flashes based on these distributions should be more physically meaningful than one based on the distribution of flashes over the entire area covered by the network and contaminated by different sampling and measuring biases. Having obtained samples that are more representative of the true populations, we proceed to compare the signal strengths of negative and positive flashes.

## 5. COMPARISON OF POSITIVE AND NEGATIVE SIGNALS

As anticipated in Figures 2 and 3, the distributions of Figure 4 have basically the same median. The positive distribution, however, has a much larger percentage frequency of small signals, especially for signal strengths less than 20. Above that value, there is a rapid decrease in relative frequency that extends to a signal strength level of 100. After that point, the relative frequency of the larger values increases compared with the previous curve segment; observe how the curve turns toward the right compared with the segment between the signal strength values of 20 and 100. By comparison, the negative distribution seems much smoother and more regular.

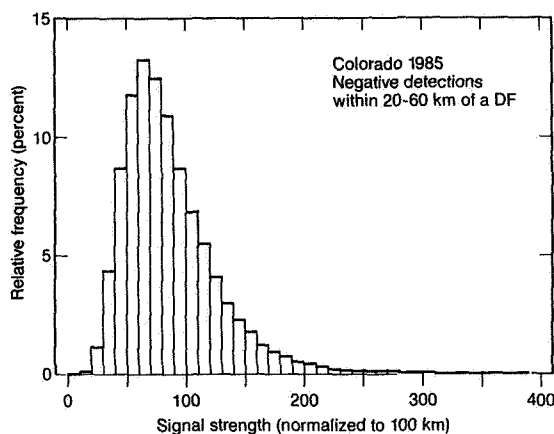


FIGURE 5. Normalized peak signal strength for negative flashes within 20-60 km of a DF.

Figures 5 and 6 show the distributions of Figure 4 in histogram form for the close-in range of 20 to 60 km. The positive distribution is highly skewed towards very small signal values, having the maximum frequency between 20 and 30. The negative distribution, on the other hand, has a maximum frequency at signal strengths between 60 and 70, and the skewness is not as large. It should also be kept in mind that because of the higher acceptance threshold for positive flashes mentioned above, the true proportion of weak positive signals could be even higher.

The positive distribution, then, appears to be markedly different in shape from the negative one, showing a large percentage of very weak flashes and a small percentage of intermediate ones. Although this result is hinted at in the observations of [17] in Sweden and [3] in Japan, to our knowledge, the importance of this high percentage of weak positive flashes in the distribution has not been emphasized before.

Before the physical nature of these weak positive flashes is discussed, however, it is important to consider how representative are the resulting frequency distributions of signal strength of the thunderstorms in northeast Colorado during the summer. As can be seen from Figures 5 and 6, the most marked difference between positive and negative flashes lies in the frequency of signals at or below 40 LLP units. A total of 216 positive flashes were

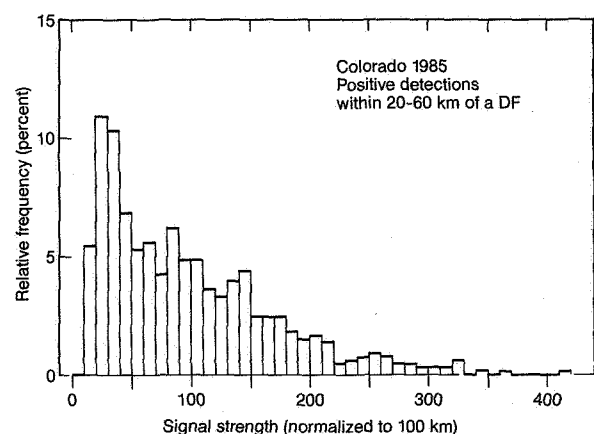


FIGURE 6. Normalized peak signal strength, as in Figure 5, but for positive flashes.

observed in that range on 46 different summer days. Thirteen of those days had three or more of the weak positive flashes, and eight of those 13 days had seven. The weak flashes have their peak frequency between 1500 and 1600 MST, coinciding with the peak diurnal convective activity in the region [18]. These flashes are also fairly well distributed around the DFs, although their frequency drops dramatically with range after about 60 km from the antennas as explained above in connection with Figure 3. In addition, when the frequency distributions of both positive and negative flashes of all signal strengths are computed for a ring of 20 to 60 km around each of the three DFs separately, the three distributions for each polarity are very similar to each other and the two sets are very similar to Figures 5 and 6. Thus, the weak positive flashes are not the result of just a few atypical storms in a few particular localities, but come from thunderstorms that are part of the regular diurnal cycle of convection throughout the summer. Also, within the region where they can be detected, the weak positive flashes are geographically well distributed in numbers and belong to fairly representative signal strength distributions.

It has been suggested, however, that the very weak positive signals close to the DFs are not from cloud-to-ground flashes [17]. In the absence of independent evidence showing that these signals indeed come from cloud-to-ground positive flashes, there are basically three possible explanations for these results:

- a. The weak signals do come from positive CG flashes and because of their weak signal strength are detected only when a flash occurs very close to a DF.
- b. The weak signals come from intracloud discharges with waveshapes similar to inverted return strokes, are detected by the positive stroke circuits in the DFs, and are improperly classified as positive cloud-to-ground lightning. Since these are intracloud discharges, their signal amplitudes are small relative to cloud-to-ground flashes and are preferentially detected only near the DFs. Because the waveshapes are similar to those of real cloud-to-ground strokes, it would be very difficult to discriminate against them except by further increasing the acceptance threshold for positive flashes. It is strange, however, that

similar intracloud discharges with *negative* return stroke waveshapes are not being detected (compare frequency distributions in Figures 5 and 6). Also, it must be remembered that these signals refer to flashes that were detected by two or three DFs with a mean separation of about 80 km. Very weak intracloud discharges close to an antenna would not have been detected by another at those distances. Furthermore, a study [22] of the correctness of the polarity assignments of direction-finding equipment similar to the one used in the present study but for a high gain system, concluded that the acceptance criteria for positive flashes are adequate, provided that the distances of the flashes to the DFs are less than 600 km. Another study [23] recently considered positive flashes detected by a similar DF network and examined the waveforms simultaneously detected by an extremely low frequency (ELF) system. The conclusion was that no more than 15% of the positive flashes detected by the DFs with signal strengths of less than 50 are false detections. The percentage is probably even lower, the study concluded, because the very weak positive flashes produce ELF signals that are close to the ELF system's noise level.

c. These are signals with waveshapes that do not correspond to return strokes (in contradistinction to "b" above) and should be rejected by the positive stroke detection circuit as not fitting the waveshape criteria for cloud-to-ground strokes, but because of their small signal strengths they are not recognized as such. These signals could well come from very weak but legitimate intracloud flashes which are being improperly classified as CG flashes or they could come from non-stroke discharges such as k changes. In this case, a modification to the waveshape criteria logic could filter out these weak signals.

More work will have to be done to explain the large percentage of weak positive detections. In view of the growing importance of lightning data and the proliferation of lightning detection networks, the problem should be given serious consideration when the data are used for operational and research applications. If the weak positive signals are shown to come from real cloud-to-ground positive flashes, it should be realized that there is a larger proportion of weak, positive flashes to ground than would appear from

previous studies and that, when all things are considered, the median signal strength values are about the same for positive and negative flashes. It also should be realized that, at least for medium- and low-gain systems, storms near the DFs would appear to have a larger proportion of positives flashes than would storms farther away. The details of the deformation with range of the frequency distributions of signal strength would depend on the particular configuration of the network and to some extent on the conductivity characteristics of the surrounding terrain.

If the weak signals are shown to be from intracloud or cloud-to-cloud discharges (with return-stroke-like waveshapes or not), then it should be realized that, as far as positive flashes are concerned, data from closer than about 100 km from a DF might give an erroneous picture of cloud-to-ground lightning activity.

## 6. CONCLUSION AND DISCUSSION

Using the lightning data of one entire year from northeastern Colorado, a comparison has been made of the magnitude of the peak signal strength of the first return strokes of positive and negative flashes. When the data from a large region around the DF (300 km) are considered together, the positives appear to have a median signal strength that is almost twice as large (1.8 times) as that of the negatives. The overall sample, however, tends to indicate that the two resulting distributions are quite different in regard to the very weak signals. These signal strength distributions based on positive and negative flashes from widely different distances, however, contain some sampling and measuring biases. One of the most important sampling problems is the inevitable bias with range against flashes with weak signals. This range bias has very different effects on the sampling of flashes of different polarity owing to the basic difference in the skewness and spread of the original distributions. In addition, there is a bias against large signals caused by the saturation of the DFs by flashes that strike close by.

The particular way in which the different sampling and measuring biases affect the signal distributions with range depends on

the gain of the network. The Colorado network used in this paper has a medium-to-high gain. In networks with lower gain, the range detection bias would produce an even more dramatic modification of the signal strength distributions with range. Networks with high gain would see weaker flashes much farther away and the modifications to the signal distributions would be noticed only at larger distances.

Frequency distributions of the peak signals of flashes observed a small distance from the DFs best reveal the fundamental differences between negatives and positives. Both appear to have the same median signal strengths, but the positive sample has a larger proportion of very small signals. The positive sample lacks the large percentage of signals of intermediate values that are frequent in the negative group. The two distributions are more similar in their relative frequency of large values, but the positive sample, although it is about 15 times smaller, contains the largest values of peak signal.

That some positive strikes can transfer to earth very large charges and have very large currents is not denied by the present data set. It should also be kept in mind that positive strokes have longer time to peak current, and large continuing currents following the peak discharge. However, once the range bias is taken into account by considering only flashes close to the DFs, the present Colorado data tend to indicate that, relative to the negative, the positive distribution appears to have a larger percentage of flashes with very small values, a smaller percentage yielding intermediate ones, about the same proportion of large values, and a few flashes with values that are larger than any in the negative distribution. The medians of the two distributions, however, are about the same.

The larger percentage of weak signals detected close to the DFs has not been emphasized earlier, nor are there any independent data obtained by other methods in Colorado for studying their physical nature. The results of [23], however, lend weight to their being real cloud-to-ground positive flashes. In any case, the results reported here should be taken into account when positive

flash data from magnetic direction finders are used, especially for medium-and low-gain systems. It appears that frequency distributions for positive and negative flash signal strength are indeed different and that the detection bias with range, inherent in the system, produces different results as it operates on the different distributions.

## ACKNOWLEDGEMENTS

The Program for Regional Observing and Forecasting Services (PROFS) of NOAA in Boulder, Colorado operated the network and collected the lightning data used in this study. The assistance of R. Ortiz of NSSL, Boulder, in plotting a portion of the data is appreciated.

## REFERENCES

1. Hagenguth, J.H., and J.G. Anderson, Lightning to the Empire State Building. *Trans. AIEE*, 71 (Pt. 3), 641-649, 1952.
2. Berger, K., Novel observations on lightning discharges: Results of research on Mount San Salvatore. *J. Franklin Inst.*, 283, 478-525, 1967.
3. Brook, M., M. Nakano, P. Krehbiel, and T. Takeuti, The electrical structure of the Hokuriku winter thunderstorms. *J. Geophys. Res.*, 87, 1207-1215, 1982.
4. Takeuti, T., M. Nakano, M. Nagatani, and H. Nakada, On lightning discharges in winter thunderstorms. *J. Meteorol. Soc. Japan*, 51, 494-496, 1973.
5. Takeuti, T., Z. Kawasaki, X. Funaki, N. Kitagawa, and J. Huse, Notes and correspondence on the thundercloud producing the positive ground flashes. *J. Meteorol. Soc. Japan*, 63, 354-358, 1985.
6. Cooray, V., and S. Lundquist, On the characteristics of some radiation fields from lightning and their possible origin in positive ground flashes. *J. Geophys. Res.*, 87, 11203-11214, 1985.
7. Rust, W.D., D.R. MacGorman, and R.T. Arnold, Positive cloud to ground lightning flashes in severe storms. *Geophys. Res. Lett.*, 8, 791-794, 1981.
8. Beasley, W.H., M.A. Uman, D.M. Jordan, and C. Ganesh, Positive cloud to ground lightning return strokes. *J. Geophys. Res.*, 88, 8475-8482, 1983.
9. Fuquay, D.M., Positive cloud-to-ground lightning in summer thunderstorms. *J. Geophys. Res.*, 87, 7131-7140, 1982.
10. Orville, R.E., R.W. Henderson, and L.F. Bosart, An east coast lightning detection network. *Bull. Amer. Meteorol. Soc.*, 64, 1029-1037, 1983.
11. Orville, R.E., R.A. Weisman, R.B. Pyle, R.W. Henderson, and R.E. Orville, Jr., Cloud-to-ground lightning flash characteristics from June 1984 through May 1985. *J. Geophys. Res.*, 92, 5640-5644, 1987.
12. Orville, R.E., R.W. Henderson, and L.F. Bosart, Bipole patterns revealed by lightning locations in mesoscale storm systems. *Geophys. Res. Lett.*, 15, 129-132, 1988.
13. Reap, R.M., and D.R. MacGorman, Cloud-to-ground lightning: Climatological characteristics and relationships to model fields, radar observations, and severe local storms. *Monthly Weather Review*, 117, 518-535, 1989.
14. Holle, R.L., A.I. Watson, R. Ortiz, and R.E. López, Spatial patterns of lightning, radar echoes, and severe weather in mesoscale convective systems. *Preprints, Conference on Atmospheric Electricity*, October 22-26, Kananaskis Provincial Park, Alberta, Canada, American Meteorological Society, Boston, 721-726, 1990.
15. Rutledge, S.A., and D.R. MacGorman, Cloud-to-ground lightning in the 10-11 June 1985 mesoscale convective system observed during PRE-STORM. *Mon. Wea. Rev.*, 116, 1393-1408, 1988.
16. Murty, R.C., S. Israelsson, E. Pislér, and S. Lundquist, Observations of positive lightning in Sweden. *Preprints, 5th Symposium on Meteorological Observations and Instrumentation*, April 11-15, Toronto, Ontario, Canada, American Meteorological Society, Boston, 512-515, 1983.
17. Christensen, U., and S. Israelsson, Relationships between radar echo characteristics and lightning parameters for a thunderstorm in Sweden. *Weather*, 42, 166-176, 1987.
18. López, R.E., and R.L. Holle, Diurnal and spatial variability of lightning activity in northeastern Colorado and central Florida during the summer. *Mon. Wea. Rev.*, 114, 1288-1312, 1986.
19. Krider, E.P., R.C. Noggle, and M.A. Uman, A gated, wideband magnetic direction finder for lightning return strokes. *J. Appl. Meteor.*, 15, 301-306, 1976.
20. Krider, E.P., R.C. Noggle, A.E. Pifer, and D.L. Vance, Lightning direction-finding systems for forest fire detection. *Bull. Amer. Meteor. Soc.*, 61, 980-986, 1980.
21. Uman, M.A., D.K. McLain, and E.P. Krider, The electromagnetic radiation from a finite antenna. *Amer. J. Phys.*, 43, 33-38, 1975.
22. Brook, M., R.W. Henderson, and R.B. Pyle, Positive lightning strokes to ground. *J. Geophys. Res.*, 94, 13295-13303, 1989.
23. MacGorman, D.R., and W.L. Taylor, Positive cloud-to-ground lightning detection by a direction-finder network. *J. Geophys. Res.*, 94, 13313-13318, 1989.

**Predicting the Onset and Cessation of Natural Lightning Hazards:  
Capabilities of Existing Sensor Systems as Illustrated by Two Case Studies**  
*by M. Maier and L. Maier*

No paper available.

**Session 14A, Friday 10:15**  
**Lightning Mapping Systems 3**  
**Thomson, Chairman**

## LIGHTNING MAPPING SYSTEM

C. Lennon and L. Maier

National Aeronautics and Space Administration  
John F. Kennedy Space Center, Florida

### ABSTRACT

A new Lightning Detection and Ranging (LDAR) System is being implemented at the Kennedy Space Center, Florida. The first operational use is expected in the late summer of 1991.

The system is designed to map the location of In-Cloud and Cloud-to-Ground Lightning based on the Time Of Arrival (TOA) of electromagnetic radiation. The system detects VHF radiation and is designed to map the volumetric extent of lightning. The system implements two independent antenna arrays to provide a fast data quality check, as necessary for a real-time warning system. The system performance goals and a comparison with a similar system implemented in the mid 1970s is made.

### INTRODUCTION

In this paper we describe a Lightning Mapping System that is under development at the John F. Kennedy Space Center. The system is an improved version of a system that was used during the Thunderstorm Research International Program (TRIP 76-78)[1]. The final form of the original system is described by Poehler and Lennon in NASA Technical Memorandum [2]. This early NASA system used digital waveform recorders and digital computers to provide a near real-time display of lightning pulse locations. The NASA system was an automated version of a system developed by Proctor[3] which determined the time differences manually from film records.

### PRINCIPAL OF OPERATION

Lightning discharges produce a series of broadband VHF pulses. By detecting the TOA of these pulses, at widely separated sites, the location of the source of radiation can be computed.

The coordinates of the receiving sites are listed and plotted on a map of the Kennedy Space Center (KSC) in Figure 1. Lightning-produced RF pulses are received at the remote sites and are processed by Log Video Detectors (LVDs). The resulting series of video pulses are transmitted to the Central LDAR site (Site 0) by microwave links. The physical configuration of the system assures that the direct RF pulses

will arrive at the Site 0 prior to the retransmitted pulses from the remote sites. Advantage is taken of the early arrival of the pulses at the Site 0 to trigger the system.

When a pulse exceeds a threshold at the Site 0 the system is triggered, opening a data analysis period which extends for 100 microseconds. During this analysis window the system determines the time of occurrence (apparent TOA) of the largest amplitude pulse for each of the seven data channels. At the end of the analysis period the time and amplitude data for each channel will be collected, and the event will be tagged with the time of day to the nearest microsecond. This data will be buffered and the system will be re-armed within 10 microseconds. Figure 2 illustrates the time tagging process using a simplified series of lightning pulses. At the completion of the data gathering process data is transmitted to a group of computers for testing, calculation of the source locations, and display.

### COMPUTER CONFIGURATION

A block diagram of the equipment located at the LDAR Site 0 is shown in Figure 3.

The function of the display computer is to develop software for the VME system, to load both operating system and software for the VME system, and to provide lightning location displays. The display computer will receive source locations from the VME system for display.



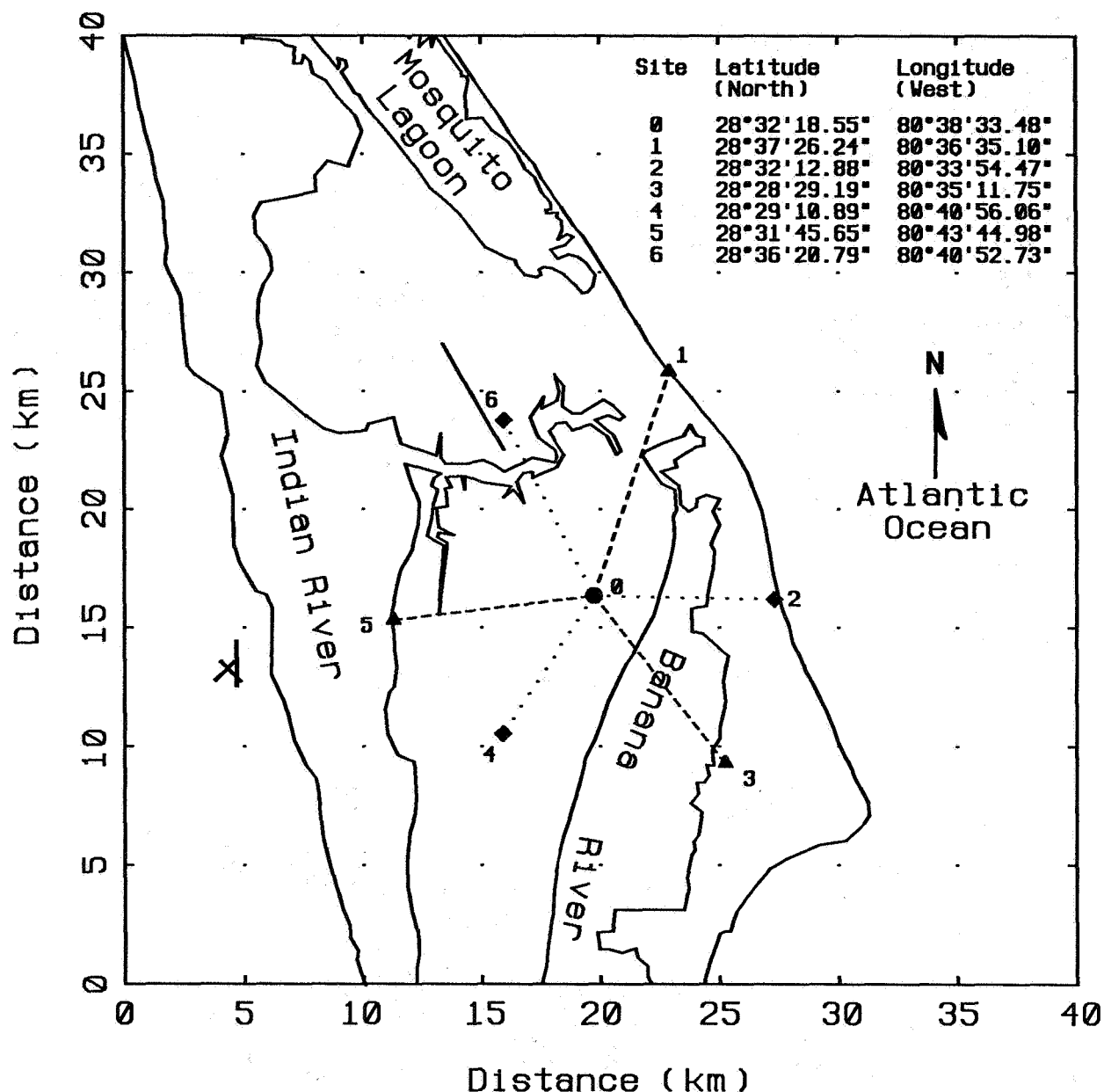


Figure 1. LDAR site locations (see text for further description).

#### DATA OUTPUT/DISPLAY

The function of the VME System is to ingest TOA data, perform validity tests, compute X, Y, and Z coordinates, store data on magnetic tape, and to transmit X, Y, Z-coordinate data to the display computer. The VME System is housed in a 20-slot card cage and uses multiple on-board computers for parallel processing of the TOA data. In addition the VME System is interfaced to a Digital Audio Tape (DAT) for mass storage of the TOA raw data (1.2 Gbytes).

The LDAR system will provide output data for displays in the following two formats.

First, the display computer will generate a near real-time display. This display will be converted to the National Television Standards Committee (NTSC) format and will be distributed to KSC and the Air Force's Operations Control Center by a combination of wideband cable and operational television circuits.

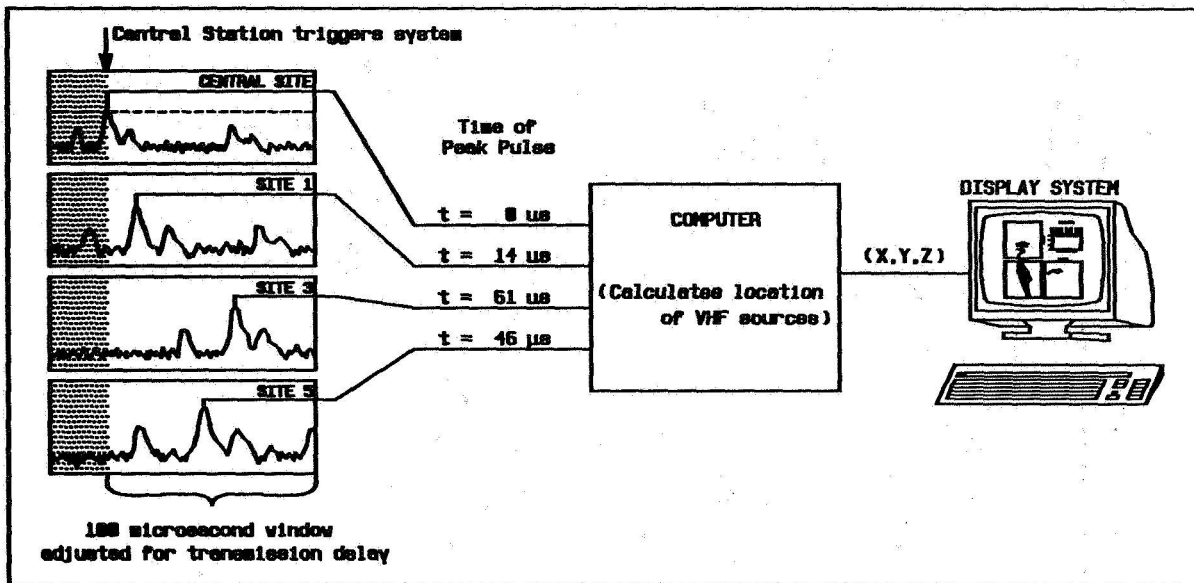


Figure 2. Time tagging process.

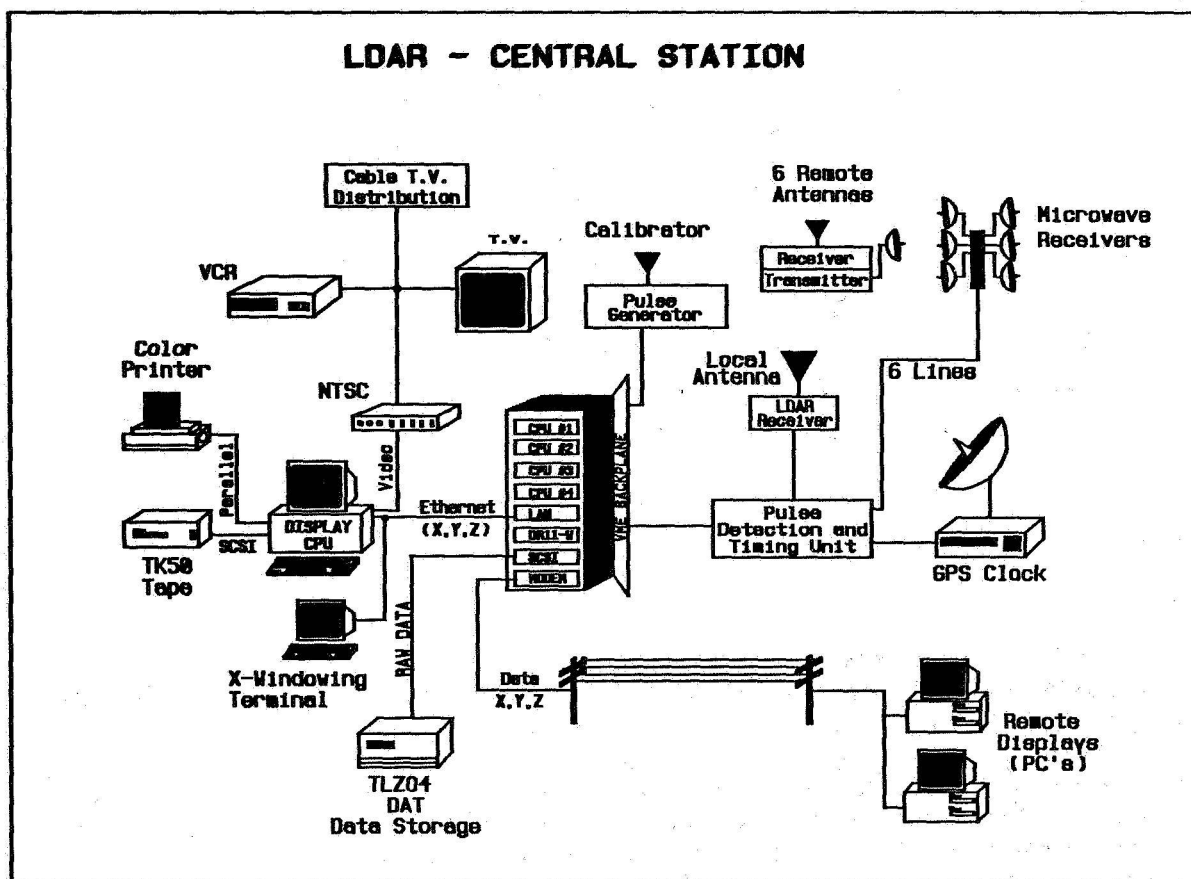


Figure 3. Block diagram of central station.

Secondly, the VME System will transmit the X, Y, Z coordinates of lightning sources. This data will be broadcast as an RS-232 format signal over a 19-gauge wire pair. This signal will be available to anyone having access to the KSC communications system. This arrangement will allow users to tailor displays to meet their requirements (e.g., a Plan Position Display, PPD, centered on Complex 39A.)

The display generated for dissemination by the local cable television network is unique, and the format of

the display is shown in Figure 4. The PPD portion of the display (A) is at the lower left of Figure 4.

This part of the display shows a map of the KSC area that is centered on the location of the LDAR Site 0 ( $X=0$ ,  $Y=0$ ,  $Z=0$ ). The scale of the map can be changed as an operator function. When a lightning pulse is detected its location will be computed in the X, Y, Z coordinate system. The X, Y location of the point will be plotted as a point in the PPD portion of the display.

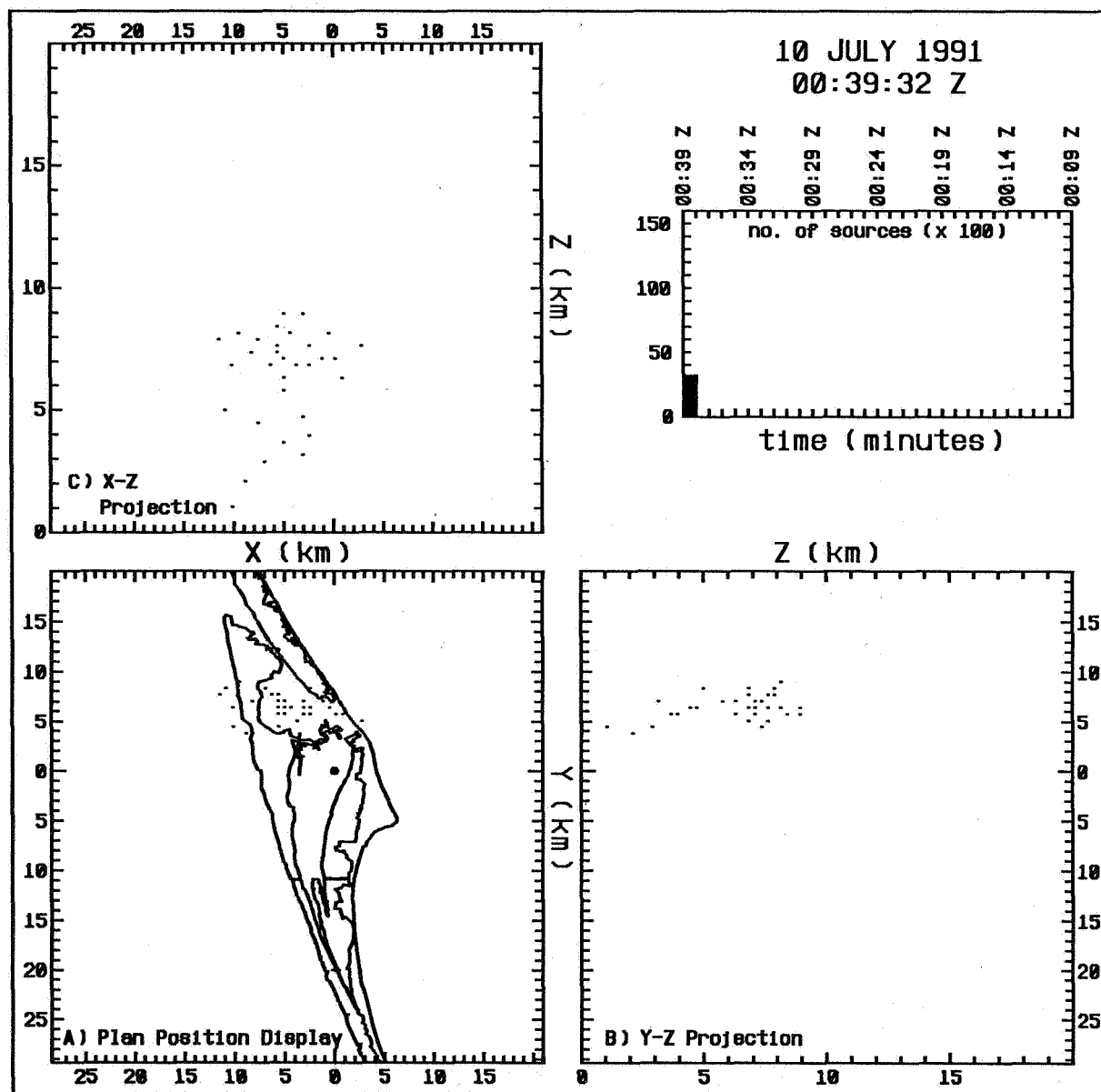


Figure 4. LDAR real-time display (see text for description).

Coupled with the PPD are two more displays that show the X, Z and Y, Z projections of the same points plotted on the PPD. These displays give the operator (observer) a view of the height profile of the discharges as seen by an observer located west of the event (Display B) or south of the event (Display C). The relationship between projections for 5 VHF sources is illustrated in Figure 5.

An additional sub-display is provided in the upper right-hand corner of the composite display (Figures 4

and 5). This display is a histogram depicting number of pulses per unit of time. The unit size of the ordinate axis (events per unit of time) will be a variable that is compatible with the lightning activity and display capacity.

Lightning pulses that fall outside of the display coverage will not be plotted or added to the histogram. A cursor will flash indicating that the system is detecting lightning activity outside of the selected display area.

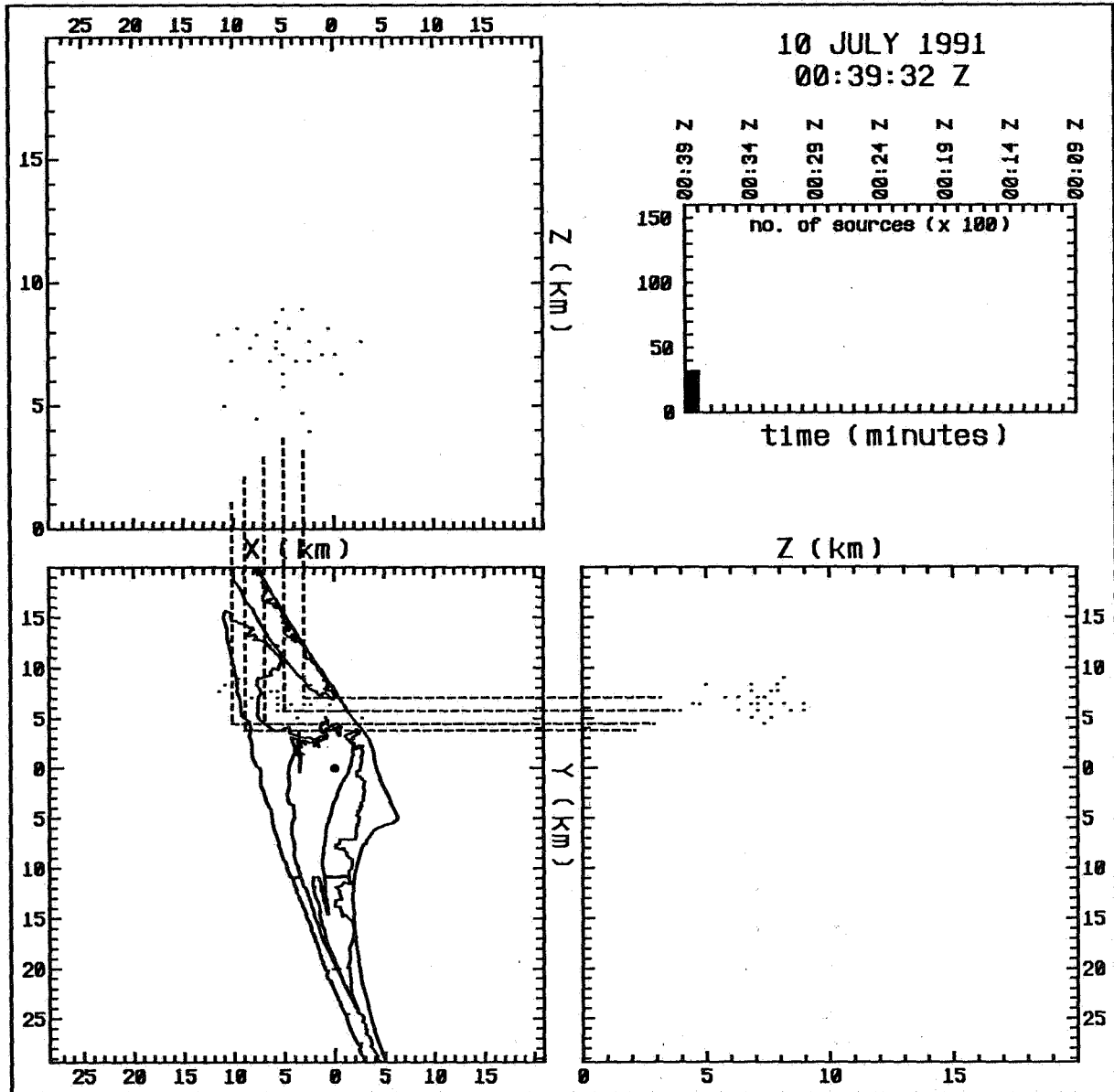


Figure 5. Demonstration of inter-relationship of projections on the LDAR real-time display.

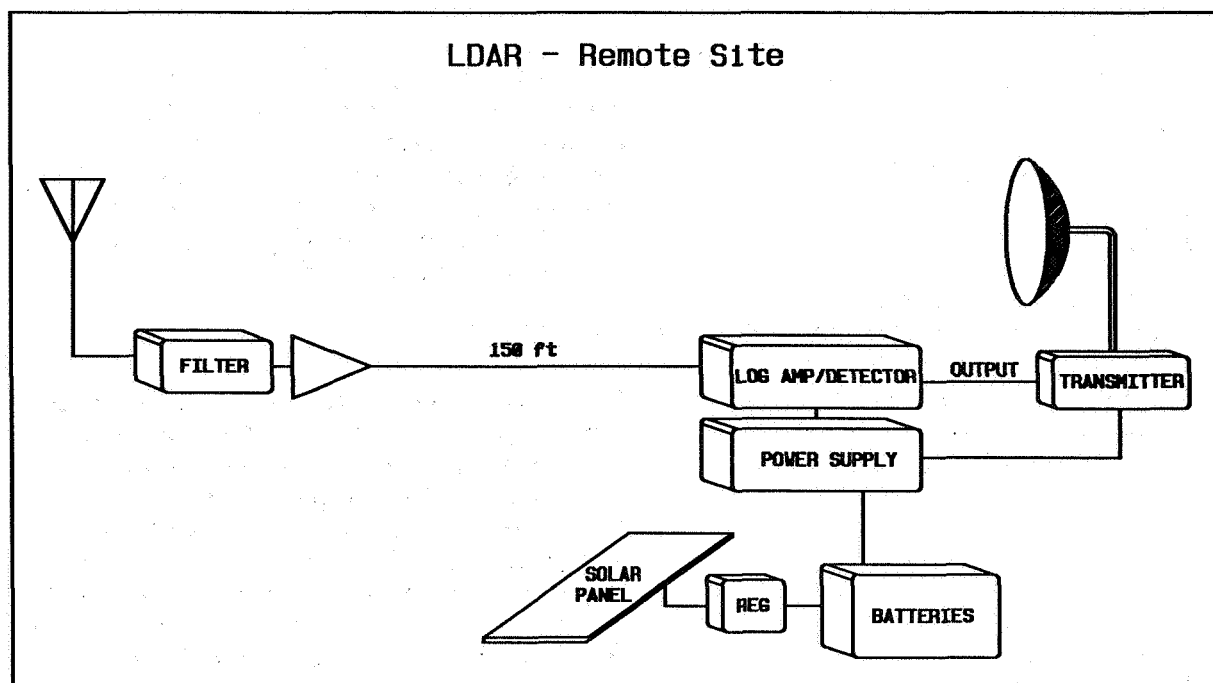


Figure 6. Block diagram of LDAR remote site.

Another feature to be added to the display is the use of color to represent temporal variations in the data. The most recent data will be displayed in bright red with earlier events being displayed in yellow, blue or green. The time interval assigned to each color will be determined during the check-out and certification phase of system development.

#### LDAR RECEIVERS/ANTENNA

A block diagram of an LDAR receiver is shown in Figure 6. The basic LDAR receiver is built around an Adams Russel Model 1CLA351 logarithmic amplifier. Amplifier specifications are provided in Table I.

TABLE I. Log amplifier specifications.

Frequency range	60-300 MHz
Input Dynamic Range	75 dB minimum
Tangential Sensitivity	-75 dBm
Rise Time	10 Nanoseconds (maximum)
Function	Logarithmic Video Detection
Linearity (Log Output)	$\pm 1.5$ Db

The frequency response of the receiving system is limited by the addition of a filter between the logarithmic amplifier and the antenna. Two sets of filters are available for selecting a system operating frequency of either  $63 \pm 3$  MHz or  $225 \pm 3$  MHz. This design easily accommodates changes to the operating frequency in the range between 60 MHz to 300 MHz by changing the input filter.

A small in-line amplifier is located near the antenna. This amplifier protects the input of the logarithmic amplifier, and it increases the signal level on the transmission line by 10 dB. By increasing the signal level on the transmission line, the effects of stray signal pickup are minimized. Power for the input amplifier is supplied via the transmission line.

The receiver package is located (adjacent to the Microwave transmitter) near the top of a 52-foot power pole. By locating the receiver close to the transmitter the possibility of stray signal pickup on the video line connecting the two is minimized.

The sensor for the receiver system is a broadband antenna covering the frequency range of 60 to 300 MHz. The antenna is specified to have hemispherical coverage, and is left hand circular polarized  $\pm 1$  dB. By using a circular polarized antenna the variation in

signal amplitude, due to variation in the polarization of the radiating source, will be minimized.

## DATA QUALITY

### SITE SELECTION

To be a useful part of a lightning warning system, the LDAR must have a high detection ratio and a near zero false alarm rate. To insure a high detection ratio the operating frequency and the locations of the receiving sites were carefully selected. Some of the criteria used in site selection are listed in Table II.

---

Table II. Site selection criteria.

---

1. Maintain "Y" Configuration
  2. Good Accessibility
  3. Located On Government Property
  4. Away From Above Ground Power Line
  5. Away from Industrial Sites
- 

### FREQUENCY SELECTION

The ambient RF signal level between 60 and 72 MHz was measured at Site 0 and at each remote site. All sites were found to have acceptable background signal levels.

An initial operating frequency of 63 MHz was chosen. This frequency is in the center of the band allocated for television Channel 3. Since there is no local Channel 3 television assignment, this frequency range is protected from local users (100 miles).

The number of lightning-produced VHF radiation impulses, as reported by Oetzel[4], peak between 50 and 100 MHz at  $10^4$  pulses-per-second, and decrease rapidly above 100 MHz. Based on these data and on operation of the earlier LDAR system at this frequency, 63 MHz was chosen as the initial operating frequency.

### TIME DELAYS

There are several system design parameters that have a direct effect on the location accuracy of the system. Some of the obvious critical parameters are: signal digitization interval, system time delays, time delay stability, and system bandwidth. The system

bandwidth (6 MHz) and digitization window ( $10^{-8}$  seconds) are fixed by design. The system delays are a function of site location, cable lengths, individual component bandwidths, and propagation delays. To insure optimum system performance, these delays must be measured and subtracted from the TOA data. To measure these delays a system calibrator has been included in the design.

### CALIBRATOR

The system calibrator consists of a high powered impulse generator AVTECH Electrosystem Ltd. Model # AVB2-C-NASA1. This generator is capable of producing a 400 volt peak-to-peak pulse into a 50 ohm load. The shape of the waveform simulates a single cycle of a 63 MHz sine wave. This signal will be applied to a vertically polarized antenna, located on top of the microwave tower at the LDAR Central site. This signal will be received at the remote site and the resulting video pulses will be transmitted back to the central site by microwave links. The time interval between the arrival of the pulse at the central site receiver and the arrival of the pulses at the output of the microwave receivers will be measured by the LDAR data processor. This is the same technique used to measure pulses produced by lightning.

Since the location of the calibrator antenna and the remote station antennas are known ( $\pm 1$  meter), the time delay to each station can be calculated. These propagation time delays are constant and will be measured by the LDAR system when the calibrator is turned on. The measured time delays will be compared to the calculated propagation delays, and the differences will be determined and entered into the LDAR software as constants.

During the system checkout and certification, the calibrator will be used at least daily to verify proper system operation and system time delay stability. Based on this data, a System Calibration Interval will be established. The calibrator provides a ready means for system function test. When the calibrator is turned on a series of points will be displayed at the center of the primary LDAR display.

### SYSTEM REDUNDANCY

The LDAR System is actually two systems. LDAR Site 0 and remote sites 1, 3 and 5 comprise System 1; and site 0 and remote sites 2, 4 and 6 comprise System 2. Since Site 0 is common, both systems operate in

TABLE III. System specifications.

Operating Frequency	60-300 MHz
Initial Implementation	63 MHz
Data Band width	6 MHz
Data Collection Rate	$10^4$ events/second (maximum)
Data Window	100 microseconds
Number of Stations	6 Remote 1 Central
Remote Station Power	Solar Panel with batteries.
Operating reserve	3 days with overcast sky.
System Location Accuracy	
Within Network	X and Y $\pm$ 30 Meters Z $\pm$ 90 Meters
Outside Network	Basic Accuracy $\propto D^2/6$ D = Distance in miles
Processing Efficiency (i.e., the number of source locations that pass all data quality criteria)	75%
False Alarm Rate	0
Data Storage:	All raw data stored on Digital Audio Tape (1.2 GByte capacity)
System Outputs:	1. Television NTSC Compatible Display 2. Pulse source location broadcast on RS-232 Circuit.
Central Station Power	120/208 Vac 60 Hz With uninterruptible Power System (UPS) backup for a one hour power outage. System air conditioners are not on the UPS.
System Timing:	All trigger events will be time tagged to nearest microsecond. Timing source is a GPS receiver.

synchronization. The coordinate data from System 1 is designated as  $X_1$ ,  $Y_1$ , and  $Z_1$ , and the coordinate data from System 2 is designated  $X_2$ ,  $Y_2$ , and  $Z_2$ . By comparing the coordinate data from the two systems ( $D_1 = D_2 \pm K_1(D)$ ,  $Z_1 = Z_2 \pm K_2(D)$ , where  $D = [X^2 + Y^2]^{1/2}$  is the horizontal distance to the source and  $K_1$ ,  $K_2$  increase as a function of distance from Site 0) wild points can easily be detected. Initially, the sys-

tem will not display data that does not pass the comparison test, although the data will be archived. Future development may include calculations of coordinates using other remote site combinations, i.e. 0, 1, 3 and 6. Experience has shown that the coordinate comparison is a very stringent test that assures that bad data will not be provided for operational use.

## COMPARISON WITH EARLIER LDAR (LDAR-1)

The principal of operation and the site locations for the two systems are essentially the same. The major differences are discussed below.

### DATA TRANSMISSION FROM REMOTE SITES

LDAR-1 used a combination of wideband video circuits and microwave links. The new system uses all microwave links.

### REMOTE STATION POWER

LDAR-1 used commercial A.C. power with battery back-up at all but one site. One microwave site used batteries which were charged by a wind driven generator. In the new system, all remote sites are operated from solar charged batteries.

### CALIBRATOR

LDAR-1 used a spark gap transmitter, which was located on the roof of the Vehicle Assembly Building. The new system uses a solid state pulse generator to drive an antenna, located on the microwave tower at the central site.

### WAVEFORM PROCESSING

LDAR-1 used eight Biomation Model 8100 waveform recorders, operated in parallel, to digitize and store the waveforms of the RF pulses. The stored data was dumped to a parallel processor that determined the time to the peak of the largest pulse in each waveform. The new system does not use waveform recorders. The new system uses a special NASA built processor that determines the time to peak, and peak amplitude on the fly.

### DATA COLLECTION RATE

LDAR-1 could process a maximum of 200 sets of waveforms per second. The present system is designed to determine the peak amplitude and time delays for  $10^4$  waveform sets per second.

### DATA COMPUTATION

LDAR-1 used a mini-computer to ingest data and compute the coordinates of the pulse sources. The coordinates were transferred to a second computer

for display and storage. The programming language was Basic with equipment drivers written in Assemble language. The new system will utilize four single board computers to ingest and parallel process the data. The output of the processors will be transmitted to a work station for display generation. The primary programming languages will be Fortran and "C".

## DEVELOPMENT SCHEDULE

The LDAR system is under construction. Barring unforeseen procurement or development problems, the system should be ready to record data by May of 1991. The software required to produce an elementary real-time display should be available by July 1991.

## OPERATIONAL RESEARCH

The LDAR System is an excellent tool for locating the source of VHF pulses produced by the lightning discharge process; but considerable work is needed to determine the best utilization of LDAR data in support of ground and launch operations at the Cape Canaveral Forecast Facility (CCFF).

LDAR will initially operate at 63 MHz, in the range between 50 and 100 MHz where VHF pulses are most numerous according to Kimpara [4]. Since the best operational frequency is not yet known, the current system is designed to operate between 60 and 300 MHz. The design of the present LDAR also allows one system to be operated at 63 MHz and the second system to be operated at 225 MHz. By operating the system at two frequencies simultaneously, it should be possible to determine whether radiation at 63 MHz and at 225 MHz originate from different regions of the cloud. This in turn will determine the optimum operational configuration.

The LDAR data should also be useful in studying the following operational concerns:

1. Time From First Detected VHF radiation (or any other easily identifiable meteorological signature) to occurrence of first ground strike.
2. Number and characteristics of lightning-producing storms that do not produce ground strokes.
3. Lightning Hazard Distance - Distance from centroid of VHF radiation or radar echo to ground contact point.



4. Tracking of electrical storms.
5. Definition of the end of electrical activity.
6. Preferred location of storms.
7. Climatological data base.
8. Comparison of VHF source volume with radar volume.
9. Lightning rate as a predictor of storm behavior.

#### FUTURE SYSTEM ENHANCEMENTS

After successful implementation of LDAR, future enhancements to both hardware and software are under consideration. Several are described below.

The current system uses the peak pulse in a 100-microsecond window from each of the 7 sites for calculating the VHF source location. The system relies on running two systems in parallel to compare data and reject erroneous locations due to using an incorrect pulse. A future enhancement would employ cross-correlation techniques in either hardware or software to assure the same pulse is identified for each site.

A simpler technique may be to use more than two site combinations to calculate pulse location. This would provide assurance that the pulse was located correctly and provide receiver statistics that may help identify maintenance needs. This technique may also be used with cross-correlation techniques to provide an indicator of system accuracy for the location of each radiation source

Another enhancement would lengthen the 100-microsecond window and overlap it with the subsequent windows at each of the remote sites to assure that the peak pulse in the window at site 0 will be available in the windows of each of the remote sites.

To improve vertical resolution, elevation angle measured from an interferometer at site 0 may be used.

#### ACKNOWLEDGEMENTS

Special recognition goes to Thomas Britt who designed and built the special hardware required to determine the TOA of the RF pulses. Also, we wish to recognize the special efforts to the technicians, Co-ops, coordinators and procurement personnel who have overcome many obstacles to make this project a reality.

#### REFERENCES

1. Pierce, E. T., The Thunderstorm Research International Program (TRIP)-1976, *Bull. Am. Meteorol. Soc.*, 57, 1214-1216, 1976.
2. Poehler, H. A. and Lennon, C. L., Lightning Detection and Ranging System, LDAR, System Description and Performance Objectives, NASA Technical Memorandum 741005, 1979.
3. Proctor, D. E., A hyperbolic system for obtaining VHF radio pictures of lightning, *J. Geophys. Res.*, 76, 1478-1489, 1971.
4. Oetzel, Pierce, Radio Emissions From Close Lightning, Planetary Electrodynamics, International Conference on the Universal Aspects of Atmospheric Electricity, Chapter IV, Pg 558, 1969.

## LIGHTNING TESTING AT THE SUBSYSTEM LEVEL

Frank Luteran  
 EMC Science Center, Inc.  
 West Conshohocken, PA 19428

## ABSTRACT

Testing at the subsystem or black box level for lightning hardness is required if system hardness is to be assured at the system level. The often applied philosophy of lightning testing only at the system level leads to extensive end of the line design changes which result in excessive costs and time delays. In order to perform testing at the subsystem level two important factors must be defined to make the testing simulation meaningful. The first factor is the definition of the test stimulus appropriate to the subsystem level. Application of system level stimulations to the subsystem level usually leads to significant overdesign of the subsystem which is not necessary and may impair normal subsystem performance.

The second factor is the availability of test equipment needed to provide the subsystem level lightning stimulation. Equipment for testing at this level should be portable or at least movable to enable efficient testing in a design laboratory environment. Large fixed test installations for system level tests are not readily available for use by the design engineers at the subsystem level and usually require special operating skills.

The two factors, stimulation level and test equipment availability, must be evaluated together in order to produce a practical, workable test standard. The neglect or subordination of either factor will guarantee failure in generating the standard. It is not unusual to hear that test standards or specifications are waived because a specified stimulation level cannot be accomplished by in-house or independent test facilities. Determination of subsystem lightning simulation level requires a knowledge and evaluation of field coupling modes, peak and median levels of voltages and currents, bandwidths and repetition rates.

Practical limitations on test systems may require tradeoffs in lightning stimulation parameters in order

to build practical test equipment. Peak power levels that can be generated at specified bandwidths with standard electrical components must be considered in the design and costing of the test system. Stimulation test equipment and test methods are closely related and must be considered a test system for lightning simulation.

A non-perfect specification that can be reliably and repeatedly applied at the subsystem test level is more desirable than a perfect specification that cannot be applied at all.

## SUBSYSTEM LEVEL TESTING BENEFITS

Why test at subsystem or black box level? Why not let the system test qualify all the subsystem boxes? Subsystem testing provides two important benefits.

First - In most cases subsystem testing saves money by ensuring that the system tests will be successful. When failure of subsystems occur during system testing, the cost of redesign and rework is escalated by a factor to ten (10) times the cost of correcting a problem identified during subsystem test (Figure 1). In fact an even more ideal situation exists when testing can be performed at the bread-board level where costs to redesign are typically one tenth (1/10) the cost of redesign at the subsystem level.

The designer who depends on system tests alone to qualify a subsystem is facing costs one hundred (100) times greater for redesign at this level over redesigns at the board level. Testing only at system level is a gamble with the odds stacked against the subsystem designer.

Second - Subsystem performance can be characterized and defined more completely for various stimulus levels. The subsystem should be tested to full threat level or even over threat levels. The

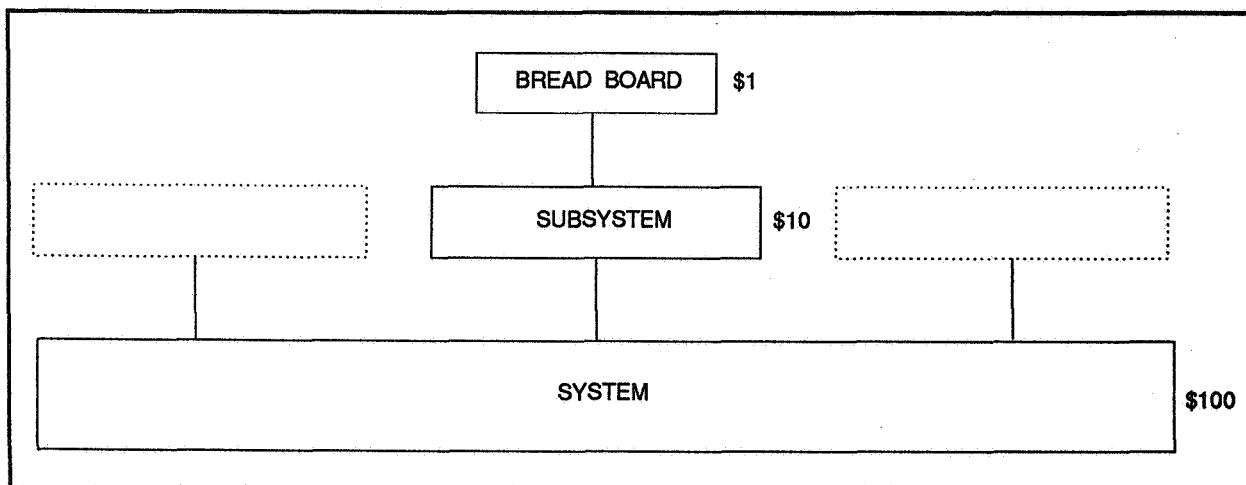


Figure 1. Test Levels.

threshold of failure can be accurately measured when the test generator can produce reduced levels as well as the full threat level. It is desirable to test at full threat level rather than at a reduced level with linear scaling to full threat level since subsystems seldom react in a linear manner except over narrow ranges at low stimulus levels.

There is typically interaction between subsystems because they share a common power supply, have a common database and have interconnections. When a massive failure occurs at system level test it is important to know which subsystem started the failure chain. The subsystem which is the source of failure and which is the victim is often difficult to identify. If threshold levels are known for each subsystem, the failure mode and propagation paths can be easily identified and corrected.

An additional benefit arises from the testing of multi-purpose or generic subsystems. Once the response of the subsystem to specific waveforms and levels is known, the response to other waveforms can be accurately predicted, thereby reducing or eliminating the testing required when the subsystem is utilized in other systems having different system test parameters.

#### DEFINING SUBSYSTEM LIGHTNING STIMULUS

The task of translating system level lightning stimulus into subsystem stimulus is not a simple task. Although certain models of lightning waveforms for

direct and near strikes have been defined, it has been observed that each year the lightning model becomes faster and more intense (Figure 2). Which-ever model is used, the system response which is the subsystem stimulus must be defined on the basis of frequency, duration, levels, and coupling modes acquired from full scale models in full threat lightning simulators.

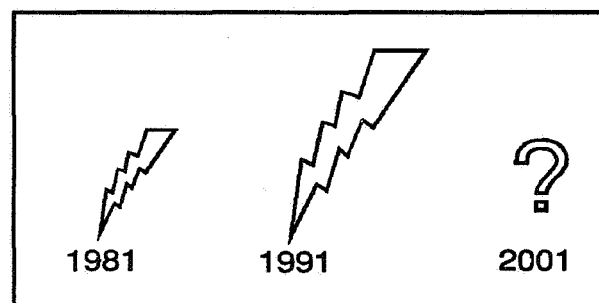


Figure 2. Lightning Stimulus.

Therefore, the criteria for defining the subsystem stimulus is the waveform stimulus that is coupled from the system to the subsystem. An example of coupled waveform stimulus can be found in MIL-STD-461C. The EMP test requirement is defined by tests specified as RS05, CS10 and CS11 for Naval equipment and CS12 and CS13 for Air Force equipment. The RS05 requirement duplicates the EMP field which is a double exponential of 50 kV per meter (Figure 3). This stimulus is used at the system level. The effect of the system stimulus is to couple damped sinusoid currents with a bandwidth of approximately 10 kHz to 100 MHz into the subsystem. The stimulus for subsystem tests CS10, CS11, CS12 and CS13 is

therefore a group of six damped sinusoid pulses at frequencies from 10 kHz to 100 MHz (Figure 4).

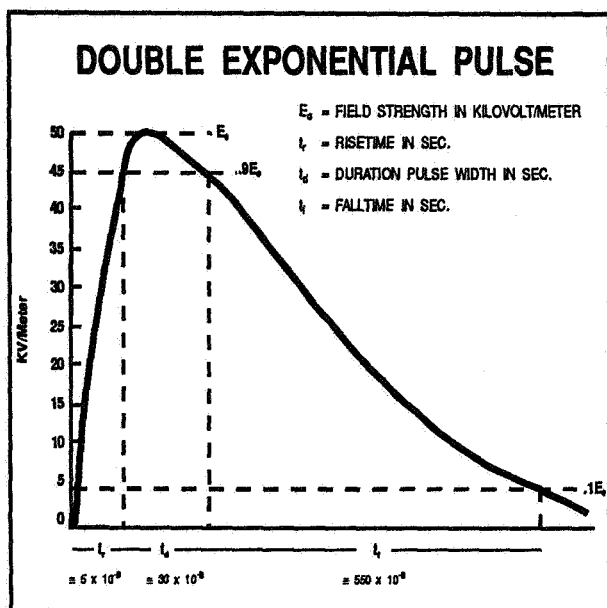


Figure 3. EMP System Waveform MIL-STD-461C RS05.

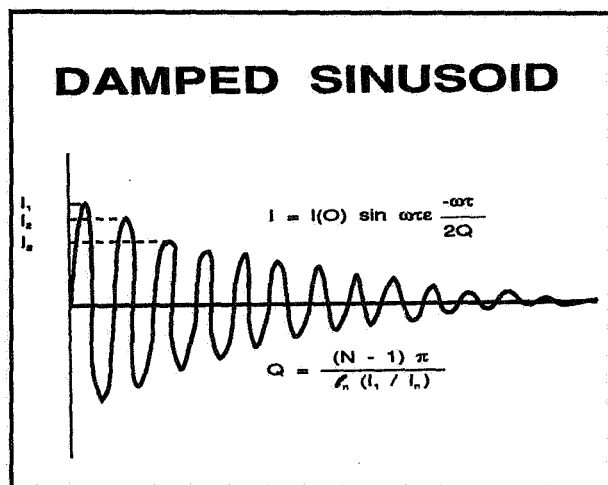


Figure 4. EMP Subsystem Waveform MIL-STD-461C CS10, 11, 12, 13.

Attempts have been made to define the lightning stimulus through various specification and advisories such as DO-160, Boeing Specs, SAE AE4L, FAA AC 20-136 and various modification of these documents. The range of waveforms include single pulse, multi-pulse and multiple bursts of double exponential and damped sinusoid waves (Figures 5, 6, 7). The levels for the various zones have been defined although with some confusion.

The purpose for the various waveshapes and levels is not adequately described in the specification and standards so it is not possible to substitute equivalent waveshapes when test equipment is not available to generate the specified waves. All too often the tests are waived when the exact waveform is not available. The use of equivalent test waveforms is an area that has not been rigorously pursued. Empirical data may suggest that a peak current or voltage and a total energy requirement is sufficient to simulate a particular threat. In this instance the test waveforms may be a rectangular pulse, a double exponential or damped sinusoid of equal energy waveforms having the same peak current. It is interesting to look at the relationship between different rise times for a fixed fall time pulse as shown in Figure 8. What appears to be a minor change in rise time relates to a significant change in total energy. It cannot be emphasized enough that equivalence of waveforms requires detailed analysis. Another factor that may have to be considered is the rise time of the waveform. Nonlinear devices such as spark gaps may not conduct if the rise time is fast and the pulse duration short. In this instance consideration of the subsystem circuit design must be made before selecting an alternate test waveform. The best person to define circuit response to alternate waveforms is the designer. When testing is performed on the designer's turf, involvement of the design team is assured. There are no guarantees that equivalent waveforms will identify circuit failure modes 100% of the time. It has been reported in some tests that rectangular pulses of a given energy and peak value will not cause circuit failure, yet an equivalent damped sine wave test produces failures approximately 10% of the time. Figure 9 shows how the energy level of a damped sinusoid may be changed by varying the  $Q$ . This characteristic provides a convenient method of controlling pulse energy level.

Although alternate means of qualification may be through analysis or expert opinion, I maintain that one good test is worth a hundred expert opinions.

## SUBSYSTEM TEST EQUIPMENT REQUIREMENTS

Test equipment acceptable for breadboard and subsystem testing must possess properties that are quite different from the test equipment used for system level tests. The obvious difference is that the subsystem test stimulus is not a reduced level of the

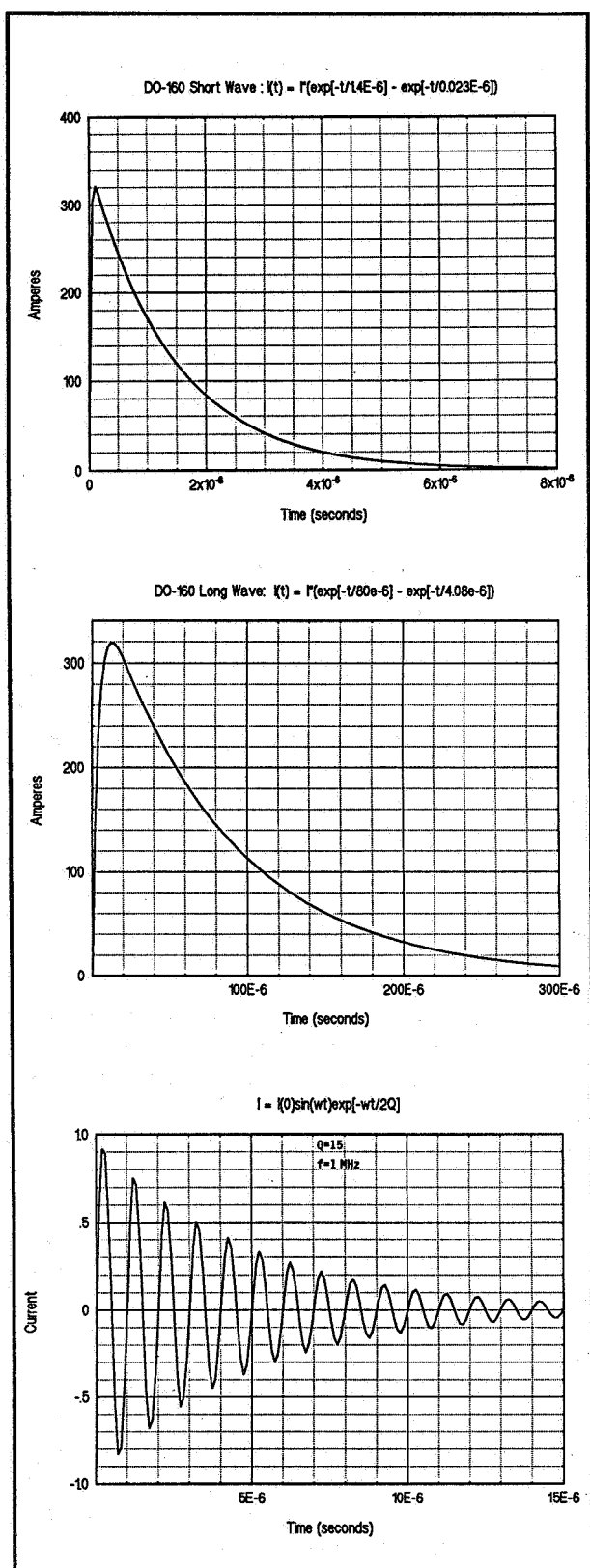


Figure 5. Single Pulse.

system test stimulus. It is critical that the system designer provide the subsystem designer with stimulus information early in the design cycle so that testing can begin as early as the breadboarding stage, but definitely not later than the subsystem test phase.

The subsystem test waveforms should be determined not only from equivalence considerations, but also from the availability of equipment and the waveforms and levels that can be produced by test generators suitable for use at the subsystem and breadboard levels.

Test equipment selection should be based upon the following characteristics:

- Portability - test equipment should come to the hardware to minimize set-up time and to be convenient for use by the design team.
- Ease of Use - design personnel should be able to operate the test equipment with minimal training. The test generators should be as familiar to the design group as an oscilloscope.
- Controllability - signal levels, polarities, source impedance, and frequencies and Q's for damped sinusoids should be variable.
- Operationally Safe - lethal voltages and energy levels are usually present in the test generators. Safety features such as interlocks, key switches, manual pulsing and standby modes should be incorporated.

Test equipment limitations should also be considered by the equipment selector. Test equipment weights are typically limited to 150 pounds for hand carry units by two people to about 1800 pounds for a console that can be wheeled through a standard doorway.

Transient generators which are suitable for generating the waveform types previously described are of store and dump design rather than of amplifier design. Using a low level waveshape generator and a power amplifier to generate the desired signal is not practical due to the high peak power required from the amplifier. A waveform requirement of 10 amp peak current through a 100 ohm load calculates to a peak power of 10 kW which could be supplied by an amplifier of about 5 kW average power. An amplifier of this size is very expensive and could only meet the

lower level waveform requirements. In comparison the store and dump design is an order of magnitude lower in cost for most of the higher level waveforms. In the store and dump generator design, energy is usually stored in a capacitor bank and then switched (dumped) into a pulse forming network. The switching element is either a spark gap or a high voltage relay. From practical and safety considerations the charging voltages are usually kept below 30 kV. The largest contributor to the weight of the generator is the energy storage capacitor or capacitors. High energy capacitors can store 8J/in<sup>3</sup> or 488KJ/m<sup>3</sup> at a weight of 10 lbs/KJ.

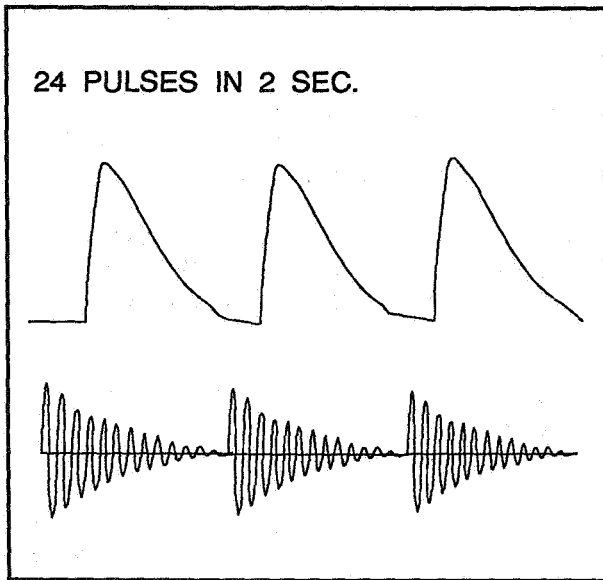


Figure 6. Multiple Pulses.

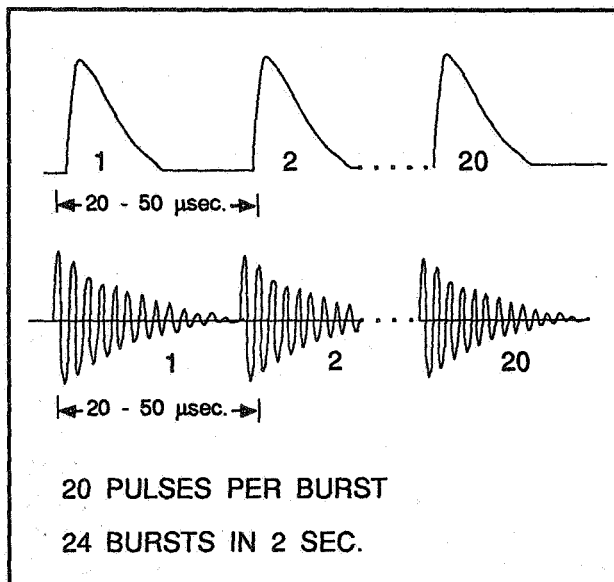


Figure 7. Multiple Bursts.

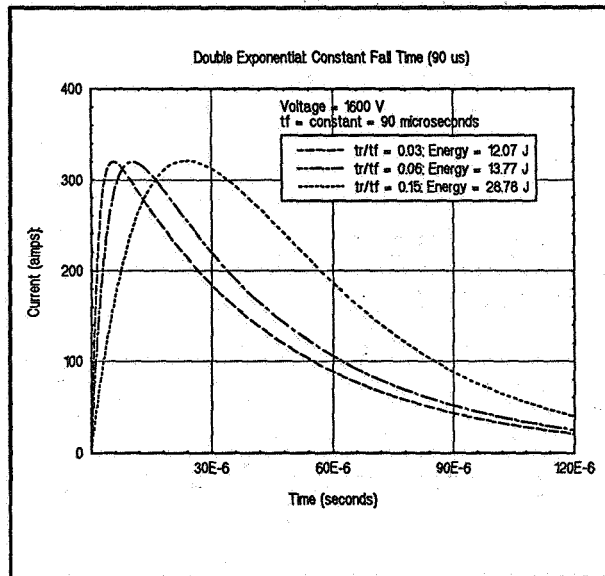


Figure 8. Time Constant-Energy Factors.

In order to provide a certain amount of flexibility in a test generator, a multiple of capacitors is preferred rather than a single large unit (Figure 10). Smaller capacitor units allow reconfiguration of the system to generate additional waveforms at low additional cost.

Multiple resistors also offer a certain amount of flexibility; however resistor changing is not usually a large expense.

Another consideration for test equipment is the type of waveform that is to be generated. The double exponential waveshapes usually require a charging voltage 15% than the generated voltage while the generation of a damped sinusoid requires a charging voltage 5% higher than the product of the peak waveform and "Q" (i.e.,  $1.05 \times V_p \times Q$ ). It is understandable why damped sinusoid generators cost more than exponential generators for equal peak voltage values.

The power requirement for the test generator is an important factor that usually is overlooked. To generate waveshapes by the charge and dump technique requires ten to twenty times the energy/power that is delivered to the subsystem under test. Although the peak power produced by the generator may be very high, the average line power requirements are within the range normally available in a design laboratory environment. A well designed transient test generator will produce waveforms that

will vary less than 10% in amplitude, rise and fall times and source impedance over the open circuit to short circuit range of the generator.

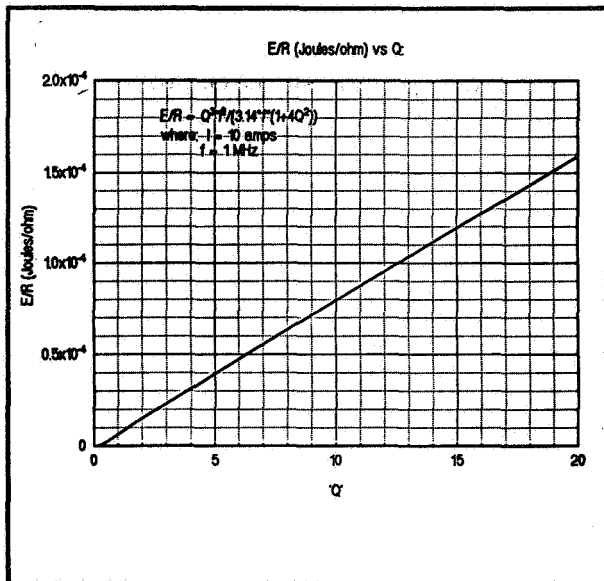


Figure 9. Q-Energy Factor.

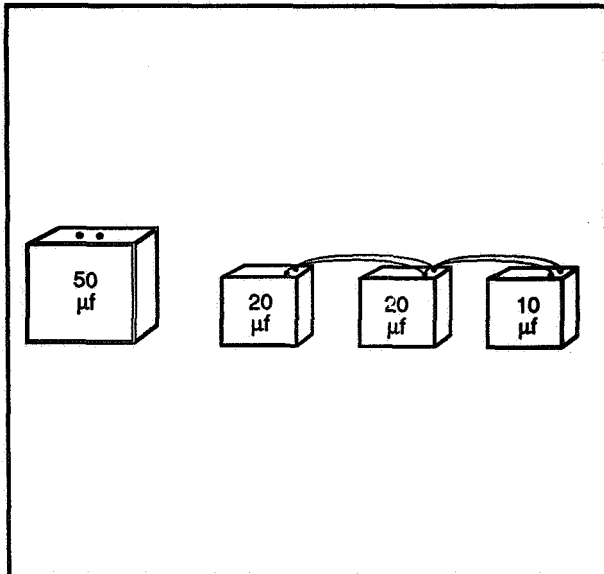


Figure 10. Modular Capacitor Design

## CONCLUSIONS

The increasing application of sensitive electronics to subsystems that are susceptible to damage by lightning requires a new test philosophy. Testing at levels below system level is practical and offers potential cost savings that can approach several orders of magnitude.

Additional efforts are required to define the test stimulus that must be applied to subsystems so that test waveforms and equivalent test waveforms can be defined. Circuit designers must be included on the test team in order to ensure that the subsystems are properly stressed by equivalent waveforms.

Test equipment is available to produce damped sinusoids and double exponentials, the most commonly specified test waveforms. Selection of test equipment must be based on a knowledge of the signal generation technique and the variable features of the equipment. Test generators should be considered an essential instrument in the design lab.

## BIBLIOGRAPHY

1. A.S. Padogorski and E.M. Podogorski, "Lightning Standards for Protection of Ground Electronic Systems," Proceedings of the 1988 International Aerospace and Ground Conference on Lightning and Static Electricity, pp 324-327, April 19-22, 1988.
2. MIL-STD-1757 (1980) MIL-STD-1957A (1983) Lightning Qualification Test Techniques for Aerospace Vehicles and Hardware.
3. FAA AC 20-136.
4. RTCA Paper No. 250-87/SC135-186 Lightning Induced Transient Susceptibility.
5. MIL-STD-461C.
6. F.D. Martzloff and T.F. Leedy, "Electrical Fast-Transient Tests: Applications and Limitations," IEEE Transactions on Industry Applications, Vol. 26, No. 1, January/February 1990.
7. K.E. Crouch, "Aircraft Lightning-Induced Voltage Test Technique Developments," NASA Contractor Report 170403, NASA 1983.

**Cloud-To-Ground Lightning Surveillance Capabilities at the U.S. Air  
Force Eastern Space and Missile Center**  
*by M. Maier and R. White*

**No paper available.**



**A Continually Recording Method for Lightning Stroke Waveform**  
*by X. Lingen, G. Chao, and L. Xinkang*

**No paper available.**

**Session 14B, Friday 10:45**  
**Specifications and Standards**  
**Reed, Chairman**

## IMPLEMENTATION OF THE FAA RESEARCH AND DEVELOPMENT ELECTROMAGNETIC DATABASE

R. L. McDowall  
Computer Resource Management, Incorporated  
FAA Technical Center, Atlantic City International Airport, NJ

D. J. Grush and D. M. Cook  
EG&G Idaho, Incorporated  
Idaho Falls, Idaho

M. S. Glynn  
Federal Aviation Administration  
FAA Technical Center, Atlantic City International Airport, NJ

## ABSTRACT

The Idaho National Engineering Laboratory (INEL) has been assisting the Federal Aviation Administration (FAA) in developing a database of information about lightning. The FAA Research and Development Electromagnetic Database (FRED) will ultimately contain data from a variety of airborne and ground-based lightning research projects. This paper contains an outline of the data currently available in FRED. It also lists the data sources which the FAA intends to incorporate into FRED. In addition, it describes how the researcher may access and use the FRED menu system.

## INTRODUCTION

A number of researchers throughout the world have conducted research on lightning. In general, once a researcher has published his data and conclusions, it is very difficult for other researchers to access that data. In the Proceedings of the 1988 International Aerospace and Ground Conference on Lightning and Static Electricity [1], Computer Resource Management, Incorporated (CRM) reported on the plans which the FAA had for the creation of a world-wide database of information on lightning. This paper presents the accomplishments made since that time.

The FAA has solicited data from a number of different sources to be compiled in a database. The aim of this database is to unite in one location information compiled by different researchers using different equipment with different research goals in mind.

At present, not all data sources contain information for all of the data fields in FRED. In addition, as other sources become available, new fields may be added to FRED. FRED's major function will be to provide a place to collect data gathered in lightning studies conducted throughout the world. The combined data will then be available to researchers in common format for analysis, allowing them to create and test lightning models.

The minimum objective for FRED will be to provide access so that users can see what information has already been collected. They can then use this

information to plan future physical or statistical research projects.

Functions currently available through FRED include average, mean, integration, differentiation, maximum, minimum, relative maxima, relative minima, waveform plots, and scatter diagrams of combinations of fields.

Functions anticipated to be available through FRED include fast Fourier transforms, standard deviation, correlations, and histograms of combinations of fields.

FRED will provide investigators with the ability to generate reports and perform statistical analyses. A number of pre-programmed reports and graphs are available to the user. These reports can be selected from the menus. Other reports may be available on request from the FAA Database Administrator (DBA):

FRED Database Administrator, ACD-230  
Flight Safety Research Branch  
FAA Technical Center  
Atlantic City International Airport, NJ 08405 USA

#### DATA

Although a number of data sources have been identified, acquisition of the data has not proceeded as rapidly as anticipated. Data have been acquired from the FAA (the CV-580 program), from the National Aeronautical and Space Administration (NASA) (the F-106 program) and from the Bureau of Land Management (BLM). Each of these data sources will be discussed below. If a user has an existing body of data, the FAA would be very interested in reviewing it for inclusion in FRED.

There are three basic types of information contained in FRED: environmental, electromagnetic, and waveform data. At a minimum, for each strike, there will be both environmental and electromagnetic data. Although FRED allows for entry of various items of data, not all sources will have entries in all data fields.

The following sections describe the data fields in FRED. All possible data fields are listed along with a description of the data they may contain. In addition, the default value for each field is given. In general, the default value will be some value that is physically or logically impossible to obtain, or will be the letter "U" or the word "Unknown".

#### WAVEFORM DATA

Waveform data consists of data points recorded either by a digital or an analog recorder. If the waveform was recorded in analog format, it was digitized before inclusion in FRED.

#### ENVIRONMENTAL DATA

Environmental data consists of data describing the environment at the time of the strike. Items such as air temperature, or precipitation type and

intensity are examples of environmental data. Table I shows the possible environmental data fields and their default or unknown values.

TABLE I. ENVIRONMENTAL DATA

FIELD	DEFAULT VALUE	FIELD	DEFAULT VALUE
ALTITUDE	-9999	AIRSPEED	-9999
OUTSIDE AIR TEMPERATURE	-9999	LATITUDE	999:99:99
LONGITUDE	999:99:99	PRECIPITATION SEVERITY	U
TYPE OF PRECIPITATION	0	TURBULENCE	U
ATTACHMENT-DETACHMENT POINT	Not Available		

#### ELECTROMAGNETIC DATA

Electromagnetic data consists of those electromagnetic parameters which can be calculated from a waveform or which can be sensed directly. Table II shows the possible electromagnetic data fields and their default values. Those fields whose default value is marked with an asterisk (\*) do not have default values.

TABLE II. ELECTROMAGNETIC DATA

FIELD	DEFAULT VALUE	FIELD	DEFAULT VALUE
SENSING PARAMETER	*	PEAK VALUE OF PARAMETER	*
PEAK RATE OF RISE OF PARAMETER	OEO	TIME TO PEAK VALUE OF PARAMETER	*
FULL WIDTH AT HALF MAXIMUM VALUE	*	TIME TO HALF MAXIMUM VALUE	*
SATURATION FLAG SET	U	ACTION INTEGRAL	blank
CHARGE TRANSFER	blank	TRIGGER THRESHOLD	-9999
SATURATION THRESHOLD	-9999	F LL SCALE	-9999

#### OTHER DATA

In addition to the data described above, FRED carries other information important to the understanding of the lightning event and its measurement. There are two basic types of other data, data describing the data source and data describing the data collection equipment. These data fields are shown in table III. Those fields whose default value is marked with an asterisk (\*) do not have default values.

#### DATA SOURCES

##### CV-580 DATA

During 1984, 1985, and 1987 the FAA conducted a program to take electromagnetic measurements of strikes to an aircraft which was flown in thunderstorms in Florida. This program was conducted jointly with the Air Force, the Navy, NASA, the National Oceanic and Atmospheric Administration (NOAA), and the Offices Nationales des Etudes et Recherches Aerospatiales

(ONERA). The program employed a Convair 580 aircraft specifically hardened against lightning. During the course of the program, the aircraft was struck approximately 60 times.

TABLE III. OTHER DATA

FIELD	DEFAULT VALUE	FIELD	DEFAULT VALUE
SOURCE TYPE	blank	MODEL NUMBER	*
SOURCE NAME	*	SENSOR TYPE	*
PRIMARY RESEARCHER	blank	LOWER FREQUENCY RESPONSE LIMIT	*
RESEARCHER'S AFFILIATION	blank	UPPER FREQUENCY RESPONSE LIMIT	*
DATE OF FLASH	*	ACCURACY	*
TIME OF FLASH	*	MANUFACTURER	*
TIME OF INITIAL SAMPLE POINT	*	MODEL NUMBER	*
PENETRATION	U	NUMBER DISCRETIZATION LEVELS	*
SENSOR LOCATION	*	NUMBER OF CHANNELS	*
DIGITIZER ID	*	MAXIMUM FM BANDWIDTH	*
SAMPLING INTERVAL	*	MAXIMUM DIRECT RECORD BANDWIDTH	*
SAMPLING WINDOW	*	FULL SCALE	*
ANALOG RECORDER ID	*	DYNAMIC RANGE	*
MANUFACTURER	*		

Three types of data were collected under this program: digital recordings, analog recordings, and manually written log sheets. The log sheets contain information about the environment: the altitude, temperature, airspeed, and precipitation and turbulence conditions. They also contain the date and time of the strike and the longitude and latitude of the aircraft when it was struck.

The CV-580 was instrumented with a variety of sensors throughout the aircraft. The number, kinds, and locations of the sensors varied from one year to the next. These sensors fed both analog and digital tape recorders. The analog recorders ran continuously during the flight, except when a tape ran out and a new tape was being mounted. Analog recordings were made for 48 of the strikes to the aircraft. The analog signals were converted to digital representations by Electro Magnetic Applications, Incorporated (EMA). This effort is described in an internal FAA report [2]. The digitized analog data and the data from the log sheets were entered into FRED by the staff at the INEL.

#### NASA F-106 DATA

Between 1981 and 1986, NASA conducted a program to study lightning at high atmospheric levels. An instrumented F-106 aircraft was flown into storm clouds. Data was collected on strikes near the aircraft, as well as strikes directly to the aircraft. Although both analog and digital waveforms were collected, only the digital will be incorporated into FRED. Additional data consists of environmental and other data similar to that collected under the CV-580 program.

#### BLM DATA

The BLM collects lightning location data on strikes in 11 western states of

FRED

FRED will be housed on equipment at the INEL Supercomputing Center (ISC) in Idaho Falls, Idaho. Figure 1 shows the relationships among the various components used to store or access FRED.

FRED will be housed on equipment at the INEL Supercomputing Center (ISC) in Idaho Falls, Idaho. Figure 1 shows the relationships among the various components used to store or access FRED.



To gain access to FRED, the user will request permission from the FAA DBA and complete the forms for INEL computer access.

93-5

## WELCOME SCREEN

The access to some of the data provided to the FAA for inclusion in FRED has been restricted by the original data owner. If a user's access to some data has been restricted, the user will see a restriction message in the Welcome Screen.

The Welcome Screen will also show the last time FRED was accessed by this User-ID and the last time FRED was updated. These dates allow the user to determine if the database has been changed since his last access, or if someone else is using his ID. From the Welcome Screen, the user can go to the User Menu or exit the system.

## USER MENU SCREEN

The User Menu Screen (shown in figure 2) allows the user to select browsing, querying, and listing functions. These functions are selected by typing the appropriate number in the Selection field. Pressing the <EXIT> key causes the user to be logged off the system.

The diagram shows a rectangular window titled "Update and System Menu". Inside this window is a smaller rectangle containing a numbered list of three options:

- 1 - Browse the SOURCE, FLASH, EMD Data
- 2 - Query by Range Limits with Plot, Statistics, Report and Data Loading Capabilities
- 3 - Waveform Processing

Below the inner rectangle, the text "Selection:" is displayed. At the bottom of the outer rectangle, the following instructions are provided:

Press COMMIT to invoke selection  
Press EXIT to exit system

FIGURE 2. USER MENU

The first function on the User Menu allows the user to browse among the records which are available to him in FRED. Selecting this option causes the system to display the Summary Data screen (shown in figure 3).

The user may scroll through the information about sources of data available in FRED. When the user has selected the source he wishes to use, he may scroll up and down through the flashes for that source. For each source there will be many records in the Flash file. Each record will correspond to one strike of lightning.

When the user has identified the flash in which he is interested, he may move to the Electromagnetic Data block. When the cursor is positioned in the Electromagnetic Data block, the user may scroll through the electromagnetic data records for the selected flash. For each flash there may be many records in the electromagnetic data file. Each record will contain information collected by one sensor from this one strike of lightning.



Summary Data Selection by Source and Flash			
Source Type Airborne Source Name CV-580 Researcher Glynn, Burkett, Jafferis, Mazur, Reazer Affiliation FAA, AF, NASA, NOAA, TSSI			
Flash ID 2	Strike Type	Flash Date 30-JUL-87	Time 19:08:23
	Attach Point	Direct Attachment	Airspeed 170 knots
	Detach Point	Not Available	Altitude 140 x 100ft
	Turbulence Severity	Light	Latitude 28:28:54 N
	Precipitation Severity	Unknown	Longitude 80:42:47 W
	Initial Strike Time	19:08:22.9442125	Air Temp. 1 degrees C
Electrical Phenomena		Visible Lightning	
Precipitation		Rain Icing	
Press COMMIT to produce a report    Press NXTREC/PRVREC to scroll within a block Press EXIT to go back                Press NXTBLK/PRVBLK to move between blocks			

FIGURE 3. SUMMARY DATA SCREEN

If a waveform has been recorded for this sensor, the user may also elect to look at information about the waveform. Invoking the waveform information calls the Electromagnetic Data screen, shown in figure 4.

ELECTROMAGNETIC Data for FLASH 16-JUL-87 14:44:52			
Waveform ID	11	Analog Recorder ID	1
Sensor ID	9	Digitizer ID	1
Sensor Location	Left Wing	Sensing Parameter	I-L
Peak Value	1.54849E+03		
Peak Rise	1.52680E+09	Peak Array Loc.	256181
Time to Peak	8.26900E+06 nsec	Peak Rise Location	356386
Full Width at Half	3.72000E+05 nsec	Time to half max.	5.00000E+02
Time to Half Max.	8.14400E+03 nsec	Sampling Window	1.04858E+03
Trigger Threshold	-9.99900E+03	Saturation Threshold	8.88320E+03
Full Scale	-9999	Saturation	U
Sensor Scale Factor	2.50000E+02	Record Scale Factor	6.94000E+00
Conversion Factor	1.00000E+00	Number Points	2097152
Data Scale Factor	1.00000E+00		
Action Integral	2.44145E+03 Amp2/sec2	Integration Start Point	141415
Charge Transfer	1.08510E+01 C	Integration Stop Point	356386
Press COMMIT to produce a report    Press DUPLICATE RECORD to load this waveform Press EXIT to go back			

FIGURE 4. ELECTROMAGNETIC DATA SCREEN

The Electromagnetic Data screen shows the user information about the waveform selected in the Summary Data screen. The bottom block contains information only if the sensor for the selected waveform is a current or "I" sensor. The other blocks will contain information for all waveforms. After viewing the data, the user may return to the previous menu to select another Source, Flash, or Electromagnetic Data record. The user may also produce a report of the waveform or request that the waveform be loaded onto the CRAY from the Electromagnetic Data screen.

#### Query Screen

The second function on the User Menu allows the user to select data from FRED. The selected data may then be viewed, plotted, reported, or used for

statistical analysis. Selecting "2" causes the system to display the Query screen (shown in figure 5).

Query of the Summary Data					
			Total Counts		
			Total Number of Flashes 10	Number of Positive Flashes 10	Number of Negative Flashes 9
Query Limits:	Min	to	Max	Selections	
Altitude	-9999		145 x 100ft	1 - Query	
Airspeed	-9999		229 knots	2 - Display Queried Results	
Air Temperature	-9999		5 degrees C	3 - Plot Using Query Limits	
Latitude	999:999:99 U		28:54:17 N	4 - Statistical Analysis	
Longitude	999:999:99 U		80:42:06 W	5 - Report Queried Results	
Dates	11-JUL-84		04-AUG-87	6 - Reset Defaults	

Selection:

Press COMMIT to invoke selection  
Press EXIT to go back

FIGURE 5. QUERY SCREEN

When this screen is invoked for the first time, the total counts reflect the total number of strikes of the relevant type in FRED. In addition, the query limits for each parameter are set to the minimum and maximum values in FRED. In general, if a numeric value is not known, it is set to the most negative value possible for the field. Alphabetic values are set to blank or "U" if unknown.

In addition to the six selections offered on this screen, the user may change values in any of the parameter fields. After changing any of the limiting parameters, the user may restore the original defaults by typing a "6" in the Selection field. This results in the restoration of the screen to the original values, but does not perform a query. As a result, the data which has already been retrieved is not reset. If the user resets the defaults and then tries to display the queried results without invoking a query first, the data will remain the same.

Typing a "1" in the Selection field of the Query screen issues a "query" to the database management system. An ORACLE query selects data from the database using the selection criteria and the limits displayed on the screen at the time the query is invoked. When the query is invoked, FRED will count the total number of flashes and the number of positive and negative flashes resulting from the query. These numbers will be displayed in the top block of the Query screen.

Typing a "2" in the Selection field will display the queried results by invoking the Source and Flash screen (shown in figure 6). If no query has been made, the Source and Flash screen will be displayed, but it will contain no data. It is imperative, therefore, that the user issue a query by invoking selection "1" before selecting this option, even if the user is interested in browsing through the entire set of FRED data.

Typing a "3" in the Selection field of the screen invokes the Graphics Menu screen shown in figure 7. This screen allows the user to plot the data

contained in the displayed limits. (The user need not execute a query to select the data.) The user may select a number from one to eight corresponding to the plots listed on the screen.

Source and Flash of the Data			
Source Type	Airborne		
Source Name	CV-580		
Researcher	Glynn, Burkett, Jafferis, Mazur, Reazer		
Affiliation	FAA, AF, NASA, NOAA, TSSI		
Flash ID 2	Strike Type	Flash Date 30-JUL-87	Time 19:08:23
	Attach Point	Direct Attachment	Airspeed 170 knots
	Detach Point	Not Available	Altitude 140 x 100ft
	Turbulence Severity	Light	Latitude 28:28:54 N
	Precipitation Severity	UnKnown	Longitude 80:42:47 W
	Initial Strike Time	19:08:22.9442125	Air Temp. 1 degrees C
Electrical Phenomena		Visible Lightning	
Precipitation		Rain Icing	

Press COMMIT to produce a report      Press NXTREC/PRVREC to scroll within a block  
Press EXIT to go back                      Press NXTBLK/PRVBLK to move between blocks

FIGURE 6. SOURCE AND FLASH SCREEN

Graphics Menu	
1.	Peak Value Vs. Latitude
2.	Peak Value Vs. Longitude
3.	Peak Value Vs. Temperature
4.	Peak Value Vs. Altitude
5.	Peak Rise Vs. Latitude
6.	Peak Rise Vs. Longitude
7.	Peak Rise Vs. Temperature
8.	Peak Rise Vs. Altitude

Press COMMIT to invoke selection      Selection:  
Press EXIT to go back

FIGURE 7. GRAPHICS MENU

When the user has made his selection, the system displays a Plot Customization screen. This screen allows the user the change the defaults used in creating the plot. When the user is satisfied with the information on the Plot Customization screen, the system will ask the user to select the device on which the plot is to be displayed. If the user wishes to display the plot on his terminal, the terminal must be compatible with Tektronix equipment.

When the plot is completed, the user returns to FRED by typing "quit" and "logout". A sample plot is shown in figure 8.

Typing a "4" in the Selection field of the Query screen and pressing <COMMIT> invokes the SQL environment. This environment allows the user to write his own SQL queries. Two sample queries are shown in figure 9. The resulting reports are shown in figures 10 and 11.

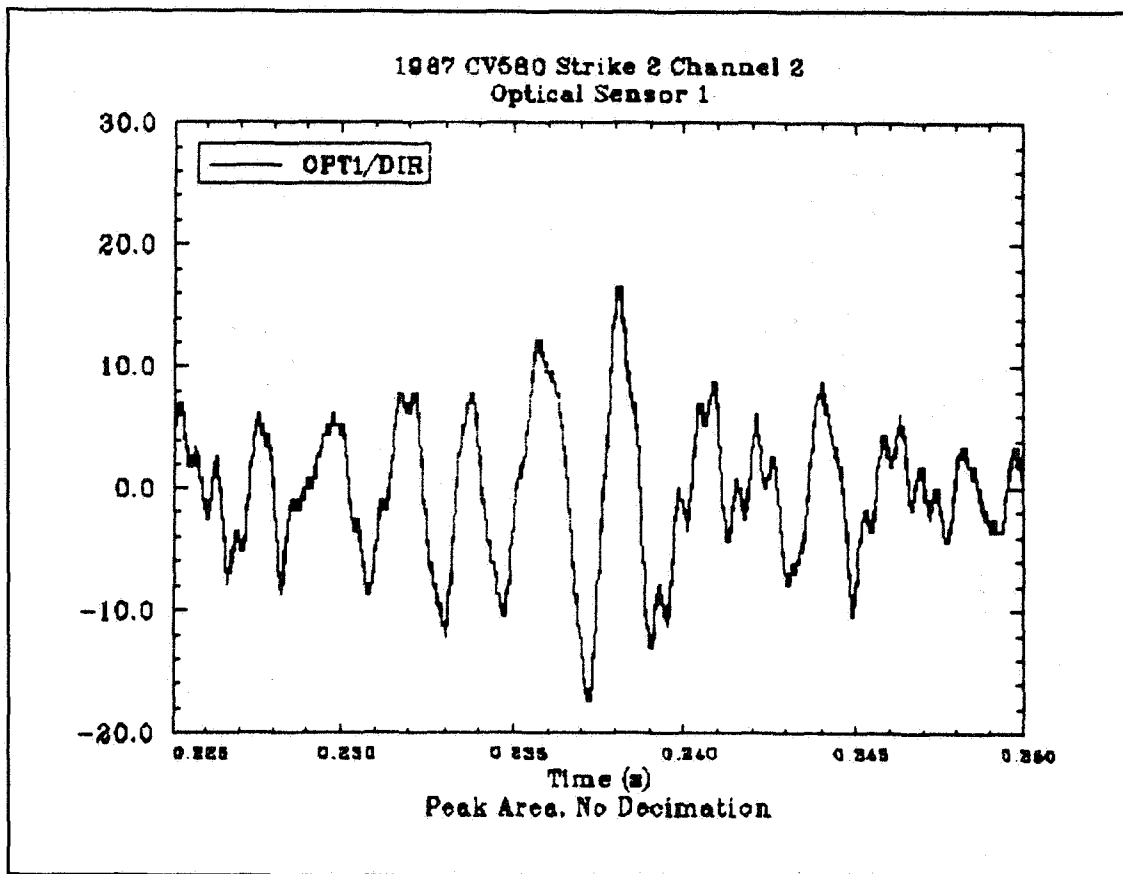


FIGURE 8. SAMPLE FRED PLOT

```

select action_integral,altitude,air_temperature
from i_param,flash,emd
where i_param.waveform_id=emd.waveform_id
and emd.flash_id=flash.flash_id
/

select action_integral,altitude,air_temperature
from i_param,flash,emd
where i_param.waveform_id=emd.waveform_id
and emd.flash_id=flash.flash_id
and action_integral=(select max(action_integral) from i_param)
/

```

FIGURE 9. SAMPLE SQL QUERY

ACTION_INTEGRAL	ALTITUDE	AIR_TEMPERATURE
-----	-----	-----
494457	145	4
698.7231	145	4
2132.234	143	-9999
3266.51	143	-9999
20671.44	143	-9999
321279.8	145	4
438.3188	145	4
465.3078	145	4
250568.6	145	4
188269.5	143	-9999
327443.9	143	-9999
ACTION_INTEGRAL	ALTITUDE	AIR_TEMPERATURE
-----	-----	-----
291.5429	-9999	-9999
218833.3	-9999	-9999
754749.2	140	5
811.6994	140	5
486.4361	140	5
422767.4	140	5
759333	140	5
523.8895	140	5
456.807	140	5
456773.4	140	-3
1055345	140	-3
68 records selected.		

FIGURE 10. PARTIAL REPORT FROM FIRST SAMPLE QUERY

ACTION_INTEGRAL	ALTITUDE	AIR_TEMPERATURE
-----	-----	-----
1055345	140	-3

FIGURE 11. REPORT FROM SECOND SAMPLE QUERY

Typing a "5" in the Selection field invokes the Report screen. This screen allows the user to select a report to be displayed and printed. The user will be prompted to enter the name of a file into which the report will be saved. This file will remain in the user's FRED directory. Management of these report files is accomplished through the waveform processing option. Files remain resident on the CRAY until the user chooses to delete them.

The report selected is displayed on the user's screen. This allows the user to capture the data for reprinting. A sample report is shown in appendix A.

### Waveform Processing

The third function on the User Menu allows the user to review the waveforms which have been loaded into his directory. Selecting "3" causes the system to display the Waveform Processing Menu screen (shown in figure 12). The Waveform Processing Menu allows the user to see and manage a listing of the waveforms he has had loaded into his directory. Because of space and cost limitations, the waveform data is stored offline on nine-track magnetic tapes. If the user wishes to view or manipulate a particular waveform, he asks to have it loaded onto the CRAY computer. Depending on the workload at the time he issues his request, it may take an hour or more to process this request.

```
Waveform Processing Menu

1 - List/Delete Waveforms Loaded in Your FRED
    Directory on the CRAY System
2 - Waveform Graphics
3 - Waveform Statistics

Selection:

Press COMMIT to invoke selection
Press EXIT to exit system
```

FIGURE 12. WAVEFORM PROCESSING MENU

### ACRONYMS

BLM	Bureau of Land Management
CRM	Computer Resource Management, Incorporated
DBA	Database Administrator
FAA	Federal Aviation Administration
FRED	FAA Research and Development Electromagnetic Database
INEL	Idaho National Engineering Laboratory
NASA	National Aeronautical and Space Administration
NOAA	National Oceanic and Atmospheric Administration
ONERA	Offices Nationales des Etudes et Recherches Aerospatiales

### REFERENCES

1. McDowall, R. L., and M. Glynn, "Lightning Information Database", Proceedings of the 1988 International Aerospace and Ground Conference on Lightning and Static Electricity, NOAA Special Report, 1988.
2. Elliott, J. R., and H. S. Weigel, "Digitization of CV-580 In-Flight Lightning Strike Analog Data from 1984, 1985, 1987", FAA Internal Report, 1990.

## APPENDIX A

## ELECTROMAGNETIC DATA INFORMATION

## ELECTROMAGNETIC DATA INFORMATION

Strike Date	Strike Time	Sens Parm	Sense Loc.	Peak Value	Units	Peak Rate of Rise	Time to Peak (nsec)	Width at 1/2 of Full		Saturation Threshold	Action Integral	Charge Transfer	Trigger Threshold
								Max.	Max.				
30-JUL-87	19:25:50	8DOT	TB	-2.8E+02	A/m	3.2E+08	5.6E+05	2.1E+05	4.6E+05	U	2.0E+04	-	-9.999E+03
		I-H	TB	1.2E+04	A	5.7E+10	5.8E+03	2.8E+03	4.0E+03	U	1.7E+06	-4.3E+01	-9.999E+03
		I-H	LW	6.7E+03	A	4.3E+10	3.3E+03	7.5E+02	3.0E+03	U	1.7E+06	-1.8E+01	-9.999E+03
		I-H	RW	8.3E+03	A	5.3E+10	1.9E+05	7.5E+02	1.9E+05	U	1.7E+06	-1.1E+02	-9.999E+03
		I-H	VS	4.2E+03	A	2.3E+10	1.0E+03	5.0E+02	8.8E+02	U	1.7E+06	-1.5E+02	-9.999E+03
		I-L	VS	2.9E+02	A	6.4E+08	5.5E+03	2.0E+03	4.5E+03	U	8.9E+03	4.5E+00	-9.999E+03
		I-L	LW	2.1E+02	A	4.4E+08	4.0E+03	1.0E+03	3.0E+03	U	8.9E+03	2.0E+00	-9.999E+03
		I-L	TB	2.0E+03	A	3.8E+09	5.1E+04	6.7E+04	9.0E+03	U	8.9E+03	1.4E+03	-9.999E+03
		I-L	RW	9.2E+02	A	4.9E+08	2.9E+06	1.8E+05	2.8E+06	U	8.9E+03	9.5E-01	-9.999E+03
		IDOT	TB	-1.9E+09	A/s	1.3E+15	1.8E+04	2.4E+04	6.5E+03	U	1.1E+11	3.0E+00	-9.999E+03
		JN	VS	-2.0E-06	C/m**2	3.9E+00	3.3E+03	2.8E+04	2.5E+03	U	5.0E-04	-	-9.999E+03
		JN	RW	-3.2E-06	C/m**2	1.4E+01	3.8E+03	4.5E+03	3.3E+04	U	5.0E-04	-	-9.999E+03
		JN	LW	-3.2E-06	C/m**2	4.9E+00	1.1E+05	5.5E+04	8.8E+04	U	5.0E-04	-	-9.999E+03
		JN-H	FF	3.2E-06	C/m**2	1.9E+00	3.5E+03	4.0E+04	2.5E+03	U	3.5E-05	-	-9.999E+03
		JN-L	FF	3.8E-06	C/m**2	2.3E+00	1.2E+05	4.1E+04	1.2E+05	U	6.9E-05	-	-9.999E+03
		JS	RW	4.4E+08	A/m/s	.0E+00	5.0E+03	4.8E+03	4.8E+03	U	2.3E+11	-	-9.999E+03
		JS	FF	1.2E+09	A/m/s	.0E+00	7.5E+02	7.5E+02	5.0E+02	U	2.3E+11	-	-9.999E+03
		JS	AF	5.6E+08	A/m/s	.0E+00	3.3E+03	7.5E+02	3.1E+03	U	2.3E+11	-	-9.999E+03
		OPT1	LF	-1.1E+01	V	1.6E+07	5.8E+05	6.2E+05	2.7E+05	U	5.7E+02	-	-9.999E+03
		OPT2	LU	-1.2E+01	V	1.9E+07	2.7E+05	6.8E+03	2.6E+05	U	5.7E+02	-	-9.999E+03
		OPT3	LA	-5.0E+00	V	1.0E+07	4.3E+05	1.6E+05	4.3E+05	U	5.7E+02	-	-9.999E+03
04-AUG-87	22:53:01	OPT4	LR	-4.4E+00	V	1.0E+07	7.1E+04	2.8E+05	7.0E+04	U	5.7E+02	-	-9.999E+03
		OPT5	LL	-8.9E+00	V	1.6E+07	3.0E+05	8.3E+03	3.0E+05	U	5.7E+02	-	-9.999E+03
		OPT6	LD	-6.7E+00	V	2.0E+07	1.6E+05	4.5E+05	1.3E+04	U	5.7E+02	-	-9.999E+03
		TRIG	NA	-2.9E+00	V	6.4E+06	6.3E+03	9.7E+04	5.5E+03	U	5.7E+01	-	-9.999E+03
		8DOT	TB	-3.3E+02	A/m	5.1E+08	4.8E+05	1.2E+05	4.8E+05	U	2.0E+04	-1.3E+02	-9.999E+03
		I-H	VS	-4.2E+03	A	2.7E+10	4.4E+04	6.0E+04	1.0E+04	U	1.7E+06	-1.2E+02	-9.999E+03
		I-H	RW	4.2E+03	A	2.7E+10	2.1E+04	2.5E+04	5.5E+03	U	1.7E+06	-1.4E+02	-9.999E+03
		I-H	LW	3.3E+03	A	2.3E+10	3.0E+05	3.8E+04	2.7E+05	U	1.7E+06	-1.4E+02	-9.999E+03
		I-H	TB	2.5E+03	A	2.0E+10	5.0E+02	1.0E+03	3.8E+02	U	1.7E+06	-1.4E+02	-9.999E+03
		I-L	VS	-1.6E+03	A	1.3E+09	5.9E+06	1.2E+06	5.4E+06	U	8.9E+03	-6.1E+00	-9.999E+03
		I-L	TB	2.4E+02	A	4.5E+08	2.5E+03	1.5E+03	1.5E+03	U	8.9E+03	2.5E-01	-9.999E+03
		I-L	RW	1.5E+03	A	9.2E+08	5.2E+06	6.0E+05	4.7E+06	U	8.9E+03	7.4E+00	-9.999E+03
		I-L	LW	3.4E+02	A	5.6E+08	3.0E+03	3.0E+03	2.5E+03	U	8.9E+03	-2.3E-01	-9.999E+03
		IDOT	TB	-1.9E+09	A/s	2.4E+15	1.2E+04	2.5E+04	1.0E+03	U	1.1E+11	-	-9.999E+03
		JN	VS	-2.0E-06	C/m**2	3.9E+00	5.3E+03	2.3E+04	3.5E+03	U	5.0E-04	-	-9.999E+03
		JN	LW	-3.4E-06	C/m**2	7.8E+00	4.5E+05	8.6E+04	4.4E+05	U	5.0E-04	-	-9.999E+03
		JN	RW	-3.9E-06	C/m**2	4.9E+00	2.9E+04	5.8E+03	2.6E+04	U	5.0E-04	-	-9.999E+03

# THE NEW SECTION 23 OF DO160C/ED14C LIGHTNING TESTING OF EXTERNALLY MOUNTED ELECTRICAL EQUIPMENT

B J C Burrows

Lightning Test and Technology, Culham Laboratory, Abingdon, Oxfordshire,  
OX14 3DB, England

## 1 INTRODUCTION

This paper introduces the new Section 23 which has only very recently been fully approved by the RTCA for incorporation into the first revision of DO160C/ED14C. Full threat lightning direct effects testing of equipment is entirely new to DO160, the only existing lightning testing is transient testing for LRU's by pin or cable bundle injection methods (see Section 22<sup>(1)</sup>), for equipment entirely contained within the airframe and assumed to be unaffected by direct effects. This testing required transients of very low amplitude compared with lightning itself, whereas the tests now to be described involve full threat lightning testing, that is using the previously established severe parameters of lightning appropriate to the Zone, such as 200kA for Zone 1A as in AC20-136<sup>(2)</sup>. Direct effects (ie damage) testing involves normally the lightning current arc attaching to the object under test (or very near to it) so submitting it to the full potential for the electric, mechanical, thermal and shock damage which is caused by high current arcing.

Since equipment for any part of the airframe require qualification, tests to demonstrate safety of equipment in fuel vapour regions of the airframe are also included.

## 2 SUMMARY OF EQUIPMENT INCLUDED AND EXCLUDED FROM THE TESTS OF SECTION 23

Examples of equipment covered in these tests are:- aerials (antennas), exterior lights, air data probes, anti-ice and de-ice equipment, and sensors. Likewise, electrical and electronic equipment such as lights and fuel quantity probes, and pumps mounted on fuel tanks and exposed to direct or swept strokes are covered by this section. Mechanical devices, for example fuel filler caps, are not covered.

Equipment such as aerials that are protected by a dielectric covering specific to that item and exposed directly to lightning attachment is included in the tests, but any aircraft specific dielectric covers over aerials such as radomes, etc, used for a specific aircraft to cover one or more aerial systems are not included. (Tests to radomes are given in other standards eg, CLM-R163<sup>(3)</sup>, MIL STD 1757A<sup>(4)</sup>, etc.)

## 3 CATEGORIES OF EQUIPMENT

Equipment is categorised as for the familiar lightning testing described in other specs <sup>(2), (3), (4), (5)</sup> using the Zone numbers as category numbers. Thus, equipment in Zone 1B is in category 1B etc. In addition to the five familiar lightning Zones (1A, 1B, 2A, 2B, 3) there is an additional category, X, which is used to designate equipment for which lightning effects are insignificant or inapplicable.

Equipment for use in fuel vapour regions requires special tests to determine freedom from sparking in the fuel vapour region when the equipment is subject to the appropriate Zone currents. Thus, equipment for any of the categories above may also be subjected to, and pass, the fuel vapour region tests, which allows the addition of the suffix 'F' after the



category, and thus the use in 'fuel vapour' designated areas, or any other area, of the airplane.

#### 4 NOVEL TEST METHODS FOR DIRECT EFFECTS TESTING

Section 23 includes four areas for which either new tests are described, or significantly improved and more closely specified tests are described. These are as follows:

##### 4.1 HIGH VOLTAGE TESTS

These tests are to determine the surface flashover/breakdown properties of specimens with dielectric covers. The novel features are the specification of the preferred waveform (using the  $V_{90}$  voltage and the UDVTM), and the specification of the test geometry using large electrodes instead of ones with an unspecified size as previously. As well as the preferred one, two alternative voltage waveforms are also described, one a fast rising waveform of  $1000\text{kV}/\mu\text{s} \pm 50\%$  and also a slow rise waveform, going to peak between 50-250 $\mu\text{s}$ , with breakdown to occur at or around peak voltage. The waveforms are shown in Figures 1a), b) and c).

These three test methods are not exactly equivalent, the first and the third are likely to give close results, but owing to the very high rate of rise of the second method significantly different test results might occur which are believed by some to be not so typical of lightning attachment to aircraft components. This test method was put in to provide consistency with the existing test specifications (eg Reference 4) but is not as satisfactory as the other two.

Significantly different test results occur depending on the specification of test electrode size. Hitherto a rod electrode has been widely used but this is not ideal since it encourages the pre breakdown streamer to occur from itself, followed by rapid breakdown, instead of streamering from the test object. A large profiled electrode as in Figure 2 coupled with waveforms a) or c) promote streamering from the test object and not from the electrode and prevent unrealistic puncture of that point of the test object nearest to the electrode, as occurs with a pointed electrode and a fast rise waveform of unlimited amplitude.

The other aspect of the test method is the specification of the electrode sizes and spacings as a function of the test specimen size. This prevents either unrealistically short gaps, or unnecessarily long gaps to be used, the former giving biased results, the latter requiring excessive voltages.

##### 4.2 HIGH CURRENT TESTS OVER DIELECTRICS

No previous test specification has called for full threat high current tests along side of a dielectric cover, where high voltage tests have shown that a surface flashover occurred. Section 23 specifies such a test by requiring that high current tests are done to demonstrate freedom from damage on the test object when an arc is initiated (using the appropriate current waveforms according the Zone) along the line of any flashovers. This is done by supporting and initiating wire (with a diameter of 0.1mm) between 5 and 15mm from the surface along the line of the flashover and driving the lightning test current components through it, so fusing the wire and causing an arc at that position. This test will then show freedom (or otherwise) from blast, shock and thermal effects of the arc.

Considerable difficulties could occur with very long arcs for very large objects in maintaining components C current for the full duration owing to the large arc drop; and stability of the arc is a problem owing to the effect of return conductors which have a very strong influence on component B and C arcs and their movement.

#### 4.3 FUEL SYSTEM TESTS

The section of fuel vapour tests describes, in considerable detail, how to perform these tests, and new material from recent work in the UK and elsewhere are included in these test requirements. Two main methods of detecting sparking or arcing are suggested, namely (i) photographic methods and (ii) gas mixture ignition tests.

Photographic and other optical methods have many advantages for engineering and certification tests on the equipment owing to the ease of identifying the location of sparks of sufficient energy which can be divided into voltage sparks or thermal sparks. By contrast, gas methods only reveal that there was at least one spark somewhere in the gas volume of sufficient energy to cause ignition. Previously, photographic methods have been too loosely defined for adequate spark detection, eg, by saying that .... "using a camera with an aperture of f/4.7 with 3000ASA film that sparks can be detected adequately". This is not the case unless the camera lens focal length and maximum distance to the spark are specified, or alternatively and more simply, by specifying the maximum field of view available at the spark distance. The latter method is the most useful, and 1m is recommended as the maximum field of view, see Figure 3. This then specifies the minimum size of image on the film and the minimum amount of light that will be incident on it. Very importantly Section 23 also requires that for any variants in photographic technique, it must be demonstrated that the technique employed can detect 200 $\mu$ J sparks, including the effect on the sensitivity of mirrors, where used for obtaining views of possible sparking sources hidden from direct view of the camera. The limitation on field view, which for a given lens in a given camera implies a maximum lens to spark distance, must not of course be exceeded by the sum of the lens to mirror plus mirror to spark site distance. Accurate focusing in any case requires these distances to be the same for all sites observed by one camera.

For gas mixture ignition tests additional details compared with those hitherto used, are presented to assist in making the test more definitive. The two important details are that: a) the gas mixture ignitability should be checked with a 1.5 to 2.0mm long 200 $\mu$ J spark, and shown to have a high ignition probability, and b) the most useful gas for making a mixture of high ignition probability with a 200 $\mu$ J spark is ethylene/air in a 1.3 to 1.4 stoichiometric mixture. Other gas mixtures such as propane/air are not sensitive enough unless oxygen enrichment is used.

The typical test set up is shown in Figure 4. This shows the usual high current connections, etc, and also the method used to ensure that the gas mixture is correct by incorporating a test cell in the output pipe with a repetitive calibrated spark. Note also the use of purge gas in the blackout region containing the camera to ensure that the whole blacked out volume will not contain the ignitable gas mixture.

For flush mounted objects the typical set up illustrated will be modified somewhat by having a gas enclosure around the object on the inside within the camera volume.

In all cases where an explosion is possible the provision of a blow out panel is important, to limit the violence of any ensuing explosion.

Pass/fail criteria for the tests will be specified in the test plan agreed before the tests commence.

#### 4.4 CONDUCTED ENTRY TESTS

For these tests a double transmission line set up is suggested as shown in Figure 5. This allows the maximum surface current density levels to be established which are flowing past the test object by scaling from the current,  $I$ , and the perimeter,  $p$ , of the electromagnetic field tight box. For fairly closely spaced return conductors (ie,  $S \leq 0.5W$ ), the surface current density  $J_s$  is given approximately by:

$$J_s = \frac{\hat{I}}{p} \text{ A / m} \quad \text{where } p \text{ is in metres.}$$

A value of  $J_s = 50\text{kA/m}$  is recommended in Section 23.

These tests are unlikely to be necessary for anything except fuel vapour region components, and will demonstrate if sparking occurs at the fixing interface to the skin.

## 5 DESCRIPTION OF LIGHTNING ZONES

A word of explanation is required to explain the meaning of the terms 'high possibility' and 'low possibility' where used for the lightning zone definitions. A mathematically correct description would be to use the term 'probability' instead of possibility since probability law and statistics in mathematics does not use the rather subjective term 'possibility'. The word probability is intended, but owing to an objection to its use from the FAA, the unfortunate substitute was possibility. In each case in these zone definitions where the word possibility is used it should be mentally converted to probability and will make proper statistical meaning.

## 6 SUMMARY AND CONCLUSIONS

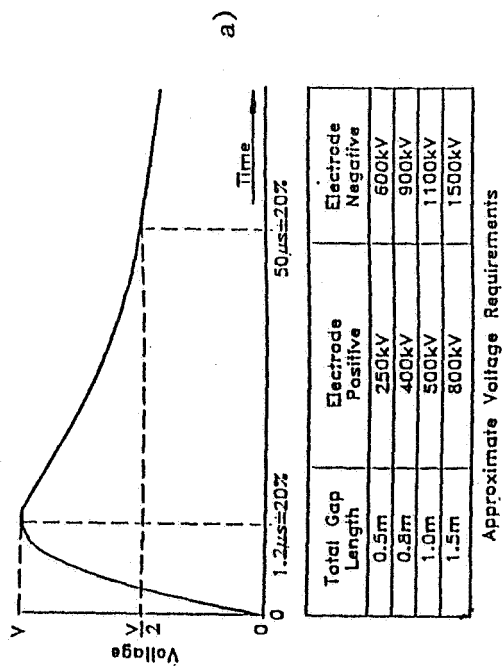
The new Section 23 fills a gap in the standards required for adequate lightning testing of aircraft components. Although progress on providing a complete set of technically sound lightning standards is good, there are still many required for satisfactory definition of the comprehensive range of tests. These additional areas are being looked at by the WG31 technical committee of EUROCAE in Europe and by SAE AE4L in the USA.

## ACKNOWLEDGEMENTS

The author would like to acknowledge the effort by co members of the EUROCAE WG31 SG2 Committee which drafted the standard and the assistance of the SAE AE4L Committee in the USA in finalising its technical content for submission to RTCA.

## REFERENCES

1. Section 22 DO160C/ED14C published by RTCA. December 1989.
2. AC20-136 FAA Advisory Circular. Protection of Aircraft Electrical/Electronic Systems Against the Indirect Effects of Lightning 1990. (Previously known as the 'Orange Book'.)
3. Phillpot J Recommended Practice for Lightning Simulation and Testing Techniques for Aircraft. Culham Laboratory CLM R163. 1977.
4. MIL STD 1757A Lightning Qualification Test Techniques for Aerospace Vehicles and Hardware. July 1983.
5. FAA Advisory Circular AC20-53A: Protection of Airplane Fuel Systems Against Fuel Vapour Ignition due to Lightning. 1985



94-5

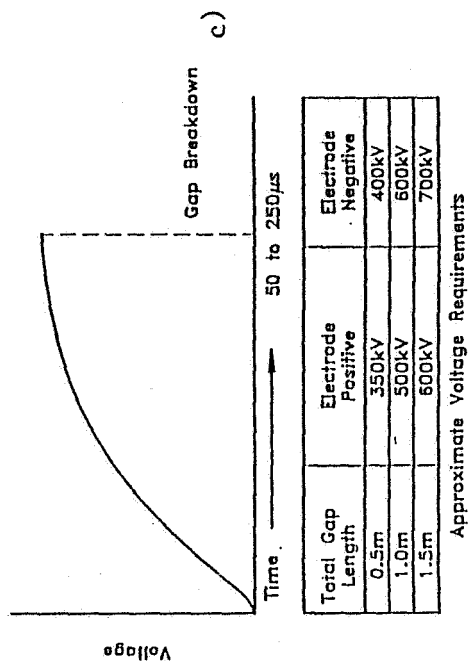
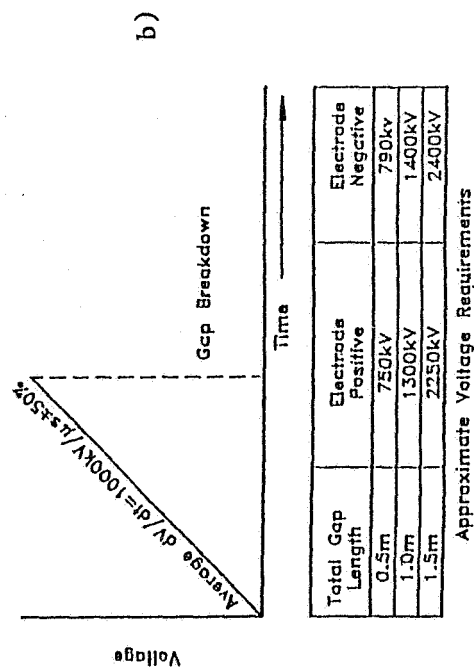
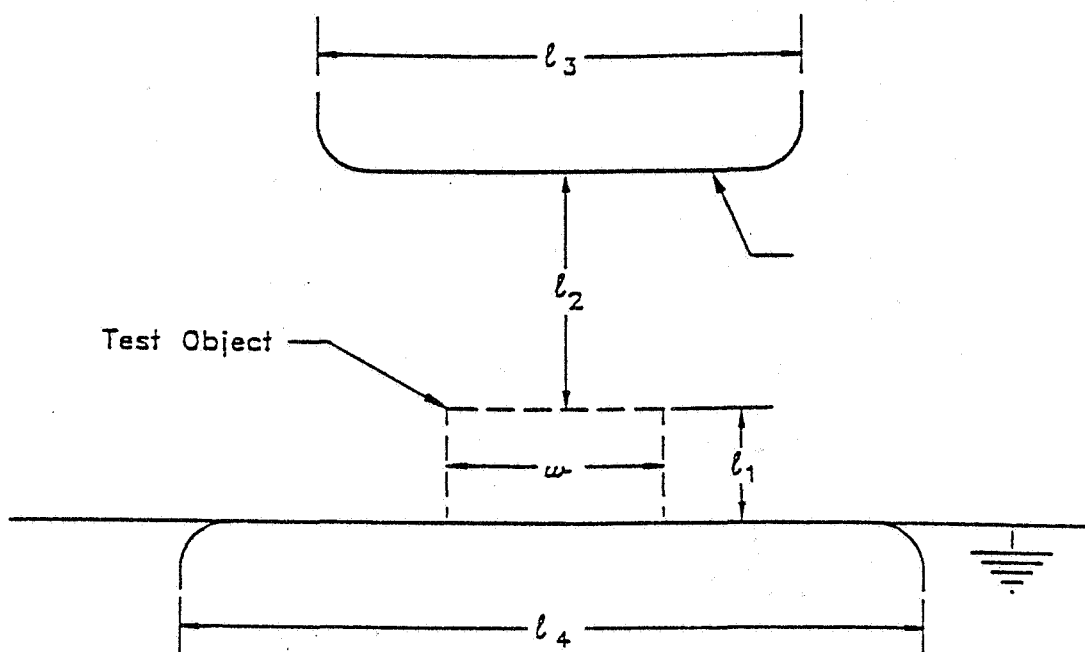


FIGURE 1 High Voltage Test Waveforms

- a) for  $V_{90}$  method.
- b) 1st alternative method.
- c) 2nd alternative method.



Note: The ground plane may be either a very broad flat one, or one with a profiled edge of width  $l_4$ .

Test Set-up Dimensions	For $w$ and $l_1 < 100\text{mm}$	For $l_1 > w$ and $l_1 > 100\text{mm}$	For $w > l_1$ and $w > 100\text{mm}$
$l_2$	150mm	$\geq 1.5 l_1$	$\geq 1.5 w$
$l_3$	$> 2 l_2$	$> 2 l_2$	$> 2 l_2$
$l_4$	$\geq l_3$	$\geq l_3$	$\geq l_3$

#### Gap and Electrode Dimensions for High Voltage Tests

Notes: The tolerance for  $l_2$  is  $+20\%$   
 $-0\%$

The values for  $l_3$  and  $l_4$  are minimum values.

FIGURE 2 TEST ARRANGEMENT AND DIMENSIONS FOR HIGH VOLTAGE TESTS

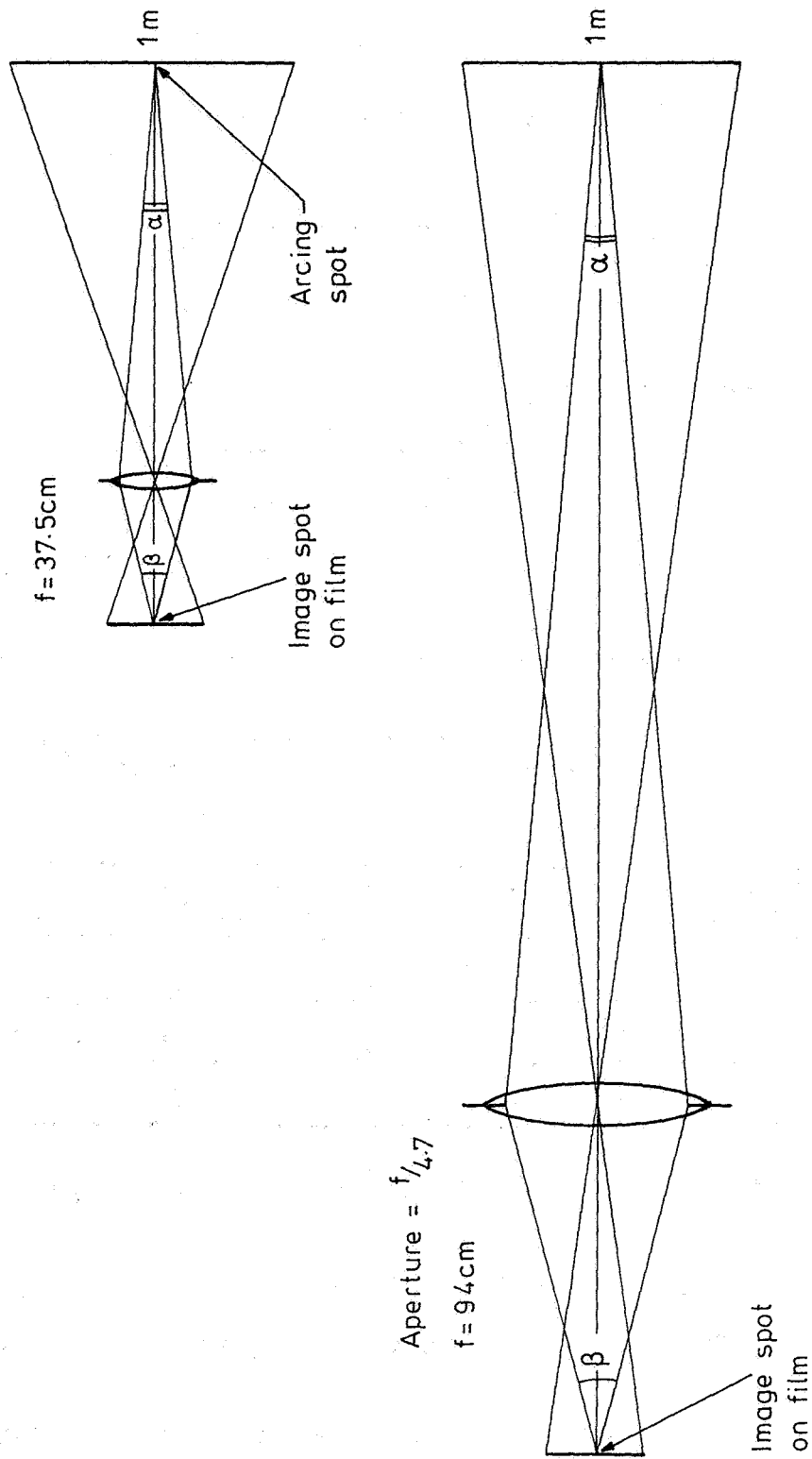


Fig 3 Comparison of different focal length camera lenses  
(Aperture sizes magnified by 3.25 for emphasis)

Note: May also need Injected Current and Voltage Recorder as in Fig. 23.5

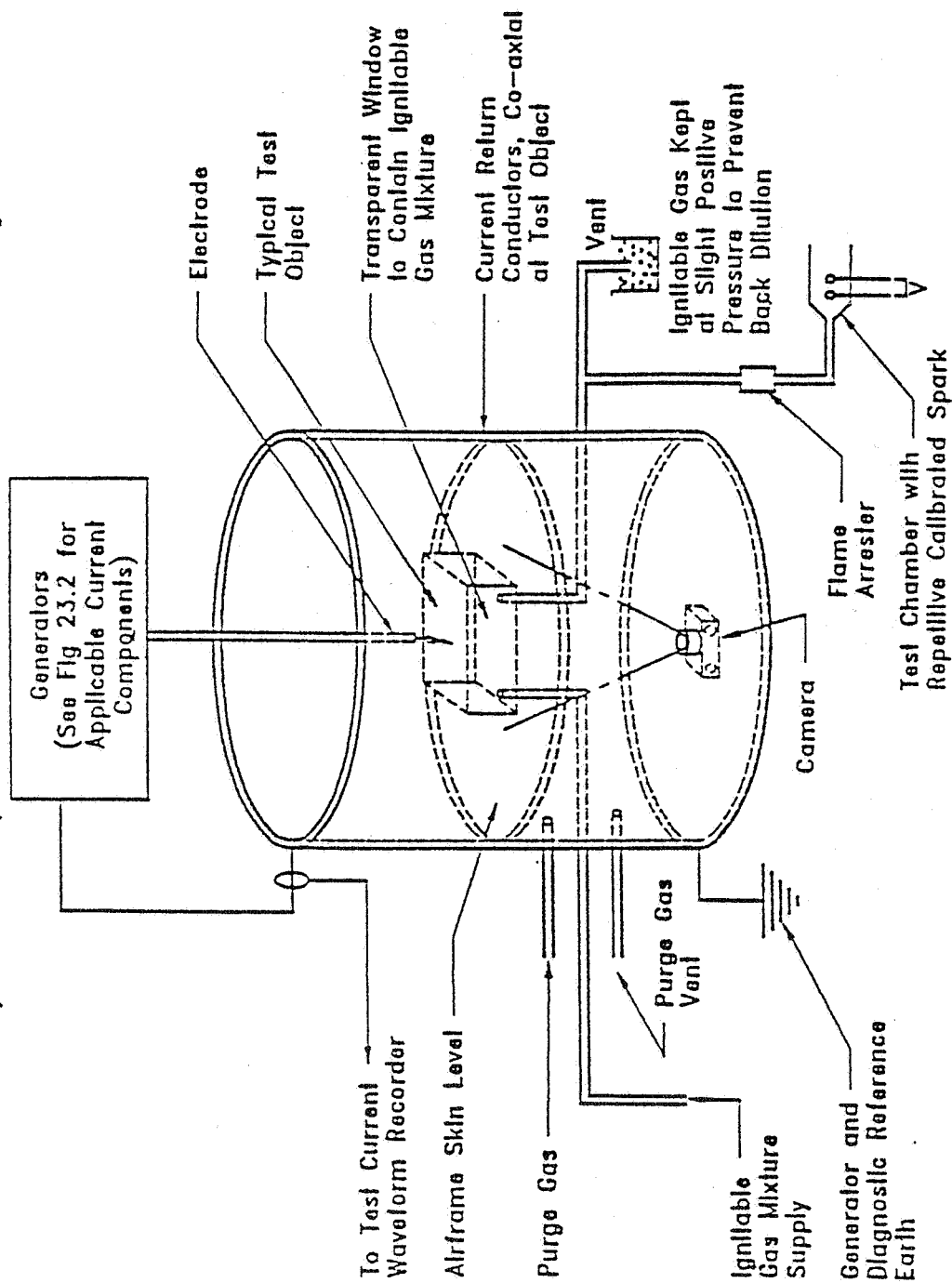


FIGURE 4 TYPICAL HIGH CURRENT SET-UP FOR FUEL VAPOR REGION REQUIREMENTS

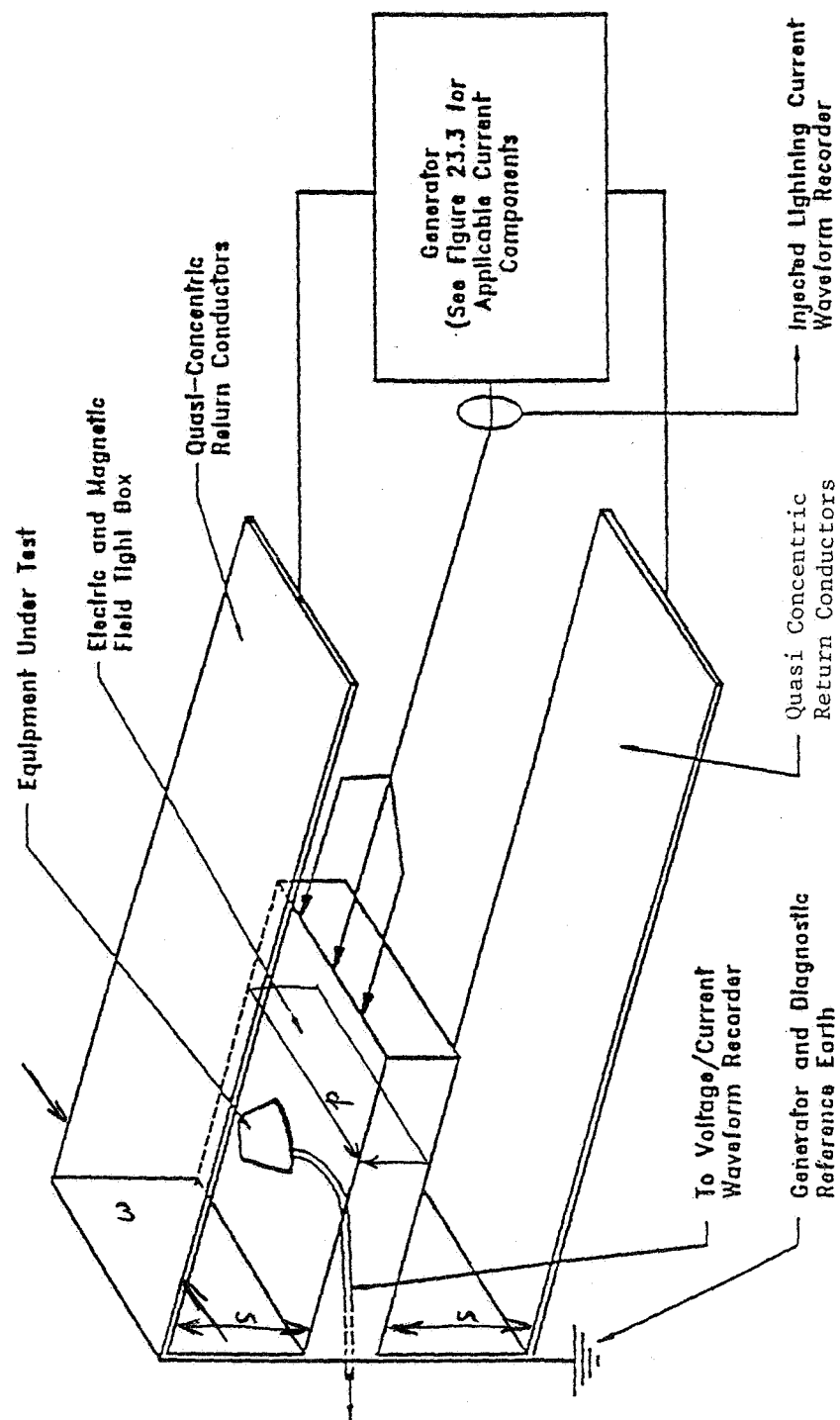


FIGURE 5 TYPICAL HIGH CURRENT SET-UP FOR NON-FUEL AREAS CONDUCTED ENTRY TESTS.



# DESIGN OF LIGHTNING PROTECTION FOR A FULL-AUTHORITY DIGITAL ENGINE CONTROL

M. Dargl, E. Rupke, K. Wiles  
Lightning Technologies, Inc., USA

## ABSTRACT

This paper describes the steps and procedures necessary to achieve a successful lightning-protection design for a state-of-the-art Full-Authority Digital Engine Control (FADEC) System. The engine and control systems used as examples in this paper are fictional, but the design and verification methods are real. Topics discussed include applicable airworthiness regulations, selection of equipment transient design and control levels for the engine/airframe and intra-engine segments of the system, the use of cable shields, terminal-protection devices and filter circuits in hardware protection design, and software approaches to minimize upset potential. Shield terminations, grounding and bonding are also discussed, as are the important elements of certification and test plans, and the roles of tests and analyses. The paper includes examples of multiple-stroke and multiple-burst testing. The paper concludes with a review of design pitfalls and challenges, and status of applicable test standards such as RTCA DO-160, Section 22. This paper will be presented in two parts; Part I - Design, and Part II - Verification.

## 1.0 INTRODUCTION

Developed in the early 1970s for military aircraft, electronic-flight and engine-control systems have found increasing application in the commercial fleets of the world. Systems such as Full-Authority Digital Engine Control (FADEC) and Fly-By-Wire (FBW) not only perform flight-critical and essential functions, but do so independently of mechanical or hydraulic backup. Currently operating commercial transport aircraft such as the Airbus A320, McDonnell Douglas MD-11, and Boeing B747-400 use full-authority electronics for engine control and some aspects of flight control. Other systems are under development.

Because FADEC and FBW systems are flight-critical, they are required by regulatory agencies to withstand the effects of a severe lightning strike to the aircraft. This paper describes and interprets the current airworthiness regulations and standards pertaining to lightning protection and provides a technical discussion of the steps that should be taken to achieve a successful protection design. This paper also reviews several design problems and ways to overcome them. Methods to verify adequacy of these designs are treated in a sequel paper [1].

## 2.0 DESCRIPTION OF SYSTEMS

Typical FADEC and FBW systems share many features that are important from a lightning-protection standpoint. In general, both types of systems are designed to convert pilot-input data, such as control stick or throttle-lever movement, into digital signals which are received by actuators at the appropriate engine controls or flight-control surfaces.

Both types of systems have similar configurations:

- The systems are widely distributed throughout the airframe, with controls in the cockpit electrically connected to actuators as far as the tail and wingtips.
- FADEC and FBW systems usually receive electric power from the aircraft power distribution buses, which are also distributed throughout the aircraft.
- The systems interface with cockpit displays, and often with general-purpose digital data buses.
- The systems are sometimes connected to externally mounted sensors and actuators.

Block diagrams of generic FBW and FADEC systems are shown in Figures 1 and 2. Figures 3 and 4 show typical locations of system components and interconnecting wiring within an aircraft and an engine, respectively.

A full FBW system controls the three main axes of flight - pitch, roll and yaw - by adjusting ailerons, rudder, elevators,

flaps, trim-tabs, etc. For each of the pilot's controls, the FBW system includes a force transducer that converts the pilot's stick, pedal or lever motion into electrical signals. These signals are transmitted to a computer and voter unit (CVU) which reads not only all the data being supplied by the pilot commands, but also data sent by aircraft motion sensors (including gyros and air-data probes) and control-surface position indicators. The CVU regularly consists of three or more separate processors operating on separate channels, sometimes asynchronously. The voter unit polls the independent processors for agreement.

This redundancy is a safety feature but it does not in itself provide adequate protection against lightning because lightning-induced effects appear simultaneously in all channels of interconnecting wiring and thus have the potential to damage components in all channels at once.

The CVU computes the optimum changes to make in the various control-surface positions in order to accomplish the pilot's commands and maintain pre-programmed flight parameters. In addition to the above connections, the CVU is also connected to the pilot's display panels and to the aircraft's main power systems, including one or more engine-driven generators and one or more batteries. The computer sends the appropriate electronic signals to secondary actuators near the control surfaces.

The secondary actuators (SA) translate the electrical signals from the CVU to mechanical motion of the flight-control surface. The SA will typically consist of an electrically activated servovalve to operate the hydraulically powered control-surface actuators. There are also differential transducers which provide the CVU and main cockpit display with feedback information on the position of the control surfaces.

FADEC systems also include cockpit controls and interfaces with other cockpit avionics, as well as engine-mounted components, which usually include the electronic control unit (ECU) whose function is to that of the CVU in an FBW system. Usually, a FADEC system is comprised of two channels, designated A and B, at each engine. The CVU interfaces with engine-mounted sensors and actuators, and with cockpit avionics. The interconnecting wire harnesses often follow different routes between engine and cockpit to protect the system against damage from an exploding engine, etc. This is referred to as *disbursed routing*. Instead of control surfaces, as found in FBW systems, FADEC systems typically control engine fuel flow, stator vane position, exhaust nozzle configuration, etc., to optimize engine performance and economy.

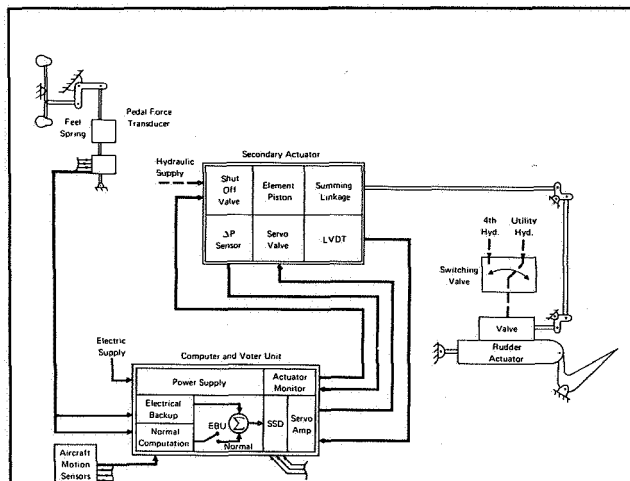


FIGURE 1 Typical FBW System

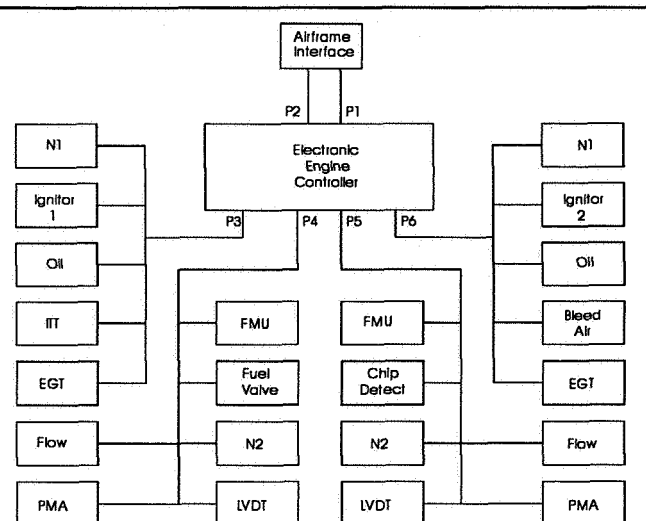


FIGURE 2 Typical FADEC Block Diagram

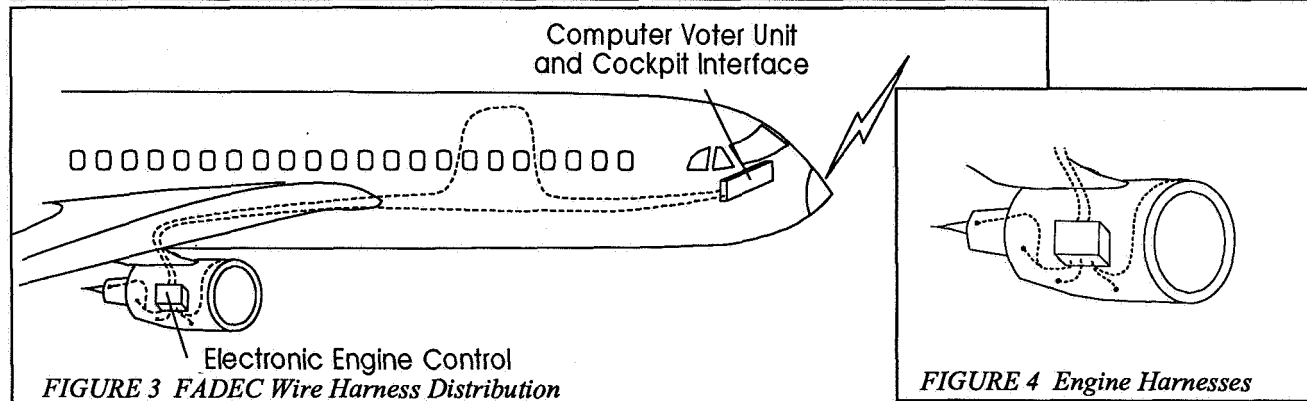


FIGURE 3 FADEC Wire Harness Distribution

FIGURE 4 Engine Harnesses

Both systems provide many challenges to the lightning-protection engineer. The amount and length of interconnecting wiring harnesses makes them susceptible to lightning indirect effects, and the location of some components near aircraft extremities results in potential susceptibility to direct lightning effects. The magnitudes of induced transients are difficult to predict because of the difficulty of describing most wiring installations in circuit or mathematical terms that can be analyzed. These complexities make numerical modeling of the waveforms and currents which might be expected in the systems very difficult. Mathematical analysis currently can predict only orders of magnitude, which are of use in formulating design goals but inadequate for verification of all but the simplest of systems.

### 3.0 REGULATIONS

Airworthiness certifying authorities around the world assume that during the operational life of an aircraft, lightning strikes will occur. Over the years, the Federal Aviation Administration (FAA) has developed several Federal Aviation Regulations (FAR) [2] which pertain to lightning. These are listed in Table I, and include FAR 25.581, which states, for transport category aircraft: "The airplane must be protected against catastrophic effects of lightning." Of more particular interest to engineers concerned with electronic control systems is FAR 25.1309 which requires that "The equipment, systems, and installations whose functioning is required by this subchapter, must be designed to ensure that they perform their

intended functions under any foreseeable operating condition." While not mentioned by name in this regulation, lightning is considered a foreseeable operating condition. To preclude any question of the applicability of FAR 25.1309 to lightning protection, the FAA has required lightning protection of flight-critical and essential avionics through the imposition of *special conditions* and *issue papers*. A special condition is written by the FAA (or similar certifying authority in another country) expressly for a particular aircraft (or modification) and has the same force and effect as a published regulation. An issue paper delineates a safety issue of particular concern to the FAA, and requests the applicant to address this issue and respond to the FAA with details. Thus, an issue paper has somewhat less force than does a special condition.

To avoid questions as to the applicability of FAR 25.1309 to lightning protection, the FAA will shortly issue FAR 25.1315, which is similar to 1309 but pertains specifically to protection of avionics against the effects of lightning. It is the first such regulation to be issued by the FAA, and will obviate the need for special conditions.

This new regulation will define *critical functions* as those whose failure would contribute to or cause a condition which would prevent the continued safe flight and landing of the airplane. Critical functions must not be affected when exposed to lightning. Essential functions are those whose failure would contribute to or cause a condition which would significantly impact the safety of the aircraft or the ability of the flight crew to cope with adverse operating conditions. Essential functions must be protected to ensure that the

TABLE 1 U.S. Federal Aviation Regulations

	Vehicle Type and Regulations			
	Aircraft		Rotorcraft	
	General Aviation	Transport	Normal	Transport
Airframe .....	23.867 .....	25.581 .....	27.610 .....	29.610
Fuel System .....	23.954 .....	25.954 .....	27.954 .....	29.954
Other Systems .....	23.1309 .....	25.1309 .....	27.1309D .....	29.1309H
Avionics .....		25.1315		

function can be recovered in a timely manner after being exposed to lightning.

Neither FAR 25.1309 nor the forthcoming FAR 25.1315 define the lightning environment for design and certification purposes. This is found in FAA Advisory Circular 20-136 [3] which will be discussed in more detail later in this paper.

Lightning protection requirements for general aviation aircraft and general and transport category rotocraft are included in Parts 23, 27 and 29, respectively, of the U.S. Federal Aviation Regulations [4], [5], [6]. The basic requirements are similar to those in Part 25, although application (and enforcement) of them to general aviation (Part 23) aircraft has not been as extensive. Lightning-protection regulations for rotocraft are also similar to the transport aircraft (Part 25) requirements, and the recent introduction of FBW and FADEC systems to these vehicles has prompted renewed attention to the helicopter lightning-protection requirements.

Military aircraft and rotorcraft must either comply with FAA standards or Mil-Stds 1757A and 1795A, depending on their role. MIL-STD-1795A describes the protection requirements and the lightning environment, and MIL-STD-1757A presents verification tests methods. Both are the same as the FAA requirements for civil aircraft. MIL-STD-1795A is of interest because it extends protection beyond flight-critical/essential systems to include those systems whose failure could endanger mission success, or result in excessive maintenance costs, on an optional basis. These mission and maintenance factors, of course, are of equal concern to owners/operators of civil aircraft, but are not a part of the civil-airworthiness requirements.

Translation of these regulations into specific aircraft design goals is left to the manufacturer. However, in order to obtain certification, the manufacturer must verify that the aircraft and its systems are protected against catastrophic effects from lightning in accordance with these regulations.

## 4.0 STANDARDS

Beyond the regulations, the FAA has issued Advisory Circulars (AC) that provide more detailed information on how to achieve successful compliance with the FARs. The first lightning-related AC was 20-53 [7] that dealt with lightning protection of fuel systems. However, the FAA recognized that this did not cover other systems, so in 1972 the Society of Automotive Engineers Committee on Electromagnetic Compatibility was asked to form a subcommittee to develop improved aircraft lightning-protection standards. This committee was designated SAE AE-4L.

Over the years, the committee issued several reports which did much to define the threats posed by lightning and to recommend design practices and test methods required to ensure protection. Of

particular importance to electronic control systems is the SAE Committee Report AE4L-87-3, called the Orange Book, which was adopted by the FAA in 1990 as AC 20-136. The subject is "Protection of aircraft electrical/electronic systems against the indirect effects of lightning."

This AC defines the electrical characteristics of lightning for use in design and verification of protection against lightning indirect effects. This AC includes recent additions to the environment that are important to indirect-effects protection, including multiple strokes and multiple bursts which are described in [8]. In addition, AC 20-136 furnishes the engineer with procedural steps which can be followed to achieve and verify a successful design. These steps, as they apply to full-authority electronic control systems, are discussed in following sections of this paper.

## 5.0 INDIRECT EFFECTS

Since most parts of an FBW or FADEC system are installed inside an airframe, lightning indirect effects are of primary concern. These effects have been described fully elsewhere [9], [10], [11], [12] and include voltages and currents induced by changing magnetic fields and/or structural voltages in the interconnecting wiring associated with FBW and FADEC systems.

Of particular concern to digital systems is the potential for upset of data processing and control functions due to the effects of the multiple-stroke and burst environments. Whereas shielding and other protection approaches may control induced transients to non-damaging levels, the low-level transients that remain intermingle with them, resulting in erroneous commands. There will be as many transients as there are strokes or pulses in the "multiple" environments, and these may change or upset computer-generated words and commands. In one well-documented case, a single additional bit induced by a lightning strike to an Atlas-Centaur rocket launched by NASA from Cape Canaveral resulted in a hard-over guidance command and loss of the vehicle shortly after liftoff [13].

## 6.0 DIRECT EFFECTS

Electronic control systems may also be exposed to the direct attachment of the lightning channel to externally mounted sensors, such as air-data probes or actuator parts. Another concern is the puncture of non-conducting skins, resulting in direct lightning current flow into control system components. Direct effects may also be caused by lightning currents being transferred to the electronic systems via cables or power supplies shared with unrelated non-critical components such as antennae, probes or lights. It is the responsibility of the lightning-protection engineer to identify possible current paths of direct entry of lightning currents to the system.

## 7.0 STEPS IN DESIGN

The most successful lightning-protection design programs occur when the process is conducted in a logical series of steps. As outlined in AC 20-136, the steps are: a) Determine the lightning strike zones. b) Establish the external lightning environment for the zones. c) Establish the interior environment. d) Identify the aircraft flight-critical/essential systems and equipment. e) Establish Transient Control Levels (TCL) and Equipment Transient Design Levels (ETDL). f) Design protection. g) Verify protection. The balance of this paper describes steps a through f. Step g is the subject of a sequel paper [1].

### 7.1 a) DETERMINE LIGHTNING-STRIKE ZONES

There are five defined lightning-strike zones which are defined as follows: 1) Zone 1A: Initial attachment point with low possibility of lightning channel hang-on. 2) Zone 1B: Initial attachment point with high possibility of lightning channel hang-on. 3) Zone 2A: A swept-stroke zone with low possibility of lightning channel hang-on. 4) Zone 2B: A swept-stroke zone with high possibility of lightning channel hang-on. 5) Zone 3: Those portions of the aircraft that lie within or between the other zones, which may carry substantial amounts of electrical current by conduction between areas of direct or swept-stroke attachment points.

The location of the zones varies from one aircraft design to another, and depends upon aircraft geometry and operational factors. Therefore individual assessments must be made for each aircraft. Methods of determination are described in [14].

The lightning currents to be expected in each zone are shown in Table 2.

TABLE 2 Current Components Applicable in Various Zones

Zone	Current Waveforms					
	A	B	C	D	Multiple Burst	Multiple Stroke
1A	X	X			X	X
1B	X	X	X	X	X	X
2A		X		X	X	X
2B		X	X	X	X	X
3	X	X	X	X	X	X

Until recently, Zone 1A was identified as extending only 18 inches aft of the leading edge extremities such as engine inlets. However, in-flight experience and laboratory tests of scale models of aircraft have shown that Zone 1A may be extended up to 6 meters aft of leading edges. Thus, most surfaces of wing-mounted nacelles are located within Zone 1A and subject to the first return stroke, current component A. Trailing edges of engine nacelles and exhaust ducts are in Zone 1B, where all four components of the lightning environment are experienced. Flight-control surfaces have similar exposures, depending on their location on the aircraft.

It must be remembered that structures and components inside surfaces in most zones are in Zone 3 and are exposed to the effects of conducted currents. Figure 5 shows typical zones on a wing-

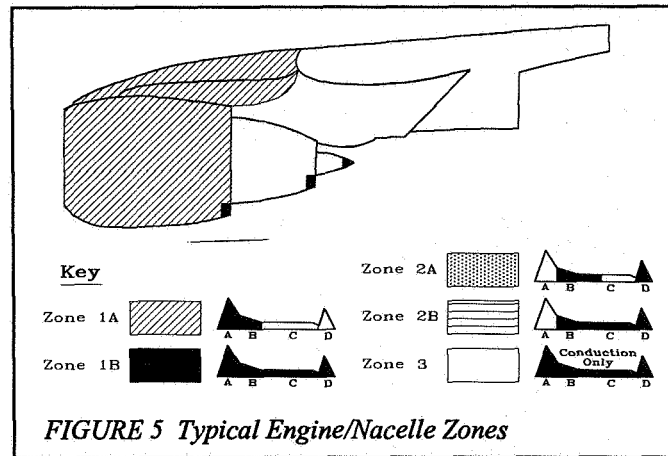


FIGURE 5 Typical Engine/Nacelle Zones

mounted engine nacelle.

Once zones have been established for a particular aircraft design, they should be documented on a drawing of the vehicle with boundaries identified by appropriate station numbers or other notation. It is appropriate for the applicant to review and obtain FAA concurrence for the zone drawings since these determine the specific components of the lightning environment that the system must withstand.

Of essential concern to the aircraft designer is the identification of the various zones and surface materials through which the flight-critical electronic control systems pass. This will aid in determining the direct and indirect effects to be expected and the protection methods required, as will be discussed later in this paper.

### 7.2 b) ESTABLISHING THE EXTERNAL LIGHTNING ENVIRONMENT

The results of recent research into characteristics of lightning encountered by aircraft has focused attention beyond the effects of cloud-to-earth lightning, to include the additional characteristics of intracloud and cloud-to-cloud lightning strikes, especially as they may affect electronic systems. Whereas the amplitude and action integrals of the currents in these strikes are usually less than those associated with cloud-to-earth flashes, other aspects, such as peak rates of change of current and multiplicity of pulses, are of particular concern.

The most significant of these results is the multiple-burst lightning environment, composed of a large number of comparatively low amplitude pulses, characterized by high rates of change (up to  $2 \times 10^{11}$  a/s) and short duration (between 1 and 10 microseconds), and occurring randomly over the lifetime of the lightning flash.

Multiple-burst phenomenon is now added to the cloud-to-earth lightning environment which includes the four basic current components and the multiple-stroke environment based on components A and D/2, as follows:

Component A: Initial High Peak Current Component B: Intermediate Current Component C: Continuing Current Component D: Restrike Current Multiple Stroke (Component A, followed by 23 Components D/2)

The multiple-burst environment, or Component H, as described in AC 20-136 Appendix III, has a peak current of 10 kA and a peak rate of rise of  $2 \times 10^{11}$  a/s.

For evaluation of the indirect effects of lightning to sensitive

aircraft electronics, it is necessary to consider both the multiple-stroke and multiple-burst environments, in addition to the basic indirect effects arising from Component A. This is because the succession of D/2 strokes or H pulses may induce corresponding pulses in data transfer circuits, for example, causing upset or cumulative damage to sensitive systems or devices, as noted previously.

### 7.3 c) ESTABLISH THE INTERNAL ENVIRONMENT

A lightning strike injects a wide assortment of electric currents into the airframe, some of which reach hundreds of thousands of amperes. These currents diffuse throughout conducting structures and are accompanied by changing electromagnetic fields, which can also penetrate to the interior of the aircraft.

The fields and structural IR voltages constitute the portion of the internal lightning environment which causes the voltages and currents on interconnecting wiring that in turn appear at sensitive equipment interfaces. In some cases, electromagnetic fields within the aircraft may penetrate equipment enclosures and compromise system operation.

The mechanisms whereby lightning currents and magnetic fields interact with electrical and electronic systems are illustrated in Figure 6.

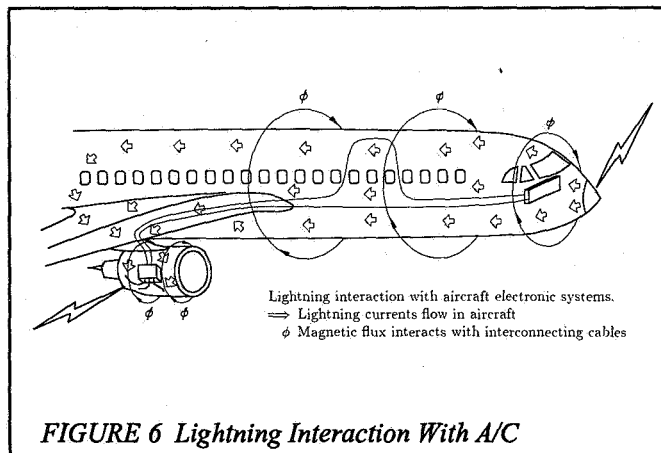


FIGURE 6 Lightning Interaction With A/C

The passage of current between fuselage and engine nacelle creates a potential difference (voltage) between the flight deck and engine-mounted computer. In an aircraft constructed of conventional aluminum, resistance is primarily in the fuselage/wing, wing/pylon and pylon/engine joints. Whereas these resistances are small, lightning-stroke currents of 200 kA can produce IR voltages of several hundred volts. These structural IR voltages may drive currents into interconnecting wires between electronic components in the cockpit and nacelle.

The lightning currents in the airframe are accompanied by changing magnetic fields which increase and decrease in amplitude along with the lightning current. A portion of these fields may penetrate through apertures in the fuselage, wing, pylon and nacelle and induce voltages in unshielded interconnected wiring or currents in the shields of shielded cables.

The multiple-burst environment is not necessarily a salient factor in a damage assessment, but can be the primary factor in a system upset. Since major electrical/electronic systems are composed of

components that are distributed throughout the aircraft, verification of compliance relative to functional upset involves consideration of the overall lightning environment to which the system is exposed. Functional upset can be a particularly important issue for digital processor-based systems in modern aircraft.

Determining the interior lightning environment is generally considered the responsibility of the airframe designer. However, sophisticated electronic control systems and equipment now being employed in aircraft, and the use of composite skins, necessitate a closer working relationship between the airframe designer and the equipment designer to fulfill the design goals of adequate lightning protection and aircraft performance and economy.

Two methods are generally accepted in determining the internal environment: Numerical analysis, as described in detail in [15] and experimental analysis [16]. Numerical analysis methods, which are still in their relative infancy, are often validated by comparison with test data on simple airframes and/or wiring installations, and then extended to address more complex installations.

The difficulty here is that in the extension, complex installations may introduce factors that affect computed results by at least one order of magnitude; yet these factors are not quantified and therefore neglected. Figure 7 shows the type of situation that can be analyzed, and in a real-life installation this approach is sometimes intended to represent.

Electromagnetic interference, from such sources as radio trans-

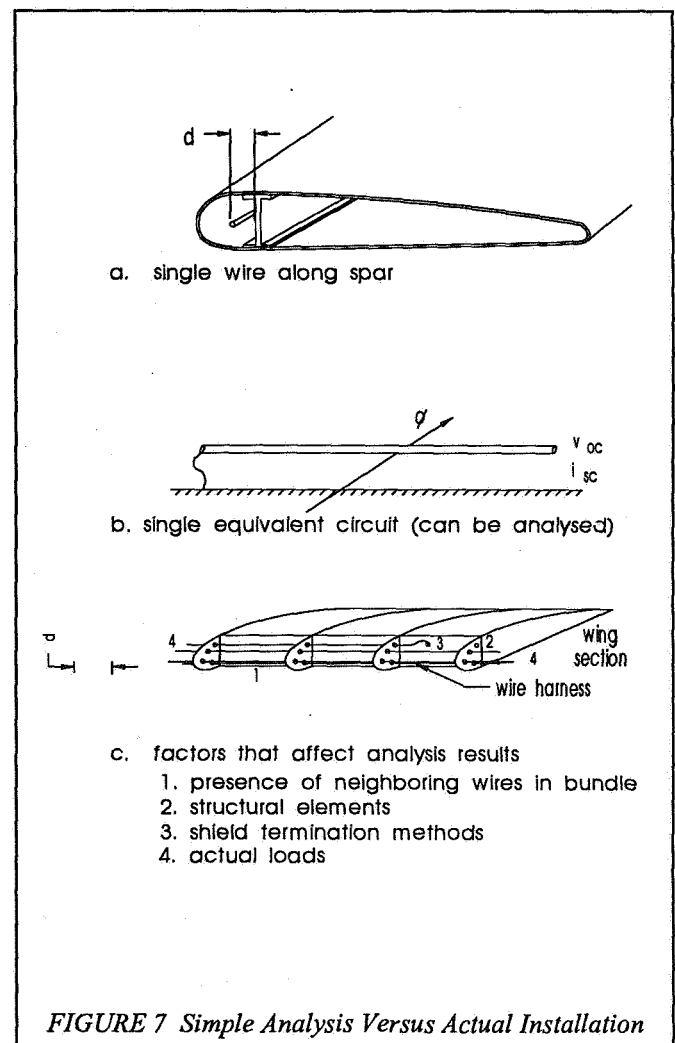


FIGURE 7 Simple Analysis Versus Actual Installation

mitters or radar systems, presents a different coupling mode than that of lightning. EMI, though present in the external environment, with the possibility of coupling with the internal environment, requires no special protection methods. An aircraft employing proper lightning protection methods will exclude adverse EMI effects.

## 7.4 d) IDENTIFY THE FLIGHT-CRITICAL/ESSENTIAL SYSTEMS AND EQUIPMENT

Flight-critical and essential systems and equipment include, but are not limited to:

- Engine parameters
- Wing anti-ice system
- Aircraft power
- Fuel-flow electrical
- Flight instruments
- Warning lights power
- Stall barrier
- Audible tone generator
- Communication system(s)
- Engine fire determination
- Navigation capabilities

In addition to identifying systems and equipment, a major consideration for the designer is to determine their locations and the routing of wiring within the aircraft and review the location of interfacing equipment which is not critical or essential but may provide an indirect (back door) for substantial lightning-induced transients. These transients may propagate from externally mounted probes or devices on the aircraft or be routed from regions with intense magnetic fields.

Complex integrated avionic systems many times display a variety of functions of which some may be critical/essential, while other functions are only supplementary and, if lost, will not significantly degrade the level of safety. Failure or loss of certain noncritical and non-essential information may be acceptable as long as the critical/essential functions are maintained. The identification of critical/essential functions should be the determining factor for what systems or portions of a system must remain operable or no affected by the lightning event.

The determination of flight-critical/essential functions and equipment should be a formalized policy. Generally, it is best to have inputs into this list from not only system designers but from other support groups such as reliability (failure-mode analysis) groups and flight-test operations. This becomes very important since flight test may be required to demonstrate the ability to safely operate the aircraft from the critical/essential equipment list. Thus the critical and essential systems (or equipment) listing becomes a key certification issue which should be well conceived and agreed to by program management.

## 7.5 e) ESTABLISH TCL AND ETDL

The Transient Control Level philosophy was originally inspired by the Basic Insulation Level (BIL), or transient coordination philosophy, used successfully in the electric power field for many years. The TCL approach follows the BIL approach to transient coordination in that targets or specifications relative to transients should be assigned both to those who design electronic equipment and to those who design wiring to interconnect such equipment, rather than allowing things to develop by chance. The TCL philosophy is illustrated in Figure 8.

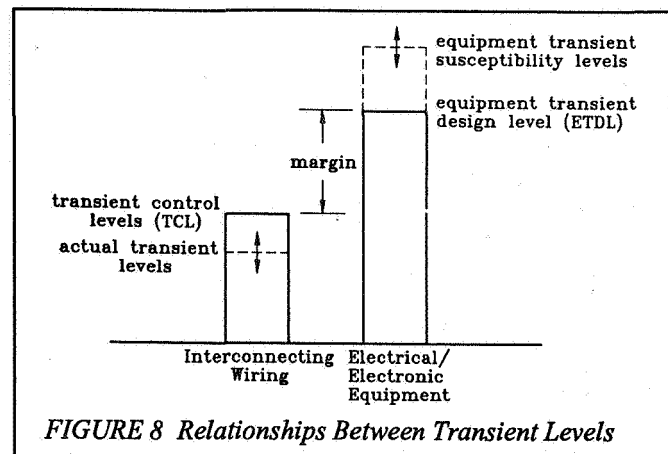


FIGURE 8 Relationships Between Transient Levels

It encompasses the following:

- **Actual Transient Level:** Ensuring that the actual transient level produced by lightning or any other source of transient will be less than that associated with the transient control level number assigned to the cable designer. The cable designer's job is to analyze the electromagnetic threat that lightning would present and to use whatever techniques of circuit routing or shielding are necessary to ensure that the actual transients produced by lightning do not exceed the values specified for that particular type of circuit.

- **Equipment Transient Design Level:** The ETDL establishes the levels of transients that must be tolerated by the equipment within a system. This tolerance can be achieved, of course, by inherent hardness or tolerance of the electronic devices within the equipment or by installation of surge-protection devices (SPDs) at the equipment terminals. The purpose of these SPDs is to limit incoming transients to levels that can be tolerated by equipment and components.

Prediction of the actual transient levels during the system design phase is difficult because of the large number of individual wires and installation configurations that abound in any complex system. Therefore, there will always be a possibility of some wires or circuits experiencing higher transients than those which have been predicted by analysis during the design phase or even those which have been measured during tests of full vehicles. In the latter case, it is never practical to measure transients in every single wire due to time constraints.

This topic of margins is very important, and one which the regulatory authorities have not formulated definite policies on. That is, the amount of the margin is uncertain in some cases. In general, the greater the degree of confidence that one has in the actual transient levels, the smaller the margin can be. Conversely, if actual transient levels, and therefore transient control levels, have been established purely by estimation or analysis techniques, or by similarity with other designs and not by test, then the authorities require use of a larger margin.

Margins as small as 50 percent and as large as 10-1 have been required in the past. Recently, several advanced flight- and engine-control systems have been certified with a margin of 2-1 when the actual transient levels in interconnecting wires have been measured and verified by aircraft tests and when the capability of the equipment to tolerate the transient design levels have also been verified by test.

Further discussion of recommended test techniques will appear in



Selection of the most appropriate method is challenging since it depends on the ultimate use of the data and the state of development of the aircraft. A simulation technique that imposes all features of the lightning in a proper time sequence is desirable but this may not be effective for subsystems or for providing design data. It is especially important that the simulation technique provide data on the system, subsystem or component equipment on line replaceable unit (LRU) responses that can be extrapolated to the values that occur when the aircraft is exposed to the real lightning environment.

Transient design and control levels are best defined in terms of the waveshapes and amplitudes of induced voltage and current transients that appear at interfaces between equipment and interconnecting wires. Specifically, this means the transients that appear on equipment connector pins. In most cases, lightning strikes will induce the maximum levels of transients between interconnecting wires and airframe ground. Therefore, the maximum induced transients will nearly always appear between connector pins and case ground. Thus it is usually preferable to design the equipment transient design levels as the levels of transients that must be withstood by the equipment between incoming connector pins and equipment case ground.

This is often referred to as a *pin specification*. Of course, in any complex system there will be many wires and pins interfacing with each piece of equipment. These wires will extend to varied locations within the aircraft and will experience varying amplitudes and waveshapes of transients. In addition, these circuits may themselves operate at a different or varied system voltage levels. For example, some incoming wires bring 115 V or 28V aircraft power to the equipment. Others, however, only transmit very small signal voltages whose amplitudes do not exceed 1V or 5V. Thus it often makes sense to establish more than one transient design level for a single piece of equipment with the individual levels being related to either the function of the incoming circuit and connector pin or the routing of that circuit through the aircraft.

Thus, for example, for a typical flight-control computer, one transient design level could be established for incoming 115V AC power circuits, a second level might be established for incoming 28V DC aircraft power circuits, and a third equipment transient design level could be established for incoming or outgoing signal and control circuits.

Frequently, each of these functions passes through the same multi-pin connector. In this example, a single connector can have pins which must withstand differing equipment transient design levels.

But in all cases, the levels would be defined as follows:

- A waveshape
- A peak voltage
- A peak current

The voltage referred to above is the maximum voltage which would be expected to appear at the open-circuit terminals of the interfacing wire with no load. This is referred to as the open-circuit voltage as shown in Figure 9 (a). The current specification is the maximum current expected to be induced in the same interconnecting circuit(s) when that circuit is shorted to ground at the equipment as in Figure 9 (b). Of course, in most cases, the load within the equipment is a finite impedance, so that neither the open-circuit voltage nor the short-circuit current will appear at the equipment in an actual lightning strike event as shown in Figure 9 (c). But if the transient design level specification is described in this manner, then the proper amplitude of transient will appear at the equipment when

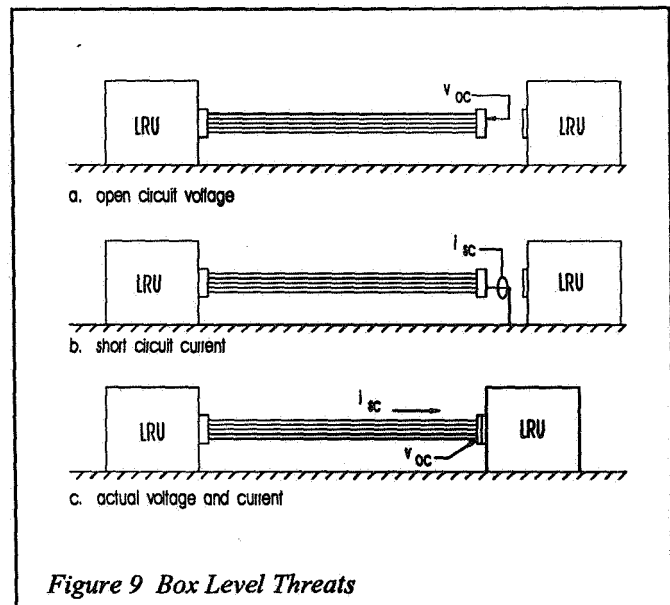


Figure 9 Box Level Threats

the equipment is tested with a test set that can also produce either the open-circuit voltage or the short-circuit current.

#### 7.5.1 CONSIDERATIONS IN ETDL SELECTION

The importance of ETDLs applicable to the equipment connector pins is that it establishes the transient levels which equipment components must withstand without burnout. This is the very basic and most important part of the ETDL specification for flight critical and essential equipment. Compliance with pin specifications will require proper selection of equipment components and/or the application of surge-suppression devices. A further discussion of protection devices is contained in Design Protection section of this paper.

Verification of compliance with pin ETDL requirements usually means the application of a pin-injection test as described in [1]. In this test, transients are applied to pins individually. This means that the equipment cannot be interconnected with other equipment on the test bench. A pin specification and pin-injection test are not capable of evaluating the synergistic effects that may occur due to the simultaneous application of transients on all incoming circuits and at all connectors within the system. It is therefore usually necessary to specify a second type of ETDL which is applicable to a fully interconnected and operating system.

This second ETDL is often a bulk cable current specification which defines the waveshape and amplitude of the total current expected to be induced in the cables which interconnect the various components of the system, such as those which connect the flight-control computer to secondary actuators in a flight-control system. For this purpose, a bulk cable current waveshape, such as waveform 1 or 5, as shown in AC 20-136 is often selected together with a peak amplitude. Amplitudes of bulk cable currents induced on intra-engine cables of a full-authority digital engine control system would range in the thousands of amperes, whereas the amplitudes of bulk cable currents circulating in cables installed within an aluminum fuselage might be less than 100 amperes.

Bulk cable current specifications are most appropriate for cables in which the bundle of wires is enclosed within an overall shield or in which most of the circuits are enclosed within individual shields, and these shields are grounded to equipment cases at each end. In this case, of course, the lightning magnetic fields induce voltages and

currents in the loop between the cable shields and the airframe. In some cases, cables may not simply extend between two pieces of equipment but may branch and extend from one piece of equipment such as a computer to several remote items such as actuators and sensors. In these cases, care must be given to selection of realistic current levels. For example, the bulk cable current at the computer end of such a cable would be the sum of the bulk cable currents entering each of the accessories which are fed from branches of this same cable.

The bulk cable current specification is viewed as a system specification, both from a component-damage and system-upset perspective. Cable shields, connectors, equipment cases and components within the equipment must, of course, withstand the effects of the specified currents flowing on the cable shields. Currents on shields will, of course, produce transient voltages in conductors and at equipment interfaces within those shields. These transients will be lower in amplitude than they would be were the shields not present or ungrounded. Nonetheless, these transients still exist and in some cases may reach damaging levels. Also, induced transients which do not meet damaging levels may still be capable of upsetting digital-processing circuits, especially when it is recalled that there will be more than one transient produced by an individual lightning flash. The bulk cable current specification therefore enables realistic induced transients to be induced simultaneously in all cables and conductors within a system. And if for verification purposes this ETDL is applied in a multiple-stroke or multiple-burst mode, it is indeed possible to evaluate system upset possibilities and/or verify that the system will not upset when exposed to the specified ETDL.

For interconnecting cables which are not shielded it may not be appropriate to specify a bulk cable current or at least a bulk cable current by itself. In these cases, the cable ETDL may be specified as both an open-circuit voltage and a short-circuit current. In this case, the open-circuit voltage is the voltage that would appear between the ends of all interconnecting wires and airframe ground when disconnected from the equipment. The short-circuit current factor is the total current that would flow from all connectors to airframe ground when these connectors are shorted to airframe ground at the equipment. Thus in this latter case the short-circuit current factor can be viewed as the sum of the short-circuit currents in all the individual wires within the cable bundle.

### 7.5.2 OTHER ASPECTS OF ETDL SPECIFICATIONS

It must be remembered that whereas ETDLs are defined as a single waveform, they do appear as multiple transients because of the

fact that lightning flashes inject more than one stroke or pulse of current through the airframe with each stroke or current pulse producing a corresponding transients. This aspect of the lightning environment has been defined as the multiple-stroke and multiple-burst environment in AC 20-136. Therefore whenever an ETDL is defined, it must be viewed as a multiple-transient threat as illustrated in Figure 10.

The first of these pulses is at the specified ETDL level and the second through the 24th of which are either at one-half or one-fourth of the specified ETDL depending upon the coupling mode. Subsequent transients which are predominantly due to changing magnetic fields would be one-half of the original ETDL. Transients which are predominantly due to structural IR effects are one-fourth of the amplitude of the original ETDL.

Thus the equipment components must be designed and verified to withstand the first ETDL transient but the subsequent 23 transients at reduced levels. Test and analysis methods for verification and compliance with this multiple-stroke specification are discussed more fully in [1].

Damaging effects of the subsequent stroke components of the multiple-stroke environment are significant and do need to be accounted for in equipment design and in the selection of surge-protection devices which will be discussed in the following section.

The damaging effects of multiple-burst transients are usually negligible and need not be considered in selection of circuit elements or SPDs. However, the multiple-burst transients are important from an upset standpoint.

### 7.5.3 PITFALLS IN ETDL SELECTION

One method of defining ETDL for system equipment has been to define the characteristics of a transient which is applied between an equipment case and a test bench ground when that case has been elevated from ground. In this case, a short cable(s) is attached to the equipment and grounded through simulated loads a short distance away from the equipment. Verification is achieved by applying the specified transient between the equipment case and test bench ground. Unfortunately, one cannot be certain of the value of the levels of actual transients applied to specific pins or electronic devices within the equipment because in most cases there exist one or more ground wires or grounded shields between the equipment and the simulated loads a short distance away.

These wires inevitably accept most of the transient energy and leave the remaining conductors relatively unexposed. Unfortunately, the method just described has been formalized in several industry specification and test requirements, including RTCA DO-160, [18] and many equipment vendors have received the misleading impression that compliance with such a specification indicates that their equipment can indeed tolerate an ETDL at its interface(s) as described earlier in this section.

Nothing could be further from the truth. Also, unfortunately, potential users of such equipment have been led astray and given the false assumption that equipment thus qualified is capable of tolerating actual transient levels that appear between individual wires and airframe ground. Fortunately, industry standards-writing groups are taking a second look at these methods and clarifying the results obtained from them as compared with the pin specification.

Flow charts demonstrating logical progression of steps toward integration of design at the airframe and component levels are shown in Figure 11.

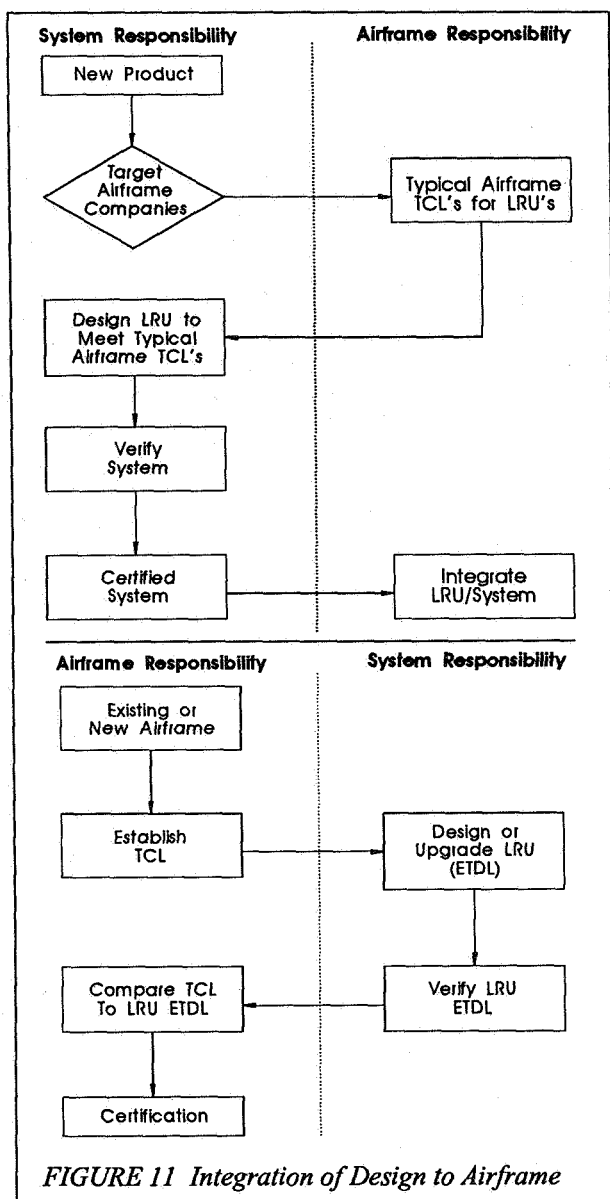


\* depending on coupling mode

- This is defined as an
  - equipment interface specification (for damage tolerance)
  - bulk cable current specification (for system upset tolerance)

FIGURE 10 Multiple Stroke Flash





## 7.6 f) DESIGN PROTECTION

To minimize the possibility of upset or damage, the ETDL should be higher than the TCL allowed to appear at equipment interfaces. In cases where the TCL plus the defined margin exceed the transient design level, additional protection must be provided. The optimum protection design is based on many factors, including level of required and provided protection, cost, weight, impact on production schedule, impact on vehicle performance, maintenance, reliability and ability to withstand other natural and man-made environments.

In general, the objective of the protection design is to:

- Reduce the level of the transient that reaches the vulnerable electric or electronic circuit.
- Decrease vulnerability of the circuits by increasing their damage and upset thresholds.
- Increase the design margin by combining elements of the above.

Design techniques commonly used to reduce transient levels include shielding, cable routing, circuit wiring type selection, terminal protection and dielectric isolation. Techniques that decrease

circuit vulnerability include circuit designs with high damage levels, high-level logic, and use of hardware and software techniques to increase circuit upset tolerance.

In order to make an electronic system immune to the effects of lightning, it is almost always necessary to make judicious use of shielding on interconnecting wiring and to provide proper grounding of these shields.

Of the different types of shields, the solid shield inherently provides better shielding than does a braided shield, and a spiral-wrapped shield can be far inferior to a braided shield in performance.

In severe environments, braided shields using two overlapping courses of braid may give shielding performance approaching that of a solid-walled shield.

Conduits should not be relied upon for protection against indirect effects since they may or may not provide electromagnetic shielding. Only if the conduit is electrically connected to the aircraft structure will it be able to carry current, and thus provide shielding for the conductors within.

The presence of a shield grounded at only one end will not significantly affect the magnitude of the voltage induced by changing magnetic fields, although a shield may protect against changing electric fields. While a shield may keep the voltage at the grounded end low, it will allow the common mode voltage on the signal conductors to be high at the unshielded end.

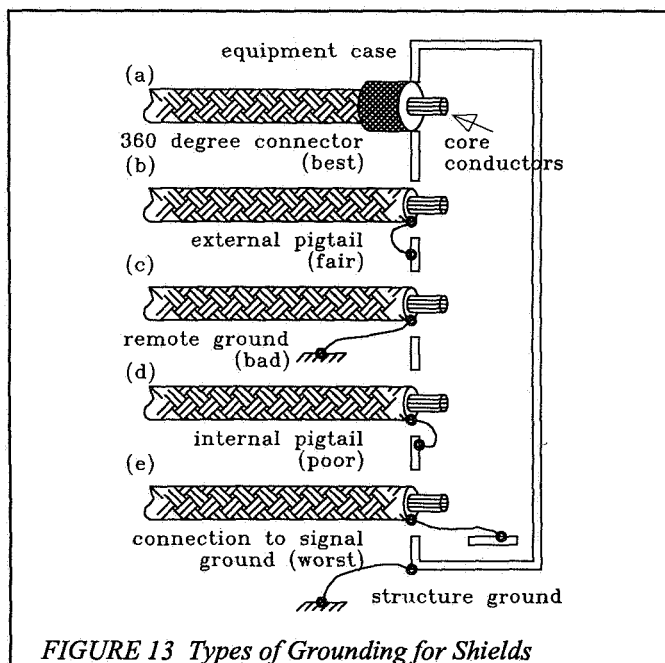
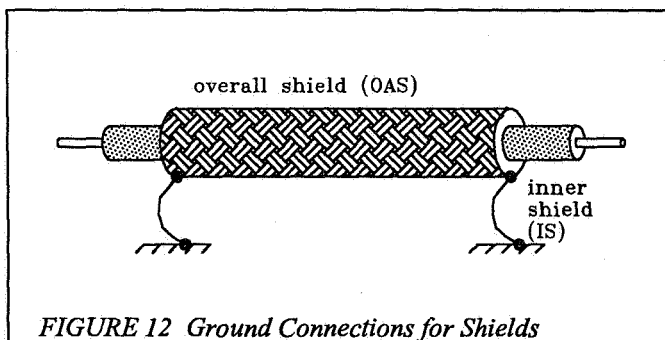
Shielding against magnetic fields requires the shield to be grounded at both ends, in order that it may carry a circulating current. It is the circulating current that cancels the magnetic fields that produce common mode voltages.

There is some virtue in staggering spacing between multiple-ground points on a cable shield, since it is theoretically possible that uniform grounding can lead to troublesome standing waves if the shield is illuminated by a sustained frequency interference source. Also, the cable may be exposed to a significant amount of magnetic field over only a small portion of its total length. If the shield is multiple-grounded, the circulating currents will tend to flow along only one portion of the cable, whereas if it is grounded at only the two ends, current is constrained to flow the entire length of the cable.

The requirement that a shield intended for protection against lightning effects must be grounded at both ends raises the perennial controversy about single-point versus multi-point grounding of circuits. For many reasons, mostly legitimate, low-level circuits need to be shielded against low-frequency interference. Most commonly, and usually legitimately, the shields intended for such low-frequency interference protection are grounded at only one end.

A fundamental concept, often overlooked is that the physical length of such shields must be short compared to the wavelength of the interfering signals. Lightning-produced interference, however, is usually broad-band and includes significant amounts of energy at quite high frequencies - frequencies higher than those the typical low-frequency shields are intended to handle. This conflict is usually too great for both sets of requirements to be met by only one shield system.

Most commonly, both sets of requirements can be met only by having one shield system to protect against low-frequency interference and a second to protect against lightning-generated interference. The lightning shield can usually consist of an overall braided shield on a group of conductors, with this overall shield being grounded to the aircraft structure at least at the ends. Within the overall shield may be placed whatever types of circuits are needed. Such an overall shield is shown in Figure 12. Other types of



grounding for shields are shown in Figure 13.

An in-depth treatment of equipment location and associated wiring can be found in [17].

Because of other constraints, the designer may not have much choice in the location of electronic equipment. But it is often possible to make improvements in the resistance to indirect effects by locating equipment in regions of the aircraft where the electromagnetic fields produced by lightning current are the lowest, and by avoiding placement in the region where fields are the highest. For example, since the most important type of coupling from the outside electromagnetic environment to the inside of the aircraft is through apertures, it follows that equipment should be located as far from major apertures as possible.

One main goal is to locate electronic equipment toward the center of the aircraft structure, since the electromagnetic fields tend to cancel toward the center of any structure. Other goals include locating equipment away from the outer skin of the aircraft, particularly the nose; and, if possible, electronic equipment should be located in shielded compartments.

Of particular importance to aircraft using large amounts of composite materials is the type of shelf upon which electronic equipment is located. Shelves are called upon to provide ground planes or reference surfaces for electronic equipment, and thus it is essential that they be highly conductive and well-bonded to the aircraft structure.

Some basic principles apply:

- The closer a conductor is placed to a metallic ground plane, the less is the flux that can pass between that conductor and the ground plane.

- Magnetic fields are concentrated around protruding structural members and diverge in inside corners. Hence, conductors located atop protruding members will intercept more magnetic flux than conductors placed in corners, where the field intensity is weaker.

- Fields will be weaker on the interior of a U-shaped member than they will be on the edges of that member.

- Fields will be lowest inside a closed member.

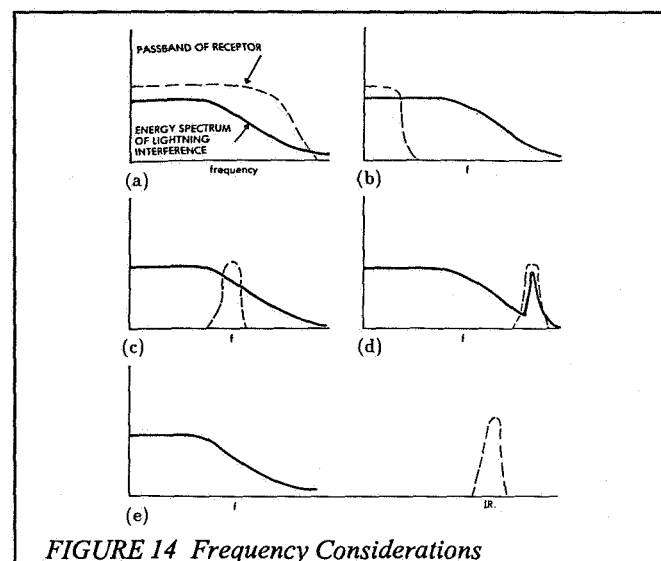
Circuit protection devices can sometimes be used to limit the amount of electrical energy that a wire can couple into a piece of electronic equipment. While one can seldom eliminate interference through the use of circuit protection devices, when judiciously used, they can virtually eliminate physical damage to electronic devices. Protective devices should be incorporated into a piece of equipment at the time it is built, not added after trouble has been experienced.

Circuit protection devices, described in [19] include:

- Switching devices
- Non-linear devices
- Circuit interrupters
- Spark gaps
- Metal oxide varistors
- Zenar-type diodes
- Reverse-biased diodes

Frequently a spark gap and a MOV, or an MOV and a surge-protecting diode, are used together to provide added protection. The higher energy device is connected close to the point where the surge may enter the system, and the lower energy device is connected close to the more sensitive components. The principle is that the high-energy device provides the primary protection and diverts the major portion of the surge energy, while the lower-energy device provides protection for the residual transients.

Protective devices cannot be operated directly in parallel since the device with the lowest clamping voltage would carry all the surge current. Impedance between the two is needed to limit the surge current in the lower energy device and allow voltage to develop that initiates conduction in the high-energy device. Best protection is obtained if the two surge protectors are physically separated, where possible.



One of the most important considerations in the control of lightning-related interference through proper circuit design lies in the fundamental observation that a device with a broad bandwidth can intercept more noise energy than can a narrow bandwidth device. Some of the considerations that derive from this observation are contained in Figure 14.

The noise produced by lightning has a broad frequency spectrum. Equipment is damaged or caused to malfunction in accordance with the total amount of energy intercepted. In a lightning flash there may be plenty of energy left in the megahertz and multimegahertz region to cause interference. The energy that is available for damage or interference may well be concentrated in certain frequency bands by the characteristic response of the aircraft or the wiring within the aircraft.

The studies of types of interference produced in aircraft by the flow of lightning current have shown that the lightning energy excites oscillatory frequencies on aircraft wiring, particularly if the wiring is based on the single-point grounding concept. If at all possible, the pass bands of electronic equipment should not include these frequencies, as does the hypothetical pass band shown in Figure 14 (d). Higher or lower pass bands would inherently be better than the one shown. As an extreme example, shown in Figure 14 (e) fiber optic signal transmission operating in the infrared region avoids the frequency spectrum associated with lightning-generated interference almost completely.

Once the ETDLs have been established, it is important to look at the protection design of individual equipment from a system standpoint when possible, and some intelligent decisions can be made.

If a system is protected on an independent basis where SPDs are installed at each end of a circuit, there is the potential for burning out

When complete insulation is not possible in the remote LRUs, it is possible to install series impedance at the interfaces of the remote LRU. Thus, in this particular case, some current will flow in the circuit, but the current will be limited by the series resistance to a level which is safe enough so that SPDs in the computer do not burn out.

When either of these two approaches is employed for protection design, it is essential that both LRUs be assigned the same ETDL and that both be verified by test, specifically by the pin-injection test described earlier and which will be discussed further in [1]. When the pin-injection test is applied to the computer interface, the open-circuit voltage of the test set will be clamped to the rated clamping level of the SPDs in the computer and current will flow through them. This current will be limited by the short-circuit current factor in the ETDL specification and, of course, the SPDs must be able to tolerate this amount of short-circuit current to pass the test. At the remote LRU, the same test set is applied to the connector pins of the same circuit. In this case, the entire test set voltage which is the ETDL open-circuit voltage level, will appear between incoming pins and case ground because there are no SPDs and no other elements or connections between incoming circuits and case ground. Thus the insulation between LRU circuit elements and case ground must be capable of tolerating the full ETDL voltage level.

A major challenge facing FADEC and FBW system designers concerns the performance of system software in the presence of indirect lightning effects. [20], [21], [22], [23]. Circuits should be designed to tolerate momentary logic upsets and to return to normal operation after a transient. Designers should avoid circuits that latch up in an abnormal mode, and use logic with high transitional levels wherever possible.

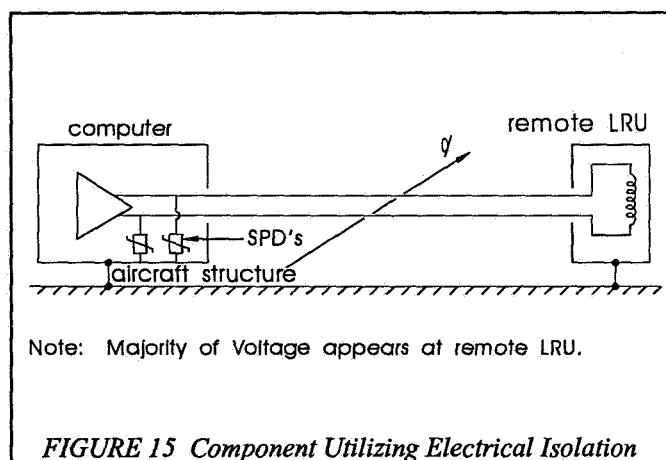
In a practical sense, upset is very difficult to prevent by shielding because the signal levels must be reduced to below the level of the logic voltage (usually a very low signal of 5 to 12V). Protection devices cannot be used because the devices, if they are set below the logic level, would effectively upset the logic. Upset hardening is often handled by software that allows the upset to occur but ensures that it will not be catastrophic to the aircraft or its operation. Optical isolation equipment is effective in reducing upset.

Following are a few examples of the software techniques that should be considered to minimize upset:

- Program execution from random access memory (RAM) is undesirable.
- Exit from temporary loops must be guaranteed.
- Return from all possible interrupts is mandatory.
- Use system cross-checking and process redundancy that involves multiple execution of a process and comparison of results.
- Use checkpoint rollback where critical information is periodically and routinely recorded on a backup or redundant-storage medium.
- Use plausibility checks that verify that information being processed or the result of computation fall within realistic bounds.
- Use timeouts for certain operations to occur.

## 8.0 CONCLUSION

This paper has discussed the first six steps in the lightning protection certification process. The sequel paper, "Certification of Lightning Protection for a Full-Authority Digital Engine Control," discusses the verification process in detail.



the SPDs at both ends of the circuit. Therefore, placing SPDs at interfaces of all LRUs within a system is not always a good idea. It adds weight and cost to the equipment. Instead, there are several alternatives which make sense from a system design standpoint. One is applying an SPD at one end of a circuit and utilizing electrical insulation between incoming elements and case ground at the other end, as illustrated in Figure 15.

Because of that insulation, no current flows. Because no current flows, no current flows through SPDs at the computer end and they are not stressed. The SPDs are there in the rare event that a transient might appear there, but they are not stressed by short-circuit currents because the remote ends of the circuit conductors are insulated from ground.

A variation consists of SPDs used at the computer as before.

---

## REFERENCES

- 1) M. Dargi, E. Rupke, K. Wiles, "Certification of Lightning Protection for a Full-Authority Digital Engine Control," International Aerospace and Ground Conference on Lightning and Static Electricity, 16-19 April, 1991.
- 2) U.S. Federal Aviation Regulations, Airworthiness Standards: Transport Category Airplanes, June 1974
- 3) "Protection of Aircraft Electrical/Electronic Systems Against the Indirect Effects of Lightning," FAA AC 20-136, 5 March, 1990.
- 4) U.S. Federal Aviation Regulations, Airworthiness Standards: Normal, Utility and Acrobatic Category Airplanes, December 1974.
- 5) U.S. Federal Aviation Regulations, Airworthiness Standards: Normal Category Rotorcraft, 1974.
- 6) U.S. Federal Aviation Regulations, Airworthiness Standards: Transport Category Rotorcraft, 1974.
- 7) "Protection of Airplane Fuel Systems Against Fuel Vapor Ignition Due to Lightning," FAA AC 20-53A, Federal Aviation Administration, Washington, D.C., 12 April, 1985.
- 8) F.A. Fisher, J.A. Plumer, R.A. Perala, "Lightning Protection of Aircraft," Lightning Technologies, Inc., 1990; Chapter 5.
- 9) Fisher et.al., Chapter 4.
- 10) Fisher et.al., Chapter 8.
- 11) Fisher et.al., Chapter 11.
- 12) Fisher et.al., Chapter 14.
- 13) NASA Report of Atlas-Centaur-67 FLTSATCOM F-6 Investigation Board, July 15, 1987.
- 14) Fisher et.al., Chapter 5.
- 15) Fisher et.al., Chapter 10.
- 16) Fisher et.al., Chapter 13.
- 17) Fisher et.al., Chapter 16.
- 18) "Environmental Conditions and Test Procedures for Airborne Equipment, Radio Technical Commission for Aeronautics.
- 19) Fisher et.al., Chapter 17.
- 20) "Damage and Voltage Breakdown Threshold Data Base Improvement Test Report," document D-180-28467-1, Boeing Aerospace Co., Seattle, Wash., 1984.
- 21) G.W. Masson, "Upset Experimentation in Computer-Based System," Eighth International Aerospace and Ground Conference on Lightning and Static Electricity, 21-23 June, 1983.
- 22) R.A. Perala, T. Rudolph, F. Erikson, "Electromagnetic Interaction of Lightning with Aircraft," IEEE Transactions on Electromagnetic Compatibility, Volume EMC-24, Number 2, May 1982.
- 23) G.M. Masson, "Intermittent/Transient Faults in Digital Computers," Compendium of Lightning Effects on Future Aircraft Electronic Systems, DOT/FAA/CT-82/30, February 1982.

# CERTIFICATION OF LIGHTNING PROTECTION FOR A FULL-AUTHORITY DIGITAL ENGINE CONTROL

M. Dargi, E. Rupke, K. Wiles  
Lightning Technologies, Inc., USA

## 1.0 INTRODUCTION

As discussed in "Design of Lightning Protection for a Full-Authority Digital Engine Control" [1], FADEC systems present many challenges to the lightning protection engineer. In addition, verification of the protection-design adequacy for certification purposes presents additional challenges. In particular, close coordination between the airframe manufacturer and the suppliers of systems and subsystems is required.

The basic requirement of the certification plan of a FADEC system is to demonstrate compliance with Federal Airworthiness Regulations (FAR) 25.1309 [2] and 25.581. Certain FAR Issue Papers may be applicable and the forthcoming FAR 25.1315 [3] will clarify some ambiguities in the FARs pertaining to lightning protection of flight-critical and essential systems. These FARs are intended for transport aircraft, but there are equivalent sections for general aviation aircraft, normal and transport rotorcraft. Military aircraft may have additional requirements.

The criteria for demonstration of adequate lightning protection for a FADEC system includes the procedures outlined in Federal Aviation Administration (FAA) Advisory Circular (AC) 20-136 "Protection of aircraft electrical/electronic systems against the indirect effects of lightning." [4] As FADEC systems, including the interconnecting wiring, are generally not susceptible to direct attachment of lightning currents, this paper deals primarily with the verification of protection against indirect effects.

It is the responsibility of the airframe manufacturer or system integrator to provide the overall assurance of adequate lightning protection. However, it is often the case that the airframer's certification plan will refer to test or analysis plans conducted by system suppliers.

## 2.0 VERIFICATION METHODS

Verification of protection against lightning indirect effects is accomplished by the following procedures:

1. Demonstrating that actual transient levels in the interconnecting wiring do not exceed the established TCLs for the wiring.
2. Demonstrating that the individual equipment will tolerate the ETDLs without component damage.
3. Demonstrating that interconnected and operating systems will tolerate the applicable ETDLs (as applied to the cables of an interconnected system) without component damage or system functional upset.

The accepted methods of verification are through similarity of design with existing systems or aircraft, mathematical analysis or through simulated lightning testing.

## 2.1 SIMILARITY

Verification by similarity must be demonstrated by detailed

comparisons of drawings, parts lists, system operating parameters and installation details. The certification plan must show that the FADEC systems, and the portions of the airframe which contain the systems, are identical to a previously certified system from a lightning-protection standpoint. Most importantly, the certification plan must show that TCLs, ETDLs and margins will remain similar. As FADEC systems are relatively new to the transport aircraft market and because of the rapidly developing technology of electronic control systems, certification entirely through similarity is rare.

## 2.2 ANALYSIS

Mathematical analysis is often used in the development stages of an aircraft, before prototypes are available, to determine the levels of lightning-induced transients that may be expected. For certification purposes, the use of "acceptable" mathematical analysis is often limited to certification documents describing lightning protection for small engineering changes. More frequently, analysis is used in conjunction with one or both of the other forms of verification. A common example is the extrapolation of the effects of high current from the results of a low-current test. Analysis should always include the worst-case scenario. Generally, verification by analysis will require significantly higher margins between TCL and ETDL than other forms.

## 2.3 TESTING

Conceptually it would be best to perform full-threat testing on fully configured and operational aircraft, performed either on a Go/No-Go basis or with a measurement and analysis scheme. This is seldom practical, however, primarily because of the cost and complexity of the required test equipment, test specimen and test facility. Therefore, to determine the indirect-effects protection of a FADEC system, testing will usually consist of two general categories of simulations: aircraft-level tests such as lightning transient analysis (LTA), used to determine the TCLs in the airframe or major sections of the airframe, and ETDL tests, performed with FADEC system components installed in the airframe. The second main category consists of a variety of bench tests performed on system components to assess protection against damage and functional upset.

## 2.4 TCL VERIFICATION

Verification of TCL will be accomplished by one of the following methods:

- Performance of a full-vehicle lightning test, in which reduced-scale pulses of current with waveforms of components A and H are circulated through the aircraft and measurements are made of actual transients induced in typical individual conductors and bulk cables associated

with the flight critical/essential systems. The measured transients are then extrapolated linearly to predict the levels that would be induced by full-threat component A and H currents. This procedure is also known as an LTA test. Measurements are made on representative circuits/cables, in accordance with a detailed test plan.

- Computation of anticipated actual transient waveforms/levels in representative wires/cables by analysis based on first principles (laws of electromagnetic effects, aircraft material properties and geometry). The analytical techniques utilized are verified by comparison with available prior test data.

- A combination of both of the above procedures. The extent to which each method will be employed will be detailed in test and/or analysis plans, to be submitted to airworthiness certifying authorities for approval.

## 2.5 ETDL VERIFICATION

Verification of compliance with the ETDLs specified is to be accomplished by tests conducted by the system or equipment vendors in accordance with test plans to be submitted by them to the airframe manufacturer for approval. Two test methods will be employed, as follows:

- Pin-injection tests in which full-scale voltage/current transients are applied (in most cases) between individual pins and case ground to verify circuit board component tolerance of the specified ETDLs.

- Bulk-cable tests, in which the specified cable ETDLs (bulk-cable currents) are transformer coupled or directly injected into interconnecting cables, with the system powered up and operating. The primary purpose of these tests is to verify that the system does not upset, although the test also verifies protection against system-related damage effects.

## 3.0 CERTIFICATION PLAN FOR A ROTORCRAFT FADEC/ENGINE SYSTEM

The following example of a certification plan for a hypothetical system provides detailed procedures applicable to most FADEC applications. This example addresses specifics for a rotorcraft FADEC/engine system, designated LTI-1000, including an Electronic Control Unit (ECU) and a Hydromechanical Control Unit (HMU). However, the general procedures and steps would be applicable for fixed-wing aircraft installation of the same or similar engine system, though changes in some of the ETDLs and TCLs may be necessary. The certification plan would begin with several brief introductory sections describing the purpose and citing the specific FAA and DoD requirements relevant to the rotorcraft. Our example begins after the opening paragraphs:

### 3.1 INTRODUCTION

- provide an overview of the system and application.

### 3.2 PURPOSE

- state goals of certification plan.

### 3.3 REQUIREMENTS

- cite specific FARs, ACs, MIL-STDs and issue papers as applicable.

## 3.4 LIGHTNING CRITERIA

The lightning environment which the helicopter (or fixed-wing aircraft) must withstand is defined in Appendix III of AC 20-136 [4] and Section 3.3 of MIL-STD-1795. [5]

These references define the same lightning environment, which is represented by current components A through D, a multiple-stroke arrangement of components A and D/2, and a multiple-burst environment. These components are fully defined in the aforementioned references and will not be described further here. They represent the characteristics of lightning-stroke currents entering, flowing through and exiting from an aircraft.

Applicability of individual components of the lightning environment to specific airframe surfaces or structures depends on the lightning strike zones of such surfaces/structures. Zone definitions are also found in AC 20-136 [4] and MIL-STD-1795A. [5]

## 3.5 STEPS IN DESIGN AND VERIFICATION

This section describes the steps being followed in design and verification of lightning protection for the LTI-1000 electronic control system. The steps described herein are similar to those in Section 7 of FAA AC 20-136 [4] (Steps a through g). Several of the steps include performance of tests. Plans for these tests are provided in separate documents, referenced herein.

### 3.5.1 Step a - Locate the lightning-strike zones

The LTI-1000 engine installed in the helicopter is not susceptible to direct lightning strikes. Instead, they are subject to lightning strikes conducted on and off the engine via the drive shaft, engine mounts, electrical wiring harnesses, fuel and drain lines. Systems and components exposed to such conducted currents are in zone 3, see Figure 1.

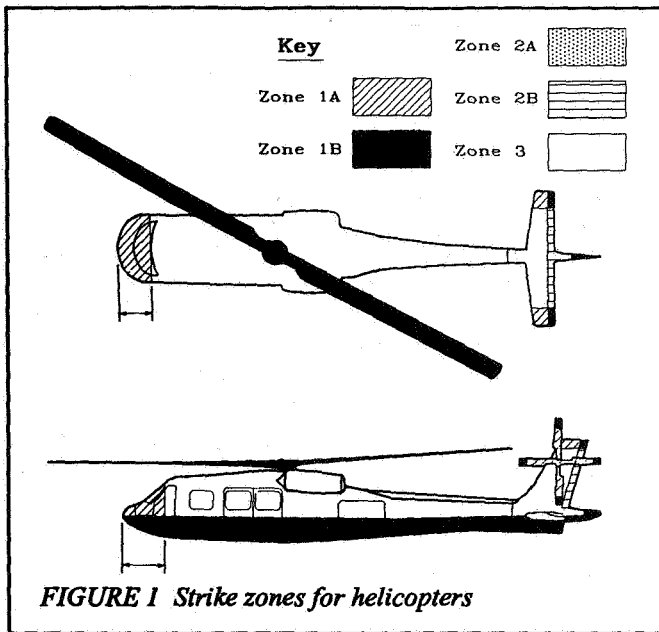
### 3.5.2 Step b - Establish the external environment for the zones

The external environment components applicable to specific zones are found in Appendix III of AC 20-136 [4], reproduced herein as Table 1.

*Table 1 - Zonal Application of the External Environment for Determination of Indirect Effects*

Zone	Current Waveforms					
	A	B	C	D	Multiple Burst	Multiple Stroke
1A	X	X			X	X
1B	X	X	X	X	X	X
2A		X		X	X	X
2B		X	X	X	X	X
3	X	X	X	X	X	X

Note: Indirect effects resulting from components B and C are usually insignificant.



Since components B and C produce insignificant indirect effects and the effects of component D are exceeded by those of component A, the LTI-1000 electronic control system is being designed to tolerate the indirect effects of current component A and the multiple-stroke and multiple-burst environments being conducted through the airframe. Since the LTI-1000 will be employed in a helicopter, the zone 3 currents will be conducted into the engine via the main rotor shaft, gearbox and engine output shaft. Lightning current will exit the engine via all other electrically continuous paths between the engine and the airframe.

### 3.5.3 Step c - Establish the internal environment

The internal lightning environment consists of lightning currents conducted into and out of the engine via the aforementioned conductive paths. The amount of lightning current that may flow in each path cannot be determined exactly by analysis, due to the complexity of the airframe and engine installation design and difficulty of quantifying electrical impedances associated with mechanical parts. However, gross estimates can be made of current magnitudes and, if simplifying assumptions are made on a worst-case basis, the resulting magnitudes will be higher than those actually experienced.

#### 3.5.3.1 Lightning-current flow paths

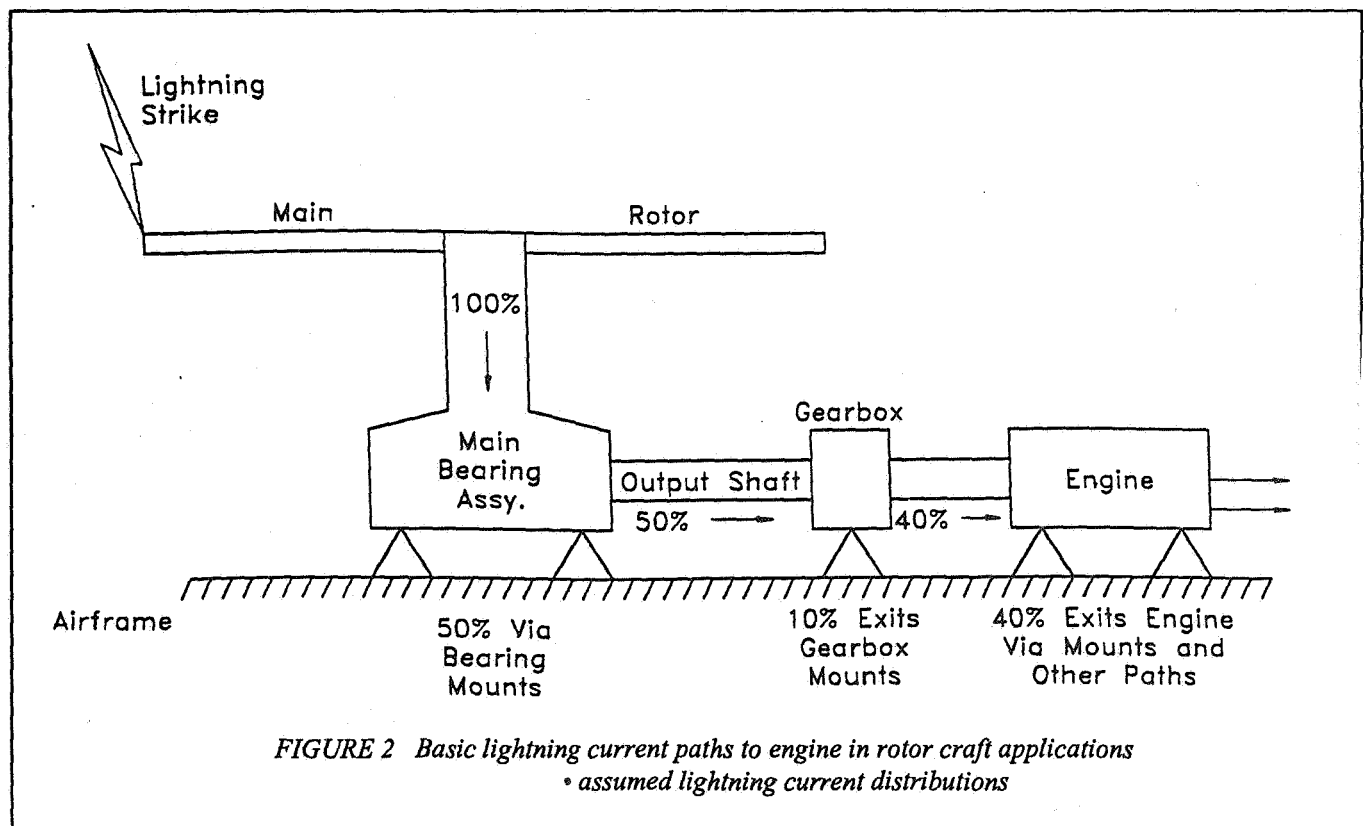
##### 3.5.3.1.1 Current entering engine

Nearly all lightning strikes to a helicopter enter the main rotor and exit from one or more of the lower extremities such as landing gear, skids, or tail boom. The lightning current path to an engine is illustrated basically in Figure 2.

Figure 2 shows a single-engine installation. In this figure, the following simplifications have been made, which result in the percentage of current entering the engine being higher than is actually expected to occur.

##### Simplifying Assumptions

- Current paths through rotor pitch control rods are omitted.
- 100% of external lightning current is expected to enter main bearing assembly.
- 50% of lightning current is assumed to flow through main bearing to output shaft(s), even though other low-impedance paths exist to the airframe via the mechanical-load paths (thrust amounts) and a variety of control and sensor paths.
- A single engine and output shaft is assumed. Twin output shafts would share the engine current, resulting in less current to each engine.





Thus, the percentages of lightning current assumed to flow into the gearbox (50%) and engine (40%) are higher than actual, though the amount of margin cannot be determined.

Accordingly, it is assumed that 40% of the applicable full-threat, external lightning-current components, (components A, D/2, and H) will enter the engine via its output shaft and exit the engine via the engine mounts and other available paths. These current magnitudes are listed in Table 2.

*Table 2 - Lightning Currents Entering Engine*

Current Component	Peak Current
A	80 kA
D/2	20 kA
H	4 kA

The currents of Table 2 represent the internal lightning environment applicable to the LTI-1000 engine.

### 3.5.3.1.2 Currents exiting engine

The lightning current that entered the engine via its output shaft will exit from the engine via a variety of conductive paths. These are listed in Table 3.

*Table 3 - Current Exit Paths from Engine Path*

Path	No.
• Engine and gearbox mounting struts	7
• Exhaust duct	1
• Common drain	1
• Plenum drains	2
• Fuel hose	1
• Engine starter harness grounds	1
• ECS wiring harness	2
• Ground strap	1
<b>Total number of paths:</b>	<b>16</b>

If the current divided evenly, approximately 5 kA would flow from the engine to the airframe via each path. Actually, the magnitude of current in each path is determined by its impedance as compared with the impedances of other paths, with the highest currents flowing in the lowest impedance paths. The shortest, most direct paths to the airframe will have the lowest impedance and the highest current. These include the gearbox and engine-mount struts.

The metal cross sections and other aspects of the struts and other mechanical paths are fully capable of conducting their share of the lightning currents and no further considerations will be given to them in this plan.

It is necessary to establish the peak amplitudes of lightning currents flowing in the shields of ECS wiring harness as these become part of the TCL and ETDL specifications. For protection design purposes, it is assumed that current is shared equally among all exit paths and that ECS shield currents are as shown in Table 4.

*Table 4 - ECS Harness Shield Currents (engine-to-airframe)*

Current Component	Peak Current
A	5 kA
D/2	1.25 kA
H	0.25 kA

The fact that the ECS shield currents do not, in fact, exceed the levels of Table 4 will be verified by test of an engine in a simulated helicopter installation, as described in Section 3.5.7 (step g).

### 3.5.4 Step d - Identify the flight-critical/essential systems

The LTI-1000 ECS is assumed to be flight-critical as the engine is being certified for single- as well as twin-engine applications. All components of this system, including the ECU, engine-mounted accessories and interconnecting wiring harness are assumed to be flight-critical.

The ECS is exposed only to lightning indirect-strike effects in accordance with its zone 3 installation. The engine and ECS are protected from direct lightning strikes by the main rotor and the engine cowlings, which are above the engine.

### 3.5.5 Step e - Establish transient control and design levels

The ETDLs represent the amplitude(s) of voltage(s) and/or current(s) that the ECS equipment is required to tolerate and remain operational without damage or system-functional upset. These levels are set higher than the maximum amplitude of transients that are allowed to be induced in interconnecting wiring and appear at equipment interfaces, which are the TCLs. The relationship between TCLs and ETDLs is illustrated in Figure 3. The ETDL is part of the specifications for the ECS electrical/electronic components. TCLs and ETDLs are defined in terms of the open circuit voltage (Voc) and the short circuit current (isc) appearing at wiring/equipment interfaces, and the currents in the shields of ECS interconnecting wiring harness. The "V" and "I" will be related by the source impedances (i.e., loop impedance) of interconnecting wiring, and different levels have been established for signal circuits and 28 VDC power circuits. The waveforms/levels defined in Appendix IV of FAA AC 20-136 [4] have been utilized to establish TCLs and ETDLs for cable shields and connector interfaces.

The equipment transient susceptibility level, also shown on Figure 3, is the amplitude of voltage or current which, when applied to the equipment, would result in damage to components or upset such that the equipment can no longer perform its intended function. This level is higher than the ETDL, and is not specified.

The TCLs and ETDLs for the single-engine helicopter installation are defined as individual connector pin-to-case (Voc) and

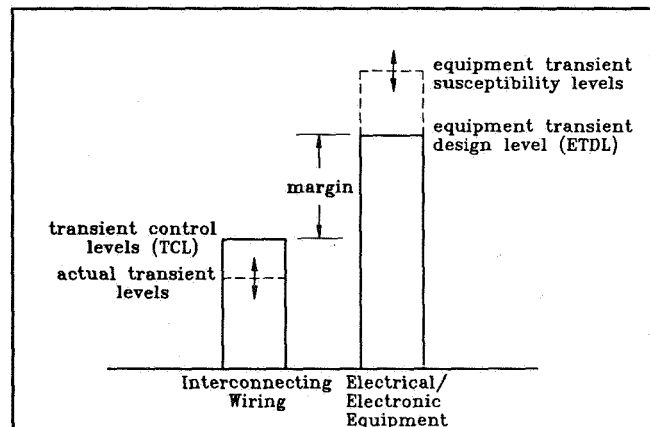


*FIGURE 3 Relationships between transient levels*



current (isc) waveforms and levels, as this condition is where the highest levels of induced effects are expected to appear in the helicopter circuits. This is the manner in which verification tests of equipment will be performed, as described in 3.5.7 (step g).

For design and verification of protection against system upset, a bulk-cable current is also defined. This represents the total voltage and/or current that can be induced in the loop formed between a complete cable shield and the adjacent engine or airframe. For overbraid shielded cables, or cables comprised entirely of individually shielded pairs, this is defined as a bulk-cable current. For verification test purposes, the levels will be directly injected or transformer coupled into the interconnecting cable while the system is powered up and operating, for the purpose of verifying protection against system-related damage and upset, as described briefly in section 3.5.7 (step g) and the referenced test plans.

All of the ETDs are defined in the multiple-stroke mode, as defined in AC 20-136 [4] (one full-amplitude transient corresponding to the first return stroke, Component A, followed by twenty-three transients corresponding to subsequent strokes, Component D/2).

Specific TCLs and ETDs established for the interconnecting wiring and electrical/electronic components are shown in Table 5.

Notes: 1. Waveforms and levels are defined in FAA AC 20-136 [4], Appendix IV.

2. Short-circuit current specification (isc) may be reduced from the level defined in AC 20-136 [4] if line-to-case ground impedance at airframe or engine-mounted accessory is determined to be greater than the impedance (5 ohms or 25 ohms) implied in the definition. In no case may the isc level be less than that produced by a 100-ohm impedance. If the isc specification is reduced in this manner, the ability of the remote interface to withstand the specified ETD must be verified by transient test.

3. The specified shield-current amplitude is the current at the ECU interface (connectors E1, E2 and E3). Currents in branches of intra-engine harness shields will be lower. The total of currents in each branch will equal the specified current at the ECU connector.

4. The short-circuit (isc) current is as specified and may not be reduced as described in Note 2.

The transient levels presented in Table 5 represent a margin of 2:1 or greater between ETDs and associated TCLs, in accordance with advice given in Section 9 of FAA AC 20-136. The TCL selections are intended to encompass the actual transient levels (ATLs) of the shielded conductors, and are generally based on an assumed harness-shield transfer impedance of 0.05 volt of conductor voltage per amp of shield current; a value typical of short-length shielded harness, such as employed between the ECU and other engine-mounted accessories. Thus, if the shield-harness TCL is 5 kA as listed in Table 5, the conductor voltage,  $V_c$  would be,

$$V_c = (0.05 \text{ V/A}) (5,000 \text{ A}) = 250 \text{ volts}$$

hence, a TCL of 300 volts for waveform 4, as defined in AC 20-136 [4].

The harness-shield TCLs have been based on experience with similar-sized engines and installations. Verification that actual-shield currents (sometimes called bulk-cable currents) do not exceed these levels will be accomplished by test of an engine with typical intra-engine and engine-airframe harnesses installed, as described briefly in section 3.5.7 (Step g) and the referenced test plans.

If actual harness-shield currents are found to be higher than the proposed TCLs, the TCLs and corresponding ETDs will be increased proportionately or a design change will be implemented to reduce the ATLs.

### 3.5.6 Step f - Design protection

The LTI-1000 ECS is designed to minimize the magnitudes of lightning-induced transients on the wire-harness shields and conductors, and to provide protection at the component (box) level in cases where expected transients would otherwise exceed component tolerance levels. Some of the protective measures incorporated in the LTI-1000 ECS design are listed in Table 6. The adequacy of each of those measures will be verified by the tests described in section 3.5.7 (step g).

*Table 5 LTI-1000 Equipment Transient Design and Control Levels*

Application	Equipment Interfaces		Waveform (Note 1)	TCL (Note 1)	ETDL (Note 1)	Remarks
	ECU	Other				
LRU connectors, pin-to-case ground	E1, E2	Engine mounted accessories interfacing with ECU	4	Level 3	Level 4	Note 2
Intra-engine harness shields	E1, E2	Engine mounted accessories interfacing with ECU	5A	5 kA	10 kA	Note 3
LRU connectors, pin-to-case ground	E3	Aircraft signal interfaces	3B 4	Level 3 Level 3	Level 4 Level 4	Note 2 Note 2
	E3	28 VDC power	4	Level 3	Level 4	Note 4
Engine-to-airframe	E3	Airframe mounted components	5A	5 kA	10 kA	Note 3

Table 6 - ECS Protective Measures

Protective Measure	Result
• Improved electrical bonding between accessories and engine	Reduces potential differences
• Shielding of all intra-engine harnesses; shields grounded at both ends	Reduces magnetic field coupling to signal conductors to insignificant levels
• Transient suppression diodes at ECU interfaces to sensitive circuits	Reduces incoming transients to levels that can be tolerated by circuit board components
• Dual-channel design and operation	Provides a second operational channel to perform control functions in the event the first is upset or damaged
• Isolation of electrical circuits from case ground at engine-mounted accessories	Reduces induced currents to low levels, reducing stress at ECU interfaces

### 3.5.7 Step g - Verify protection adequacy

The adequacy of the LTI-1000 ECS design to withstand lightning indirect effects will be verified by four series of tests. Two of these verify that actual transients induced in the interconnecting wiring do not exceed the established TCLs, and the other two verify that the ECU and other engine-mounted electrical components can safely tolerate the ETDL. These tests are described briefly in the following subsections. Complete descriptions are followed in the referenced test plans.

#### 3.5.7.1 Transient control level (TCL)

##### 3.5.7.1.1 Harness shield currents

Verification that the ECS harness-shield currents do not exceed the shield-current TCLs listed in Table 5 will be accomplished by tests of an engine with ECS components and interconnecting wire harness installed. In these tests, the simulated-lightning currents will be injected into the output shaft and allowed to exit the engine via simulated mounting struts, drains, harness shields and each of the other conductive paths listed in Table 3. These tests will be conducted on an EMI test rig, which consists of an engine case equipped with all engine-mounted accessories and suspended within a frame above a ground plane via insulating straps. This enables the actual exit paths to be simulated with metal straps, harnesses, etc. Measurements will be made of currents induced in the ECS intra-engine wiring harness, including all of its branches. These are the shield currents referred to in Table 5. The engine-airframe cable will also be represented in the test so that a measurement can be made of current in its shield. In addition, measurements will be made of currents exiting the engine via the other paths, for comparison with the original assumptions.

The ECS harness-shield current tests are described more fully in the referenced Test Plan #1.

##### 3.5.7.1.2 Conductor voltages and currents

Actual transient voltages induced in conductors within the ECS engine harness will be determined by test of an actual intra-engine harness. In this test, the shield currents determined from the engine test of section 3.5.7.1.1. will be injected into the intra-engine and measurements will be made of the voltages induced in conductors within. This test is conducted on a bench with conductors shorted to shields at remote (accessory) ends of the shield branches so that all of the conductor voltage and current can be measured at the ECU ends. Measurements will be made of induced voltage at open, ungrounded ends of conductors extending into each branch of the cable (the open-circuit voltage, Voc) and of the current flowing in the same conductors when both ends are shorted to the shield (the short-circuit current, isc) as these are the parameters by which the TCLs are defined.

Details of the intra-engine harness test are presented in the referenced Test Plan #2.

Actual transient levels in the conductors within the engine-airframe harness will not be measured during this test, as this harness is furnished by the airframe manufacturer. The TCLs and ETDLs established for the airframe interfaces in Table 5 will become part of the engine/airframe interface specification.

#### 3.5.7.2 Equipment transient design level (ETDL) verification

##### 3.5.7.2.1 Damage tolerance

Verification of ECS component compliance with the ETDLs listed in Table 5 will be accomplished by pin-injection tests, in which full-scale transients defined in Table 5 and Appendix IV of AC 20-136 [4] will be injected into equipment connector-pins, between individual pins and case grounds. These tests verify ability of circuit-

board components and protective devices to tolerate the established ETDLS without damage.

Pin-injection tests will be conducted on the ECU as well as the other ECS engine-mounted accessories. In situations where these accessories also have complied with line-to-ground, high-potential (hipot) test requirements that exceed the ETDLS, the ETDL pin tests may be waived upon presentation of hipot test reports.

The pin-injection tests are conducted on the ECU in a power-on but non-operational status. Other accessories will be tested in a power-off configuration. The pin-injection tests are described in the referenced Test Plan #3.

### 3.5.7.2.2 System functional upset

Verification of the ECS' ability to continue to perform its intended functions during and after exposure to lightning's indirect effects will be demonstrated by a system-upset test of a complete engine-mounted ECS, powered up and operating. For this test, induced multiple-stroke and multiple-burst transients are transformer-coupled or directly injected into the harness shields while the system is operating in each operational mode. These tests will be conducted on a system installed on the same engine case that was utilized for the harness-shield current tests of section 3.5.7.1.1. The test currents will be full-threat, harness-shield ETDLS as defined in Table 5, applied in the multiple-stroke mode, with one transient corresponding to current component A, as defined in Table 5 followed by 23 transients of one fourth this amplitude, corresponding to component D/2, all within two seconds, as defined in AC 20-136 [4].

The system-upset test is described in the referenced Test Plan #4.

### 3.5.7.3 Sequence of verification tests

The four tests described in the preceding subsections will be conducted in the sequence shown in Figure 4, so that the results of one

test are available to support the next and substantiate any design changes that might be necessitated by test results. In this way, the tests provide a building-block approach to certification, and allow each level of the protection to be validated.

#### Test Plan References

- #1. Engine-mounted harness-shield current test plan
- #2. Engine-mounted harness-conductor voltage/current test plan
- #3. ECS-equipment damage-tolerance test plan
- #4. ECS system functional upset test plan

### END OF "LTI-1000 CERTIFICATION PLAN"

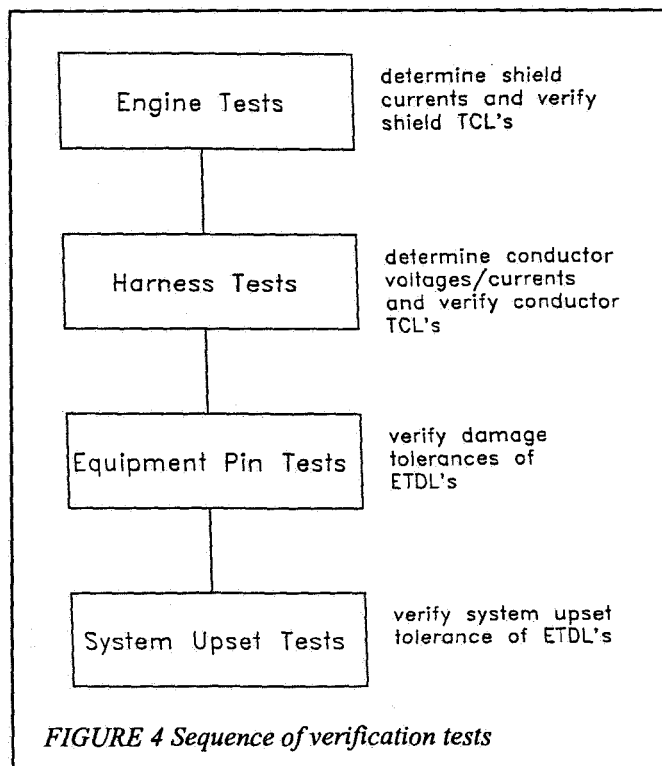
## 4.0 EXPERIMENTAL METHODS OF ANALYSIS

### 4.1 AIRCRAFT/ENGINE TCL-VERIFICATION TESTS

As noted in Section 3.5.7.1 of the certification plan for the hypothetical LTI-1000 engine, the verification that TCLs associated with intra-engine cables (i.e., between engine and engine-mounted accessories) do not exceed the specified values for these circuits, is accomplished by an LTA test of an engine housing with all engine-mounted accessories and all intra-engine wiring harnesses in place. This low-level pulse test may be conducted on an engine by itself, rather than in a completely configured vehicle, because the TCLs of interest here are associated only with engine-mounted circuits. For verification of the TCLs assigned to the engine-aircraft circuits (i.e., between engine and CVU or pilot-input force transducers) a full-vehicle LTA test may be required. LTA tests should also include measurements of bulk-cable currents, currents on cable shields, magnetic fields within structures and structural IR voltages when appropriate.

#### 4.1.1 Approach

LTA tests usually are low-level current pulse tests with the waveshapes of Component A and H as defined in FAA AC 20-136 [4] Appendix III. Other components are not used since the Components B and C produce insignificant indirect effects and the effects of Component D are exceeded by the effects of Component A. The resulting induced voltage and current transients in the aircraft wiring and harnesses will be measured and recorded by oscilloscopes located in or near the aircraft. Peak currents applied to the airframe generally can be limited to 1 kA or less to prevent any damage from occurring to the aircraft or avionic equipment. The measured data will then be extrapolated linearly to predict the actual transient levels that would appear in interconnecting wires during a full-threat, 200 kA stroke to the aircraft. An overview of the procedures and practices to conduct low-level pulse LTA tests may be found in "Lightning protection testing of full-scale aircraft to determine induced transient levels," by M.M. Dargi [6], "Lightning protection of aircraft," [7] and NASA CR-2524 "Lightning effects on the NASA F-8 digital-fly-by-wire airplane." [8] No further discussion of full-vehicle tests is provided in this paper.



## 4.2 ETDL VERIFICATION TESTS

In December 1989, the Radio Technical Commission for Aeronautics (RTCA) issued revision C of DO-160 Section 22, providing standard procedures for the conduct of lightning-induced transient susceptibility tests. Because of the rapid proliferation of sensitive electronics into more and more aspects of flight control, the trend toward lower operating voltages in these electronics, and the advent of "off-the-shelf" aeronautic devices intended for installation in a variety of applications, RTCA DO-160C Section 22 has been deemed inadequate. Since that time, the committees SAE AE4L and EUROCAE WG-31 SGI have been working on a revision. This will address, in greater detail, the waveforms, test levels, configuration of equipment-under-test (EUT), test procedures, measurement procedures, test equipment and safety procedures required for the conduct of ETDL verification tests for individual LRUs. Additional tests are usually necessary for verification of complete, interconnected FADEC and FBW systems.

As ETDL tests are generally bench tests performed by the equipment vendors to the specifications of the system integrator or airframe manufacturer, the success of the overall lightning protection for the entire aircraft may depend on the authenticity of the test simulation conducted by the equipment vendor. It may not be sufficient to perform ETDL tests, especially for system-functional upset, on a generic basis. It is preferable to perform ETDL analyses which relate to the actual configuration for the specific aircraft. Using DO-160 as a baseline, engineers should tailor ETDL tests to reflect actual operating loads, power- and signal-cable sizes, types and routing. Failure to do so could, at best, result in unnecessary expense and aircraft weight due to overdesign - at worst, underdesign.

### 4.2.1 Pin-Injection Tests

Pin-injection tests are designed to define a very specific level of damage tolerance. Depending on the type of EUT, these tests should be conducted with different methods and different pass/fail criteria.

For simple electrical/electromechanical components, such as valves, solenoids and switches, which are normally isolated from case or aircraft ground, the hipot or dielectric-withstand test is used. The EUT is unpowered and test currents are applied pin-to-case in accordance with specified ETDLs and idealized waveforms of DO-160. Figure 5a gives a typical test setup. If the EUT suffers no voltage breakdown to case, then the unit has been verified to withstand the specified damage-tolerance ETDL.

For simple electrical/electromechanical components which are normally referenced to case or local aircraft ground, a circuit-damage tolerance test is also required. In this situation, the EUT is normally powered because the follow-on currents from the power bus would accentuate any damage and make detection of potential circuit damage clearly distinguishable. Test currents are applied pin-to-case or pin-to-pin. Figure 5b illustrates a typical configuration. If no unintentional voltage breakdown to case occurs and there is no component damage, then the EUT has passed. Some equipment includes suppression devices that will intentionally shunt current to case.

For more complex electrical and electronic components - typically those containing solid-state circuitry - two possible conditions exist. When, under normal operating conditions, operating voltage constraints, impedance definitions, ground conditions and loading characteristics for the EUT are controlled by other equipment supplied by a different vendor, and the EUT manufacturer has no indication of suppression devices or filtering on interconnecting wiring, then pin tests must be performed to full specification of voltage and current.

In the second case, if loads and other operating parameters for the EUT are under the control of the EUT manufacturer, then any line-to-ground surge impedance and line-to-ground load impedance which exist in the interconnecting wiring may be used to relax test currents applied to the appropriate EUT pin. Since cable lengths and geometry play a role in surge characteristics, and they are not usually under the control of the EUT manufacturer, then relaxation of the specifications should be limited to line-to-ground transmission line impedances only - typically from full specification of 5 ohms to 50 to 100 ohms. This is usually applied only to waveforms 2 and 4, and waveform 5 if used as a pin test.

In both cases, power is applied to the unit, but loads are not interconnected. Transients are applied pin-to-case or pairs of pins-to-case under the assumption that case is power ground. Pass/fail conditions are again unintentional voltage breakdown, component damage and loss of function after the EUT is reconnected to the system. One special condition which must be considered is that testing must assess the possibility of change-of-state in the circuitry. To ensure that worst-case situations have been evaluated, circuits should be tested in both states. Because verification tests are performed under certification conditions and EUT configuration may not be altered, some developmental breadboard testing of specific circuits may be required to evaluate certain circuits in both states.

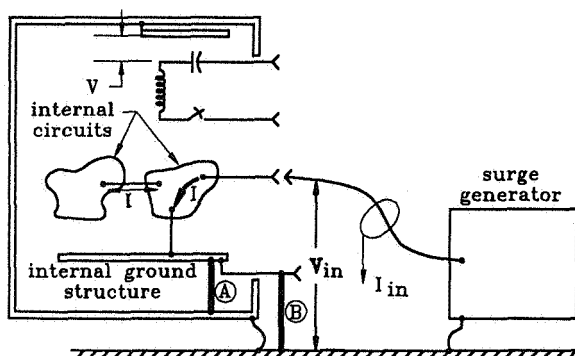


FIGURE 5a Pin-injection of an ungrounded system

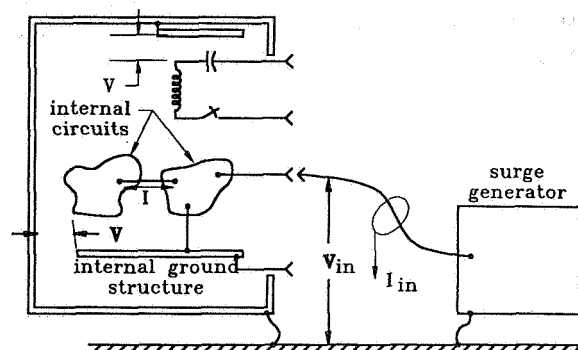


FIGURE 5b Pin-injection of a grounded system

#### 4.2.2 Functional tests

Functional tests are designed to evaluate the LRU, its wiring harnesses and its loads as an integrated and functioning system or subsystem. DO-160 is again a minimum requirement specification designed for off-the-shelf components; when that component is integrated into a system, the ETDL verification should reflect the actual configuration of the installed system. Particular attention should be given to ensure that bench tests reflect the actual lengths, orientation and operating conditions of interconnecting wiring, such as cable routing, cable size, cable types, shielding, cable branching, actual loads or load simulation. In short, transient susceptibility should be verified to actual configuration for each and every wire, not to a generic cable-bundle specification. ETDLs should be tested separately to each interface, not simultaneously to all interfaces, because this would pose a much lower threat to certain LRU interfaces. For example, if 1000 amps is specified for a connector, then 1000 amps should be applied to each connector, not 1000 amps applied to a cable bundle with many connectors. The setups illustrated in DO-160 are very generic, consisting of one LRU, with one cable and one load; most actual installations are not as simple. DO-160 must be used as a baseline and adopted to the aircraft installation. The closer the test setup is to actual installation, the less analysis will be required to correlate the test with verification requirements. The result will be increased safety, and may also reduce the use of unnecessary suppression devices. If generic tests require that every interface withstand a specified level of threat, but a thorough simulation shows that particular connectors will be subject to lower transient levels due to their actual configuration, those connectors will require less protection.

In all such tests, the EUT must be fully functional. System responses, as seen by the pilot, are monitored for unacceptable responses per specified pass/fail criteria.

## 5.0 RESPONSIBILITIES

Because it is rarely practical to perform full-threat tests on fully configured aircraft, the key to successful protection will be the degree to which the system and subsystem tests simulate actual internal lightning conditions to be expected in the complete aircraft with all components interconnected and operational. These tests will depend in turn, upon the accuracy of the airframe manufacturer's or system integrator's prediction of TCLs, the thoroughness of ETDL verification as tested by the system suppliers, and the sufficiency of the margins to account for any uncertainties in these conditions. The coordination between the airframe manufacturer and system/subsystem suppliers in this process is fundamental to adequate protection.

## REFERENCES

- 1) M. Dargi, E. Rupke, K. Wiles, "Design of Lightning Protection For a Full-Authority Digital Engine Control," International Aerospace and Ground Conference on Lightning and Static Electricity, 16-19 April, 1991.
- 2) U.S. Federal Aviation Regulations, Airworthiness Standards, Equipment, systems and installations, (all aircraft categories).
- 3) Federal Aviation Regulations, Airworthiness Standards, Transport Category Airplanes, U.S. Department of Transportation.
- 4) "Protection of Aircraft Electrical/Electronic Systems Against the Indirect Effects of Lightning," FAA AC 20-136, 5 March, 1990.
- 5) "Lightning Protection of Aerospace Vehicles and Hardware," U.S. Mil-Std 1795, U.S. Department of Defense, May 1986.
- 6) M.M. Dargi, "Lightning Protection Testing of Full Scale Aircraft to Determine Induced Transient Levels," Proceedings of the 1989 International Conference on Lightning and Static Electricity Addendum.
- 7) F.A. Fisher, J.A. Plumer, R.A. Perala, "Lightning Protection of Aircraft," Lightning Technologies, Inc., 1990.
- 8) F.A. Fisher, J.A. Plumer, L.C. Walko, "Lightning Effects on the NASA F-8 Digital-Fly-By-Wire Airplane," NASA Contractor Report CR-2524, March 1975.

## **Poster Papers Measurements**

ON ERROR SOURCES DURING AIRBORNE MEASUREMENTS OF  
THE AMBIENT ELECTRIC FIELD

B.F. Evteev

Voeikov Main Geophysical Observatory,  
Karbyshev St., 7, 194018 Leningrad, USSR

ABSTRACT

The paper addresses the principal sources of errors during airborne measurements of the ambient electric field and charge. Results of their analysis are presented for critical survey. It is demonstrated that the volume electric charge has to be accounted for during such measurements, that charge being generated at the airframe and wing surface by droplets of clouds and precipitation colliding with the aircraft. The local effect of that space charge depends on the flight regime (air speed, altitude, particle size and cloud elevation). Such a dependence is displayed in the relation between the collector conductivity of the aircraft discharging circuit - on the one hand, and the sum of all the residual conductivities contributing to aircraft discharge - on the other.

Arguments are given in favour of variability in the aircraft electric capacitance. Techniques are suggested for measuring from factors to describe the aircraft charge.

INTRODUCTION

During last years many experts sought for objective estimates of the ambient electric field (  $E$  ) measurement accuracy, and of a similar characteristics for the aircraft electric charge,  $Q$ . That aircraft is envisaged as a platform outfitted with a measurement system of several field mills.

Interest in the physical processes of cloud electrification, in the conditions for generation of both the natural and triggered lightning discharge, in the physical processes of electrification of flying vehicles, and in the dependence of such processes on the properties of environment and the vehicles themselves all stimulate further efforts in analyzing and updating measurement techniques. Moreover, reliable data are needed on the spatial and temporal variability of the atmospheric and cloud electrical parameters to verify and calibrate numerical models of cloud electrification.

The techniques available for such measurements have progressed far during all the years the aircraft laboratories have been employed for these tasks. Placing field mills at cross points of the aircraft electric neutrals has become generally accepted. Adequate placement of such mills provided for favourable conditions of their operation and excluded the effects caused by cloud and precipitation particles, hitting the mills, by the charging dielectrics, and by space charges from the corona points [1,2,3].

Significant progress in estimating the form factors at field mill mounting positions [2,3] and explicit calibration of these sensors directly

on board the aircraft [8] should be noted. Redundant sensors in the measurement system ( in excess of four ) were demonstrated to contribute to measurement accuracy [3].

The present author believes that a simple general principle may serve as a basis for a uniform approach to atmospheric measurements of the ambient electric field. Starting such measurements one has:

- a) to identify all the possible sources of the electric fields affecting each sensor and try to eliminate them;
- b) to identify and account for all the factors which might cause changes in form factors at the sensors' mounting positions;

The known factors from among their multitude are listed in Table 1. The "plus" sign in the table stands for indicate that such a factor should be accounted for, while the "minus" sign has an opposite meaning.

The factors listed under positions 1,2, and 5 of Table 1 are exhaustively treated in [2,3]. The systematic error source (position 4) is to be identified and eliminated in each given case, e.g., by coating the dielectric surfaces with conducting paints or by transferring the sensor to another position prior to measurements.

Consider in more detail the effects of other factors and the possibilities of accounting for them.

Table I

Factors to be accounted for during atmospheric measurements of the ambient electric field and the aircraft electric charge at various flight regimes

No	Factor	Flight condition			
		Outside a cloud		Inside a cloud	
		E	Q	E	Q
1.	Ambient electric field	-	+	-	+
2.	Aircraft charge	+	-	+	-
3.	Space charge at the aircraft surface	-	-	+	+
4.	Charging of fairings, domes, and other dielectric surfaces	+	+	+	+
5.	Measurement errors for form factors	+	+	+	+
6.	Aircraft electric capacitance and its variations	-	+	+	+
7.	Position of aircraft electric neutrals and their evolution	+	+	+	+
8.	Inhomogeneities in the ambient electric field	+	+	+	+



## 1. SPACE ELECTRIC CHARGE AT THE AIRCRAFT SURFACE

According to [4] there exist two causes of space charge generation at the aircraft surface, differing in their nature. First, the electric charges are redistributed at the aircraft surface affected by the aircraft self-charge and the ambient electric field. Such a redistribution results in a space charge layer appearing at the aircraft surface, its ionic spectrum differing from that in free atmosphere. The electric field in the space charge layer affects the results of atmospheric field measurements, as well as measurements of the aircraft charge itself.

I.M.Imyanitov estimated this additional field strength produced by redistribution of air ions at the surface of a charged aircraft. He demonstrated that at ionic mobility of  $K=2 \cdot 10^{-4} \text{ cm}^2/\text{V} \cdot \text{s}$  and a flight speed of  $v=50 \text{ m/s}$  the additional field strength produced by a space charge layer would be about three orders of magnitude less than that of the principal field. Apparently, the higher is the aircraft flight speed, the less will be the additional charge density, so that conversely, the additional field will also be less. Such reasoning should apparently hold for flight speeds up to the shock ionization threshold for air molecules.

The effect of corona points and of sparking dielectrics (e.g., fairing and domes, cockpit window glass, etc.) which also alter the ionic spectrum at the aircraft surface is neglected here because it may be neutralized by the means mentioned in the Introduction.

The second cause for the space charge layer to appear, beside the airframe self-charging, is that particles colliding with an aircraft flying through clouds and precipitation, also charges [4].

Generation of a space charge by cloud and precipitation particles colliding with an aircraft is directly related to the process of aircraft electrification. Consider a simplified example of the conducting sphere charging in a homogeneous stream of single mode non-charged droplets. Let the first droplet colliding with the sphere deposit a charge of  $-q$  at its surface due to contact potential difference between the droplet and the sphere substances. Having thus lost a charge of  $-q$ , the droplet will itself have a charge of  $+q$  after detaching from the sphere (before the contact the droplet was electrically neutral). The electric field between the sphere and the droplet detached from it will be determined by the charge  $-q$  of the sphere and that of the droplet ( $+q$ ).

Each following droplet contacting with the sphere will also deposit a charge  $-q$  at the sphere. With the total charge accumulated by the sphere growing the new droplets detaching from it will carry away with them a part  $m$  of charge  $Q$  of the sphere, which will be proportional to the surface charge density at the sphere and to the electric capacitance of the droplet detaching from it [5,6]. The droplets with a charge of  $(+q - mQ)$ , detaching from the sphere and flying over it after detachment all contribute to the space electric charge forming, which has to be accounted for in our description of the process.

When the charge transferred by the colliding droplet equals that carried away by the detaching droplet ( $q = mQ$ ), the charge of the sphere reaches its equilibrium state, and the droplets further detaching from the sphere will remain uncharged.

If we prevent, in some way, the sphere from reaching its equilibrium charge (e.g., letting a charge leak from the sphere via the isolation

resistance) a space charge produced by a stream of droplets detaching from it and carrying with them the charge opposite in sign to that of  $Q$ , will be constantly present around the sphere.

Consequently, if the surface charge density at the droplet detachment point at the surface of that sphere  $\sigma_i$  is such that the charge transferred by the droplet is equal to that carried away, a stream of such particles will produce no volume electric charge around the sphere. If the surface charge density at that point  $\sigma_i$  exceeds the respective equilibrium charge density,  $\sigma_e$ , the detaching droplets will produce a space charge above the sphere of the same sign as that of the sphere itself. On the other hand, if the surface charge density,  $\sigma_i$ , at the detachment point is less than the equilibrium density,  $\sigma_e$ , the stream of such droplets will generate a space charge of a sign opposite to that of the sphere.

Since the charge distribution over the aircraft surface is highly inhomogeneous and is strongly intensified at wing tips, tail empennage, the airframe nose, one may safely assume that areas of  $\sigma_i > \sigma_e$ ,  $\sigma_i < \sigma_e$ , and  $\sigma_i = \sigma_e$  may be found at the aircraft frontal surface.

To study explicitly the aircraft electrification features current sensors were mounted at the wing attack edge [4]. Metal plates safely isolated from the airframe served for such sensors. Each wing attack edge housed two such plates. One of them (plate 1) was placed approximately 1 meter off the hull, and the other (plate 2) - further out, close to the wing tip. It was assumed that such a placing would result in  $\sigma_2 > \sigma_e$ ,  $\sigma_1 < \sigma_e$ . Measurements conducted with an aircraft model had demonstrated that  $\sigma_2 \gg \sigma_1$ . The plates' profiles followed exactly the wing contour. Therefore conditions for the slip-stream at the plated wing area and the neighbouring areas could be considered identical. The plates were of wing metal, so that on the account of similarity in the aerodynamic and surface properties of wing proper and the plate one could assume the conditions of charge separation and droplet fragmentation at both surfaces to be identical. We had to neglect the differences in plate currents due to peculiarities of a slip-stream around a swept wing (the sweep angle difference between the positions of two plates was about  $5^\circ$ ).

Analyzing the currents to plates measured in flight we found that :

1. The current to plate 1 (positioned close to the hull) is always of the same sign as the overall aircraft charge;
2. If currents at both plates were of the same sign, the current to plate 2 was less than that to plate 1;
3. If currents to plates were of different signs, the current modules at plate 2 could be larger than that to plate 1. In the latter case the current to plate 2 coincided in its sign with the currents through the plane point dischargers.

The latter results indicates a strong collector discharge of the plane at its wings' attack surface, at least in the zone of wing tips.

The measured currents  $I_{p1}$  and  $I_{p2}$  may be used to calculate the conductivity  $\lambda_c$ , due to the collector effect. Having the value  $\lambda_c$

is important, since it shows whether the plane is charged via the process typical for well-isolated bodies, or the situation is the opposite, and the discharge through the aircraft point discharges ( $\lambda_d$ ), competing with  $\lambda_c$  is constantly holding the overall charge  $Q$  of the aircraft to a level  $Q < Q_e$ . Here  $Q$  is an equilibrium value of  $Q_e$ , with point dischargers disconnected.

Fig.1 shows part of a plane wing with current sensors, and the elements are shown from the circuit of plane discharge to the atmosphere.

The current  $I_p$ , recorded by the instruments connected to each plate is  $I_p = I_c - I_{cp}$ , where  $I_c$  is the charging current through a plate, and  $I_{cp}$  is the collector current from that plate.

Since the conditions for charge separation on each plate are the same, the difference between  $I_{p1}$  and  $I_{p2}$  will be produced by differences in the respective collector effects only, resulting from significant differences in the surface charge densities  $\sigma_1$  and  $\sigma_2$  at both plates.

It follows from the electric scheme in Fig. 1:

$$\begin{aligned} I_{p1} &= V_a (\lambda_d + \lambda_c + \lambda_{cp2}) \\ I_{p2} &= V_a (\lambda_d + \lambda_c + \lambda_{cp1}) \end{aligned} \quad (1)$$

Here  $V_a$  is the aircraft potential;  $\lambda_{cp1}$ ,  $\lambda_{cp2}$  are the discharging aircraft conductances due to the collector effect at plates 1 and 2, respectively.

It follows from (1) that

$$\lambda_{cp1} - \lambda_{cp2} = \frac{I_{p1} - I_{p2}}{V_a} = \frac{\Delta I_p}{V_a} \quad (2)$$

Here  $I_{p1}$ ,  $I_{p2}$ ,  $V_a$  are the respective values measured in flight.

Since plate 2 is positioned close to the wing tip, and  $\sigma_2 \gg \sigma_1$ , we approximately have:  $\lambda_{cp2} \gg \lambda_{cp1}$   
It may be assumed then that:

$$\lambda_c \cong \lambda_{cp2} \frac{\alpha_a}{d_{p2}} \cdot \frac{L}{\ell_p} \quad (3)$$

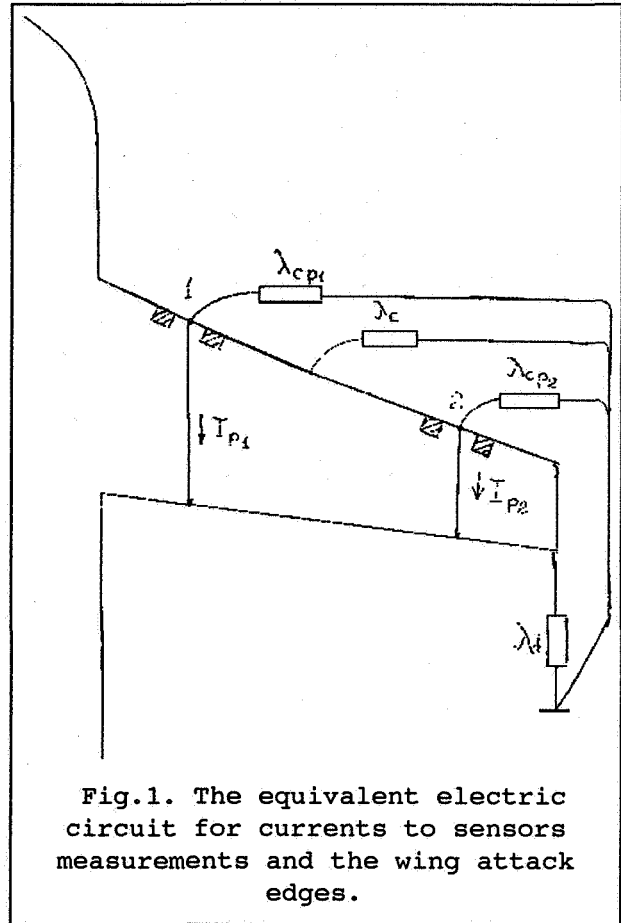


Fig.1. The equivalent electric circuit for currents to sensors measurements and the wing attack edges.

Here  $\alpha_{p2}$  is the relative surface charge density at the wing around plate 2;  $\alpha_a$  is the average relative surface charge density for all the droplet capturing surfaces;  $L/l_p$  is the total aircraft capturing zone to plate zone lengths' ratio.

We have calculated  $I_{p1}$ ,  $I_{p2}$ ,  $Q$  in liquid droplet clouds from the measured currents (flight level: 4.2 km; air speed: 650 km/hr) and found  $\lambda_c = 10^{-9} \text{ Ohm}^{-1}$  for these conditions. The value of  $\lambda_d$  for the same conditions is approximately  $2 \cdot 10^{-9} \text{ Ohm}^{-1}$ . It is experimentally found that  $\lambda_c$  is proportional to squared air speed [9], and  $\lambda_d$  is linear on that speed [10]. Besides,  $\lambda_c$  also depends on the cloud water content and the size of droplets colliding with the aircraft [6,7,12]. Studying electrification of a Tu-104 aircraft empirical expressions were found to relate the values of  $\lambda_d$  and  $\lambda_c$  with the medium and aircraft characteristics. These expressions may be used to estimate the change in  $\lambda_c / \lambda_d$  ratio in the aircraft discharge circuit, and to assess the regime of aircraft charging.

According to [7]  $\lambda_c \approx D \cdot w \cdot v / r$ ,  $\lambda_d \approx B \cdot v \cdot (P_0/P)^{0.4}$ . Here  $w$  is the cloud water content,  $v$  is the air speed;  $r$  is the cloud droplet average radius. We have for the Tu-104 aircraft  $D \approx 0.9 \cdot 10^{-15} \text{ Cm} \cdot \text{m}^2 \cdot \text{s}^2 \cdot \text{kg}^{-1}$ ,  $B \approx 10^{-11} \text{ Cm} \cdot \text{s} \cdot \text{m}^{-1}$ .

Computational results on  $\lambda_c / \lambda_d$  for two air speeds of 100 and 200 m/s are shown in Fig.2 for cloud droplet radii 10, 20, 30, and 100  $\mu\text{m}$ , and the cloud water content raised to 2  $\text{g}/\text{m}^3$ . It follows from these computations that  $\lambda_c < \lambda_d$  for large droplet size clouds only. Fine droplet size clouds and clouds of high water content always give  $\lambda_c > \lambda_d$ . Higher air speeds resulting in more intense droplet fragmentation upon collision with the aircraft surface, increase the role of  $\lambda_c$  in aircraft discharging process, as compared with that of  $\lambda_d$ . That means that at higher air speeds the point at the wing edge where  $\sigma_i = \sigma_e$  moves closer to the airframe. Inversely, that point will move to wing tip at low cloud water contents and in particles of large droplet size.

We may conclude that because of a change in cloud properties above and below the wing the density of the space charge formed by droplets fragmenting upon collision with the aircraft, will be minimum within the possible shifting range of the  $\sigma_i = \sigma_e$  at wing end point. Below we shall estimate the limits of that range. To do that we also have to account for the conductivity of the aircraft engine exhaust gases, i.e. consider the value  $(\lambda_c / (\lambda_d + \lambda_e))$ .

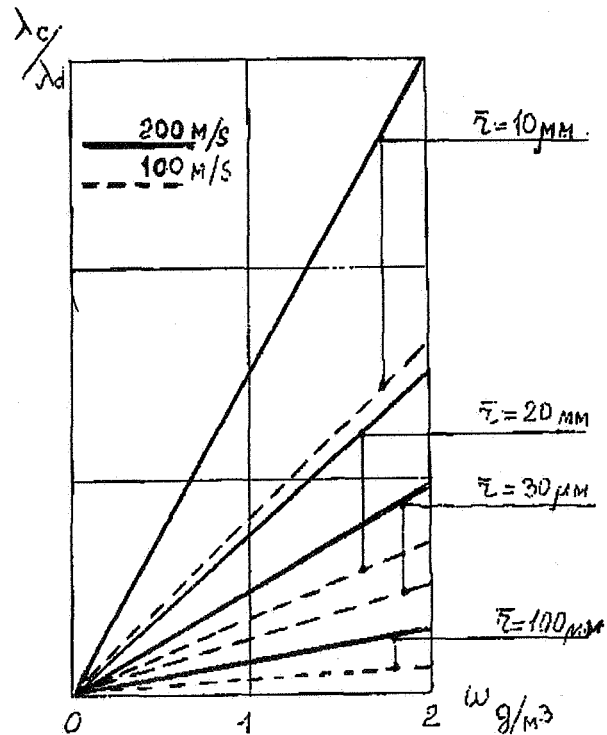
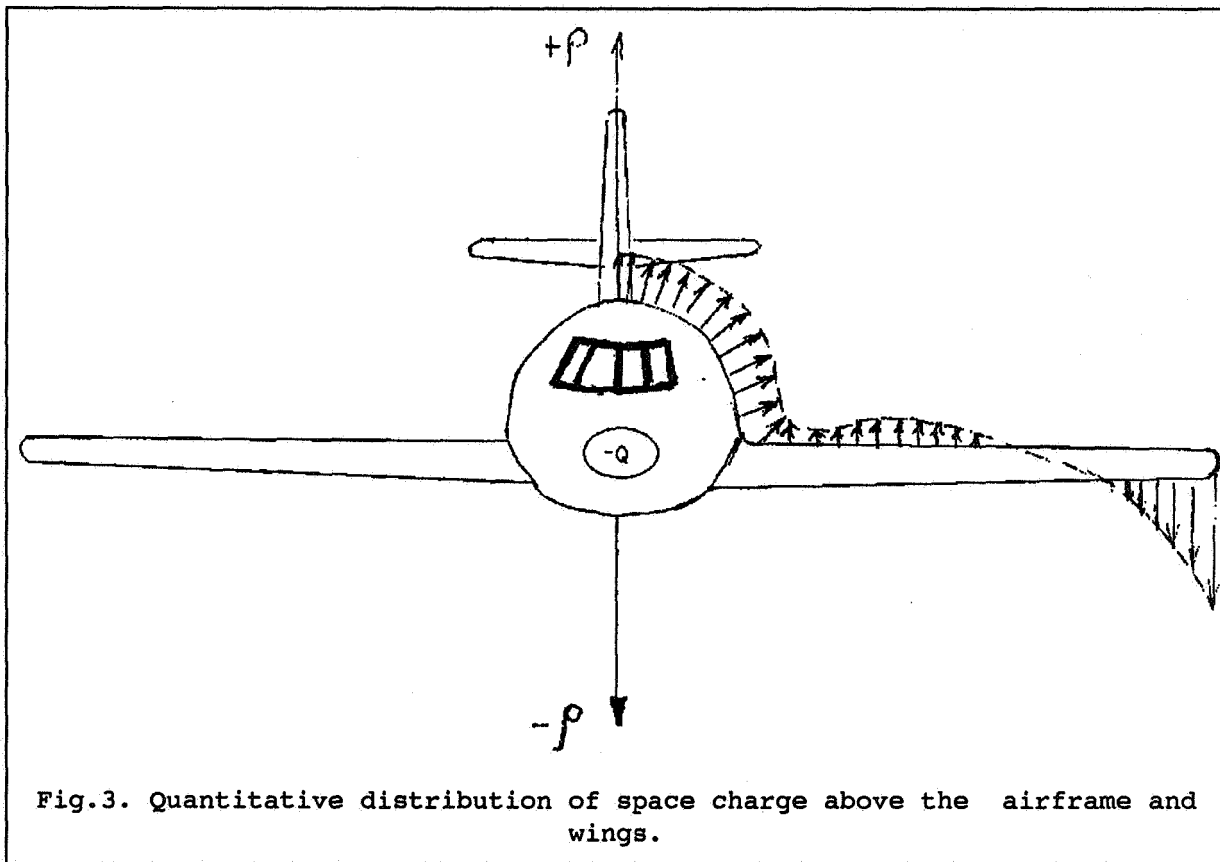


Fig.2. The effective electric conductances  $\lambda_c$  and the  $\lambda_d$  ratio for various flight conditions.

If our reasoning is correct, the airframe would apparently be slipstreamed by an airflow with a high density of space charge. The nose part of the air frame being non-symmetrical in the vertical, these flows may considerably differ above and below the frame.

Prof. Imyanitov [4] estimated the additional field strength due to these changes. He demonstrated that it may be comparable or even exceed the ambient electric field and the field of the aircraft electric charge. Considering also the effect of the space electric charge, the airframe should not be considered the best place for mounting the measurement system sensors.

From that point of view a better place to fit much sensors would appear to be the wing edge, where  $\sigma_i = \sigma_e$ . (see Fig 3)



## 2. THE ELECTRIC CAPACITANCE OF THE AIRCRAFT AND THE POSITION OF ELECTRIC NEUTRALS

As an isolated conducting body the aircraft has a certain electric capacitance. This capacitance is usually assumed to be constant, since it is determined by the characteristic linear size of the airframe. The high-temperature rocket jet exhaust are known to increase the respective length of a rocket conductive body by almost a factor of two. However, significantly lower exhaust temperatures of the turboprop and jet engines precluded even suggesting a possibility of such an effect for aircraft.

Trinks and Haseborg [11] studied electric fields at the Earth surface after an aircraft passed above the observation site. They recorded the

position of a hypothetical chargecenter of the aircraft using a little sensor had a small load resistance and indicated that center point as the signal passing its zero. Studies by these authors demonstrated that the charge center was biased to the artificial tail, and for some aircraft types even got behind the actual tail end. This experimental fact may only be explained by the effect of low-temperature gas jets, which appears to be capable of somewhat "elongating" the airframe. Another simple measurements may be applied to assess the role of the engines' exhaust jets. It is enough to compare the surface charge distribution over a model aircraft with its actual distribution over the frame in a longitudinal electric field. Two flight legs are needed for such an experiment; one leading to, and another - from a thundercloud. Comparing the relative distribution of the induced charges along the airframe with that along the model should demonstrate whether a displacement takes place of the electric neutrals. The positive result of such an experiment would testify to airframe "elongation", hence - to an increase in the aircraft capacitance.

Modelling the exhaust jets by as conducting cylinders attached to the aircraft model, the same relative displacement of the electric neutrals may be obtained as that actually observed. The capacitance of such a system would serve a better presentation of the actual aircraft capacitance in flight.

### 3. INHOMOGENEITY OF THE AMBIENT ELECTRIC FIELD

Form factors at sensor locations are estimated in a homogeneous electric field. Using such factors to calculate the components of the ambient field vector and the aircraft charge in case that field is significantly inhomogeneous, would lead to noticeable errors in  $E$  and  $Q$ . Apparently, the longer is the base, at which the sensors are placed to compute  $E$  and  $Q$  from their signals, the more homogeneous should the ambient field be, if only we went to stay within the prescribed error limits for both the field and the charge. However, it is advisable to position the sensor along small bases to achieve high spatial resolution in  $E$ . We again return to the already discussed option: of placing sensors at aircraft wings: the wing thickness is an order of magnitude less than the diameter of the hull. Placing two sensors along a wing chord would result in obtaining information on the longitudinal field component from a small base. The field transverse component may be measured by any pair of sensors in a differential circuit. Such a system features the needed redundancy, it may be positioned in the zone of minimal effect from space charges (see Fig. 4), and moreover, placing these sensors at wing may help estimate the form factors directly in flight.

### 4. FORM FACTORS FOR THE AIRCRAFT CHARGE

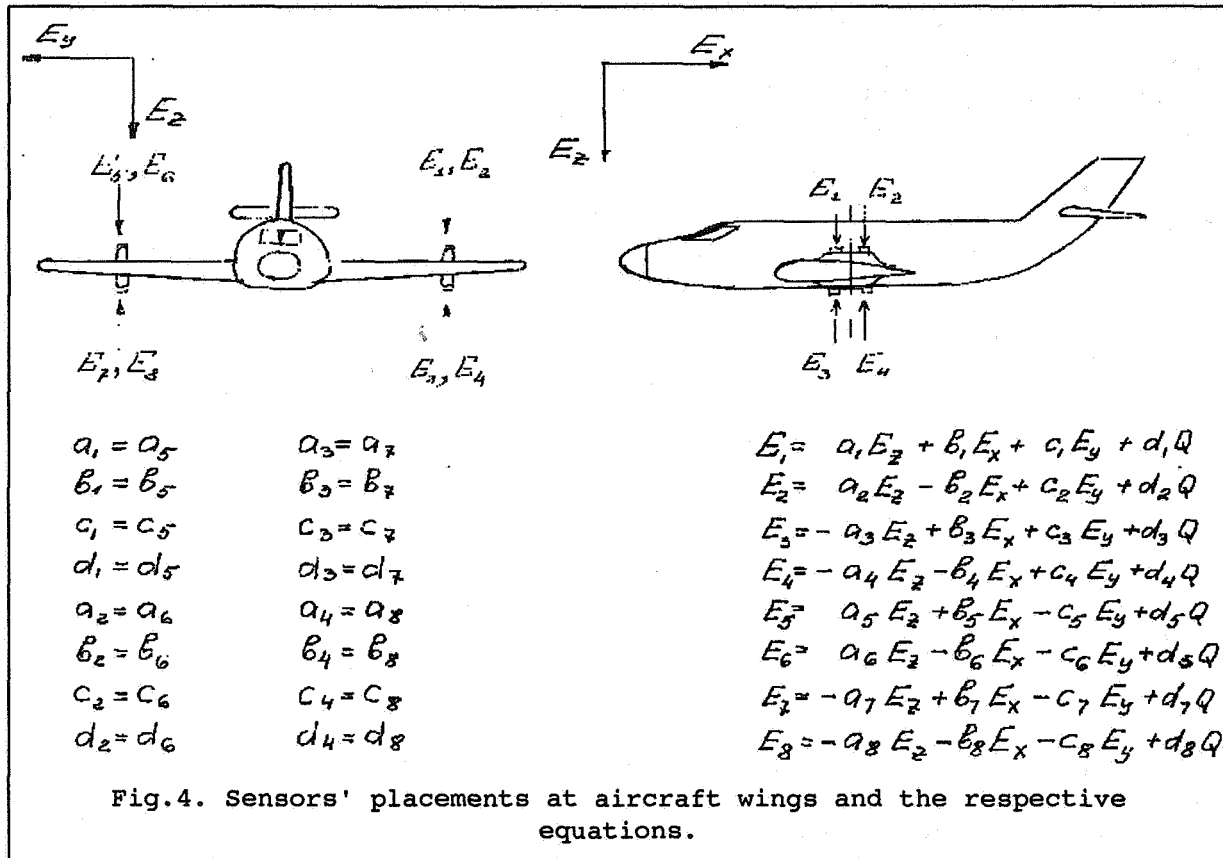
An approach is well known to estimating, model and flight testing the form factors, which relate the ambient electric field with the local one at the sensor locations [2,3,8,13].

Of certain interest are ways and means for estimating such factors, which relate the aircraft charge and the field at sensor locations. One of such means may be measuring the field produced by a charged aircraft flying by the surface field sensors at a low altitude [11]. The aircraft charge may be calculated if the flight level is accurately known. The second approach

to that task is artificial charging of an aircraft from an on board source. Controlling the charging current and making sure that the charge only leaks via air and the exhaust jets conductances (these values may be measured and accounted for) we may compute the running charge value:

$$Q = \int_0^{t_1} i \Delta t$$

where  $i$  is the measured charging current. Then one may compare the running value of  $Q$  with local fields at sensor positions to retrieve the respective form factors.



#### CONCLUSION

Increasing the measurement accuracy for both the electric field and charge of a flying vehicle is seen as a solvable problem. The present paper put forward the problem certain considerations on that problem for critical attention of the scientific community. They touch on the need to account for additional space charges resulting from the appearance of an aircraft in airspace, on the techniques for estimating the actual aircraft capacitance seen as an isolated body; on the possible changes in form factors caused by a displacement of the aircraft electric neutrals, because of the influence from the attached conducting engine exhaust jets.

It is believed that preparing an aircraft laboratory for in-flight measurements in the free atmosphere should include the following steps:

1. Estimating external factors which interfere with the measurements - the presence of charging fairings, of the corona points, and the space charge distribution at the aircraft surface;
2. Estimating form factors at an aircraft model or via numerical simulation;
3. Updating form factors (for both field and charge) at the aircraft;
4. Adjusting the electric capacitance and form factors in the computational matrix;
5. Estimating the admissible limits of spatial and temporal variability of the signals measured to retrieve the ambient electric field in the aircraft environment.

#### Acknowledgement

The author express his sincere gratitude to Drs. L.Ruhnke, M.Glynn, and V.Mazur who updated him on the latent developments in the discussed field.

#### REFERENCES

1. Imyanitov I.M. Modern Instruments and Techniques for Studying the Atmospheric Electricity. // TTTI. Moscow. 1957.
2. Mazur V., Ruhnke L.H., Rudolph T.H. Effect of E-field mill location on accuracy of electric field measurements with instrumented airplane. 1986. Int. Aerospace and Ground Conf. on Lightning and Static Electricity, Dayton, Ohio, p.31.1-31.7.
3. Hewitt K.L., Kositsky J., Maffione R.A., Thayer T.S. On the accuracy of an aircraft-borne ambient electric field measuring system. Proc. 1989 Int. Conf. Lightning and Static Electricity. Univ. of Bath. UK. 26-28 Sept. 1989, p. 7A. 1.1-7A, 1.8
4. Imyanitov I.M. Aircraft Electrification in Clouds and Precipitation. // Gidrometeoizdat. Leningrad. 1970. 211 p.  
Imyanitov I.M. // Ibid. English Translation by Foreign Technology Division. U.S. Air Force Systems Command. Report FTD-HC-23-544-70. 1970
5. Imyanitov I.M. On the problem of the Electrostatic Charging Mechanism. // Doklady USSR Ac. Sci. 1958. v.121. N 1. p. 93-96.
6. Evteev B.F., Selvikyan Ya.V. Electrification of Bodies in a Stream of Droplets. // Trudy GGO (MGO Proc.) 1982. N 455. p. 10-25.
7. Bryljov G.V., Gashina S.V., Evteev B.F., Kamaldina I.I. // Characteristics of the Electrically Active Zones in Stratiform Clouds. // Gidrometeoizdat. Leningrad. 1989. 158 p.
8. Anderson R.V., Bailey T.C. Experimental calibration of an aircraft vector electric field meter system. 1986. Int Aerospace and Ground Conf. Lightning and Static Electricity. Dayton. Ohio. p. 33. 1-33. 13.
9. Evteev B.F. Estimating the Collector Effect in Aircraft Discharge. // Trudy GGO (MGO Proc.) 1980, n 424. p. 115-120.
10. Studying the Characteristics of Aircraft Corona Points at Various Flight Conditions. / Aleksandrov V.S., Evteev B.F., Ziganov N.P., Markchev N.T. // Trudy GGO (MGO Proc.) 1980. N 424. p. 125-128.
11. Trinks H., Haseborg T.L. Application of charging effects: ranging of aircraft. Proc. Int. Aerospace Conf. Lightning and Static Electricity. Oxford. 23-25 March. 1982. p E9. 1-E9. 8.



12. Danilov Yu.I., Evteev B.F., Kazak R.R., Kaprans A.A., Selvikyan Ya.V. On Studying Bodies Electrification in Aerosol Streams. // Trudy GGO (MGO Proc.) 1977. N 350. p. 101-111.
13. Evteev B.F. Measuring the Electric Field Strength at a Model Aircraft Surface. // Trudy GGO (MGO Proc.) 1972. N 277. p. 130-133.
14. Imyanitov I.M., Kolokolov V.P. Studying the Distribution of Induced and Self-Charge at Aircraft Surface. // Trudy GGO (MGO Proc.) 1956. N 58. p. 8-16.
15. Easerbrook C.C., Rudolph T.H., Easterbrook K. Estimating Electric Field Enhancement Factors in Aircraft Utilizing a Small Scale Model: A Method Evaluation. Proc. 1988 Int. Aerospace and Ground Conf. Lightning and Static Electricity. April 19-22, 1988. Oklahoma City, Oklahoma. USA.

LIGHTNING TO THE UPPER ATMOSPHERE:  
A VERTICAL LIGHT PULSE FROM THE TOP OF A THUNDERSTORM  
AS SEEN BY A PAYLOAD BAY TV CAMERA OF THE SPACE SHUTTLE

William L. Boeck  
Niagara University  
Niagara University, NY 14109

Otha H. Vaughan, Jr. and Richard Blakeslee  
NASA Marshall Space Flight Center  
Huntsville, AL 35812

Bernard Vonnegut  
State University of New York at Albany  
Albany, NY 12222

Marx Brook  
New Mexico Institute of Mining and Technology  
Socorro, NM 87801

John McKune  
NASA Johnson Space Center  
Houston, TX 77058

ABSTRACT

An examination and preliminary analysis of video images of thunderstorms as seen by a payload bay TV camera of the Space Shuttle has provided examples of lightning in the stratosphere above thunderstorms. These images were obtained on several recent Shuttle flights while conducting the Mesoscale Lightning Experiment (MLE). MLE was an experiment to obtain night time images from space of large storm complexes with lightning. These images are being used to provide data for the design of specialized instrumentation which will provide quantitative measurements of global lightning. Eight video sequences have been selected because they illustrate near vertical discharges in the stratosphere above thunderstorms. Although there are previous reports in the literature, these are the first images from the viewpoint of an orbiting spacecraft. The written material is primarily a companion to a video presentation.

BACKGROUND

An examination of video imagery, obtained from space, has revealed several examples of electrical discharges, associated with thunderstorms, that penetrate the stratosphere. This phenomena is now being studied in detail and this paper will present several examples and preliminary conjectures about these unusual discharges. This paper is intended to be a companion to a video poster presentation. The content of this paper will provide notes and ancillary information to

supplement the video imagery. The full motion video is emphasized because the human vision system does a good job of identifying a transient event in the presence of a noisy background scene. Most of the events are poorly illustrated by still photographs of the original video.

The video was obtained by the Mesoscale Lightning Experiment (MLE) which employed Shuttle payload bay cameras to observe lightning discharges from large thunderstorm complexes. The video is being analyzed to develop storm flash rate statistics, and location information to simulate observations that are to be made in the future by the Lightning Imaging Sensor (LIS), now a part of the Earth Observing System Program. A summary of data from the first MLE Shuttle flight (STS-26) was prepared by Vaughan[1].

There have been previous reports of discharges above thunderstorms that do not seem to be descriptions of ordinary lightning channels that terminate in the clear air. In particular some descriptions mention discharges that extend to extreme heights. In the last century C. V. Boys [2] wrote "...I should like to refer to an observation which I made about the year 1876, as in a life's observation of lightning the phenomenon then accompanying every flash is one I have seen on no other occasion." "A storm one evening in the autumn had passed directly over the village of Wing in Rutland and moved away to the north, leaving a clear starlit sky above the thundercloud, with the stars of the Great Bear in their lowest position far above. When the storm was distant about ten miles and more, for every flash seen in the rain cloud and below, and simultaneous with it, there was one or more very slender flashes of typical lightning form from the cloud upwards and many times as long as the usual kind of lightning below. According to my recollection, these reached one-third or perhaps half-way towards the stars of the Great Bear, and in one instance there were seven of these flashes going simultaneously into the clear sky."

Recently Vaughan et al [3] reported a number of eye witness accounts of vertical lightning observations. Although most of the reports could be taken as descriptions of lightning channels that terminate in clear air rather than in a cloud, there are exceptional cases. In particular Lloyd F. Willett reports "About 50 mi west of San Antonio, Texas, at a flight level 41,000 msl, I observed a strong shaft of lightning go directly up and discharge into the ionosphere." J. Richard Fisher [4] has written a detailed description of his observations. "...I noticed that some of the lightning flashes were accompanied by a faint plume of light extending from the top of the thunderhead above the pool of light from the lightning discharge. The tops of these thunderheads were quite dark, so the light plume was definitely not diffuse light from the lightning in the lower clouds. My only size scale was the height of the tallest clouds, which I assumed to be about 10 km. From this I estimate that the light plumes were about 10-20 km high and a few kilometers wide with their

bases at the tops of the clouds. All the plumes were vertical as best I could determine at night, and they appeared at exactly the same time as the lightning flash."

A strange slow moving upward discharge was reported by Everett [5]. "- a luminous trail shot straight up to 15 degrees or so, about as fast as, or rather faster than, a rocket, and of very similar appearance, but with minute waves, like ribbon lightning. It was hardly as bright as most lightning. ... One of the trails turned off, as shown; the others were about vertical as seen from here. Each grew up steadily from below, and then disappeared at once. The upper end was definite, and did not branch or spread."

Franz et al [6] have captured a video image of two vertical plume discharges simultaneously extending into the clear sky above a thunderstorm. The report of Franz et al provided further incentive for a more detailed examination of the video scenes of lightning obtained during recent Shuttle missions. Two of the vertical events that occurred during Mission STS-32 have been presented in a previous video poster paper [7].

#### VIDEO OBSERVATIONS

Some of the authors describe lightning events that they have observed visually to be similar in appearance to a rocket launch [5] with a glowing trail and one video example we have seen seems to fit the description of rocket lightning. The general appearance is of bright peak appearing at the top of the cumulus tower which then moves upward leaving a luminous trail behind.

Case 1. While the Space Shuttle STS-34 was on orbital pass 45, a storm was observed over Australia. The storm came into view at 12:07:10 GMT on October 21, 1989 and was tracked until it passed out of view at 12:12:20 GMT. The camera strayed off the storm from 12:07:34 GMT until 12:08:42 GMT. The storm appeared to be a supercell storm which had a thick anvil that obscured the illuminated cloud except along the side and at a central location, which we presume to be an overshooting turret. This same storm was observed by a satellite of the USAF Defense Meteorological Satellite Program (DMSP) about ten minutes later. The storm complex had frequent multiple stroke lightning with an average rate of 33.2 flashes per minute. One hundred thirty five flashes were recorded, fifty five before the "rocket" lightning and seventy nine afterwards. None of the other flashes appeared to be abnormal.

Six video examples (five from the viewpoint of space) have the appearance of thin luminous fingers of glowing gases stretching into the stratosphere above a thunderstorm. The term "cloud flash" will be used in this paper to describe a cloud mass that is illuminated from within by an electrical

discharge. The lightning channel either within or below the cloud is not seen from space. Also the TV images do not have the time resolution to identify all lightning strokes in a flash. Consequently all phenomena, including cloud-to-ground strokes, that produce a continuous period of cloud illumination will be grouped together and called a cloud flash. All the examples are relatively low resolution images of events that were at a considerable distance from the TV camera.

Case 2. The first example was a storm as seen from the ground on the northwestern side of Lake Superior in North America by Franz et al [6]. "The flash was separated into two fountain-like jets as imaged by the TV, but the two structures were simultaneous within the 17-ms time resolution of the TV sweep." They recorded the flash on July 6, 1989 at 04:14:22 GMT. They estimate the flash was about 20 km in vertical extent at a distance of 250 km. This image contains more detailed structures than the images obtained by an orbiting camera. There was no cloud-to ground event detected by lightning location networks simultaneous with the flash.

Case 3. This event was identified in video imagery taken during orbit 140 of Space Shuttle STS-32 on January 18, 1990. The shuttle had passed over the Gulf of Mexico and proceeded East of Florida over the Atlantic Ocean. The camera was viewing the Southeastern section of the United States which was illuminated by moonlight. The video images showed that the cloud flash began with a relatively small spot which remained faint for 12 frames (30 frames per second). The size of the cloud flash expands to a maximum over the next five frames. Seventeen frames after the beginning of the event two fingers appeared at 07:23:26 GMT. The next two frames show the intensity of the fingers decreasing with a distinct blob at the upper end of each finger. The cloud illumination continued after the fingers disappeared for a total cloud flash time of 34 frames. The length of the discharge above the thunderstorm was estimated to be about 35 km.

Case 4. The third example of a finger like discharge was obtained on October 21, 1989 while the Shuttle STS-34 was on orbit 44. The camera was viewing Northern Australia. The earth was dark and cloud outlines could not be seen. The vertical event accompanies an extremely bright cloud flash which produced a reflection on the vertical stabilizer of the Shuttle. The vertical discharge appears near the horizon as two distinct fingers. There is some brightening at the top of the discharge at the beginning of the full discharge. This brightening is a common feature in other examples. The cloud flash begins six frames before the stratospheric event. The fingers appear at 10:34:20, brighten in the next frame then gradually fade in two more frames. The brightest part of the fingers was near the top while the dimmest section was at the

cloud top. The total event occupies 26 frames. The next cloud flash from the vicinity of the vertical event was 42 seconds later.

Case 5. This example was obtained from the Shuttle STS-41 during orbit 9 on October 6, 1990. The camera was viewing central Africa. There were a number of active thunderstorm cells in a large cloud bank that was brightly illuminated by moonlight. The location of interest was in view for two minutes and 33 seconds. A total of four cloud flashes were observed at the location of the vertical flash. This area was adjacent to an area which was much more electrically active. A single vertical line is observed at 23:37:07 GMT and was visible in three frames. The cloud flash started ten frames earlier and continued for a total of 23 frames.

Case 6. This example is included for completeness. The vidicon had been exposed to extreme levels of light and several images were burnt into the screen. There are some features apparent in the full motion video that are obscured in the still frames. The images were obtained on October 8, 1990 while the Shuttle STS-41 was passing over West Africa on orbit 41. A moonlit scene of a large complex of thunderstorms comes into view at 23:41:45 GMT. The location of interest was visible for three minutes and only a few flashes were seen near there. The cloud flash lasted 41 frames in total. The single vertical line was seen at 23:43:31 GMT, 13 frames after the start of the cloud flash.

The next examples are grouped together because they appear to be single discharges with a width much greater than the thin finger like examples presented above. These examples will be referred to as columnar discharges. There is insufficient information to determine whether these are two distinct types of stratospheric discharges or merely an indication of the range of natural variation.

Case 7. The first example of what we call a columnar discharge was obtained from Shuttle STS-32 while on Orbit 132. The scene on January 17, 1990 was too dark identify cloud areas. Some of the stars appear enlarged either because of image saturation or because of poor lens focus. Although there may be some lack of precise focus, the width of the discharge is much wider than the finger type of discharge. The view is of East Africa with a active multi-cell thunderstorm complex near the horizon. The event starts as a small spot and then increases in size for 14 frames. The fifteenth frame at 18:53:28 GMT shows a semicircular glow around the edge of the cloud which is connected to a vertical column with a flat top. In the next frame the column intensifies and develops a small peak. The intensity of the column decreases over five frames from its first appearance with the upper blob remaining brighter than below. The cloud

flash for the entire event continues for 112 frames total. In the absence of visual clues, no estimate is provided for the flash rate of the location of interest.

Case 8. The second example of a columnar discharge was found in video during Orbit 55 of the Shuttle STS-31. The scene on April 28, 1989 is dark with only a few other flashes visible over West Africa. The cloud flash was located at about 7.5 N, 4 E over the Gulf of Guinea. The discharge at 03:35:59 GMT appears to be a column with a distinct blob of illumination at the top (see fig 1.). Several stars were located in the scene. The angular separation of the stars was used to calibrate the distances in the scene. The length of the vertical column was approximately 34 km. Nine frames of the cloud flash pass before the stratospheric discharge appears. The columns are visible for four frames out of a total of twenty-five frames for the event. There was no apparent lightning activity on the horizon for a minute before the vertical event. A weak flash was seen on the horizon 40 seconds after the vertical flash.

Case 9. The third example is also a columnar type of discharge. In this case the background noise in the TV transmission partly obscures any details of the image. Shuttle STS-31 was over East Africa on orbital pass 37. A single vertical column was observed at 22:22:43 GMT on April 26, 1990.

## DISCUSSION

Some features appear to be common among the various video observations of stratospheric lightning.

These flashes are clearly a part of series of thunderstorm discharge processes. The vertical event typically occurs about a half second after the cloud illuminates due to electrical discharge processes. The video imagery obtained from a viewpoint above the thunderstorm shows the clouds illuminated from within and does not present evidence to distinguish between intracloud events and cloud-to-ground strokes. The cloud remains illuminated after the vertical event, typically for a large fraction of a second.

The flash appears as a singular event which penetrates the stratosphere. Repeated vertical events have not been captured on video but several eyewitnesses have observed them.

In most cases the discharges appear to be aligned nearly with the vertical. The vertical extent of the flash is established within the time resolution of one video frame. The observations to date do not contain convincing evidence of the direction of propagation.

The width of the luminosity seems to vary considerably between events. Some examples show a very thin or even several thin vertical lines while others are much broader plumes. Several examples show some sort of darkened region below the top of the discharge.

The typical stratospheric flash accompanies a cloud flash in a cell that exhibits a low flash rate, about one flash per minute. The movement of the Shuttle limits the observation time of any location to several minutes at most. There is insufficient information to determine whether the observed low flash rate is a characteristic of the storm and its environment or an aspect of the individual storm life cycle.

The geographic distribution of events is biased by the limited opportunities to observe them. The major limitations are the number and duration of Shuttle missions, the inclination of the trajectory, and the inability to observe these phenomena during daylight. The examples do include Northern and Southern hemisphere cases, oceanic and continental storms. Thus it appears that the conditions for these stratospheric discharges may occur over most regions of the globe.

A rough estimate of the frequency of occurrence of stratospheric lightning can be made from the volume of MLE observations. This estimate is biased by the impression that the vertical discharge could not be identified against a bright background. Consequently all cases that have been observed appear near the horizon. We estimate that vertical flashes can occur with a frequency of the order of one in five thousand total lightning flashes. These vertical events are unusual but not rare.

These observations of stratospheric lightning raise additional questions. If these vertical events are not that rare, why are there so few reports of vertical lightning? Why did it take until 1990 to get images of vertical flashes? Some partial answers can be given. The phenomena is unusual. The visual impression is so fleeting that there is no clear recall of the event. Written reports emphasize repeated events when the attention of the observer was focussed on identifying the next unusual visual event. The video camera observations were discovered during replay. The luminance of vertical lightning is much less than the cloud flash it accompanies. Vertical events can not be identified against a bright background. If intervening clouds block the view of the sky above the cell in question, the event will not be observed. The video cameras that were used to document this phenomena were special low light level video cameras capable of recording events near the threshold of human vision; and were pointed in the right direction at the right time.

#### CONCLUSIONS



More measurements are needed to identify the physical processes producing the visible glow. Spectroscopic analysis of the optical emissions should yield information about the atomic processes. There is some hope that limb scanning type satellite instruments may observe some of these stratospheric events. We are now working with scientists who make observations in the radio frequency spectrum to help identify the radio signature of these events. We conjecture that the conditions for stratospheric lightning, some combination of thunderstorm electrical fields or electric field changes as well as some stratospheric conditions, may often exist before and return after the vertical event as well as at near by cells. It may necessary to necessary to postulate some external, possibly ionizing, event to explain the infrequent and localized occurrence of these phenomena.

We intend to continue to gather observations from further Shuttle flights and make quantitative analyses of selected video scenes.

---

1 Vaughan, O.H., Jr. (1990). "Mesoscale Lightning Experiment (MLE): A View of Lightning as Seen From Space During the STS-26 Mission", NASA TM-103513, 61 p.

2 Boys, C.V. (1926). "Progressive Lightning", Nature, Vol. 118, pp. 749-750.

3 Vaughan, O.H., Jr. and Vonnegut, B. (1989). "Recent Observations of Lightning Discharges From the Top of a Thundercloud Into the Clear Air Above", Journal of Geophysical Research, Vol. 94, pp. 13179-13182.

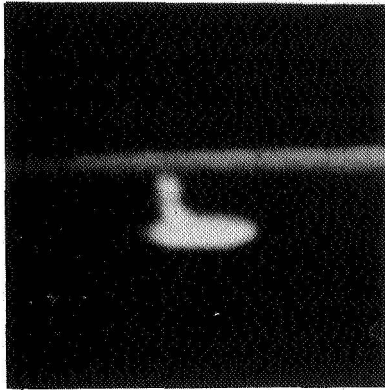
4 Fisher, J.R. (1990). "Upward Discharges Above Thunderstorms", Weather, Vol. 45, pp. 451-452.

5 Everett, J.D. (1903). "Rocket Lightning", Nature, Vol. 68, p. 599.

6 Franz, R.C., Nemzek, R.J., Winckler, J.R. (1990). "Television Image of a Large Upward Electrical Discharge Above a Thunderstorm", Science, Vol. 249, pp. 48-51.

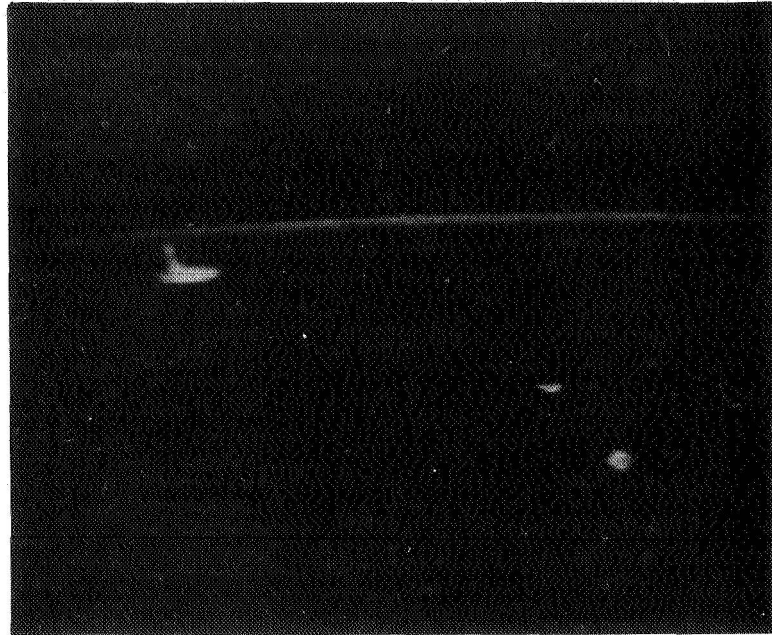
7 Boeck, W.L., Vaughan, O.H. Jr. (1990). "Lightning Observations From the STS-32 Space Shuttle Mission", Transactions of the American Geophysical Union, Vol. 71, p. 1241.

Figure 1



Blow-up of  
Vertical Discharge

ORIGINAL PAGE  
BLACK AND WHITE PHOTOGRAPH



Vertical Discharge from a Thunderstorm Cell Located At  
Limb Of Earth. Note Small Storm Cells Illuminated by  
Lightning in Foreground

N91-32721

**A STUDY OF POINT DISCHARGE CURRENT OBSERVATIONS IN THE THUNDERSTORM  
ENVIRONMENT AT A TROPICAL STATION DURING THE YEAR 1987 AND 1988**

G.K. MANOHAR, S.S. KANDALGAONKAR AND S.M. SHOLAPURKAR  
INDIAN INSTITUTE OF TROPICAL METEOROLOGY, PUNE - 411 008, INDIA

**ABSTRACT**

In the present paper the results of the measurements of point discharge current observations at Pune, India, during the years 1987 and 1988 are presented by categorising and studying their number of spells, polar current average durations and current magnitudes in day-time and night-time conditions. While the results have shown that the thunderstorm activity occupies far more day-time than the night-time the level of current magnitudes remains nearly the same in the two categories.

**INTRODUCTION**

It is well-known that high electric field beneath the thunderstorms produce electric discharge (point discharge current - PDC) at the tips of grounded natural and artificial objects. Most of the recent laboratory and field observational studies on PDC (Ette [1]; Dawson [2]; Standler and Winn [3]; Rahman and Saunders [4] and Sivaramkrishnan [5]; Kamra [6]; Kamra and Varshneya [7]; Rao and Ramanadham [8]; Selvam et al., [9]; Kamra [10] and Manohar et al., [11]) were concerned with the relative efficiencies of the natural and artificial objects and the splashing of rain-drops on sea surface to produce discharges; the net amount of annual charge transferred to the earth by PDC and the functional relationship of electric field and PDC along and aloft the ground surface etc.

In the present work the authors recorded a total of 266 spells of PDC during 41 thunderstorms of the years 1987 and 1988 at Pune (18°32'N, 73°51'E, 559 m ASL). The total duration of the thunderstorm activity on each day, when PDC spells were recorded, was arbitrarily grouped in two major periods : day-time (D) and night-time (N). The PDC activity thus separated in two time periods was studied in details. Results pertaining to some other aspects of the subject matter are also described. In this respect the present work is a deviation from the routine as it has attempted to locate differences in the seasonal day-time (D) and night-time (N) PDC activity.

**INSTRUMENTATION, DATA AND METHOD OF ANALYSIS**

The point discharge element consisted of a platinum/10% iridium needle 0.5 mm diameter and about 2 cm long erected on a mast on the third floor terrace at height 14 meters above ground level. Current through the needle was carried by a coaxial cable and fed to an operational amplifier system. The output from the amplifier system was recorded on a 1 mA strip chart ink recorder run at speed 1 cm per minute during the entire life period of thunderstorm. The instrument could record current in the range  $\pm 0.05$ -4.50  $\mu$ A. The recording system was calibrated in the laboratory before its installation during the seasons. During the two years namely 1987 and 1988 at Pune

thunderstorm activity was noticed on 41 days which primarily occurs during the pre and post-monsoon seasons (March-early June and September-November). The total span of the thunderstorm activity was reckoned as the duration between the first and last spell of PDC. Each spell of PDC of either polarity, which occurred during the span of thunderstorm on a day, was analysed for per spell average current intensity by using 1 minute interval values during the spell. There were a total of 266 such spells of current in the range of a few minutes to an hour or so. The initial and the end timings as well as the duration in minutes of each spell was noted.

This data was then classified into day-time (D) and night-time (N) periods. Spells during the period 1200-2200 hours IST were termed as (D) time and during period 2200-1200 hours IST as (N) time (actually no thunderstorm activity was noticed beyond premorning hours) since in the tropical region major thunderstorm activity is restricted to AN-night hours and in very exceptional cases the activity persists beyond night hours.

A detailed statistics of PDC activity during the (D) and (N) time periods of pre and post monsoon seasons of the years 1987 and 1988 of either polarity is furnished in Table I.

Daily total duration of PDC and the daily span of thunderstorm activity was used to obtain the ratio of the two quantities. The daily ratios thus obtained were then plotted against daily durations of thunderstorms. A line of best fit for the data points was obtained by the method of the least squares (Fig. 1).

As explained earlier, there were a total of 217 and 49 spells of PDC during (D) and (N) time periods in the two years 1987 and 1988 (Table I). Frequency distribution of number of spells of PDC in time interval 1-10, 11-20, 21-30 .... minutes was made and expressed as percentage of the total in each category (Fig. 2).

Daily surface data on maximum air temperature, evaporation, sun-shine duration and humidity in the AN hours was obtained from IMD (India Meteorological Department) Observatory Pune on all the days of thunderstorms. The mean values of the above parameters and some other information in relation to the thunderstorm activity for the two seasons for the two years is given in Table II.

## **RESULTS AND DISCUSSIONS**

1. In Table I a detailed statistics of the PDC activity of either polarity for (D) and (N) time category for the pre and post-monsoon seasons of the years 1987 and 1988 is furnished. The data sets indicated that mutual comparison in many ways among the data can be made and may reveal useful informations. Some salient features of the PDC in the (D) and (N) are described.

- (i) From Sr.No. 4 it is noted that the respective positive (D) durations : 639, 527, 692 and 317 were higher than the (N) : 42, 98, 71 and 89 in the range 3.6 to 15.2 and similarly the negative (D) durations were higher than the (N) in the range 2.3 to 9.4.

- (ii) From a similar comparison it is also noticed that positive as well as negative (D) number of spells were higher than the (N) in the range 3 to 7 times.
- (iii) Also, from Sr.No. 5 it is noted that the per spell positive duration during the (D) was higher than the (N) in the range 1.0 to 2.5 times whereas the per spell negative duration during (D) was higher than the (N) in the range 0.9 to 1.6.
- (iv) And, from Sr.No. 6 it is noted that the positive (D) average current was higher than the (N) in the range 0.93 to 1.9 whereas the negative (D) average current was higher than the (N) in the range 0.78 to 1.2.

2. In Figure 1 the daily spans of thunderstorm durations and PDC ratios as explained earlier are plotted for 31 days data out of 41 days (data on 10 days was not considered when activity was at odd hours - see Table II). The equation for the straight line fitted by the regression method is  $Y = -456.56X + 544.59$ . For the maximum value of  $X = 1$  the value of  $Y$  comes as 88 minutes. For lower values of  $X$  the values of  $Y$  increase. This feature perhaps suggests that thunderstorm activity of prolonged durations may be comparatively less efficient in producing point discharges than the brisk ones.

3. As explained earlier, in Figure 2 is shown the frequency distribution of (D) and (N) number of spells of PDC. The (D) figure indicates that the distribution is exponentially decreasing with a long tail and is governed by the equation  $Y = 0.01 + 58.6e^{-0.05X}$ . It is noticed from figure that (D) point discharge currents of durations 1-10 minutes have maximum frequency and during (N) the maximum frequency occurs for currents with durations 11-20 minutes. It is to be noted that the extreme edge of spell durations of PDC during (D) extends upto 90 minutes whereas during night time a cut-off occurs between 50-60 minutes.

4. In Table II we have furnished the values of meteorological and related thunderstorm parameters during the two seasons of the two years to serve the purpose of general interest. We have also given at Sr. No. 3 of this table the details of the occasions when thunderstorm activity was at odd hours. From this information it is to be noted that occasions of thunderstorm activity at odd hours are higher and more frequent during the post-monsoon seasons. Information at Sr.No. 4 of this table also suggests that the post monsoon thunderstorms either may be relatively weakly electrified or the activity may be occurring from isolated cells active at different times unlike the massive heat thunderstorms active during limited time and over area. At Sr.No. 5 of the same table meteorological ground based information in relation to thunderstorm situations is furnished. Inter seasonal comparison of the mean values of the four surface meteorological parameters brings out the difference between them which promote the development of thunderstorm activity. Pre monsoon season values, particularly of the maximum air temperature and humidity, 38.3°C and 38% respectively, are strikingly different from those in the postmonsoon, 31.9°C and 70%.

The observation of nearly two times higher value of humidity, at the surface levels, in the AN hours in the postmonsoon season needs some consideration.

Such higher value of humidity suggests that ions are immobilized in the lowest region of the atmosphere that may inhibit the magnitude of PDC which is perhaps reflected from the day-time pre monsoon season average value ( $.55 \mu\text{A}$ ) and post monsoon season value ( $.34 \mu\text{A}$ , Table I, Sr.No. 5).

### **CONCLUSIONS**

The relative estimates obtained of PDC in the D and N time conditions need a back-up before generalization could be possible. Since different parts of the world have different thunderstorm activities at different times such estimates would be of significance in the earth's electric budget studies and in planning some crucial activities such as air navigation, safety of power line system etc.

**ACKNOWLEDGEMENT** : The authors are thankful to Dr(Mrs.) A. Mary Selvam and Dr. A.S.R. Murty for support and encouragement in pursuing the studies. Thanks are also due to Sh. M.I.R. Tinmaker for typing the manuscript.

#### LIST OF REFERENCES

- [1] Ette, A.I.I., 1966, Laboratory studies of point-discharge from multiple points in irregular configuration, J. Atmos. Terr. Phys., 28, 983-99.
- [2] Dawson, G.A., 1969, Pressure dependence of water-drop corona onset and its atmospheric importance, J. Geophys. Res., 74, 6859-6868.
- [3] Standler, R.B. and Winn, W.P., 1979, Effects of coronae on electric fields beneath thunderstorms, Q.J.R.M.S., 105, 285-302.
- [4] Rahman, M.K. and Saunders, C.P.R., 1988, Corona from splashing water drops, J. Atmos. Terr. Phys., 50, 545-555.
- [5] Sivaramkrishnan, M.V., 1957, Point discharge current, earth's electric field and rain charges during disturbed weather at Poona, I.J.M.G., 8, 379-390.
- [6] Kamra, A.K., 1968, Charge transfer in the atmosphere by point discharge, J. Geomagnetism and Geoelectricity, 20, 111-113.
- [7] Kamra, A.K. and Varshneya, N.C., 1968, Local potential gradient development during excess point discharge current, J. Geomagnetism and Geoelectricity, 20, 221-224.
- [8] Rao, A.M. and Ramanadhan, R., 1979, Study of transfer of charge by point discharge in the atmosphere, Pure and Applied Geophysics, 117, 904-912.
- [9] Selvam, A.M., Manohar, G.K., Kandalgaonkar, S.S., Ramachandra Murty, A.S. and Ramana Murty, Bh.V. 1980, Electrical phenomena in pre-monsoon thunderstorms, VI Inter. Natl. Conf. on Atmos. Elec., England, 28 July-1 Aug. 1.
- [10] Kamra, A.K., 1989, Charge transfer by point discharge below dust storms, Geophys. Res. Letters, 16, 127-129.
- [11] Manohar, G.K., Kandalgaonkar, S.S. and Sholapurkar, S.M. 1990, Some characteristics of point discharge current during two premonsoon season thunderstorm at Pune, Current Science, 50, 367-370.

TABLE I. STATISTICS OF THE POINT DISCHARGE CURRENT ACTIVITY, PUNE

Year	1987						1988					
	Premonsoon			Postmonsoon			Premonsoon			Postmonsoon		
S.N	7			16			10			8		
1. Total days of Thunderstorms												
2. Duration of PDC in minutes	1098			1303			1410			917		
3. Positive and Negative duration in minutes	+ 681 - 417			+ 625 - 678			+ 763 - 647			+ 406 - 511		
4. Daytime/Nighttime (D) (N) durations in minutes. No. of spells	D 639	N 42	355	D 527	N 98	528	D 692	N 71	585	D 317	N 89	357
	18	3	15	33	6	46	30	5	20	27	9	28
5. Average duration per spell and ratio of D/N per spell duration	35	14	24	16	16	11	23	14	29	12	9	13
	2.5		1.6	1.0		0.6	1.6		1.4	1.3		0.9
6. Av. current per min. ( $\mu$ A)	.59	.31	.73	.43	.46	.34	.35	.30	.55	.28	.21	.32
												.41



TABLE II. SOME CHARACTERISTICS OF METEOROLOGICAL AND THUNDERSTORM PARAMETERS, PUNE

S.No	Year Season	1987		1988	
		Premonsoon	Post monsoon	Premonsoon	Post monsoon
1.	Av. time of initiation and cessation of Thunderstorm activity	1612 IST 1900	1617 IST 1852	1630 IST 2000	1827 IST 2033
2.	Duration of PDC (minutes) mean max. mini.	157 351 100	81 218 8	141 246 30	115 294 3
3.	Occasions when activity was at odd hours.	On one occasion activity started after 2200 hrs and ended at mid-night.	On three occasions activity persisted during midnight time.	On one occasion activity ended at mid-night hours.	On one occasion activity started and ended in the early morning hours. On two occasions activity started after midnight and ended subsequently.
4.	Mean ratio of PDC duration to total duration of thunderstorm activity	.91	.45	.75	.64
5.	Mean values of surface i. Max air temp °C ii. Evaporation (mm) iii. Sun-shine (hrs) iv. Humidity (%)	38.3 8.6 8.1 30	31.9 3.5 4.6 70	38.0 8.6 8.2 38	31.1 5.4 6.6 69

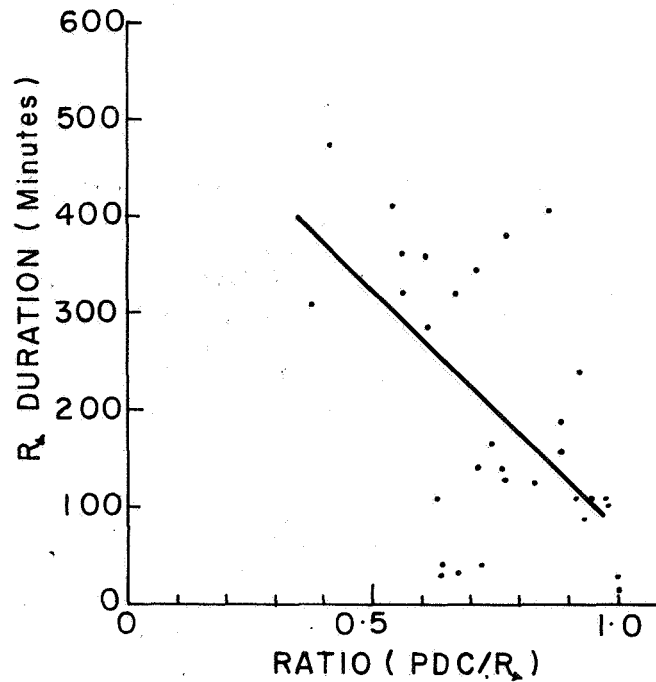


Figure 1. Daily Ratios of (PDC/R) Duration Versus Thunderstorm Duration

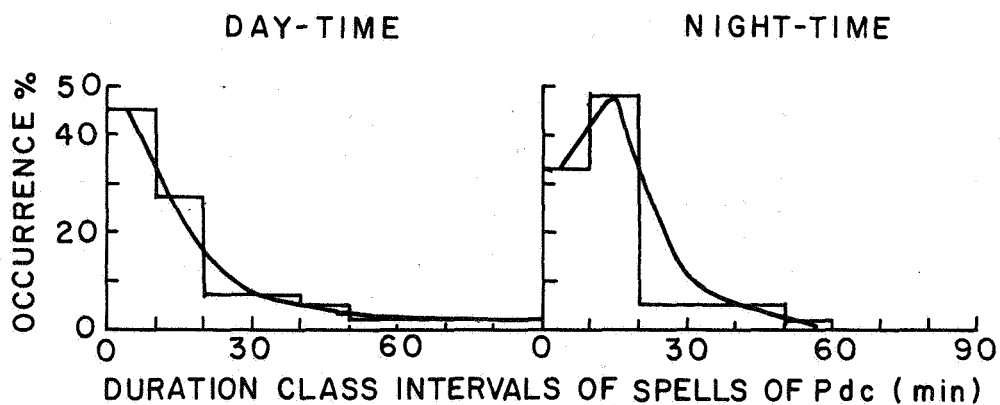


Figure 2. Frequency Distribution of Number of Spells of PDC in Given Time Intervals for Day-Time and Night-Time Conditions

# PORTABLE COMBINED OPTICAL AND ELECTRIC FIELD CHANGE INTRACLOUD LIGHTNING DETECTOR

Ralph Markson  
Airborne Research Associates  
46 Kendal Common Road  
Weston, MA 02193  
(617)899-1834

## BACKGROUND

Optical lightning detection has been used at research institutes for years and movie cameras equipped with optical lightning detectors were operated by astronauts on several Space Shuttle missions to detect lightning in clouds within the field of view during daylight and at night. The optical lightning detector reported here is the first such device available commercially. The addition of a flat plate antenna section, which responds to electric field changes, provides the advantages of both types of detectors in a single compact unit. Flat plate antenna sensors also have not been available as an inexpensive commercial product in the past. By combining both signals in a coincidence circuit false alarms are essentially eliminated.

## OPTICAL LIGHTNING DETECTION

Lightning emits optical signals which in some respects are easier to detect and interpret and more reliable indicators than longer wavelength electromagnetic radiation. In daylight, depending on background light intensity, cloud-to-ground lightning can be observed visually, but intracloud lightning is rarely seen. At night the human eye sees essentially all lightning from clouds within the field of view. The optical lightning detector provides close to nighttime visual sensitivity during daylight. Intracloud lightning in the upper portion of brightly sunlit clouds is sensed as easily as cloud-to-ground discharges. The optical lightning detector offers some important advantages over other types of lightning detection including:

- ability to report intracloud lightning
- close to 100% detection efficiency within about 20 km or further (depending on visibility)
- can determine if specific clouds contain lightning
- low cost (less than 1% of mapping systems)
- no installation or maintenance
- no requirement for AC power
- no requirement for communications between remote sensors and central processor
- reliability
- portability
- simplicity of operation

The limitations of an optical detector are:

- does not provide range
- azimuth may be inaccurate if light is reflected from other clouds
- nearby clouds or rain can block view of more distant lightning (but flat plate antenna will sense them)

#### INDUCTION FIELD CHANGE LIGHTNING DETECTION

The current second generation optical lightning detector includes a flat plate field change detector in order to improve performance. The antenna is the shiny metal plate on the end of the instrument. This section can be operated independently or in coincidence with the optical section. Improvements include:

- coincidence mode: elimination of false optical signals which can occur from reflections off raindrops or other objects or from windows within buildings
- field change mode: ability to detect distant lightning when optical visibility is obstructed
- omnidirectional (no need to aim instrument at clouds)

Electric field change detection has been selected as the best way to use non-optical emissions, rather than "sferics" type emissions such as one hears on an AM radio. The problem with using radio static signals for lightning detection is that such signals decrease slowly ( $1/R$ ) with distance in the far field and are reflected from the ionosphere. Thus they propagate for long distances; one has no idea if the flashes are nearby or a few hundred miles away. If range is purposely limited by reducing sensitivity, only the more energetic cloud-to-ground flashes are received and the earlier intracloud discharges are missed. However, by sensing VLF field changes in the "near field" where signal intensity decreases rapidly with distance ( $1/R^3$ ), one can eliminate reception of distant signals without decreasing sensitivity for nearby flashes.

Use of this flat plate antenna section makes it possible to survey for lightning for about 50 km in all directions on days with limited visibility without having to point the detector at specific clouds. Such omnidirectional sensing can be done before there are any nearby visible clouds. It is best to use this mode outdoors since electric signals are screened from the interior of buildings with metal structure.

When threatening clouds appear, the instrument can be switched to the "optical" or "both" (coincidence) mode to see if these clouds contain lightning. In any of the three operational modes the unique staccato sound signature characteristic of lightning (caused by the strokes within each flash) can be heard; this is useful for distinguishing lightning from any noise sources.

## **DISTANCE TO LIGHTNING**

In the early part of a storm, when lightning is occurring only once every few minutes or a few times per minute -- so that individual flashes (beeps from the instrument) can be associated with subsequent thunder -- it is possible to determine the distance to the discharge. This classic "flash to bang" method works because sound travels 1 mile in 5 seconds. The technique is useful for distances up to about 8 km, or possibly as much as 15 km on occasion, depending on sound propagation and lightning frequency.

## **RANGE**

The detector's range is essentially line-of-sight. However, it is capable of picking up lightning from clouds behind those in the foreground because of light transmission through the thin veil of high cirrus clouds which is often present near thunderstorms. Thus, the range is not usually restricted to the closest clouds and it is on the order of 50 km with other clouds between the source and detector. The range can be as much as 150 km in clean air with no clouds between the detector and clouds with lightning.

## **CIRCUIT FEATURES**

The accompanying block diagram shows the components of the circuitry. A highpass filter and bandpass filter restrict signals essentially to lightning (and strobe lights when operated in the purely optical mode). The detection threshold automatically adjusts to a level just below that of the variable background light intensity to maximize sensitivity. The timing diagram illustrates how the optical and field change sections trigger when the threshold is exceeded and how the signal is maintained for 50 ms to aid in hearing the pulses (strokes). This diagram illustrates how both signals must be on for the coincidence circuit to respond.

## **PHYSICAL SPECIFICATIONS**

The M-10 dimensions are 18 cm (7.0 in) x 10 cm (3.8 in) x 3.5 cm (1.3 in). It weighs 450 gm (1 lb). A fitting in the base allows it to be mounted on a camera tripod so it can easily be pointed toward suspicious clouds without having to hold it in position by hand for an extended period of time. (It also can be supported by any convenient object.) It can be heard 20 meters away when background noise is low. The instrument is powered by two 9 volt alkaline transistor batteries which are inserted into molded housings when the back plate is removed. The detector beeps every 3 seconds when the batteries need replacement.

## **APPLICATIONS**

To date over 100 optical lightning detectors are being used at universities and golf courses as well as government laboratories and field test sites. A half dozen observers covering the KSC test area could tell with 100% reliability if any visible clouds over or near the region contained any kind of lightning.

**Errors in Electric Field Measurements Using Instrumented Aircraft**  
*by B. Evteev*

**No paper available.**

**Characteristic Features of Small, Average, and Large Ion Concentrations  
in Different Mobility Ranges, During Thunderstorms at Poona, India**  
*by G. Srivastava*

**No paper available.**

## LT-23

## THE FEEDBACK VIBRATING CAPACITOR FIELDMETER

by

James R. Vosteen and William E. Vosteen  
Monroe Electronics, Inc.  
Lyndonville, NY 14098

*This paper was presented at the 1991 International Conference on Lightning and Static Electricity  
April 16-19, 1991 at Cocoa Beach, Florida USA*

## ABSTRACT

A redesign effort was undertaken starting in the fall of 1988 to replace our Models 1019A and 1019B fieldmeter probes resulting in greatly improved performance. Extensive testing was conducted to confirm performance of the new design and to evaluate outdoor atmospheric applicability. We will discuss theory of operation, design improvements, performance, proper use, maintenance, and applications for the new intrinsically safe design.

## INTRODUCTION

The feedback vibrating capacitor fieldmeter was first developed in 1965 by Robert E. Vosteen [1], founder of Monroe Electronics, Inc., to address problems a manufacturer of coated film was having with its production lines during winter months when humidity is low and static events are more prevalent. The client did have field mills at the time. They were custom made in house for their own use.

The stator was made from copper clad glass epoxy printed circuit board material etched to 18 equal segments. The rotor was made from stainless steel. Regular calibration was required due to changes in impedance of the glass epoxy from surface contamination, possible charge holding characteristics of the glass epoxy and contact potential differences of the bare copper and stainless steel.

Bearing noise from motors of 25 years ago was also a problem and little was known about contact potential at the time. The calibration procedure was a real ordeal as remembered by one of their employees who used to do it.

By incorporating a feedback null seeking technique, calibration of the vibrating capacitor probe was made extremely stable over time being little affected by changes in impedance due to surface contamination of the electrode insulator or changes in modulator efficiency. Zero drift was about 2% due mostly to contact potential of the gold plated electrode and aperture plate.

Field mill design has improved immensely since those days. Much improved motors, better insulating materials, better knowledge of contact potentials and better mechanical and electronic design has resulted in extremely accurate and stable modern instruments.

Regular calibration is still required if the mill is used in an environment where the electrode stator insulators can get contaminated thereby changing their insulating properties and calibration.

The film manufacturer uses Monroe Electronics' vibrating capacitor fieldmeters exclusively and have units 20 years old still in use. They are presently embarking on a replacement program to take advantage of the increased performance and stability of the new design probes which we will proceed to describe. One of our goals in the redesign effort was to close certain performance gaps between our previous design and state of the art field mills.



## PRINCIPLE OF OPERATION

The sensitive electrode "senses" the field to be measured through the aperture in the probe gradient cap. The A.C. signal induced on this electrode is proportional to its excursion path length and the strength of the ambient field. The polarity of this field determines phase. This signal and a reference signal from the oscillator are fed into a phase sensitive detector whose output feeds a D.C. integrating amplifier. The output of this amplifier is used to drive the electrode to a potential just sufficient to neutralize the net field at the sensitive electrode.

This feedback principle and null seeking operation combine to make a remarkably stable and highly accurate instrument.

## DESIGN IMPROVEMENTS

A new patented low noise pre-amp [2] was employed which reduced noise by a factor of 10.

Electrode size was increased from 0.5 inch to 0.625 inch resulting in an approximate 50% increase in area which translates to conversion efficiency or gain. Alloy 304 stainless steel was used wherever possible for the electrode and for parts viewed by the electrode. Research [3] has shown stainless steel to be a superior material for reducing contact potential effect in fieldmeters.

If increased speed of response is deemed by the user to be more important than low noise then the pre-amp gain can be changed to increase speed 10% to 90% to a maximum of 50 milliseconds. A time of 250 milliseconds is typical in the low noise mode.

The gradient cap on the new design is at ground potential whereas the old one was at driven shield potential. This enhances the intrinsically safe design, hardens the unit to static discharge and may improve measurement accuracy in high fields.

Better purging is designed into the 1019E version for reliable performance under extremely dirty conditions. An air column surrounds the gradient cap as well as exiting through the gradient cap aperture. The old design purged through the aperture only and charge-carrying contamination could deposit on the gradient cap altering measurements being taken.

### Applications

There are now three fieldmeter mainframes used to cover a range of application.

1. Model 245 is a single channel battery powered unit used for trouble shooting static hazards and taking of measurements where a.c. power is not available.
2. Model 273 is a single channel unit with 2 symmetrical alarm levels. Relays are supplied via barrier strip to allow automated control of chart recorder, external alarms or high voltage supplies, etc. Optional battery power is available.
3. Model 171 is a multichannel (2 to 16) unit for monitoring and alarming more than one site at a central location. Up to 1000 feet of probe cable may be used on all instruments.

All units are 1019E & F compatible. The E probe is designed with long term monitoring in mind and has better purging capabilities and better shielding of cables for noise reduction. The F probe is the same probe head but much smaller and is used for short term monitoring or where small size is of importance. These units are used in monitoring:

A. Charge accumulation

1. Fueling monitoring
2. Filling stations/processes
3. Painting operations
4. Explosives handling
5. Solid rocket manufacturing processes
6. Read-write head analysis
7. Mixing processes
8. Transport systems ducting, pipe lines, etc.

B. Coating processes

1. Metal coating
2. Paper coating
3. Film coating
4. Solvent coating

C. Atmospheric monitoring

1. H V D C transmission lines
2. Research
3. Lightning hazard warning

Intrinsic Safety [4]

Probes have been certified Class I, Division 1, Groups C & D intrinsically safe by Factory Mutual Research Corporation when used with approved barriers. With purging and interlocks, Division 1, Groups A & B requirements can be met [5].

Sensitivity

Sensitivity is controlled by hole size in the gradient cap. Ranges from  $\pm 10$  kV/m to 2MV/m are possible. The larger the hole size, the greater the sensitivity and the lower the full scale field strength.

It is recommended that the range of most interest to the user should be the approximate mid-range of full scale sensitivity.

Some degradation in speed of response will be noticed on the more sensitive ranges due to loss of feedback gain because of the larger aperture sizes.

Calibration

Calibration is done using the parallel plate method. The probe is placed flush with a grounded plane and a voltage is applied to a parallel plate a set distance from the probe. A minimum ratio of 5:1 width of plate to distance between plates is recommended [6]. Using this method, kV/M, kV/cm and kV/in sensitivities can be calibrated. Larger fixtures with greater distance (10cm) between plates are considered optimum but are not always practical and can be of some danger to the user due to high voltages required. Well made fixtures with spacings of 1cm to 1 inch have been found to correlate well with the larger fixtures.

Testing was performed to compare the 1cm fixture to the 10cm fixture and check linearity.

## Equipment List

### Calibration Fixture #1 (10cm)

Dimensions: plates 58.7cm x 58.7cm  
insulators 10cm

### Calibration Fixture #2 (1cm)

Dimensions: plates 15.2cm x 15.2cm  
insulators 1cm

Monroe Electronics Model 152A  $\pm 10$ kV Coronaply

Monroe Electronics Model 241  $\pm 3$ kV reference supply

Monroe Electronics Model 175-57 1000:1 divider

Data Precision 2540A1 digital voltmeter

Monroe Electronics Model 273 fieldmeter with 1019F-3 probe (1kV/cm or 100kV/M)

The Model 152A was used for the 2kV to 10kV range. Output was checked and adjusted using the 175-57 divider and 2540A1 meter. The Model 241 is a 0.05% instrument and no adjustments were required in the 1V to 1000V range.

The fixtures were placed on a cardboard box to isolate them from leakage to the benchtop. The fieldmeter was calibrated at full scale on the 10cm fixture. 10kV at 10cm = 100kV/m and 10.000 VDC output. Voltage applied was then reduced 1 decade at a time and fieldmeter output measurements taken. The last (mV) digit on output voltages flashed  $\pm 1$  due to noise. The F model probes have a lesser degree of shielding on the probe cable and therefore may exhibit a greater degree of noise from local sources. As can be seen from the data, the output was linear within 0.05% and sensitive to 10V/m. When the same test was then performed on the 1cm fixture without re-calibration, full scale output started at 1000V at 1cm = 9.846VDC. This was noted to be about 1.5% difference. Some of this difference is attributed to variation in calibration distance. Other factors such as field convergence may be affecting calibration at the close spacing. The accuracy of your calibration is correlated directly to how well you know your plate spacing, flatness and adequate size as described earlier to insure straight field lines.

## Cleaning

When cleaning is required (the probe is disassembled and) the gradient cap is removed. At this time, care must be taken not to drop the probe or allow the electrode to receive any blows or contact with anything but the solvent cleaner. It is fairly fragile and can be fractured from its insulator if exposed to excessive force. The electrode should not be pushed on as this can alter the magnetic set of the transducer possibly altering the performance. Recommended solvent for cleaning purposes is Miller Stephenson MS160/C02 or technical grade isopropyl alcohol. Any other solvent may attack conductive polymer used in manufacturing and render probe inoperable. Flush the electrode and transducer with a spray and dry with light application of Aero Duster (MS222) or clean dry low pressure air. Clean the gradient cap with same solvent and wipe dry with a lint free wipe. Re-assemble gradient cap to base making sure it is well seated. A short bake in an oven at 75°C will drive off any residue solvent and help to stabilize the probe.

## Purging

Purging is highly recommended when any long term monitoring (more than 24 hours) is undertaken. The only place purging may not be required is in a clean room or other similar ultra clean environment. Due to the close spacings used in the probe particulate contamination will cause zero drift due to charge holding characteristics of contaminants.

Well filtered air is recommended and filtered inert gas such as argon or nitrogen can be used where air may not be compatible with the environment being monitored.

Existing gas supplies to be used for purging should be equipped with dedicated filtering for purging use only. Supply filters are available capable of removing 99.99% of 0.1 micron oil, water and dirt when properly maintained per manufacturer's instructions. Replaceable in line filters can also be used to further enhance filtering. Zero drift should be monitored and re-zeroed as required at intervals determined by the user to keep error within acceptable limits. If excessive zero drift is observed the probe should be disassembled, cleaned and recalibrated. Air filter maintenance should be done at this time also. Recalibration is required only after disassembly of the probe. Calibration is unaffected by contaminants.

### Environmental Testing

Hundreds of hours of tests have been performed to establish working parameters of the probes.

A Tenney environmental chamber has been used for indoor testing of humidity and temperature effects. The probes have been found to work well in specified temperature ranges of -30°C to +100°C and 0 to 100% humidity (non-condensing). Temperature drift has been found to be about 0.5% from -30°C to 100°C. A test was performed to check performance at 10°C increments through the full temperature range. Data taken involved zero drift, calibration, speed of response (which equates with overall gain) and noise. A zero offset of around 2% is induced starting at around 80°C to 90°C. This only takes place on an initial ramp up to 100°C. The probe can then be re-zeroed and will hold within 0.5% zero drift over the temperature range. Calibration was found to hold within 0.05% through the full temperature range.

Speed of response is degraded starting at about 60°C to 70°C. A probe exhibiting a 10% to 90% speed of 250 milliseconds at room ambient will degrade to 500 milliseconds at these higher temperatures. This is probably due to loss in modulator efficiency. There is also some loss of performance at temperatures below 0°C although to a much smaller degree. Noise was found to remain stable through the temperature range varying only 2-3 mV peak to peak.

### Drift Under Working Conditions

Our old design probe has a platinum/palladium/gold thick film over ceramic electrode viewing a gold plated stainless steel gradient cap. The use of stainless steel in these parts has greatly reduced observable drift rates. Contact potential and modulator efficiency are known to be the largest factors effecting drift. Modulator efficiency in field mills is vastly superior to that of the vibrating capacitor and greater spacings of electrode to vanes are possible with this combination greatly reducing contact potential effects. A larger more powerful modulator with a larger electrode could be used to enhance stability but intrinsic safety of the present design would most probably be lost.

Outdoor drift rates are probably a worst case due to changes in air pollution levels and the chemical cocktail always present in the atmosphere. Fluctuating temperature and humidity also will affect drift.

Observed zero drift outdoors usually runs less than 0.1% per day, <0.5% per week and <1% per month. These guideline parameters may be better or worse depending on air quality and weather conditions of a given location. The user would determine drift rates through checks and decide on a zeroing schedule compatible with the accuracy of measurements required.

Indoor drift rates are usually much lower. A probe was left running unpurged on a bench in the factory in a zero field and drift was less than 0.1% for a period of three weeks. In a clean room situation drift would probably be lower yet. Conversely, in extremely dirty conditions or chemically contaminated atmospheric drift may be enhanced. Attention to good purging practices will minimize drift under all conditions.

### Development Of Outdoor Probe And Fixture

Feasibility testing was done at New Mexico Tech. Langmuir Laboratory in November - December 1988 with the help of Dr. William Rison [7]. We compared the signals of our Model 245/old 1019A with their E-100 field mill, which was designed for airborne applications by Dr. William P. Winn, for a period of six weeks. These mills are in use for ground level measurements at several research and military installations in New Mexico. Little attention was paid to getting absolute calibration of measurements. We were most interested in seeing how well the instruments would track under similar conditions. The signals on the chart recorder were nearly identical for the period. The main discrepancy noted was zero drift of the 1019A. It would quickly (within 48 hours) drift off about 2% of full scale or 200V/m and then stabilize. This made it impossible for accurate measurements of ambient E-field to be taken.

The outdoor fixture in use at the time was that of a downward facing probe viewing a grounded wire mesh grid. A probe height of approximately 14" gave the same reading as one facing upward flush with the ground. The NM Tech fixture was also downward facing but at a greater distance from ground and viewing ground. It was explained by Bill Winn that this arrangement works like an antenna enhancing the E-field by a factor determined by comparison with an upward facing flush mounted mill. The face of the mill is at approximately 1 meter, giving an enhancement factor of about 7:1, i.e. 60 kV/m at the face of the mill gave 8.4 kV/m in the fixture. It is felt that under most conditions, the earth itself is an adequate static ground. Unusual geological situations do exist where the earth is not a good ground. In this case a grounded wire mesh grid or plate should be provided for the fieldmeter to view.

Our latest design outdoor fixture 1019G is patterned after the New Mexico Tech design. There are several advantages:

1. Reasonable manufacturing cost
2. Good portability
3. Stable in high wind conditions
4. Works well in adverse conditions (rain, snow, etc.)
5. Enhances performance factors of the fieldmeter used
6. Excellent for long term monitoring at fixed sites

The probe faces downward at a height of approximately 1 meter. The full scale sensitivity of the probe is 20kV/m which becomes 5kV/m when used on the fixture. Our enhancement factor is 4:1 where the Tech fixture is 7:1 at approximately the same height. Our probe is equipped with a round 6 inch diameter field normalization plate which also works as a roof keeping rain from the probe aperture. This plate allows less of the E-field converging on the fixture to reach the electrode therefore making the enhancement factor less. Each design of fieldmeter will have its own enhancement factor when used in this downward facing mode.

A rain proof NEMA enclosure is attached to the fixture for permanent installations. This contains a small air pump with filters for purging, an electrical box for AC connections and a dry place for probe connections. It is recommended that all wiring to a permanent installation be run in buried conduit and be well grounded.

The probe is equipped with a self regulating heater which will enhance performance at low temperature and keep the probe free from condensation which can deposit contaminants over time and degrade performance. Temperature inside the probe is raised about 20°C at -30°C and stops working completely at about +50°C. At +20°C the temperature inside is about +33°C; at +30°C, it is about +36°C and at +40°C, about +41°C.

The  $\pm 5$ kV/m full scale range was selected because the range of most interest in lightning hazard warning is in the  $\pm 3$ kV/m range. Bill Rison suggested that an adequate speed of response for the probe would be around 200 milliseconds. This will allow the user to detect lightning discharge in the range of 3 - 5km radius with use of a chart recorder. The spikes seen at this distance would be on the order of the ambient field at 100 to

200V/m. Gain was added at the pre-amp to reach this speed with some increase in noise to about 10 - 12 mV peak to peak. This level still allows for a maximum sensitivity of less than 5V/m. The gradient cap can be changed for wider range measurements should they be desired, the 4:1 enhancement factor being constant.

Many months of outdoor year around testing have been done. No probe failures have been noted. They have survived normal and severe weather conditions well.

At present we are doing a final evaluation with the help of Bill Jafferis at NASA atmospheric science laboratory. Initial results look promising. The unit tracks well with the on-site field mills in ambient E-fields. As of this writing no storms have passed by and outputs need to be compared under higher fields. We also plan to check fixture calibration with a flush mounted mill and adjust it if required.

### Conclusion

This new design has proven itself to be a significant improvement over the old design. Further studies are needed in material selection and mechanical design considerations to minimize contact potential effects.

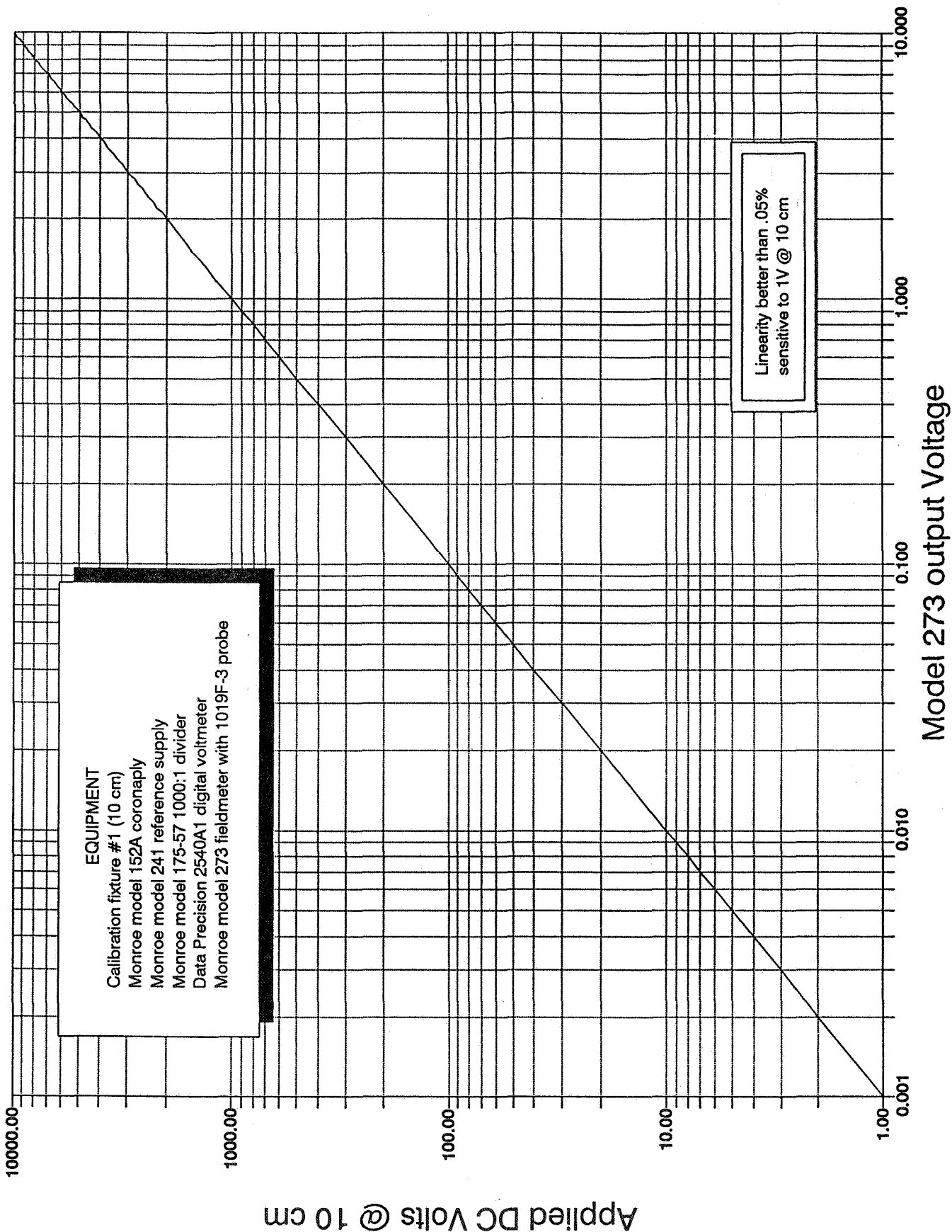
### Acknowledgments

The authors wish to thank (in alphabetical order) Bill Jafferis, Launa Maier, Charlie Moore, Bill Rison, and Bill Winn for all their help and cooperation in the development of the outdoor fixture.

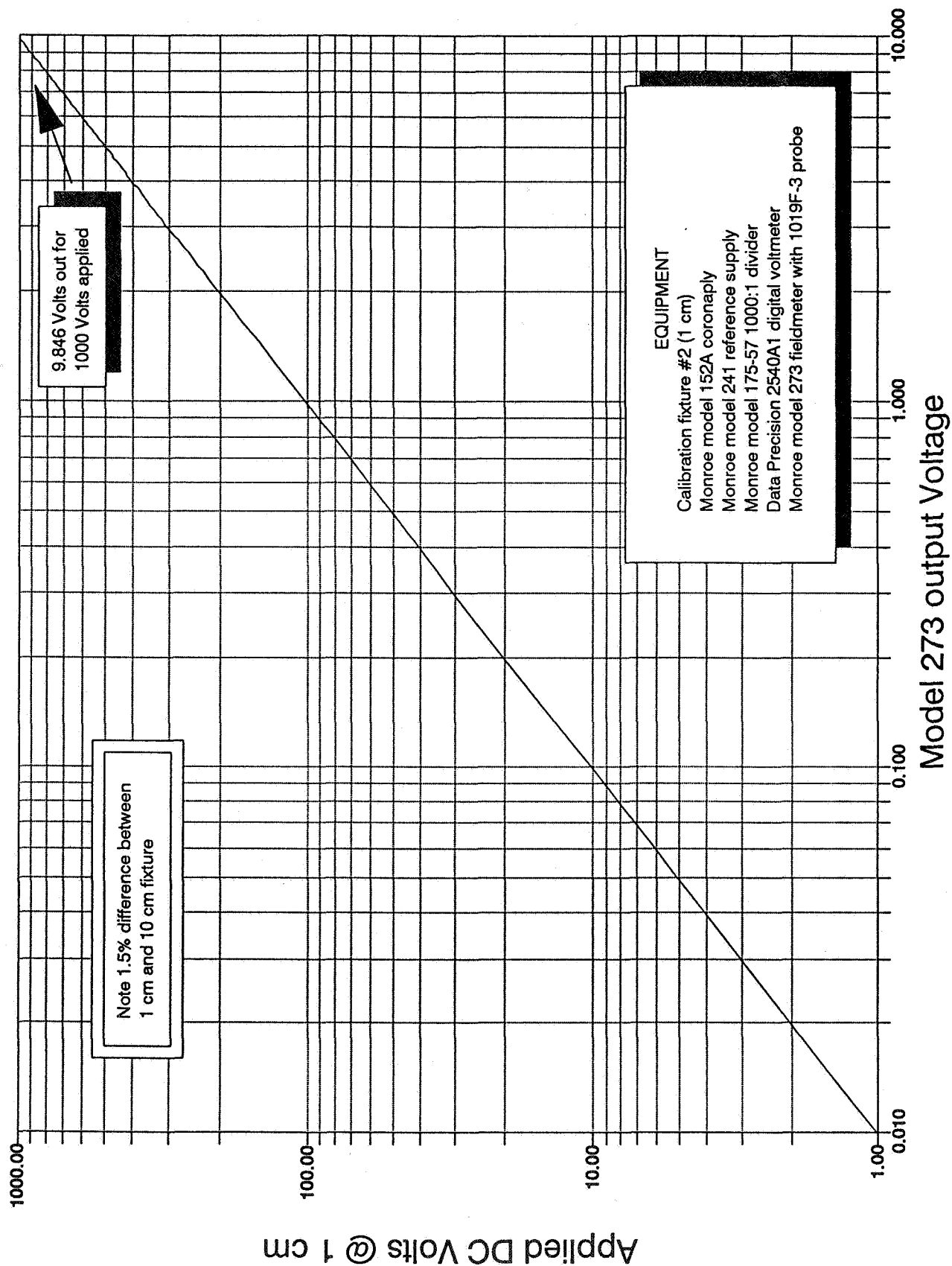
### REFERENCES

1. *Electrostatic Potential and Field Measurement Apparatus Having a Capacitor Detector With Feedback to Drive the Capacitor Detector to the Potential Being Measured* by Robert E. Vosteen U.S. patent #3,611,127.
2. *Amplifier With D.C. Compensation* by Mason F. Cox U.S. patent #4,785,237.
3. *Contact Potential And Surface-Charge Effects In Atmospheric Electrical Instrumentation* by J.C. Willet and J.C. Bailey Naval Research Laboratory Washington D.C. Memorandum report 5063.
4. *Stahls Intrinsic Safety Primer*, R. Stahl, Inc., 150 New Boston Street, Woburn, MA 01801.
5. NFPA Standard 496, *Purged and Pressurized Enclosures for Electrical Equipment*, National Fire Prevention Association, 1 Batterymarch Park, Quincy, MA 02269
6. *A Review of Current Electrostatic Measurement Techniques And Their Limitations* by William E. Vosteen, Monroe Electronics, Inc., Lyndonville, NY 14098.
7. *Lightning Protection For High Explosives And Instrumentation Using A Field Mill System* by William Rison, Geophysical Research Center New Mexico Institute of Mining And Technology, Socorro, New Mexico 87801 and Gerald P. Chapman Mission Research Corporation, 1720 Randolph Road S.E., Albuquerque, New Mexico 87106-4245.

# Calibration Linearity and Sensitivity



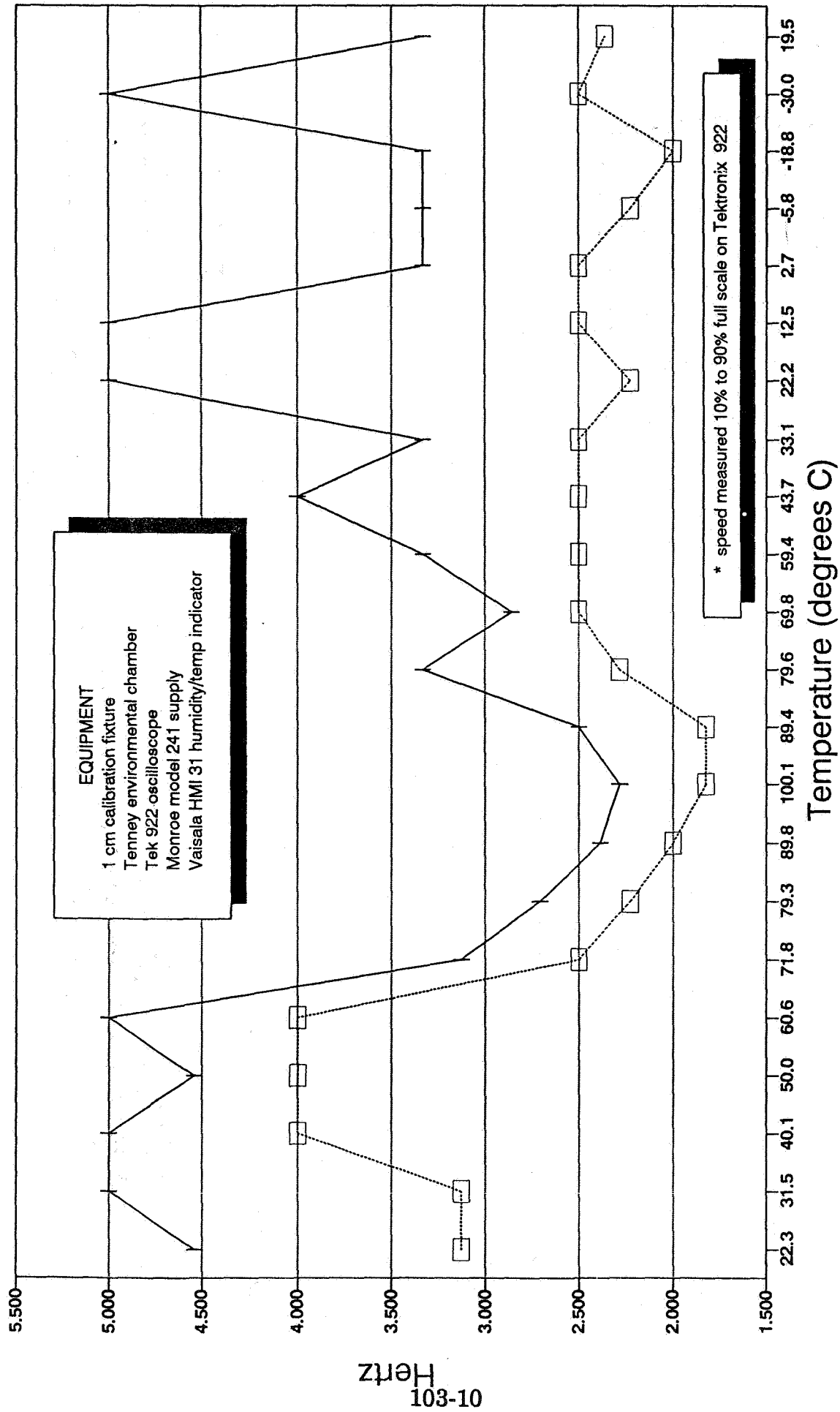
# **1 cm Fixture with Probe cal at 10 cm** **273 Fieldmeter with 1019F-3 Probe**





# Speed of response over temperature \*

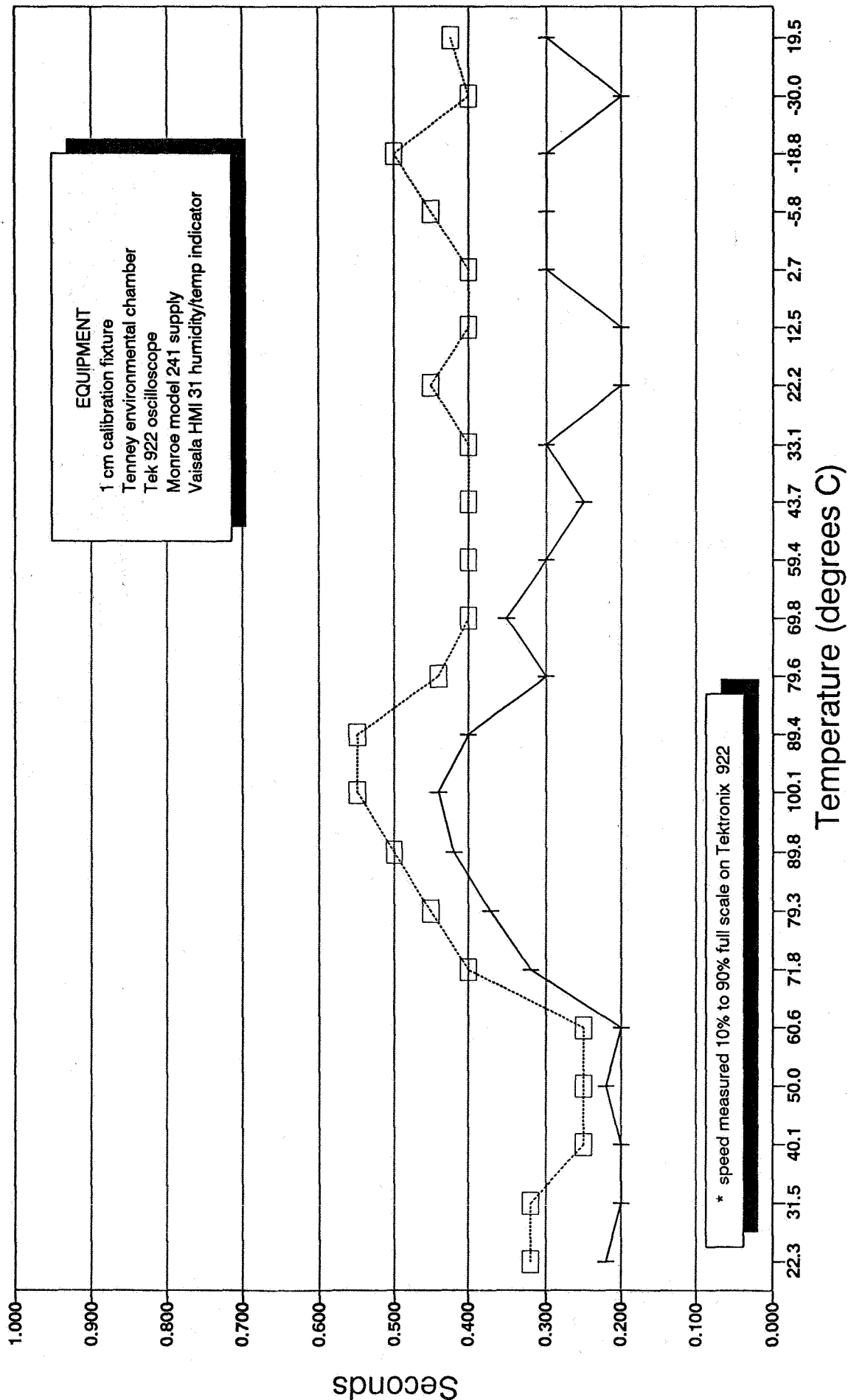
## 273 Fieldmeter with 1019E-4



Probe 1 — Probe 2

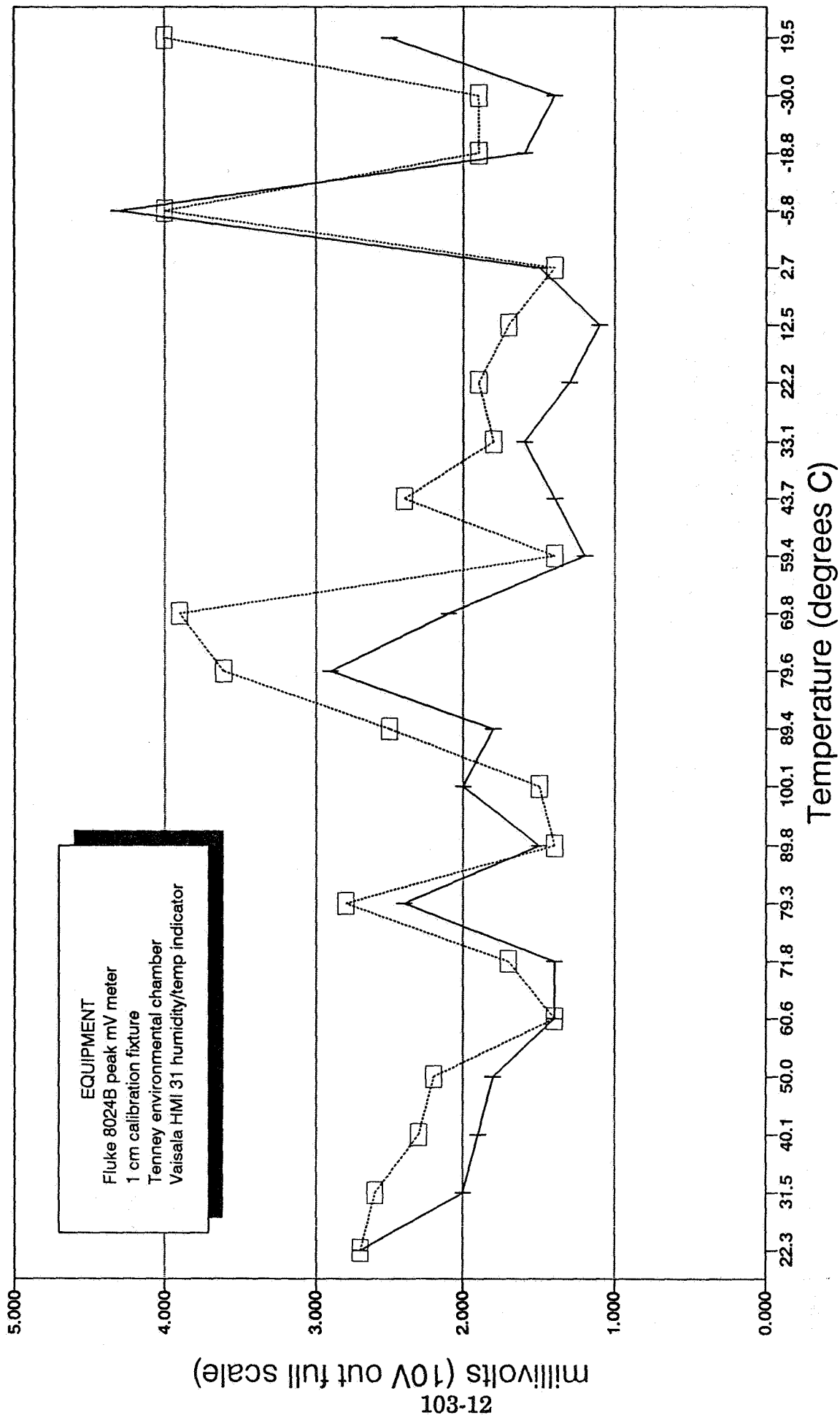
# Speed of response over temperature \*

## 273 Fieldmeter with 1019E-4



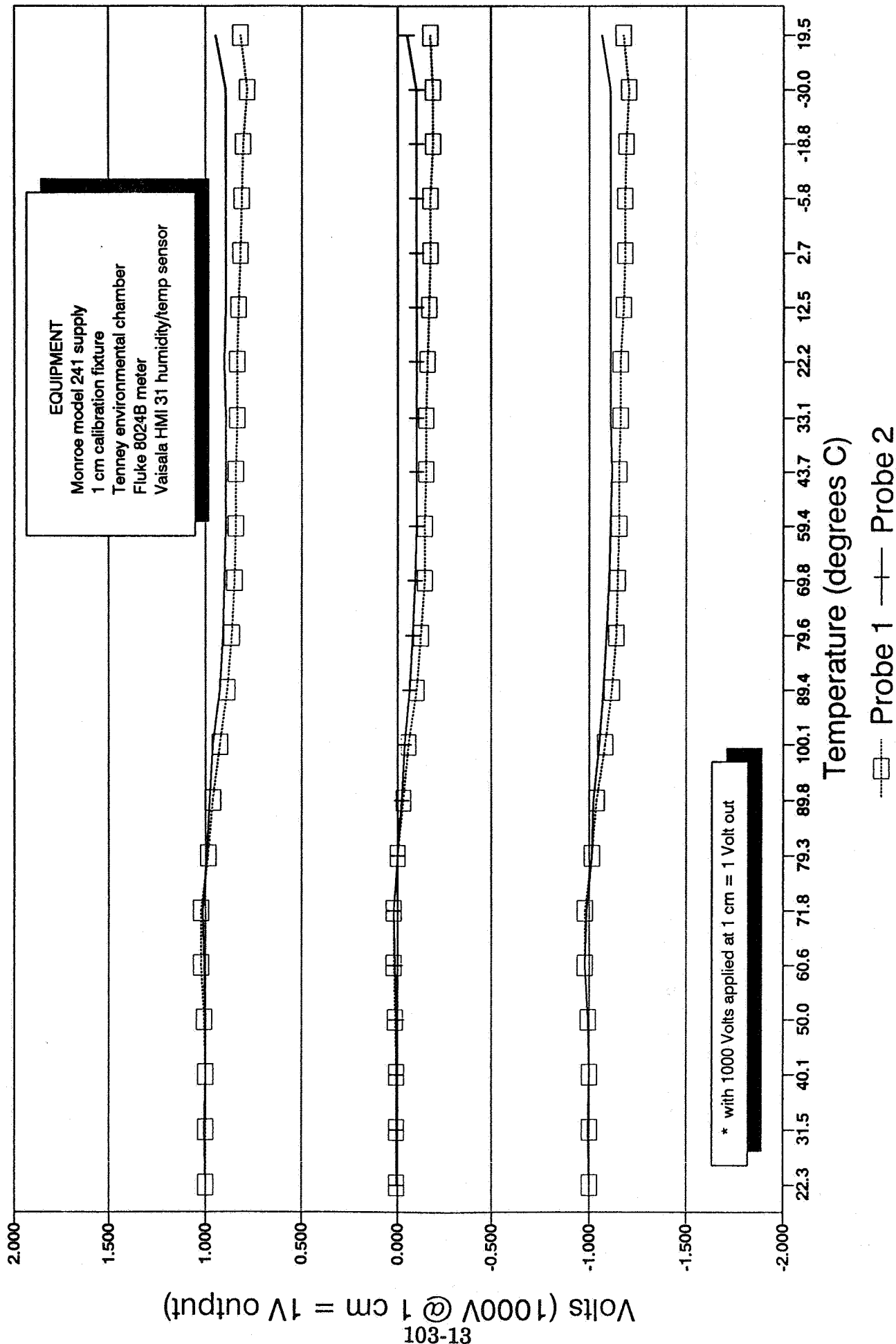
Probe 1 — Probe 2

# Noise over temperature 273 Fieldmeter with 1019E-4



# Zero drift/calibration over temperature \*

## 273 Fieldmeter with 1019E-4



N.I. Petrov and G.N. Petrova

Branch of All-Union Electrotechnical Institute, 143500 Istra, Moscow region, USSR

## Abstract

The dependences between the different parameters of a leader in lightning theoretically are obtained. The physical mechanism of the instability leading to the formation of the streamer zone is supposed. The instability has the wave nature and is caused by the self-influence effects of the space charge. Using a stability condition of the leader propagation a dependence between the current across a leader head and the its velocity of moving is obtained. The dependence of the streamer zone length on the gap length is obtained. It is shown that the streamer zone length is saturated with the increasing of the gap length. A comparison of the obtained dependences with the experimental data is resulted.

## 1 Introduction

A consideration of leader discharge propagation is based on the investigation of charged particles moving in electric field. A particle moves in the potential created by all others charges. The calculation of that self-consistent potential is a difficult mathematical problem. Therefore it is important to construct an alternative approach for the analysis of such self-consistent problem. Particularly, an approach similar to the one used nonlinear wave theory for analysis of the self-influence effects in a nonlinear media turns out to be effective. At such approach a leader process is described by the nonlinear wave equations of evolution type, which from the continuity equations for the particles and Poisson equation for the electric field may be obtained. Note, that the nonlinear wave equation being constructed for the complex wave function  $\Psi(x, y, z, t)$ , determined from the condition  $\rho = |\Psi|^2$ , where  $\rho$  is the charge density. Such approach allows to understand the physical picture of many effects in leader process, in particular, the mechanism of instability, leading to the streamer corona formation.

In this paper a qualitative consideration of physical processes in a leader discharge caused by the self-influence effects is suggested.

## 2 Streamer zone formation

Leader process begins from the formation of streamer corona, consisting of multitude individual streamers. It is known that the streamers formation is caused by the avalanche-streamer transition. However a series of peculiarities of streamer have not a physical explanation so far. In particular the physical picture of the keeping of streamer head radius along the all its trajectory is not known. It is necessary to solve the two-dimensional equations for explanation of this effect:

$$\frac{\partial n}{\partial t} = \frac{1}{e} \operatorname{div} j + \alpha v n + w, \quad (1)$$

$$\frac{\partial \rho}{\partial t} = \alpha v n + w, \quad (2)$$

$$\operatorname{div} E = \frac{4\pi e}{\epsilon} (\rho - n), \quad (3)$$

where  $j = en\mu E + eD\nabla n$  is the current density,  $n$  and  $\rho$  are number density of electrons and positive ions, respectively,  $\alpha$  is the ionization coefficient,  $v$  is the drift velocity,  $D$  is the diffusion coefficient,  $w$  is the charges produced due to the gas photoionization per volume and time.

A quasiclassical approach for the analysis of this system of equations allows to elucidate the physical picture of streamer radius preservation. Coulomb repulsive interaction between the charges, leading to the decrease of particles number and the ionization in the potential created by the same charges, which lead to the increase of charge number are the basic processes keeping the streamer radius. A next qualitative analysis may be presented. The growth of number of charges in some region on at the time  $dt$  is determined by the expression

$$dQ_+ = v_i Q dt, \quad (4)$$

where  $v_i = \alpha v$  is the ionization coefficient. The decrease of the particles at the same time  $dt$  from this region because of Coulomb interaction is equal to

$$dQ_- = 4\pi \rho r^2 dr = 4\pi \rho r^2 v dt, \quad (5)$$

where  $\rho$  is the mean density of charges,  $v = \mu E_r = \mu Q / 4\pi \epsilon r^2$ ,  $\mu$  is the mobility of the electrons,  $E_r$  is the electric field at the streamer head with radius  $r$ . A stationary propagation of streamer take place at the fulfilment of equality

$$dQ_+ = dQ_- \quad (6)$$

Hence it follows that the mean density of charges and the radius of streamer are equal

$$\rho \approx \alpha \epsilon_0 E_0, \quad (7)$$

where  $E_0 \approx E_r$  is the external electric field,

$$r_0 \approx \frac{3v}{v_i} = \frac{3}{\alpha}, \quad (8)$$

i.e., is determined by only the gas properties.

Note that at the  $r < r_0$ ,  $dQ_+ < dQ_-$  and the conductivity  $\sigma$  is insufficient in order to oust the field from this region in consequence of Maxwell relaxation at the time  $t \sim 1/\nu_i$ . Therefore the radius  $r$  grows to value  $r_0$ , i.e., when the Maxwell relaxation time  $\tau_m = 1/4\pi\sigma$  is compared with the conductivity growth time  $t \sim 1/\nu_i$ . Later on the growth of streamer radius is ceased because of the quickly ousting of field from the streamer head forward. It is noted that such picture occurs in the electronegative gases, where the influence of processes in a channel is not essential. In the electropositive gases the radius of the streamer depends also on the conductivity of a channel and must be greater than the  $r_0 \approx 3/\alpha$ . A charge of the head of streamer may be evaluated

lated as follows:

$$q_0 = \frac{4\pi}{3} \rho \alpha^3 = \frac{4\pi}{3} \alpha \epsilon_0 E_0 \left(\frac{3}{\alpha}\right)^3 = 10^2 \frac{\epsilon_0 E_0}{\alpha^2} \quad (9)$$

At the  $E_0 = 24$  kV/cm and  $\alpha = 10^2$  cm<sup>-1</sup> in air we obtain, that the  $q_0 = 2.4 \cdot 10^{-12}$  C or  $N_e = 10^7$ . In  $SF_6$  for the development of streamer the field  $E_0 = 89$  kV/cm is necessary. Then the  $\alpha = 0.75 \cdot 10^2$  cm<sup>-1</sup> and the streamer charge is equal to  $q_0 = 1.6 \cdot 10^{-12}$  C ( $N_e = 10^7$ ). A process in the streamer channel influence on its development only up to distance  $l \sim \psi_{tr}/\psi_0$ , where  $\psi_0$  is the attachment coefficient ( $\psi_0 \sim 10^{-7}$  sec in air). At further removing from the electrode a streamer head lose the conductive connection with its, but the necessary intensification of field on the head is ensured because of its polarization in the external electric field.

A such mechanism allows to explain the dependence of streamer velocity on the value of external electric field. So, from the system (1-3) may be obtained

$$\psi_{tr} = \frac{\partial n / \partial t}{\partial n / \partial x} = v_0 + \alpha \psi_0 \epsilon_0 + w, \quad (10)$$

where  $\alpha(E) = A \exp(B/E)$ ,  $E$  is the electric field,  $A$  and  $B$  are constant,  $v_0 = v_{min} \sim \epsilon_0 / \tau_m \sim \mu E_0$ .

From here one can see that the streamer velocity has the threshold character of dependence on the external electric field. This leads to the quickly stopping of streamer at the decrease of field lower the critical value  $E_{cr}$ .

In the nonuniform gaps the critical field is reached only near by electrode. However in the long gaps only the numerous streamers are propagated, which form the streamer zone. Elucidation of physical mechanism of instability leading to the formation of streamer zone is of interest. When the charge density reaches the critical value, the breaking into the threads (streamers) is occurring, i.e. the analogy with the breaking of light beam or acoustics wave in nonlinear media is exist. Note that the instability leading to the formation of streamer zone has the wave nature and is not connected with the temperature instability. The role of critical power in this case the critical charge density in the leader head plays, and besides the number of streamers is equal to  $N_{str} = Q/q_0$  at the inculcate into the gap of charge  $Q$ .

### 3 Physical picture of leader propagation

Characteristic peculiarity of propagation both positive and negative leaders is the essential influence of the space charge of the streamer zone. Formation of a new leader head and its moving is caused owing to the self-influence processes and the ability of streamers to propagate in the region of the weakly field.

#### 3.1 Pinching effect in the leader front

As the mechanism of a pinch usually the low-temperature overheating instability is suggested [1]. However the time of pinching in this case is determined by the thermal processes. A next physical picture of the pinch not connected with the thermal processes may be suggested. Because of the nonuniform distribution of the electric field at the leader front the distribution of charges created in this field turn out to be also nonuniformity, i.e. the nonuniform distribution of conductivity  $\sigma(r, x) = e \mu n(r, x)$  is formed. The axis region of the head has the greater conductivity. Therefore the electric field is ousted from there forward quickly than the from periphery regions. The ousting time of field is determined by the Maxwell

relaxation time of charges  $\tau_M \sim 1/4\pi\sigma$ . Thus the cross electric field is created, pinching the charges into the axis region and leading to the pinch of the head. The velocity of pinching is determined by the degree of non-uniformity of conductivity and Maxwell relaxation time  $\tau_M$ .

#### 3.2 Plasma clots formation

It is known [1], that at the front of the streamer zone of negative leader the plasma clots are formed, from which in the opposite direction the positive volume leader is propagated. A physical mechanism of the plasma clot formation is not clear. Lower the physical mechanism of plasma clot formation is suggested. It is known that the streamers starting out of the leader tip are connected with the leader head galvanically up to the distance approximately of few centimeters. A maximum length is determined by the disintegration time of the plasma in the old parts of the streamer channel  $l_{max} = v_0/\nu$ ,  $\nu = 1/\tau$  is the electron detachment frequency. This time in air is equal to  $\tau \sim 10^{-10}$  sec. A further propagation of the streamers take place at the absence of the galvanic connection with the leader tip. The losses of the energy are compensated at the expense of the external electric field energy. The plasma formations with the length of approximately 1 cm are polarized in the electric field. A force acting on the dipoles in the nonuniform electric field equal to

$$\vec{F} = \vec{p} \nabla \cdot \vec{E},$$

where  $\vec{p} = q \vec{l}$  is the dipole moment,  $\vec{E}$  is the electric field.

Hence it follows that the plasma dipoles draw in the strong field region, i.e. the focusing of dipoles take place. Note that the formation of plasma clot not depends on the polarity of leader and take place also in a positive leader.

#### 3.3 Stepped leader propagation mechanism

A continuous or stepped propagation of a leader to be take place in the dependence on the polarity and the humidity. A negative leader propagates only in the stepped form. A positive leader may to propagate both continuous and stepped forms.

Two forms of the stepped propagation of positive leader may be suggested. The first of these is connected with the feeding difficulties of the leader channel, and the second with the formation of plasma clot at the front of streamer zone, analogically to the negative leader. In the first case the time pause between the steps or the flashing of the leader channel is not connected with the length of the streamer zone and the velocity of the leader and not has a periodic character. In the second case the pause time between the steps by the velocity of the leader and the length of streamer zone is determined. This it seems leads to the decrease of the time interval between the steps when the leader approaches to the ground. A schematic picture of stepped propagation of a leader is presented in fig. 1.

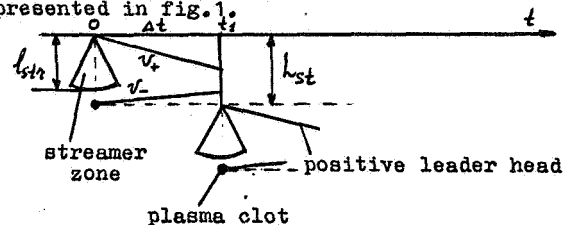


Fig. 1

It is seen from fig.1 that the pause time between the steps depends on the velocities of the positive  $V_+$  and negative  $V_-$  leaders and the streamer zone length  $l_{st}$ . Effective velocity of the stepped leader propagation or the mean leader velocity is determined as the

$$v_{eff} = \frac{H}{t} = \frac{N L_{st}}{N \Delta t} \approx \frac{L_{st}}{\Delta t}, \quad (11)$$

where  $H$  is the gap length,  $t$  is the full time of leader propagation,  $N$  is the number of steps. As it follows from (11) at the  $\Delta t \approx \text{const}$  the effective velocity of stepped leader grows with the increasing of streamer zone length.

#### 4 Optimal parameters of leader

A stability propagation of a leader is possible at the establishment of balance between the processes in the channel, leader head and streamer zone (Fig.2). In particular, a

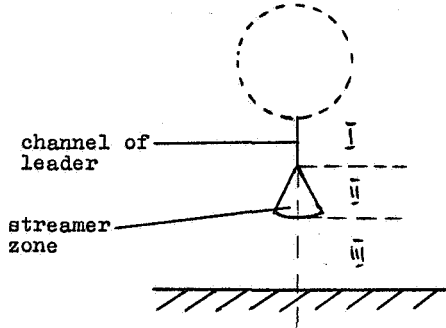


Fig.2

full current flowing in each these regions must be the same. In a channel the current is determined in the main by the conduction current

$$i_c = \sigma E_c \pi r_c^2, \quad (12)$$

where  $r_c$  is the channel radius,  $\sigma$  is the conductivity. In a streamer zone the displacement current caused by the moving of charges flows

$$i_s = q \cdot v_l, \quad (13)$$

where  $q$  is the charge per unit length,  $v_l$  is the leader velocity. Finally at the front of streamer zone the "clean" displacement current, not connected with the charges moving takes place

$$i_j = \epsilon_0 \frac{\partial E}{\partial t} \cdot S, \quad (14)$$

where  $S$  is the area of streamer zone front. Note that  $q \sim E_s \cdot l_s$  and  $S \sim l_s^2$ , where  $E_s$  is the electric field in the streamer zone,  $l_s$  is the streamer zone length. Hence it follows the correlation

$$j_h \cdot r_h^2 \sim \epsilon_0 E_s l_s v_l \sim \epsilon_0 \frac{\partial E}{\partial t} \cdot v_l \cdot l_s^2, \quad (15)$$

where  $\partial E / \partial t$  is the derivative of electric field along the propagation direction of leader at the streamer zone front,  $j_h$  is the current density in the leader head,  $r_h$  is the radius of leader head. Note that the electric field in the streamer zone is kept along the all its length [2]. A pinch of leader head takes place at the reaching of critical power  $W_{cr} = j_h E_h^2 = \sigma_h E_h^2$ , where  $\sigma_h = j_h \cdot \rho_h = \text{const}$ . Since  $E_h \sim r_h$ , then  $j_h \sim r_h$ . Then from (15) we obtain the correlation  $r_h^2 \sim l_s \cdot v_l$ .

#### 4.1 The velocity of leader

The velocity of leader analogically to the velocity of streamers is determined by the effective ionization coefficient  $\alpha_{eff}$  before the head:

$$v_l = v_0 + \alpha_{eff} \cdot v_0 \cdot r_h \quad (16)$$

It is seen from (16), that at the  $\alpha_{eff} r_h \ll 1$  the velocity of leader is constant. Therefore  $l_s \sim r_h^2$ . The current in the head  $i_h \sim r_h^2 \sim l_s$ , where  $j_h \sim E_s \cdot l_s$  is the potential of leader head. At the  $\alpha_{eff} r_h \gg 1$   $v \sim \alpha_{eff} \cdot v_0 \cdot r_h$  and the streamer zone length is proportional to the square of head radius  $l_s \sim r_h^2$  ( $l_s / r_h^2 = \text{const}$ ). For the current in the leader head we obtain

$$i_h \sim r_h^2 \sim l_s^2 \sim v_l^2 \quad (17)$$

Hence it follows that the current grows with the increase of potential of leader head as

$$i_h \sim \varphi_c^{3/2}$$

and the velocity

$$v_l \sim i_h^{2/3} \sim \varphi_c^{1/3}$$

The velocity dependence on the current flowing across the leader head is presented in fig.3.

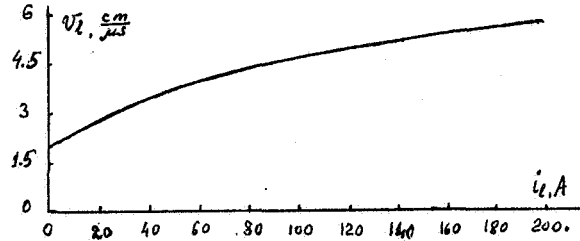


Fig.3

#### 4.2 The streamer zone length

From (15) the equation for the determining of the dependence of streamer zone length on the gap length may be obtained:

$$\epsilon_0 \frac{\partial E}{\partial t} (l_s, H) \cdot v_l \cdot l_s^2 = q \cdot v_l \quad (18)$$

It is known that the electric field intensity is determined by the equation

$$E = \text{grad } \varphi$$

where  $\varphi = \varphi_1 + \varphi_2$  is the sum of the potential  $\varphi_1$  created by the electrode and the potential  $\varphi_2$  created by the space charge of the streamer zone.

The potential  $\varphi$  is the solution of Poisson equation  $\Delta \varphi = 4\pi \rho$  and may be obtained from the integral equation

$$\varphi = \iint \frac{\rho dS}{\epsilon_0 R} + \iiint \frac{\rho(r) dv}{\epsilon_0 R} \quad (19)$$

where  $dS = R^2 \sin \theta \cdot d\theta \cdot d\alpha$ ,  $R$  is the radius of electrode,  $\rho = e \cdot E_s / 4\pi$  is the surface charge density,  $E_s$  is the electric field on the electrode surface,  $R$  is the distance between the element of charge and the point of observing,  $dv = r^2 dr \sin \theta \cdot d\theta \cdot d\alpha$ ,  $\theta$  is the angle of integration.

The distribution of the charge density along the radius of streamer zone may be determined on the known electric field from the equation

$$\text{div } E = 4\pi \rho \quad (20)$$

Since the electric field intensity in the streamer zone is not changed along the all

its length [3] then from (20) we obtaine

$$\rho(r) = \frac{\rho_0 \cdot r_0}{r}, \quad (21)$$

where  $E_A = \rho_0 \cdot r_0 / k$  is the electric field near the leader head. Integrals (19) may be calculated analytically. Calculating the derivative  $\partial E / \partial x$  and substituting its to the equation (18) the equation for determining of the dependence  $l_{st} = f(H)$  may be obtained. Fig. 4 shows the calculated value of streamer zone length  $l_{st}$  as a function of gap length  $H$ .

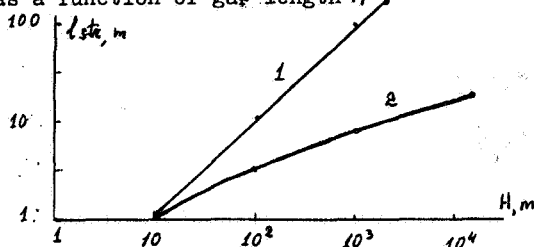


Fig. 4

It is found that when the influence of electrode is not take into account the streamer zone length grows linearly to the gap length (curve 1). The streamer zone length is saturated when the influence of electrode is take into account (curve 2).

### 5 Fractal nature of lightning

It is known that even at the identical external conditions (gap geometry, atmosphere conditions, applied voltage) the characteristics of discharge behave accidentally. In particular the trajectory of lightning represents something crooked line changing from case to case. However it may be showed that the channel dynamics is described by the deterministic equations, i.e. the chance picture of trajectory is determined by the internal properties of leader, but not the external chance influences. A series of quantitative characteristics may be introduced which allow to differ the one picture of discharge from other. These are fractal dimensions. So, the channel length of lightning  $L$  measured by the put on the sections with the length  $\epsilon$  depend on the minimal length  $L_{min}$  by the degree manner

$$L(\epsilon) = \epsilon \left( \frac{L_{min}}{\epsilon} \right)^D,$$

where  $D$  is the fractal dimension, changing in the interval  $1 < D < 2$ . Fractal dimension  $D$  change at the changing of characteristic length of straight sections of channel and its orientation angle. In one's turn this characteristic length is connected with the streamer zone length that determines the parameters of the electromagnetic radiation of lightning. Therefore the amplitude-frequency characteristics of lightning radiation also possess by the fractal nature. This property may be used for the re-establishment of the channel parameters on the characteristics of the electromagnetic radiation.

A growth of streamer zone of leader may be described also on the basis of the growth law of branching physical system, possessing by the fractal properties. The fractal dimension  $D$  of the streamer zone may be determined by means of calculation the number of streamers branches (or the streamers heads), keeping in the sphere with radius  $R$  at different  $R$ :

$$N(R) = \int \rho(r) \cdot r^{d-1} \cdot dr = R^D, \quad (22)$$

where  $\rho(r)$  is the density distribution of streamers head,  $d$  is the space dimension. Hence it follows that the charge density distribution satisfies the law

$$\rho(r) \sim r^{D-d} \quad (23)$$

It is known that the electric field intensity in the streamer zone is kepted along the its length [2]. From the Poisson equation  $\text{div } E = 4\pi \rho$  we obtaine, that this take place at the  $\rho(r) \sim r^{-1}$ , i.e. at the  $D = 2$  in three-dimensional space. Therefore the streamer zone represent the fractal structure with the dimension  $D = 2$ .

### 6 Discussion and conclusion

The dependences obtained above may be used at the calculating of leader parameters in lightning. Using the relations (17) we can evaluate the streamer zone length  $l_{st}$  or the leader head potential  $\mathcal{U}_h$  of lightning. It is known [3] that the streamer zone length is equal to  $l_{st} = 1$  m and  $\mathcal{U}_h = 500$  kV in the laboratory gaps at the leader current  $i_e = 1$  A. A characteristic current of leader in lightning is equal to  $i_e = 100$  A [4]. Hence we obtain that the characteristic streamer zone length is equal to  $l_{st} = 20$  m, and the potential of leader head  $\mathcal{U}_h = 10$  MV, that agrees with the experimental observations.

In table 1 some values of current in leader  $i_e$ , radius of leader  $r_A$ , potential of leader head  $\mathcal{U}_h$ , velocity of leader  $v_e$ , streamer zone length  $l_{st}$  for different gap length  $H$  are presented. At the current in leader  $i_e = 1$  A the values of parameters are presented from the laboratory experiments in long air gap.

Table 1

$i_e, A$	$r_A, mm$	$\mathcal{U}_h, MV$	$v_e, cm/\mu s$	$l_{st}, m$
1	1	0.5	2	1
10	1.1	2.4	2.2	4.8
100	2.3	10.6	4.6	21.2

It is seen from table that the calculated values agree with the experimental data obtained for lightning. Added relations between the parameters are related to the leader stage of discharge. However these determine also the characteristics of discharge in the return stroke stage. So, streamer zone length determines a duration of return stroke current, connected with the neutralization of space charge around the channel. As was shown above, streamer zone length is saturated at the growth of gap length. This explains the slow change of the duration of return stroke current from case to case. Note that streamer zone length determines also the amplitude value of return stroke current.

The obtained correlations may be used at the determining of such parameters of lightning as the potential of cloud, current and space charge neutralized by return stroke on the characteristics its electromagnetic radiation.

### References

1. E. M. Bazelyan, I. M. Razansky, Spark discharge in air. Novosibirsk, Nauka, 1988.
2. E. N. Chernov, A. V. Lupeiko, N. I. Petrov, Electric field measurements in long air spark using a Pockels device. All-Union Conf. on Physics of Gas discharge. Proceedings of Conf. Omsk, 1990, p. 192-193.
3. Les Renardieres Group: Positive discharge in long gaps. Electra, 1977, v. 53, pp. 31-153.
4. M. A. Uman, Lightning. New York: Mc-Hill, 1969.



# Poster Papers Meteorology

N91-32724

ON CHARGING OF SNOW PARTICLES IN BLIZZARD

HISASHI SHIO

Department of Physics  
Hokkaido University of Education  
Iwamizawa 068: JAPAN

ABSTRACT

We investigated the causes of the charge polarity on blizzard consisted of the fractured snow crystals and the ice particles. As a result, the charging phenomena showed the characteristics on blizzard as follows:

- i) In the case of the blizzard with snowfall the fractured snow particles drifting at near the surface of snow field (Lower area: Height 0.3 m) had positive charge, while those drifting at higher area (Height 2 m) from the surface of snow field had negative charge. However during the series of blizzard two kinds of particles positively and negatively charged were collected in equal amounts in Faraday Cage. It may be considered that a snow crystal with electrically neutral properties were separated into two kinds of snow flakes charged positively and negatively by destroying of snow crystal.
- ii) In the case of the blizzard consisted of irregularly formal ice drops generated by peeling off the hardened snow field, the charge polarity on irregularly formal ice drops salting over the snow field was particularly controlled by the crystallographic characteristics on the surface of the snow field hardened by the powerful wind pressure.

## INTRODUCTION

Magono et al. [2] has reported that the charge polarity of particles was dependent on the vertical distance from snow fields according to measurements of the electrostatic potential gradient in blizzard without snowfall at Mt. Teine (Height: 1023 m). Latham et al. [3] explained the charging phenomena in blizzard with the temperature gradient effect which was presented in Latham and Mason [1]. Latham [4] also investigated the vertical electric field strength near snow cornice on Bridger Ridge (Height: 2590 m), and suggested that the appropriated condition to the development of cornice is due to the electrostatic force being generated between the snow field and the charged snow particles under the comparatively low velocities of drifting snow particles. Shio et al. [5,6], and Shio [7,8] pointed out shortcoming of the temperature gradient effect in relation to the frictional phenomena, and suggested that the polarity on frictional electrification, is concerned with the different characteristics on crystallization, and the hardness effect of specimen.

In this paper, in order to observe the relation between the crystallographic properties on snow field and the electrostatic phenomena in blizzard the measurements of the charging on snow particles were carried out with Faraday Cage and Wells and Gerke's Horizontal Field Method [9]. While, snow particles were collected by Replica Method, in the most windy season we carried out the measurements at Sugatami area of Mt. Asahidake (Height: 1970 m), in the lowest

temperature season being colder than  $-30^{\circ}\text{C}$  at Tomamu area.

## RESULTS AND DISCUSSION

During those observations the charging tendency may be divided into two groups, namely whether the snowfall was or not in blizzard.

### BLIZZARD WITH SNOWFALL

An example of this condition is shown in Fig. 1. Estimates have been made of the charging on particles drifting in the higher area in the blizzard during from 12 h 48 min to 12 h 55 min, while in the lower area during from 12 h 56 min to 13 h 04 min. The charging curve became repeatedly to be beyond the value which could be measured by using the static potential electrometer as shown by the arrows E, and then, Faraday Cage was earthed. At 12 h 49 min and 12 h 55 min, the charging curve suddenly changed from negative sign to positive sign, while at 13 h 1 min the reversal tendency on comparing the result as above appeared. Fig. 2 shows an example of the trajectory of particles moving unnaturally into the Faraday Cage at 12 h 49 min and 12 h 55 min. At those times the electrometer shows the inversion on sign of charge. It is estimated that those particles had acquired a strong positive charge and were absorbed into Faraday Cage by pulling of the strong electrostatic forces induced by the negative charge accumulated in the Faraday Cage. Fig. 3 shows the charge densities against the measuring periods. Since the ambient temperature being  $-19^{\circ}\text{C}$  is always about  $-2^{\circ}\text{C}$  colder

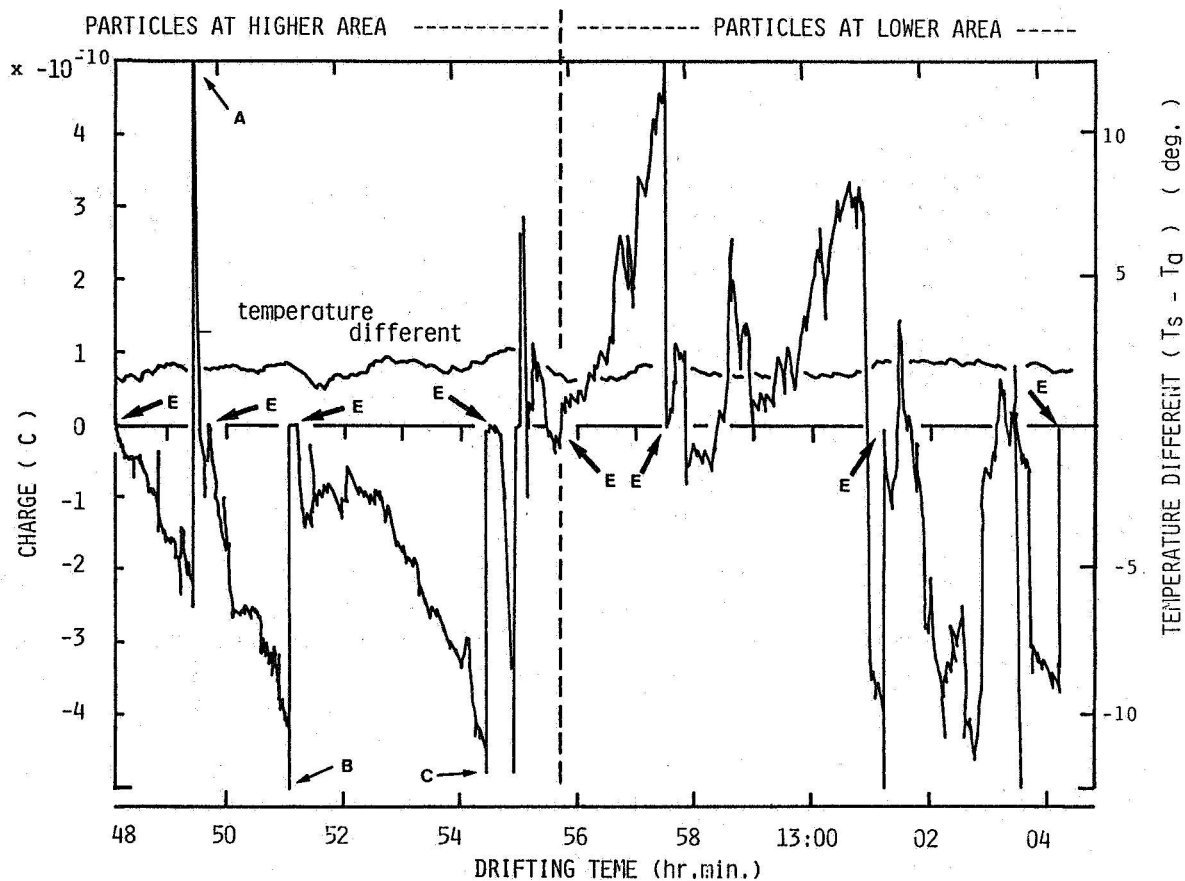


Fig.1. Charge against drifting time. Higher area: 12h 48min to 12h 55min. Lower area: 12h 55min 30sec to 13h 4min 10sec. Arrows A, B and C show the points where the stored charge is over the regions measured possibly using the electrometer, then, it was earthed as shown by arrow E.

ORIGINAL PAGE IS  
OF POOR QUALITY



Fig.2. Trajectory of particles moving unnaturally into Faraday Cage.

than at the point of about 0.1 m above the snow field, same temperatures of the

drifting particles is below that of the snow field. On the basis of the temperature gradi-

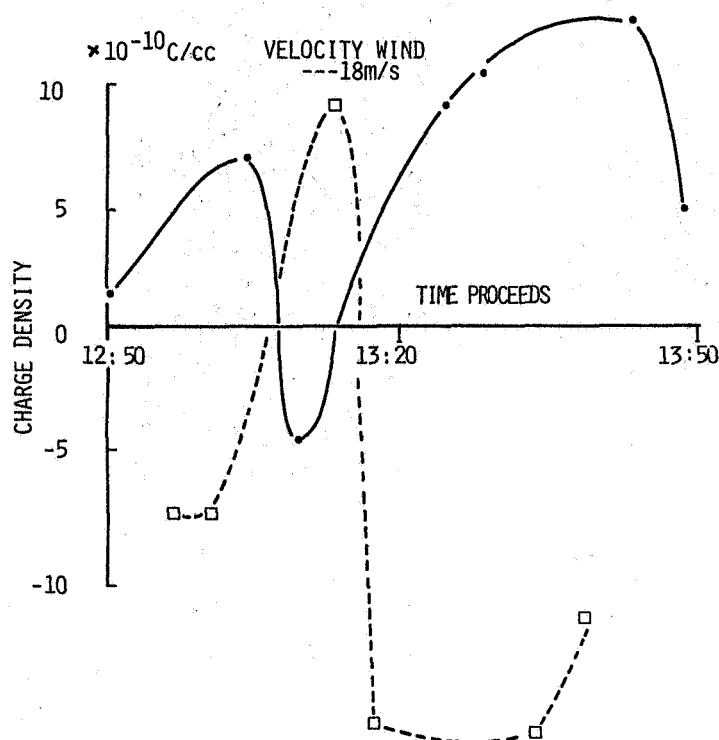


Fig.3. Charge densities against drifting time. Open squares: Charging at higher area. Solid circles: Charging at lower area.

ent the particles should always be positively charged regardless of the height above snow field. However fig. 3 does not show its tendency. The wind velocity was 18 m/s at 10 m above the snow field and 2 m/s at 0.3 m. After measuring of charge the volume of the particles precipitated in Faraday Cage was accurately measured by melting of it. The charged densities show the accumulated charge vs. the particles precipitated in Faraday Cage during 8 min interval. It shows that the snow particles have negative charge at higher area and positive charge in the lower area. The sign of charge densities was dependent upon the vertical distances from snow field except in the

period between 13 h 01 min to 13 h 15 min when the charging curve was changed with the change of wind direction.

Since Yoshida [10] and Magono et al [2] reported the relation between the charging ice particles and their size, in order to examine how the charge polarity depends on the size of snow flakes we investigated the correlation frequency of the sign of charge on snow flakes against those size using Wells and Gerke's method. The results are shown in Fig. 4 and Fig. 5. Fig. 4 shows a trajectory of a charged particles falling in the parallel electric field of D.C. and A.C. Fig. 5 shows that the charge on par-

ORIGINAL PAGE IS  
OF POOR QUALITY

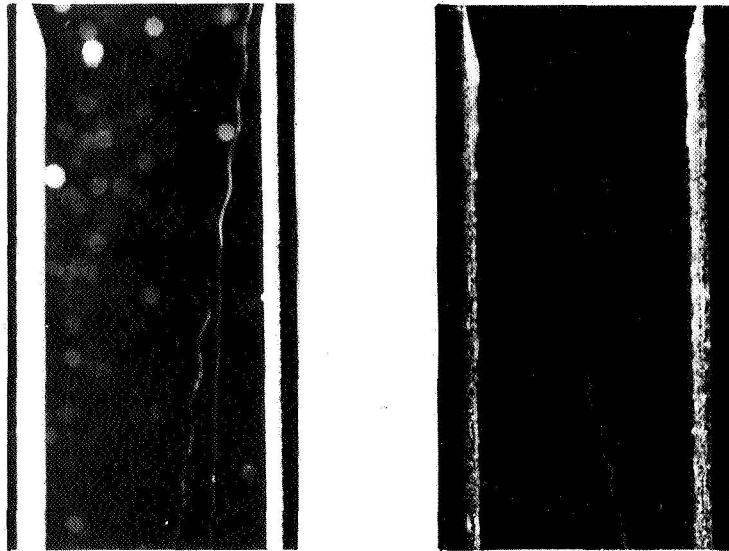


Fig.4. Trajectory of the moving particles with positive charge in electrostatic field with A.C and D.C. electric power. The destroyed particle was made by blowing off the fresh snow with compressed air.

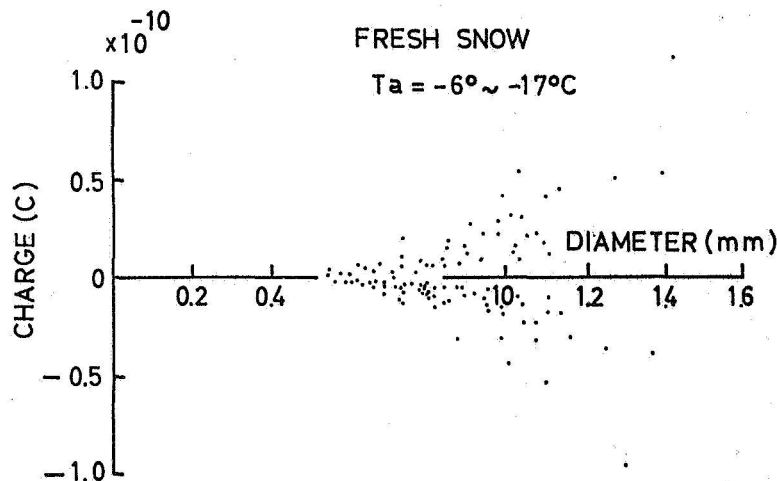


Fig.5 Charge of the destroyed particle against its size.

ticles against their diameters distributed uniformly with in the range smaller than  $\pm 10^{-10}$  C. The size of the particle which was fixed on slide glass by the replica method are shown by green diameter. The charge on the the particle was uniformly distributed in the positive and negative range.

Latham [ 4 ] reported the charge per one crystal was  $- 4 \times 10^{-14}$  C , which is close to the value of the maximum charge deduced by Latham et al. [ 3 ]. On comparing the result as above, its result shows greater quantity of the charge per one crystal. We could not confirmed the

strong relation between the charge polarity and the size of the particle made by destroying of the fresh snow. However, the charge polarity

on the drifting particle in blizzard was a function of distance from the surface of snow field.

# BLIZZARDS WITH IRREGULAR ICE DROPS GENERATED BY PEELING OF THE HARDENED SURFACE OF SNOW FIELDS

An example of observation is shown in Fig. 6 and 7. Fig. 6 shows the data obtained in daytime, fig. 7 is data after sundown. The wind velocity-

ties were 16 to 17 m/s at 10 m, and 5 to 6 m/s at 0.3 m above the surface of snow field. In the daytime the particle always acquired negative charge regardless of height from the surface of snow field. However, after sundown the direction of wind was suddenly changed from wind-

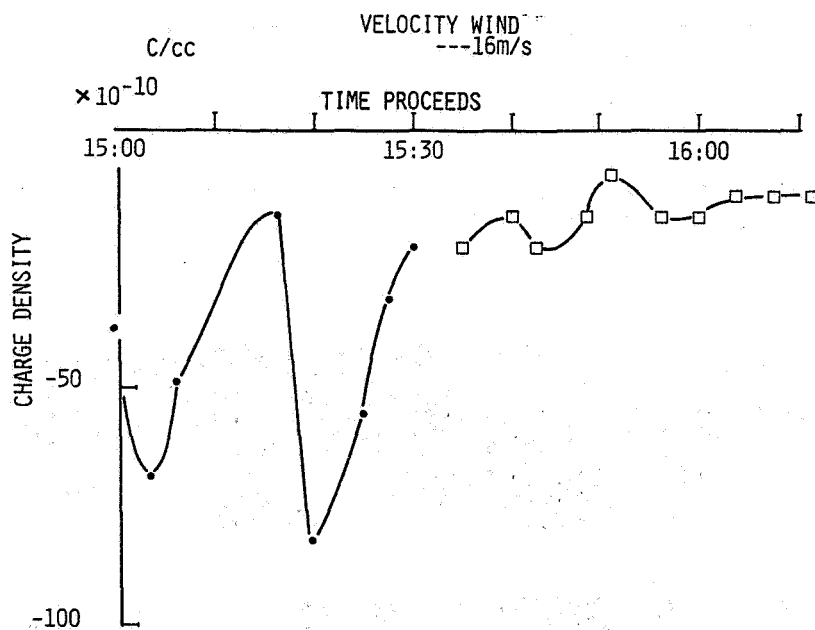


Fig. 6. Charge densities on particle collected in blizzard without snowfall in daytime.

ard to leeward and simultaneously the charge was changed from negative to positive regardless of height from the surface of snow field.

In order to investigate the relation between the inversion of sign of charge and the change of direction of wind,

we observed about the crystallographic characteristics of ice plate made of snow lumps collected from the various snow field at the windward areas and at the leeward area under polarimicroscope. The result is shown in Fig. 8. It appears that the hardened

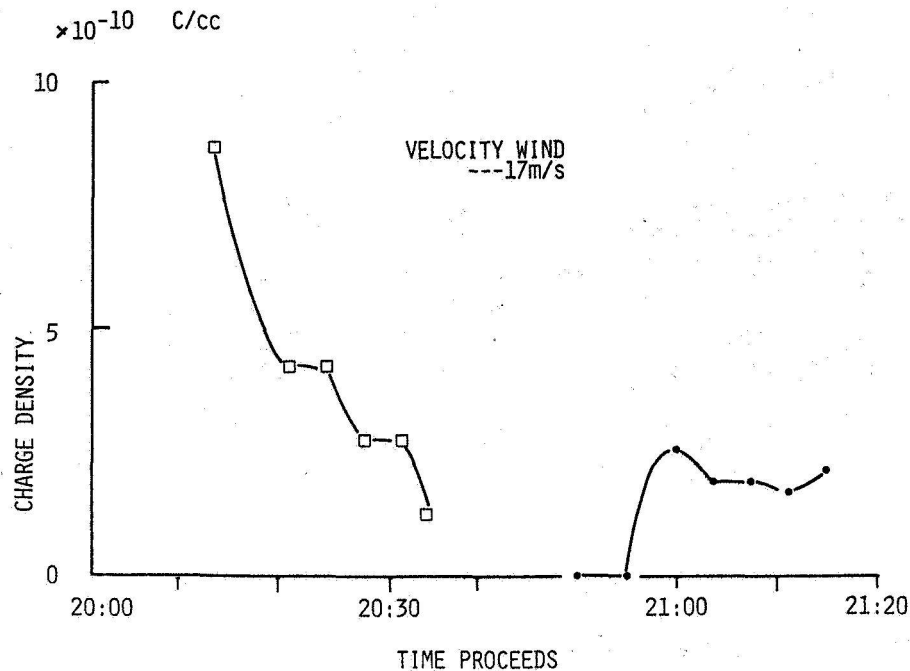


Fig. 7. Charge densities on particle collected in blizzard without snowfall after sundown.

ORIGINAL PAGE IS  
OF POOR QUALITY

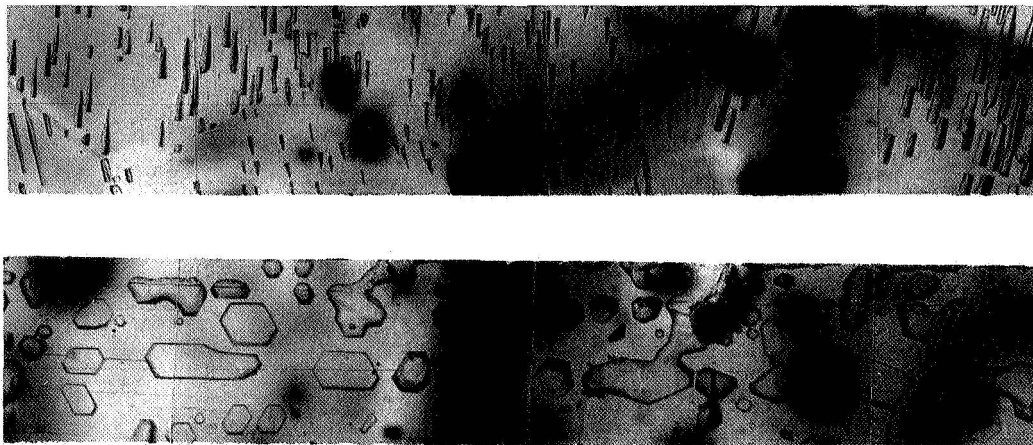


Fig. 8. Crystal orientation of hardened snow field determined by pits. The upper photo. is surface of hardened snow field oriented nearly with prism plane, collected at windward. The lower photo. shows its surface with nearly basal plane, collected at leeward.

snow field surface with similar crystallographic orientation was centered on a specific area. In order to determine



between the charge polarity on ice particle generated by peeling of the hardened snow field and the anisotropy of the peeled surface of snow field, the charge on ice particle peeled from the snow lump collected at the hardened snow fields by compressor was measured using Faraday Cage. The result is shown in Fig. 9. As the result, the ice particle peeled from the surface with an angle crys-

tallographic orintation of  $0^{\circ}$  to  $30^{\circ}$  against the C-axis acquired positive charge, the particle with an angle of  $60^{\circ}$  to  $90^{\circ}$  against the C-axis acquired negative charge at ambient temperature below  $-7^{\circ}\text{C}$ . At temperature above  $-7^{\circ}\text{C}$  both groups of particle were always electrified positively.

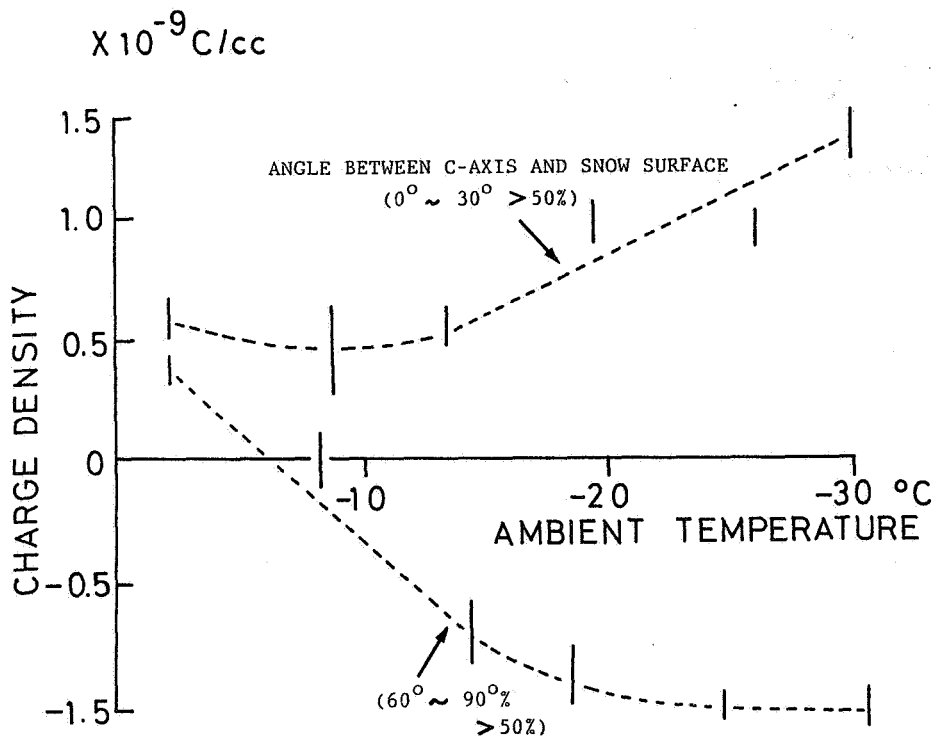


Fig. 9. In room experiment, by compressor the charge on ice particle made by peeling of the hardened snow field against anisotropy of surface of snow field.

#### CONCLUDING REMARKS

The result may be summarized as follows:

i) In the case of blizzard with fresh snow the charging phenomena of fractured snow flake were dependent on the destruction effect of fresh snow crystal.

Whether the snow flake were generated by collision with each other or by friction of fresh snow crystal on the surface of snow field.

ii) In the case of blizzard without fresh snow at ambient temperature below  $-7^{\circ}\text{C}$  the

charge polarity was dependent on the anisotropy of the hardened surface of snow field. At temperature above  $-7^{\circ}\text{C}$  the

fractured irregular shapeless flake was positively charged regardless of the anisotropy of surface of snow field.

#### REFERENCES

- 1) Latham, J., and Mason, B.  
J.Pro.Soc.A. 280. (1961) 523
- 2) Magono, C, and Sakurai, K.  
J.Meteor.Soc.Japan. 41. (1963) 211
- 3) Latham, J., and Stow, C. Quar.  
J.R.Meteor.Soc. 93. (1967) 55
- 4) Latham, J. J.Glaci. 19. (1970) 375
- 5) Shio, H., and Magono, C.  
Planetary Electrodynamics. Vol. 1. (1969) 309
- 6) ——— J.Meteor.Soc.Japan. 50. (1972) 159
- 7) Shio, H., J.Meteor.Soc., Japan. (1978) 56. (1978) 489
- 8) ———, Pro. Atmospheric Electricity (1983) 229
- 9) Wells, P.V. and Gerke, R.H., J.Amer.Chem.Soc., 41 (1919) 312
- 10) Yosida, Z., Low Temp. Sci., 1 (1944) 149

**On the Interactions of Positive Streamers With Hydrometeors**  
*by T. Verma*

**No paper available.**

# **Poster Papers**

## **P-Static**

**Development of a Portable P-Static Simulation Test Set**  
*by W. Devereux*

**No paper available.**

**Poster Papers  
Aerospace Vehicles  
Test Criteria and Techniques**

A SIMULATED LIGHTNING EFFECTS TEST FACILITY  
FOR TESTING LIVE AND INERT MISSILES AND  
COMPONENTS

Jeffery D. Craven, James A. Knaur, and Truman W. Moore, Jr.  
Dept. of the Army, Redstone Technical Test Center, Redstone Arsenal, Al.

Thomas H. Shumpert  
Auburn University, Auburn, Al.

ABSTRACT

Details of a simulated lightning effects test facility for testing live and inert missiles, motors, and explosive components is described. The test facility is designed to simulate the high current, continuing current, and high rate-of-rise current components of an idealized direct strike lightning waveform.

The Lightning Test Facility has been in operation since May, 1988, and consists of three separate capacitor banks used to produce the lightning test components, a permanently fixed, large, steel safety cage for retaining the item under test should it be ignited during testing, an earth covered bunker housing the control/equipment room, a charge/discharge building containing the charging/discharging switching, a remotely located blockhouse from which the test personnel control hazardous testing, and interconnecting cables.

I. INTRODUCTION

One of the problems associated with simulated lightning testing of inerted missiles and inerted explosive items containing electrically initiated explosive trains is to determine the interaction of the propellants and explosives with the simulated lightning environment. There have been concerns raised in the past that propellants and explosive materials may be susceptible to the indirect effects (radiated fields) of lightning. The large missile lightning test facility was designed and built to simulate lightning strikes on missiles and other items which contain less than 100 pounds of detonable material up to several thousand pounds of propellant materials. The primary objective of testing at this facility is to determine whether a hazard exists to personnel or area equipment should the Unit Under Test (UUT) be struck by lightning. These tests may also be conducted on shipping containers containing live missiles to determine if hazards exist in stockpile or shipping configurations. The secondary objective of this testing is to determine whether the UUT suffers major damage which prevents its use or which requires extensive repairs before it can be used.

II. IDEALIZED DIRECT STRIKE LIGHTNING WAVEFORM

The test facility is designed to simulate components A (high current), C (continuing current), and D (high  $\partial I/\partial t$ ) of the direct strike lightning idealized current test waveform shown in Figure 1 [1 and 2]. These

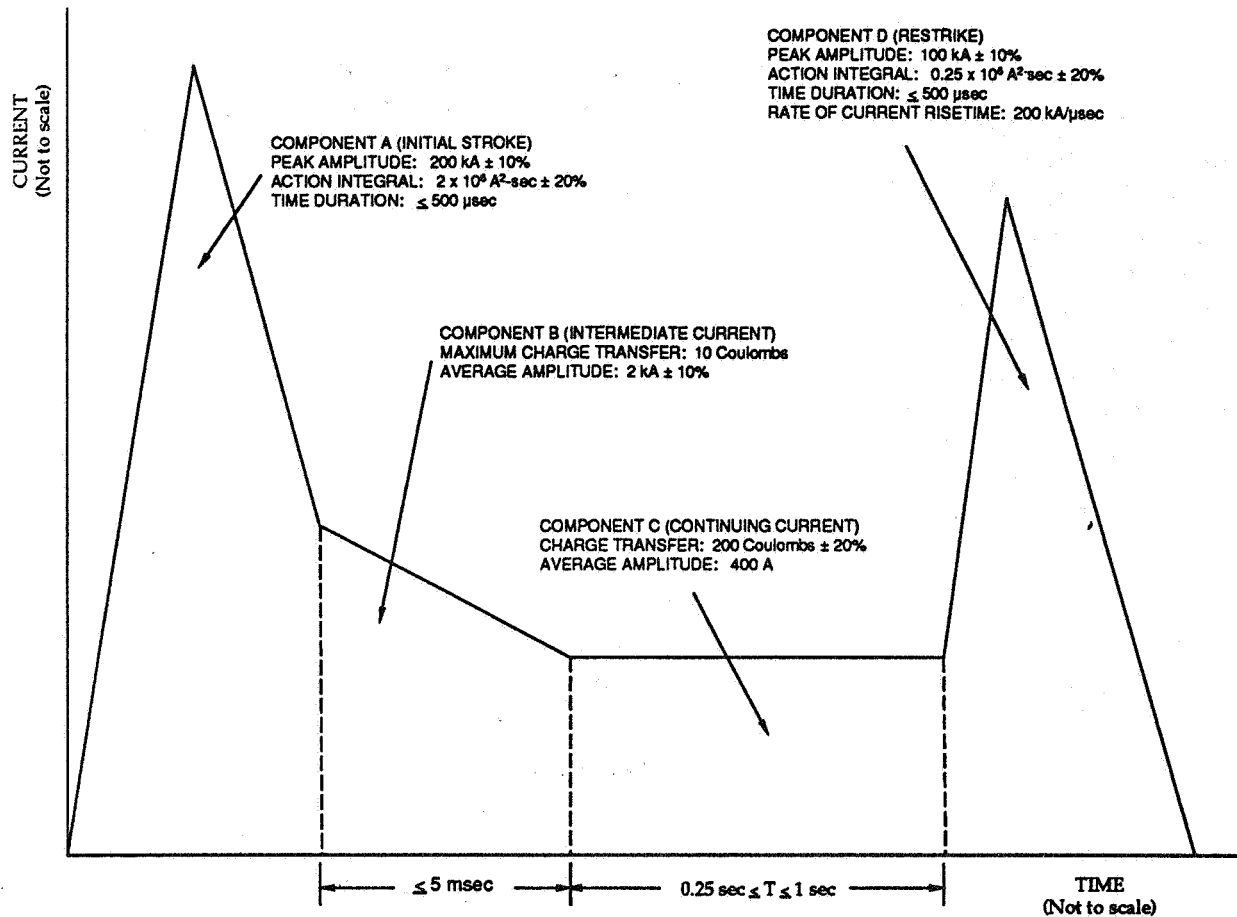


**Figure 1. Idealized Direct Strike Lightning Waveform.**

components are intended to reproduce the significant effects of the natural environment and are therefore independent of vehicle type or configuration. The idealized component specifications are as follows:

- |                                |  |
|--------------------------------|--|
| High Current:                  | Peak current = $200 \text{ kA} \pm 10\%$<br>Action integral, $\int I^2 dt = 2 \times 10^6 \text{ A}^2 \text{ sec} \pm 20\%$<br>Time duration $\leq 500 \mu\text{s}$  |
| Continuing Current:            | Charge transfer = $200 \text{ C} \pm 20\%$<br>Average amplitude = 400 A<br>Time duration: $0.25 \text{ sec} \leq T \leq 1 \text{ sec}$   |
| High $\partial I/\partial t$ : | Peak amplitude = $100 \text{ kA} \pm 10\%$<br>Action integral, $\int I^2 dt = 0.25 \times 10^6 \text{ A}^2 \text{ sec} \pm 20\%$<br>Current rate - of - rise = $2 \times 10^{11} \text{ A/sec} \pm 10\%$<br>Time duration $\leq 500 \mu\text{s}$ |



### III. DESCRIPTION OF THE TEST FACILITY

The test facility consists of three separate capacitor banks to produce the lightning test components, a permanently fixed large steel safety cage for retaining the unit under test should it be ignited during test, an earth covered bunker housing the control/equipment room, a charge/discharge building containing the charging/discharging switching, a remotely located blockhouse from which test personnel control hazardous testing, and interconnecting cables (see Figure 2). The safety cage is designed to retain large missiles should they become propulsive during test. A smaller, removable secondary cage can be installed inside the larger cage to retain smaller test items. The high current and continuing current components are normally simulated simultaneously in one test event, and the high  $\partial I/\partial t$  component is simulated in a separate test event (see Figures 3, 4, 5, and 6 for block diagrams of the systems).

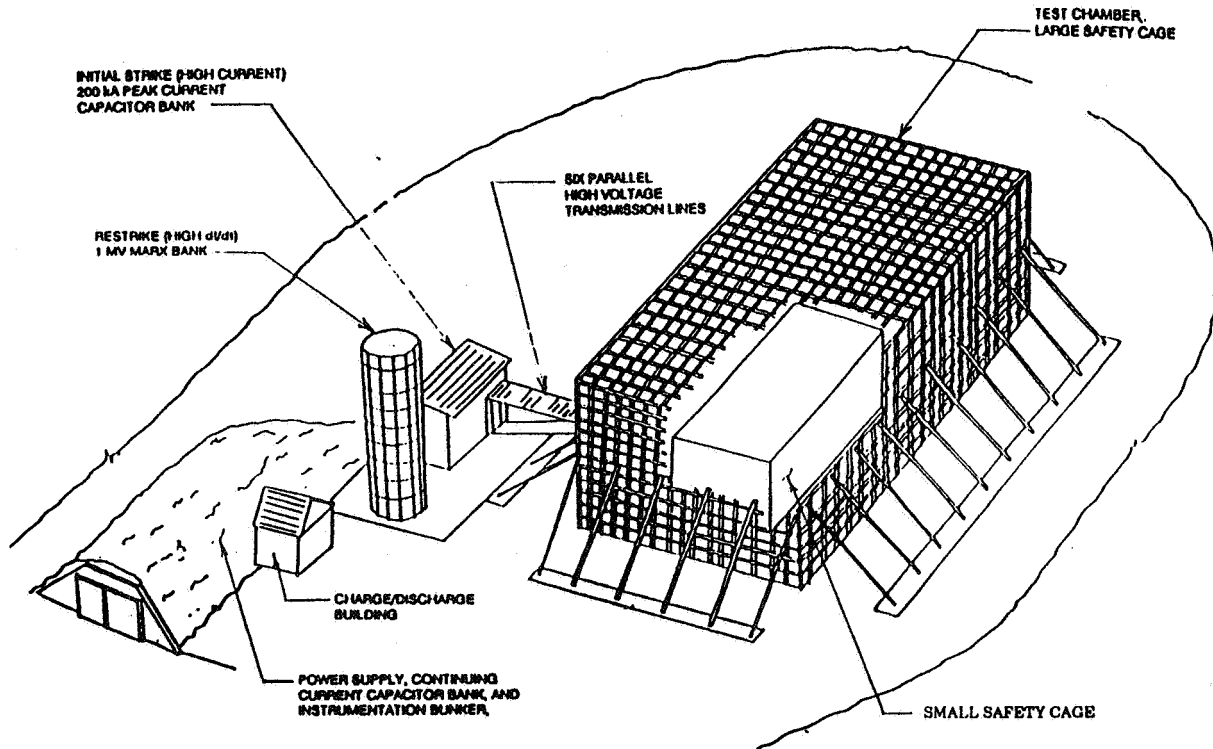
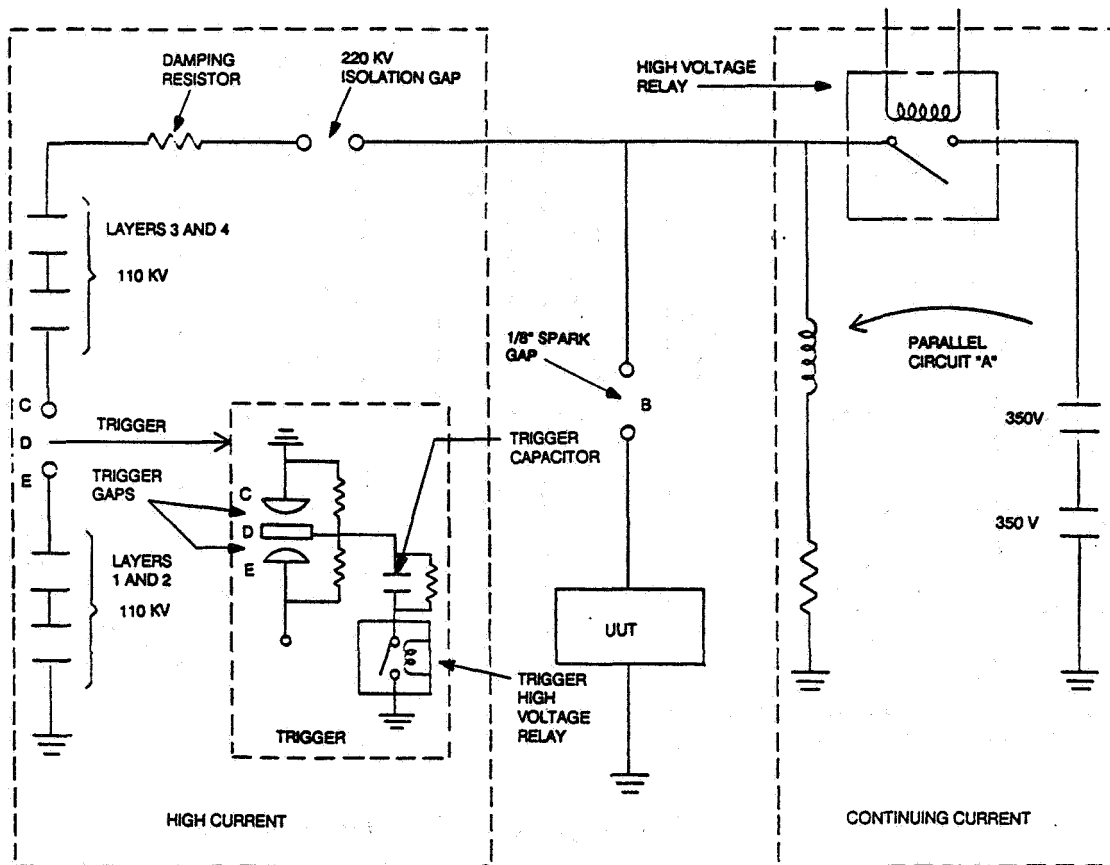


Figure 2. Test Facility Overview.

#### A. HIGH CURRENT SYSTEM

The high current system, Figure 4, consists of 480 capacitors each rated at 60 kV and 1.875  $\mu\text{F}$ . It is constructed in 4 layers with 120 capacitors in



- NOTES: 1. Charge each of the 480 capacitors in the high current bank,  $1.875 \mu\text{F}$  per capacitor, to 55 kV, and charge each of the 392 capacitors in the continuing current bank, approximately  $3000 \mu\text{F}$  per capacitor, to 400 V.
2. Activate the continuing current to start current flow in parallel circuit "A". 20 ms later the high current is activated. After the high current breaks down a path across B, an  $1/8"$  spark gap, the continuing current flows across the gap into the UUT.

**Figure 3. High Current/Continuing Current Abbreviated Schematic.**

parallel on each layer. Layers 1 and 2 are connected in series, as are layers 3 and 4. Each layer consists of 10 removable modules with 12 capacitors per module. Individual capacitors are fused in order to prevent the entire bank from dumping into a capacitor fault. Layers 1 and 2 and layers 3 and 4 are charged in parallel to approximately 110 kV and discharged in series to form a two-stage Marx bank with an output voltage of 220 kV. The bank is fired by a triggered spark gap located between layers 2 and 3. An output isolation gap is located above layer 4 to isolate the load from the bank. A damping resistor is also located above layer 4; it consists of three Franklin 60 kV, 240 kJ resistors connected in series, providing a total resistance of 0.63 ohms. The bank is charged by power supplies whose leads are routed through a switching system located in the Charge/Discharge Building, where charging

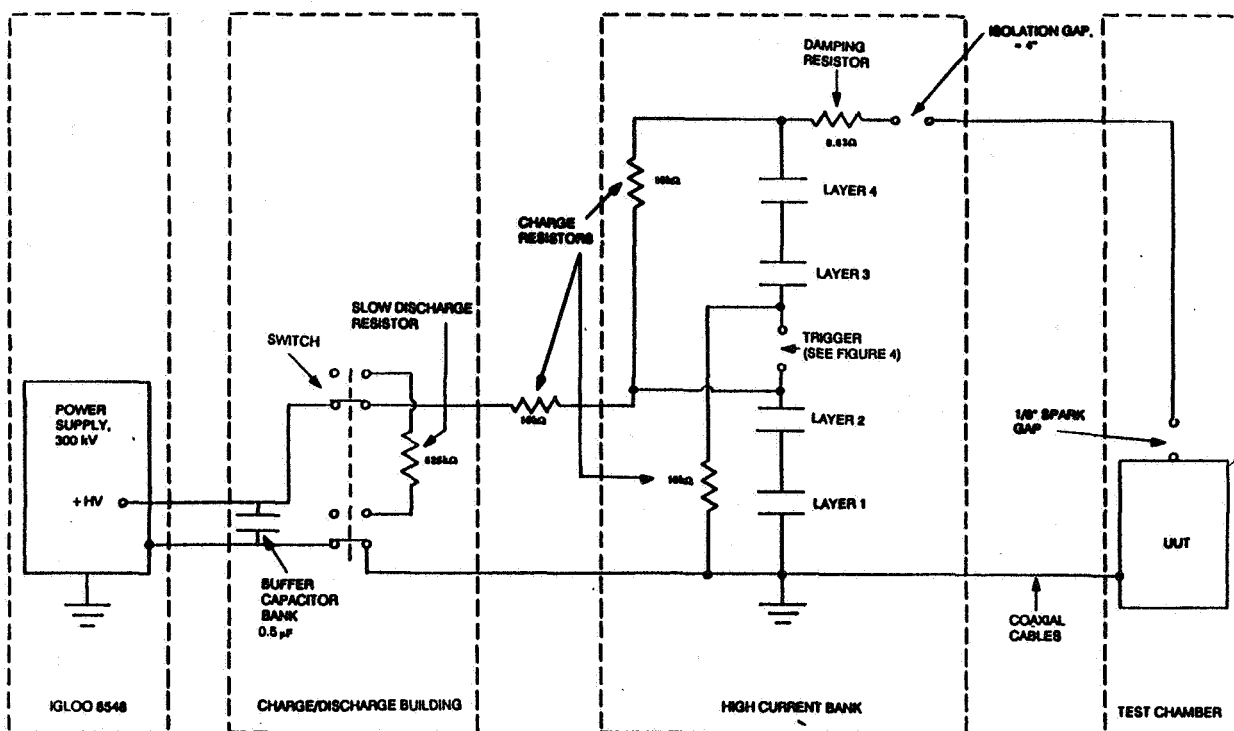


**Figure 4. High Current System Schematic.**

and slow discharging of the bank can be accomplished by remotely operated pneumatic switches.

The high current bank is fired by the triggered spark gap located between capacitor layer 2 and layer 3 about 20 ms after the continuing current circuit is activated. The trigger center electrode is pulled to ground potential by the high voltage relay causing an overvoltage of the other half of the gap.

The high current/continuing current transmission lines must penetrate the safety cages, which are electrically conductive and grounded, without loss of current. This transmission system consists of six large parallel high voltage cables connected to ten smaller high voltage cables. The large cables penetrate the large safety cage and the smaller cables penetrate the secondary safety cage. The smaller cables can be routed within the secondary safety cage to the desired test location on the UUT. The center conductors of these cables are tied to a tungsten probe tip. During testing for these current waveform components, the probe tip is placed one eighth inch from the test item, and the current return path to the generator is through the coax shields. During this test, the UUT must be isolated from the ground plane and safety cage walls to assure that the entire current load returns via the coax shields.

## B. CONTINUING CURRENT SYSTEM

The continuing current bank, Figure 5, consists of two layers of electrolytic capacitors connected in series. Each layer contains one hundred ninety six 450 V, 3000  $\mu\text{F}$  capacitors in parallel. The total measured capacitance is 0.37 F when charged to a nominal value of 750 V. This bank is charged with a 1000 V, 5 A power supply. The charge leads are connected to the capacitor bank via a charge relay mounted on the bank. This bank is fired with a high voltage relay, triggered by a pneumatic switch, which triggers a high voltage relay to fire the high current bank. The current flows via connecting cables to the high current bank coaxial cables and thence to the UUT. An 8 mH inductive parallel circuit at the load stores the continuing current energy until the high current bank discharges and ionizes the air at the spark gap. This small, approximately 1/8 inch gap isolates the current from the UUT. After approximately 20 ms, the high current bank is fired and arcs across this gap, thus allowing the continuing current to flow from the parallel circuit to the UUT. Slow discharging can be accomplished by manually closing a switch on the bank, which places a large resistive load on the capacitors.

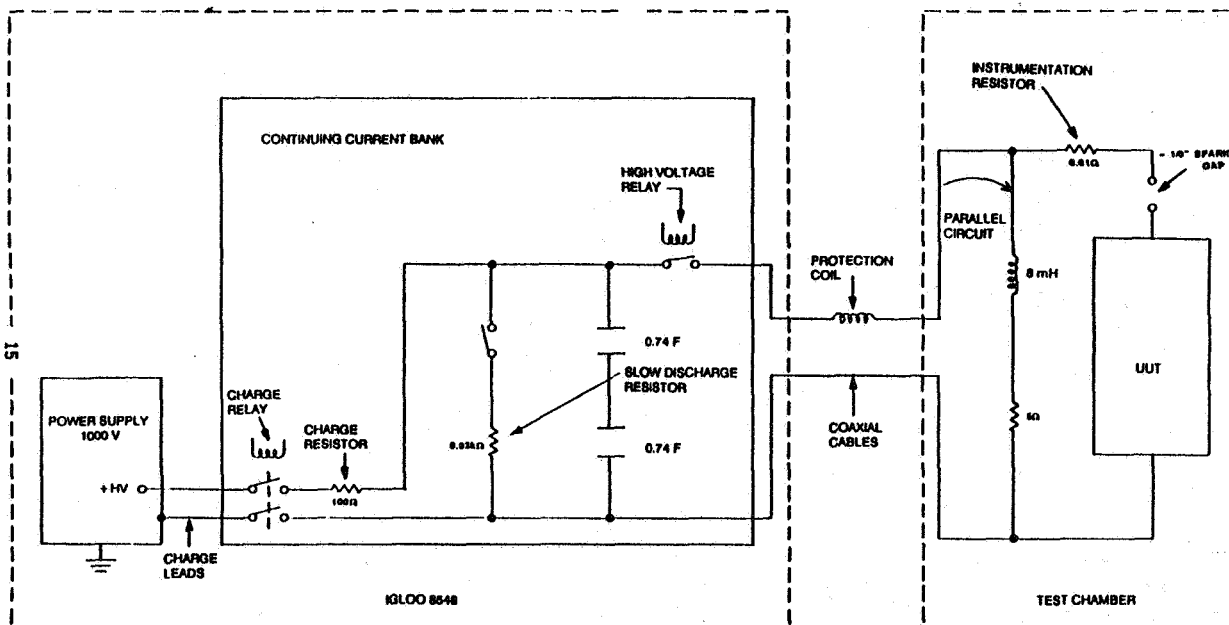


Figure 5. Continuing Current System Schematic.

## C. High $\partial I/\partial t$ SYSTEM

The high  $\partial I/\partial t$  bank, Figure 6, is an 18 stage Marx bank with a total capacitance of 0.9375  $\mu\text{F}$ . Each stage, consisting of nine 60 kV, 1.875  $\mu\text{F}$  capacitors in parallel, is normally charged to 42 kV to provide a total output voltage of 756 kV. The 18 stages are charged in parallel via a group of charge resistors by a 100 kV power supply. Charging is activated with a remotely operated pneumatic switch, located in the Charge/Discharge Building. The

bank is triggered remotely by a pneumatic switch. The trigger pulse is divided resistively and delivered to the first 4 spark gaps in the large Marx bank. The bank can be slowly discharged in the Charge/Discharge Building by switching in a large resistive load to ground.

Energy from the Marx bank is delivered to the peaking capacitor/spark gap assembly via a one-inch insulated conductor. The insulated conductor runs from the high  $\partial I/\partial t$  bank isolation gap to the top of the peaking capacitor/spark gap assembly large corona ring inside the large safety cage. The peaking capacitor bank has a total capacitance of  $0.027 \mu\text{F}$  and a maximum voltage capability of 2.2 MV. The peaking capacitor bank consists of two parallel stacks of Maxwell capacitors. Each stack contains twenty two  $0.3 \mu\text{F}$ , 100 kV capacitors in series. The secondary frequency created by the peaking capacitor increases the risetime of the pulse to meet the  $200 \text{ kA}/\mu\text{s}$  requirement.

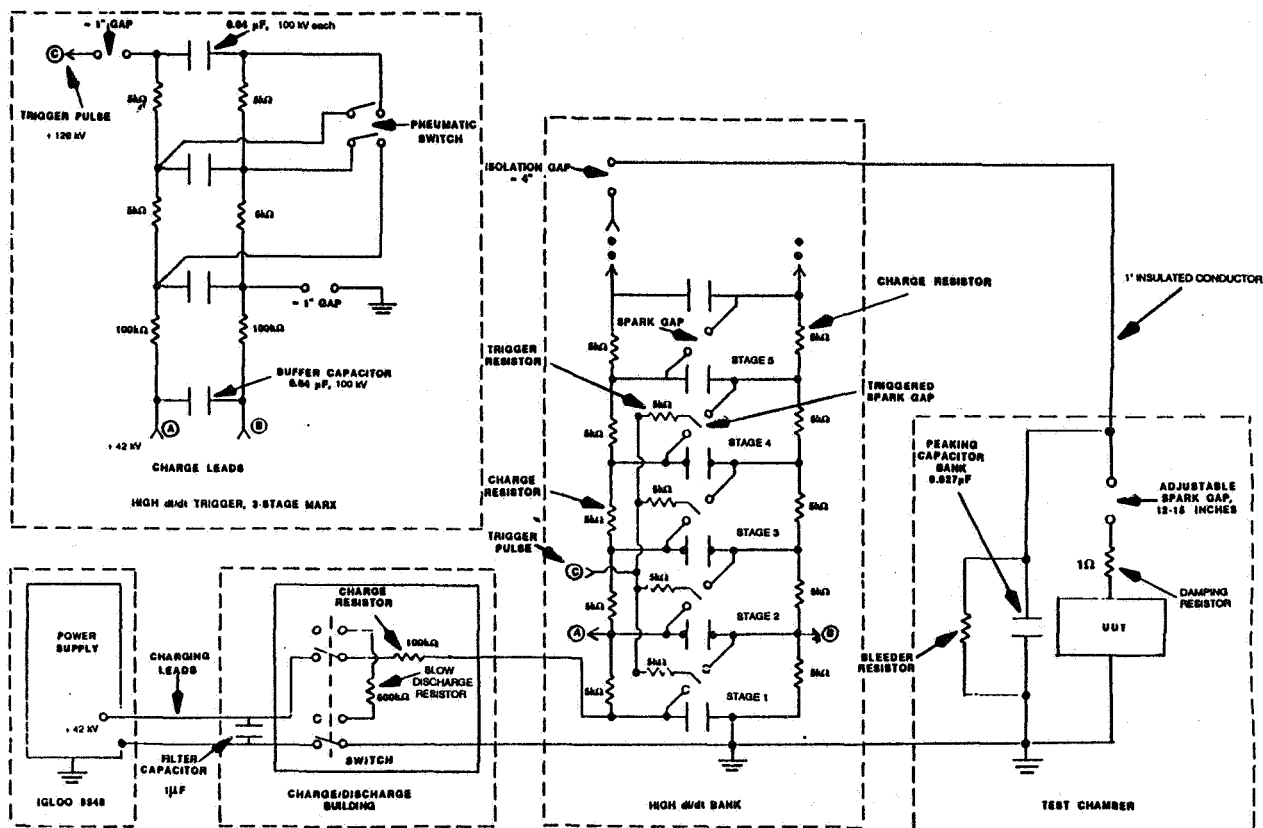


**Figure 6. High  $\partial I/\partial t$  System Schematic.**

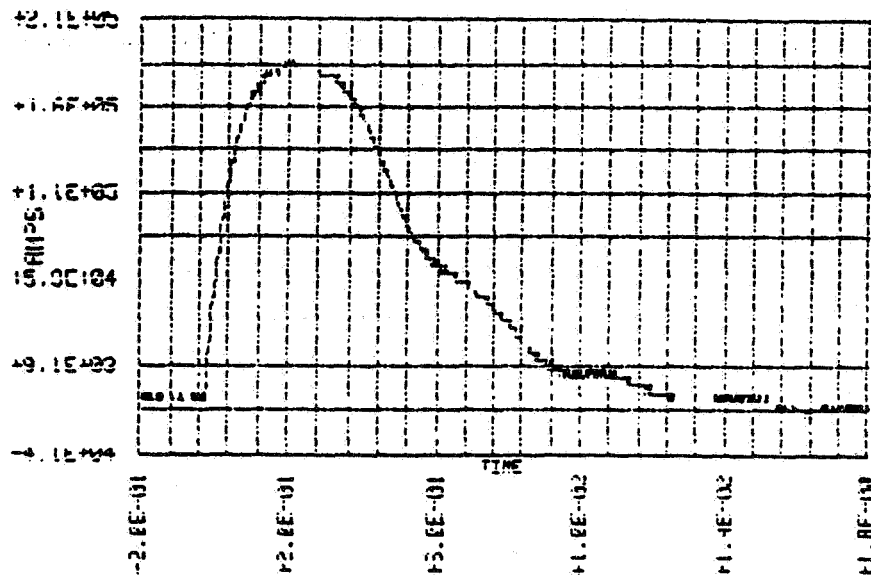
The peaking capacitor circuit utilizes a large spark gap located above the secondary safety cage. This spark gap spacing determines the peak current and rate-of-rise of the test current waveform. A down-conductor, extending through the secondary safety cage, is attached directly to the test item. A one ohm damping resistor is located between the spark gap and the UUT.

#### IV. DATA ACQUISITION AND SYSTEM CALIBRATION

Calibration waveforms for the high-current, continuous current, and high  $\partial I/\partial t$  current components of the simulated lightning waveform are obtained by connecting a load of known impedance to the output of the generator and measuring the current that flows through it. Separate instrumentation is required for each of the lightning component waveforms. Instrumentation to monitor the high current and high voltage component waveforms is identical, though, except for the attenuation/gain settings on the fiber optic receivers (see Figures 7, 8, and 9 for waveforms from an actual test). The equipment used to generate and record these measurements is as follows:

##### A. HIGH CURRENT INSTRUMENTATION

A Pearson Model 1080 Current Probe (400 Amps/Volt, 200 kA max.) is utilized as the sensor for the high current waveform measurement, Figure 7. The current probe is installed on the center conductor of the High Current/Continuing Current Discharge Probe. The high current waveform measurement is telemetered via a Nanofast Model OP-300 Fiber Optic System (Self-calibrating with a 1 volt, 1 MHz square wave signal). The signal



PEAK CURRENT: 196372.59254 AMPS  
INTEGRAL: 12.9432263939 Coulombs  
ACTION INTEGRAL: 1621496.57 A\*2 Sec

**Figure 7. High Current Component Waveform Measurement.**

can be recorded on a Hewlett-Packard Digitizing Oscilloscope (Model 54111D, 54200D, or 54510A) or a Tektronix Programmable Digitizer (Model 7612D or 7912A/D) and reduced on a Hewlett-Packard Model 9000 PC 308 Vectra Computer with a Hewlett-Packard Model 9122 Disk Drive.

## B. CONTINUING CURRENT INSTRUMENTATION

An in-house designed 0.01 ohm Nichrome ribbon series resistor (100 Amps/volt) is utilized as the sensor for the continuing current waveform measurement, Figure 8. The Nichrome resistor is installed in-line with the continuing current transmission line. The continuing current waveform measurement is telemetered via a Meret Model MDL281-4-C Fiber Optic System. The signal can be recorded on a HP Digitizing Oscilloscope (Model 54111D, 54200D, or 54510A) or a Tektronix Programmable Digitizer (Model 7612D or 7912A/D) and reduced on an HP Model 9000 PC 308 Vectra Computer with an HP Model 9122 Disk Drive. The continuous current measurement system is calibrated by flowing a known DC current through the series resistor and recording the output of the HP Oscilloscope.

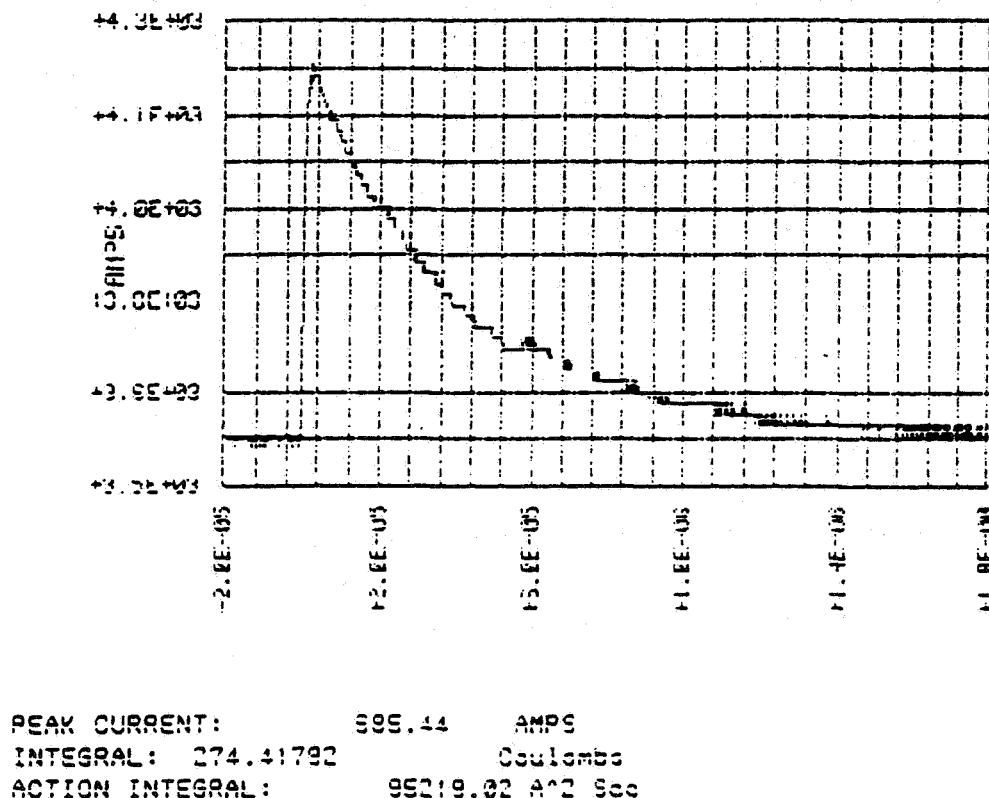


Figure 8. Continuing Current Component Waveform Measurement.

## C. HIGH $\partial I/\partial t$ INSTRUMENTATION

A Pearson Model 1080 Current Probe is utilized as the sensor for the high rate-of-rise current waveform measurement, Figure 9. The current probe is installed on the center conductor of the High Voltage Down Conductor. The

high voltage waveform measurement is telemetered via a Nanofast Model OP-300 Fiber Optic System. The signal can be recorded on a HP Digitizing Oscilloscope (Model 54111D, 54200D, or 54510A) or a Tektronix Programmable Digitizer (Model 7612D or 7912A/D) and reduced on an HP Model 9000 PC 308 Vectra Computer with an HP Model 9122 Disk Drive.

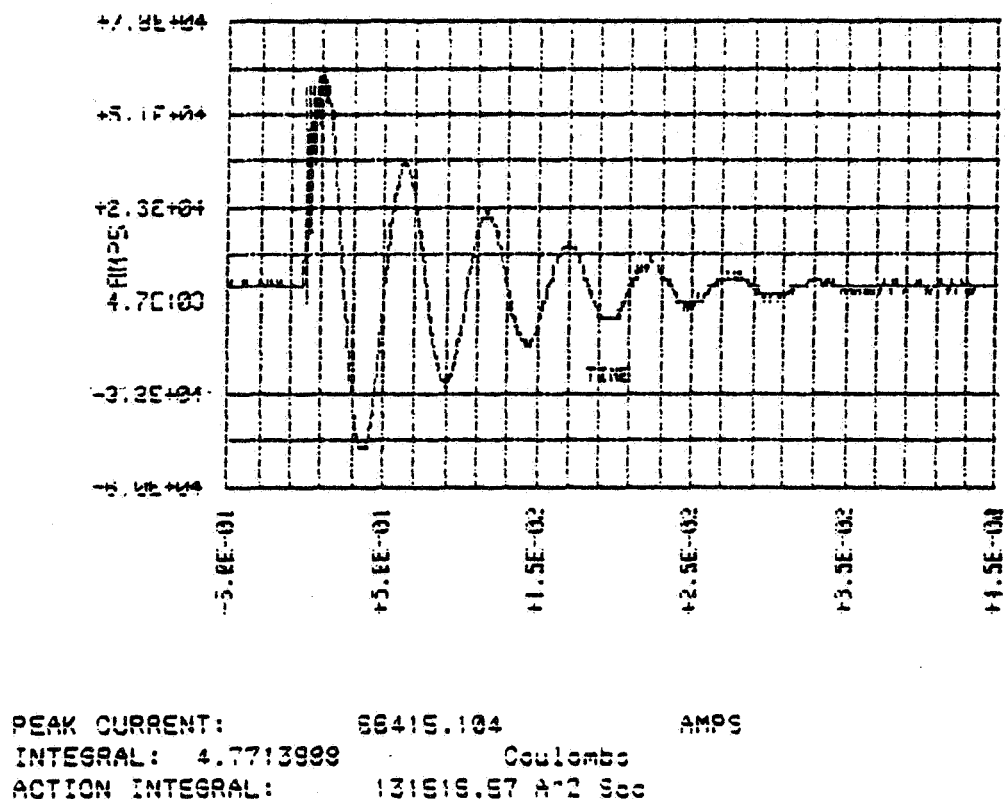


Figure 9. High  $\partial I/\partial t$  Component Waveform Measurement.

## V. CONCLUDING REMARKS

A simulated lightning test facility for testing live and inert missiles and components has been described. Although primarily designed for testing live missiles, this facility can be used to test inert hardware which could be susceptible to the effects of lightning, such as military vehicles and components, and aerospace hardware.



## DISCLAIMER

Use of trade names or manufacturers in this report does not constitute an official endorsement or approval of the use of such commercial hardware or software.

## REFERENCES

[1] MIL-STD-1757A, Lightning Qualification Test Techniques for Aerospace Vehicles and Hardware, 20 July, 1983.

[2] "Operating Procedures, Test Area 5 Large Missile Lightning Test Facility, MICOM Special Report SR-RD-TE-90-11, December 1989, prepared by Kenneth K. Mitchell COLSA, INC.

## **Poster Papers Modeling**

## ELECTRON DISTRIBUTION FUNCTIONS IN ELECTRIC FIELD ENVIRONMENTS \*

Terence H. Rudolph

Electro Magnetic Applications, Inc.  
 12567 West Cedar Drive, Suite 250  
 Lakewood, Colorado 80228-2091  
 U.S.A.  
 (303) 980-0070

## ABSTRACT

The amount of current carried by an electrical discharge in its early stages of growth is strongly dependent on its geometric shape. Discharges with a large number of branches, each funnelling current to a common stem, tend to carry more current than those with fewer branches. The fractal character of typical discharges has been simulated using stochastic models based on solutions of the Laplace equation [1, 2]. Extension of these models requires the use of electron distribution functions to describe the behavior of electrons in the undisturbed medium ahead of the discharge. These electrons, interacting with the electric field, determine the propagation of branches in the discharge and the way in which further branching occurs.

This paper reports on the first phase in the extension of the referenced models, the calculation of simple electron distribution functions in an air/electric field medium. Two techniques are investigated. The first is the solution of the Boltzmann equation in homogeneous, steady state environments. The second is the use of Monte Carlo simulations. Distribution functions calculated from both techniques are illustrated. Advantages and disadvantages of each technique are discussed.

## 1.0 INTRODUCTION

An electrical discharge is often said to have a "fractal" character. This usually means that the discharge is heavily branched, often to the point of seeming diffuse. The branching character is important, in that it allows the discharge to generate more current than is possible for a single channel. In a loose sense, the tip of each branch may be thought of as producing a fixed amount of current, which is then funnelled back along the branch to the base of the discharge.

Models have been developed which predict the branching behavior of electrical discharges [1, 2]. These models embody rules which determine how a discharge will grow incrementally. The rules are generally stochastic in character and based on static solutions of Laplace's equation. A more physical way of defining the growth rules is to use the local electron distribution function at the ends of the discharge branches. The distribution function contains information about the electrons' velocity behavior in the electric field environment and can be used to probabilistically define the direction of a branch's subsequent growth. It can also be used to predict the likelihood of a branch bifurcating into more branches.

This paper reports on the first phase of a multi-phase effort, the methodology needed for the calculation of electron distribution functions in an electric field environment. Two techniques are investigated: solution of Boltzmann's equation and a Monte Carlo procedure. Subsequent efforts in this area are intended to apply the derived distribution functions to discharge growth models and then to apply the models to discharges occurring on actual systems.

In its most general form the electron distribution function,  $F$ , describes exactly the positions and velocities of all of the electrons in a system as a function of time. This form is impractical to deal with, however, so simpler, reduced distributions, usually designated  $f$ , are defined. The reduced distribution of most interest here is the single particle distribution function, which is derived by integrating  $F$  over the position and velocity coordinates of all but one of the electrons in the system under consideration. This leaves the function  $f(x,v,t)$ , where  $x$  represents three spatial coordinates and  $v$  three velocity coordinates.

---

\* This work was sponsored by Harry Diamond Laboratories under Contract DAAL02-89-C-0075.

Various physically measurable quantities can be derived from  $f$  by taking moments over  $v$ . One of these is the density variation in space, given by,

$$n(x,t) = n_0 \int f(x,v,t) dv \quad (1)$$

Here  $n_0$  is defined to be the average density of the system  $\frac{N}{V}$ , where  $N$  is the total number of electrons and  $V$  is the total volume of the system. The mean velocity of the electrons (e.g., a drift velocity of the electrons in an electric field) is found from the first moment.

$$V(x,t) = \frac{\int v f(x,v,t) dv}{\int f(x,v,t) dv} \quad (2)$$

The denominator of Equation 2 represents a normalization of the distribution function. In many cases  $f$  is scaled so that this denominator is unity. The second moment of the distribution function can be identified with a pressure tensor. An infinite number of moments can be defined, but they begin to lose simple physical meanings when one goes beyond the second.

The physical meaning of  $f$  itself is as follows. The quantity  $n_0 f(x,v) dx dv$  is the total number of electrons in the volume  $dx dv$  centered on  $(x,v)$ . Therefore  $f(x,v)$  is in some sense the probability of finding a particular electron in  $dx dv$  centered on  $(x,v)$ .

## 2.0 SOLUTION OF THE BOLTZMAN EQUATIONS

The evolution of the electron distribution function is described by the Liouville theorem [3]. Although somewhat simplified, this theorem essentially states that, in the absence of interactions between particles, the total time derivative of  $f$  is zero.

$$\frac{df}{dt} = 0 \quad (3)$$

Expanding, one finds,

$$\frac{\partial f}{\partial t} + \frac{\partial f}{\partial x} \cdot \frac{\partial x}{\partial t} + \frac{\partial f}{\partial v} \cdot \frac{\partial v}{\partial t} = 0 \quad (4)$$

or,

$$\frac{\partial f}{\partial t} + v \cdot \frac{\partial f}{\partial x} + a \cdot \frac{\partial f}{\partial v} = 0 \quad (5)$$

Here  $a$  is the acceleration experienced by the electrons from external forces (e.g., electric fields, magnetic fields, gravity). Equation 5 is commonly known as the collisionless Boltzmann equation, or the Vlasov equation. When collisions, either with other electrons or background particles, are taken into account, a source term must be included on the right hand side of Equation 5. The form of this source term can be quite complicated and is often written formally as  $\left(\frac{\partial f}{\partial t}\right)_{\text{coll}}$ . With the addition of this source term, Equation 5 becomes the full Boltzmann equation.

$$\frac{\partial f}{\partial t} + v \cdot \frac{\partial f}{\partial x} + a \cdot \frac{\partial f}{\partial v} = \left(\frac{\partial f}{\partial t}\right)_{\text{coll}} \quad (6)$$

As was done with the distribution function itself, moments can be taken of the Boltzmann equation. This is done by multiplying both sides of the equation by  $v^n$ , where  $n$  represents the desired moment, and then integrating over all velocity space. The zeroth order moment of the Boltzmann equation reduces to a statement of

conservation of particles. The first order moment reduces to conservation of momentum, and the second order moment to conservation of energy.

A form for the collision source term in Equation 6 can be derived if one makes some assumptions about the physical situation. For example, in a fully ionized gas, collisions are generally coulombic in nature, and therefore long range. Under these conditions Fokker-Planck theory is appropriate for calculating transport properties. Alternatively, the case considered here is one of a weakly ionized plasma in which nearly all interactions take place between electrons and neutrals. These collisions can usually be treated as elastic, at least for low electron energies. In addition, because the electron-neutral collisions are not long range, they can be assumed to be of very short duration (effectively instantaneous) compared to the time the electron spends between collisions. These assumptions allow one to derive an explicit form for the collision term. The derivation involves a consideration of the mechanics of electron scattering into and out of a specified region of velocity space. The appropriate collision term is shown below.

$$\left(\frac{\partial f}{\partial t}\right)_{\text{coll}} = n_n \int d\mathbf{v}_1 \int d\Omega \frac{d\sigma}{d\Omega} |\mathbf{v} - \mathbf{v}_1| [f(\mathbf{v}') f_n(\mathbf{v}_1) - f(\mathbf{v}) f_n(\mathbf{v}_1)] \quad (7)$$

In Equation 7  $f_n$  is the distribution function of the background neutrals.  $n_n$  is the average density of these neutrals.  $\mathbf{v}_1$  defines the velocity space of the neutral particles and  $\Omega$  is a solid angle.  $\frac{d\sigma}{d\Omega}$  represents the differential cross section for the scattering processes under consideration and can be quite complex. The scattering cross section is generally a function of  $\mathbf{v}'$ . Note the presence of the factor  $|\mathbf{v} - \mathbf{v}_1|$  in the integrand. This factor expresses the fact that no collisions can occur unless there is a relative velocity between the electrons and the background particles. The bracketed terms in the integrand represent two specific types of collisions. The first term, sometimes called a 'scattering in' term, defines those collisions which scatter electrons from all other velocities  $\mathbf{v}'$  to the velocity of interest  $\mathbf{v}$ . The second term, the 'scattering out' term, defines those collisions which scatter electrons from the velocity of interest  $\mathbf{v}$  to any other velocity. Hence the 'scattering in' term is in a sense a source term in Equation 7, while the 'scattering out' term is a sink term. The balance of these terms along with the forcing terms from the left side of Equation 6 determines the behavior of  $f$  in a particular volume of velocity space.

It can be shown that for a proper choice of  $f$ , the collision term can be made to vanish. This choice is a function only of  $\mathbf{v}$ , and therefore in the absence of external forces ( $\mathbf{E}$ ,  $\mathbf{B}$ , etc.) it is an equilibrium solution of the Boltzmann equation. This distribution is known as the Maxwell-Boltzmann distribution and is shown below.

$$f_0(\mathbf{v}) = \left(\frac{m}{2\pi k T_e}\right)^{3/2} \exp\left(-\frac{m\mathbf{v}^2}{2k T_e}\right) \quad (8)$$

In this expression  $T_e$  is the electron temperature. It characterizes the size of the distribution in velocity space.

Even given the explicit form for the collision term of Equation 7, the Boltzmann equation is very difficult to solve without further simplifications. In Section 2, a variety of simplifications to the collision term will be considered. In addition, there are some general assumptions that cover all work reported here. The first is that steady state will be assumed. The distribution function relaxes in time on the scale of several collision times. This will generally be on the order of a few tens of picoseconds for electrons in typical electric fields.

A second assumption is that of homogeneity. That is, the electron distribution function will be assumed to be independent of  $\mathbf{x}$ . This will be a reasonable approximation locally if the electric field is uniform over several electron mean free paths. The electron mean free path in air is approximately  $10^{-6}$  m. Hence it takes at least 1000 collision times for the electron to move a millimeter, even if it is assumed to move in a straight line. This time is much longer when the actual drift velocity of the electron distribution is used, rather than the straight line speed. Then if the electric field is uniform over fractions of millimeters the homogeneity approximation is acceptable.

The third basic assumption is that only electric field external forces are present. The effect of static magnetic fields that may be present will be ignored. The acceleration term under this assumption becomes  $a = -\frac{eE_z}{m}$ , and Boltzmann's equation reduces to,

$$-\frac{eE}{m} \frac{\partial f}{\partial v_z} = \left( \frac{\partial f}{\partial t} \right)_{\text{coll}} \quad (9)$$

Note here that E is assumed to be oriented along the positive z axis, but the z subscript will be suppressed.

In Equation 9 f is now considered to be solely a function of v. This means that f can be written in general as  $f(v_x, v_y, v_z)$  or, given the cylindrical symmetry,  $f(v_r, v_z)$ . The electric field E can be treated as a parameter, so there will be a family of distribution functions based on the value of E.

The Maxwell-Boltzmann distribution given by Equation 8 represents an equilibrium solution of Boltzmann's equation in the absence of an electric field. This is the distribution to which collisions, and the collision term of Equation 9, drive the system. A simple way to think of the right hand side of the equation, therefore, is as a term tending to force the system back to equilibrium. Modeling this mathematically can be accomplished simply by replacing the full collision term with a relaxation process as shown below.

$$\left( \frac{\partial f}{\partial t} \right)_{\text{coll}} = -\frac{f(v) - f_0}{\tau} \quad (10)$$

Here  $f_0$  is the Maxwell-Boltzmann equilibrium distribution,  $f(v)$  is the (perturbed) distribution in the presence of the electric field, and  $\tau$  is an average collision time for electron-neutral interactions.  $\tau$  can be replaced, if desired, by its inverse, the collision frequency  $\nu$ . The simplified Boltzmann equation then becomes,

$$\frac{eE}{m} \frac{\partial f}{\partial v_z} = \nu (f - f_0) \quad (11)$$

The form of Equation 11 can be interpreted in much the same way as the more general Equation 7. The first term on the right hand side can be thought of as a term scattering electrons out of the volume  $dv$  centered on v. The second term represents scattering of electrons into the volume  $dv$  centered on v from all other velocities. Replacement of the full collision term with a relaxation term as in Equation 11 constitutes what is called the Krook model.

## 2.1 LINEARIZED SOLUTION OF KROOK MODEL

If the electric field strength is small enough, one expects the distribution function f to differ only slightly from the equilibrium distribution  $f_0$ . To investigate this regime, f may be considered as the sum of  $f_0$  and a (small) perturbation  $f_1$ .

$$f = f_0 + f_1 \quad (12)$$

This leads to a linearized solution for f in cylindrical coordinates.

$$f(v_r, v_z) = f_0 + f_1 = \left( \frac{m}{2\pi k T_e} \right)^{3/2} \exp \left( -\frac{m(v_r^2 + v_z^2)}{2k T_e} \right) \left( 1 - \frac{eE v_z}{\nu k T_e} \right) \quad (13)$$

Equation 13 is the solution to the linearized Krook model. Note in particular the last term in the equation. This term can be negative if E or  $v_z$  are too large. Because f must be everywhere nonnegative, this represents a lowest order limit on the value of E which can be allowed in the linearized model.

Figure 1 shows contours of the distribution function f as calculated from Equation 13 for  $E = 3$  MV/m. The electron-neutral collision frequency,  $\nu$ , was chosen to be  $1 \times 10^{12} \text{ s}^{-1}$ , and the electron temperature (of the unperturbed distribution  $f_0$ ) was chosen to be 300° K. The figure shows contours of f, with the dashed lines

indicating negative (nonphysical) values. The contours represent a projection of the full three dimensional distribution function. Rotation about the left side of the figure reproduces the third dimension. It should be noted that the linearized Krook model gives physically realistic solutions only for much lower values of electric field ( $\sim 100$  KV/m).

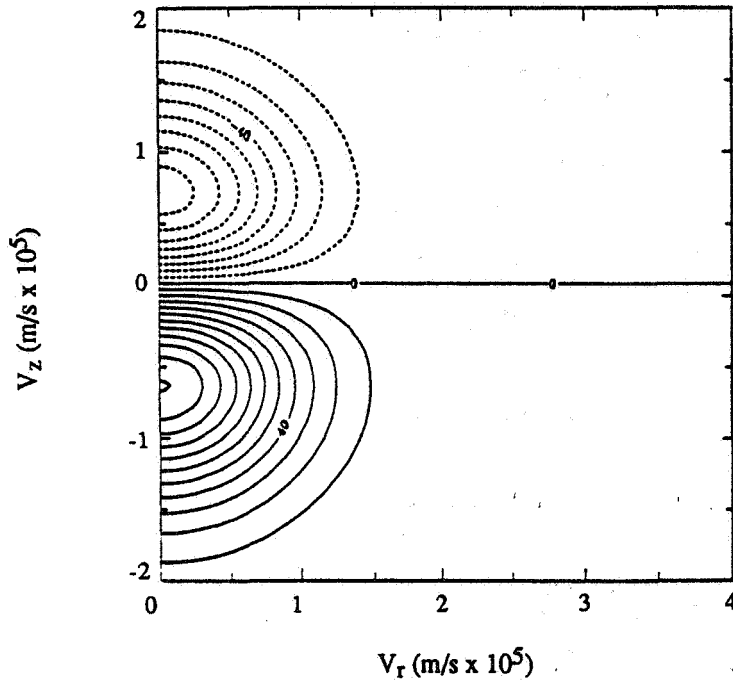


Figure 1 Linearized Krook Model Distribution Function,  $E = 3$  MV/m. Peak Value is  $1.11 \times 10^{-15}$

## 2.2 KROOK MODEL SOLUTION WITHOUT LINEARIZATION

Although linearization of Equation 11 leads to a simple solution in the Krook model, it is not necessary to linearize to obtain a solution. Equation 11 as it stands is a simple first order linear differential equation with constant coefficients and can be integrated directly. First, rewriting the equation in a more suitable form,

$$\frac{\partial f}{\partial v_z} - \frac{mv}{eE} f = -\frac{mv}{eE} f_0 \quad (14)$$

With the application of an integrating factor, Equation 14 becomes,

$$\frac{\partial}{\partial v_z} \left[ f \exp\left(-\frac{mv}{eE} v_z\right) \right] = -\frac{mv}{eE} f_0 \exp\left(-\frac{mv}{eE} v_z\right) \quad (15)$$

In integrating the equation some care must be exercised in choosing limits of integration. If one integrates over  $v_z$  from  $-\infty$  to  $v_z$ , the left hand side evaluated at  $-\infty$  may or may not vanish depending on the behavior of  $f$  at large negative  $v_z$ . More convenient is to integrate from  $v_z$  to  $+\infty$ . At  $v_z \rightarrow +\infty$  the left hand side vanishes unless  $f$  grows faster exponentially than the integrating factor decays. But the distribution function  $f$  must go to zero as  $v_z$  approaches infinity to be normalizable, so this is not a problem. Substituting for  $f_0$  and performing the integration on the left hand side of Equation 15 leads to,

$$f(v_r, v_z) = \frac{mv}{eE} \left( \frac{m}{2\pi kT_e} \right)^{3/2} \exp \left( \frac{mvv_z}{eE} - \frac{mv_r^2}{2kT_e} \right) \int_{v_z}^{\infty} \exp \left( -\frac{mv_z'^2}{2kT_e} - \frac{mvzv_z'}{eE} \right) dv_z' \quad (16)$$

After some manipulation the closed form solution for  $f(v_r, v_z)$  becomes,

$$f(v_r, v_z) = \frac{m^2 v}{4\pi e k T_e} \exp \left[ -\frac{mv_r^2}{2kT_e} + \frac{mv}{eE} v_z + \frac{mkT_e}{2} \left( \frac{v}{eE} \right)^2 \right] \operatorname{erfc} \left( \sqrt{\frac{m}{2kT_e}} v_z + \sqrt{\frac{2kT_e}{m}} \frac{mv}{2eE} \right) \quad (17)$$

It may be noted that Equation 17 is significantly more complex than Equation 13, the linearized Krook solution. Another difference is that  $f(v_r, v_z)$  as calculated from Equation 17 is everywhere positive, as required for distribution functions.

Figure 2 is a contour plot of Equation 17 for electric field value of 3 MV/m. The figure is analogous to Figure 1 for the linearized solution. This solution is much more physically reasonable than that of Figure 1.

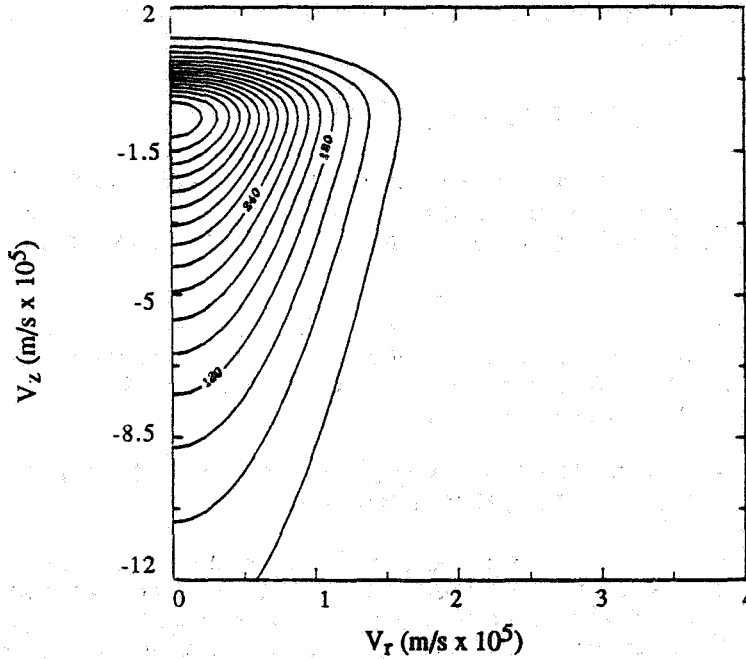


Figure 2 Krook Model Distribution Function,  $E = 3$  MV/m

### 2.3 DISCUSSION OF KROOK MODEL

Because the Krook model is one of the easiest to deal with in the solution of the Boltzmann equation, it is of interest to briefly examine some implications of the approximations made. One of these is the form of the Boltzmann collision integral in the Krook model. In the Krook model  $\tau$  is defined to be a mean time between collisions, and can be related to a mean collision frequency,  $\nu$ . Defined as means, these quantities are not functions of velocity. Physically, however, they should be functions of velocity (or more accurately, speed), and  $\tau$  should be a function of velocity in Equation 10. The faster an electron moves through an essentially unmoving background, the more collisions it experiences in unit time. The mean free path of the electron may remain constant, but the time between collisions cannot. Then, because  $\nu$  should be monotonically increasing



with the speed of the electron, the relaxation term on the right of Equation 11 should be less important for electron speeds resulting in collision frequencies below the mean, and more important for electron speeds resulting in collision frequencies above the mean. This will tend to raise the distribution function  $f$  at low speeds and decrease it at higher speeds, leading to contours which appear more squashed than the extended distributions shown in Figure 2.

A second issue has to do with normalization of the distribution. Recall from Equation 1 the normalization requirement on the function  $f$ , essentially that the integral of  $f$  over all velocity space must equal one. Consider now the Krook model of the Boltzmann equation (Equation 11), repeated below.

First, assume that  $v$  is not a function of velocity, and integrate both sides of the equation over all  $v_z$  ( $-\infty$  to  $+\infty$ ). The left hand side is identically zero, because  $f$  is assumed to vanish as  $v_z \rightarrow \pm\infty$ . Passing  $v$  through the integrals on the right hand side leads to,

$$\int f \, dv_z = \int f_0 \, dv_z \quad (18)$$

Then  $f$  will be properly normalized as long as  $f_0$  is a normalized distribution, which it is when the Maxwellian distribution is used.

Now consider what happens when  $v$  is allowed to be a function of electron speed. The left hand side still vanishes, for the same reason as before. The collision frequency on the right hand side, however, can no longer be passed through the integral, so one finds,

$$\int v(|v|) f \, dv_z = \int v(|v|) f_0 \, dv_z \quad (19)$$

Now even though  $f_0$  may be normalized, Equation 19 does not require the normalization of  $f$ . In general a normalized solution of Equation 11 cannot be found for this case, because the equation is nonlinear with the introduction of  $v(|v|)$ . Hence the simple Krook model does not adequately handle the case of collision frequency which is a function of electron speed.

A more realistic model would allow the collision frequency  $v$  to vary with the speed of the electron,  $v \propto |v|$ , or use the full Boltzmann collision integral. Both of these techniques were tried under this effort, but were found to lead to serious computational complexities beyond the scope of the effort. The interested reader is referred to Reference 4 for the details of these calculations.

### 3.0 ELECTRON DISTRIBUTION FUNCTION CALCULATION USING MONTE CARLO TECHNIQUE

The difficulty in dealing with any but the simplest cases in the Boltzmann collision term leads one to search for more convenient ways to calculate the electron distribution function. An obvious technique which has become practical only with the advent of digital computers is to simulate the motion of a large number of electrons. The simulation should include the effects of electric field force and interactions with the background neutral gas. Randomness is introduced into the simulation through the parameters of the collisions that the electrons undergo.

The Monte Carlo simulation proceeds in the following way. An electron is dropped at  $t = 0$  with no velocity into a medium containing an electric field. The electric field is assumed, without loss of generality, to be oriented along the positive  $z$  axis of a cylindrical coordinate system. The electron will be continuously accelerated by the electric field and will experience collisions with the background gas that randomly change its velocity. The distance the electron travels between collisions,  $\lambda$ , is based on its mean free path in the medium and is a random variable. Given  $\lambda$ , the next step in the simulation is to calculate the time  $\Delta t$  that the electron takes to travel that distance.  $\Delta t$  depends on the initial velocity of the electron (its velocity immediately after the preceding collision), the distance  $\lambda$ , and the strength of the electric field. After the time  $\Delta t$  the electron is assumed to experience a collision with a background particle. The parameters of the collision, consisting of an impact parameter and an angle, are random variables. The collision calculation is the point at which a variety of physical models for electron/background interaction can be included. A simple model is considered here, in which

the electrons and background particles are assumed to behave as hard spheres. The sequence of steps above is continued for the given electron until a time  $t_0$  is reached, at which time the electron velocity is frozen in place. A second electron is then released with zero velocity and the sequence repeated. The time  $t_0$  is chosen so as to ensure that each electron has undergone a large number of collisions before its velocity is frozen.

After a large number of electrons have been simulated (up to one million in the work reported here) a distribution function can be derived from the final calculated velocities of the electrons. Normalizations are necessary to account for the transformation from an intrinsically three dimensional electron motion to a two dimensional distribution function.

The study of electron motions in Monte Carlo simulations has been considered by a number of researchers [5-8]. The technique has been used to study the growth of ionization in electron avalanches and electron diffusion. It is well respected in that far more realistic physics can be included than in more analytically oriented techniques. For example, it is possible in principle to include very complex variations in collision cross section with electron energy in a Monte Carlo calculation. This is extremely difficult in Boltzmann equation approaches. The present work is restricted to simple hard sphere collisions because of resource restrictions, not because more physics is difficult to include in the Monte Carlo framework.

To demonstrate the Monte Carlo technique a simulation was undertaken to determine the electron distribution function in an airlike medium with an electric field strength of 300 kV/m. The value of 300 kV/m was chosen to avoid the physical process of ionization which in principle should be included for high intensity electric field cases. Ionization is of course a highly inelastic process and would invalidate the simple hard sphere scattering model used here. Inclusion of ionization processes can be accomplished through the use of additional random variables which define the probability of inelastic versus elastic collisions and the implementation of different scattering models for the two processes. In general the additional random variables need to account for varying scattering cross sections as a function of electron energy.

As mentioned above, the simulation reported here used elastic hard sphere collisions only. A total of one million electrons were simulated. Each of the electrons was followed for 20 picoseconds ( $t_0$ ), a time which allows on the average about twenty collisions with the background gas. Ideally, it would be desirable to have more collisions per electron. The simulation was truncated at 20 picoseconds to limit computer resource usage. The mean free path chosen for the simulation was  $6.88 \times 10^{-7}$  m. At the end of the 20 picosecond simulation time the velocity of each electron was recorded and a new electron started. The distribution of final energies of all the electrons is shown in Figure 3. The distribution approximates quite well the analytically predicted distribution, known as a Druyvesteynian. The actual distribution function of the electrons is shown in Figure 4. The raggedness of the contours in Figure 4 requires some explanation. Although one million electrons were simulated, the vast majority of these electrons end up with final velocities having large  $r$  components. Required normalization reduces the importance of these electrons and increases the importance of those having small  $r$  components of velocity in the final distribution. This normalization, however, means that a relatively small number of electrons determines the electron velocity distribution function, resulting in statistical fluctuations in the contours of Figure 4. Adding more electrons to the simulation would eventually result in smoother contours, but an order of magnitude increase may be necessary.

Comparison of the distribution of Figure 4 with that of Figure 2 reveals the same general behavior, as expected. More exact comparisons would require a larger number of electrons to be simulated, as well as a longer simulation time, both beyond the scope of this effort. For simple cases in which a Boltzmann solution is possible, it is clear that the Boltzmann technique is both faster and simpler. The main advantage of the Monte Carlo technique is in its ability to add complex physical processes without correspondingly complex increases in difficulty. That is, the Monte Carlo technique takes significant computer resources to generate a distribution function even in simple cases, but the extension to more realistic physics is not difficult or significantly more costly. Solutions of the Boltzmann equation are fast and inexpensive for simple cases, but very difficult for more realistic cases.

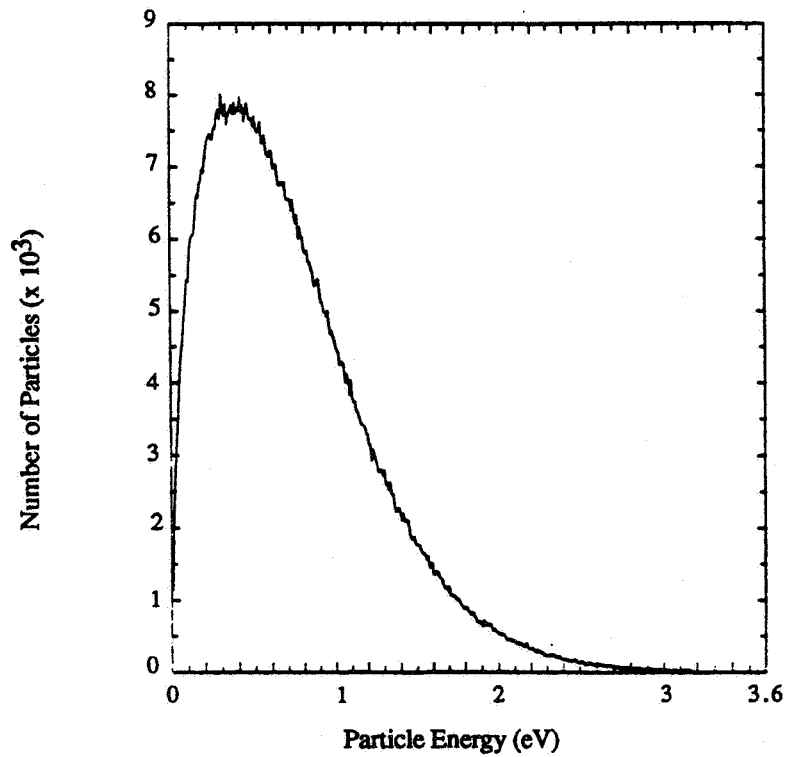


**Figure 3** Distribution of Electron Energies at Conclusion of Monte Carlo Simulation of One Million Electrons. The Fundamental Form of the Distribution is Known as a Druyvestinian

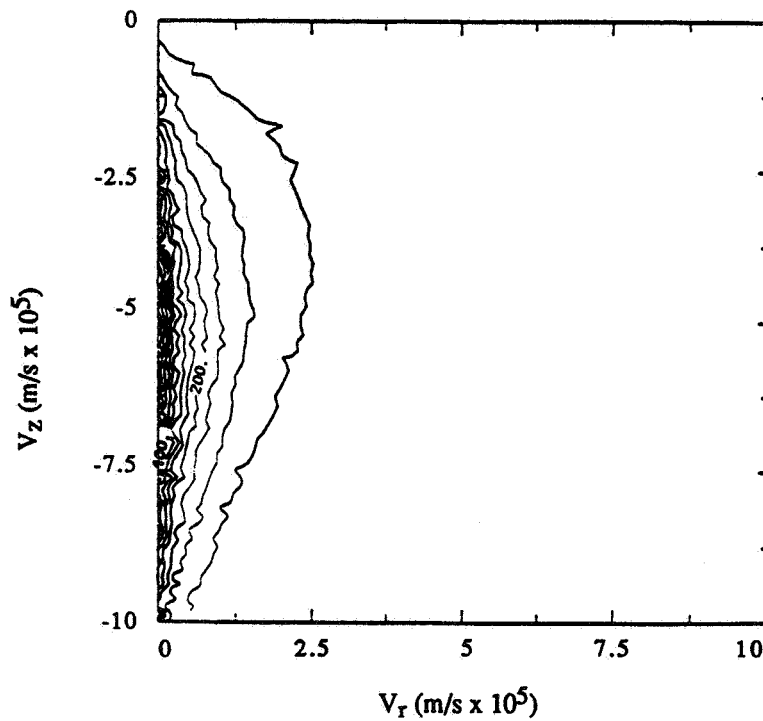


**Figure 4** Electron Distribution Function From Monte Carlo Simulation of One Million Electrons. The Function is Unnormalized

## REFERENCES

1. Niemeyer, L., L. Pietronero, and H. J. Wiesmann, "Fractal Dimension of Dielectric Breakdown," *Phys. Rev. Letters* **52**, No. 12, March 19, 1984.
2. Pietronero, L., and H. J. Wiesmann, "From Physical Dielectric Breakdown to the Stochastic Fractal Model," *Z. Phys. B - Condensed Matter* **70**, 87-93, 1988.
3. Krall, N. A., and A. W. Trivelpiece, "Principles of Plasma Physics," McGraw-Hill, New York, 1973.
4. Rudolph, T., "Electron Distribution Functions in Disturbed Environments," EMA-90-R-47, September 1990.
5. McIntosh, A. I., "Computer Simulation of an Electron Swarm at Low E/p in Helium," *Aust. J. Phys.* **27**, 1974, pp. 59-71.
6. Braglia, G. L., "The Diffusion and Drift of Electrons in Gases: A Monte-Carlo Simulation," *Physica* **92C**, 1977, pp. 91-112.
7. Reid, I. D., "An Investigation of the Accuracy of Numerical Solutions of Boltzmann's Equation for Electron Swarms in Gases with Large Inelastic Cross Sections," *Aust. J. Phys.* **32**, 1979, pp. 231-254.
8. Reid, I. D., and S. R. Hunter, "Comparison Between the Boltzmann and Monte Carlo Simulation Methods for the Determination of Electron Swarm Transport Coefficients in Molecular Hydrogen," *Aust. J. Phys.* **32**, 1977, pp. 255- 259.

N91-32727

CHARGE TRANSFER DURING INDIVIDUAL COLLISIONS IN ICE  
GROWING BY RIMING

*Eldo E. Avila and Giorgio M. Caranti*

Facultad de Matemática Astronomía y Física, Universidad Nacional de Córdoba

Laprida 854, 5000 Córdoba, Argentina.

ABSTRACT

The charging of a target growing by riming in a wind tunnel has been studied in the temperature range of  $(-10, -18^{\circ}\text{C})$ . For each temperature, charge transfers of both signs are observed and according to the environmental conditions one of them prevails. The charge is more positive as the liquid water concentration is increased at any particular temperature. It is found that even at the low impact velocities used (5 m/s) there is abundant evidence of fragmentation following the collision.

## Introduction

Many experimental studies about charge transfer while the target in a wind tunnel or the rimer in a cloud chamber grow by riming involve multiple collisions (Reynolds et al, 1957, Takahashi 1978, Jayaratne et al 1983). This made difficult to establish the mechanism or mechanisms of charging. The measured electrical current in these experiments were the result of many collisions and therefore a null result could simply be due to equal numbers of positive and negative charge transfers.

Jayaratne et al (1983) observed while working on multiple collisions that the charge current dropped significantly when the steam supply was cutoff. This result is subject to different interpretations. It should be noted that the crystals would grow at expenses of the droplets which dissipate very soon.

Recently, there have been attempts of measuring the charge transfer when only very few crystals impacted at a given time (low frequency of collisions) in order to infer the charge transferred per collision. Kumar and Saunders (1989) measured the charge transfer between ice crystals and a previously rimed target at low frequency. The cloud droplets were also drawn past the target so it is expected that some riming was simultaneous to the charging. Unfortunately, there was not a quantification of the amount of riming the target was undergoing.

There are a number of mechanism being proposed as responsible for the charge transfer. Among them the contact potential (Buser and Aufdermaur 1977), the liquid like layer (Baker and Dash 1989), the presence of charged dislocations on the surface (Keith and Saunders 1989). Each mechanism seems to explain part of the observations.

Baker et al (1987) working on multiple collisions experiments arrived to the

conclusion that the sign depended on the relative rate of growth of the interacting particles, the fastest growing particle would get positive charge. Keith and Saunders (1990) also measuring multiple collisions arrived at a different conclusion and they suggest that charged dislocations on the surface of the interacting particles are responsible for the observed transfers. This process would also yield only one sign for a given set of conditions. Nevertheless, there is evidence that under the same target surface and particle conditions it is possible to obtain a mixture of signs. In fact, Avila et al (1988), measured single collisions and found a that almost invariably there was not a single sign.

Caranti et al 1991 studied individual collisions of ice crystals with a target growing by vapor deposition. They showed direct evidence that at least on a target subject to these conditions the breaking of protuberances on the surface could be associated with the charge deposited on the target. This work is extended here to riming and further support to the physical model presented in that work is given.

### Experimental Set up

The arrangement was basically the same as in Caranti et al 1991. The experiments were carried out in a wind tunnel placed inside a cold room. On top of which the drop generator [Abbott and Cannon 1972] was installed. This generator produces water drops of a uniform size which can be selected in a relatively wide range. Both the repetition rate and the charge placed on the drops can be controlled. In the present experiment only sizes close to  $100\ \mu\text{m}$  were used. Each drop formed at laboratory temperature is frozen as it falls through a liquid air cooled region of the tunnel. After freezing the particle has a free fall of more than 50 cm that allows for thermalization. There is an acceleration zone where cold room air

enters the tunnel and drags the particle with it to collide the target at the wanted speed. In this reported work the velocity was 5 m/s.

Figure 1 shows the working section of the tunnel. Twelve centimeters upstream from the target there is an induction ring sensing the charge on the frozen drops. The target is a copper cylinder 4 mm in diameter connected on an end with a sensitive charge amplifier capable of detecting charges larger than 2 fC. The amplifier has associated with it a time constant of about 100 ms. Eight centimeters downstream from the target there is another induction ring with the purpose of detecting the products of the collisions. The two rings were electrically interconnected and to another amplifier. Since the total time of passage of a particle at 5 m/s between the two rings would be 40 ms and the repetition rate about 1 s there is no aliasing.

Unlike the previous experiment and due to the added complexity the cloud drawn past the tunnel impose in this case the signals from the target and from the rings were not added. This helped to distinguish better the origin of pulses that looked like transferences to the target but they were actually transferences to the rings. The noise levels were also kept at manageable levels by this arrangement.

So each charge transfer event has several pulses associated with it. The first pulse comes from the upstream induction ring and is recorded on the ring channel. The amplitude of this pulse is proportional to the initial charge that the particle brings and its duration is of approximately 4 ms, depending on the velocity. The second pulse recorded on the target channel is separated about 24 ms from the first originates in the target and it is related both to the induction of the initial charge of the particle and to the transfer itself. This latter event is distinguished from a near miss because of the mentioned 100 ms decay. Finally, any byproducts



of the collision namely the original particle and/or fragments if they are produced are detected at the second ring and recorded on the ring channel . The signals are both magnetically recorded for later process and measured in real time using a digital oscilloscope (Tektronik 2020). As before the shape of each pulse contains a welth of information and therefore it is better to analize them on a one by one basis.

The cloud was generated outside the cold room by boiling water. The water vapor was conducted inside by several tubes. The first brass section at the outside was cooled by evaporation. Next, a corrugated plastic section entered the cold room followed by a 1 m brass section that ensured thermalization. The cloud entered a small chamber that sorrounded the tunnel and was drawn into the tunnel through two symetrically placed tubes positioned between the first induction ring and the target. This disposition ensured a minimum flow perturbation and therefore no significant increase in the number of particles that miss the target was found.

Ultrasonic generators were also used but in the end steam was preferred because it lacked appreciable charge density resulting in a clearer signal.

## Experiments and Results

The charge transfer was measured in individual collisions between  $100\text{ }\mu\text{m}$  ice particles at 5 m/s and an target undergoing simultaneous riming.

The measurements were carried out for ambient temperatures ( $T_a$ ) between  $-10$  and  $-18\text{ }^{\circ}\text{C}$ . The ambient relative humidity was lower than saturation and within the range of 60 to 80 % over ice according to the cold room cycle. This made necessary monitoring the cloud liquid water concentration during each run

in order to take into account the cloud dilution. Typical effective values were around  $0.5 \text{ g/m}^3$ .

The determination of the liquid water concentration (LWC) was done by weighting the mass of water collected by the target during a given time. LWC is then calculated dividing the mass by the corresponding time interval times the cross sectional area of the target and the air velocity. This procedure of course assumes an unity collection efficiency and therefore the term "effective" LWC.

Figure 2 shows typical charge transfer pulses. The upper trace represent the signal coming from both rings simultaneously. The lower trace shows the signal originated in the target. In general it is possible to distinguish the rebounding initial particle from the fragments because of their different masses. Their respective downstream ring pulses can be resolved due to the different times they take to attain the air velocity, resulting in unequal time delays for the downstream ring passage. In Figure 2a the positive charge transfer is clearly seen in the target signal after the passage of a particle through the first induction ring. The ring signal also shows the postimpact passage of two particles through the second ring. Figure 2b shows an interesting case of probable trapping of the impacting particle but with the emission of a fragment. A case of negative charge transfer is seen in Figure 2c. In a similar fashion as in Figure 2a there are fragments detached from the target showing that fracture occurs irrespective of the sign of the charge transfer. In all cases a check of the conservation of charge is made; assuming the target is initially uncharged the sum of all charges (target and downstream ring) after the collision should be equals to that of the incomming particle before the impact. This ensures that possible interactions of the rebounding particles with the tunnel walls do not affect the interpretation of results.

The initial charge on the impacting particle was not taken into account in previous work mainly because the charge transfer experiments involved smooth ice targets. In the present case the surface of the target is so uneven that there is a greater possibility of partial trapping in which the incoming particle spends more time in contact with the target maybe transferring its initial charge. Nevertheless, these cases are easily detected from the oscilloscope pulses.

Figure 3 shows the histograms for three runs with an effective LWC of  $0.2 \text{ g/m}^3$  at different temperatures ( $-10$ ,  $-15$  and  $-18^\circ\text{C}$ ). There is a mixture of signs with a dominance of the positive pulses in all three runs. Figure 4 shows data taken at slightly higher LWCs. The data corresponding to  $-12^\circ\text{C}$  was taken at  $0.3 \text{ g/m}^3$  while the data for  $-15$  and  $-18^\circ\text{C}$  was taken at  $0.5 \text{ g/m}^3$ .

A first observation from these Figures is that as the LWC is increased it is necessary decrease the temperature in order to obtain negative charge transfers. The charge magnitudes are comprised in the range  $\pm 50 \text{ fC}$  in accordance with the observations of Gaskell and Illingworth (1980). From a statistical point of view it is important to mention that about 50% of recorded events are observed to produce fragments. Moreover, there is a proportion of events similar to that illustrated in Figure 2b which cannot be categorize with total certainty as fractures but they have a high probability of being so, bringing the total to about 80%.

## Discussion

Caranti et al (1991) noted that for a smooth ice target just placed into the wind tunnel the charging was different from that of a target that had the opportunity to grow new ice on it. They observed a mixture of signs during the initial growth from the vapor and suggested that the presence of both signs could be

associated to two different kind of surfaces.

They also suggested that the transfer of negative charge observed when the ice particles collide with an evaporating ice substrate could be caused by a contact potential difference between the interacting ice surfaces. In fact, *Caranti and Illingworth* [1983] found a relatively strong contact potential change when ice was rimed or was subjected to rapid freezing. A similar change could not be associated to vapour growth, which prompted Caranti et al (1991) to suggest that the positive transfers were probably caused by the fragmentation of dendrites from the surface of the growing particle.

The phenomenological model they proposed was based on the fact that significant temperature gradients are created when a particle grows. Fracture under these gradients can be a source of charge for the measured transfers. In that work it is shown that the sign of the charge transfer follows the sign of temperature gradient. When the surface was growing by vapor deposition the charge left on the target was positive.

The droplets landing on the target form structures or piling up as long as the their influx does not go over the limit of wet growth. This piling up are inherently fragile and could break under impact (or even without). During this accretion process the temperature gradients are caused by the release of freezing latent heat. The heat released has also the overall effect of warming up the the whole accretion. Now, a droplet landing on top of a pile will heat up the outer end of it, creating a outward pointing temperature gradient  $\nabla T$ . Neighbouring piles will also be heated but by vapor deposition since the freezing drop is a strong vapor source. On the other hand the piles away from a freezing drop and evaporating will have an inward pointing  $\nabla T$ .

The fraction of piles having a given sign of the gradient will be related to the droplet influx and therefore to the product of LWC and the air velocity. The other parameter, this fraction of piles is related to is the temperature. As the temperature is lowered the time it takes for a droplet to freeze diminishes and on average its influence on the surroundings also decreases. The probability a collision results in the fracture of a pile with a given  $\nabla T$  will be related to this fraction.

The results illustrated in Figures 3 and 4 are consistent with the above description. In fact, the fraction of positive pulses at a given  $T$  is clearly proportional on the LWC (all runs were at the same air velocity). So much that in certain runs there were only positive pulses. The influence of the temperature is also seen in those figures.

### Conclusion

Several researchers working on multiple collisions (eg. Kumar and Saunders 1989) argue that given a particular set of environmental conditions the charge transfers would have only one sign. The results presented here show that most of the time there is a mixture of signs and that the environment influence only which one is the dominant.

The fracture charging is observed to work in a wide range of temperatures and for impact velocities relevant to cloud physics.

It is important to stress the large proportion of collisions followed by fracture observed. There is evidence that the size of the fragments will allow them to grow from the vapor as any other ice crystal in the cloud. Therefore this is a viable multiplication mechanism.

## References

Abbott, C. E., and T. W. Cannon, A droplet generator with electronic control of size, production rate, and charge, *Rev. Sci. Instrum.*, **43**, 1313-1317, 1972.

Avila, E.E., G.M. Caranti and M.A. Lamfri, Charge reversal in individual ice-ice collisions, *Proc. 8<sup>th</sup> International conference on atmospheric electricity* 245-250, Uppsala, Sweden, 1988.

Baker B., M.B. Baker, E.R. Jayaratne, J. Latham and C.P.R. Saunders, The influence of diffusional growth rates on the charge transfer accompanying rebounding collisions between ice crystals and soft hailstones. *Q. J. R. Meteorol. Soc.*, **113**, 1193-1215, 1987.

Baker M.B. and Dash J.G. Charge transfer in thunderstorm and the surface melting of ice *J. Crystal Growth*, **97**, 770-776, 1989.

Buser O. and A.N. Aufdermaur, Electrification by collision of particles on ice or metal target in *Electrical processes in the atmospheres*, Steinkopf Darmstadt, 1977.

Caranti J.M., E.E. Avila and M.A. Ré, Charge transfer during individual collisions in ice growing from vapor deposition. *J. Geoph. Res.* in press. 1991.

Caranti J.M. and A.J. Illingworth, The contact potential of rimed ice. *J. Phys. Chem.* **87**, 4125, 1983.

Gaskell W. and A.J. Illingworth, Charge transfer accompanying individual collisions between ice particles and its role in thunderstorm electrification. *Q. J. Roy. Met. Soc.* **106**, 841-854, 1980.

Jayaratne E.R., C.P.R. Saunders and J. Hallett, Laboratory studies of the charging of soft hail during ice crystals interactions. *Quart. J. Roy. Met. Soc.* **109**, 609-630, 1983.

Keith W.D. and C.P.R. Saunders, Charge transfer during multiple large ice crystal interactions with a riming target. *J. Geophys. Res.* 94, 13103-13106, 1989.

Keith W.D. and C.P.R. Saunders, Further laboratory studies of the charging of graupel during ice crystals interactions. *Atm. Res.* 25, 445-464, 1990.

Kumar P.P. and C.P.R. Saunders, Charge transfer during single crystal interaction with a rimed target. *J. Geophys. Res.* 94, 13099-13102, 1989.

Reynolds S. E., M. Brook and Mary Foulks Gourley, Thunderstorm charge separation . *J. Meteor.* 14, 426-436, 1957.

Takahashi T., Riming electrification as a charge generation mechanism in thunderstorms. *J. Atmos. Sci.* 35, 1536-1548, 1978.

## Figure Captions

**Figure 1.** Left: vertical cross section of the working stage of the wind tunnel. The target is a cylindrical rod. The arrow indicates the flow direction. Right: horizontal cross section along the A-A line. The steam is generated outside the cold room and is thermalized before entering this stage.

**Figure 2.** Typical events with particles of  $100\text{ }\mu\text{m}$  impacting at  $5\text{ m/s}$ . Top trace: added signals from the two induction rings. Bottom trace: the target signal. (See text for description)

**Figure 3.** Charge transfer histograms taken at three temperatures. The effective liquid water concentration LWC was  $0.2\text{ g/m}^3$ .

**Figure 4.** The same as in Figure 3 but for LWC  $0.5\text{ g/m}^3$ .



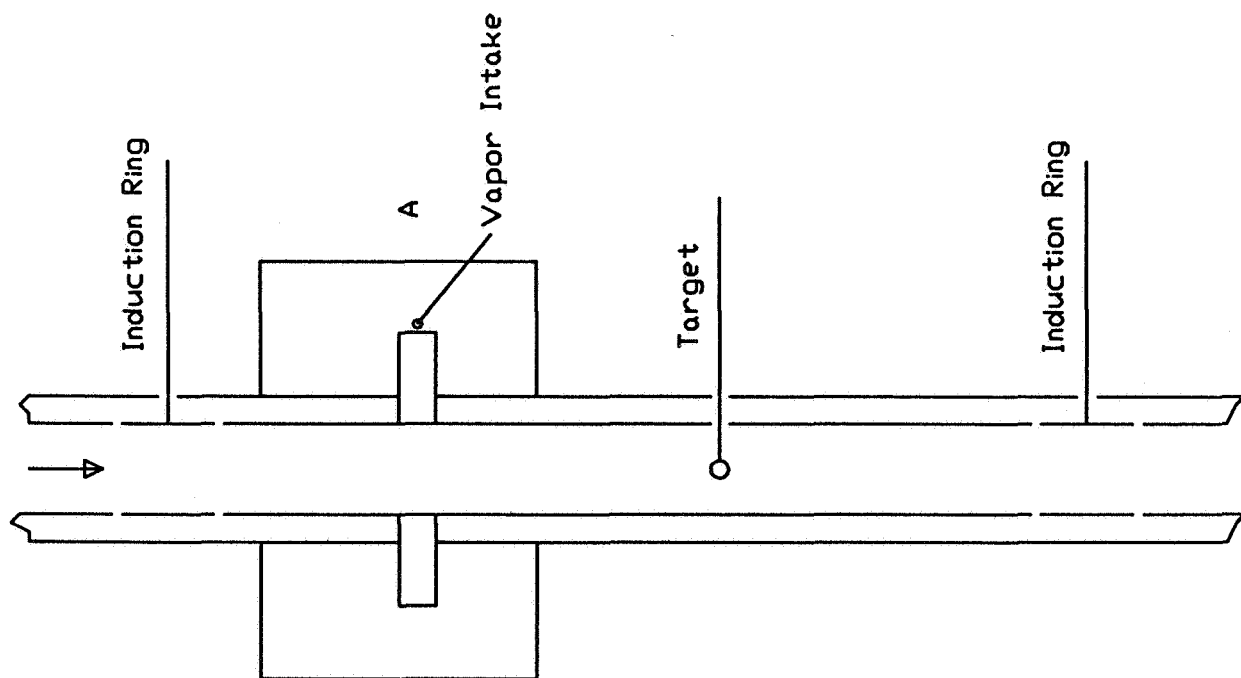
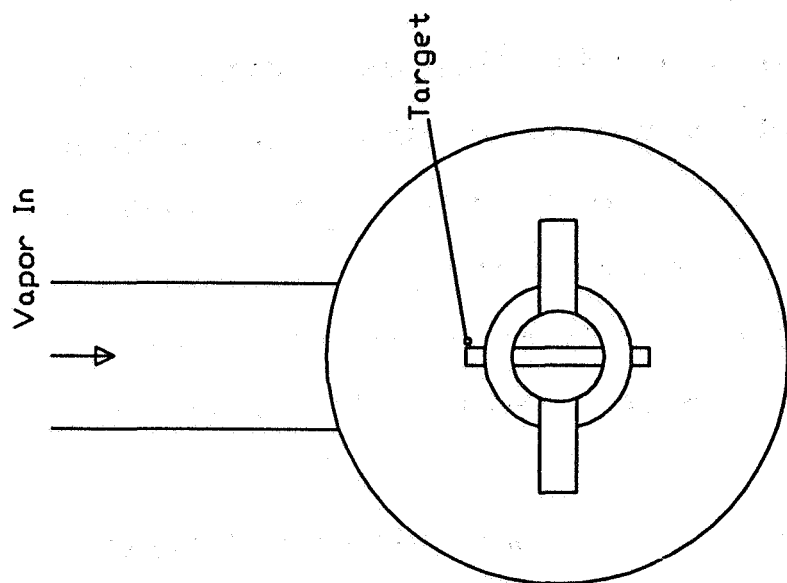


Figure 1

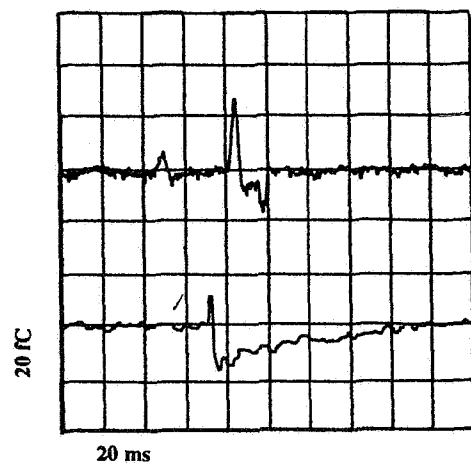
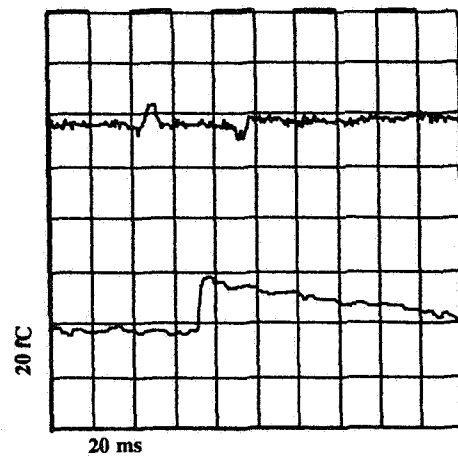
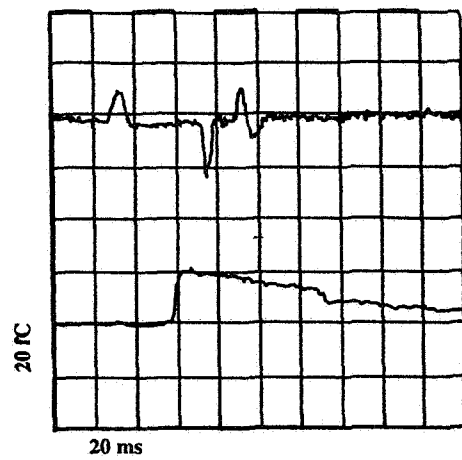


Figure 2

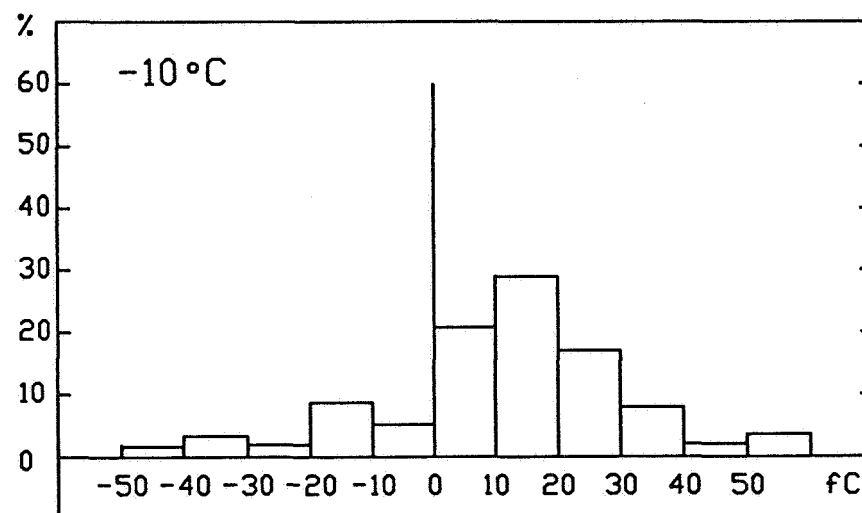
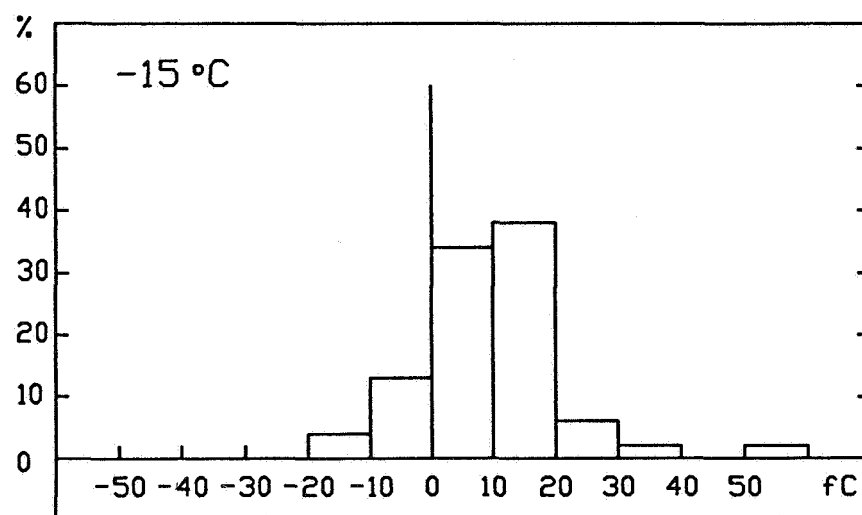
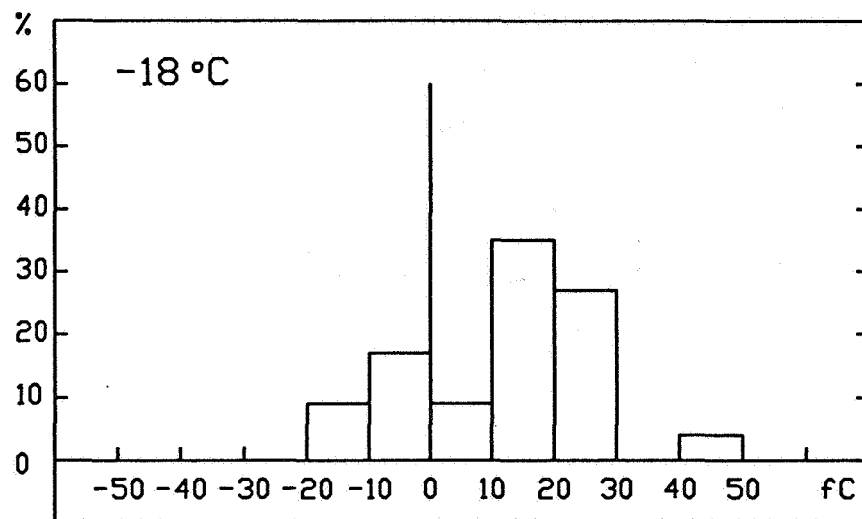


Figure 3

## HOW TO CREATE BALL LIGHTNING

Robert K. Golka, Jr., Box 676, Brockton, MA 02403  
U. S. Air Force, Flight Dynamics Laboratory

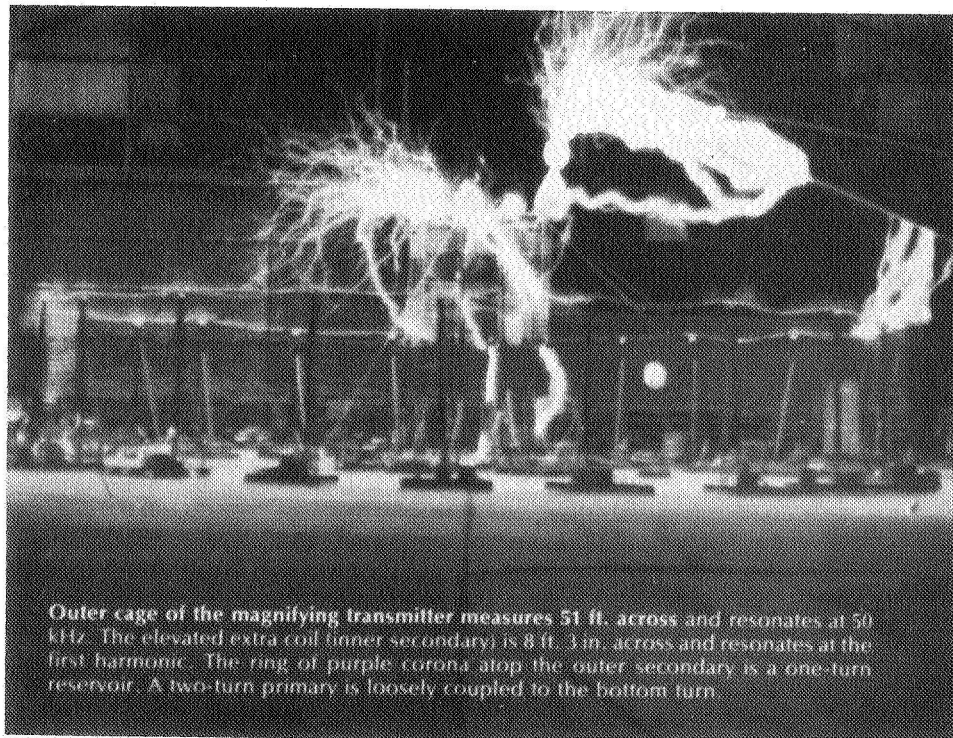
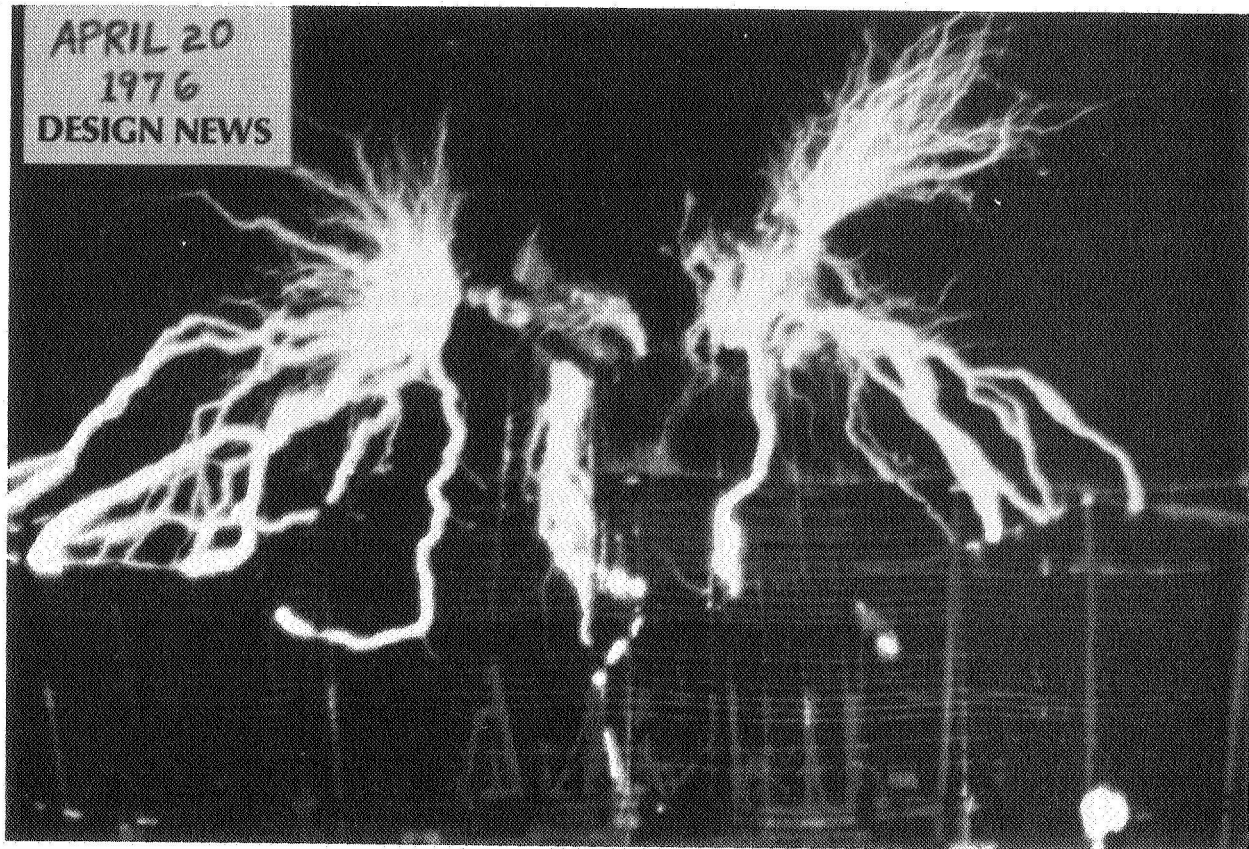
At last the discovery of how to produce ball lightning on a command and controlled basis has been discovered by Robert K. Golka, Jr. It took 23 years and thousands of failures to develop the techniques. Similar plasma balls have appeared in dwellings on rare occasions and on commercial and military aircraft during flight.

The type Golka has created are similar to what has come into airplanes during flight and that have appeared in WW-2 submarines during maneuvers. They consist of a liquid metal core or kernel surrounded by a metal vapor boundary layer. It has characteristics very much like a drop of water bouncing and dancing for a few seconds on a hot cast-iron stove. With higher power input to the fireball it can be made to flow and travel higher from a surface or ground area.

What does one need to make ball lightning?

1. A transformer of 150,000 watts capable of providing approximately 10,000 amperes at 15 volts 60 cycle.
2. Thick one inch cables of stranded wire leading into a 3 x 4 x 1 foot plastic tank.
3. Quarter inch thick 4" x 6" aluminum plate to be used as one of the discharge electrodes, the other electrode being the heavy (400 MCM) copper wire with the insulation stripped back 6 inches.

By shorting the cable against the aluminum plate under water, quarter inch fireballs or lightning balls will appear out of the water and dance around on its surface. Of course, protective clothing and goggles are necessary. These lightning balls sometimes dance right out of the tank onto the floor. They seem to be hot to the touch only if you squeeze them. They are a brilliant white color indicating a slow combustion of aluminum. If higher temperatures are reached and different metals are used, the color of the fireballs will be different. It appears that the ball is spinning or the inside kernel is spinning. With the stated ampere and voltage ratios, they have lasted for almost 2 seconds. More power in would increase their lifetimes. Other variations are currently under investigation. The high temperature limits of these fireballs is now being studied.



EXPERIMENTAL MODELLING OF LIGHTNING INTERACTION PHENOMENA WITH A  
FREE POTENTIAL CONDUCTING OBJECTS

E.N.Chernov, A.V.Lupeiko, N.I.Petrov

Branch of All-Union Electrotechnical Institute, 143500 Istra, Moscow region, USSR

## Abstract

A laboratory experiments has been conducted to investigate the physical processes of the development of long air discharge and their interaction with a free potential conducting objects. Space-time development of the lightning phenomena in the gaps was registered by the moving-image camera and optoelectronic transducer. The electric field in the different points of a gap was measured using a Pockels device both in the leader stage and the stage of return stroke. Experimental results of the streamer zone length measurements in the gaps with length of up to 65 meters are presented. Extrapolation on the lightning case shows that the streamer zone length of the leader in the lightning composes only the few tens meters. A physical processes of the interaction of a positive and negative long sparks with the isolated objects are investigated. In particular the striking probability of isolated conducting spheres with different diameters in the dependence on the location in the gap is investigated. It is obtained that the striking probability of the spheres smaller than the critical size equal to zero near the electrode. The striking probability of the spheres with the diameters greater than the critical is the unity near the electrode. The physical picture of the observed effects is supposed.

## 1 Introduction

It is well known that both the lightning and the spark discharge in a long air gap are characterized by the leader mechanism of the propagation. Therefore a series of properties of lightning discharge are displayed also in the long air gap discharge. This allows to put the task of modelling of lightning orientation processes on the objects in the laboratory. The different factors influence on the spark discharge channel orientation: a gap geometry, parameters of a leader, atmosphere conditions and others. Many papers was suggested to the investigation of striking probability of a free potential objects (see, for example, [1-3]). In [1] it is shown that the striking probability is increased with the growth of conductivity and capacity of the object. In [2] the striking probability of the objects in the dependence on the its spacing in the gap is investigated. It is shown that near the earth surface the striking probability is increased. In paper [3] the results of investigation of the polarity effect in the interaction of spark with a free potential object are presented.

The basic effect of the orientation of a leader discharge is connected with the flow of electric field, closed on the object, i.e. the orientation is determined by the degree of field distortion by the object and most probably in the direction of field intensification. However the effects of space charges interaction also influences on the striking probability. The investigation of striking probability dependence on the charge of the leader also is of interest for lightning protection of aircrafts.

In this paper the influence of polarity of the applied voltage and the parameters of the streamer zone on the striking probability of the free potential objects are investigated.

## 2 Experimental technique

Measurements are carried out in rod-plane and toroid-plane gaps. Impulses with the duration  $T_i = 7500 \mu s$  and the front duration  $t_f$  from 2 to  $1200 \mu s$  were forming on an outlet of High-Voltage Generator HVG-9MV and energy capacity 1.35 MJ. The space-time development of the lightning phenomena in the

gap was registered by the moving-image camera and optoelectronic transducer. The electric field in the various point of the gap was measured using a Pockels device. The sensor is a primary transducer optically connected by fiber guides of up to 150 m long with a light source and a photodetector. A light source is a semiconductor laser with emission wavelength of  $0.86 \mu m$ . Recorded frequency band is 50 MHz.

In the experiments the models of aircrafts and metallic spheres with the diameters 4, 10, 30, 50 cm are used. The objects on the different distance from the high-voltage electrode both inside of the streamer zone and the outside of its are placed. The streamer zone length was measured with the help of a photoelectronic recorder. The trajectories of the spark channel were recorded using a two photocameras, mounted under the angle  $90^\circ$ . The striking probability was determined from 100 breakdowns for each case. The applied voltage was equal to 90% of the breakdown probability. Investigations are carried out in the gaps with the length of up to 25 meters long under application of voltage pulses of positive polarity and of up to 12 meters under negative polarity voltage. The sparks from the HVG top, which is the toroid with the ratio of external radiuses  $8/2$  m have the length from 50 to 80 meters.

## 3 Experimental results

## 3.1 Positive polarity

The main parameters characterized the leader are the streamer zone length, electric field intensity and the space charge of the streamer zone.

## 3.1.1 The streamer zone length

It is important to reproduce the stage of free development of leader with the chance distortions of the channel trajectory in the experiments on the modelling of lightning striking of the aircrafts. This is ensured in the case when the streamer zone length  $l_{stz}$  of developing leader is much shorter than the gap length  $d$ . It is known that the streamer zone length of leader in the its initial phase of development  $l_m$  depends on the front duration of the applied voltage.

At the sharply impulse front the streamer zone length occupies the significant part of the gap already in the initial phase of leader development. The dependences of streamer zone length on the front duration of the applied voltage for different gaps obtained using photoelectric transducer are presented in fig.1. It can be seen that the discharge at the  $\tau_f = 2 \mu s$  is characterized by

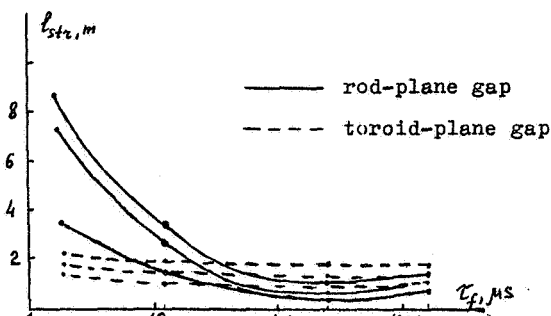


Fig.1. The variation of streamer zone length  $l_{str}$  as a function of voltage front duration  $\tau_f$ . 1-  $d=5m$ ; 2-  $d=10m$ ; 3-  $d=15m$ .

significant length of streamer zone and for the gap with length  $d=4m$  consists from only one final stage. The critical duration of voltage front  $\tau_{cr}$  is exist at which the streamer zone length takes the minimum value. Note, that the breakdown voltage is minimal at the critical duration of the front. It is seen from fig.1 that the change of streamer zone length in the gap rod-plane essentially more then in the gap toroid-plane. The streamer zone lengths versus from the gap length at the critical front duration  $\tau_{cr}$  of the applied voltage are presented in the fig.2.

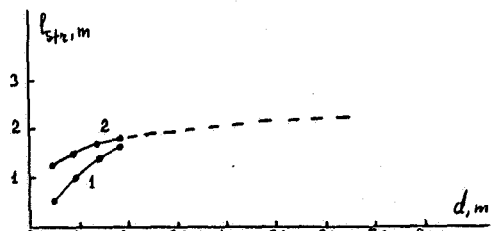


Fig.2. The variation of streamer zone length  $l_{str}$  as a function of gap length  $d$ .

The streamer zone length  $l_{str}$  in the gap rod-plane in the dependence on the gap length  $d$  is described by the expression

$$l_{str} \approx 0.18 d^{3/4}, [m] \quad (1)$$

In the gap toroid-plane this dependence have the form

$$l_{str} \approx 1 + 0.15 d^{1/2}, [m] \quad (2)$$

Approximation of the streamer zone length on the large length of gaps by formula (2) is represented in the fig.2 with the drawing line. It is seen that the streamer zone length is saturated at the large gap length. So, at the gap length  $d=100m$  the streamer zone length, calculated by the formula (2), is equal to  $l_{str} \approx 2.5m$ . Note, that the streamer zone length of leader developing from the HVG top is equal to  $l_{str} \approx 2.8m$  at the influence of impulse (2/7500  $\mu s$ ), when the breakdown take place with the overstrain.

### 3.1.2 The electric field intensity

Oscillograms of the electric field intensity change are represented in figs.3-6. Figures 3 and 4 correspond to gap breakdown case of  $d=6m$  and  $d=12m$  under application of voltage pulse (300/7500  $\mu s$ ). Maximum value

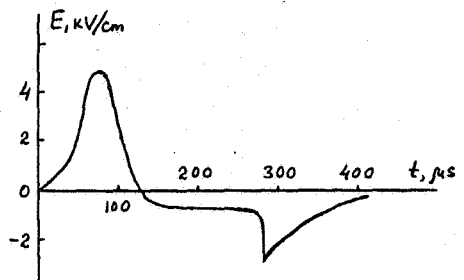


Fig.3. Electric field in the streamer zone of leader.  $d=6m$ ,  $h=0.6m$ .

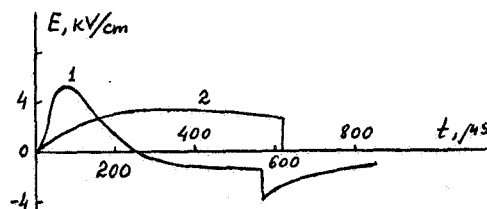


Fig.4. Electric field in 12m rod-plane gap. 1-  $h=0.8m$ ; 2-  $h=4m$ .

of electric field intensity is achieved at sensor placing on the longitudinal axis of streamer zone and is equal to 5 kV/cm, time of attainment of this maximum at change of sensor position in gap being determined by velocity of leader propagation. Curves 1 correspond to case of streamer zone passage through the sensor. It is seen from the figures that the polarity of electric field intensity is changed. In the oscillograms one can separate two stages corresponding to different physical processes. First stage corresponds to leader one of discharge development, second stage corresponds to neutralization of the space charges. Time of discharge forming grows with increase of gap length and is defined by leader propagation velocity  $v_l$  ( $t=d/v_l$ ). Field intensity is decreased moothly after breakdown. Half-decay time or neutralization time of the space charge  $\tau$  grows with increase of gap length. So, at the length  $d=6m$ , time  $\tau \approx 100 \mu s$ , and at  $d=12m$   $\tau$  is 400  $\mu s$ . In case when the sensor is beyond a leader cover the neutralization stage is not registered by the sensor (fig.4, curve 2).

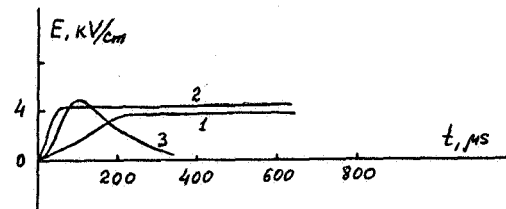


Fig.5. Electric field in 18m rod-plane gap. 1-  $h=4m$ ; 2-  $h=0.8m$ ; 3-  $h=1.6m$ . 300/7500  $\mu s$ .

At absence of breakdown the field oscillogram was changed depending on availability or absence of uncompleted leader in gap (fig.5). In last case the sensor placing beyond a streamer corona from the rod end reproduced change

of electrode field in rod-plane gap (fig.5, curve 1). Inside the streamer corona at absence of leader the electric field repeats form of applied voltage however velocity of field growth is defined not by the steepness of voltage rise, but a dynamics of the space charge in the streamer zone and depends on distance from the rod end (fig.5, curve 2). A availability of the uncompleted leader in the gap the field change inside the streamer corona takes place analogically to breakdown case. However change of field polarity is not observed in this case (fig.5, curve 3). Change of front duration of applied voltage (15/7500  $\mu$ s) is not affected on the qualitative picture of field behaviour (fig.6). Note only that for-

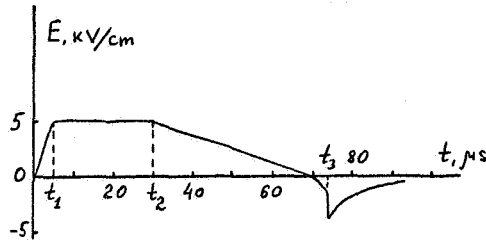


Fig. 6. Electric field in 4 m rod-plane gap.  
 $h = 0.7$  m;  $\tau_f/\tau_i = 15/7500$   $\mu$ s.

ming time of breakdown is decreased essentially because of increase of leader propagation velocity and increase of streamer zone length in the final stage. Fig. 6 corresponds to the gap length  $d = 4$  m. Time moment  $t = 0$  coincides with the beginning of voltage application,  $t_1$  coincides with contact moment of the streamer zone with the sensor. When the sensor is placed inside the streamer zone time  $t_1$  is determined by propagation velocity of ionization front of the streamer corona  $t_1 = h/v_{stz}$ . Velocity is constant at different distances from the rod end and is equal to  $v_{stz} = 2 \cdot 10^8$  cm/s. Electric field intensity is not changed also along the full length of the streamer zone and is equal to  $E_{stz} = 5$  kV/cm. Electric field intensity begins to decrease after the leader head. Time interval  $\Delta t = t_2 - t_1$  is defined by velocity of leader propagation. In this case leader velocity is equal to  $v_l = 3 \cdot 10^8$  cm/s. The leader reaches the plane at the moment time  $t_3$ . Further the change of electric field intensity is connected with the processes of neutralization of charges accumulated in the discharge gap. Time of charges neutralization is correlated with the streamer zone length and the gap length.

### 3.1.3 Space charge of streamer zone

Using the Gauss theorem we can to evaluate the value of space charge, carried out by leader:

$$Q_{stz} = \epsilon_0 \oint E_{stz} dS = \epsilon_0 E_{stz} l_{stz} \Omega, \quad (3)$$

where  $\epsilon_0 = 8.85 \cdot 10^{-12}$  F/m is the dielectric constant,  $E_{stz}$  is the electric field in the streamer zone,  $l_{stz}$  is the streamer zone length. On the known intensity of electric field in the streamer zone the potential of leader head also may be obtained:

$$\varphi_l = E_{stz} \cdot l_{stz} \quad (4)$$

Setting in (4) the expression (2) for streamer zone length  $l_{stz}$ , we have

$$\varphi_l = E_{stz} (1 + 0.15 d^{1/2}), [V] \quad (5)$$

At the characteristic gap length  $d \approx 3$  km for the lightning it is followed from here, that the potential of the leader head composes  $\varphi_l \approx 4.6$  MV, and the streamer zone length equal to  $l_{stz} \approx 9.2$  m. This is not contradicted with the experimentally observing value of streamer zone length in the lightning [4]. In fig. 7 the per unit length charge  $q = 2\pi\epsilon_0 E_{stz} l_s$  versus from the gap length is presented. It is seen from figure, that the per

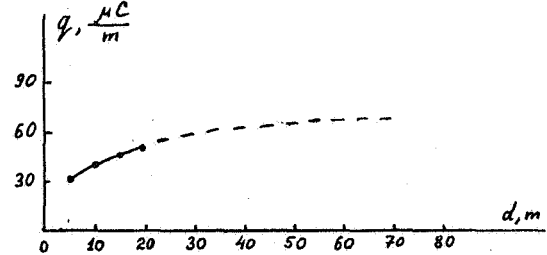


Fig. 7. The charge per unit length as a function of the gap length.

unit length charge of leader is saturated at the growth of gap length. It is known [4], that the space charge distributed around the lightning channel is neutralized in the return stroke stage and is composed

$$Q = \int i dt = 1 \text{ C}$$

for the mean current  $i \approx 20$  kA with the duration  $\Delta t \approx 50$   $\mu$ s. Approximately a such charge is followed at the evaluating of  $q \approx 2\pi\epsilon_0 E_{stz} l_s$  using the expression (2) for the lightning channel length  $d \approx 3$  km:

$$Q = q \cdot d \approx 300 \frac{\mu\text{C}}{\text{m}} \cdot 3000 \text{ m} = 0.9 \text{ C}$$

### 3.1.3 Striking probability of aircraft models

Lower the experimental dependences of striking probability of aircraft models in the gap rod-plane are resulted. In figs. 8, 9 the dependences of striking probability  $P$  of models with length  $l_m = 1.15$  m on the distance  $h_m$  up to high-voltage electrode at the different value  $\tau_f$  and  $d$  are presented. It is

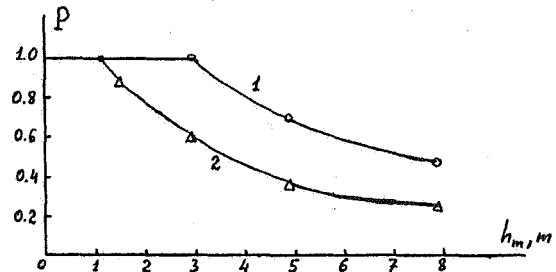


Fig. 8. The striking probability as a function of distance from the electrode. 1-  $\tau_f = 15$   $\mu$ s; 2-  $\tau_f = 600$   $\mu$ s.  $d = 3$  m.

seen from figures that the probabilities  $P$  are maximum near the electrode and is decreased with the removing from it. Fig. 10 shows a change of striking probability of model placed on the fixed distance  $h_m$  from the electrode at the increase of gap length. It can be seen that the striking probability decreases with the increase of gap length. It is known that the essential influence on the striking probability of models turns out the discharge processes beginning from the model. Fig. 11



shows the discharge development until the striking of model. It is seen from figure that the positive discharge begins from the model after the contact of the streamer zone of direct leader with the model. Note that the itself leader channel is found on the distance  $l_{str}$  from the surface of model.

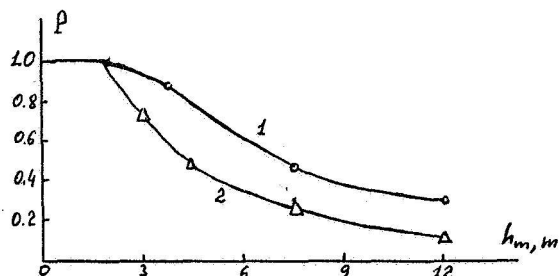


Fig. 9. Striking probability as a function of distance from the electrode.  $d=12m$ ; 1-  $\tau_i = 15 \mu s$ ; 2-  $\tau_i = 600 \mu s$ .

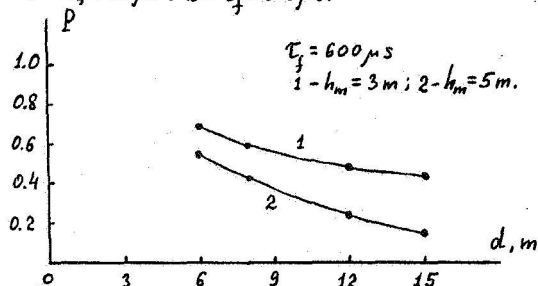


Fig. 10. Striking probability of aircraft model as a function of a gap length.  $\tau_i = 600 \mu s$ ; 1-  $h_m = 3m$ ; 2-  $h_m = 5m$ .

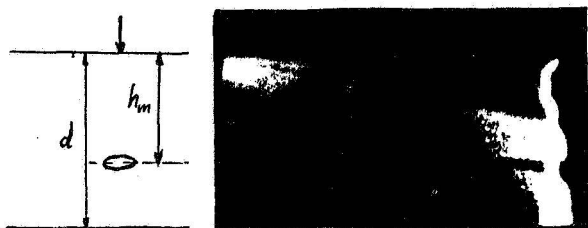


Fig. 11. Discharges development in the gap positive rod-model-plane.  $d=8m$ ,  $h_m=5m$ .

### 3.1.4 Striking probability of metallic spheres

As was shown above the corona discharge processes begin from the objects until the contact its by the leader channel. Elucidation of the role of this processes on the orientation of leader channel is of interest. Lower the results of the investigation of the positive leader orientation to the metallic spheres, from which the corona processes is absent, are presented. Experimental investigations have been carried out in the rod-plane gap. The positive switching impulse voltages ( $15/7500 \mu s$  and  $300/7500 \mu s$ ) were applied to the rod electrode. The striking probability of conducting spheres with different diameters in the dependence on the applied impulse voltage parameters and on the situation of spheres in the gap are measured. The spheres with the diameters  $D=4, 10, 30, 50$  were used. The spheres were placed in the gap at the different distance from the rod end both inside of streamer zone and outside its.

The streamer zone length was measured using the moving-image camera. For gap length  $d=6m$  the streamer zone length was equal to  $l_{str} = 0.6m$  and  $l_{str} = 2m$  at the applied voltage impulse  $\tau_i/\tau_i = 300/7500 \mu s$  and  $15/7500 \mu s$  accordingly. The trajectories of sparks channel were recorded using a two photocameras, mounted under the angle  $90^\circ$ . In figs. 12 and 13 the dependences of a striking probability of the spheres with different diameters from the distance between the sphere and rod are presented. From figures it can be seen that the striking probability in the dependence on the leader charge  $Q_e$  and the inductive charge  $Q_{in}$  may be either increasing or decreasing function of distance between the object and high voltage electrode. Striking probability of the spheres smaller than the definite size equal

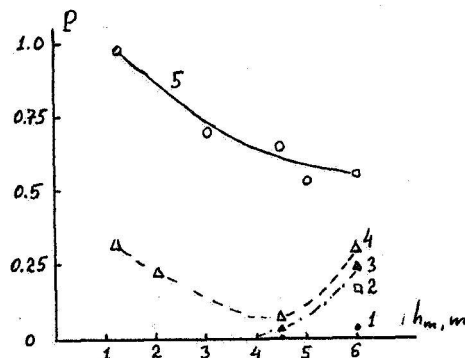


Fig. 12. Striking probability of spheres at the applied voltage  $300/7500 \mu s$ .

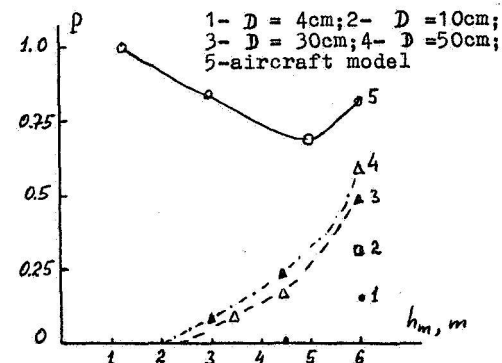


Fig. 13. Striking probability of spheres at the applied voltage  $15/7500 \mu s$ .

to zero near the electrode. At the exceeding of critical size the striking probability becomes the unit near the rod and decrease with the removing from it. The charge of the streamer zone grows also at the increasing of gap length that must to change the striking probability of object. So, the sphere with the diameter  $D=50cm$  in the gap with length  $d=6m$  situated on the distance  $1m$  from the rod end is struck with the probability  $P=0.3$ . At the gap length  $d=8m$  this sphere is never struck. The charge of the streamer zone at this is increased two times. The obtained results may be explained proceed from the next physical picture of leader discharge orientation. Propagation of leader takes place mainly in the direction of field intensification, created by the object. At the contact of object by the streamer zone the object is charged with the positive charge. This is increases the flow of electric field, closed on the object. If the charge of streamer zone turns out to be more than the inductive negative

charge then the repulsive electric field is appeared. This explains the existence of critical parameters (critical size of object or critical charge of leader) at exceeding of which the mechanism of leader orientation is changed.

### 3.2 Negative polarity

The striking probability of objects is increased at the negative polarity of leader approximately on 25% in relation to the positive polarity (fig.14).

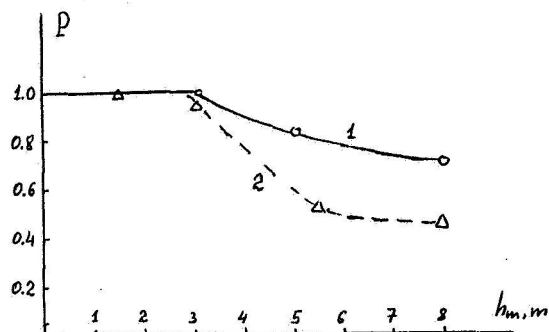


Fig. 14. Striking probability of aircraft model as a function of the distance from the electrode.  $d = 8$  m; 1-  $\tau_f = 15$   $\mu$ s; 2-  $\tau_f = 600$   $\mu$ s.

Explanation of this may be obtained from the analysis of discharge photochronograms, presented in figs. 15, 16. It is seen from figures that the contrary positive leader develops from the object. It is noted that the condition of the development of contrary positive leader is the touching of object by the front of streamer zone. In the lower part of gap the discharge develops in the form of slow corona. In table 1 the experimental values of the velocities of contrary  $v_+$  and direct  $v_-$  leaders, the develop time up to its close  $\Delta t$ , the channel length of direct leader  $l$  and the streamer zone length of negative leader  $l_s$  in the beginning of the final jump phase of discharge are presented. Note that the parameters of the direct negative leader and the contrary positive discharge practically is not depended from the front duration of the applied voltage impulse  $\tau_f$  and the gap length  $d$ . These parameters not depends also on the effective velocity of the stepped negative leader development in the upper part of gap, which at the  $d = 12$  m grows up to 5-10 cm/ $\mu$ s. Note, that the development of the contrary leaders takes place in the unbroken form. The velocity  $v_-$  coincides with the velocity of negative leader, developing in the "pure" gap, and the value  $v_+$  agrees with the measurements values of positive leader head velocity of leader developing from the volume. In all case the aircraft model participates in the formation of new leader step. The step formation time not depends on the presence of the model and composes in average 30-35  $\mu$ s. It is seen from table, that the length of direct leader channel  $l$  in the moment of birth of contrary leader at the constant distance between the model and high voltage electrode depends on the  $\tau_f$ , that may be caused by the different value of space charge or the streamer zone length. By this reason the value  $l$  must to increase at the growth of gap length that is observed in the experiments. It is noted that the development of the contrary leader takes place from the moment of contact of the streamer zone of

direct leader. However, the growth of distance  $(h_m - l)$  is observed with the increasing of gap length and for the gap length  $d = 12$  m the value  $(h_m - l)$  coincides with the streamer zone length of negative leader in the final jump phase.

Table 1. Characteristics of discharge in the gap negative rod-model-plane

$d/h_m$ , m/m	$\tau_f$ , $\mu$ s	$v_+$ , cm/s	$v_-$ , cm/s	$\Delta t$ , $\mu$ s	$l$ , m	$l_s$ , m
8/3	15	$3.7 \cdot 10^6$	$0.8 \cdot 10^6$	35.0	0.7	2.7
	300	$3.3 \cdot 10^6$	$0.6 \cdot 10^6$	30.0	1.15	2.4
12/7	15	$3.3 \cdot 10^6$	$1.0 \cdot 10^6$	31.0	4.1	2.9

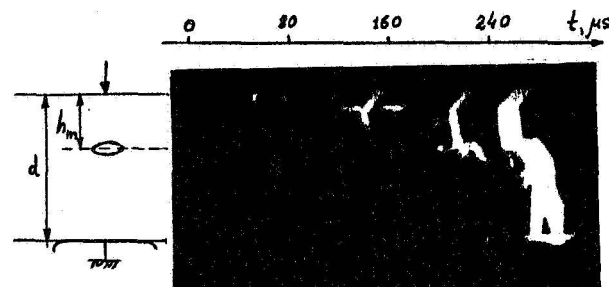


Fig. 15. Photochronogram of discharge processes in the gap negative rod-model-plane.  $d = 8$  m; -300/7500  $\mu$ s;  $h_m = 3$  m.

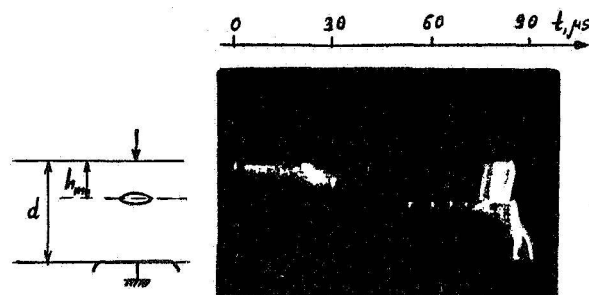


Fig. 16. Photochronogram of discharge processes in the gap negative rod-model-plane.  $d = 8$  m; -15/7500  $\mu$ s;  $h_m = 3$  m.

#### 4 Discussion

The results adduced above are related to the object striking in laboratory discharge gap. Elucidation of the role of obtained effects in lightning striking of real objects is of interest. Let us evaluate a characteristics of objects and lightning at which the repulsion effect turns out to be essential. The charge carried by the streamer zone of leader may be evaluated on the known value of electric field in the streamer zone using the Gauss theorem:

$$Q_{str} = \epsilon_0 \oint E_{str} dS = 2\pi\epsilon_0 E_{str} l_{str}^2 (1 - \cos\theta_0) \quad (6)$$

where  $l_{str}$  is the streamer zone length,  $\theta_0$  is the top angle of the streamer zone,  $E_{str}$  is the electric field in the streamer zone,  $\epsilon_0$  is the dielectric constant.

The electric field in the streamer zone  $E_{str}$  approximately is 5 kV/cm. The angle  $\theta_0$  is equal as a rule to 30°-90°. The value of inductive charge  $Q_{in}$  depends on the capacity of the object or of its geometrical sizes. So, for the sphere with a diameter  $D$  we have:

$$Q_{in} = \frac{3\pi}{4} \epsilon_0 E D^2 \quad (7)$$

From (6) and (7) we obtain that

$$\frac{Q_{str}}{Q_{in}} \sim \frac{8}{3} \frac{l_{str}^2 (1 - \cos\theta_0)}{D^2} > 1,$$

i.e. the essentially repulsion effect takes place for the objects with the linear size smaller than the streamer zone length

$$D \leq \sqrt{\frac{8}{3} (1 - \cos\theta_0)} l_{str}$$

At the length of gap  $d = 6$  m and the front durations of applied voltages  $\tau_f = 300 \mu s$  and  $\tau_s = 15 \mu s$  the streamer zone length is equal to  $l_s = 0.6$  m and  $l_{str} = 2$  m, accordingly. The charges of streamer zones are equal to  $Q_s = 3.5 \mu C$  and  $Q_{str} = 34 \mu C$ . In lightning the streamer zone length composes a few ten meters. At the length of streamer zone  $l_{str} = 10$  m the charge approximately is equal to  $Q_{str} \approx 150 \mu C$ . The repulsion effect of this leader must take place for the objects with the size  $L \leq 5$  m.

Note that the physical picture of leader orientation described above not accounts a series of effects influencing on the striking probability of object. In particular the corona discharges from the sharp projections of objects are not take into accounted. Experiments show that the striking probability of sphere with a projection of rod form essentially depends on the location of projection on the sphere. The projection that is the cathod electrode, not influences on the striking probability of sphere. So, the sphere of the diameter  $D = 50$  cm with the cathod projection by length of 10 cm was not in the least struck, and with the anode projection the striking probability becomes 100%. Essential influence of the anode projection on the striking probability is noted also in paper [3].

#### 5 Conclusion

Thus, the values of the streamer zone length of leader in the gaps with length up to 80 meters are experimentally obtained. Extrapolation of these results on the lightning shows that the streamer zone length of lightning with a channel length  $L \approx 3$  km composes only 9.2 m.

Electric field intensity in the streamer zone of positive leader composes  $E_{str} \approx 5$  kV/cm

and not depends on the gap length. This allows to calculate the potential of leader head in lightning. So, at the streamer zone length  $l_{str} = 10$  m the potential of leader composes  $\varphi_L = 5.0$  MV.

A next characteristics essentially influence on the striking probability of objects: position of object in the discharge gap, degree of field distortion by object and degree of compensation of inductive charge by the charge of streamer zone. It is necessary to take into account these effects at the determining of the orientation height of leader.

It is shown that the contrary discharges, developing from the object, also essentially influence on the striking probability.

#### References

1. A. P. Belyakov, I. S. Stekolnikov, Influence of different factors on the development of spark discharge. - *Elektrichestvo*, 1938, 3, pp. 25-28.
2. E. M. Bazelyan et al. Lightning striking of aircrafts. - *Elektrichestvo*, 1980, 3, pp. 48-50.
3. B. Hutzler, C. Riquel, J. P. Riu. High voltage laboratory tests and lightning phenomena. - 10 th Int. Aerospace and Ground Conference on Lightning and Static Electricity. Paris, 1985, pp. 191-196.
4. M. A. Uman. Lightning. New York: Mc-Graw-Hill, 1969.

# **Poster Papers**

## **Ground Protection**

N91-32730

DIFFUSE DISPERSIVE DELAY  
and the  
TIME CONVOLUTION / ATTENUATION of TRANSIENTS \*  
Burt J. Bittner (LS) Sr Staff  
Electronic Systems Division, HARRIS Corp.  
Troutman Blvd. Bldg 20, Palm Bay, Fl. 32905

Introduction:

The Fourier analysis of transients often neglects the phase-delay characteristics and unfortunately if the phase-delay data is retained the computer data shows only the phase angle and loses the real  $2\pi t$ , time-delay parameters. Lossy, conductive materials all have a time delay that are (equ 1.2) sq-rd functions of the conductivity, permeability and the inverse of frequency which "spreads-out" the time of arrival of transients propagating through the material to the extent that "CW" measurements of shielding effectiveness are not - by themselves - a true evaluation of transient protection. Test data and analytic evaluations are presented to show (claim!) that relatively poor 100 Khz shielding of 12 Db can "effectively" provide an EMP transient reduction of 100 Db. and more-importantly demonstrates several techniques for lightning-surge attenuation as an alternative (or addition) to "crow-bar", spark-gap or power-zener type clipping which simply reflects the surge.

A time-delay test method is shown which allows CW testing - with a convolution program to define a "Transient Shielding Effectivity" where the Fourier phase characteristics of the transient are known or can be broadly estimated.

CONCLUSIONS

Even very thin shields significantly alter the wave-form of transients due to phase-delay, not attenuation - which is very small at LF (<.1 Mhz).

Shielding effectiveness - for transients - cannot be evaluated simply by a convolution of the CW measurements techniques. This is an error of magnitude - usually >20 Db.

Transient shielding with higher permeability materials such as 0.8 oz NICKEL is equivalent to 3 oz Copper.

\* This work is protected under the author's Patent #4,823,228 and HARRIS Patent Disclosure RA-559, H2722 by Bittner and Reed

NOTICE:

The following is a cursory abbreviated synopsis of this ongoing investigation. The original paper is being revised due to new developments and will be available - by June, 1991.

Those wishing a copy can write to the author at:  
2580 CLINTON Drive NE  
PALM BAY, FL. 32905

In evaluating a transient due to Lightning, Switching or EMP each spectral component (in the frequency domain) starts at zero amplitude at  $t = 0$  and reaches a maximum as shown in the Figure 1 below - which is somewhat misleading since "Log of time" does not adequately emphasize the much greater delay at lower frequencies. The 2 plots to the right show how much more delay the wave experiences propagating through nickel foil, 0.6 oz, and 9 oz copper, 0.0126".

Fig 2 provides the solutions for the time delay - the solid line - and the attenuation - the dashed line and emphasizes that at 200 KHz the attenuation has only reduced the wave amplitude to 0.6 (-4.4 dB) but has delayed the wave 600 nanosec ( $\pi/4$ ) so that the wave cannot constructively recreate the incident transient due to this time distortion.

- the equations of Fig 2 are shown more clearly below [ref 1]:

$$V_{cu} = \left( \frac{2\omega}{\mu\sigma} \right)^{1/2} = 0.415 (f)^{1/2} \text{ M/S}$$

VELOCITY

ARRIVAL TIME  
 $t = 257 \times 10^{-6} (f)^{-1/2}$  SECONDS  
AMPLITUDE =  $A_0 e^{-\alpha d} = A_0 e^{-0.0016 (f)^{1/2}}$

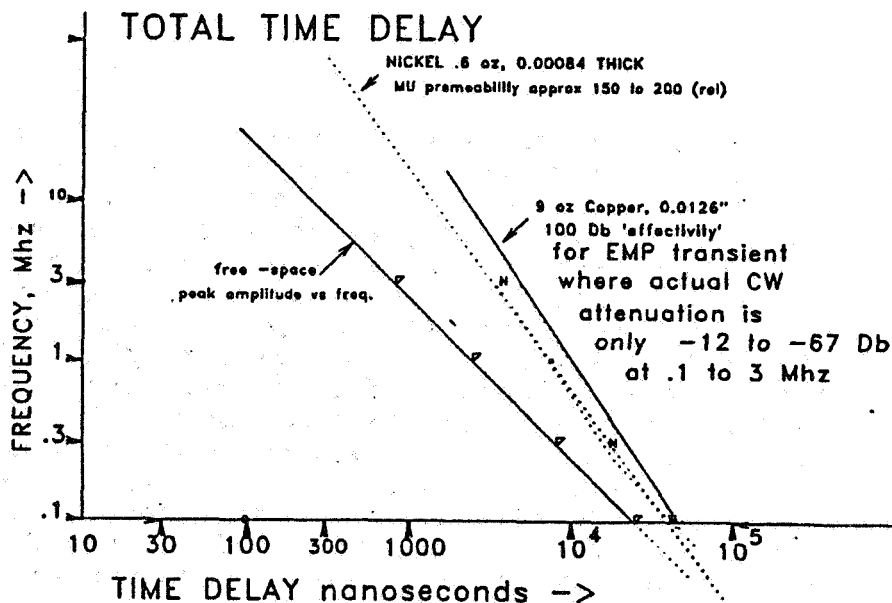


Figure 1

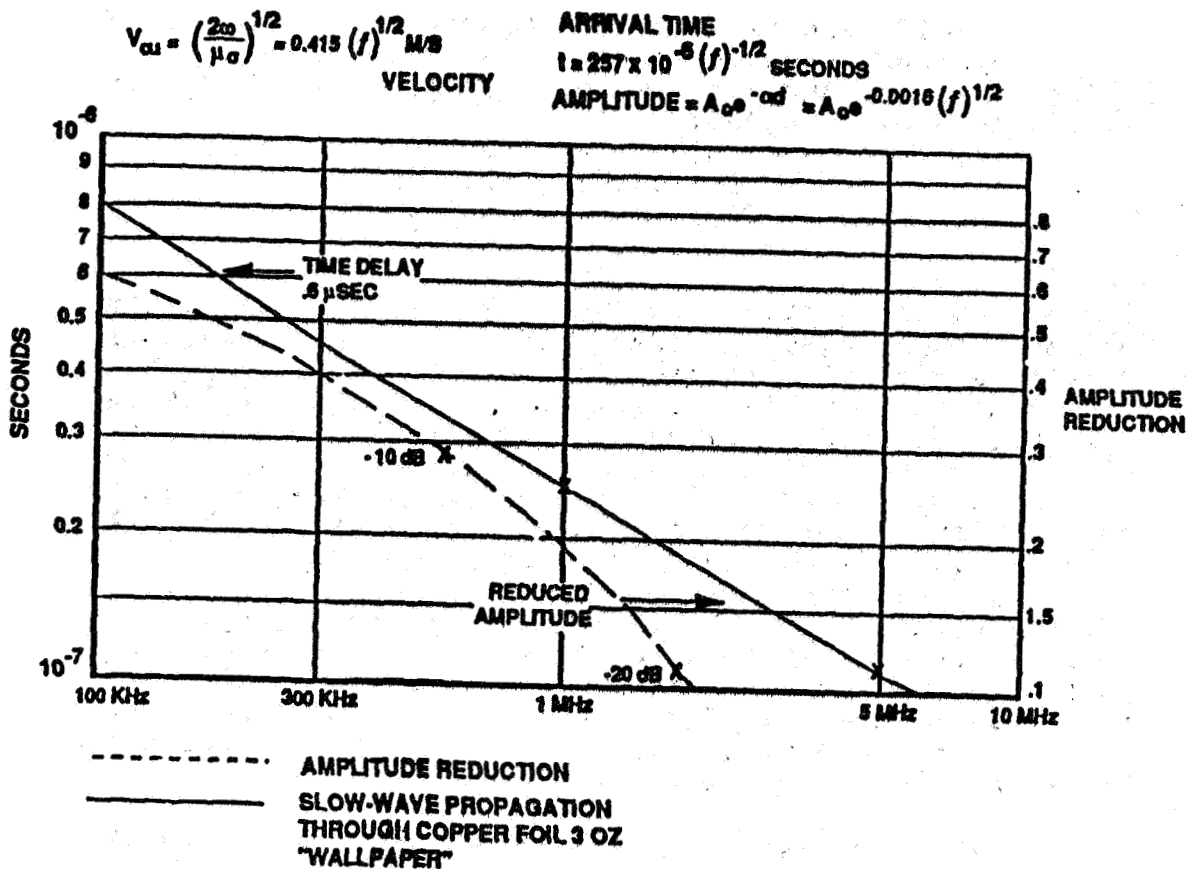
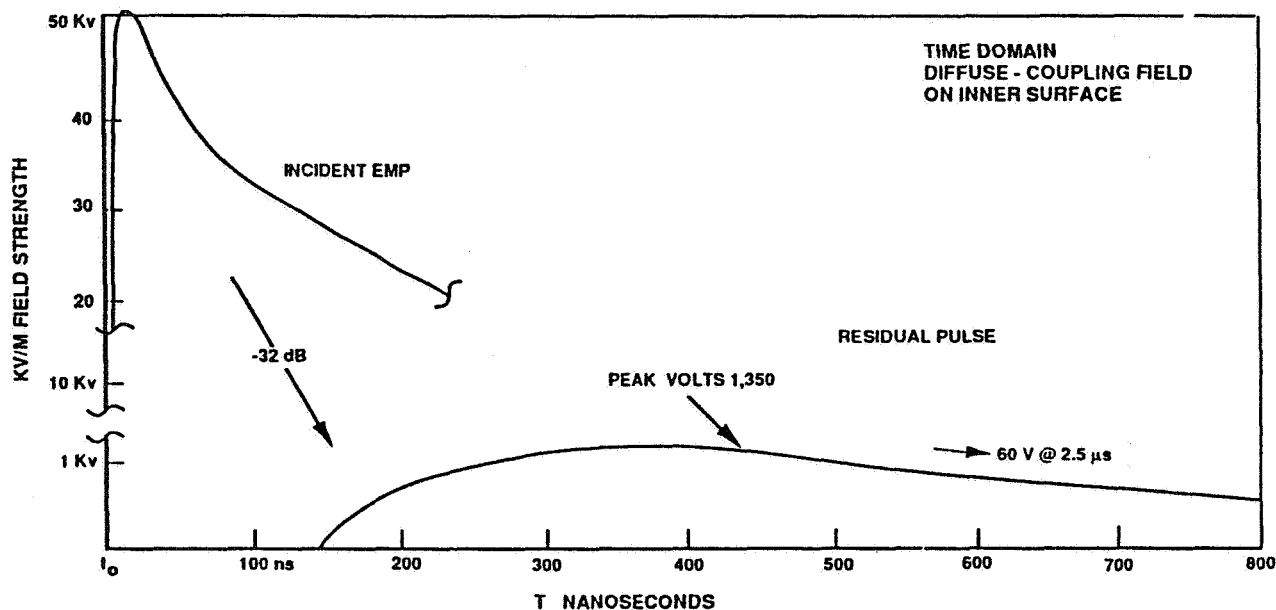


Figure 2

It is often noted that the frequency domain spectrum of lightning and EMP is only 20 to 50 millivolts per Hz and only the convolution simultaneously creates the fairly large [2] peak amplitudes.

Figure 3 demonstrates how an analysis of transient propagation through a conductive material results in a reduction of the classic HEMP of 52 KV down to less than 1.4 Kv with the peak delayed nearly 400 nanosec. and much of the energy delayed to over 0.8 microseconds - this time-delayed reconstruction / convolution is a time-consuming computational process and in this figure the amplitude was presumed constant up to 2 Mhz at 3 mv and 2 mv to 10 Mhz (- A much more elegant program is needed here! - an inverse Fourier ?). This is a true representation of the dispersive delay as it modifies the transient - and cannot be easily reconstructed using just CW test methods since penetration through cracks or ports will combine with the diffuse wave because the time differential amplitudes are lost.



#### EMP FIELD AT INSIDE SURFACE

USUALLY REDUCED FURTHER BY:

- LOWER INTRINSIC IMPEDANCE AT LOWER FREQUENCIES,  $R_s = F(f)^{1/2}$
- STRUCTURES "APERTURES" CANNOT SUSTAIN/INTERCEPT LONG ( $> 3$  MHz) WAVES  
i.e.; A VERY INEFFICIENT ANTENNA

BASIC AMPLITUDE VS TIME (TIME DOMAIN)

$$= A_0 \exp -15.1 d(f)^{1/2} \sin \omega t$$

$$A_0 = 0.0037 \text{ V/MHz to 2 MHz (0.002 TO 10 MHz)}$$

SUM AMPLITUDE COMPONENTS AT (CONVOLUTE)

$$T = \sum t + 257 \times 10^{-6} (f)^{-1/2} \text{ SECONDS}$$

$$t = 25 \text{ nsec to 3 MICROSEC}$$

$$d = \text{THICKNESS (0.0042")}$$

$$f = \text{FREQUENCY (150 KHz to 10 MHz)}$$

$$\omega = 2\pi f \text{ RADIANS}$$

FIGURE 3

Figure 4 illustrates some examples of dispersive time delay that are of engineering significance if shielding from transients is of importance. Note that about 3 oz Nickel (permeability over 100) or 9 oz copper can provide about 100 dB reduction in transients which is mentioned in the proposed MIL-STD-188-125.

Examples are also given for the equivalent '5 mho' sea-water and our newly developed ISIG (TM) thermoplastic which is about six times more conductive than sea-water and is used on the exterior of power and coax cables to absorb the common-mode transients - and in some cases as an overlay for each wire in twisted pairs.

HP has furnished me a fiber-optic circuit that appears to give good data when comparing the phase of the incident CW illumination with the signal inside the shielded enclosure - but it still doesn't provide the total time delay properties of the enclosure and can be very misleading where the CW leakage signal exactly, destructively cancels the diffuse propagated signal.



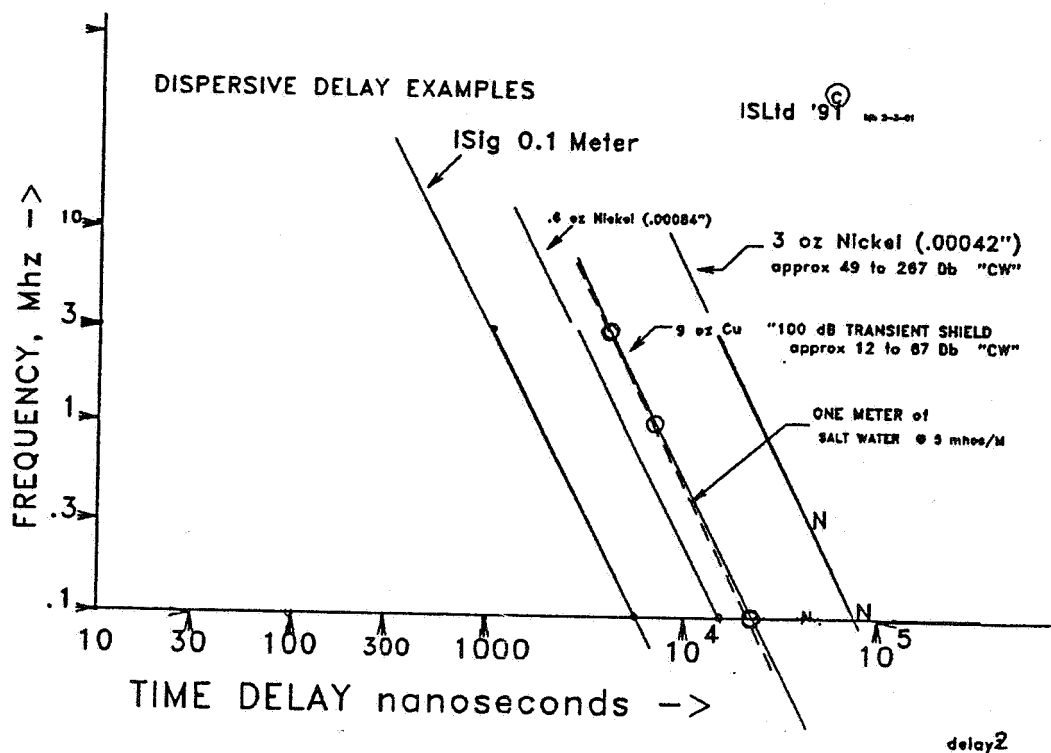


Figure 4

Note should be made that this diffuse delay characteristic is often present on signals intercepted from hi-data rate digital sources - which significantly distorts the waveform intercepted.

references:

- [1] E.C.Jordan "Electromagnetic Waves and Radiating Systems" Prentice-Hall, 1950
- [2] Frederick M. Tesche, Paul R. Barnes "Transient Response of a Reclosure and Control Unit - - -" IEEE EMC Trans May 1990 p 113
- [3] F. M. Tesche  
- adv. copy "ON THE USE OF THE HILBERT TRANSFORM FOR PROCESSING MEASURED CW DATA"  
- in the HPM issue of EMC Trans. IEEE -

## ADVANCES IN LIGHTNING PROTECTION THAT SATISFIES CONTEMPORARY STANDARDS

by Roy B. Carpenter, Jr. of LEC, Inc.  
Boulder, Colorado

### INTRODUCTION

Recent years have experienced a flurry of activity in lightning protection circles and protection technology. Most of the development in protection technology has been limited to some form of electrical and electronic circuit protectors. However, there has been some activity in the stroke protection field. Most of these have involved "bigger and better" stroke collectors (air terminals), including the radioactive variety. One or more of these developments resulted in low impedance down conductors.

All except one company has been concentrating in the field of what may be termed a "Collector-Diverter" System in some form. In contrast, LEC, Inc. of Boulder, Colorado has developed a lightning strike prevention system and has successfully completed installation of over 1000 systems in many of the lightning active areas of the world. That system is known as the Dissipation Array® System (DAS®). Although the DAS has achieved an impressive record for preventing strikes to large areas and tall structures, it has not yet been included in any of the recognized standards such as NFPA-76 or UL 96. There are many reasons given why the DAS is not part of an accepted standard but perhaps the most valid reason is that there is no standard that provides for such a revolutionary concept. All standards provide for stroke collection; the DAS facilitates stroke prevention. The demands on system design are, therefore, significantly different. To resolve that problem and provide a stroke prevention system that does qualify under UL 96, LEC has developed an Ionizer (the main component of the DAS) that also qualifies as an air

terminal. Further, it is a far more effective air terminal if used alone. This paper describes the LEC Spline Ball Ionizer® (SBI) and the Spline Ball Terminal™ (SBT) families and how their use in a conventional lightning protection system can achieve strike prevention in a conventional setting.

### LIGHTNING AS IT INFLUENCES A PROTECTION SYSTEM

Lightning is usually initiated by a downward moving channel of charge starting from the cloud and moving toward the earth in steps. These channels are termed "Step Leaders" because they move in steps. As these channels or leaders move toward the earth, the electrostatic field between them and earth-bound objects rises rapidly.

The primary question is "where will that step leader terminate?" To that end, a great deal of research has been accomplished and recorded. It seems that the stroke termination is a function of two definable factors in addition to random chance.

RANDOM CHANCE we are told determines the path the leader will take until that leader reaches the "Point of Discrimination". Refer to Figure 1.

THE POINT OF DISCRIMINATION is that point in the leader descent path where the strike point is determined; and is also the beginning point of the last step. It is, therefore, about one full step from earth. This distance is also referred to as the "striking distance".

THE STRIKING DISTANCE is the length of the path between the Point of Dis-

crimination and any potential strike terminus regardless of direction. It may also be considered the maximum distance between the tip of the leader and the stroke terminus. The Striking Distance and the step length are approximately the same value. Both are statistical quantities dependent on the intensity of the ensuing lightning strike. These values are estimated via Figure 2. Note that these steps and the striking distances vary from a low of approximately 20 meters to a high in excess of 200 meters. However the average is only about 20 meters for a negative stroke which is the most common. For a positive stroke, the average exceeds 45 meters.

Placing these data in perspective, we know that after the leader reaches the Point of Discrimination the strike point has been determined. Before that time, the path is random and indeterminate. Therefore, only the objects or facilities within the strike zone are at risk. As illustrated in Fig. 1, a tall tower can be just outside the strike zone and not take a strike while a blade of grass within the strike zone could be struck. Upward moving streamers tend to "compete" for the downward moving leader; the first to connect closes the circuit creating the flash channel.

Pertinent to this paper is the occasional horizontal paths taken by some leaders. When leaders approach a structure at some angle, the approaching leader creates a high electrostatic field between. This causes the potential to rise high enough to stimulate any discontinuity to pass into the streamer mode. That streamer may then "reach out" and collect the leader causing sharp changes in the leader path. Often 90 degree turns have been observed to be caused by this phenomena.

#### CONVENTIONAL COLLECTORS (AIR TERMINALS)

Conventional collectors or air terminals are devices deployed to intercept an incoming step leader and divert the related energy to earth by some preferred path. Lightning rods are typical of these units and the most widely used.

These rods take on various configurations from pointed to blunt and some times offer several secondary points. The usual application calls for the rods to be mounted in such a way that they will collect a stroke entering their cone of protection. Refer to Figure 3. In practice we find that the so called "Cone of Protection" assumption is never 100 percent effective. Cones of even 10 degrees have been used with varying degrees of success. It appears that the smaller volume of the assumed cone of protection, the more effective it is in collecting the stroke leader if the height is not significant. Because the cone of protection theory has proven ineffective, the utility industry moved to the "Rolling Sphere" concept also illustrated. This reduced the assumed "protected volume" significantly and appears to more accurately describe the protected volume, but is still not 100% true.

The foregoing limitation can best be understood from Figure 4. Industry standards are based on the premise that the collecting volume is described as a cone of 45 degrees around the vertical centerline of the air terminal for a full 360 degrees in azimuth. However, it appears that Figure 5 more closely approximates the air terminal's collection capability. This is a function of the inability of the air terminal to propagate effective streamers as the angle from the vertical increases. This also explains why tall structures are often struck below the top.

#### HYBRIDS (DISSIPATING AIR TERMINALS)

As used herein, a hybrid air terminal is one that primarily functions as an Ionizer, but when saturated, "fails" as an air terminal. In addition, when properly designed, properly deployed and used in some quantity, they will function as a DAS® and conceivably approach 100 percent effectiveness as a stroke prevention system.

The LEC Spline Ball Ionizer® (SBI) and the Spline Ball Terminal™ (SBT) were developed as an optimized hybrid air terminal. Figures 6 and 7 illustrate the two configurations. Both the SBI and SBT provide the required point spacing to maximize the ionization current. At the same time they provide a point oriented for at least every 5 degrees in azimuth for the full 360 degrees and a full 120 degrees in elevation. As a result, there is no direction from which a leader can approach that would not have a collective point oriented directly toward it and many backup points close by.

Both the SBI and SBT have been reviewed by Underwriters Lab and have been listed as Air Terminals, usable as such in any UL 96 based lightning protection system where UL listed terminals are specified.

#### USING THE SBI AND SBT IN STANDARDS BASED SYSTEMS

Standards such as NFPA-78, UL96A, NAV FAC DM4, Army 385-100 are based on the use of a single point lightning rod known as the air terminal or some other form of stroke collector. However, since UL has listed the SBI and SBT, these assemblies can be used in place of the single point terminal. In most cases they can be used as a direct replacement. The SBT is designed to fit into the conventional lightning rod mounting plate.

Figure 8 illustrates a typical NFPA-78 building protection system that has been converted to a Hybrid Stroke Pre-

tection System. Model SBT-24 hybrids are used in the required locations around the periphery. The Model SBI-48 hybrids are used in the required locations down the middle of the building.

In addition to the standard demands, location and separation distance between SBT or SBI's are a function of two factors:

1. The percentage of strokes to be eliminated (an energy related factor), and
2. The potential strike zone physics.

All are traced off against cost. Of particular concern to this paper is the criteria for the location and spacing of the SBT for successful operation as an air terminal.

As general criteria:

1. For a system that must satisfy UL 96A and/or other standards, the SBT-24 is 24 inches high and may be used as described by the following:
  - a. Space each SBT 25 feet apart, but no more than 2 ft. from the edge of the facility.
  - b. Space each row of SBT's no more than 50 ft. apart.
  - c. Interconnect rows at no more than 50 ft. intervals
  - d. Ground each row at least every 100 ft.
2. For a non-standard, Collector-Diverter Concept based on the SBT, the following rationale may be applied:

**NOTE:** A non-standard system is one based on the premise that a standard per se does not need to be satisfied. It also follows that since the numbers of SBT's required are reduced, the dissipation capability is reduced and the major protection mode may be that of a collector-diverter concept instead of a DAS.

The object of a Collector-Diverter system is to provide an efficient collector and a safe diversionary path. The diversionary path parameters are defined by UL 96A and 1.d above.

The collector efficiency is related to its ability to produce streamers that will propagate toward the downward moving leader as it approaches the Point of Discrimination. As illustrated in Figure 1, the Strike Zone for that leader is a discrete volume dependent entirely on the energy in the leader. High energy leaders have strike distances of up to 180 meters for the common negative polarity and as short as about 15 meters. Positive stroke distances are much longer. From these data it is evident that to provide a 100 percent effective collection function, the SBT must be within the strike zone of the lowest energy leader and it must be the most prominent streamer generator within that zone.

The design problem is related to the site situation as well as the facility. Since the portential between the leader tip and the closest streamer generator (point or sharp edge) will be highest, it will be the stroke terminus. This premise is true only if there are no other streamer generating objects close enough to compete with it.

Based on the foregoing, and the desire to collect the weakest stroke, it would appear that a separation distance equal to the strike distance would be the maximum safe separation. Therefore, a spacing of no more than 15 meters or approximately 50 ft. should be safe. However, a 40 ft. separation would offer a margin of safety.

A properly completed standards based system which is composed of the LEC Spline Ball Ionizer® hybrid system

and will provide us with two modes of protection:

1. A stroke prevention mode that reduces the risk of a strike to the protected facility in proportion to the size of that facility, the size and number of SBI/SBT's used.

NOTE: When the SBT/SBI based system is used and the number of units are in the order of 100 or more, the risk of a strike should be less than one chance in 1000. That is equal to a DAS.

2. A Stroke Collector-Diverter System that is far superior to any system now in use because it collects strokes entering the "protected" area from any direction and angle.

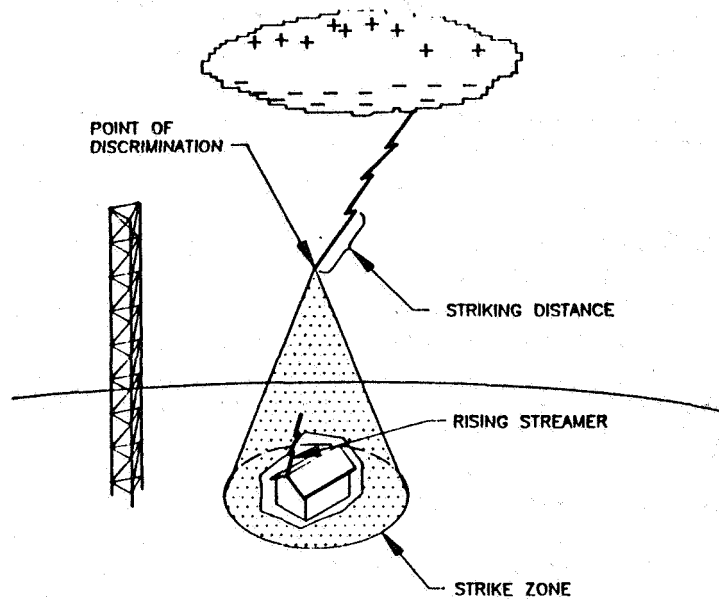


**FIGURE 1, THE STROKE PATH FACTORS**

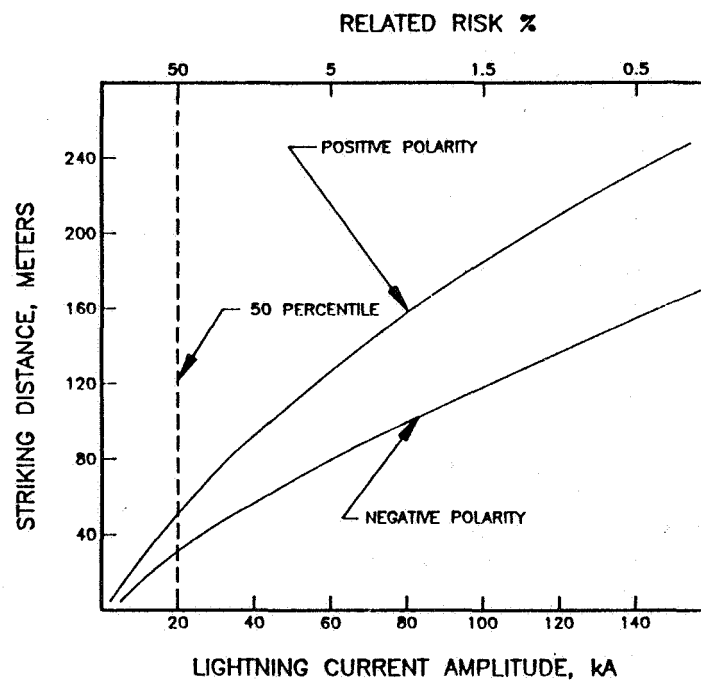


**FIGURE 2, STRIKING DISTANCES OF NEGATIVE AND POSITIVE LIGHTNING STROKES**

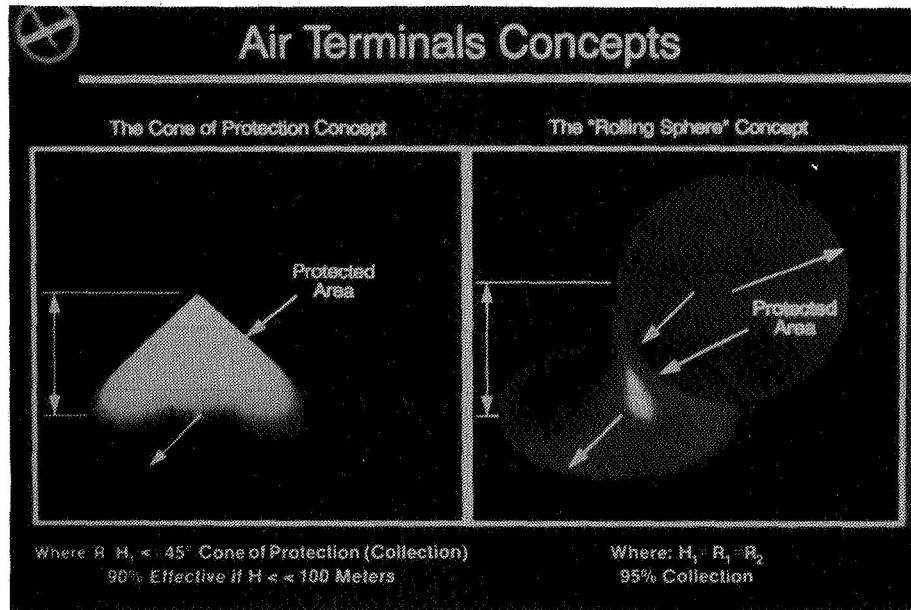


FIGURE 3.

# STROKE COLLECTION EFFICIENCY CONVENTIONAL AIR TERMINAL

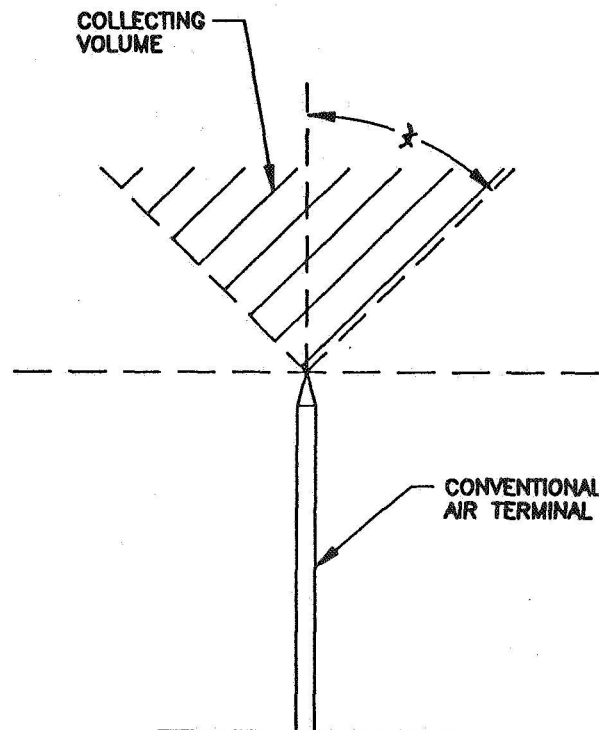


FIGURE 4.

## STROKE COLLECTION EFFICIENCY CONVENTIONAL AIR TERMINAL

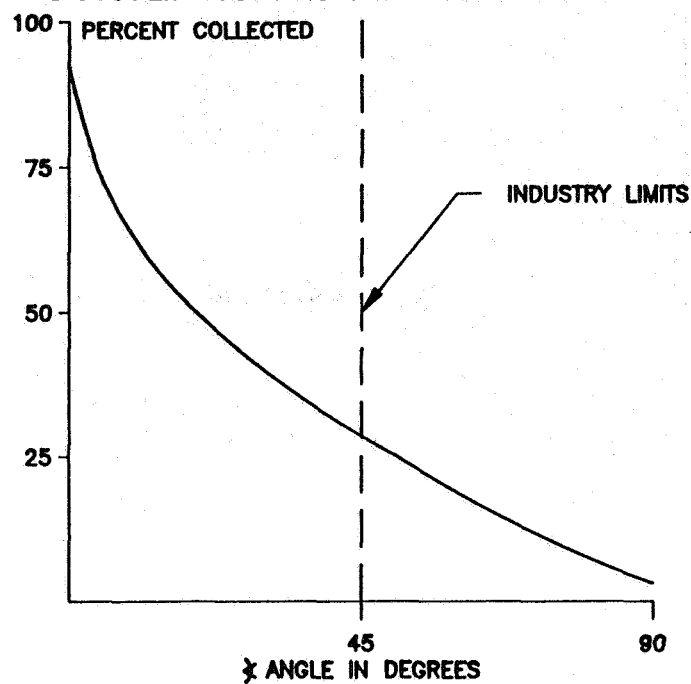


FIGURE 5.

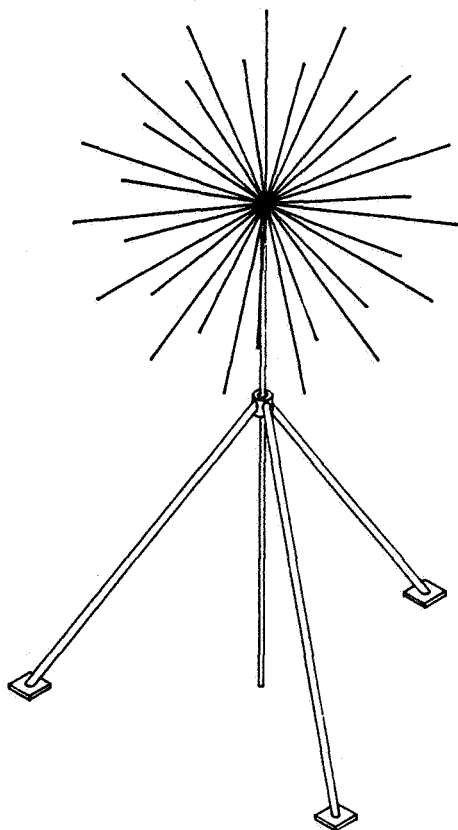


FIGURE 6: SBI ON TRIPOD



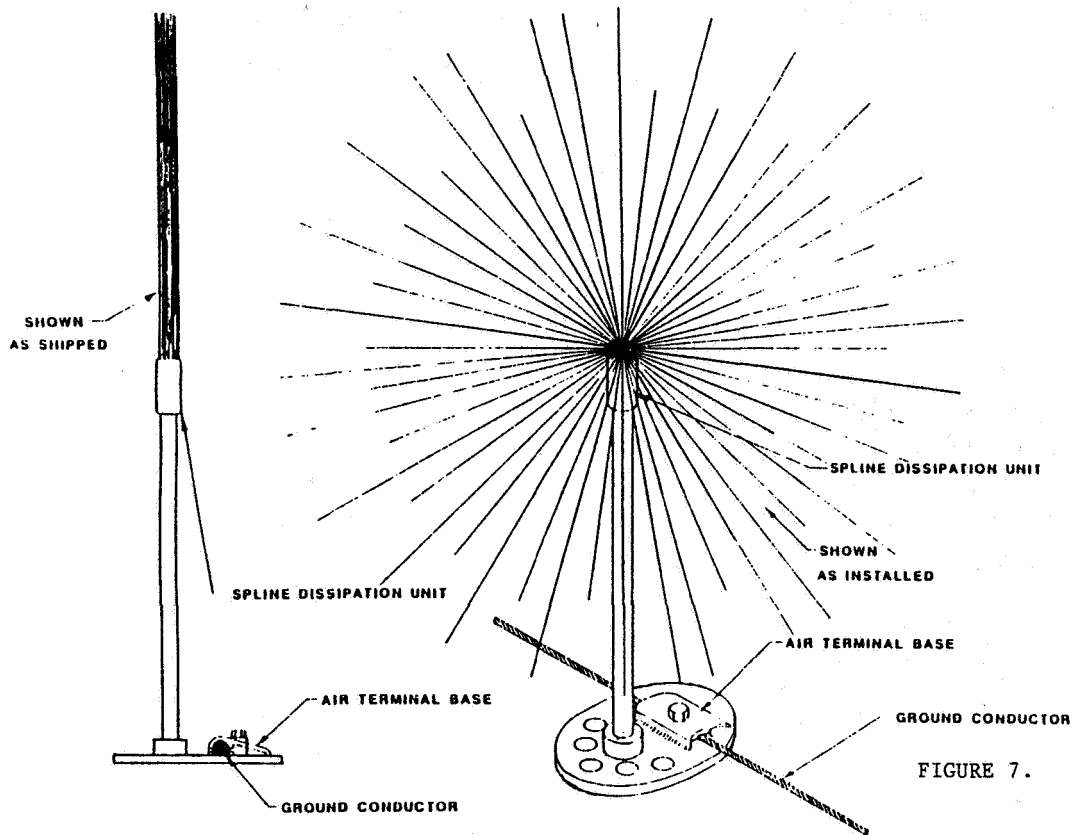


FIGURE 7.

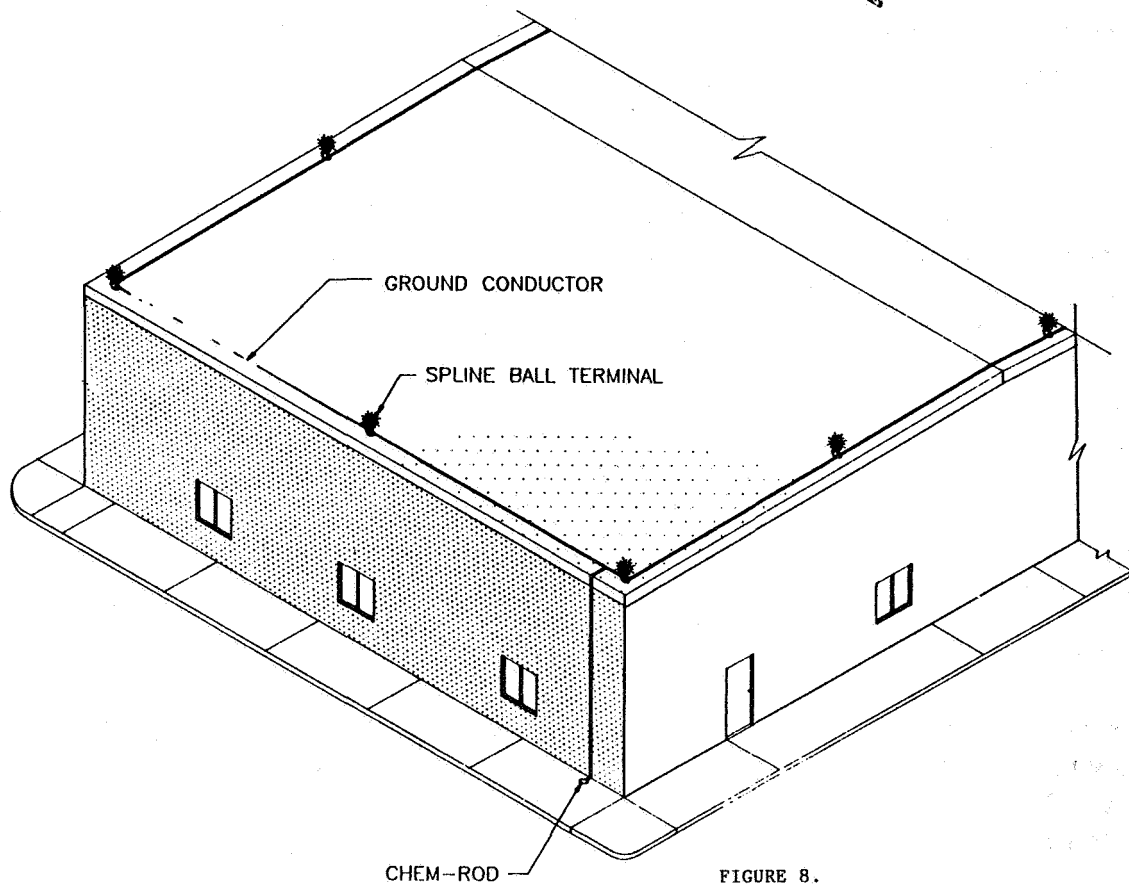


FIGURE 8.

# **CIRCUIT PROTECTION DEVICES FOR TRANSIENT SUPPRESSION**

Richard Childers  
Electromer Corporation

## **ABSTRACT**

Electrical Overstress (EOS) transients - brief but powerful voltage surges - are a major threat to virtually all electronics equipment. As electronics equipment becomes denser, and as chip geometries shrink, the likelihood of EOS transients increases. Therefore, more designers are using transient suppressors to protect electrical circuits from damage due to EOS threats such as lightning, electrostatic discharge, and electromagnetic pulses.

Currently the major transient suppression devices are gas discharge tubes, metal-oxide varistors (MOVs), and zener diodes. The gas discharge tubes and varistors are designed to handle high energy transients while the zener diodes provide only low energy protection. Of these devices, no one type meets all the criteria of an ideal transient suppressor.

Electromer Corporation has developed a series of transient voltage suppression components based on a patented, specially formulated PolyClamp<sup>®</sup> material. PolyClamp<sup>®</sup> components are a new class of transient voltage surge suppressors that extend the range of protection offered by transients protectors. The PolyClamp<sup>®</sup> transient surge suppressors provide low capacitance, high energy capability, and packaging flexibility.

A wide variety of applications can be protected by PolyClamp<sup>®</sup>. A tube and ferrule configuration is designed to be used with MIL/Aerospace style connectors and is designed to meet the applicable environmental, mechanical, and electrical requirements as defined by SAE, and United States and European defense standards performance requirements. This paper compares PolyClamp<sup>®</sup> to current transient surge suppressors and describes typical performance and design.

## **INTRODUCTION**

Transient suppressors of the type discussed above, as well as the Electromer PolyClamp<sup>®</sup> devices, operate by shunting the incoming EOS transient to ground, thereby clamping the circuit voltage to a tolerable level. The transient suppression device is in parallel with the electronics circuitry to be protected.

EOS transients can enter electronics equipment through several paths. Antenna cables and other signal lines are very susceptible to picking up EOS transients. Power supply lines, both AC and DC, are frequently carriers of the transients. In fact, virtually any cable or wire connected to the equipment is a potential path for transporting the EOS transient to the

sensitive electronics. Therefore, transient suppression is necessary at practically all input/output lines to electronics equipment.

The ideal transient suppressor is at a very high or infinite resistance during normal operating conditions and is essentially electronically invisible to the other circuitry. The presence of an EOS transient causes the ideal transient suppressor to rapidly switch to a low resistance state, shunting the transient to ground and preventing the other electronics circuitry from experiencing damaging overvoltage conditions. The transient suppressor is said to clamp the transient voltage to a safe level. Gas discharge tubes clamp the transient voltage to a very low level by creating a virtual short circuit to ground. Varistors and zener diodes as well as PolyClamp<sup>®</sup>, have a specified voltage clamp level.

The ideal transient suppressor should have zero leakage current, very low capacitance, high energy handling capability, and response time in the sub-nanosecond range. PolyClamp<sup>®</sup> products can be tailored to very nearly meet these ideal specifications.

In addition to the performance benefits PolyClamp<sup>®</sup> components offer a packaging flexibility that is not available with gas discharge tubes, diodes, or varistors. PolyClamp<sup>®</sup> transient suppressors are moldable into many configurations including tubes and ferrules, pin and ferrules, and arrays. The packaging flexibility allows form, fit, or function customization for packaging and cost advantages.

## **PERFORMANCE OF POLYCLAMP<sup>®</sup> COMPONENTS**

### **(a) Clamp Voltage**

PolyClamp<sup>®</sup> clamp voltage, the voltage at which the device switches to a low resistance state, can be controlled both by formulation and by the dimensions of the device itself. Currently there are two PolyClamp<sup>®</sup> formulations available. These formulations, combined with precise dimensional control, allow a broad range of devices to be made over a wide range of clamp voltages, 30 to 1000 volts.

### **(b) Energy Capability**

The typical energy handling capability of PolyClamp<sup>®</sup> devices is approximately 10 Joule/cc. For applications requiring large energy dissipation, the size of the PolyClamp<sup>®</sup> device can be increased to accommodate the specific requirement. The excellent energy handling characteristics of PolyClamp<sup>®</sup> make it a rugged device with broad applicability in transient suppression applications.

### **(c) Response Time**

An important feature of any transient suppression device is the response time to an EOS transient. This is especially true for fast rising transients. The rise time of a transient pulse can be thought of as the time for the transient to rise from essentially zero volts to the peak amplitude of as many as several thousand of volts. Fast rise times are usually considered

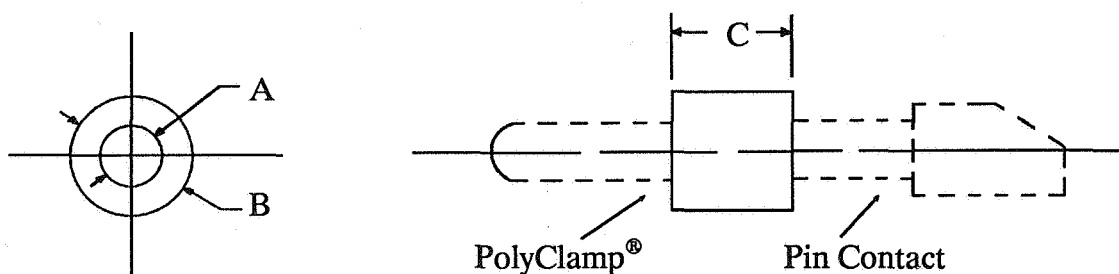
sub-nanosecond range. The nature of the PolyClamp® performance is that of a foldback device with response times less than 100 nanoseconds.

#### (D) Packaging Flexibility

PolyClamp® is a moldable plastic semiconductor device, and because PolyClamp® formulations are moldable, a wide variety of shapes and geometries can be fabricated. This is particularly desirable for nearly every application including connector inserts, printed circuit board traces, leaded devices, wire insulation, IC packaging, gaskets, housings, customer retrofit parts, etc. PolyClamp® offers many advantages in its manufacture. The raw materials are generally standard and easily obtainable. Processing of the PolyClamp® formulations is done by standard plastic processing technology. Finely divided powders are incorporated into a polymer matrix using Banbury or two-roll mill mixing. Curing of the polymer matrix is done according to usual procedures for the polymers used in the particular formulation. All materials are non-toxic and stable under widely varying conditions.

A typical tube and ferrule PolyClamp® specification and design follows:

Voltage Clamp Range	50-90 Volt
Response Time	< 200 nanoSeconds
Energy Handling	> 10 Joules/cc
Capacitance	< 10 picoFarads
Off State Resistance	> 10 <sup>8</sup> ohms @ 100 volts
On State Resistance	< 2 ohms
Operating Temp.	-55 to 155 °C



DIM:	Pin dia.	A dia.	B dia.	C
Size 22	0.030	.033	0.073	0.300
Size 20	0.040	0.043	0.118	0.300
Size 16	0.062	0.066	0.141	0.300
Size 12	0.094	0.098	0.170	0.300

## DESCRIPTION OF EXISTING TRANSIENT SUPPRESSORS

Below is a detailed discussion of varistors, zener diodes, and gas discharge tubes.

### Varistors

Varistors are ceramic devices formed by sintering together metal oxide powders at high temperatures. The resulting solid material is composed of individual metal oxide grains separated from each other by grain boundaries of finite thickness. These grain boundaries contain various impurities and dopants important to the varistor operation. It is the grain boundaries, generally characterized as Schottky barriers, that give rise to the voltage clamping characteristics.

Because of the grain boundaries, varistors have inherently high capacitance, an undesirable feature for most applications. This high capacitance plus other factors cause varistors to have inadequate response times to fast rising EOS transients. The resulting voltage overshoot can be very damaging to the electronics equipment to be protected.

### Zener Diodes

Zener Diodes are P-N semiconductor junctions which are specifically made to operate in the reverse breakdown mode in response to a voltage transient. Response times to EOS transients are generally quite fast. However a major problem is the energy handling capability. Because of its thickness and construction, the semiconductor junction of the zener diode has very low energy handling capability. Another consideration is the relatively high capacitance associated with the zener diode junction.

In comparison, the PolyClamp<sup>®</sup> conduction mechanism is a bulk effect and therefore PolyClamp<sup>®</sup> devices have substantially greater energy capability.

### Gas Discharge Tubes

Gas discharge tubes are composed of a gas-filled tube enclosing two metallic conductors which are separated by a small gap. Under normal conditions the resistance between the two conductors is essentially infinite. When a large enough voltage is applied to the conductors, an arc is ignited across the gap and the conductors are virtually shorted together. The time to form and develop the arc can be quite long relative to the rise time of an EOS transient, resulting in large voltage overshoots before the clamping effect takes place. The very slow response time renders gas discharge tubes inadequate for suppressing fast rising EOS transients.

Gas Discharge Tubes do not reset. This means that after triggering the internal electrical arc in response to an incoming transient, all power to the circuit must be removed in order to extinguish the arc and restore the Gas Discharge tube to its off state. PolyClamp<sup>®</sup> automatically resets to high resistance when the incoming transient is past.

## General Description of PolyClamp<sup>®</sup> Devices

PolyClamp<sup>®</sup> Protection Devices are used as a parallel element in electrical circuits. A simple circuit diagram is shown below in Figure 1.

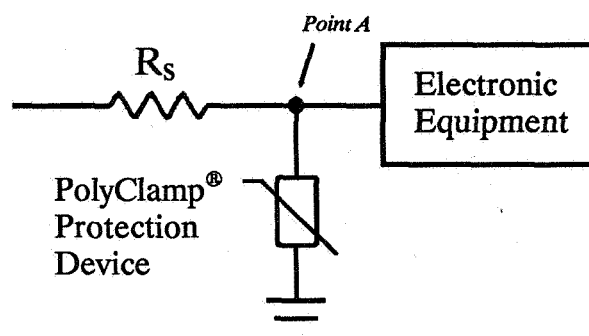


Figure 1 - Simplified Circuit Using Voltage Clamping Device

The source impedance  $R_s$  shown in Fig. 1 is present in all applications, although it may not be contained in a single circuit element as shown. For applications such as telephony, where long signal lines are involved, the source impedance is comprised of distributed resistance, capacitance, and inductance. For wiring in aircraft or buildings there are again distributed values which can effectively be combined into a single source impedance element for the present analysis.

The role of source impedance is not always fully appreciated when discussing voltage clamping elements such as PolyClamp<sup>®</sup> Protection Devices. The total voltage of the overvoltage transient is shared between the source impedance and the PolyClamp<sup>®</sup> Protection Device, the voltage clamping element. Example: using a PolyClamp Device with a rated clamping voltage of 30 volts, and an incoming overvoltage transient of 3000 volts magnitude, there would be a voltage of 30 volts at Point A in Figure 1. The rest of the transient voltage, 2970 volts, would be shared or dropped across the source impedance  $R_s$ . Thus the electronic equipment in Figure 1 is effectively protected from damaging exposure to excessive voltage levels. This example should help illustrate the role and importance of source impedance.

## Response to Lightning

A typical lightning threat is illustrated in Figure 2. This pulse shape is described in ANSI/IEEE C62.41-1980 (formerly IEEE 587) and is often referred to as an 1.2x50 waveform. The voltage level can be as high as 6000 volts with up to 3000 amps of current. The 1.2x50 designation refers to a rise time of 1.2 microseconds and a fall time to 50% amplitude of 50 microseconds.

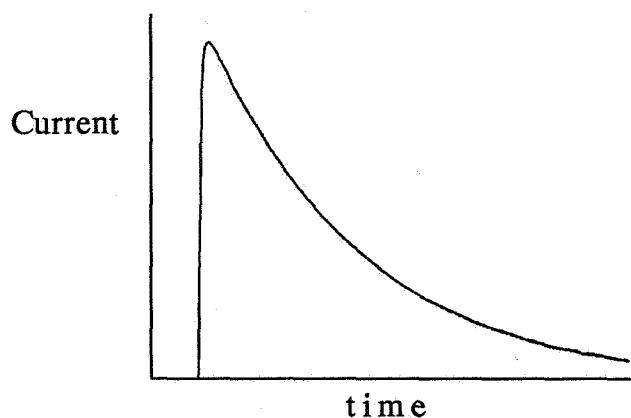


Figure 2 - 1.2x50 Lightning Pulse

Figure 3 below illustrates the response of an ideal voltage clamping device to the lightning threat of Figure 2. Note the sharp clamping action, primarily because the Ideal Device responds instantaneously. In addition, the Ideal Device has virtually no capacitance, has an infinite off-state resistance, and is capable of absorbing extremely large amounts of energy.

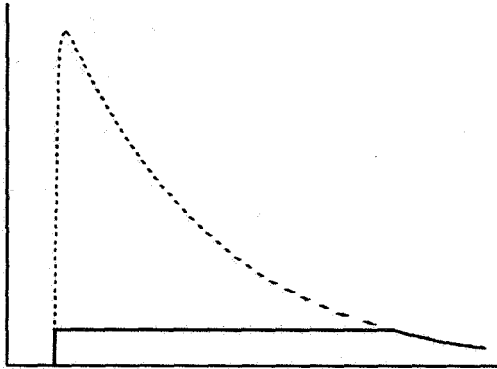


Figure 3 - Response of the Ideal Voltage Clamping Device

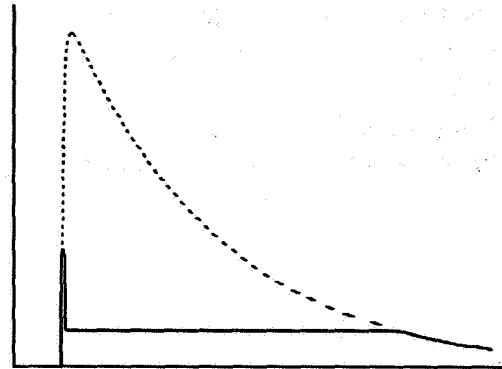
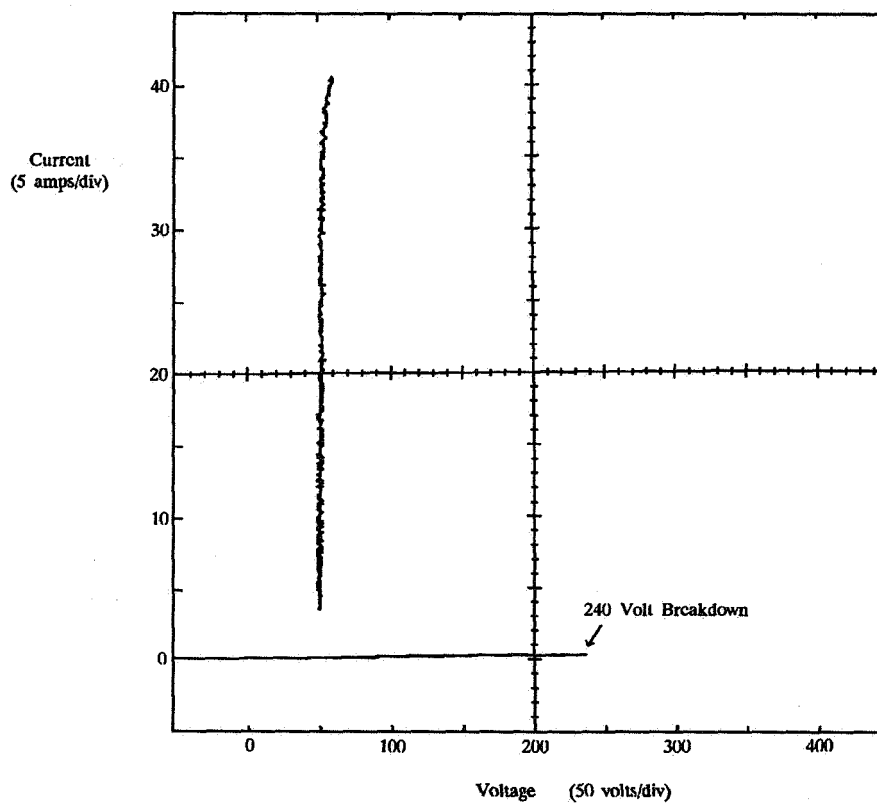


Figure 4 - Response of PolyClamp® Protection Device

Figure 4 above shows the response characteristics of the PolyClamp® Protection Devices to the lightning pulse of Figure 2. The PolyClamp® device is a foldback device with the I-V curve shown in Figure 5 below.



PolyClamp<sup>®</sup> Protection Devices have very low capacitance and handle large energy levels. Energy values of up to 10 joules per cc of material are within the capability of the devices. Depending on the device size, peak power levels of greater than 5000 watts are obtainable in connector applications.

The response of a PolyClamp<sup>®</sup> Device to longer lightning pulses, such as the 10x1000 pulse (10 microsecond risetime, 1000 microseconds to 50% amplitude) or the 50x500 pulse (e.g.) LEMP-EFA-1 requirement), is essentially the same as in Figure 4 except of course that the clamp region lasts for a much longer time period. Below in Figure 6 are actual voltage and current responses to a 6,000 volt 1.2x50 lightning pulse.

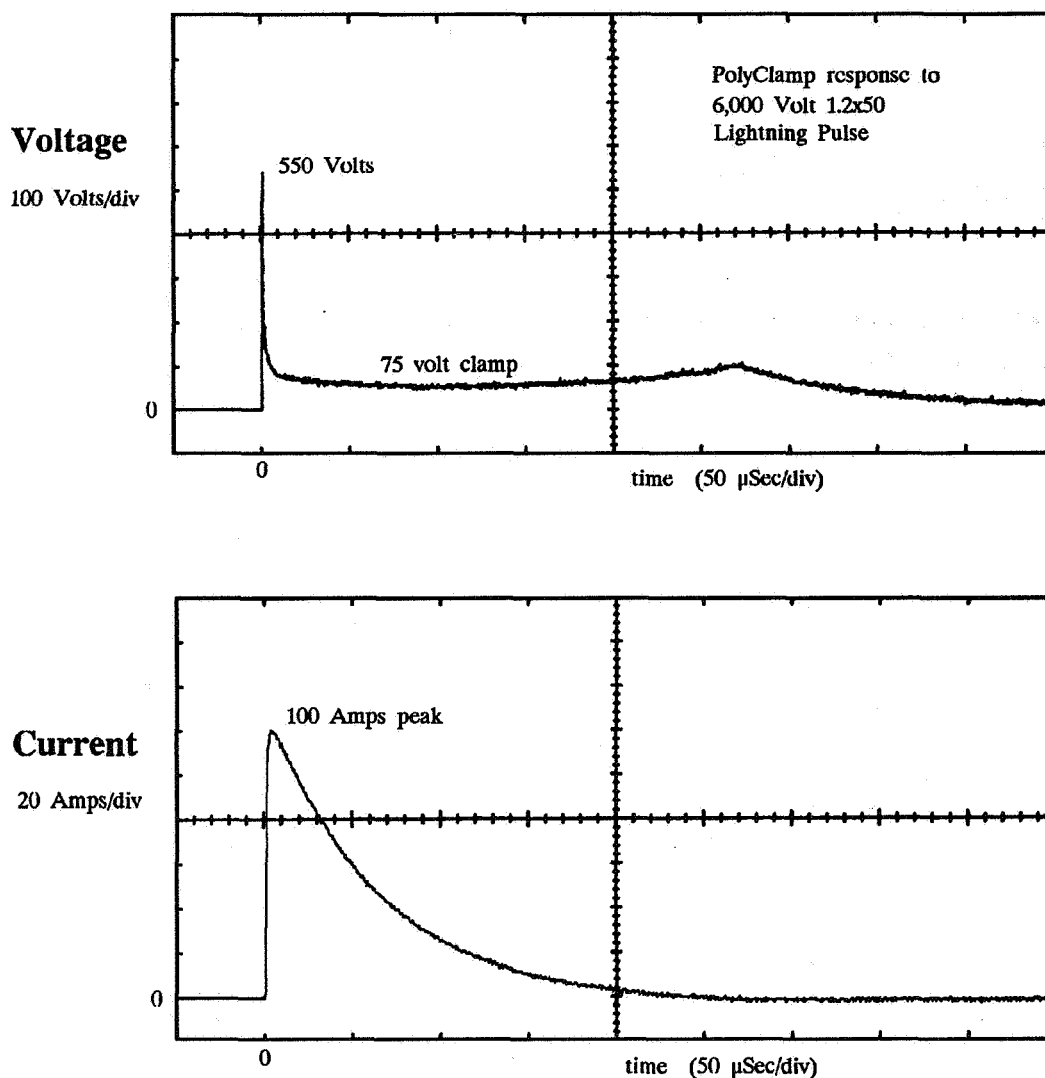


Figure 6 - PolyClamp<sup>®</sup> response to 1.2x50 Lightning Pulse.



## Response to EMP/NEMP

The oscillatory pulse characteristic of induced transients from the NEMP-EFA-1 test waveform (DEF STAN 59-41) is illustrated in Figure 7. This waveform in this Figure is a damped 30 Mhz pulse of several thousand volts amplitude.

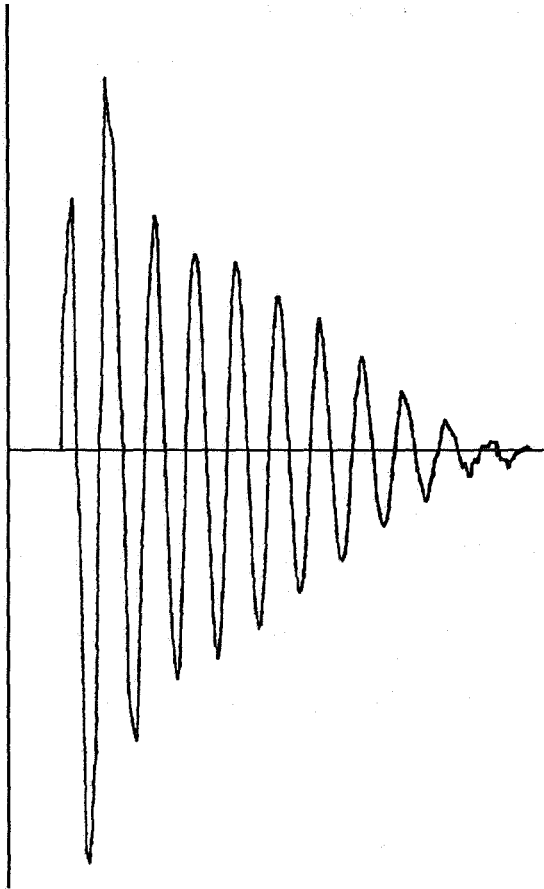


Figure 7 - EFA EMP/NEMP Pulse

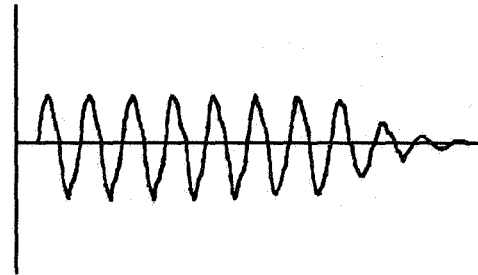


Figure 8 - Response of Ideal Voltage Clamping Device

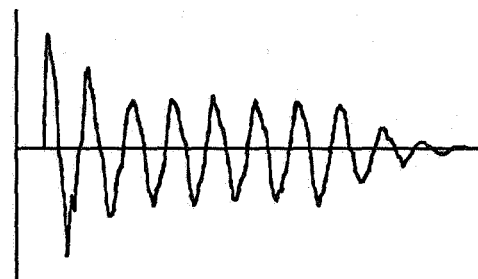


Figure 9 - Response of PolyClamp<sup>®</sup> Protection Device

The response of the Ideal Voltage Clamping Device is shown in Figure 8, and the response characteristics of the PolyClamp<sup>®</sup> Protection Device is shown in Figure 9.

The induced current with the PolyClamp<sup>®</sup> Protection Device in the circuit (Figure 9) was 30 amps. Note the PolyClamp<sup>®</sup> Device exhibits a small "overshoot" at the front of the waveform. The switching speed to reach rated clamp voltage is typically 1/4 microsecond.

Figure 9 illustrated the dramatic clamping action of the PolyClamp<sup>®</sup> #22 Tubular Protection Device designed for use in connector applications. The low capacitance and low insertion loss makes this product ideal for avionics electronics.

## **ADVANTAGES OF PolyClamp OVER EXISTING TRANSIENT SUPPRESSORS**

Existing transient suppressors include varistors, gas discharge tubes, and zener diodes. The following Table compares the performance characteristics of existing transient suppressors with both the ideal device and with PolyClamp®.

Compared to Spark gaps, Zener diodes, and MOV's, PolyClamp® Products have:

- Packaging Flexibility
- Very High Energy Capability
- Low capacitance (pF)
- Highly reliable, rugged, single unit construction

## **SUMMARY**

A wide variety of applications can be protected by PolyClamp® Transient Voltage Suppression devices. The extremely low capacitance of PolyClamp® devices makes them well suited for use with network and high-frequency applications. In addition, wide service range and high energy-handling capability make them useful for low level data signal and heavy duty power protection. Performance stability demonstrated during MILSPEC performance testing, temperature extremes, and mechanical testing ensure reliability of the material and product configuration.

# EVALUATING LIGHTNING HAZARDS TO BUILDING ENVIRONMENTS USING EXPLICIT NUMERICAL SOLUTIONS OF MAXWELL'S EQUATIONS \*

Richard S. Collier, Paul M. McKenna and Rodney A. Perala

Electro Magnetic Applications, Inc.  
12567 West Cedar Drive, Suite 250  
Lakewood, Colorado 80228-2091  
U.S.A.  
(303) 980-0070

## ABSTRACT

Lightning hazards to buildings and their internal environments can be described in terms of electric and magnetic fields (and their time derivatives) and the resulting direct and induced electrical currents which are found in and around critical locations of the building during a lightning strike. The space and time distributions of such fields and currents follow solutions of Maxwell's Equations providing that appropriate initial and boundary conditions can be supplied in the regions of interest and that a method of solution can be applied.

Building environments can be electromagnetically complex, because they consist of a variety of inhomogeneous materials (e.g., concrete with rebar) which may be either conducting or partially conducting. In addition, the structures usually have metallic penetrations such as electrical cables or plumbing, as well as a lightning protection system including an earth ground of some type.

The objective of this paper is to describe the lightning hazards to such structures using advanced formulations of Maxwell's Equations. The method described is the Three Dimensional Finite Difference Time Domain Solution. It can be used to solve for the lightning interaction with such structures in three dimensions and include a considerable amount of detail. Special techniques have been developed for including wires, plumbing and rebar into the model.

Some buildings have provisions for "lightning protection" in the form of air terminals connected to a ground counterpoise system. It is shown that fields and currents within these structures can be significantly high during a lightning strike. Time lapse video presentations have been made showing the electric and magnetic field distributions on selected cross-sections of the buildings during a simulated lightning strike.

## 1.0 INTRODUCTION

Lightning hazards to building environments can be described in terms of electric and magnetic fields (and their time derivatives) and the resulting direct and induced electrical currents which are found in and around critical locations of the facility during a lightning strike.

The space and time distributions of such fields and currents follow solutions of Maxwell's Equations providing that appropriate initial and boundary conditions can be supplied in the regions of interest and that a method of solution can be applied.

This paper describes the results of a numerical computer model which applies Maxwell's Equations to describe a specified lightning attachment to a specific building or facility. The result shows how electromagnetic fields and currents are distributed in space and time in and near the facility during a simulated lightning strike. Time lapse video presentations have been made showing these distributions on selected cross-sections of the buildings.

---

\* Work sponsored by Picatinny Arsenal Under Contract # DAAA21-89-C-0176

Examples are given; 1. For an earth covered storage igloo with iron rebar re-enforced concrete walls, and 2. For a rectangular building with cinder-block walls and a metal roof. Both structures have provisions for "lightning protection" in the form of air terminals connected to a ground counterpoise system. It will be shown that fields and currents within these structures can be significantly high during a lightning strike.

## 2.0 DESCRIPTION OF THE NUMERICAL MODELS

The numerical model of the structure and surrounding environment is based upon a finite difference time domain solution of Maxwell's equations. The solution technique is explicit and accurate to second order in the time and spatial increments, which in these models correspond to the three dimensional cartesian coordinate increments as obtained by Merewether and Fisher [1] with further discussion by Collier and Perala [2].

A problem space containing the facility and surrounding environment is divided into rectangular cells. Each cell has a staggered spatial grid, as shown in Figure 1, composed of the vector components of E and H. There are approximately one million cells in the lightning strike problem spaces discussed in this paper. The cell dimensions  $\Delta x$ ,  $\Delta y$  and  $\Delta z$  are 12"x6"x6" for the igloo and 6"x12"x12" for the building. The field components in each cell are calculated numerically via the finite difference form of Maxwell's Equations [1].

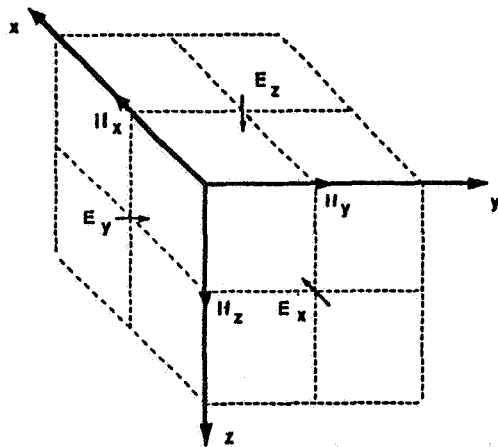


Figure 1 Staggered Spatial Grid

### MAXWELL'S EQUATIONS

$$\mu \frac{\partial \mathbf{H}}{\partial t} + \nabla \times \mathbf{E} = \mathbf{M} \quad (1)$$

$$\epsilon \frac{\partial \mathbf{E}}{\partial t} + \sigma \mathbf{E} - \nabla \times \mathbf{H} = -\mathbf{J} \quad (2)$$

$$\nabla \cdot \mathbf{E} = \frac{\rho}{\epsilon} \quad (3)$$

$$\nabla \cdot \mathbf{H} = 0 \quad (4)$$

In addition to the appropriate boundary and initial conditions, the material properties at each cell location must be specified. This consists of the magnetic permeability,  $\mu$ , in equation (1); the conductivity,  $\sigma$ , in equation (2) and the dielectric constant,  $\epsilon$ , in equations (2) and (3). If the material is homogeneous within the cell (for example, volumes of air, soil, concrete, etc.) then the appropriate values of  $\mu$ ,  $\sigma$ , and  $\epsilon$  are included in the time advance equations for the cell in question.

If the material properties are inhomogeneous in each cell (detailed structure, etc.) then a decision must be made on how to represent the properties in each cell. In some cases average properties are sufficient and in other cases they are not. Special considerations are available for treating apertures in metal walls and also for pipes and thin wires (radii much smaller than cell dimensions) which may run throughout the problem space. These pipes and wires can be carriers of high current.

The buildings and facilities of interest usually have a great deal of "thin wire" situations in the form of signal and power lines, rebar in reinforced concrete, pipes, plumbing, metal poles, the lightning protection air terminals, down conductors, counterpoise, etc.

The thin wires and rods are implemented in a self consistent fashion by making use of the telegrapher's transmission line equations. The telegrapher's equations (5), (6) are a one dimensional solution of Maxwell's in terms of currents,  $I_w$ , and voltages,  $V_w$ , on the wires, which are required to have diameters less than cell size (spatial increment). The per unit length inductances and capacitances are defined (7), (8) with respect to the cell size and the wire diameter,  $2a$ .

The One Dimensional Transmission Line Equations are:

$$\frac{\partial V_w}{\partial z} = -L_w \frac{\partial I_w(k)}{\partial t} - I_w R_w + \hat{E}z(i_w j_w, k) \quad (5)$$

$$\frac{\partial I_w}{\partial z} = -C_w \frac{\partial V_w}{\partial t} - G_w V_w \quad (6)$$

where  $L_w$  and  $C_w$  is the in-cell inductance and capacitance of the wire per unit length.

$$L_w = \frac{\mu_0}{2\pi} \ln \left( \frac{\Delta y}{2a} \right) \quad (7)$$

$$C_w = \frac{2\pi\epsilon E_r(a)}{V_w} = \frac{2\pi\epsilon}{\ln \left( \frac{\Delta y}{2a} \right)} \quad (8)$$

$G_w$  is the in-cell conductance from the wire to the surrounding conductive medium

$$G_w = \frac{\sigma}{e} C_w \quad (9)$$

The wire resistance per unit length,  $R_w$ , is obtained by considering the surface conduction of the metal in question using the skin depth obtained for a frequency of 1 MHz. The resistance for pipes, wire, iron rebar, etc., is normally on the order of  $10^{-3}$  Ohms/meter. In practice, the major results at early time seem to be relatively insensitive to variations of the resistance.

In the computer code, the wires and pipes are embedded into the staggered grid and are driven by the electric field component (see equation (7)) calculated by the three dimensional solution of Maxwell's equations. In order to maintain electrical charge conservation, this wire current must also be injected back into the driving electric field component as a source current via Maxwell's Equation (2). At the interconnections, which are voltage nodes, Kirchoff's law is invoked. At locations where the wires are situated in the soil or concrete, the wires are in electrical contact with the soil or concrete with in-cell conductance given by  $G_w$  in equation (9). This is also true of the facility ground wire which is in contact with the soil.

Complex networks of thin wires (e.g., concertina or metal rebar mesh embedded in conducting concrete) are included in the model by a vectorized extension of the transmission line formalism. Vectorized average wire currents coincide with the electric field vectors in each cell and a corresponding average inductance and resistance is associated with each wire current vector. Six component tensors exist at the cell corners (nodes) describing the equivalent transmission line voltages, wire capacitance, and conductance to the embedding medium. A 36 component connectivity tensor exists at each node describing the ways that wires are connected at the nodes.

At the boundaries of the problem space, some termination condition must be applied to both the counterpoise extensions and the power and signal lines and metal pipes entering the problem space. The boundary condition is applied at current nodes and is the equivalent of the Mur boundary condition applied to the magnetic fields [2].

### 3.0 THE LIGHTNING STROKE CURRENT WAVEFORM AND INJECTION

The problem is initiated by imposing a pre-determined lightning wave form from the top edge of the problem space to a specific point on the structure. In a typical computational case described below, the lightning current waveform is characteristic of a 1% stroke of negative lightning. The lightning current,  $I(t)$ , is given as a function of time by

$$I(t) = 1.1 \times 10^5 \sin^2 \left( \frac{\pi t}{10^{-6}} \right) \text{ A}$$

$$0 \leq t \leq .5 \times 10^{-6} \text{ s} \quad (10)$$

$$I(t) = 1.1 \times 10^5 \sin^2 \left( \frac{t - .5 \times 10^{-6}}{5 \times 10^{-5}} \right) \text{ A}$$

$$.5 \times 10^{-6} < t$$

which has a peak current of 110 kA occurring at .5  $\mu$ s. The lightning current appears without propagation delays in a line of vertical electric fields ( $E_z$ ) from the top of the computational volume to the attach point. The lightning current is injected into the electric fields by dividing the current by the cell area whose normal is parallel to the vertical direction. This becomes the source current density,  $J$ , in Maxwell's equation (2). A number of different parameters are studied: lightning stroke attachment location, soil electrical conductivity, structure wall rebar composition, and power box attachment at the walls and ceiling. These parameters are varied in order to provide environments based upon the range of situations which could be encountered.

The computer model contains features of interest such as, soil, concrete, rebar, counterpoise, etc., which are included in the computer model in a modular form. These separate features may be included or excluded from the model by calling subroutines specific to the features desired. The computations are performed on a CRAY II computer. Typical run times are 1 hour of computer time for each microsecond of real time.

#### 4.0 LIGHTNING STRIKE MODELS

The analysis of the preceding sections has been applied to two structures: (1) an earth covered storage igloo with iron rebar reinforced concrete walls as shown in Figure 2 and, (2) a rectangular constructed building with a metal roof as shown in Figure 3.

The igloo interior is completely surrounded with either metal or iron rebar which forms a "leaky" electromagnetic shield for the interior. A schematic drawing of the igloo vertical mid-cross-section is shown in Figure 4.

The building is made of concrete block outer walls with no rebar, a metal roof, and concrete with rebar floor and inner walls with rebar. Thus the building cannot be considered as having a contiguous shielding effect.

For both models the numerical computer output from a simulated lightning strike may be categorized as follows:

1. Contour Plots - These are "snapshots in time" of the electric and magnetic field structures on a plane cross-section of the building at some time after the initiation of the strike.
2. Time Dependent Plots - these are time dependent graphs of electric and magnetic fields at selected points in the problem space. Currents and voltages on thin wires and rods also have time dependent plots at selected points.
3. Current Arrays - These are spreadsheet tabulations of wire currents in specific areas of the building.
4. Field Maxima - These are computer searches at selected times to find the maximum electric and magnetic fields and the maximum time derivative of the magnetic field within a specified boundary inside the building.
5. Time lapse video presentations showing the magnitudes of the electric and magnetic fields on specific plane cross-sections of the buildings.

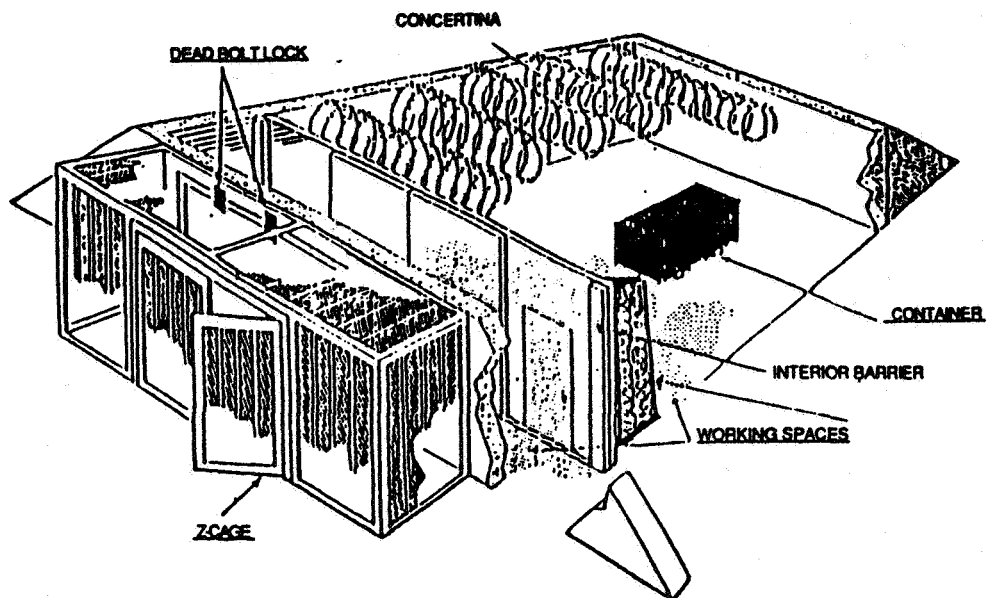


**Figure 2 Earth Covered Storage Igloo -- Lightning Strike Model**

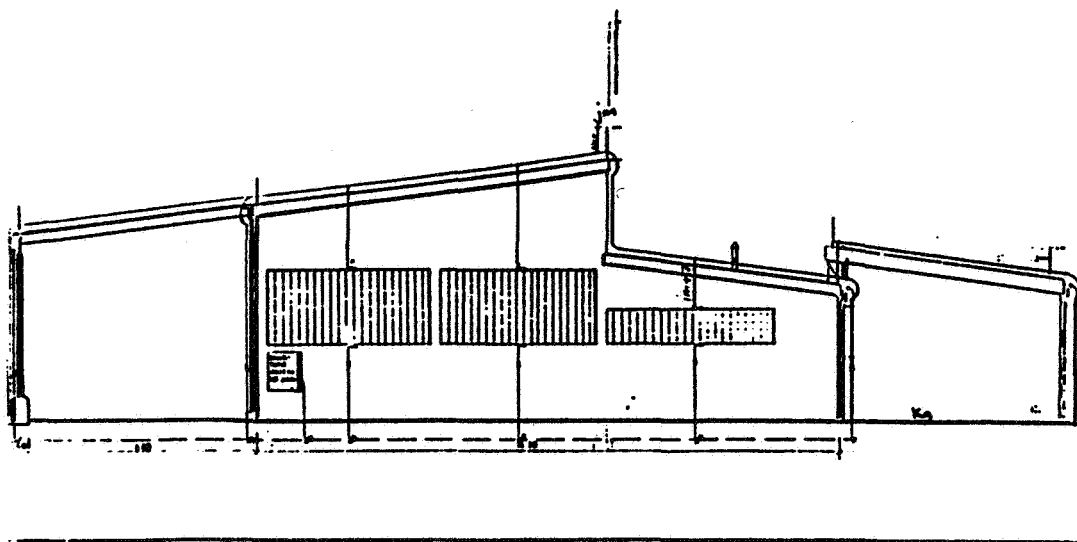


**Figure 3 Building - Right Side View With Window Screens and Lightning Protection System**

Figure 5 shows a contour plot of the vertical mid-plane longitudinal cross-section of the igloo corresponding to the schematic in Figure 4. The electric field pattern outlines some of the prominent features of the igloo, i.e., the z-cage, soil berm over the igloo, headwall, backwall, etc. The vectors show the projection of the electric field vector at each cell onto the mid-plane at a time 1  $\mu$ sec after the initiation of the strike. The length of the vector is proportional to the logarithm of the electric field. The contour lines show lines of equal electric field magnitude labeled as powers of 10 of the field magnitude in volts per meter. For example, the line labeled 4.0 represents field magnitudes of 10,000 volts/meter.

Figure 6 shows a contour plot on a vertical x-z plane of the building cutting through wire mesh on the window nearest the strike. The view is as if looking from the back of the building. The field patterns show essential geometrical features of the model, i.e., roof, supporting I-beams, outer wall, etc.

The window mesh, a wire grid covering the building windows, is being charged (note E-field vectors pointing away from the mesh) and appears to focus the electric field into the interior of the building. The field levels are very high within the building approaching 1 Megavolt/meter (contours are labeled as powers of 10 of the electric field magnitude).

In this case, Figure 6, the lightning protection system is not connected to the metal roof. At .462  $\mu$  seconds the top of the roof is positively charged and the bottom of the roof is negatively charged.

Figure 7 shows the effect of adding an I-beam (perpendicular to the contour plane) with a hanging metal cable hoist. The field at the bottom of the hoist is on the order of a few megavolts/meter and represents a potential for arcing between the hoist and the floor rebar (or any other piece of grounded equipment). In this case the lightning protection system is in contact with the metal roof which is also in contact with the I-beam.

Figure 8 shows time dependent plots, corresponding to Figure 7, of the lightning injection current (given by equations (12)), the electric field and wire voltage in the middle of the window screen, and the voltage between the hoist hook and the floor rebar. This is a case showing that connecting the lightning protection system to the building structure can enhance the hazard inside the building.

## 5.0 TIME LAPSE VIDEO PRESENTATIONS

The video tape shows computer calculated electric and magnetic fields on two different vertical plane cross-sections of the igloo (see Figure 4). The presentation begins with a view of the right-hand side of a transverse cross-section and ends with a view of the longitudinal vertical mid-cross-section (see Figures 4 and 5) and a plane offset from the mid-cross-section.

The data shown is calculated by a Cray II computer using a finite difference form of Maxwell's Equations. The resulting data pertinent to the video display is taken from the Cray II computer results and displayed on an IBM PC compatible EGA screen. These EGA screens have twice the resolution of the VHS video tapes.

The graphic frames are displayed at a rate of about 3 frames per second. Each frame occurs in simulated real time in 50 nanosecond intervals. There are then 20 frames per 1 microsecond simulated real time showing the time development of the electric and magnetic fields for each typical computer run. The time is shown in the upper left-hand corner of the screen.

The electric and magnetic field magnitudes are shown at each finite difference cell on the plane. The colored dots represent the field magnitude ranges at each cell. Vectors centered on the dots also exist at each cell showing the direction of the field projection onto the plane. The scale of values are shown in the video tape. There are approximately 1 million finite difference cells in the entire problem space.

The peak magnitude of the lightning current is 110 KA and the rise time is .2 microseconds. The lightning attaches to the igloo on the rear lightning protection air terminal near the vent chimney of the igloo.

The charge collecting on the rebar may be noted by observing electric field vectors pointing away from the ceiling and back wall in both directions.



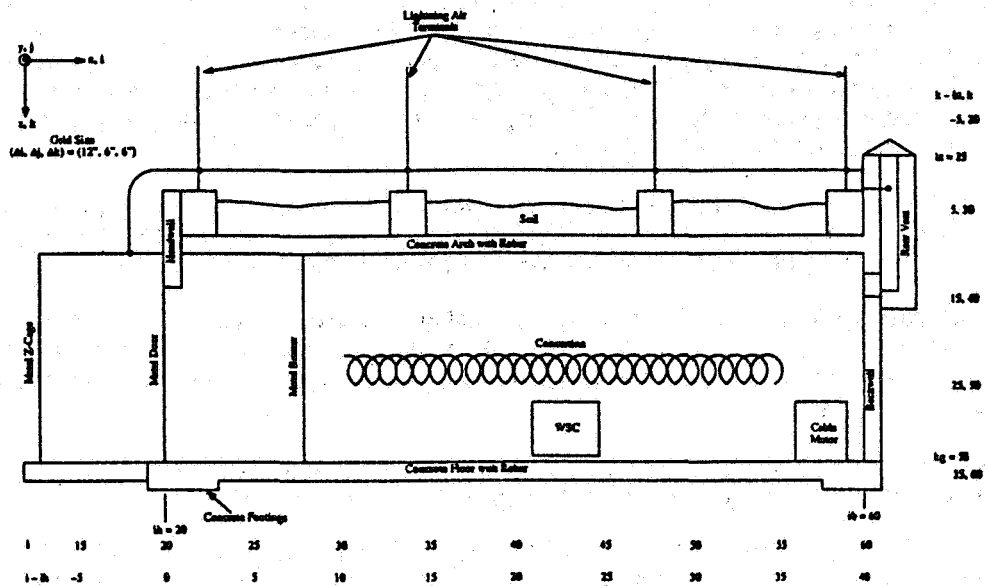


Figure 4 Igloo Vertical Cross-Section at  $j = j_m = 75$

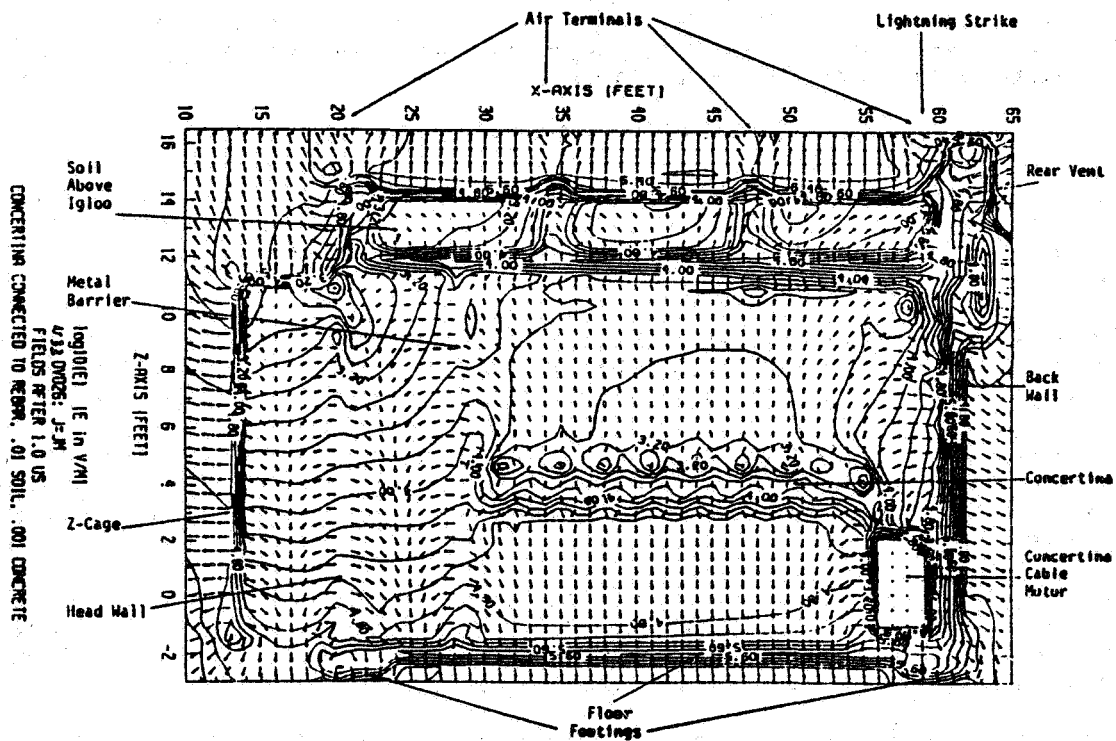


Figure 5 Electric Field Vector and Magnitude Contour Plot for Vertical Mid-Cross-Section of Igloo

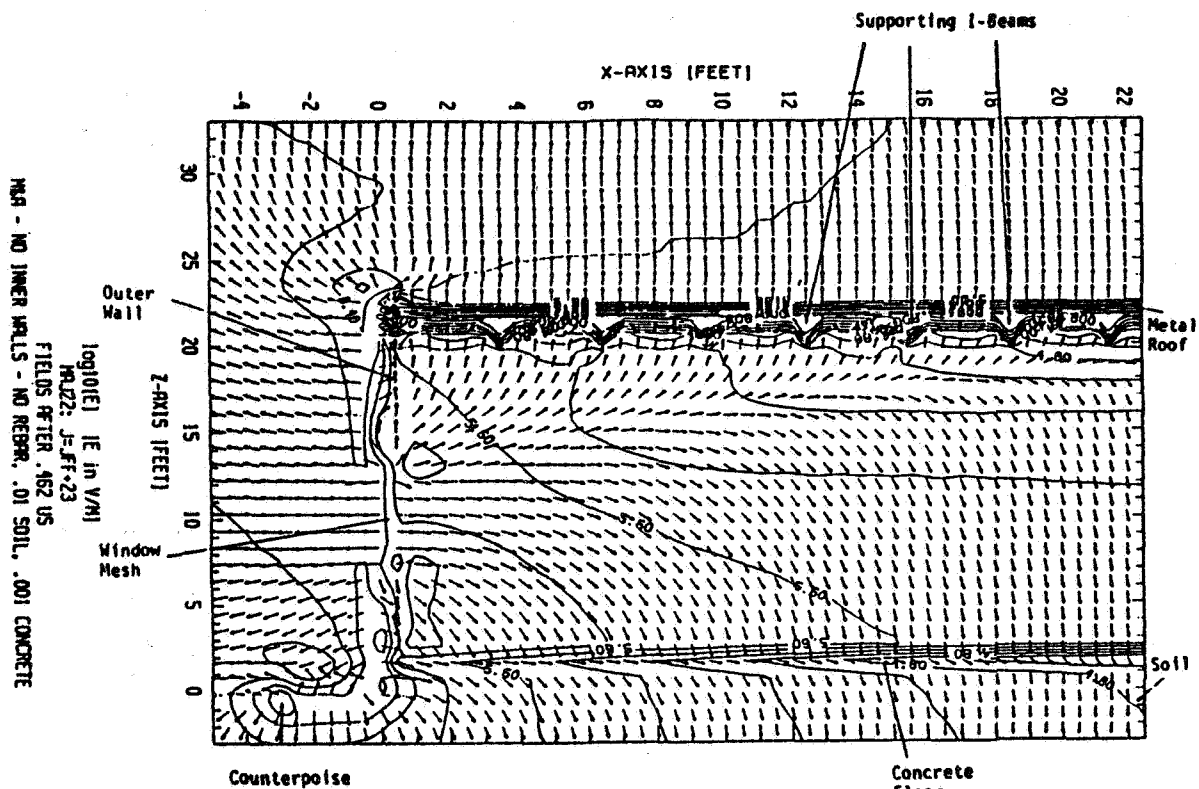


Figure 6 Electric Field Vector and Magnitude Contour Plot for a Vertical Plane Passing Through the Window Mesh of the Building

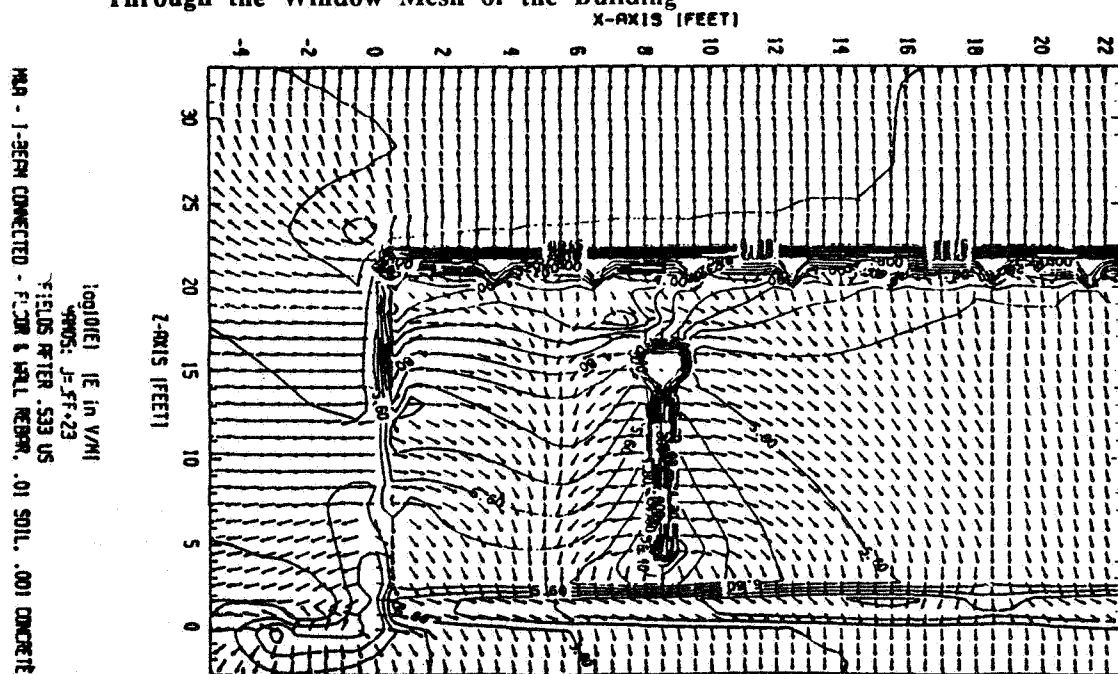
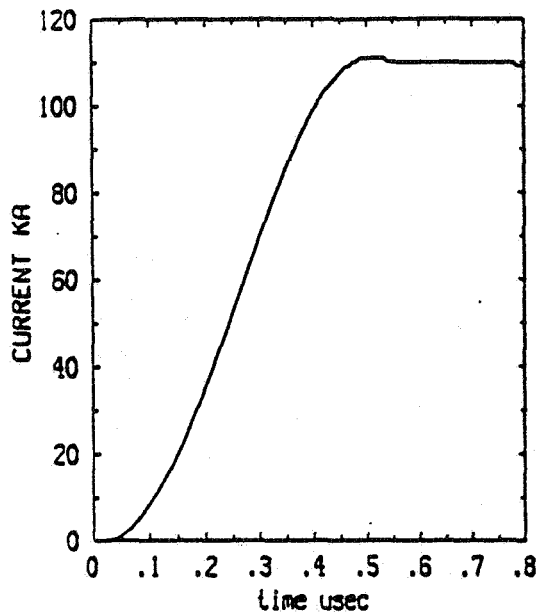
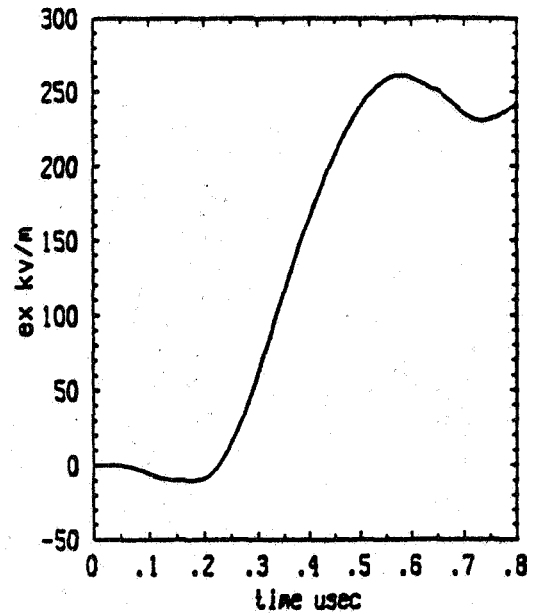


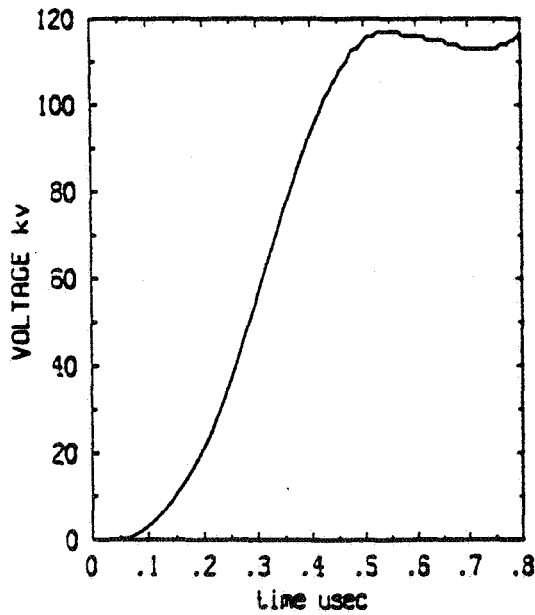
Figure 7 Electric Field Vector and Magnitude Plot for Building Showing the Effect of an Internal I-Beam and Metal Cable Hoist



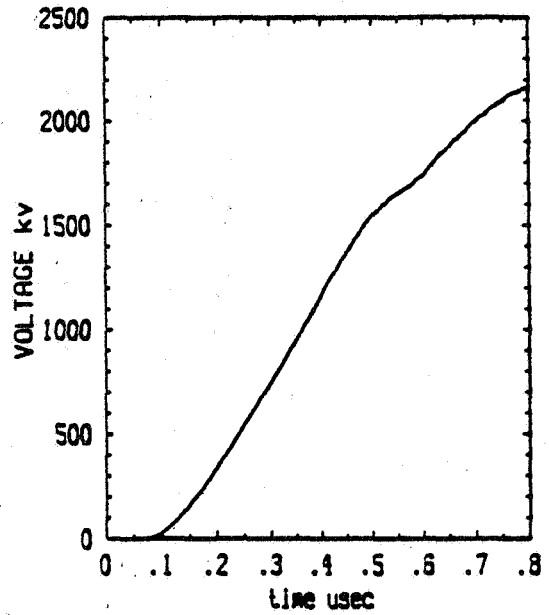
INJECTION CURRENT - M&A Ir,jm,kr-2  
FLOOR REBAR - INNER WALL & I-BEAM - CON  
.01 SOIL-.001 CONCRETE-DATASETS MAMOS



EX-FIELD  
Ir+1, jff+23,kr+14  
MIDDLE OF WINDOW SCREEN



WIRE VOLTAGE  
Ir, jff+23,kr+14  
MIDDLE OF WINDOW SCREEN



HOIST HOOK  
Ir+17, jff+23,kr+21 to 23  
HOIST HOOK TO FLOOR REBAR

Figure 8 Time Dependent Plots of Building Fields and Lightning Injection Current

It is noted that the largest fields are near the floor and are on the order of 100 Kvolts/meter at 1  $\mu$ sec. This is due primarily to capacitive coupling of charge on the rebar which, again, is enhanced by electrical contact between the lightning protection system and the igloo metal structure.

## **6.0 CONCLUSIONS**

A numerical computer model of Maxwell's Equations has been applied to buildings typical of munitions storage and handling structures to calculate potential hazards due to lightning strikes. It is seen that detailed electromagnetic field profiles and currents may be calculated which estimate in a realistic manner the hazardous areas in and around the facility. A time lapse video representation has been produced which shows the electric and magnetic field magnitudes on plane cross-sections of the building during a simulated lightning strike.

## **7.0 REFERENCES**

1. Merewether, D.E., and R. Fisher, "Finite Difference Solution of Maxwell's Equations for EMP Applications," Electro Magnetic Applications, Inc. Report, EMA-79-R-4, Final Revision, 1/15/82.
2. Collier, Richard S. and Rodney A. Perala, "Evaluation of Lightning Hazards to Munition Storage Handling, and Maintenance Facilities with the use of Advanced Methods for Solutions of Maxwell's Equations," presented at the Twenty-Fourth DoD Explosives Safety Seminar, Adam's Mark Hotel, St. Louis, Missouri, 28 - 30 August 1990.

N91-32734

VOLTAGES INDUCED ON A POWER DISTRIBUTION LINE  
BY OVERHEAD CLOUD LIGHTNING

Ziad Yacoub                      Marcos Rubinstein                      Martin A. Uman  
Ewen M. Thomson                      Pedro Medelius

Department of Electrical Engineering  
University of Florida, Gainesville 32611

ABSTRACT

Voltages induced by overhead cloud lightning on a 448 m open-circuited power distribution line and the corresponding north-south component of the lightning magnetic field were simultaneously measured at the NASA Kennedy Space Center during the summer of 1986. The incident electric field was calculated from the measured magnetic field. The electric field was then used as an input to the computer program, EMPLIN, written and provided by Dr. F. Tesche, that calculated the voltages at the two ends of the power line. EMPLIN models the frequency-domain field/power line coupling theory found, for example, in Ianoz et al. [1]. The direction of the source, which is also one of the inputs to EMPLIN, was crudely determined from a three-station time delay technique. We find reasonably good agreement between calculated and measured voltage waveforms.

For publication in the Proceedings of the 1991 International Conference on Lightning and Static Electricity, Cocoa Beach, Florida, USA, April 16-19, 1991.

# VOLTAGES INDUCED ON A POWER DISTRIBUTION LINE BY OVERHEAD CLOUD LIGHTNING

Ziad Yacoub                      Marcos Rubinstein                      Martin A. Uman  
Ewen M. Thomson                      Pedro Medelius

Department of Electrical Engineering  
University of Florida, Gainesville 32611

## ABSTRACT

Voltages induced by overhead cloud lightning on a 448 m open-circuited power distribution line and the corresponding north-south component of the lightning magnetic field were simultaneously measured at the NASA Kennedy Space Center during the summer of 1986. The incident electric field was calculated from the measured magnetic field. The electric field was then used as an input to the computer program, EMPLIN, written and provided by Dr. F. Tesche, that calculated the voltages at the two ends of the power line. EMPLIN models the frequency-domain field/power line coupling theory found, for example, in Ianoz et al. [1]. The direction of the source, which is also one of the inputs to EMPLIN, was crudely determined from a three-station time delay technique. We find reasonably good agreement between calculated and measured voltage waveforms.

## I. INTRODUCTION & EXPERIMENT

Lightning electromagnetic fields interact with electric power lines to induce currents and line voltages. There are two major types of lightning: ground flashes and cloud flashes. In general, lightning between cloud and ground causes higher voltages on power lines, either by direct strike or by the inducing effects of nearby events, than does lightning within or between clouds or from cloud to air (all commonly known as cloud lightning).

There have been several studies [e.g., 2-3] in which theoretical results obtained from the time domain model developed by Agrawal et al. [4] were compared to the corresponding measured waveforms. The comparison reveals reasonable agreement. These studies were conducted for fields from distant ground lightning.

Overhead or nearly overhead cloud lightning differs from ground lightning in that the source is elevated, producing total electric fields that are primarily horizontal, whereas in ground flashes at the same distance say 5 Km, the horizontal field component is, for the ground conductivity at the NASA Kennedy Space Center (KSC), about 30 to 50 times smaller than the vertical [5]. For this reason, cloud flashes can provide a unique simulation of the response of a power line to elevated electromagnetic sources such as nuclear weapons exploded in the upper atmosphere, so called HEMP, and to test available theory describing that interaction. In the present paper, an example of the measured induced voltages on an open-circuited 448 m long, 10 m high power distribution line due to overhead cloud flashes will be compared with the predictions of the computer program EMPLIN which is based on the frequency domain model of field/power line interaction described, for example, in Ianoz et al. [1]. The results given in this example consist of:

(1) the measured induced voltages at both ends of the power line, (2) the measured north-south component of the horizontal magnetic field, and (3) the calculated incident electric field that was obtained from the measured magnetic field using the theory of the reflection of radiation fields from a finite conducting earth and specialized approximations [6]. The data were recorded on day 232 in 1986 at the Atmospheric Science Field Laboratory of the NASA Kennedy Space Center. For more details regarding the experiment, consult the paper in this conference by Rubinstein et al.

## II. DATA

A lightning waveform was classified as a component pulse of a cloud discharge if it was one of the cloud radiation pulses that have been documented by Krider et al. [7], Weidman and Krider [8], and Levine [9] and if the pulse peaks of the induced voltages at the two ends of the power line were of opposite polarity, an important characteristic of the response of an open-circuited power line to an elevated source producing essentially horizontal electric field [6]. About 385 cloud discharge events were identified.

## III. ANALYSIS

To model the measured voltages for an overhead cloud event using the EMPLIN code, values for the conductivity  $\sigma$ , the elevation angle  $\Phi$ , the azimuth angle  $\phi$ , and the polarization angle  $\alpha$  (see Figure 1) need to be chosen. We were able to use a three-station time delay technique, where the three stations are the two end voltages of the line and the north-south component of the magnetic flux density, to determine crudely the direction of the source. Other factors also helped us in narrowing the ranges chosen for the direction angles, such as comparing the properties of the measured end voltages for the particular cloud event with the ideal voltage response given in Yacoub [6].

Figure 2 shows the north-south component of the measured horizontal magnetic field, the corresponding calculated incident electric field, and the measured east-end and west-end voltages of the open-circuited line for a typical cloud discharge waveform. In the example given, the combination of the direction angles was first reduced to the smallest region possible using the factors mentioned earlier. The next step was to try different combinations of  $\alpha$ ,  $\Phi$ , and  $\phi$  in that region, searching for the best fit to the measured voltage waveshapes. The conductivity of the ground was then varied within a certain range to change subtle waveform characteristics, such as pulse widths and sudden and narrow amplitude variations. Varying the conductivity changes the overall amplitude of the induced voltages as well as the relative amplitudes of adjacent peaks.

The combination that gave the best similarity to the measured voltages was:  $\alpha = 350^\circ$ ,  $\phi = 90^\circ$ , and  $\Phi = 80^\circ$ . Conductivities of  $1.6 \times 10^{-2}$ ,  $1.0 \times 10^{-2}$ ,  $0.5 \times 10^{-2}$ , and  $0.25 \times 10^{-2}$  were tried with the above combination of angles. The results are shown in Figure 3. Figure 3 clearly shows how, as we decrease the conductivity from  $1.6 \times 10^{-2}$  to  $0.25 \times 10^{-2}$ , the pulse peak structure at the east and west ends of the line changes to best resemble the measured voltage responses in Figure 2. Also, note that the overall amplitude of the voltage responses in Figure 3 increases as the conductivity is decreased. Again, the conductivity of  $0.25 \times 10^{-2}$  gives the best comparison in overall amplitude and

waveshapes between the calculated and measured voltages. Better amplitude agreement between theory and experiment is obtained if we double the calculated field. Reducing the elevation angle of the source reduces the overall amplitudes of the calculated voltages and also change the relative amplitudes of the initial pulse to the adjacent same polarity pulse. This is illustrated in Figure 4 where an elevation angle of  $40^\circ$  is used. This results in a voltage decrease of an order of magnitude, worsening the agreement with experiment.

#### IV. DISCUSSION

We have presented an example of a test of the computer code EMPLIN using induced voltages on a 448 open-circuited power distribution line from overhead lightning. In spite of the many parameters involved in the coupling of the overhead electromagnetic waves to the power line; the limitations experienced in determining the direction of the incident electric field to an acceptable degree of accuracy; the lack of exact knowledge of effective site conductivity for reflection of overhead electromagnetic waves; and the fact that the incident electric field, the input to EMPLIN, was not available for the cloud discharge events and had to be calculated from the north-south horizontal magnetic field component; we were able to show that EMPLIN can predict, fairly well, the induced voltage waveshapes on power lines from elevated sources while there is a factor of two discrepancy between calculated and measured voltage amplitudes.

#### V. ACKNOWLEDGEMENTS

Research sponsored by the U.S. Department of Energy, Office of Energy Management, under Contract No. DE-AC05-84OR21400 with Martin Marietta Energy Systems. We would like to thank Dr. Fred Tesche for providing the EMPLIN program.

#### REFERENCES

1. Ianoz, M., C. A. Nucci, F. M. Tesche, Transmission line theory for field-to-transmission line coupling calculations, Electromagnetics, vol. 8, 171-211, 1988.
2. Master, M. J., M. A. Uman, W. Beasley, and M. Darveniza, Lightning induced voltages on power lines: Experiment, IEEE Trans. PAS, PAS-103, 2519-2529, 1984.
3. Rubinstein, M., A. Y. Tzeng, M. A. Uman, P. J. Medelius, E. M. Thomson, An experimental test of a theory of lightning-induced voltages on an overhead wire, IEEE Trans. EMC, EMC-31, 376-383, 1989.
4. Agrawal, A. K., H. J. Price, and S. H. Gurbaxani, Transient response of multiconductor transmission lines excited by a non-uniform electromagnetic field, IEEE Trans. EMC, EMC-22, 119-129, 1980.
5. Thomson, E. M., P. J. Medelius, M. Rubinstein, M. A. Uman, J. Johnson, and J. W. Stone, Horizontal electric fields from lightning return strokes, J. Geophys. Res., 93, 2429-2441, 1988.



6. Yacoub, Z., Voltages induced at both ends of a test power line by overhead cloud lightning flashes at the Kennedy Space Center in 1986, MS Thesis, University of Florida, Gainesville, Florida, 1990.
7. Krider, E. P., G. J. Radda, and R. C. Noggle, Regular radiation field pulses produced by intracloud discharges, J. Geophys. Res., 80, 3801-3804, 1975.
8. Weidman, C. D., and E. P. Krider, The radiation fields wave forms produced by intracloud lightning discharge processes, J. Geophys. Res., 84, 3159-3164, 1979.
9. Levine, D. M., Sources of the strongest RF radiation from lightning, J. Geophys. Res., 85, 4091-4095, 1980.

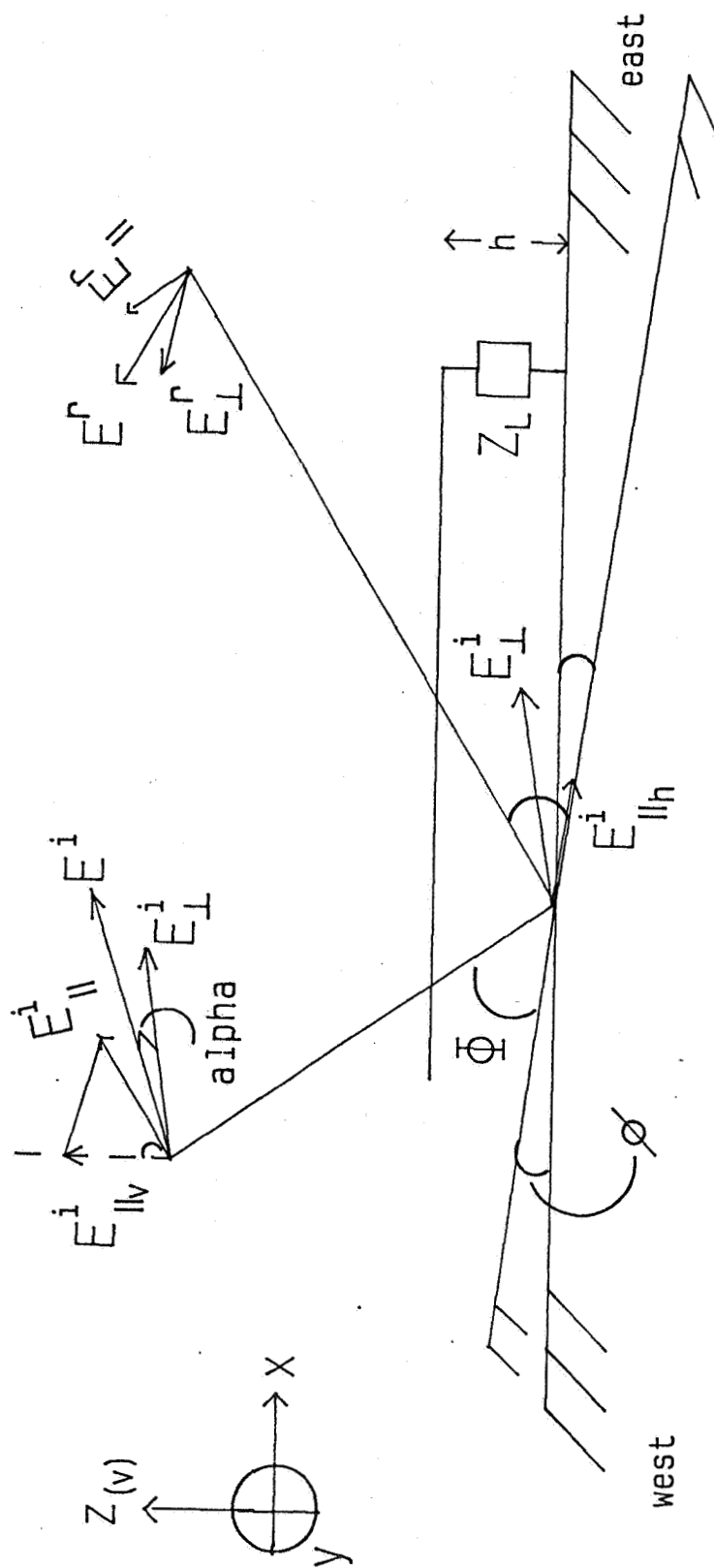


Figure 1. Geometry of an incident EM wave on an overhead power line. The direction angles  $\alpha$ ,  $\phi$ , and  $\phi_h$  are also defined.  $E^i$ ,  $E^i_{||v}$ , and  $E^i_{\perp}$  are all in a plane perpendicular to propagation.  $Z_L$  is the load at either end of the power line which is at a height  $h$  above the ground.

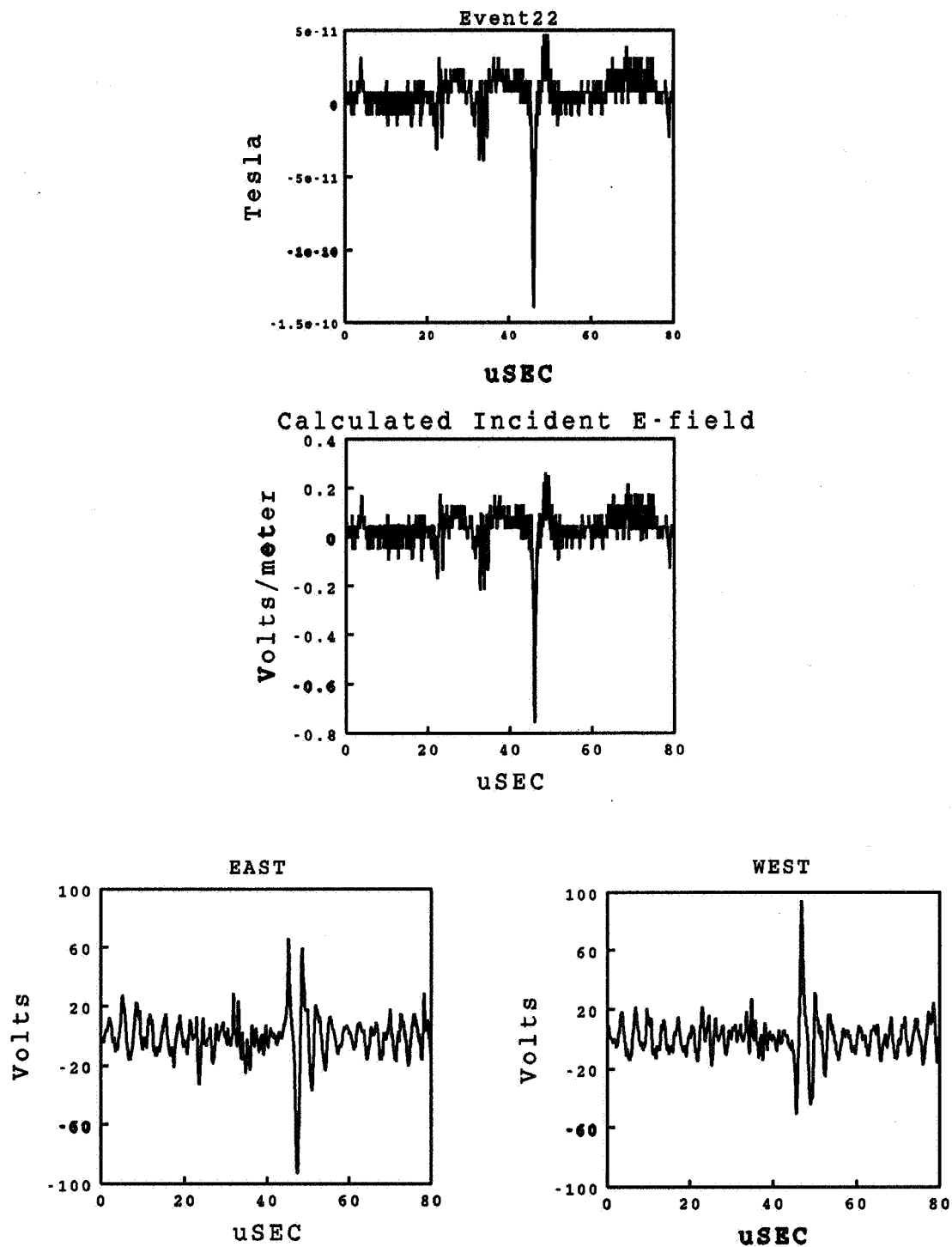


Figure 2. (top) Measured north-south component of the magnetic field, (middle) calculated incident electric field, (bottom) measured east and west end voltages.

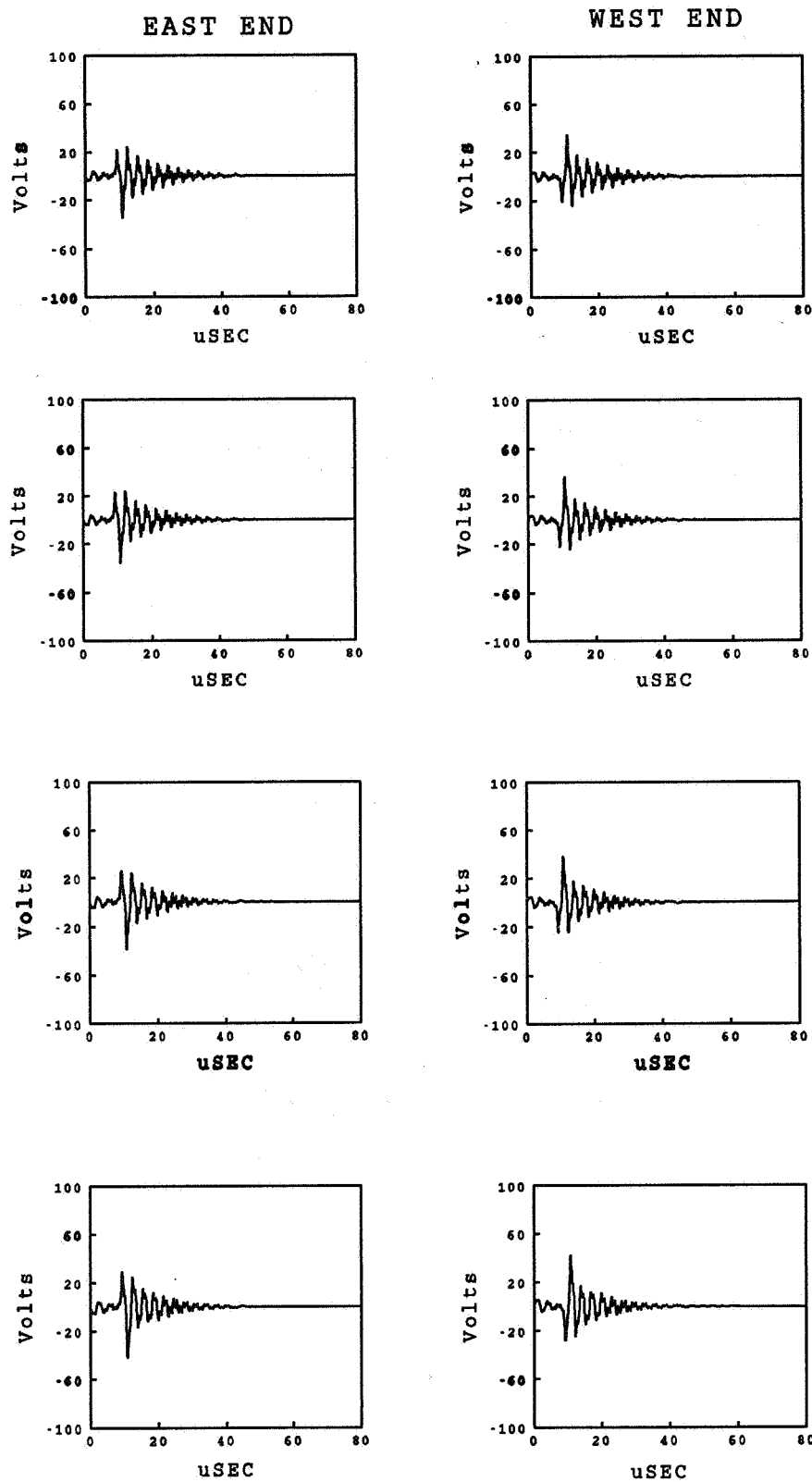


Figure 3. Calculated east and west end voltage responses:  $\alpha = 350^\circ$ ,  $\phi = 90^\circ$ ,  $\phi = 80^\circ$ . From top to bottom, conductivity used is: 0.016 mho/m, 0.01 mho/m, 0.005 mho/m, and 0.0025 mho/m.

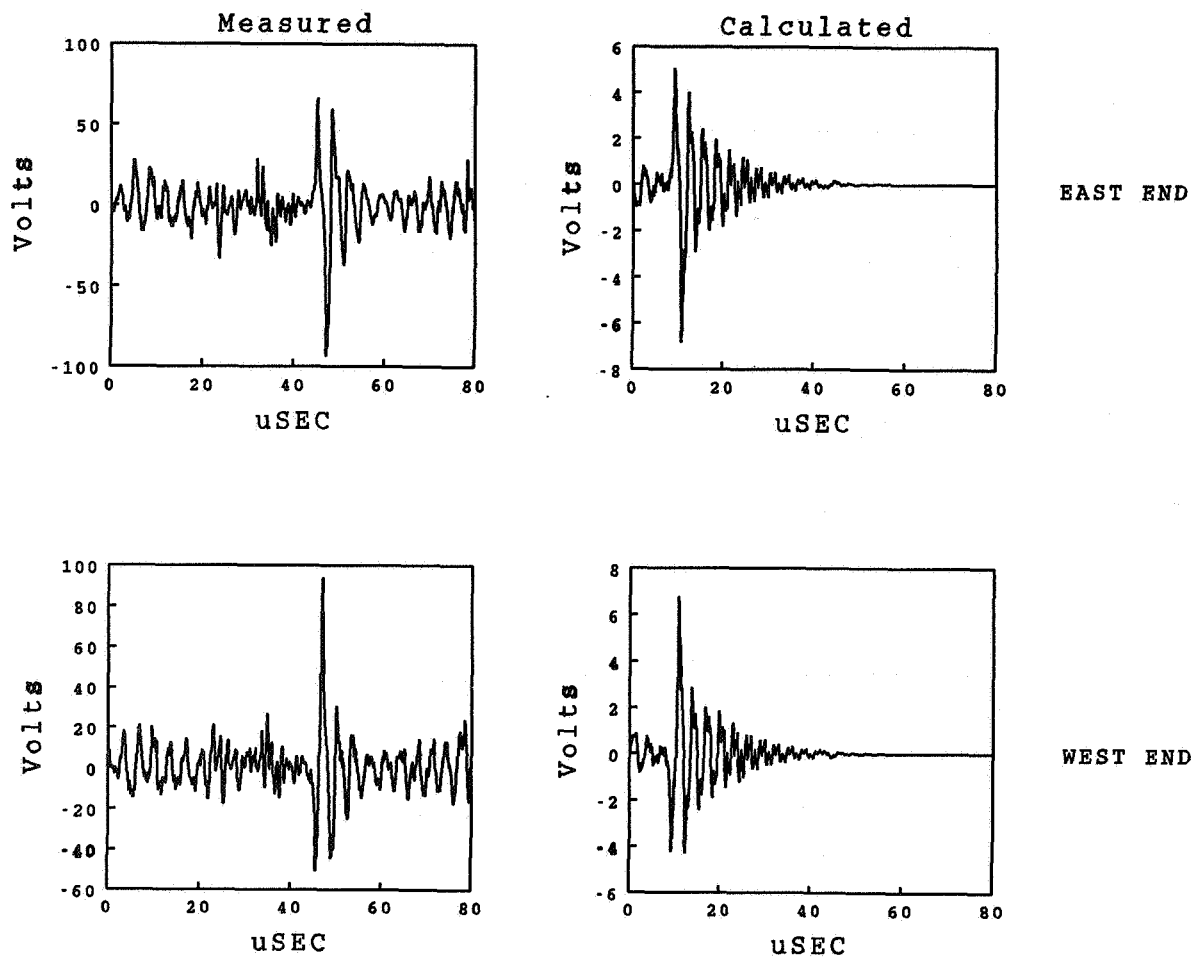


Figure 4. Measured and calculated voltage responses when the elevation angle is reduced to  $40^\circ$ . Conductivity is still 0.0025 mho/m. Note different scales on measured and calculated voltages.

N91-32735

GUIDELINES FOR A PROPOSED LIGHTNING PROTECTION POLICY  
OF A GOLF ASSOCIATION OR TOURNAMENT SPONSOR.

by Dr. Charles C. Hillyer

WHY SHOULD A LIGHTNING PROTECTION POLICY BE FORMULATED?

Lightning causes many deaths and injuries on golf courses every year. Players, contestants, caddies, spectators, officials and sponsors of golf events need to take every precaution for the protection of persons against lightning.

Recently, a decision by an Appeals Court in the State of Tennessee awarded a large damage claim to the survivors of three men killed by lightning while playing golf on a course owned by the State of Tennessee. This decision has drawn the focus of widespread attention to the role of Management Risk Responsibility regarding Lightning Protection and Safety.

The Decision was based on four points of Failure to Provide:

1. A Lightning Protection Policy.
2. Lightning Protection Information.
3. Lightning Warning.
4. Lightning Shelters.

The following guidelines and comments will attempt to address these items of "Failure to Provide." Individual critique and comments are solicited and will be welcomed.

Golf Associations have supported several programs of research on the early detection and warning of lightning. While many significant improvements have been made in this area, we are convinced, in recognition of the unpredictable nature of lightning, there is no equipment, instrumentation or other known method that can guarantee completely failsafe advance warning for lightning strikes.

During 1991, several Golf Associations will continue to conduct on site evaluation of various detection devices. One of these devices is relatively simple to operate and is very affordable, the M-10 Lightning Detector, developed by Airborne Research Associates of Weston, Mass. This new instrument is being appraised by the Southern Golf Assn, the USGA, PGA, the TPC tour events and others.

Page 2.

It must be understood by all persons associated with golf tournaments, and other outdoor applications, that these instruments are operated on an experimental basis. They can detect lightning, but do not pinpoint its location. Distance from the observer to the lightning strike must be calculated by timing the interval between an audible signal from the instrument to the sound of its thunder as received by the observer. This is called TOFTI. (Time-Of-Flash-Thunder-Interval.) Approximately five seconds between flash and thunder indicates one mile, etc.

This technique will work in the early stages of a storm when lightning is not too frequent, because it is necessary to be able to identify the specific thunder sound with the lightning which caused it. When lightning is quite frequent, this can not be done. However, at such a stage it is obvious that a storm exists. The early first detection stage is important.

These instruments have capability to detect lightning under adverse visibility conditions and may prove to be a valuable adjunct, even if in this area alone. They can also provide on site data supplemental to that obtainable from NOAA/NWS, the FAA and other reliable sources of severe weather information.

Contestants, officials and spectators, should be encouraged to learn, practice and apply the principles of TOFTI in order to assist in the pursuit of their personal responsibility for evaluation of lightning proximity.

Diligent effort will be made by the Tournament Committee to provide weather and lightning information and warning, to the greatest extent of their ability. However, due to the unpredictable nature of individual lightning strokes, the Sponsor and/or the Host Club must not be expected to assume responsibility for property or physical loss or damage from lightning or other adverse weather factors. (This paragraph, in particular, may need editing with a fine tooth comb by the Sponsor and Host Club legal advisors.)

THE ULTIMATE RESPONSIBILITY FOR AN INDIVIDUAL'S PROTECTION AND SAFETY, IS THE RESPONSIBILITY OF THE INDIVIDUAL.

A LIGHTNING ALERT: Will be instituted when weather forecasts and local observations indicate Thunderstorms in the area.

A LIGHTNING WATCH: Will be instituted when Lightning has been detected and determined to be within approximately (15 miles ??? ) of the golf course. The Lightning Watch will be issued by radio to all Committee personnel. Under this condition, all personnel will be alerted to seek visual detection of any lightning, its azimuth from the individual observer and calculation of its distance by use of TOFTI, and report this information to the Tournament Chairman immediately.

DISCONTINUING PLAY: IMPORTANT! IT SHOULD BE MADE CLEAR AND UNDERSTOOD, THAT: THE COMMITTEE CAN NOT AND DOES NOT IMPLY, TO ANY DEGREE, THAT THERE IS ANY ASSURANCE OF SAFETY FROM LIGHTNING PRIOR TO SOUNDING THE DISCONTINUE PLAY SIREN.

THE SIREN IS SOUNDED TO ADVISE THAT PLAY IS NO LONGER PERMITTED after that time, and procedure is then in accordance with provisions under the Rules of Golf.

REMINDER: The USGA Rules of Golf, page 105, under Protection of Persons Against Lightning: "Attention is called to Rules 6-8 and 33-2d." "The USGA suggests that players be informed that they have the right to stop play if they think lightning threatens them, even though the Committee may not have specifically authorized it by signal."

DISCONTINUE PLAY: When lightning is determined to have struck within varying distances of the course, depending on the speed of approaching storm, and numerous other factors, the Discontinue Play Sirens will be sounded as three successive wails and may be repeated. At that time, it is mandatory that play be suspended. The contestant must then elect, at his/her own discretion; to either mark and lift the ball at that time, or, he/she may complete the hole being played. The contestant must then seek shelter without delay; the nearest, safest shelter available.

(See TAKING SHELTER, USGA Poster reprint on page 4.)

WHEN SHOULD THE DISCONTINUE PLAY SIREN BE SOUNDED? ? ? ? ?

This question involves such a high degree of sensitivity and disagreement that it has been practically impossible to elicit definite answers.



Much of this disagreement may be attributed to widespread lack of adequate information and insufficient comprehension of the behaviour of lightning. There is also grave concern, on the part of many sponsors, over the possibility of their increasing their liability and litigational factors through the use of what they consider, overly precise terms for decision on safety parameters when stated in miles or minutes. The decision to "blow the siren" is usually dismissed as a "judgement call". A judgement based on WHAT?

In considering the "Failure to provide information", as stated in the Tennessee Decision, one might well consider that by withholding information on the basis for the "judgment call" it could backfire. Thereby, the sponsor would be at greater fault and would have increased the factor of liability and litigation. In my opinion, that information should not be withheld, since denial of its use could diminish the ability for the individual's judgement to determine his danger and need to seek safety measures for protection from lightning.

It is the author's further opinion that in general, when lightning is within approximately 5 miles of the playing area, the course should be clear of personnel. This parameter is, of course, subject to many variables, including speed of the approaching storm, evacuation time to available shelter, etc. However, there are some who feel that the 5 mile parameter is far too conservative, while from the standpoint of others, it would be considered much too liberal. Thereupon lies a wide range of disagreement.

NOTE: Lightning does not necessarily travel to earth beneath the apparent thundercloud; indeed, a high percentage of ground discharges occur at the edges of the clouds or from wispy clouds near the main convective cloud. Another example of this is that lightning can come to earth from the high cirrus anvil "blow-off" cloud at the top of thunderstorms and may travel many miles or tens of miles downwind from the central portion of the storm. "Residue clouds" at the middle altitudes formed at the latter stages of thunderstorms also cause lightning many miles away from the original storm clouds. Note that regions downwind of thunderclouds are subject to such lightning approaching. Clouds can be hazardous when they are 5, 10 or more miles away, depending on conditions. Therefore, the official upon whose judgement rests the decision to discontinue play must be keenly aware that a lightning stroke may reach ground at a widely variable distance from the ground vertically below its cloud source. Thus, some general considerations for discontinuing play when the last calculated lightning strike is within 6-10 miles.

**RESUMING PLAY:** Play should NOT be resumed until there has been substantial evidence that the trailing edge of the thunderstorm has passed no less than several, perhaps 5 - 6 miles distant and its forward progress has been determined to be in a direction downwind and away from the playing area.

Play MAY NOT be resumed until the Committee has issued the Resume Play Siren. One long wail of the siren. This signal may be repeated.

**WARNING POSTERS:** The Lightning Posters published by the USGA are readily available. Recommendation is made that these posters should be required, with distribution to include: The Clubhouse, Pro Shops, Locker Rooms, Practice Range, Starters Tents, Rangers, Tennis Facilities, Swimming Pool Area, Snack Buildings, Maintenance Barn, Cart Barn and in each on Course Shelter.

**SHELTERS:** The USGA Lightning Safety Posters provide this information clearly. The Host Club can provide supplemental information of locations of specific shelters and the maximum capacity for each shelter. Evacuation ZONES may be provided, to insure access to the assigned shelters within minimum time/distance availability and to avoid overcrowding of the facilities. Golf carts must NOT occupy space within these shelters if access for human occupancy is jeopardized, diminished or excluded. This information may be published, provided to each contestant and displayed with each USGA poster.

**TEMPORARY SHELTER FACILITIES:** (During tournaments and other special events. Upon long range advisory of anticipated thunderstorms, a Host Club may arrange for several large School Buses, or the like, to be placed at strategic locations about the golf course, to provide supplementary emergency shelter for contestants, caddies and equipment.

**AUDIBLE WARNING SYSTEM:** Every effort should be made to provide a permanent siren or horn warning system that is audible at every point of the golf course. The Host Club should be advised of the new necessity for such a system and the advantages a permanent system would afford its members.

**THE ULTIMATE RESPONSIBILITY FOR AN INDIVIDUAL'S PROTECTION AND SAFETY, IS THE RESPONSIBILITY OF THE INDIVIDUAL.**

Page 6.

Supplementary Note: A four or five page lightning protection policy would admittedly be quite a bit to expect a contestant to read. However, with the increased significance of liability for sponsors it may be worthwhile to consider:

a. At the time of contestant Registration, distribute a copy of the full content of the Lightning Protection Policy to each contestant. In that manner, the contestant will have been provided with the policy information. In addition, this would provide an updated source of some much needed general information on lightning behaviour, and procedures employed to help protect the individual and for the general public. Then, of course, we must leave the burden of responsibility of assimilating and applying the information up to the judgement of the individual.

THE ULTIMATE RESPONSIBILITY FOR AN INDIVIDUAL'S PROTECTION AND SAFETY, IS THE RESPONSIBILITY OF THE INDIVIDUAL.

(or),

b. The full content of the Lightning Protection Policy may be provided to the Officers and Directors of the Sponsoring Organization, and the Host Club Committee. The contestants could then be provided with an abridged edition of the Policy, to the extent considered necessary (???) for their individual information assimilation and protection and for the liability protection for the Sponsors.

(and)

c. That a Committee be appointed and charged with the responsibility of final formulation and management of the ultimately adopted Lightning Protection Policy.

---

Prepared by Dr. Charles C. Hillyer, President, Communications And Weather Research Foundation and Director of Research and Development, Southern Golf Association, March 1991. This paper/proposal is submitted in the Form of presentation of some Guidelines for the purposes of study and refinement by those who may realize the need of establishing a Lightning Protection Policy.

---

SEE ADDENDUM NEXT PAGE:

Page 7.

**ADDENDUM:**

On April 22, 1991, after this paper had been presented, the author received supplemental legal information. On April 8, 1991, a release for publication was issued, advising that a new decision has been made on the rulings in the litigation referenced in the paper. The earlier Appeals Court decision has been reversed by the Supreme Court of Tennessee.

Accordingly, further appraisal on this aspect of the paper will be necessary. The results of additional study will be presented at a later date.

# INFLUENCE OF CHANNEL BASE CURRENT AND VARYING RETURN STROKE SPEED ON THE CALCULATED FIELDS OF THREE IMPORTANT RETURN STROKE MODELS

Rajeev Thottappillil

Martin A. Uman

Department of Electrical Engineering  
University of Florida  
Gainesville  
Florida

Gerhard Diendorfer

Department of Electrical Power Engineering  
Technical University of Vienna  
Vienna  
Austria

## ABSTRACT

Recently Nucci et al. [1] compared five return stroke models using an identical current at the channel base of each. Diendorfer and Uman [2] introduced a new model which reproduces remarkably well the experimentally observed characteristics of the fields both close to and far from the return stroke channel. Both Nucci et al. [1] and Diendorfer and Uman [2] used a channel base current that is typical of measured subsequent stroke current of both natural lightning and triggered lightning. Though the channel base current adopted in each paper is within the range of measured currents, they differ in the detailed wave shape. The first part of this paper compares the calculated fields of the Traveling Current Source (TCS), Modified Transmission Line (MTL), and the Diendorfer-Uman (DU) models with a channel base current assumed in Nucci et al. [1] on the one hand and with the channel base current assumed in Diendorfer and Uman [2] on the other hand. The characteristics of the field wave shapes are shown to be very sensitive to the channel base current, especially the field zero crossing at 100 km for the TCS and DU models, and the magnetic hump after the initial peak at close range for the TCS model. In the second part of the paper the DU model is theoretically extended to include any arbitrarily varying return stroke speed with height and a brief discussion is presented of the effects of an exponentially decreasing speed with height on the calculated fields for the TCS, MTL, and DU models.

## INTRODUCTION

There are a number of lightning return stroke models that have been used to calculate remote electric and magnetic fields given an assumed current at the base of the channel and an assumed speed of the return stroke. Nucci et al. [1] compared five of the most used models, namely, Bruce-Golde

(BG), Transmission Line (TL), Master-Uman-Lin-Stadler (MULS), Travelling Current Source (TCS), and Modified Transmission Line (MTL) models, assuming similar currents at the channel base. For the assumed channel base current, all of the models gave reasonable values of fields although the charge and current distributions along the channel were quite different

for the different models. Nucci et al. [1] also discuss the reasons for the differences in the calculated fields for the different models and the ability of the models to reproduce the measured characteristics of the fields. Nucci et al. [1] did not deal with the influence of the variability of the channel base current on the predictions of the models, but a general discussion on the subject is available in Cooray and Orville [3], though not specific to the models discussed here. Also, Diendorfer and Uman [2], after introducing a new model (henceforth called the DU model), discuss the influence of the some of the channel base current parameters on the calculated fields. Although Nucci et al. [1] and Diendorfer and Uman [2] each assumed a channel base current that is typical of the measured currents for subsequent strokes in both natural and triggered lightning, the two current wave shapes differ in detail. In this paper we compare the calculated fields for the TCS, MTL, and DU models assuming both the current adopted by Nucci et al. [1] and the current adopted by Diendorfer and Uman [2] (henceforth called the Nucci current and the DU current, respectively) and show that some of the characteristics of the fields predicted by the models are very sensitive to the current waveshape assumed at the channel base and, further, that the extent of variation in the characteristics of the field depends on the specific model. Finally, we extend the DU model theoretically to include return stroke speed variation as an arbitrary function of height and present calculated fields for the specific case of an exponentially decreasing return stroke speed with height for the TCS, MTL, and DU models.

## RESULTS

The Nucci current and the DU current are compared in Fig.1. The DU current has a narrower peak, a small

hump after the peak, and a faster decay than the Nucci current. The small differences in peak currents and front rise times influence mostly the field rise times and peaks and do not influence significantly the overall wave shape of the fields. For field calculation with the MTL model a current decay constant of 2000 m is assumed which is the same as in Nucci et al. [1]. When fields are calculated with the DU model, two time constants, 0.6  $\mu$ s and 5.0  $\mu$ s, are adopted just as in Diendorfer and Uman [2]. Fig.2 shows the electric fields at a distance of 100 km for the DU current and the Nucci current and a constant return stroke speed of 1.3e08 m/s. From Fig.2a it is seen that with the DU current at the channel base the TCS model field (line 2) crosses zero around 50  $\mu$ s while it does not cross zero within 100  $\mu$ s with the Nucci current (curve 5). Similarly, the DU model field crosses zero around 55  $\mu$ s with the DU current at the channel base (curve 3) while it does not do so within 100  $\mu$ s with the Nucci current (curve 6). The choice of base current does not appreciably affect the zero crossing time (around 30  $\mu$ s) of the MTL model fields (curves 1 and 4). Also note that for the given channel base current the TCS and DU model fields are different only for the first 30  $\mu$ s or so, and after that they are almost the same with the DU fields being slightly higher. Fig.2b shows the same fields as in Fig.2a for the first 5  $\mu$ s. The initial peak fields are higher with the DU channel base current for all the models. The initial peak fields are the smallest for the DU model, less than half of the TCS model values and slightly greater than half of the MTL model values. Figs.3a and 3b show, respectively, the electric and magnetic fields at a distance of 5 km for the models with a constant return stroke speed of 1.3e08 m/s and with DU and Nucci currents at the channel base. For a given model the fields produced by the DU current at the channel base are larger for the first few tens of

microseconds, but becomes less than the fields produced by the Nucci current at the channel base at later times. For a given base current the electric fields produced by the TCS and DU models are very similar (see the pairs 2, 3 and 5, 6 of Fig.3a) after about 20  $\mu$ s, with the electric fields of the TCS model always being larger than the corresponding DU model electric fields. The magnetic fields for the TCS and the DU models are roughly equal after about 40  $\mu$ s for the given channel base currents (see Fig.3b). Also for the fields at 5 km, the magnetic hump after the initial peak of the TCS model is more prominent with the DU current than with the Nucci current (see Fig.3b).

The DU model was derived for a constant return stroke speed in Diendorfer and Uman [2]. The DU model can be generalized to include a variable return stroke speed that is an arbitrary function of height. It can be shown mathematically [4] that the return stroke channel current  $i(z', t)$ , where  $z'$  is the height above the ground, is given by

$$i(z', t) = i(0, t+z'/c) - i(0, z'/V_{av}(z') + z'/c) * \exp[-(t - z'/V_{av}(z'))/\tau] \quad (1)$$

where  $V_{av}(z')$  is the return stroke speed averaged over a height  $z'$  defined by

$$V_{av}(z') = \frac{z'}{\int_0^{z'} \frac{dz''}{V(z'')}} \quad (2)$$

$c$ , the speed of light, and  $\tau$ , the time constant for discharging the charge on the leader. An exponential decrease in speed given by

$$V(z') = V * \exp[-(z'/\lambda)] \quad (3)$$

where  $V$  is the speed at ground level. The factor  $\lambda$  in equation (3) is a

constant whose value is chosen as 2000 m. The speed at ground level is taken as  $1.3 \times 10^8$  m/s for all three models. The DU current is assumed at the channel base for the purpose of comparing the fields produced from the constant speed case with the variable speed case. The other parameters of the three models are the same as previously given.

Fig.4 shows the effect of an exponentially decreasing speed on the electric fields produced by TCS, MTL, and DU models at 100 km. The zero crossing time of the TCS and DU models are earlier by about 15  $\mu$ s (compare curves 2, 3 with 5, 6 respectively), but the zero crossing time of the MTL model is not affected very much. Also the hump after the peak of the TCS and DU model fields are less prominent with a decreasing speed.

#### DISCUSSION

After a time of about 35  $\mu$ s the DU channel base current amplitude is smaller than the corresponding Nucci current and at 100  $\mu$ s the DU current is only about half of the Nucci current. The lower channel base currents at later times results in lower currents along the channel at later times for all the models. Hence the fields produced at 5 km by a given model for the DU current at the channel base are smaller than the fields produced by the Nucci current at the channel base after the first few tens of microseconds. The fields at 100 km are dominated by the radiation term caused by the time rate of change of current all along the channel. As discussed in Nucci et al. [1], the time derivative of the current is positive at the return stroke wave front for the TCS and MTL models and negative at all points below the wave front for the TCS model and a few meters below the wave front (because of the finite rise time of the current) for the MTL model. For the DU model the time derivative of the current is positive at the wave front and a few meters below it and negative at all

other points. The fields at 100 km cross zero at the time that the contribution to the fields from the negative current derivatives become dominant. The amplitude of the derivative of the current is determined by the amplitude, rate of rise, and rate of decay of the current. With the DU current at the channel base, the amplitude of the currents at later times along the channel are smaller for all the models, and hence there are earlier zero crossing times (by more than 50  $\mu$ s) for the TCS and DU models. The zero crossing time of the MTL model is not very sensitive to the channel base current because in the MTL model, as the current from ground travels up the channel, it decays exponentially and the current value and its derivative at the top sections of the channel are only a small fraction of their values at the bottom sections, irrespective of the current at ground. For the same return stroke speed at ground, a decreasing speed with height delays the time at which the return stroke wave front reaches a given height, which in turn causes the smaller currents at the tail of the channel base current to appear at lesser height when compared to the constant speed case. This also causes the field at 100 km to cross zero earlier (by about 15  $\mu$ s for an exponential speed decay constant of 2000 m) for the TCS and the DU models. The zero crossing of the MTL model is not very sensitive to the assumed variation in speed for same reason mentioned above.

#### CONCLUSION

The fields calculated by the three return stroke models studied are sensitive to the channel base current characteristics and to the return stroke speed, but the different models respond in varying degrees to the above parameters. The differences in the predictions may be experimentally measurable. In that case, design of an

experiment for the simultaneous measurement of the return stroke speed, the channel base current for long duration, and the fields, both close and far from the channel might allow a determination of the best existing model or could make possible the development of a better model.

#### ACKNOWLEDGEMENT

This research was supported in part by NSF grant ATM 8807449 and by the U.S. Department of Energy, Office of Energy Management, under contract No. DE-AC05-84OR21400 with Martin Marietta Energy Systems.

#### REFERENCES

- [1] Nucci C. A., G. Diendorfer, M. A. Uman, F. Rachidi, M. Ianoz, and C. Mazzetti, Lightning return stroke current models with specified channel-base current: a review and comparison, *J. Geophys. Res.*, 95, 20395-20408, 1990.
- [2] Diendorfer G. and M. A. Uman, An improved return stroke model with specified channel-base current, *J. Geophys. Res.*, 95, 13621-13644, 1990.
- [3] Cooray V. and R. E. Orville, The effects of variation of current amplitude, current rise time, and return stroke velocity along the return stroke channel on the electromagnetic fields generated by return strokes, *J. Geophys. Res.*, 95, 18617-18630, 1990.
- [4] Thottappillil R., G. Diendorfer, and M. A. Uman, Extension of the Diendorfer-Uman lightning return stroke model to the case of a variable return stroke speed, Submitted Nov. 1990 to the *J. Geophys. Res.*.



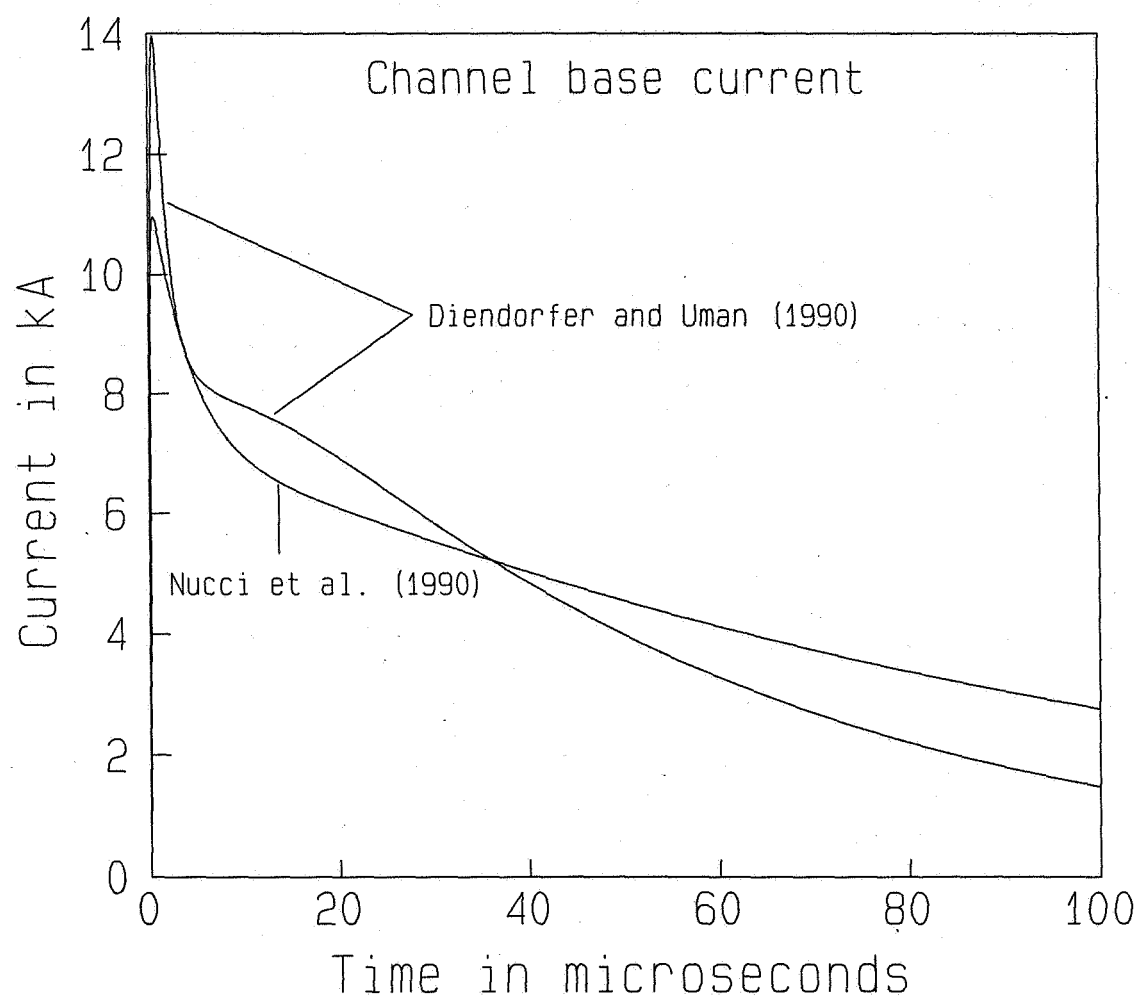


Fig.1 Channel base currents

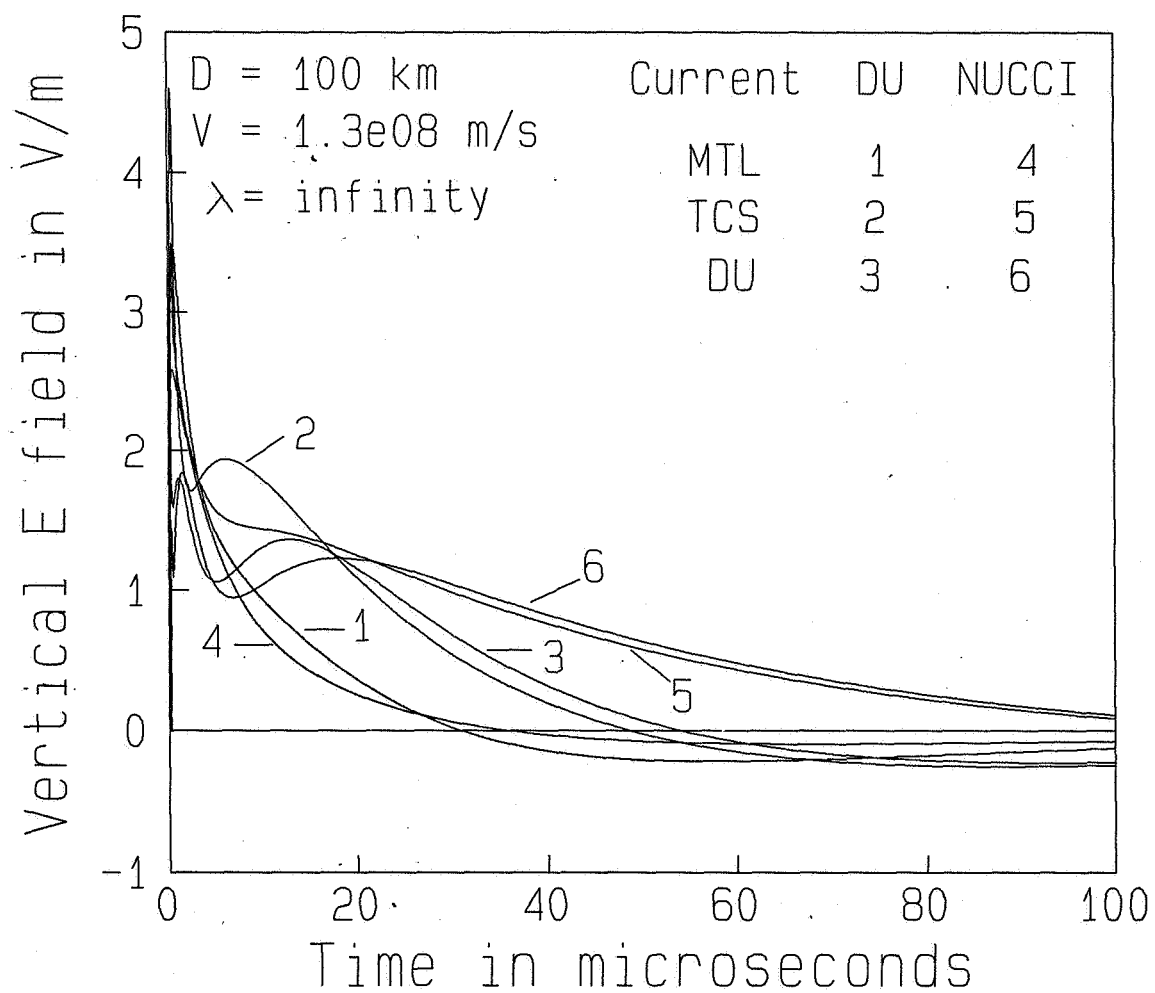


Fig.2a Electric fields at 100 km of the MTL, TCS, and DU models  
 with currents shown in Fig.1 at the channel base. Note  
 the difference in time at which the fields cross zero.

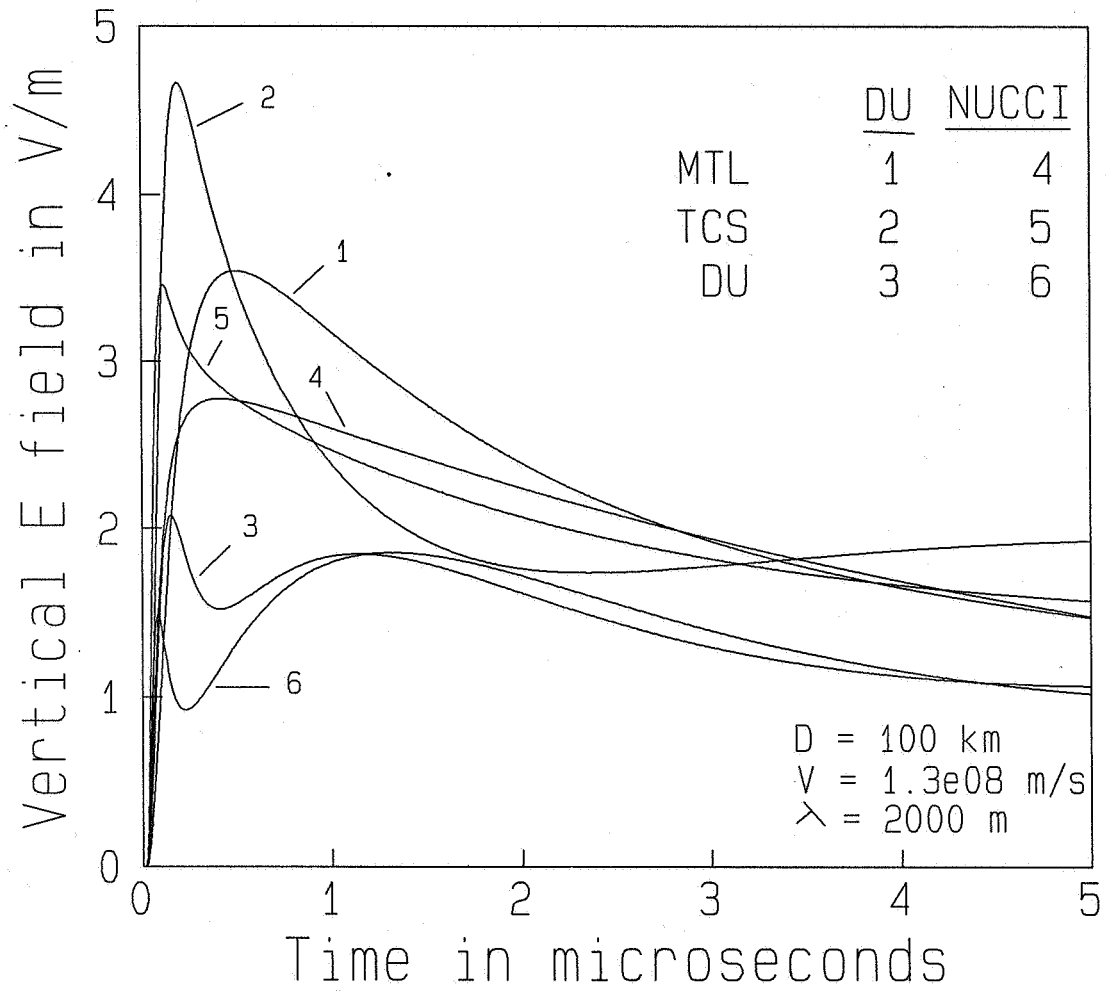


Fig.2b Electric fields at 100 km of the MTL, TCS, and DU models with currents shown in Fig.1 at the channel base. Note the difference in the initial peaks.

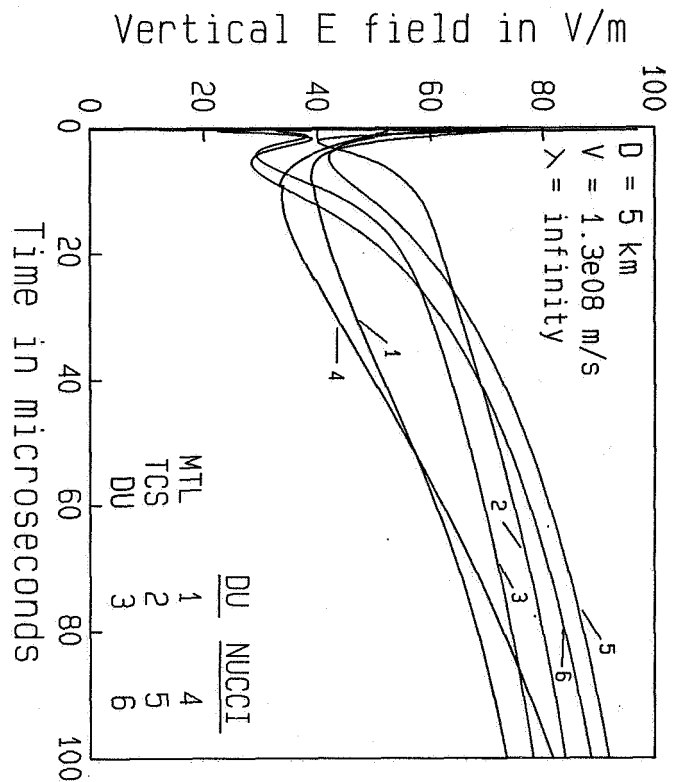


Fig.3a Electric fields at 5 km of the MTL, TCS, and DU models with currents shown in Fig.1 at the channel base.

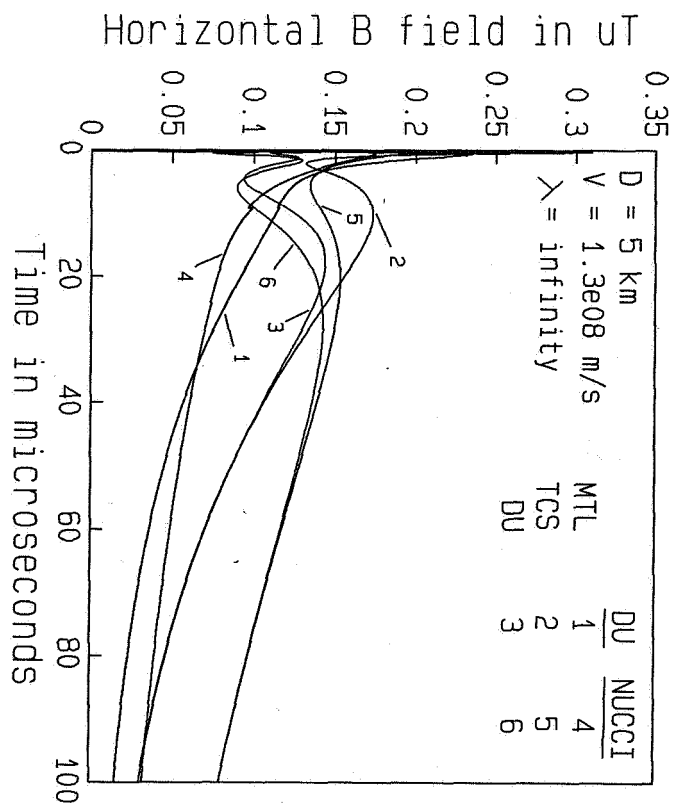


Fig.3b Magnetic fields at 5 km of the MTL, TCS, and DU models with currents shown in Fig.1 at the channel base.

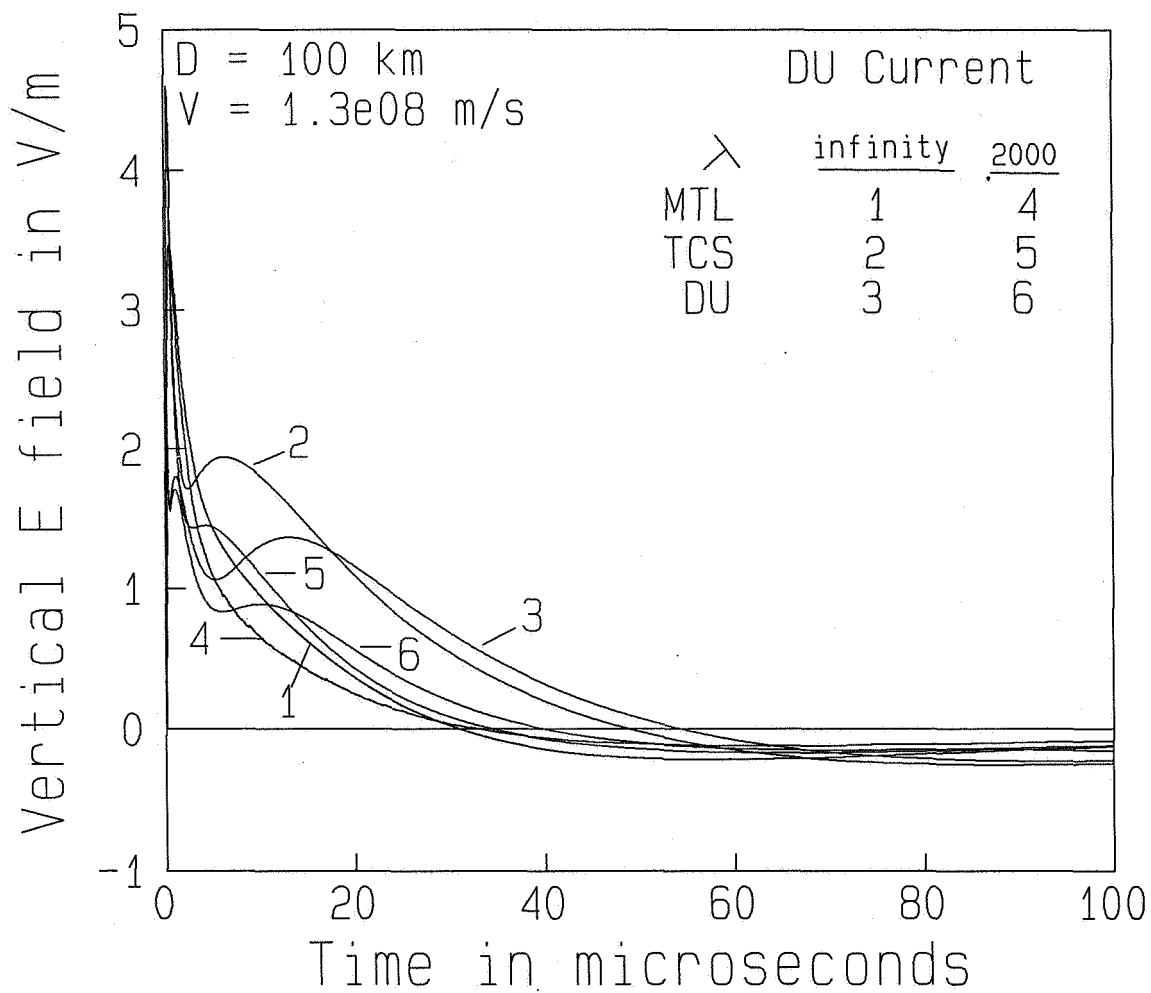


Fig.4 Electric fields at 100 km of the MTL, TCS, and DU models with DU channel base current for the cases of constant return stroke speed and decreasing return stroke speed with height.

## HIGH CURRENT PULSE TESTING FOR GROUND ROD INTEGRITY

Lawrence C. Walko

Pulse Power Group  
Aero Propulsion and Power Directorate  
Wright Laboratory  
Wright-Patterson Air Force Base, Ohio

## ABSTRACT

A test technique was developed to assess various grounding system concepts used for mobile facilities. The test technique involves applying a high current pulse to the grounding system with the proper waveshape and magnitude to simulate a lightning return stroke. Of concern were the step voltages present along the ground near the point of lightning strike. Step voltage is equated to how fast the current pulse is dissipated by the grounding system. The applied current pulse was produced by a high current capacitor bank with a total energy content of 80 kilojoules. A series of pulse tests were performed on two types of mobile facility grounding systems. One system consisted of an array of four 10 foot copper-clad steel ground rods connected by 1/0 gauge wire. The other system was an array of 10 inch long tapered ground rods, strung on stainless steel cable. The tests were performed by personnel from the Wright Laboratories Aero Propulsion and Power Directorate and the 1839 Engineering Installation Group of the Air Force Communications Command. The tests were performed adjacent to a concrete pad at the top of what is known as the Accelerated Runway in Area B, Wright-Patterson AFB. This paper focuses on the pulse test technique used and its relevance to actual lightning strike conditions.

## INTRODUCTION

A series of tests using high current pulses similar to lightning return strokes were performed to evaluate the risk to personnel and equipment from the step potentials generated near grounding systems during lightning strikes [1]. Two types of grounding systems were evaluated. One system employed the conventional long ground rod and the other used a short rod. A low resistance to ground was achieved by the short rod system by employing a larger number of ground rods than the conventional type.

## LIGHTNING SIMULATION TEST

The tests were conducted to determine the effectiveness of the grounding systems in dissipating the energy from a lightning stroke. The more rapidly the lightning currents could be dispersed throughout the soil the lower the step potentials would

be. The problem facing the test program was that in actual use a grounding system would not have the current return path as in the test circuit. In reality the lightning currents would disperse into the ground. This phenomenon had to be duplicated to some degree to insure that the test was realistic and was valid. The following sections describe the test setup and how this current dispersion was achieved and validated.

#### TEST SETUP

Current Pulse Generator. The current pulse was produced by a generator consisting of two capacitor banks, each with a capacitance of 8 microfarads. Each capacitor bank can be charged to 100 kilovolts resulting in a total charge voltage, when triggered, of 200 kilovolts and a resultant capacitance of 4 microfarads. Total energy content of the pulse generator is 80 kilojoules. The output current waveshape was a damped sinusoid with parameters such as current rate-of-rise, peak magnitude and fall time determined by generator capacitance, C, total circuit inductance, L and circuit resistance, R. The current pulse generator is shown in Figure 1 in place at the test site.

Test Site and Ground System. The test site had to be an open area with standard soil conditions with approximate earth resistivity,  $\rho$  of  $10^2$  to  $10^3$  ohm-meters. The site had to be large enough to accommodate a ground rod system and have the simulated lightning return stroke currents dissipate evenly into the surrounding soil. There could not be any drainage pipes, electrical conduits or unknown buried debris where the ground array was located.

The test site chosen was adjacent to the top of the Accelerated Runway, a sloping concrete area in Area B at Wright-Patterson AFB. At the top of the Accelerated Runway there is a level concrete pad. This was an ideal location for the AC power generators, the capacitor banks producing the simulated lightning pulse and supporting control equipment, and the van housing the data acquisition equipment. The ground systems tested were placed in the soil adjacent to the concrete pad so that the length of the leads from the capacitor bank were kept to a minimum. An effort was made to maintain a low inductance test circuit by using 12" wide aluminum flashing for the leads. The return lead to the capacitor bank was not directly connected to the ground array. Instead, a separate rod was driven to a point below the soil surface and adjacent to one of the array ground rods and the return lead was attached to this separate rod. What was then created was a gap below the surface that the pulse current had to arc across. This circuit configuration encouraged the pulse current to diffuse into the soil and not flow along the wires connecting the ground rods on the surface.

## INTERACTION OF LIGHTNING RETURN STROKES AND GROUND ROD SYSTEMS

When lightning strikes a ground rod or ground rod array a situation exists as shown in Figure 2. The current,  $I$ , disperses radially in a hemispherical fashion [2]. The current density,  $J$ , in amperes per square meter, at a distance,  $X$ , in meters from the center of the hemisphere is:

$$J = \frac{I}{2\pi X^2} \quad \text{Amps/meter}^2 \quad (1)$$

If  $\rho$  is the resistivity of the earth in ohm-meters, the current density produces an electrical-field strength,  $E$ , given in volts per meter as:

$$E = \rho J = \frac{\rho I}{2\pi X^2} \quad \text{volts/meter} \quad (2)$$

The step potential,  $V$ , created by the current pulse on the surface of the ground is a line integral of the  $E$  field strength from the point of attachment to any distance  $X$ . If:

$$V = \int_0^X E dx = \frac{\rho I}{2\pi} \int_0^X \frac{dx}{X^2} \quad \text{volts} \quad (3)$$

then:

$$V = \frac{\rho I}{2\pi} \int_0^X X^{-2} dx = -\frac{\rho I}{2\pi X} \quad \text{volts} \quad (4)$$

With the step potential directly proportional to soil resistivity and lightning current, and inversely proportional to distance from the lightning strike, the step potential between point a and point b as illustrated on Figure 2 can be minimized by insuring that the lightning current will flow along a good conductive path which includes the ground rods, interconnecting leads and low soil resistivity.



## TEST TECHNIQUE VALIDITY

As noted previously, the test was performed with an additional gap located below ground. When the pulse generator was triggered the pulse current would flow along the ground rod system and into the ground. Evidence of this taking place was found when the ground rod adjacent to the return path rod was dug up. Pitting and discoloration of the ground rod was observed at the point where arcing would occur. The breakdown of that gap below ground can be observed as discontinuity on the measured step potential waveshape. Figure 3a and 3b show an applied current pulse and a step potential. The voltage waveshape is upheld until the buried gap breaks down and then is abruptly truncated. This buried spark gap would not exist in reality but for the first tens of microseconds an accurate simulation takes place where the test results can be recognized as valid data. Also, pitting and burning were detected where the steel wire ground lead interfaces with the short ground rods. This is evidence of the simulated lightning current arcing from the leads to the ground rod to ground. In actuality, this is what would happen as the currents flow to ground and disperse through the soil.

Further proof of validity is shown by viewing Figures 4a and 4b, showing the locations where the step potentials were measured. Profiles of these voltages are shown in Figures 5a and 5b. The voltages are highest near the point of current application. They decrease and increase in relation to how close the measured voltages are to the ground rod. When the step voltage is measured outside of the ground rod configuration a gradual decrease is observed. If all current were flowing on the ground rod interconnecting wires no discernible step voltage would be observed.

## CONCLUSIONS

There are many factors that determine whether or not a good, low impedance ground system can be formed. Soil characteristics are a dominant factor. The proper moisture content and granularity are important to insure low impedance. Resistance to earth measurements of the ground system can insure the system is properly installed. This paper has shown that a high current pulse technique can be used in addition to the resistance to earth measurements to depict a ground system under the dynamic effect of a lightning strike. Through a controlled dispersion of the simulated lightning currents and measurements of surface step voltages the proper safe design of a ground system can be attained.

## REFERENCES

1. Bailey, J. W.: Surface Wire Grounding System Step Potential Study, 1839 EIG Engineering Report Number EMC-89-29, Aug. 1989.
2. Taylor, R. E.: Radio Frequency Interference Handbook, NASA SP-3067, 1971.

ORIGINAL PAGE  
BLACK AND WHITE PHOTOGRAPH

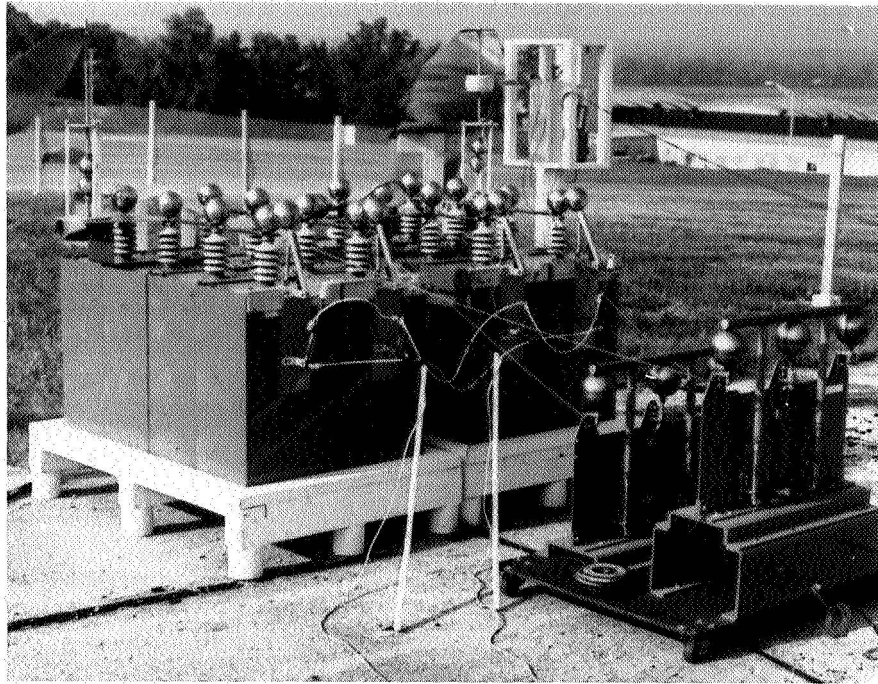


Fig. 1. CURRENT PULSE GENERATOR

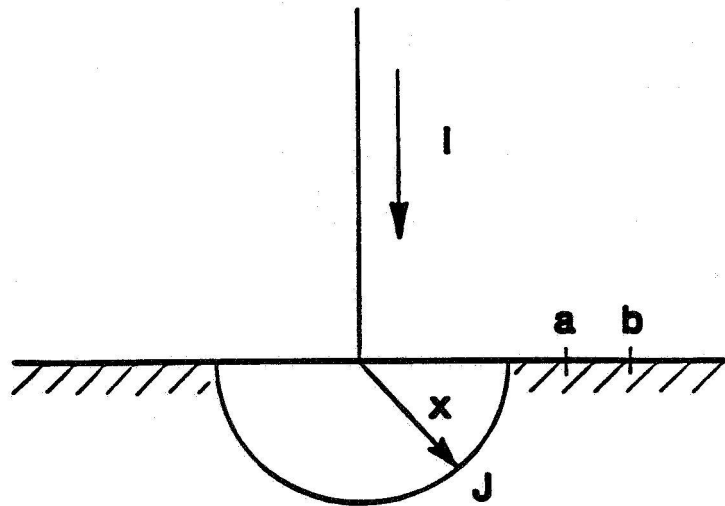
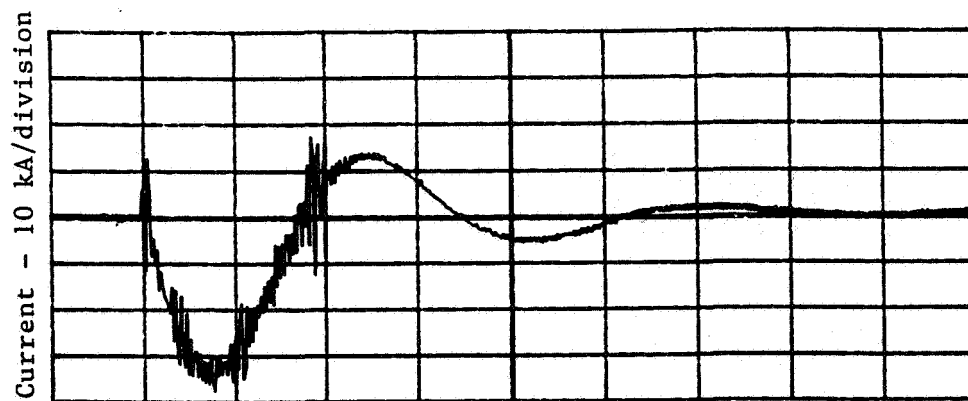
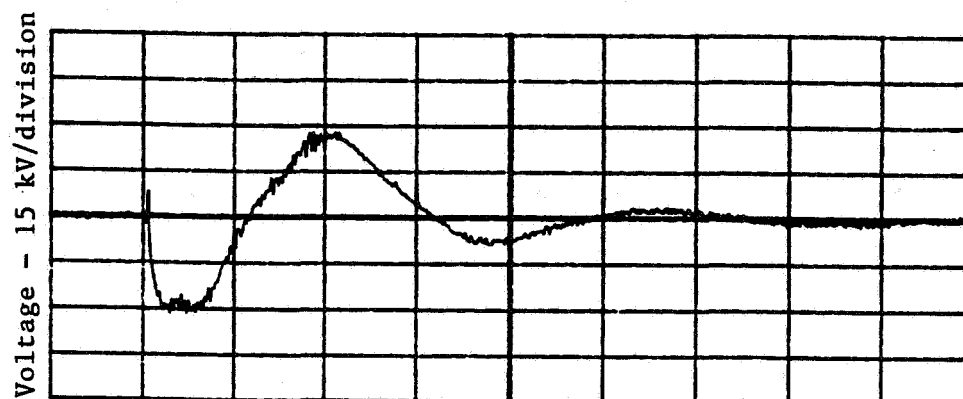


Fig. 2. LIGHTNING CURRENT DISPERSION IN EARTH SHOWN AS CURRENT DENSITY,  $J$ , AT  $x$  DISTANCE FROM POINT OF LIGHTNING ATTACHMENT



Time - 20  $\mu$ s Per Division

Fig. 3a. APPLIED LIGHTNING CURRENT



Time - 20  $\mu$ s Per Division

Fig. 3b. MEASURED STEP POTENTIAL

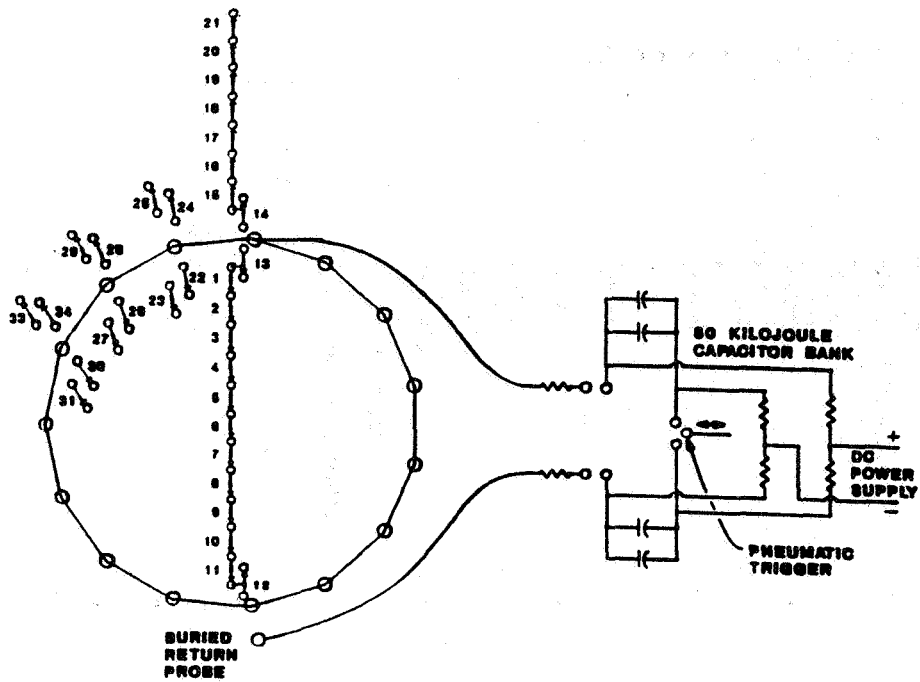


Fig. 4a. SHORT GROUND ROD SYSTEM

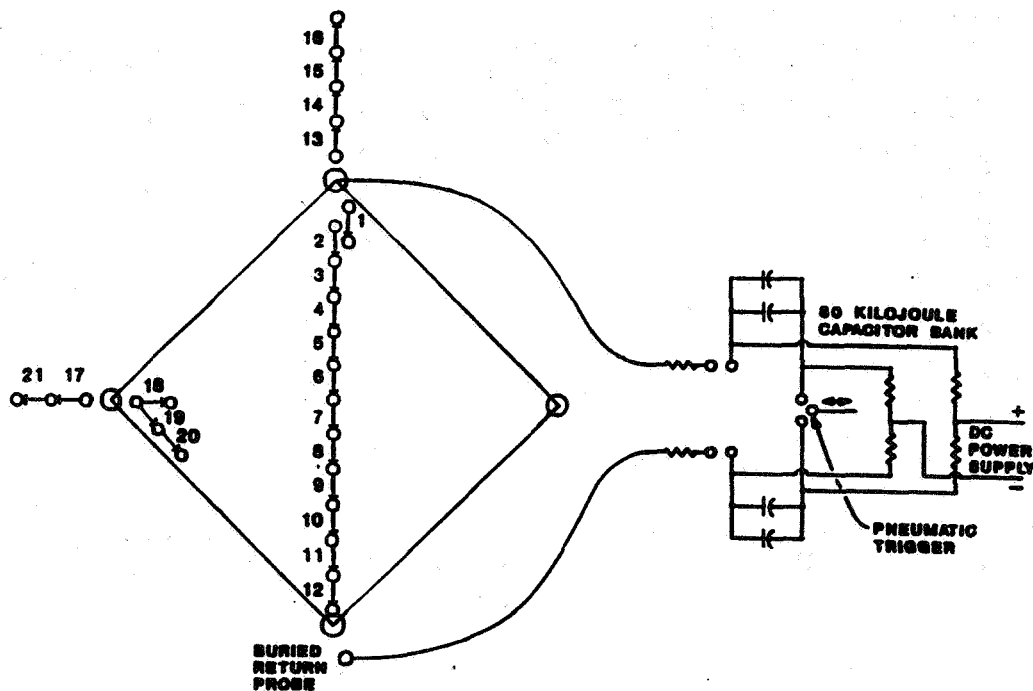


Fig. 4b. LONG GROUND ROD SYSTEM

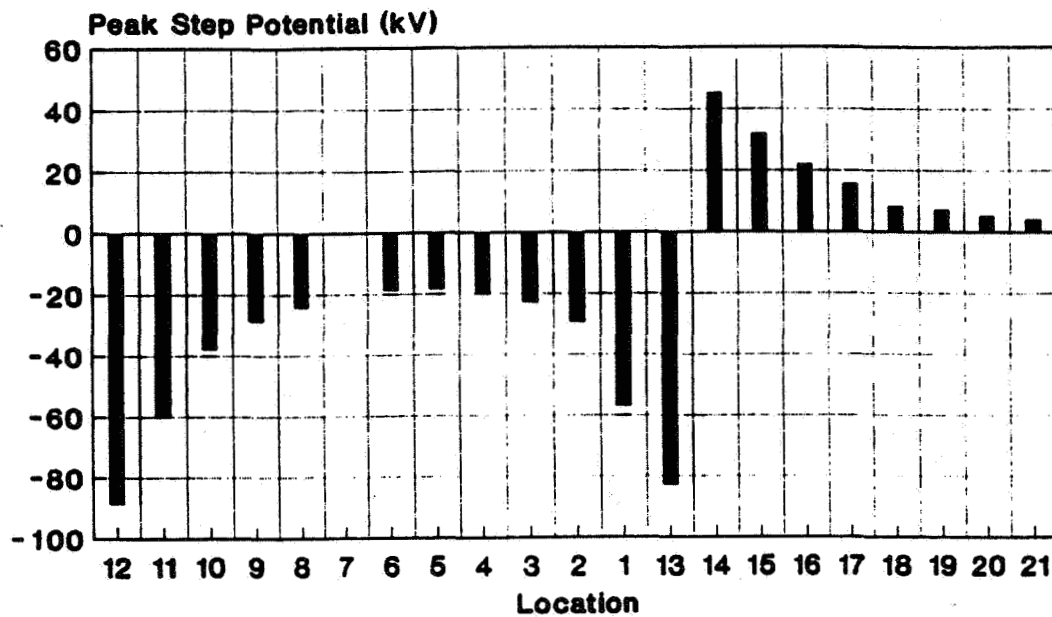


Fig. 5a. SHORT GROUND ROD SYSTEM

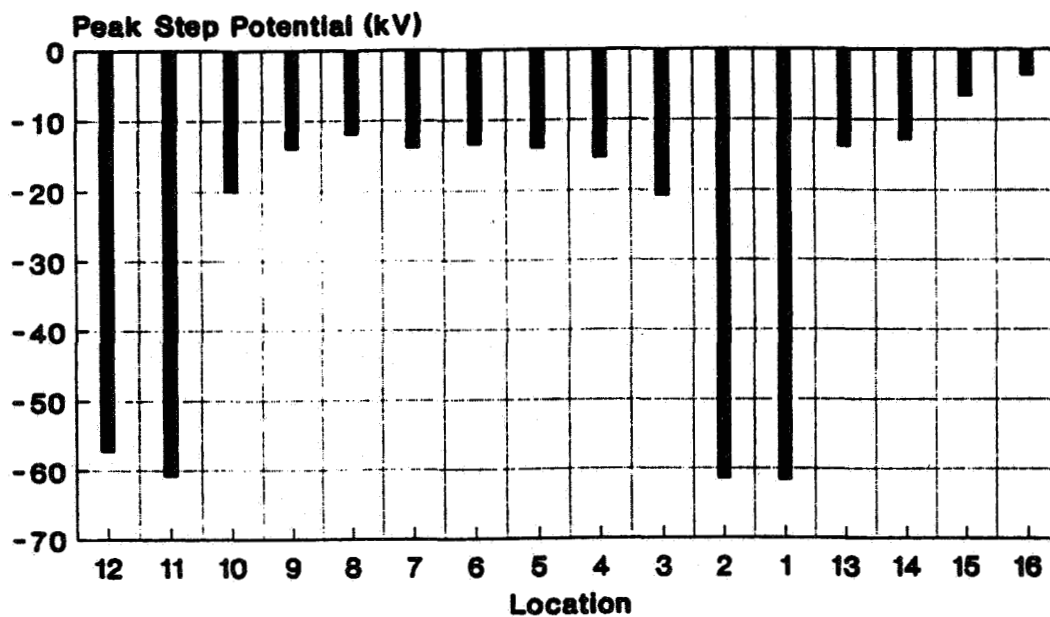


Fig. 5b. LONG GROUND ROD SYSTEM



## Report Documentation Page

1. Report No. NASA CP-3106, Vol. II		2. Government Accession No.		3. Recipient's Catalog No.	
4. Title and Subtitle  1991 International Aerospace and Ground Conference on Lightning and Static Electricity				5. Report Date August 1991	
				6. Performing Organization Code	
7. Author(s)				8. Performing Organization Report No.	
				10. Work Unit No.	
9. Performing Organization Name and Address  John F. Kennedy Space Center Kennedy Space Center, FL 32899				11. Contract or Grant No.	
				13. Type of Report and Period Covered Conference Publication	
12. Sponsoring Agency Name and Address  National Aeronautics and Space Administration Washington, D.C. 20546				14. Sponsoring Agency Code	
15. Supplementary Notes  This publication supersedes NASA CP-10058, Volume II					
16. Abstract  The proceedings of the 1991 International Aerospace and Ground Conference on Lightning and Static Electricity, which was held at the Howard Johnson Plaza Hotel, Cocoa Beach, Florida, on April 16 to 19, 1991, are reported. The conference was sponsored by Kennedy Space Center and the National Interagency Coordination Group (NICG), which consists of research experts from the National Aeronautics and Space Administration, the Federal Aviation Administration, Department of Defense, the National Oceanic and Atmospheric Administration, in concert with the Florida Institute of Technology.					
17. Key Words (Suggested by Author(s)) Aerospace Vehicles   Lightning   Standards Electrostatics   Mapping Meteorological   Modeling Electromagnetic   Coupling Specifications   P-static				18. Distribution Statement  Unclassified - Unlimited  Subject Category 47	
19. Security Classif. (of this report) Unclassified		20. Security Classif. (of this page) Unclassified		21. No. of pages 460	
				22. Price A20	